UNIVERSITAT POLITÈCNICA DE CATALUNYA
BARCELONATECH
Departament de Teoria del Senyal
i Comunicacions

Daniel Pascual Biosca

Design and Performance Analysis of Advanced GNSS-R Instruments Back-end

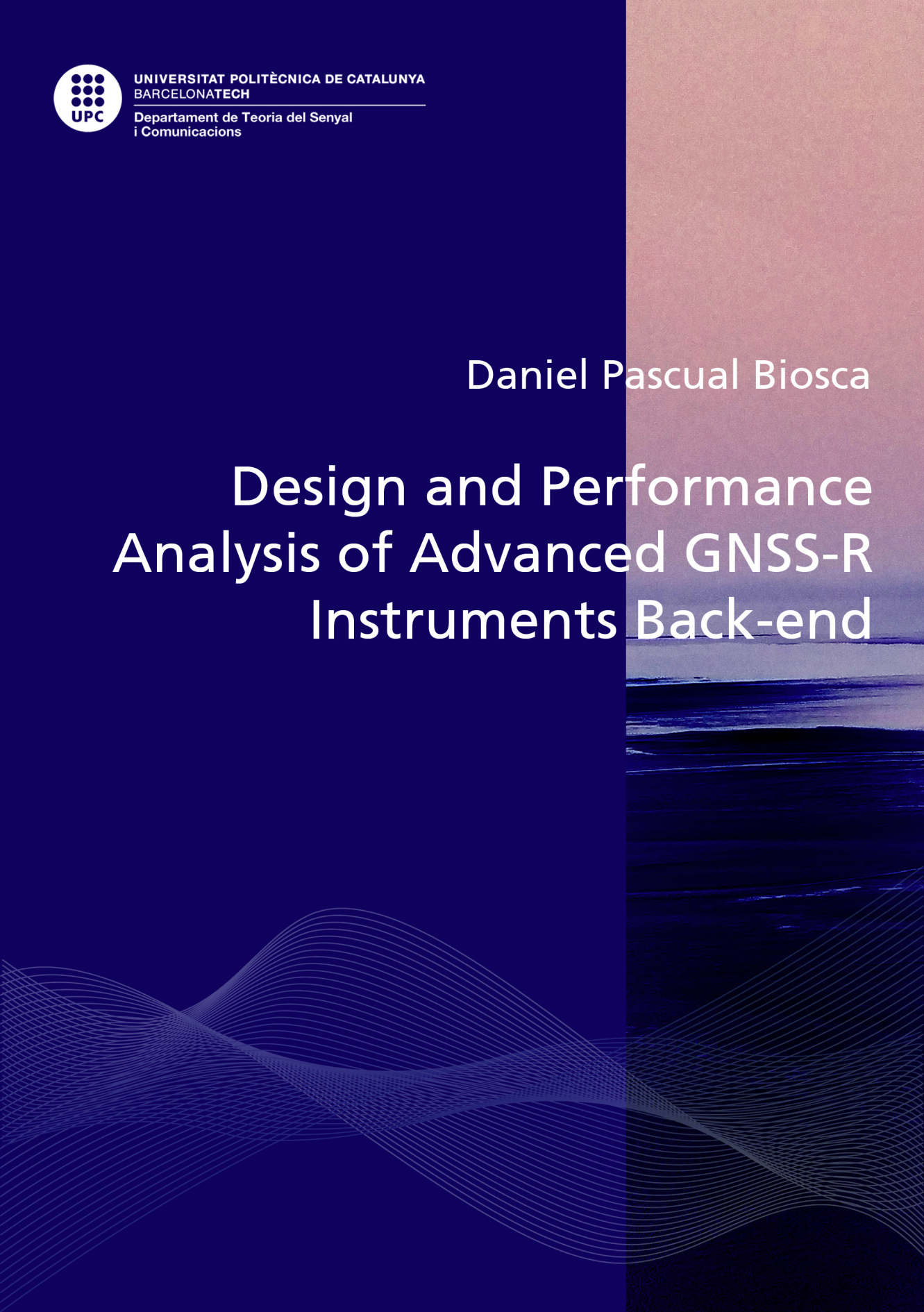

UNIVERSITAT POLITÈCNICA DE CATALUNYA BARCELONATECH

Design and performance analysis of advanced GNSS-R instruments back-end

Daniel Pascual Biosca

UNIVERSITAT POLITÈCNICA DE CATALUNYA
BARCELONATECH
Departament de Teoria del Senyal
i Comunicacions

Design and Performance Analysis of Advanced GNSS-R Instruments Back-end

Author

Daniel Pascual Biosca

Thesis Advisors

Prof. Adriano José Camps Carmona

and

Dr. Hyuk Park

A thesis submitted to the
Universitat Politècnica de Catalunya - BarcelonaTech (UPC)
in partial fulfillment of the requirements for the degree of
DOCTOR OF PHILOSOPHY

PhD program on Signal Theory and Communications
Remote Sensing Laboratory (RSLAB) Group
Barcelona, November 2020

Design and performance analysis of advanced GNSS-R instruments back-end, *D. Pascual*, PhD thesis, UPC, Barcelona, 2020.

Author IDs
IEEE Member: 92322625
ORCID: 0001-8517-2415
Scopus: 55584840200
Researcher: C-9642-2014
Google Scholar: 4p1Y62sAAAAJ
Social
GitHub: danipascual
StackExchange: danipascual

The author of this PhD thesis has received financial support from the grants FPI-UPC with reference 48-739 from Universitat Politècnica de Catalunya - BarcelonaTech (UPC) and from the FPI-MINECO with project reference AYA2011-29183-C02-01 and with researcher reference BES-012-052203 from Ministerio de Economía y Competitividad; and has been employed as researcher at the Universitat Politècnica de Catalunya - BarcelonaTech (UPC) with an open call with reference code 150-739-107.

Acknowledgments

I want to start this section by expressing my gratitude to my advisor Adriano. I appreciate not only his knowledge, his great intuition and optimistic view of any results, but also his patience with this never-ending thesis. Thanks to him I have had student grants, participated in collaborative projects, assisted several congress, and published as much as I could. Before starting the thesis, someone said to me that the advisor is more important than the thesis topic. Without wanting to undervalue my work, I can say that I now understand just what that person meant.

Thanks also to Valery Zavorotny and Nereida Rodriguez for all the time they dedicated to review my manuscript. I really appreciate the time you dedicated to read it and all the comments you sent me.

The work done in this thesis is in fact, a joint effort by the author and Raul Onrubia in his respective thesis. Without his contributions, this thesis could not have been done at all. To him, I give my most sincere gratitude. It has been a rough ride, but throughout the years, we have created an eternal bond.

I want to give a special mention to Jorge Querol for helping me with the FPGA related topics, and for his comments and observations on my work. I will certainty remember the unnecessarily long lasting coffee breaks, the spice challenges and the ridiculous discussions about the most stupid of topics. We could actually write another thesis from the ramblings and musings of our procrastination.

I also want to give a heartfelt thanks to Dr. Hyuk Park. His advice, not only for work related topics, but also for general life affairs, has been useful and appreciated. Somehow he has been like an older brother to me.

I would also like to thank the following undergraduate students for their valuable contributions: Oriol for the GPU processing; Claudia for developing the initial calibration system; Lidia for building the MIR software, and Manuel for performing the thermal analysis of the beamformers. Without their help, this thesis would have taken even longer.

Last but not least, I want to give my thanks to a set of people who in one way or the other, have also taken part in the thesis. The technicians Albert, Enric, Joaquim, Josep and Ruben for soldering, manufacturing, packaging and even last minute drives to the airport; the department secretary Aynie for all the (absurd) bureaucratic issues; the aircraft pilot Jon Johanson; the Prof. Jeff Walker and Dr. Christoph Rudiger from Monash University; my father Rafel for helping me in the C++ coding; Ginger for trying to improve my English writing style (although without much success I would say); and Phil for the awesome cover design.

Needless to say that these years would not have been the same without the company of other Phd students with whom I have happened to met during these years: Adrian, Alberto, Alessio, Ali, Domenicho, Dongliang, Estefany, Fran, Giuseppe, Isaac, Israel, Joan Adrià, Jordi, Juanfran, Miriam, and Roger.

And finally, I want to thank my parents, grandmother, friends, Ginger, psyfamily, housemates and whoever has had the patience when not able to spend time with me and to keep asking "what is your thesis about?" and "when will you finish?".

Well, finally here it is!

Abstract

GNSS reflectometry (GNSS-R) is a set of techniques that uses the reflected GNSS signals over the Earth's surface as opportunity signals for remote sensing applications. The use of signals of opportunity for scatterometry was first proposed in 1988. In 1993, the European Space Agency (ESA) suggested to use those signals as a tool to estimate sea height anomalies in an attempt to detect tsunamis before they reach the shore. Since then, GNSS-R has been a subject of topical interest, and has proven its feasibility for a diverse number of applications in land, ice and water bodies, from ground-based, airborne and space-borne instruments. To this day, more than 430 journal articles have been published in peer-reviewed journals with GNSS-R related topics, and there are sessions devoted to GNSS-R in the most important remote sensing congress. Furthermore, in the coming years, several GNSS constellations will co-exist with more than 140 satellites, transmitting new signals with advanced modulations and at different frequencies. This will broaden the number of applications of GNSS-R, and enhance the precision of its estimates.

The are two main advantages of GNSS-R with respect to dedicated technologies. Firstly, its high temporal resolution and spatial coverage. There are several GNSS satellites in view at any time from any point on Earth, except in the latitudes of the polar circles. As a matter of fact, at the moment writing this and from a latitude of 52 degrees, there are 37 GNSS satellites in view with an elevation angle higher than 20 degrees. Secondly, the cost of a GNSS-R instrument is significantly smaller than an equivalent classic one (either altimeter, scatterometer or radiometer) in terms of performance, as there is no need of a transmitter. In fact, for some applications, a GNSS-R instrument can be as cheap as a commercial GNSS chip receiver with an integrated antenna. Nowadays, those kind of chips are found in most massive market devices such as cell phones. The main drawback of GNSS-R with respect to classic technology, is its reduced precision. To be more specific, more processing has to be carried out in order to achieve a similar performance. This is mainly due to the extremely reduced power of the received signals, which are typically well below the instrument noise. There is then a trade-off between precision and temporal and spatial resolution when choosing GNSS-R instead of well established technology such as conventional radar scatterometers or altimeters.

This Ph.D. thesis has its roots in the ESA project PARIS-IoD, which aimed to study the feasibility of GNSS-R for sea altimetry from a space-borne instrument. The PARIS-IoD would have been a mission demonstrator for a future constellation of GNSS-R satel-

lites. Unfortunately, the project was canceled shortly after starting this thesis. However, some of the questions that have arisen during the initial phase of the project, have been the goals of this Ph.D.

The thesis has two objectives. The first one is to solve some theoretical issues required for the development of next generation of GNSS-R instruments. The second one is to participate in the development of an airborne GNSS-R instrument mimicking the one intended for the PARIS-IoD, and to use it in field campaigns. The main feature of this instrument is that it has two dual-band (L1/L5) array antennas, with two beams per band that are analog steered towards the desired satellite and reflection point.

As for the theoretical objectives; this thesis investigates five topics.

Firstly, the thesis gives closed-form expressions of the so-called Woodward Ambiguity Functions (WAFs) of the modern GNSS signals as function of the receiver bandwidth. The motivation behind this work is that these equations can be later used in simulators in order to create reference models based on different physical magnitudes.

Secondly, the thesis finds the optimum receiver bandwidth for each GNSS signal in terms of altimetric precision. The idea behind this study is that using a large bandwidth produces sharper waveforms, which translates into a higher resolution. However, the thermal noise increases as well with the bandwidth. Thus, there is an optimum bandwidth that minimizes the altimetric error.

Thirdly, the thesis studies the impact of sampling the GNSS signals with 1-level on the GNSS-R observables in terms of precision and of sensitivity to changes in the physical magnitudes. This work has importance because if 1-level samples were to be used, then the hardware requirements in terms of FPGA resources, transmission rate, hard drive write speed, and storage capacity will be reduced.

Fourthly, the thesis discusses different architectures for real-time correlators in FPGAs compare to those in GPUs. Results show that GPUs can be used for real-time, with the advantage of being much more flexible and easier to program.

Finally, the thesis investigates the cross-talk phenomena, or interference between GNSS satellites in the iGNSS-R technique. Results show that this kind of interference is not a problem in space-borne missions, but it does have an impact on airborne and ground-based ones. In such cases, antenna arrays with large directivity should be used.

Returning to the instrument design objective, this thesis has two main goals. Firstly, to build the signal processing units inside the receivers and in the transmitter used to generate the calibration signal, and to develop the software to control both. Secondly, to process the data from different airborne fields campaigns using the GPU software mentioned above. The results have shown the feasibility of MIR for soil moisture estimation, sea altimetry, sea state, topography and water body/land transitions.

Contents

List of Tables

List of Figures

Acronyms

ACF AutoCorrelation Function.

ADC Analog-to-Digital Converter.

AF Ambiguity Function.

AGC Automatic Gain Control.

AltBOC Alternative BOC.

ALU Arithmetic Logic Unit.

ANN Artificial Neural Networks.

ARNS Aeronautical Radio Navigation Service.

AWGN Additive White Gaussian Noise.

BOC Binary Offset Carrier.

BPSK Binary Phase-Shift Keying.

CAF Cross-Ambiguity Function.

CBOC Composite BOC.

CDBOC Complex Double Binary Offset Carrier.

CDF Cumulative Distribution Function.

CDMA Code Division Multiple Access.

cGNSS-R conventional GNSS-R.

CORTO COmpact Reflectometer for Terrain Observations.

CPU Central Processing Unit.

CRB Cramér-Rao bound.

CYGNSS Cyclone Global Navigation Satellite System.

DAC Digital Analog Converter.

DC Direct Current.

DDA Delay Doppler Altimetry.

DDM Delay-Doppler Map.

DEM Digital Elevation Model.

DFT Discrete Fourier Transform.

DGNSS Differential GNSS.

DLL Delay Lock Loop.

DME Distance Measuring Equipment.

DNF Data Not Found.

DoF Degree of Freedom.

DR Dynamic Range.

DSP Digital Signal Processing.

DSSS Direct-Sequence Spread Spectrum.

DUC Digital Up-Converter.

EGM96 Earth Gravitational Model 96.

EM Electromagnetic bias.

ESA European Space Agency.

FDMA Frequency Division Multiple Acces.

FEC Forward Error Correction.

FFT Fast Fourier Transform.

FIFO First In First Out.

FIR Finite Impulse Response.

FLL Frequency Lock Loop.

FPGA Field Programmable Gate Array.

GEO Geostationary Earth Orbit.

GEROS-ISS GNSS REflectometry, Radio Occultation and Scatterometry onboard ISS.

GigE Gigabit Ethernet.

GNSS Global Navigation Satellite System.

GNSS-R GNSS Reflectometry.

GNSS-RO GNSS-Radio Occultation.

GPIO General Purpose Input/Output.

GPS Global Position System.

GPSDO GPS disciplined oscillator.

GPU Graphics Processing Unit.

GSO GeoSynchronous Orbit.

HPF High Pass Filter.

I²C Inter-Integrated Circuit.

ICD Interface Control Documents.

ICGC Institut Cartográfic i Geológic de Catalunya.

IF Intermediate Frequency.

iGNSS-R interferometric GNSS-R.

IGSO inclined GSO.

iid independent and identically distributed.

IMU Inertial Measurement Unit.

IP Intellectual Property.

IPT Interference Pattern Technique.

ISS International Space Station.

ITU International Telecommunication Union.

LEO Low Earth Orbit.

LFSR Linear Feedback Shift Register.

LHCP Left Hand Circular Polarization.

LNA Low-Noise Amplifier.

LO Local Oscillator.

LoS Line-of-Sight.

LRM Low Resolution Mode.

LSB Least Significant Bit.

LUT LookUp Table.

MALYGNSS Multi-band Airborne L-band reflectometrY with GNSS.

MBOC Multiplexed BOC.

MEO Medium Earth Orbit.

MIR Microwave Interferometric Reflectometer.

MSB Most Significant Bit.

MTU Maximum Transmission Unit.

N/A Non Available.

NTP Network Time Protocol.

P^{2}EPS PAU/PARIS End-to-End Performance Simulator.

PARIS Passive Reflectometry and Interferometry System.

PARIS IoD PARIS In-orbit Demonstrator.

PC Pulse Compression.

PDF Probability Density Function.

piGNSS-R partial interferometric GNSS-R.

PLL Phase Lock Loop.

ppb parts-per billion.

PPS Pulse-Per-Second.

PRF Pulse Repetition Frequency.

PRN Pseudo-Random Noise.

PSD power spectral density.

QPSK Quadrature Phase Shift Keying.

RCS Radar Cross-Section.

RF Radio-Frequency.

RFI Radio Frequency Interference.

rGNSS-R reconstructed GNSS-R.

RHCP Right Hand Circular Polarization.

RMS Root Mean Square.

RMSE Root Mean Square Error.

RNSS Radionavigation Satellite Service.

SAR Synthetic Aperture Radar.

SBAS Satellite Based Augmentation System.

SD Secure Digital.

SDR Software Defined Radio.

SIR Signal-to-Interference Ratio.

SMA SubMiniature version A.

SMOS Soil Moisture and Ocean Salinity.

SNR Signal-to-Noise Ratio.

SPI Serial Peripheral Interface.

SRP Specular Reflection Point.

SRTM3 Shuttle Radar Topography Mission 3.

SSD Solid-State Drive.

SWH Significant Wave Height.

UART Universal Asynchronous Receiver-Transmitter.

UDP User Datagram Protocol.

UHD USRP Hardware Driver.

UPC Universitat Politècnica de Catalunya.

USRP Universal Software Radio Peripheral.

VHDL VHSIC Hardware Description Language.

VHSIC Very High Speed Integrated Circuit.

WAF Woodward Ambiguity Function.

WGS84 World Geodetic System 84.

XCO Crystal-Controlled Oscillator.

ZV Zavorotny-Voronovich.

List of main symbols and constants

B baseband bandwidth of an ideal square filter.

β Gabor bandwidth in Hz.

B_{opt} optimum baseband bandwidth.

c speed of light.

d discrete Doppler frequency independent variable.

$Y(\tau, \nu)$ Delay-Doppler Map (DDM).

$Y(\tau, \nu, t)$ time-varying DDM.

$|Y(\tau, \nu)|^2$ power DDM.

$< |Y(\tau, \nu)|^2 >$ averaged power DDM.

$\delta(\tau)$ Dirac delta function.

f frequency independent variable in Hz.

f_b subcarrier frequency of a BOC modulation.

f_c carrier frequency.

f_r chip rate of a PRN.

f_s sampling frequency.

h_r receiver height over the WGS84 ellipsoid.

k discrete frequency independent variable.

k_B Boltzmann's constant.

Λ triangle function.

λ signal wavelength.

m discrete delay independent variable.

n discrete time independent variable.

N_{coh} digital coherent correlation length.

N_{in} number of incoherent averages over a DDM or a waveform.

ν Doppler frequency independent variable.

ν_{sp} Doppler frequency of the reflected specular signal.

ν_d direct signal Doppler frequency.

ν_r reflected signal Doppler frequency (full path).

ν_{sc} Doppler frequency of the reflected scaterometric delay.

$R_x(\tau)$ autocorrelation function (ACF) of a time-domain signal $x(t)$.

$\sum(\tau, \nu)$ Radar Cross-section (RCS) including several receiver parameters.

$Si(x)$ sine integral function.

$S_x(f)$ Spectrum of a time-domain signal $x(t)$.

τ delay independent variable.

τ_{sc} DDM geometric delay center found in a correlation window of length T_{coh}.

τ_{sp} specular delay of the reflected signal.

τ_{pk} direct signal delay.

τ_r reflected signal delay (full path).

τ_{sc} scaterometric delay of the reflected signal.

τ_Λ width of the main peak of the ACF of a GNSS signal.

T_c duration of a PRN code.

T_{coh} coherent correlation integration length.

t time independent variable.

t_b period of a BOC sub-carrier frequency.

t_r PRN chip period.

t_s sample period.

θ_e^d elevation angle of a GNSS satellite as seen from the receiver.

θ_e^r elevation angle of a GNSS satellite as seen from the specular reflection point.

U_{10} wind speed at ten meters above the sea.

$|\chi(\tau,\nu)|^2$ Woodward Ambiguity Function (WAF).

$w(\tau)$ delay waveform.

W_τ DDM width in the delay domain.

W_ν DDM width in the Dopper domain.

$X(f)$ Fourier transform of a time-domain signal $x(t)$.

$x(t)$ time-domain signal.

$x[n]$ sampled signal.

Part I

Introduction and Theoretical Background

1

Chapter 1
Introduction

THIS chapter first presents the motivation behind the thesis and provides the context of the challenges addressed. It then details the goals, and finally, the structure and the main contents of each chapter are given.

1.1 Motivation

The motivation of this thesis was born from the idea initially given back in 1988 [1], which suggested using the Global Position System (GPS) reflected over the ocean for sea scatterometry measurements from space. In 1993, the use of those signals in combination with the direct signals were also proposed for altimetry [2]. This latter concept was named Passive Reflectometry and Interferometry System (PARIS). The use of not only the GPS signals but from any other Global Navigation Satellite System (GNSS) for remote sensing purposes was called GNSS Reflectometry (GNSS-R).

The operating principle of GNSS-R is to receive the reflected GNSS signals over an area of interest, and simultaneously, the ones transmitted by the GNSS satellites known as direct signals. The signals are then combined in order to obtain the desired measurement. This type of configuration is known as multistatic radar, as the transmitters and the receiver are at different locations. In contrast, classic sea altimeters such as the ones used in the missions TOPEX/Poseidon and in the Jason and Cryosat series are nadir-looking, which reduces their swath and temporal resolution. Figure 1.1 compares both configurations.

Classic radar altimeters need weeks, if not months, to map the whole Earth. For this reason, despite having centimeter accuracy, they are not useful for tsunami warning as they are for climatology. On the other hand, a constellation of a few satellites receiving GNSS-R signals, would cover the whole Earth, and in principle, detect tsunamis before they reach the coastline. However, the fact that the power of those signals is very small, limits its accuracy. One should bear in mind that a typical power of a direct signal is -125 dBm, which is smaller than the average power noise of any instrument. The power of the reflected signal can be several tens of dB below. The trade-off between the temporal

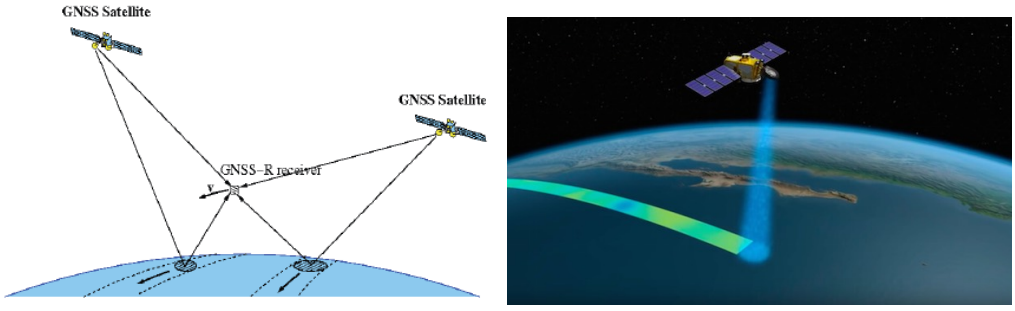

(a) **(b)**

Figure 1.1: Artist concepts of a GNSS-R scenario with two transmitters (a), and of a classic radar altimeter (b). From [`https://gssc.esa.int/navipedia/index.php/File:Gnss-r.png`] and [`https://sealevel.jpl.nasa.gov/gallery`].

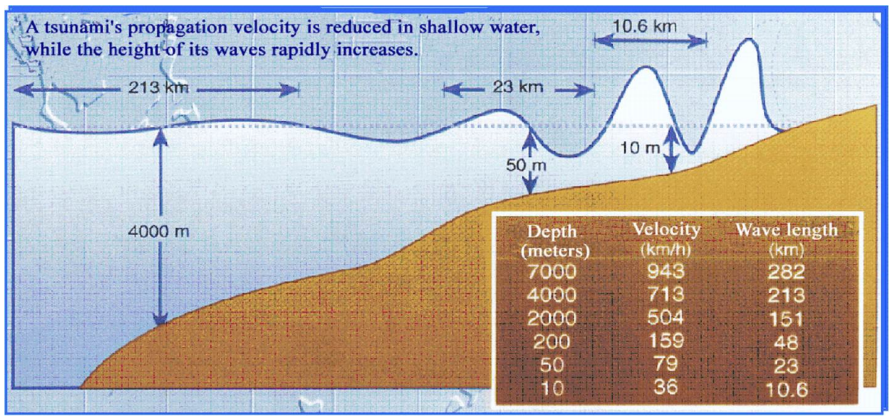

Figure 1.2: Cross-section of a tsunami moving from the deep ocean to the coast. From [https://commons.wikimedia.org/wiki/File:Gjendja_e_termeteve.jpg]

resolution and the accuracy that a GNSS-R sensor can achieve, has been, and still is, a subject of study by the scientific community. Some results will be given in the course of this thesis.

In order to give context to the reader on how important the accuracy is, Fig. 1.2 shows the propagation of a tsunami from its origin in the deep waters to the shallow ones. In the deep ocean, the height of the tsunami wave is just few tens of centimeters and travels at a speed of up to 1000 km/h. As the tsunami reaches the coastline, it slows down to tens of kilometers per hour because its energy is compressed into a much smaller volume, which translates also into a rapid increase of the wave height. There are reports of waves rising up to 30 meters.

The very first measurement of a tsunami taken by a radar altimeter was done during the catastrophic event in Sumatra in December 2004. By chance, the Jason-1 satellite overflew that area just 2 hours after the earthquake. The mean sea level obtained with Jason-1 is shown in Fig. 1.3. In the open ocean, the maximum sea surface elevation gain was about 50 cm above the average level from the previous days. The tsunami wave was followed by a surface depression of 40 centimeters below the average level.

During the 20 years after the introduction of the PARIS concept, GNSS-R has been studied not only for sea altimetry, but also for a large number of different remote sensing applications. Some of them are: sea ice detection; polar ice thickness and age; sea surface wind speed value and direction; target detection over sea; typhoon monitoring; and soil moisture and biomass estimation. There have been many experiments done from aircrafts and hot air stratospheric balloons, and even three space missions have been fully devoted to GNSS-R measurements. At the moment of writing this chapter, there are at least 431 articles published in peer-reviewed journals regarding GNSS-R.

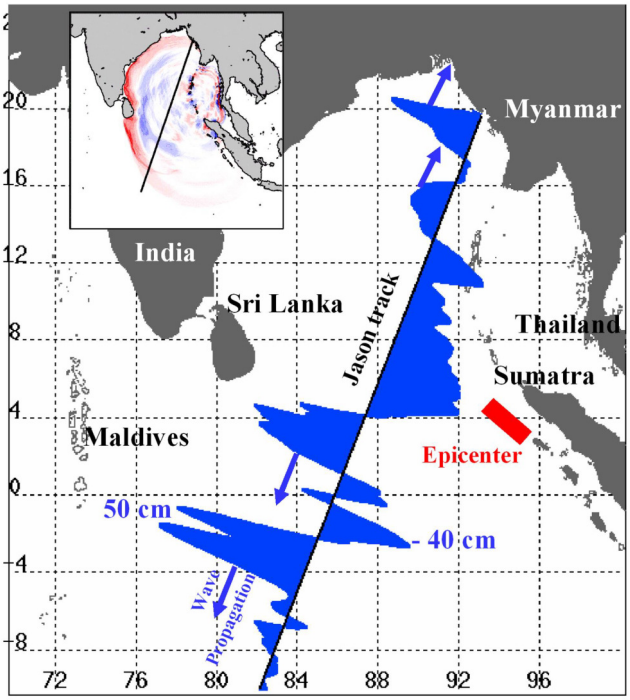

Figure 1.3: Sea surface anomalies measured by Jason-1 two hours after the Sumatra earthquake of December 26, 2004. From [`https://www.jpl.nasa.gov/spaceimages/details.php?id=PIA07219`]

Going back to the issue of altimetry, the European Space Agency (ESA) launched the project PARIS In-orbit Demonstrator (PARIS IoD) [3] as proof of concept of PARIS. A GNSS-R instrument was planned to be mounted on-board a satellite specifically designed for said mission. Among the instrument requirements, there was the use of large multi-band antenna arrays with analog beamforming, and the real-time processing of the GNSS-R. The project had to be carried out between several contractors. Among them was the Universitat Politècnica de Catalunya (UPC), specifically the Passive Remote Sensing Laboratory (RSLab), a research group from the Signal Theory Department (TSC), under the supervision of Prof. Adriano Camps. By then, Prof. Camps and his group had already experience in the GNSS-R field, as they were applying it to estimate the sea state. This would later be used as a correction parameter in the sea salinity values obtained from another ESA mission called Soil Moisture and Ocean Salinity (SMOS). In addition, the group lead by Prof. Camps, also had experience on land applications and on reflection simulators. To this date, the RSLab has participated in 65 of the 431 articles mentioned above.

Among the several Ph.D. thesis published by the RSLab, the one of Dr. Valencia in 2012 [4] was under the scope of the PARIS IoD mission. His research was mainly focused on the design of a GNSS-R instrument and to state the challenges involved in such instruments. His thesis has been the starting point of the present one and that of Dr. Onrubia [5].

Unfortunately, the PARIS IoD mission was canceled shortly after starting this Ph. D. In an attempt to continue the PARIS concept, the ESA launched the GNSS REflectometry, Radio Occultation and Scatterometry onboard ISS (GEROS-ISS) project [6]. As its names suggests, the idea was to place a GNSS-R instrument on-board the International Space Station (ISS). That would in principle, reduce the cost that PARIS IoD would have had, as no dedicated satellite or launch would have been needed. Sadly, the project was also canceled after the preliminary studies.

The author once heard Dr. Martín-Neira in a workshop saying that, we (referring to our civilization) can land a small vehicle on Mars, but cannot detect tsunamis before they reach the coastline. Without undervaluing the benefits that the space exploration gives to humanity, the author believes that the ESA or any other space agency, will eventually realize the importance of tsunami detection and bring back the PARIS concept.

1.2 Goals

The main goal of this thesis is to participate in the development of GNSS-R instrument with similar capabilities to those of the instrument intended for the PARIS IoD mission. These requirements are: to have high directivity array antennas with analog beamsteering, and to process the GNSS-R signals in real-time using the two main GNSS-R techniques, known as conventional (cGNSS-R) and interferometric (iGNSS-R). The antennas must be dual-band (L1/L5), multi-constellation (GPS/Galileo/BeiDou-2) and able to generate two beams per band.

Since this thesis has its roots in the PARIS IoD project, some research that needed to be held in the first phase of the mission has been investigated here as well. Said research includes: the study of the precision of the *new* GNSS signals for altimetry; to contribute to a reflection simulator lead by Dr. Park [7] by giving closed-form expressions to generate those signals; and to asses the impact of the so-called cross-talk, or interference from undesired GNSS satellites on the GNSS-R observables of the tracked one in (iGNSS-R). By *new* signals, the author is referring to the signals which by then were just starting to be transmitted by the advanced GPS satellites, and by the Galileo and BeiDou-2 constellations.

The instrument developed here is named Microwave Interferometric Reflectometer

(MIR), and it is actually a joint effort between the author and Dr. Onrubia in his respective Ph. D. thesis [5]. The author contribution to the instrument is to implement the signal processing unit; to build the software to control the receivers; and to process some of the data obtained from field campaigns. The work done by Dr. Onrubia was to design, manufacture, test and calibrate the antenna arrays and hardware, and to program the software that controls the beamformers.

Although the original objective of both Ph. D. thesis were clear, they were co-dependent and sometimes even overlapped. Thus, some tasks have been adapted during the course of both Ph. D. thesis. However, the main objective change with respect to the planned one, was to replace the real-time processing by raw data saving, and to process it afterwards. The reason behind this, is that several problems were encountered when processing the new GNSS signals. Those new signals give better precision with respect to the well-known classic GPS, but they require a more complex acquisition and tracking system. The details will be given later in this thesis, and some ideas for real-time processors are also explained. Saving the raw data requires sampling the signals using only 1 level, in order not to saturate the bus with the host computer. Still, the amount of data generated during the field campaigns was enormous. This translated into two new objectives. Firstly, to study the impact of 1 level sampling on the GNSS-R observables. Secondly, to build a dedicated software to process the data at high speed.

In summary, the objectives of Ph. D. this thesis are:

- To study the feasibility of the new GNSS signals for GNSS-R retrievals, and to compare them with the existing ones.
- To contribute on modeling those signals for a simulator on constant evolution managed by Dr. Hyuk Park of the RSLab [7].
- To asses the impact of the cross-talk interference, especially in space missions.
- To give a guideline for real-time correlators on Field Programmable Gate Arrays (FPGAs).
- To research the impact of 1-level sampling in the GNSS-R observables in terms of precision and sensitivity.
- To design the Digital Signal Processing (DSP) blocks inside the FPGAs of MIR, and to build the software that configures these devices.
- To develop a software tool running over a Graphics Processing Unit (GPU) to obtain GNSS-R observables at high speed.

- To validate the feasibility of MIR as a remote sensing instrument, by retrieving different physical magnitudes obtained from several field campaigns.

1.3 Outline

This Ph. D. thesis is divided into six parts, which contain a total of twelve chapters, plus five appendices. The outline is the following:

- Part I: Introduction and Theoretical background
  - Chapter 1 states the motivation and historical background behind this thesis. Then, the goals and objectives are given. Finally, this outline is drawn.
  - Chapter 2 explains the GNSS systems and signals. It focuses on the theory required for the following chapters. That is to say, the generation of those signals, and the equations that define them in the time and frequency domains.
  - Chapter 3 summarizes GNSS-R as a remote sensing tool. It first introduces the mathematical models involving the reflection process, the most common observables and their retrieval techniques. It then gives a comprehensive list of past and current instruments devoted to sea altimetry.
- Part II: Contributions to Theoretical Aspects of GNSS-R
  - Chapter 4 derives analytic expressions of the so-called AutoCorrelation Functions (ACFs). These functions are required in order to simulate the impact of the sea conditions and of the instrument parameters on the observables. These models are then used as reference in order to infer the sea state from for real measurements.
  - Chapter 5 analyzes the precision of the GNSS-R signals for altimetry as function of the receiver bandwidth. An optimum bandwidth that minimizes the error is given for each signal.
  - Chapter 6 investigates the cross-talk effect on the ground-based instruments, as well as on airborne and space-borne missions. It first studies the statistics of such interferences, and it then assesses their impact on the altimetric precision.
  - Chapter 7 examines the impact of sampling GNSS-R signals using only 1 level on the precision of different magnitudes, and on the sensitivity of those to changes in the physical ones. The study is performed using different coherent and incoherent averaging values.

  - Chapter 8 gives design considerations for GNSS-R real-time correlators. It starts with methods to generate clean GNSS replicas in FPGAs. It then gives different implementations of correlators for FPGAs and for GPUs.

- Part III: MIR Instrument: Description and Results from the Field Campaigns

  - Chapter 9 describes the MIR instrument and its precursor MALYGNSS. It first gives a brief summary on the hardware, and on the calibration of each of the subsystems that conform the instrument. It then focuses on the DSP units and on the software running in the host computer.
  - Chapter 10 gives the results from an airborne field campaign performed over the Barcelona cargo harbor with the MALYGNSS instrument. The aim of such experiment was to retrieve the sea state from the coherence of the reflected signals by analyzing the time-decorrelation of its observables.
  - Chapter 11 gives the preliminary results from the airborne field campaigns performed in Australia with MIR. The research is focused on water-body transitions, soil moisture estimation, sea altimetry, and land topography. It also assesses the cross-talk impact on the observables.

- Part IV: Conclusions and Future Research Lines

  - Chapter 12 draws the conclusions and suggests future research lines.

- Part V: Appendices

- Part VI: Bibliography and List of Publications

2

Chapter 2
GNSS Systems

This chapter gives an overview of the current and future GNSS systems. It first gives a brief summary of the satellite constellations properties and the allocated spectrum bands used to transmit the signals. The structure and the modulation of such signals is then studied, and the properties of their autocorrelation functions are shown. Finally, closed-form expressions for the signals spectra are given.

2.1 Introduction

The history of GNSS is a history of political and economic conflict among the main powers of the world. The first GNSS system was the GPS, developed by the United States Air Force in the late 70s. It was originally military, and although it was soon open for civilian use, it is ultimately dependent on the United States Armed Forces. From then on, other countries and partners have developed their own satellite navigation constellations, either global or regional. However, the cost of developing and maintaining such systems is high and the progress has been very slow. As the commercial market has become more and more appealing, the development has speed up, and currently there are 4 constellations at different development stages. In addition to the American GPS, the constellations that are currently operational are the Galileo from the European Union; the Chinese BeiDou-2, also known as BeiDou Satellite Navigation System or BDS, and formerly known as COMPASS; GLONASS (Russian acronym for Global Navigation Satellite System) from the Russian Federation; and the Indian Regional Navigation Satellite System (IRNSS), also known as NAVIC, for the Hindi term "sailor". This chapter will focus on the GPS and Galileo signals, as are the signals studied hereafter in this thesis. However some BeiDou-2, GLONASS and IRNSS information is given here for the sake of completeness.

The main goal of any satellite navigation system is to provide global or regional continuous position, navigation and velocity determination in a three-dimensional space, either on the Earth or even in the space. Another consequent application is precise timing and synchronization between distant users. In order to do so, GNSS systems provide different *services* dependent on the user requirements. There are typically open standard services for the vast majority of commercial applications such as car or pedestrian

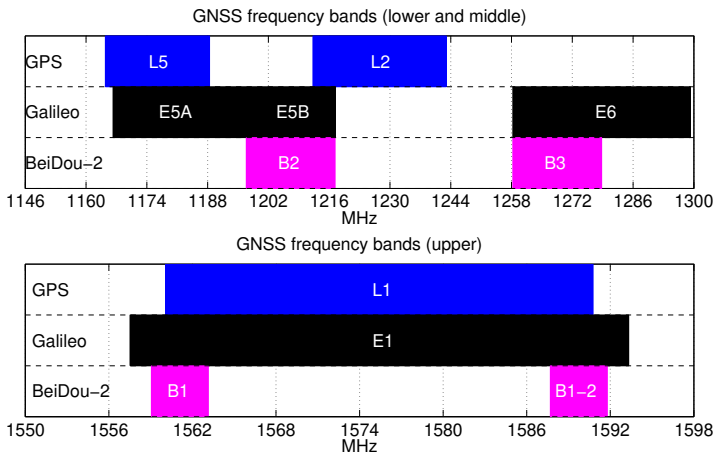

Figure 2.1: Current GNSS frequency bands allocation.

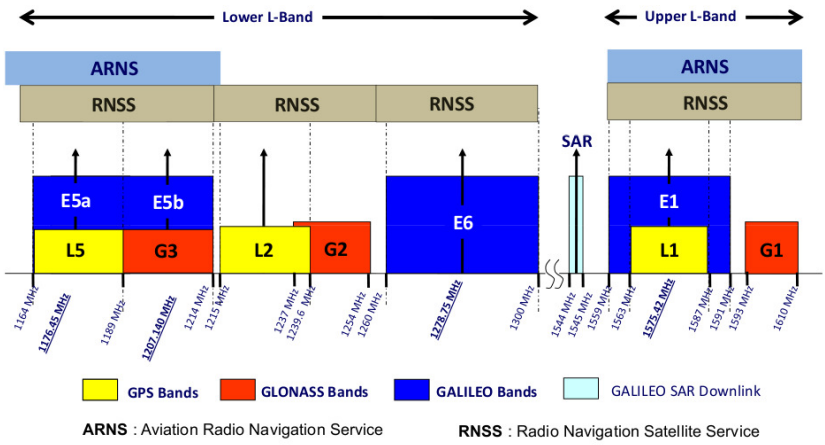

Figure 2.2: Allocation of GPS, Glonass and Galileo bands along the ITU reserved ARNS and RNSS bands. From [`https://gssc.esa.int/navipedia/images/f/f6/GNSS_navigational_frequency_bands.png`]

navigation, and precise encrypted services for military or government-authorized partners that require high accuracy on high-dynamic platforms. Each service is transmitted at different bands so that the receivers can correct the errors introduced by the ionosphere, while at the same time allows backward compatibility. The GPS and Galileo signals providing open access services are the GPS L1 C/A, L1C, L5 and L2C, and the Galileo E1OS and E5. The restricted services are sent in the GPS L1 M, L1 P and L2C, and in the Galileo E1 PRS and E6 PRS signals. A summary of the properties of these signals is found in Table A.1, and of BeiDou-2 signals in Table A.2.

The International Telecommunication Union (ITU) classifies the GNSS systems under Radionavigation Satellite Services (RNSSs), which also includes for example aircraft surveillance technologies or the Differential GNSS (DGNSS), in wich a network of ground-based reference stations broadcast differential information to users in the surrounding region. In fact, stand-alone GNSS systems are not suitable for critical positioning scenarios like civilian aviation or inside harbor navigation, since the accuracy, availability and integrity requirements are not met. The answers of the GNSS systems to this drawback are several. Firstly transmit services at different bands, proving the ability to correct for ionospheric delays by making multiple frequency measurements, as is one of the main causes of positioning error. Secondly, is the development of the so-called Satellite Based Augmentation Systems (SBASs), formed by a network of ground-based stations (as the aforementioned DGNSS), and also additional satellites in certain locations, typically Geostationary Earth Orbit (GEO) above the region desired to be enhanced, but also dedicated orbits over certain regions of the Earth. It is worth mentioning here that most receivers

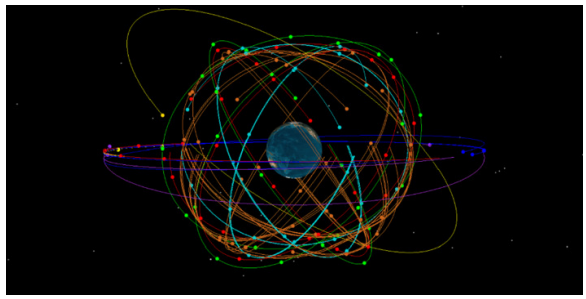

Figure 2.3: Samples of GNSS orbits over a three-day period, including the complete GPS, Galileo and BeiDou-2 constellations.

also integrate an Inertial Measurement Unit (IMU), and a compass together with the GNSS solutions with Kalman filters for added robustness.

Any new GNSS system is designed to minimize the interference among the existing ones, while ensuring interoperability between them. Some issues to be addressed for a correct interoperability are the coordinate and time reference systems, the Radio-Frequency (RF) bands allocation, and the modulations to be used within these bands, so as to mitigate the cross-interference between systems (e.g. [8] for a study of the impact between signals on GNSS-R retrievals).

The bands used in GNSS systems are shown in Fig. 2.1 and the construction of their signals will be explained later in this chapter. These bands are protected bands of transmissions for any other systems. However, the GPS L5 and Galileo E5 bands are shared with the Aeronautical Radio Navigation Service (ARNS) band, which is used to transmit the Distance Measuring Equipment (DME) signals (see Fig. 2.2). The DME signals are used for aircrafts to determine their positions from ground stations. The DME channels are spaced 1 MHz, and have a spectra of 100 kHz width, much narrower than any GNSS signal. However, their signal strength is several orders of magnitude higher than GNSS signals are, and may create interference. A detailed study of their impact in the GNSS-R scope is given in [9].

2.2 Constellations

Most of the GNSS systems use Medium Earth Orbit (MEO) satellites (the so-called Walker constellations [10]), but there are also GEO and GeoSynchronous Orbit (GSO) satellites over certain locations. The constellations are chosen so as to guarantee certain number of visible satellites with high elevation angles. As an example, Fig. 2.3 shows an snapshot map view of the orbits of several satellites. The constellation parameters of the GPS, Galileo and BeiDou-2 are summarized in Table 2.1, and are explained next.

Table 2.1: GNSS constellations summary.

System	Constellation	MEO Parameters
GPS	Walker 24/6/1 + spare satellites	i = 55° e = 0° a = 26560 km
Galileo	Walker 27/3/1 + spare satellites	i = 56° e = 0° a = 29601 km
BeiDou-2	MEO: Walker 24/3/1 + spare satellites GEO: 5 IGSO: 3	i = 55° e = 0° a = 27840 km

GPS

The core GPS constellation consists of 24 satellites allocated in six orbital planes equally spaced with an inclination of 55°, at an altitude of 20200 km, and with an orbital period of almost 12 hours. There are additional spare satellites which increase the total number of satellites up to 32. Those satellites are used for better coverage or in case of failure of the main ones. Each satellite transmits several services depending on its version (see Table 2.2), and their position in the constellation is given in Table 2.3. The newest satellites transmit at three different bands: L1 (1.57542 GHz), L2 (1.2276 GHz), and L5 (1.17645 GHz).

The GPS system has several SBAS. These systems are: WAAS (Wide Area Augmentation System) in North America, CWAAS in Canada, EGNOS (European Geostationary Navigation Overlay Service) in Europe, MSAS (Multi-Functional Satellite Augmentation System) in Japan, GAGAN (GPS and GEO Augmented Navigation) in India, SACCSA in South/Central America and Caribbean, and QZSS (Quasi-Zenith Satellite System) also in Japan. The QZSS is specially intended for urban canyons as they are common in the metropolitan areas of Japan. Figure 2.4 plots the coverage maps of said systems.

Table 2.2: GPS constellation status as on 2019/1/29. Non-transmitted signals are marked with a cross. The M signals of Block III can be steered independently from the other signals.

Block	Launch period	Operational or testing	L1				L2			L5
			P(Y)	C/A	L1C	M	P(Y)	L2C	M	
I	1978-1985	0			X	X		X	X	X
II	1989-1990	0			X	X		X	X	X
IIA	1990-1997	8			X	X		X	X	X
IIR	1997-2004	12			X	X		X	X	X
IIR-M	2005-2009	8			X			X	X	X
IIF	From 2010	12			X					X
III	From 2014	1				S			S	
Total		41								

Table 2.3: GPS satellites identifiers and PRN assignation as on 2019/1/29.

PRN	NAVSTAR	USA	NORAD	COSPAR	SVN	Launch Date	Block	Plane	Slot
1	66	232	37753	2011-036A	63	2011/7/16	IIF	D	2
2	56	180	28474	2004-045A	61	2004/11/6	IIR	D	1
3	72	258	40294	2014-068A	69	2014/10/29	IIF	E	1
4									
5	64	206	35752	2009-043A	50	2009/10/17	IIR-M	E	3
6	70	251	39741	2014-026A	67	2014/5/17	IIF	D	4
7	62	201	32711	2008-012A	48	2008/3/15	IIR-M	A	4
8	74	262	40730	2015-033A	72	2015/7/15	IIF	C	3
9	71	256	40105	2014-045A	68	2014/8/2	IIF	F	3
10	75	265	41019	2015-062A	73	2015/10/30	IIF	E	2
11	46	145	25933	1999-055A	46	1999/10/7	IIR	D	5
12	59	192	29601	2006-052A	58	2006/11/17	IIR-M	B	4
13	43	132	24876	1997-035A	43	1997/7/23	IIR	F	6
14	49	154	26605	2000-071A	41	2000/11/10	IIR	F	5
15	60	196	32260	2007-047A	55	2007/10/17	IIR-M	F	2
16	51	166	27663	2003-005A	56	2003/1/29	IIR	B	1
17	57	183	28874	2005-038A	53	2005/9/26	IIR-M	C	4
18	35	96	22877	1993-068A		1993/10/26	IIA	D	6
19	54	177	28190	2004-009A	59	2004/3/20	IIR	C	5
20	47	150	26360	2000-025A	51	2000/5/11	IIR	E	4
21	52	168	27704	2003-010A	45	2003/3/31	IIR	D	3
22	53	175	28129	2003-058A	47	2003/12/21	IIR	E	6
23	55	178	28361	2004-023A	60	2004/6/23	IIR	F	4
24	67	239	38833	2012-053A	65	2012/10/4	IIF	A	5
25	65	213	36585	2010-022A	62	2010/3/29	IIF	B	2
26	73	260	40534	2015-013A	71	2015/3/25	IIF	B	5
27	68	242	39166	2013-023A	66	2013/5/15	IIF	C	2
28	48	151	26407	2000-040A	44	2000/7/16	IIR	B	3
29	61	199	32384	2007-062A	57	2007/12/20	IIR-M	C	1
30	69	248	39533	2014-008A	64	2014/2/21	IIF	A	6
31	58	190	29486	2006-042A	52	2006/9/25	IIR-M	A	2
32	76	266	41328	2016-007A	70	2013/5/2	IIF	F	1

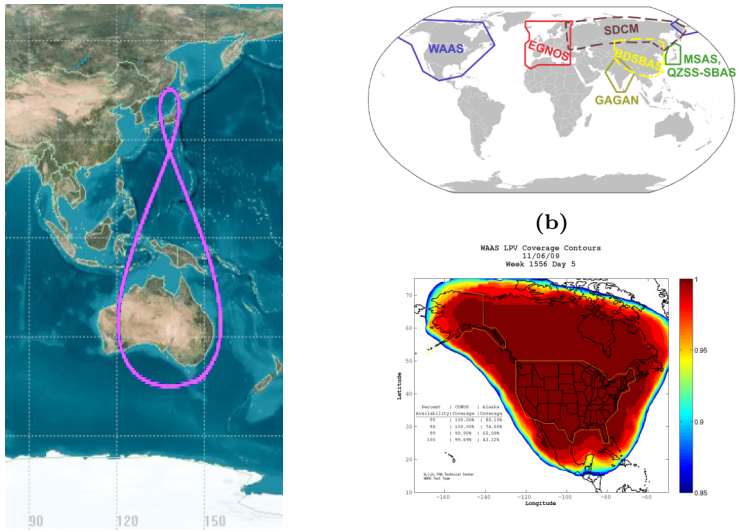

Figure 2.4: Example of regional systems coverage maps: (a) QZSS orbit [`https://commons.wikimedia.org/wiki/File:Qzss-45-0.09.jpg`]; (b) some SBAS [`https://commons.wikimedia.org/wiki/File:SBAS_Service_Areas.png`]; and (c) WAAS coverage contour map [`https://commons.wikimedia.org/wiki/File:WAAS_service_area.png`]

Galileo

The Galileo system is being built by the European Union and the ESA, and it is expected to be finished by the end of 2020. The space segment will consist of 30 satellites (27 operational and 3 spare) distributed in 3 equally spaced orbital planes with an inclination of 56°, with a semi-major axis of 29600 km, and a period of 14 h 21 min. Table 2.4 gives the position of the satellites in the constellation. The signals are transmitted at 3 different bands named E1 (1.57542 GHz), E6 (1.27875 GHz) and E5 (1.191795 GHz).

BeiDou-2

BeiDou-2 is a *multi-stage* system from China, and it is planned to be concluded by the end of 2020. By multi-stage is understood that the system will be gradually upgraded until its final stage, but providing navigation capabilities from the first one. Its constellation will consist of 35 satellites: 24 MEO, 5 GEO, and 3 inclined GSO (IGSO). The MEO satellites will operate in 3 equally spaced orbits with an inclination of 55°, at an altitude of 21568 km. Table 2.5 gives the position of the satellites in the three constellations. The BeiDou-2 signals are currently transmitted at 4 bands: B1-2 (1.58974 GHz), B1 (1.561098 GHz), B2 (1.20714 GHz), and B3 (1.26852 GHz), but they will be upgraded to B1 (1.57542 GHz), B2 (1.191795 GHz) and B3 (1.26852 GHz). BeiDou-2 will also have its own SBAS named BeiDou Satellite-Based Augmentation (BDSBAS).

Table 2.4: Galileo satellites identifiers and PRN assignation as on 2019/1/29.

PRN	NORAD	COSPAR	SVN	Common name	Launch Date	Plane	Slot	Status
1	41550	2016-030B	E210	Galileo-FOC FM10	2016/5/24	A	2	Operational
2	41549	2016-030A	E211	Galileo-FOC FM11	2016/5/24	A	6	Operational
3	41860	2016-069B	E212	Galileo-FOC FM12	2016/11/17	C	8	Operational
4	41861	2016-069C	E213	Galileo-FOC FM13	2016/11/17	C	3	Operational
5	41862	2016-069D	E214	Galileo-FOC FM14	2016/11/17	C	1	Operational
6								
7	41859	2016-069A	E207	Galileo-FOC FM7	2016/11/17	C	6	Operational
8	41175	2015-079B	E208	Galileo-FOC FM8	2015/12/17			Operational
9	41174	2015-079A	E209	Galileo-FOC FM9	2015/12/17	C	2	Operational
10								
11	37846	2011-060A	E101	Galileo-IOV PFM	2011/10/21	B	5	Operational
12	37847	2011-060B	E102	Galileo-IOV FM2	2011/10/21	B	6	Operational
13	43567	2018-060D	E220	Galileo-FOC FM20	2018/7/25	B	1	Commissioning
14	40129	2014-050B	E202	Galileo-FOC FM2	2014/8/22	Ext		Testing
15	43564	2018-060A	E221	Galileo-FOC FM21	2018/7/25	B	2	Commissioning
16								
17								
18	40128	2014-050A	E201	Galileo-FOC FM1	2014/8/22	Ext		Testing
19	38857	2012-055A	E103	Galileo-IOV FM3	2012/10/12	C	4	Operational
20	38858	2012-055B	E104	Galileo-IOV FM4	2012/10/12	C	5	Unavailable
21	43055	2017-079A	E215	Galileo-FOC FM15	2017/12/12	A	3	Operational
22	40545	2015-017B	E204	Galileo-FOC FM4	2015/3/27	B	3	Unavailable
23								
24	40889	2015-045A	E205	Galileo-FOC FM5	2015/9/11	A	8	Operational
25	43056	2017-079B	E216	Galileo-FOC FM16	2017/12/12	A	7	Operational
26	40544	2015-017A	E203	Galileo-FOC FM3	2015/3/27	B	8	Operational
27	43057	2017-079C	E217	Galileo-FOC FM17	2017/12/12	A	4	Operational
28								
29								
30	40890	2015-045B	E206	Galileo-FOC FM6	2015/9/11	A	5	Operational
31	43058	2017-079D	E218	Galileo-FOC FM18	2017/12/12	A	1	Operational
32								
33	43565	2018-060B	E222	Galileo-FOC FM22	2018/7/25	B	7	Commissioning
34								
35								
36	43566	2018-060C	E219	Galileo-FOC FM19	2018/7/25	B	4	Commissioning

Table 2.5: BeiDou/COMPASS satellites identifiers and PRN assignation as on 2019/1/29.

	Common Name	COSPAR	NORAD	Sat. Cat. Name	PRN	Launch Date	Orbit	Status
BeiDou-2	BEIDOU G1	2010-001A	36287	BEIDOU 3	C01	2010/1/16	GEO 140.0°E	Oper.
	BEIDOU G6	2012-059A	38953	BEIDOU 16	C02	2012/10/25	GEO 80°E	Oper.
	BEIDOU G7	2016-037A	41586	BD-2-G7	C03	2016/6/12	GEO 110.5°E	Oper.
	BEIDOU G4	2010-057A	37210	BEIDOU 6	C04	2010/10/31	GEO 160.0°E	Oper.
	BEIDOU G5	2012-008A	38091	BEIDOU 11	C05	2012/2/24	GEO 58.75°E	Oper.
	BEIDOU IGSO 1	2010-036A	36828	BEIDOU 5	C06	2010/07/31	55° IGSO 118°E	Oper.
	BEIDOU IGSO 2	2010-068A	37256	BEIDOU 7	C07	2010/12/17	55° IGSO 118°E	Oper.
	BEIDOU IGSO 3	2011-013A	37384	BEIDOU 8	C08	2011/4/9	55° IGSO 118°E	Oper.
	BEIDOU IGSO 4	2011-038A	37763	BEIDOU 9	C09	2011/7/26	55° IGSO 95°E	Oper.
	BEIDOU IGSO 5	2011-073A	37948	BEIDOU 10	C10	2011/12/1	55° IGSO 95°E	Oper.
	BEIDOU M3	2012-018A	38250	BEIDOU 12	C11	2012/4/29	MEO Slot A07	Oper.
	BEIDOU M4	2012-018B	38251	BEIDOU 13	C12	2012/4/29	MEO Slot A08	Oper.
	BEIDOU IGSO 6	2016-021A	41434	BEIDOU IGSO-6	C13	2016/3/29	55° IGSO 95°E	Oper.
	BEIDOU M6	2012-050B	38775	BEIDOU 15	C14	2012/9/18	MEO Slot B04	Oper.
	BEIDOU IGSO 7	2018-057A	43539	BEIDOU IGSO-7	C16	2018/7/29	55° IGSO 95°E	Oper.
BeiDou-3	BEIDOU-3 MEO-1	2017-069A	43001	BEIDOU-3 M1	C19	2017/11/5	MEO Slot B07	Oper.
	BEIDOU-3 MEO-2	2017-069B	43002	BEIDOU-3 M2	C20	2017/11/5	MEO Slot B08	Oper.
	BEIDOU-3 MEO-3	2018-018B	43208	BEIDOU 3M6	C21	2018/2/12	MEO Slot B06	Oper.
	BEIDOU-3 MEO-4	2018-018A	43207	BEIDOU 3M5	C22	2018/2/12	MEO Slot B05	Oper.
	BEIDOU-3 MEO-5	2018-062A	43581	BEIDOU 3M9	C23	2018/7/29	MEO Slot C07	Oper.
	BEIDOU-3 MEO-6	2018-062B	43582	BEIDOU 3M10	C24	2018/7/29	MEO Slot C01	Oper.
	BEIDOU-3 MEO-11	2018-067B	43603	BEIDOU 3M12	C25	2018/8/24	MEO Slot C02	Oper.
	BEIDOU-3 MEO-12	2018-067A	43602	BEIDOU 3M11	C26	2018/8/24	MEO Slot C08	Oper.
	BEIDOU-3 MEO-7	2018-003A	43107	BEIDOU 3M3	C27	2018/1/11	MEO Slot A04	Oper.
	BEIDOU-3 MEO-8	2018-003B	43108	BEIDOU 3M4	C28	2018/1/11	MEO Slot A05	Oper.
	BEIDOU-3 MEO-9	2018-029A	43245	BEIDOU 3M7	C29	2018/3/29	MEO Slot A02	Oper.
	BEIDOU-3 MEO-10	2018-029B	43246	BEIDOU 3M8	C30	2018/3/29	MEO Slot A03	Oper.
	BEIDOU-3 MEO-13	2018-072A	43622	BEIDOU 3M13	C32	2018/9/19	MEO Slot B01	Oper.
	BEIDOU-3 MEO-14	2018-072B	43623	BEIDOU 3M14	C33	2018/9/19	MEO Slot B03	Oper.
	BEIDOU-3 MEO-15	2018-078B	43648	BEIDOU 3M16	C34	2018/10/15	MEO Slot A01	Oper.
	BEIDOU-3 MEO-16	2018-078A	43647	BEIDOU 3M15	C35	2018/10/15	MEO Slot A07	Oper.
	BEIDOU-3 MEO-17	2018-093A	43706	BEIDOU 3M17	C36	2018/11/1	MEO Slot C04	Oper.
	BEIDOU-3 MEO-18	2018-093B	43707	BEIDOU 3M18	C37	2018/11/1	MEO Slot C06	Oper.
	BEIDOU-3 GEO-1	2018-085A	43683	BEIDOU 3G1	C59	2018/11/1	GEO 144.2°E	Comm.
BeiDou-3S	BEIDOU I2-S	2015-053A	40938	BD-20	C18	2015/9/29	55° IGSO 95°E	Test.
	BEIDOU I1-S	2015-019A	40549	BD-17	C31	2015/3/30	55° IGSO 95°E	Test.
	BEIDOU M1-S	2015-037B	40749	BD-19	C57	2015/7/30	MEO Slot A01	Test.
	BEIDOU M2-S	2015-037A	40748	BD-18	C58	2015/7/30	MEO Slot A06	Test.

IRNSS

This system is designed to be autonomous and to cover the India sub-continent. It is developed by the Indian Space Research Organization, and when completed, will have 3 GEO and 4 GSO satellites. The bands used are L5 (1.17645 GHz) and S (2.492028 GHz).

GLONASS

Russia's current system consists of 24 satellites distributed over 3 equally spaced orbital planes with an inclination of 65.8°, with a semi-major axis of 25510 km, and with a period of 11 h 15 min. GLONASS also has spare satellites which currently complete the constellation with 29 satellites. The signals are transmitted at three different bands: L1 (1.57542 GHz), L5 (1.17645 GHz), and L3 (1.20714 GHz). In the future, GLONASS will also have its own SBAS, named System for Differential Correction and Monitoring (SDCM).

2.3 Signal model

The GNSS signals carry the information necessary for the receivers to compute their position. The new signals also contain Forward Error Correction (FEC) techniques to mitigate the impact of the channel. In the case of the private or regulated signals, the data is also encrypted.

The bandwidth of the data signals is only of few tens of bits/second (bps), but it is *spread* over a wider bandwidth with a *ranging* code up to several Mchips/s (Mcps). This spreading technique is called Direct-Sequence Spread Spectrum (DSSS). The term *chip* is a fundamental unit of transmission, and differs from a *bit* because it is not used for the transmission of any data. The reasons for this frequency expansion are several. Firstly, the location accuracy is better the wider the spectrum is; secondly, it reduces the multipath impact in harsh environments; thirdly, it mitigates the effect of Radio Frequency Interference (RFI) signals; and fourthly it allows to distinguish satellites by using each of them a different ranging code. This method to distinguish transmitters sharing the same frequency band is called Code Division Multiple Access (CDMA), and is the one used in the GPS, Galileo and BeiDou-2 systems. However some GLONASS signals also use the Frequency Division Multiple Acces (FDMA) along with the CDMA. The FDMA technique ensures a better interference rejection, and cross-correlation between different signals as compared to the CDMA used in the other systems. However, the receivers need to have a larger bandwidth and are more complex.

As an example of the DSSS technique, Figure 2.5 shows the Probability Density Function (PDF) and the Cumulative Distribution Function (CDF) of a signal with a rate of 50 Hz before and after being spread with a code with a rate of 1.023 MHz. These are the rates used in the GPS L1 C/A signal. Note that both signals have the same power, but the peak power is reduced by about 40 dB after the spreading.

The GNSS signals transmitted by the satellites using the CDMA technique, can be modeled as

$$x_t(t) = \sqrt{2P}\sum_k e_k b_k \cos(2\pi f_c t) - \sqrt{2P}\sum_l e_l b_l \sin(2\pi f_c t), \tag{2.1}$$

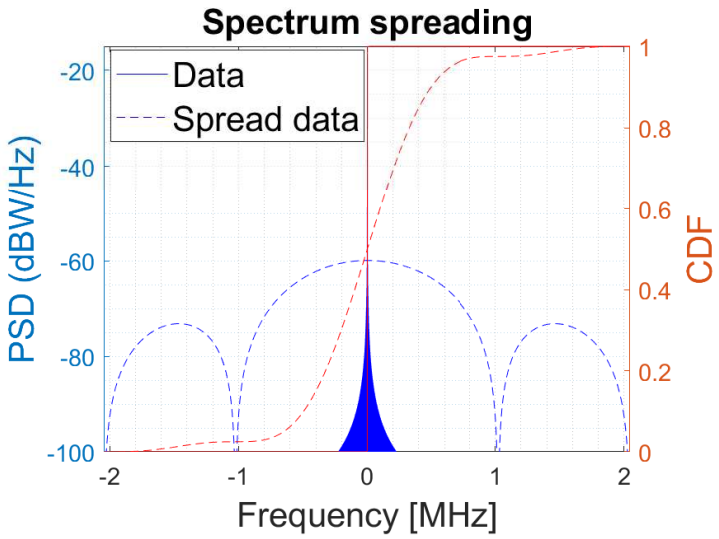

Figure 2.5: Spreading of a data signal with an original rate of 50 Hz to 1.023 MHz.

where P is the transmitted power, $e_i = C_i D_i$ is the spreading of a data signal D_i with a code C_i, b_i is a Binary Offset Carrier (BOC) subcarrier, and f_c is the carrier frequency.

The spreading code may be formed by a *primary* code c_i and a *secondary* code CS_i: $C_i = c_i \cdot CS_i$. The subcarrier may be created by combining several subcarriers. All the sequences are binary, except some BOC subcarriers. However, in these latter cases, the BOC signals are chosen so as to create a constant power envelope. Except the data signals, the other terms are cyclically repeated, but the period and rates may be different for each of them. All the terms are optional, but at least one ranging code and one data signal are present. When a signal is not conveying any data, it is usually referred as a *pilot* component.

The received signal in a Line-of-Sight (LoS) scenario (i.e. without multipath, echoes or similar phenomena), after the down-conversion, is an attenuated, delayed, Doppler shifted and noisy version of the transmitted one

$$x_r(t) = \frac{1}{\sqrt{L}} x(t - \tau_d) e^{-j2\pi f_d t} + n(t). \tag{2.2}$$

The received power is in fact extremely low. Typical power values can be as low as 10^{-16}W (see Tables A.1 and A.2 for the minimum guaranteed powers on the Earth's surface).

The basic principle of operation that a receiver perform to get its position is

1. To find which satellites are in view by cross-correlating the received signal $x_r(t)$

with a data-less locally generated clean replica $r(t)$ for several Doppler frequencies

$$Y(\tau,\nu) = \frac{1}{T_{coh}} \int_{T_{coh}} x_r(t)\, r^*(t-\tau)\, e^{j2\pi\nu t} dt, \tag{2.3}$$

where T_{coh} is the correlation length. This latter term is called Cross-Ambiguity Function (CAF), and if the satellite is present and the received signal is high enough, it will present a peak in the correlation plane at $[\tau_d, f_d]$. The receiver decides that a satellite is present if the latter peak is above a certain threshold. Since *a priori* the satellites in view are unknown, the receiver must perform the same operation for all the possible ranging codes. The peak search may be done over power $|Y(\tau,\nu)|^2$, or over power averages, but eventually, the data sent by the satellites must be extracted from the phase jumps of the peak due to a data bit transition.

2. To continuously track the peak over the delay/Doppler plane. This is typically done with Phase Lock Loops (PLLs) for the carrier phase and with Delay Lock Loops (DLLs) for the code delay.

3. To estimate the range to the satellites in view, named *pseudo-range*. The prefix *pseudo* comes because of the clock errors of the receiver and the transmitter. The latter is provided in the satellite navigation message, and it is, in fact, a critical factor for the accuracy of any GNSS system. The clocks carried on board satellites are atomic and are continuously monitored and synchronized by the control segment in the ground monitoring stations.

4. To compute the position to the satellites in view using the ephemeris data broadcasted in their navigation messages. Actually, the satellites do not send their ephemeris, but parameters that solve complex equations. The satellites also send an *almanac*, which is a simplified ephemeris of the rest of the satellites of the constellation. This is done to help the receiver during the acquisition process to have an initial clue on where the $[\tau_d, f_d]$ may be. The ephemeris and alamanac information are organized into *frames* and *subframes*, which are updated in the order of few seconds or minutes respectively.

5. To solve the receiver position by triangulation using the pseudo-ranges, the satellite positions, and the clock, ionospheric and other corrections. At least four satellites are needed to get the position, and not three because the clock of the receiver is not synchronized with the ones in the satellites. It can take just milliseconds to measure the range to a satellite, but it is the delay in the initial acquisition and the time required to decode ephemeris data that makes a typical GNSS receiver slow to produce a first position.

Before going further on this chapter, it is worth to give here some comments regarding the CAF term described above. In the case of a signal received with LoS, (2.3) can be expressed as

$$Y(\tau,\nu) = \frac{1}{L}\chi(\tau-\tau_d,\nu-f_d), \tag{2.4}$$

where $\chi(\tau,\nu)$ is the so-called auto-ambiguity function of $r(t)$ or just Ambiguity Function (AF) [11, ch. 7]

$$\chi(\tau,\nu) = \frac{1}{T_{coh}}\int_{T_{coh}} r(t)\, r^*(t-\tau)\, e^{j2\pi\nu t} dt. \tag{2.5}$$

When the signal is not in LoS or in the case of the GNSS-R reflections, the CAF depends as well on the AF, but also includes additional complex parameters. Models for the CAFs of the GNSS-R signals are given in next chapter.

The power function of the AF is called the Woodward Ambiguity Function (WAF). For the GNSS signals used in this Ph. D. thesis, it can be expressed as [12]

$$|\chi(\tau,\nu)|^2 = |R_r(\tau)|^2 \cdot \mathrm{sinc}^2(T_{coh}\nu), \tag{2.6}$$

where $R_r(\tau)$ is AutoCorrelation Function (ACF) of $r(t)$

$$R_r(\tau) = \frac{1}{T_{coh}}\int_{T_{coh}} r(t)\, r^*(t-\tau)\, dt, \tag{2.7}$$

and

$$\mathrm{sinc}(x) = \sin(\pi x)/\pi x. \tag{2.8}$$

Hence, it is necessary to understand the basics on the creation of the signals, in order to obtain their ACFs. For illustrative purposes, Fig. 2.6 plots the $|R_r(\tau)|$ of some signals.

2.4 Codes

Each GNSS satellite spreads the data signal using a different code. These codes are usually referred as Pseudo-Random Noises (PRNs). This is so because they present similar properties to those of the Additive White Gaussian Noise (AWGN), in terms of autocorrelation and cross-correlation with the codes from the other satellites. As aforementioned, some of those codes are actually the combination of several. Their creation is explained next.

2.4.1 Primary codes

Most of the GNSS codes are generated with Linear Feedback Shift Registers (LFSRs), but some of the modern ones are given as random memory codes which cannot be created with any LFSR. A LFSR produces a cycling sequence of a given length. The repetition

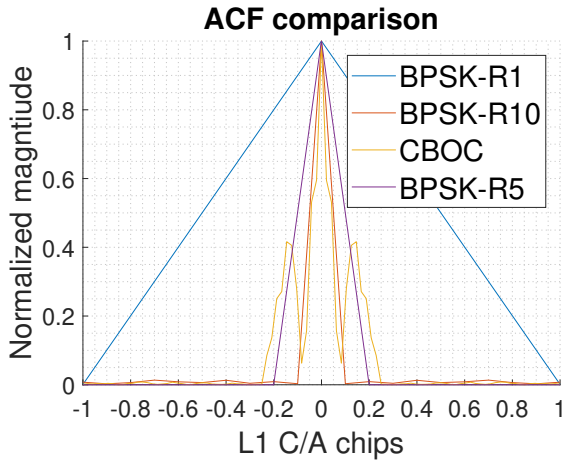

(a)

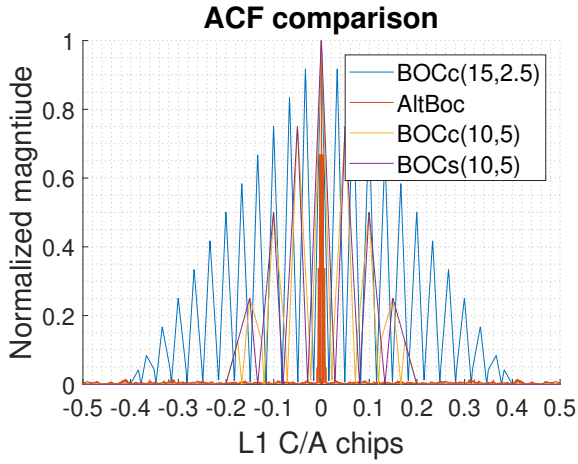

(b)

Figure 2.6: Comparison of the ACFs of different GNSS modulations.

period depends on the *taps* used to update the new value of the first register. For a LFSR of n registers, there is an optimum tap combination that generates a sequence of length $2^n - 1$. This sequence is called maximum length sequence (MLS) or m-sequence, and there is no other sequence of the same length. The initial value of the registers is called *seed*. Two LFSR with the same tap positions and different seeds, will generate the same sequences, but one delayed with respect to the other. The speed at which the LFSR *shifts*, is given by clock frequency.

Since the m-sequence is unique, the GNSS codes are actually a complex combination of several codes, sometimes even a time multiplex between them. These basic codes can be memory codes or the combination of several LFSRs. The LFSRs are designed by

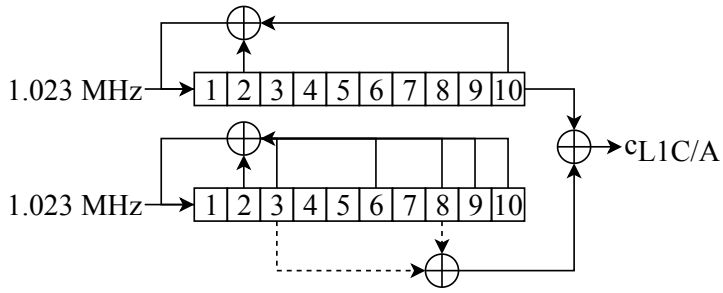

Figure 2.7: GPS L1 C/A code generation.

means of the driven clock frequency, seeds, taps, and *phases*, which are the registers used to generate the output. In some cases, it is also desirable to reset the LFSR to its original state before its natural end. The codes that will be needed to develop these thesis are the ones used in the signals GPS L1 C/A and L5, and the Galileo E1OS and E5. The following paragraphs explain their generation.

GPS L1 C/A

The GPS L1 C/A signal is a real signal formed a single code [13]. The ranging codes are formed by combining two LFSRs of 10 registers, driven with a clock frequency of 1.023 MHz. The tap positions of both registers are fixed, and their seeds are all ones for all the PRNs. The code is created by adding the last register of the first LFSR with two registers of the second LFSR. These two phases are different for each PRN. This results in a code of length 1023 chips or 1 ms. A sketch of the PRN generation is shown in 2.7.

GPS L5

The GPS L5 signals are complex signals, and they have a different code for the in-phase and quadrature components [14]. The GPS L5I and GPS L5Q codes are obtained by combining a principal code and a secondary code. The principal codes are formed with 2 LFSRs of 13 registers each, driven with a clock frequency of 10.23 MHz. One LFSR is shared between both components, has fixed taps, and its seed is all ones for all the PRNs. The LFSR is reset before its natural end. The other two LFSRs have also fixed taps, but their seeds are different for each satellite. The code is created from the last registers of the LFSRs. This results in a code of length 10230 chips and 1 ms.

The secondary codes are memory codes named Neufarm Huffman codes, and are driven with a clock frequency of 1 kHz. The codes have a different length for both components: 10 chips or 10 ms for the I, and 20 chips or 20 ms for the Q, and are the same for all the PRNs. A sketch of the PRNs generation is shown in 2.8.

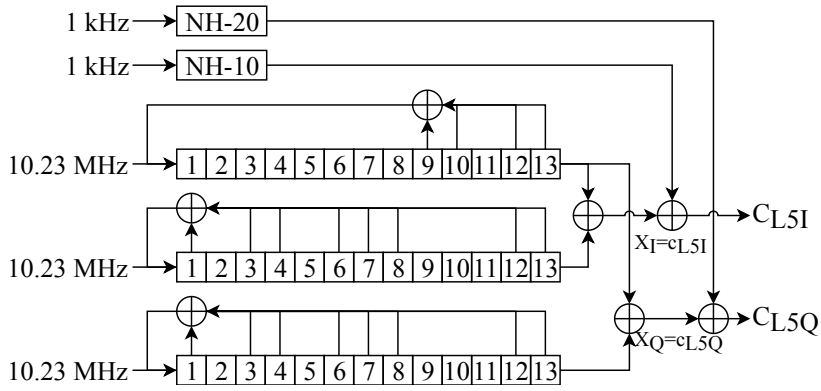

Figure 2.8: GPS L5 code generation.

Galileo E1OS

The Galileo E1OS signal is composed of two codes, named E1B and E1C [15]. The E1B code is created with one code, whereas the and E1C is a tiered code. The primary codes are random memory codes of length 4092 chips, different for each PRN, and driven with a clock frequency of 1.023 MHz, resulting in duration of 4 ms. The secondary code of the E1C is a memory code of length 25 chips, fixed for all the PRNs and driven with a clock frequency of 250 Hz, resulting in a duration of 100 ms.

Galileo E5

The Galileo E5 signal is a complex signal [15]. It is composed of 4 codes, named E5aI, E5aQ, E5bI and E5bQ. All these codes are tiered codes constructed from two codes. The preliminary codes are created with two LFSRs of 15 registers and driven with a clock frequency of 10.23 MHz. The tap positions of both registers are different for each component, but fixed for all the PRNs. The seeds are different for each component and satellite. The code is created from the last position of both registers. These results in a code of length 10230 chips or 1 ms. The secondary codes are a memory codes driven with a clock frequency of 1 kHz. Each code has a different length: 20 chips for the E5aI, 100 chips for the E5aQ, 4 chips for the E5bI, and 100 chips for the E5bQ, resulting in a duration of 4, 20 or 100 ms. The codes of the E5aI and E5bI are fixed for all PRNs, whereas for the E5aQ and E5bQ are different. A sketch of the PRN generation of the E5aI code is shown in 2.9.

2.4.2 Secondary codes

The coherent correlation time T_{coh} in (2.3) is usually set to the duration of the primary code. In principle, a larger time would produce a higher correlation peak, and the estima-

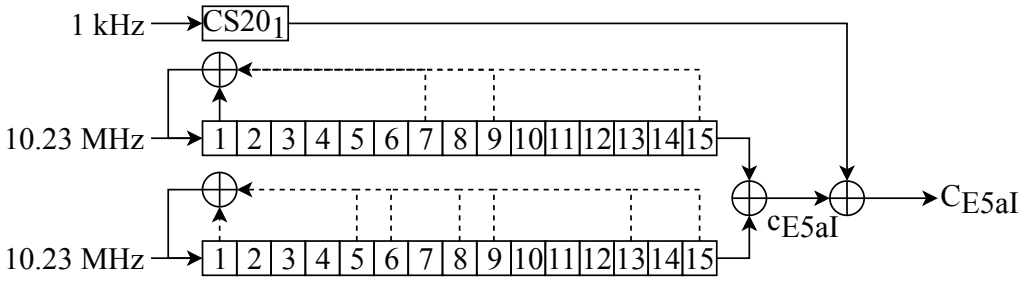

Figure 2.9: Galileo E5aI code generation.

tion of its position would be better. Although this is true, two issues must be considered. Firstly, the length cannot be arbitrary large because a too large correlation would blur the phase information required to demodulate the data bits. Secondly, since the codes are cyclic, enlarging the correlation length would produce additional peaks, so that the tracking may become complex. For these reasons, some GNSS signals provide pilot signals, that together with large secondary codes, allow longer integration times without concerning for any data bit transition. The benefits of this on the CAFs will be shown in next section. Figure 2.10 shows the relative length of the secondary codes with respect to the primary codes, and Fig. 2.11 shows their time plot.

It is worth mentioning here that the Doppler resolution required to find a peak in the CAF function is inversely proportional to T_{coh}. Trying to acquire a signal for first time with the full secondary code may take too much time. Receivers usually start acquiring with the short signals and iteratively improve their position with the secondary codes.

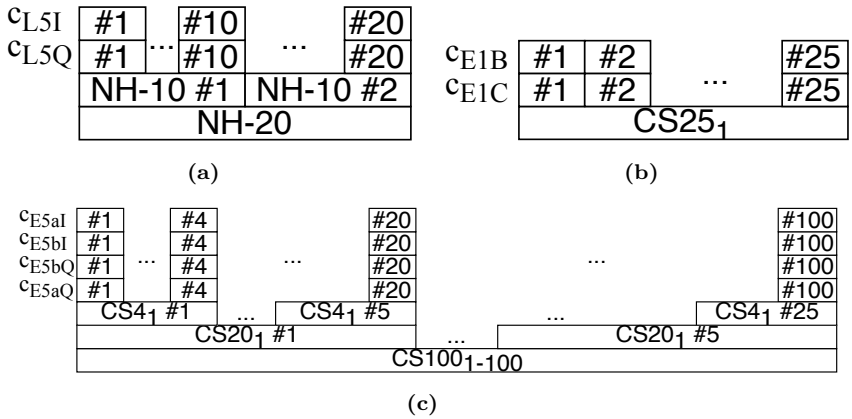

Figure 2.10: Secondary codes length: (a) GPS L5, (b) Galileo E1OS, and (c) Galileo E5.

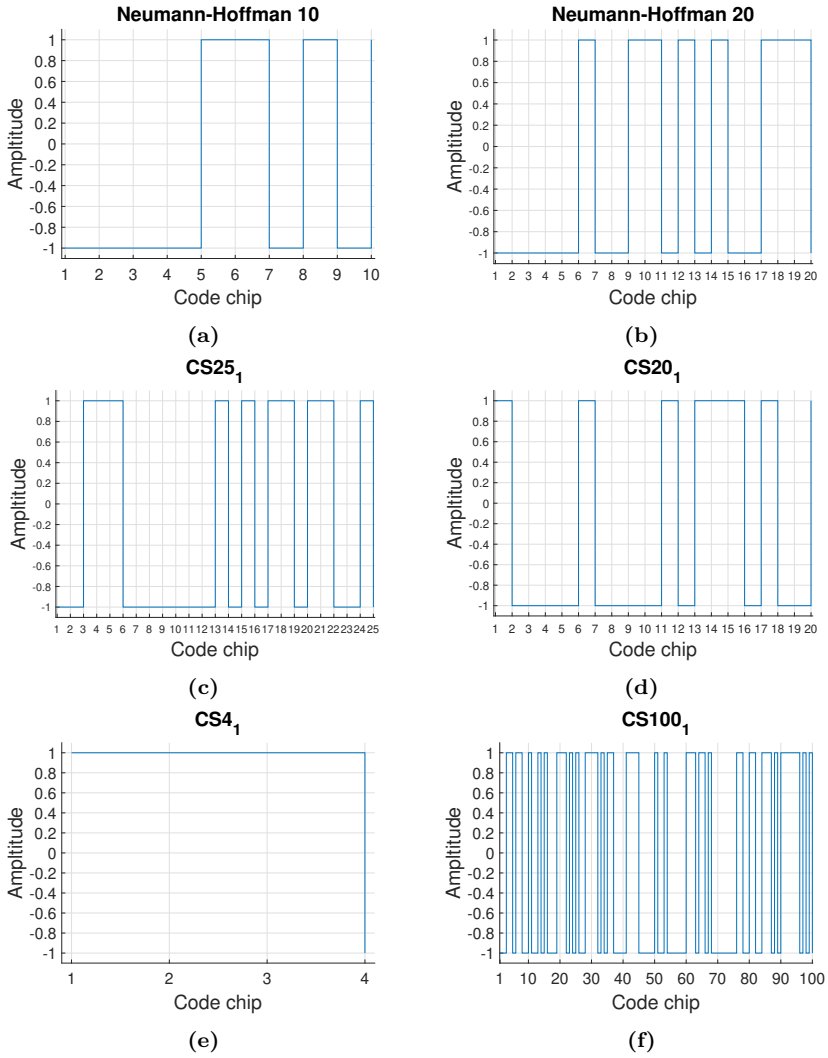

Figure 2.11: Some secondary codes: (a) NH-10 used for all the GPS L5I components, (b) NH-20 used for all the GPS L5I components, (c) $CS25_1$ used for all the Galileo E1C components, (d) $CS20_1$ used for all the Galileo E5aI components, (e) $CS4_1$ used for all the Galileo E5bI components, and (f) $CS100_1$ used for the E5aQ component of PRN 1.

2.5 Signals modulation

The modulation used in the first GNSS signals is the Binary Phase-Shift Keying (BPSK). These include the GPS L1 C/A, L1 P, L2C, L2 P, L5; and the BeiDou-2 B1, B1-2, B2, and B3 signals. However, the new signals use improved modulations called BOC [16], which add square subcarriers to the original ranging codes. This results in a frequency shift of the main spectrum lobe from the carrier frequency, and in a multi-peak ACF. The

BOC modulations were originally conceived to reduce interference with the BPSK signals emitted at the same band (see Fig. 2.1, but also to increase the positioning accuracy [17]. However, they require a more complicated acquisition and tracking scheme. The general expression for a BOC modulation is usually written as BOC(n,m) which refers to a code chipping rate of $f_r = m \cdot 1.023$ MHz and a subcarrier frequency of $f_b = n \cdot 1.023$ MHz. Depending on the phase of the subcarrier, the modulation can be sine-phased ($\mathrm{BOC_s}$) or cosine-phased ($\mathrm{BOC_c}$). The expressions of the subcarrier functions are

$$\begin{aligned} b_{BOCs,f_b} &= \mathrm{sign}\left(sin\left(2\pi f_b t\right)\right), \\ b_{BOCc,f_b} &= \mathrm{sign}\left(cos\left(2\pi f_b t\right)\right), \end{aligned} \tag{2.9}$$

where $\mathrm{sign}\left(t\right)$ is the sign function. The GPS M signals use a $\mathrm{BOC_s}$(10,5), the future versions of the BeiDou-2 B1 and B3A will use a $\mathrm{BOC_s}$(14,2) and $\mathrm{BOC_s}$(15,2.5) respectively, and the Galileo E6A uses a $\mathrm{BOC_c}$(10,5).

Some signals combine several BOCs into a more complex modulations, such as the modified Alternative BOC (AltBOC) and the multiplexed BOC or MBOC(6,1,1/11). The modified AltBOC differs from a BOC by using two complex subcarriers instead of a single real. Under *modified* it is understood that the subcarriers are not square pulses, but chosen to obtain a constant envelope. An AltBOC can also be processed as two independently Quadrature Phase Shift Keying (QPSK) signals with shifted carrier frequencies. The MBOC(6,1,1/11) modulation can be obtained by different ways. One is the composite BOC or CBOC(6,1,1/11) which is the addition of a $\mathrm{BOC_s}$(1,1) with a $\mathrm{BOC_s}$(6,1), with a power distribution of 10/11 and 1/11 respectively. The second method is called time multiplexed BOC or TMBOC(6,1,4/33), which is the addition of a $\mathrm{BOC_s}$(1,1) with a time multiplex of another $\mathrm{BOC_s}$(1,1) with a $\mathrm{BOC_s}$(6,1) with a power distribution of 29/33% and 4/33% respectively. The power distribution between the continuous $\mathrm{BOC_s}$(1,1) and the multiplexed signal is 3/4 and 1/4 respectively. The Galileo E5 signal uses an AltBOC(15,10), the GPS L1C implements the TMBOC(6,1,4/33), the Galileo E1OS adopted CBOC(6,1,1/11), and the future BeiDou-2 B1 will use a MBOC(6,1,1/11).

Tables A.1 and A.2 give a comprehensive summary of all the modulations of the GNSS signals. This PhD thesis will implement software programs to process the GPS L1 C/A, L5 and the Galileo E1OS and E5 signals, which are explained next.

GPS L1 C/A

The GPS L1 C/A is a BPSK signal (see the I/Q diagram in Fig. 2.12a). Its constructed by combining one ranging code and one data signal. The baseband expression is

$$x_{L1CA}\left(t\right) = c_{L1CA}\left(t\right) d_{L1CA}\left(t\right). \tag{2.10}$$

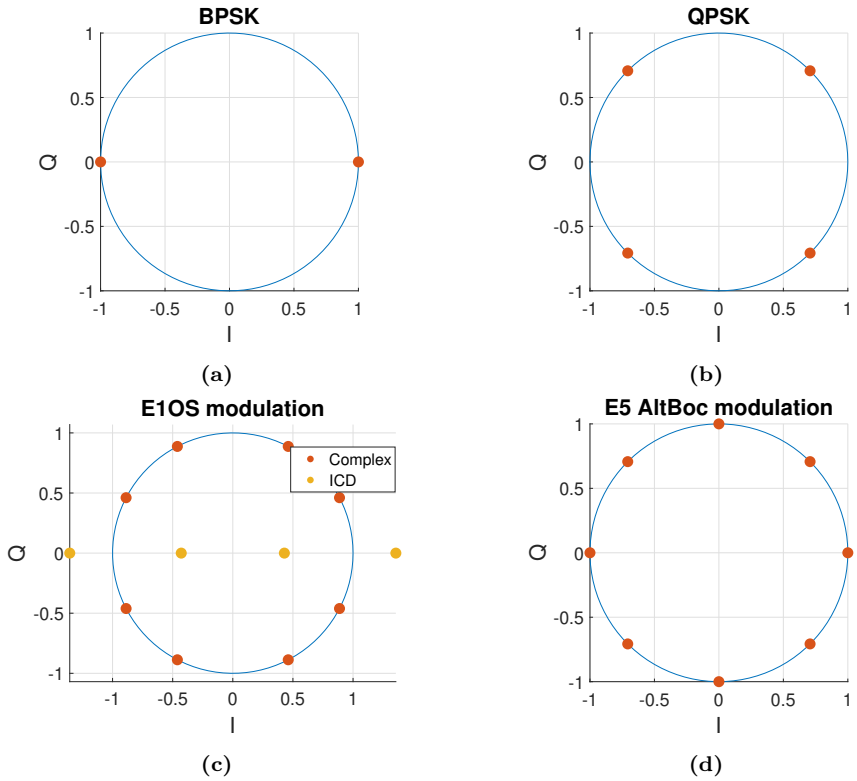

Figure 2.12: GNSS modulations I/Q diagram: (a) BPSK as used in GPS L1 C/A and L2C, and BeiDou-2 B2; (b) QPSK as used in GPS L5 and BeiDou-2 B1 and B3, and Galileo E6CS; (c) CBOC(6,1,1/11) as used in GPS L1C, Galileo E1OS, and in the future version of BeiDou-2 B1; and (d) constant power envelope AltBOC as used in Galileo E5 and in the future version of BeiDou-2 B2.

Figure 2.13 plots an example of the ACF of a code, and the cross-correlation of this code with another one from the same family. Note that the cross-correlation terms are not zero, and neither are the terms outside the peak in ACF. This is so because the PRNs are not orthogonal, but *quasi-orthogonal* to one another. Nevertheless, these terms lay about 26 dB below a ACF peak power. A similar effect happens with all the other GNSSs signals, although with an even larger power ratio.

GPS L5

The GPS L5 is a QPSK signal (see the I/Q diagram in Fig. 2.12b). It contains two ranging codes and one data signal. The complex baseband expression is

$$x_{L5}(t) = \frac{1}{2\sqrt{2}} C_{L5I}(t)\, d_{L5}(t) + j \frac{1}{2\sqrt{2}} C_{L5Q}(t)\,. \tag{2.11}$$

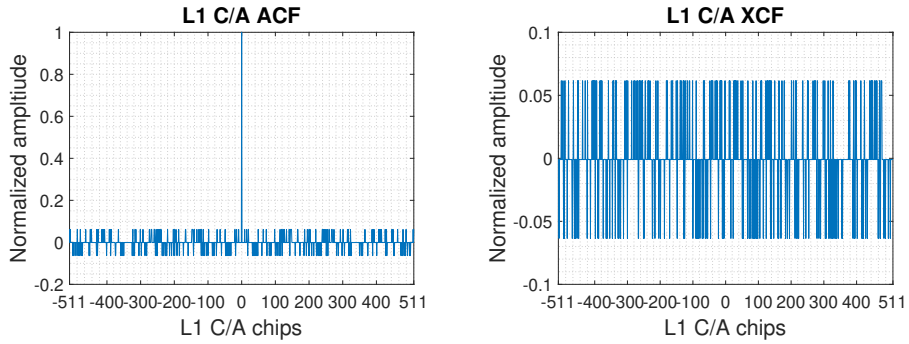

(a) (b)

Figure 2.13: Correlation properties of GPS C/A codes: (a) example of autocorrelation function for a C/A code and (b) example of a cross-correlation between two different C/A codes.

The ACFs of the L5 signals are similar to those of the L1 C/A signals, except that they are 10 times narrower due to the higher chip rate (see Fig. 2.6). The power ratio between the noise terms and the peak is about 40 dB.

If the GNSS signal is very weak, the cross-correlation peak may be blurred by the noise of the receiver. The GPS L5 signals are more resilient to the instrument noise by taking advantage of the secondary codes. Enlarging the coherent length in (2.7) up to the duration of a complete secondary code, the ACFs of Fig. 2.14b is obtained. Note that the peak power has increased by about 13 dB. Bear in mind, that enlarging the cross-correlation length in signals that do not have secondary codes (as for example L1 C/A) would produce something similar to Fig. 2.14a. In this case, the peak power has also increased by 13 dB, but as many new peaks have appeared as codes fit in the correlation.

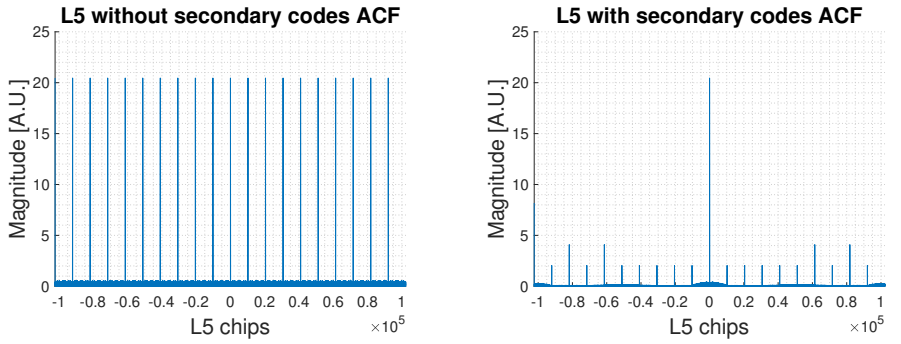

(a) (b)

Figure 2.14: Auto-correlation function of the GPS L5 signal (a) without secondary codes, and (b) with secondary codes.

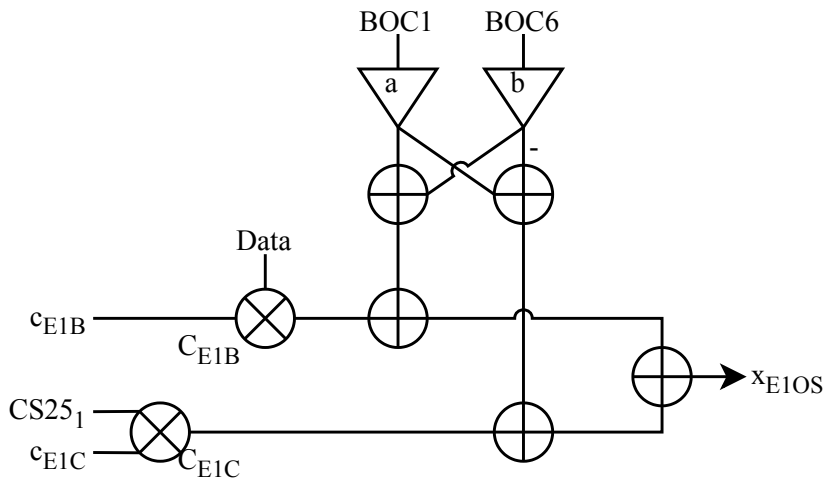

Figure 2.15: Generation of the Galileo E1OS signal as given by the ICD.

Galileo E1OS

The Galileo E1OS uses a CBOC modulation. The Interface Control Documents (ICD) [15] defines the E1OS as a real signal, generated with 2 ranging codes and one data signal

$$\begin{aligned} x_{E1OS}(t) = &\frac{1}{\sqrt{2}} C_{E1B}(t) \left(\alpha b_{BOCs,f_b^6}(t) + \beta b_{BOCs,f_b^1}(t) \right) \\ &- \frac{1}{\sqrt{2}} C_{E1C}(t) \left(\alpha b_{BOCs,f_b^6}(t) - \beta b_{BOCs,f_b^1}(t) \right) \end{aligned} \tag{2.12}$$

with $f_b^1 = 1.023$ MHz, $f_b^6 = 6.138$ MHz, $\alpha = \sqrt{1/11}$, $\beta = \sqrt{10/11}$, and with

$$\begin{aligned} C_{E1B}(t) &= c_{E1B}(t)\, d_{E1}(t)\,, \\ C_{E1C}(t) &= c_{E1C}(t)\,. \end{aligned} \tag{2.13}$$

The construction of the signal is shown in Fig. 2.15. The I/Q diagram of this modulation is given by the yellow points in Fig. 2.12c. To the author's surprise this modulation has not a constant power envelope. In fact, some of the people involved in the design of the Galileo signals, published an early article in [18] showing an E1OS I/Q diagram like the one in red in Fig. 2.12c. This modulation can be obtained by converting (2.12) into complex by

$$\begin{aligned} x_{E1OS}(t) = &\frac{1}{\sqrt{2}} C_{E1B}(t) \left(\alpha b_{BOCs,f_b^6}(t) + \beta b_{BOCs,f_b^1}(t) \right) \\ &- 1j \frac{1}{\sqrt{2}} C_{E1C}(t) \left(\alpha b_{BOCs,f_b^6}(t) - \beta b_{BOCs,f_b^1}(t) \right) \end{aligned} \tag{2.14}$$

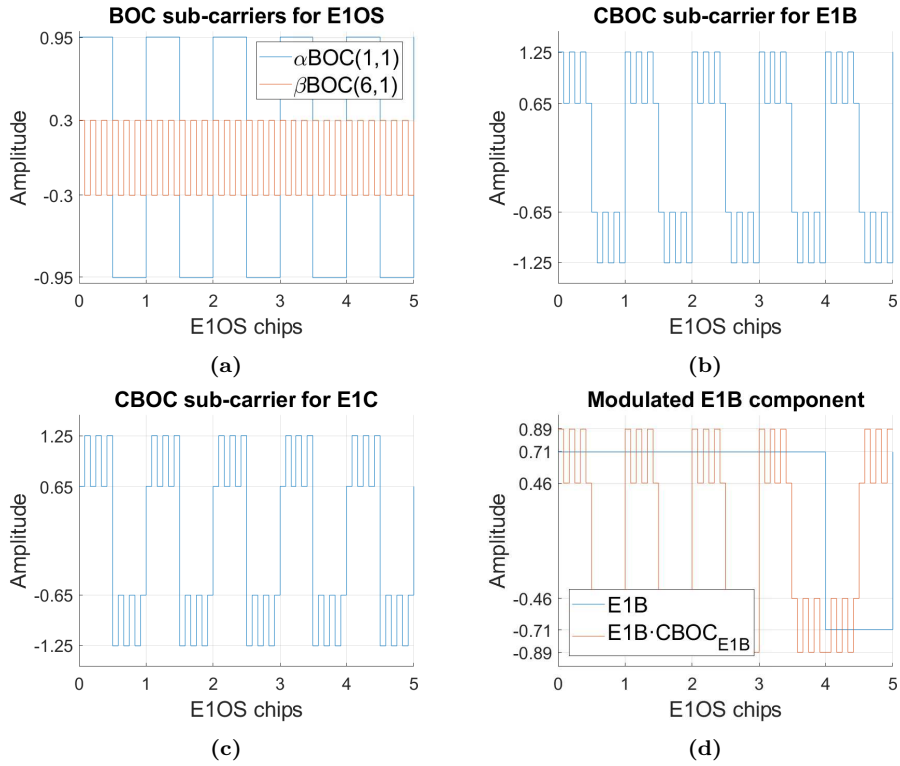

Figure 2.16: BOC subcarriers for the E1OS signal: (a) BOCs(1,1) and BOCs(6,1) sequences, (b) CBOC subcarrier for E1B branch, (c) CBOC subcarrier for E1C branch, and (d) example of a modulated E1B PRN.

The subcarriers and an example of a modulated E1B branch are plotted in Fig. 2.16. Note that the modulation has 4 different values, as opposed to the +/- 1 values in the BPSK or QPSK modulations.

The ACF of the E1OS signal is shown in 2.17a. Observe that although the rate of the spreading code is the same as that of L1 C/A, the ACF peak is narrower. Note also that the ACF presents additional peaks aside from the main one. Similar to the L5 signals, the E1OS signals allow to extend the length of the correlation above the code duration. As an example, Fig. 2.17b shows the resulting ACF when the correlation length is set to the duration of a complete secondary code. Note that the peak power has increased by about 41 dB.

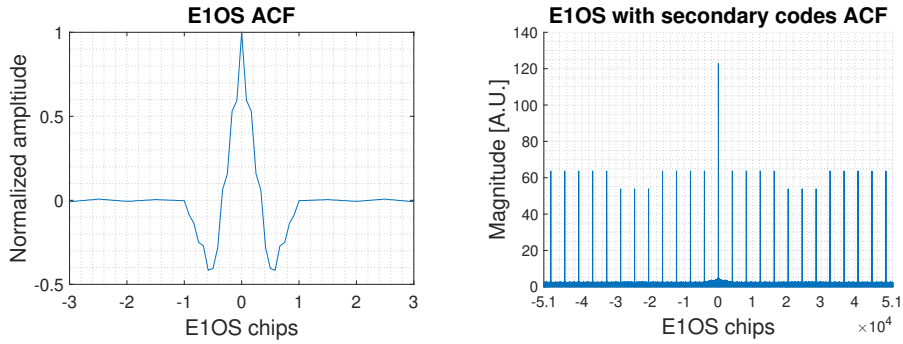

(a) (b)

Figure 2.17: Autocorrelation of the Galileo E1OS signal (a) without using the secondary codes and (b) using the secondary codes.

Galileo E5

The Galileo E5 signal is an AltBOC with constant power envelope (see the I/Q diagram in Fig. 2.12d) and its construction is shown in Fig. 2.18. It has 4 ranging codes and 2 data signals

$$\begin{aligned} x_{E5}(t) = & \frac{1}{2\sqrt{2}} \left(e_{E5aI}(t) + j e_{E5aQ}(t)\right) \left(b_1(t) - j b_1\left(t - t_b^{E5}/4\right)\right) \\ & + \frac{1}{2\sqrt{2}} \left(e_{E5bI}(t) + j e_{E5bQ}(t)\right) \left(b_1(t) + j b_1\left(t - t_b^{E5}/4\right)\right) \\ & + \frac{1}{2\sqrt{2}} \left(\bar{e}_{E5aI}(t) + j \bar{e}_{E5aQ}(t)\right) \left(b_2(t) - j b_2\left(t - t_b^{E5}/4\right)\right) \\ & + \frac{1}{2\sqrt{2}} \left(\bar{e}_{E5bI}(t) + j \bar{e}_{E5bQ}(t)\right) \left(b_2(t) + j b_2\left(t - t_b^{E5}/4\right)\right), \end{aligned} \tag{2.15}$$

where $t_b^{E5} = 1/15.345$ MHz is the period of the subcarrier frequencies, and with

$$\begin{aligned} e_{E5aI}(t) &= C_{E5aI}(t)\, d_{E5aI}(t), & \bar{e}_{E5aI}(t) &= e_{E5aQ}(t)\, e_{E5bI}(t)\, e_{E5bQ}(t), \\ e_{E5aQ}(t) &= C_{E5aQ}(t), & \bar{e}_{E5aQ}(t) &= e_{E5aI}(t)\, e_{E5bI}(t)\, e_{E5bQ}(t), \\ e_{E5bI}(t) &= C_{E5bI}(t)\, d_{E5bI}(t), & \bar{e}_{E5bI}(t) &= e_{E5bQ}(t)\, e_{E5aI}(t)\, e_{E5aQ}(t), \\ e_{E5bQ}(t) &= C_{E5bQ}(t), & \bar{e}_{E5bQ}(t) &= e_{E5bI}(t)\, e_{E5aI}(t)\, e_{E5aQ}(t), \end{aligned} \tag{2.16}$$

and where $b_1(t)$ and $b_2(t)$ are the subcarrier functions

$$b_1(t) = \sum_i \alpha \sqcap\!\sqcup \left(t - i t_b^{E5}/8\right), \tag{2.17a}$$

$$b_2(t) = \sum_i \beta \sqcap\!\sqcup \left(t - i t_b^{E5}/8\right), \tag{2.17b}$$

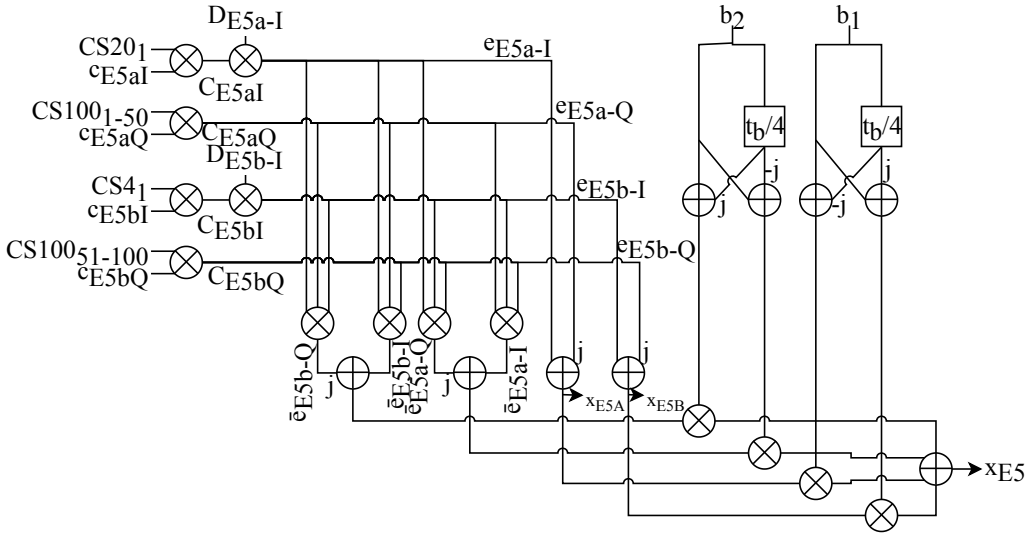

Figure 2.18: Generation of the Galileo signals E5 AltBOC, E5A and E5B.

where $\sqcap\!\sqcup(t)$ is a unitary pulse for $0 < t < t_b^{E5}$, and the coefficients α and β are given in Table 2.6. Equation 2.15 can also be expressed with the quadrate phase components as

$$\Re\{x_{E5}(t)\} = \frac{1}{2\sqrt{2}}\left[b_1(t)\left(e_{E5aI}(t) + e_{E5bI}(t)\right) + b_1\left(t - t_b^{E5}/4\right)\left(e_{E5aQ}(t) - e_{E5bQ}(t)\right)\right.$$
$$\left. + b_2(t)\left(\bar{e}_{E5aI}(t) + \bar{e}_{E5bI}(t)\right) + b_2\left(t - t_b^{E5}/4\right)\left(\bar{e}_{E5aQ}(t) - \bar{e}_{E5bQ}(t)\right)\right], \tag{2.18a}$$

$$\Im\{x_{E5}(t)\} = \frac{1}{2\sqrt{2}}\left[b_1(t)\left(e_{E5aQ}(t) + e_{E5bQ}(t)\right) + b_1\left(t - t_b^{E5}/4\right)\left(-e_{E5aI}(t) + e_{E5bI}(t)\right)\right.$$
$$\left. + b_2(t)\left(\bar{e}_{E5aQ}(t) + \bar{e}_{E5bQ}(t)\right) + b_2\left(t - t_b^{E5}/4\right)\left(-\bar{e}_{E5aI}(t) + \bar{e}_{E5bI}(t)\right)\right]. \tag{2.18b}$$

The subcarriers and an example of in-phase and quadrature E5 signal are plotted in Fig. 2.19. Note that when one of the components has zero amplitude, the other one has an amplitude of 1 or -1.

The ACF obtained by using as correlation length, the duration of the primary code is shown in Fig. 2.20a. If the length is extended so as to include the secondary codes, the ACF changes as in Fig. 2.20b. Note that the power of the peak has increased by 61 dB.

Table 2.6: Galileo E5 AltBOC sub-carrier coefficients.

i	**0**	**1**	**2**	**3**	**4**	**5**	**6**	**7**
2α	$\sqrt{(2)}+1$	1	-1	$-\sqrt{(2)}-1$	$-\sqrt{(2)}-1$	-1	1	$\sqrt{(2)}+1$
2β	$-\sqrt{(2)}+1$	1	-1	$\sqrt{(2)}-1$	$\sqrt{(2)}-1$	-1	1	$-\sqrt{(2)}+1$

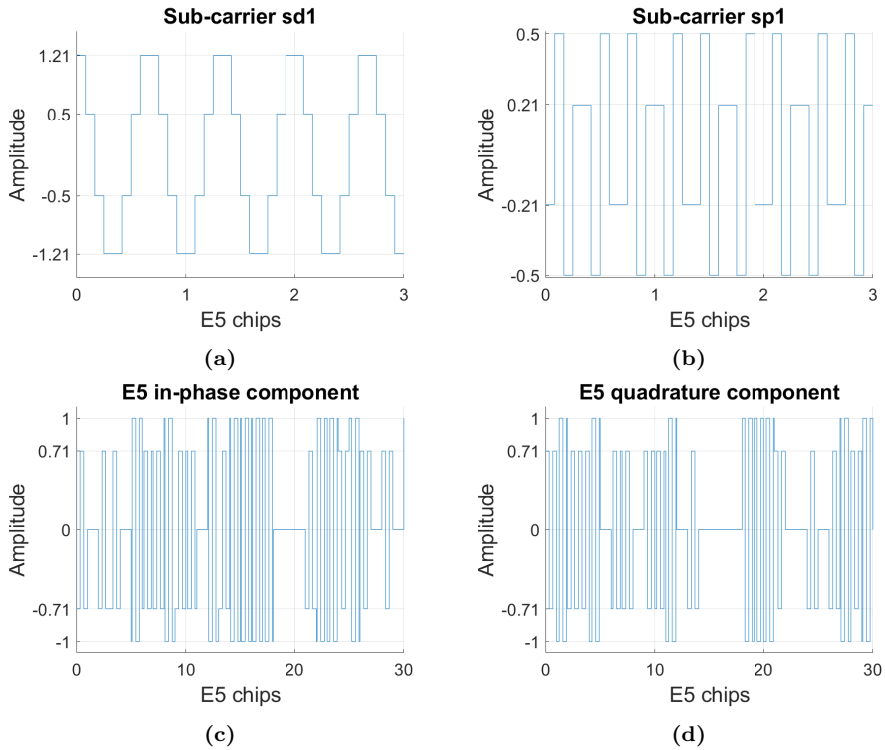

Figure 2.19: BOC subcarriers for the E5 signal: (a) subcarrier sd1, (b) subcarrier sp1, (c) example of a modulated E5 in-phase component, and (d) example of a modulated E5 quadrature component.

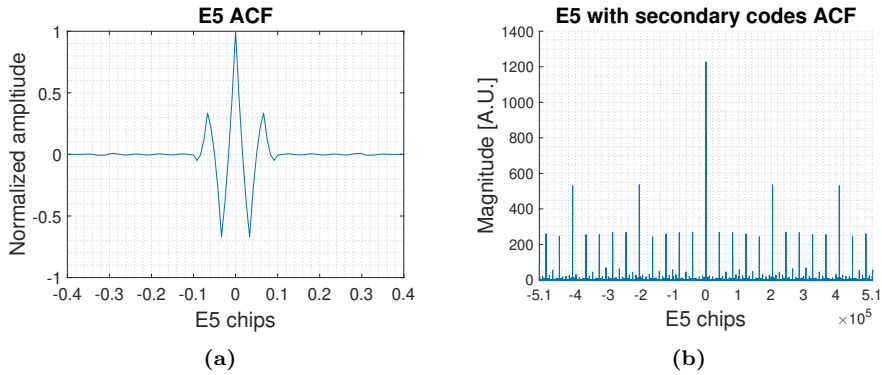

Figure 2.20: Autocorrelation of the Galileo E5 signal (a) without using the secondary codes and (b) using the secondary codes.

2.6 Signals spectrum

The spectrum of the GNSS signal given in (2.1) is

$$S_x(f) = |X(f)|^2, \tag{2.19}$$

where $X(f)$ is the Fourier transform of $x(t)$. The spectrum of the BPSK/QPSK modulations (used in GPS L1 C/A, L2C, L5; BeiDou-2 B2, B1, B3; and Galileo E6CS signals) is given by the well-known equation

$$S_{BPSK}(f) = \frac{f_r^2}{(\pi f)^2} \sin^2\left(\frac{\pi f}{f_r}\right), \tag{2.20}$$

or alternatively by

$$S_{BPSK}(f) = \operatorname{sinc}^2\left(\frac{f}{f_r}\right). \tag{2.21}$$

The equation describing the spectrum of the BOC-based modulations is different for the sine-phased than for the cosine-phased subcarriers [16]. In the cosine case, it is also different for the odd than for the even ratios between the chip and subcarrier rates [16]. For the signals that contain different BOC modulations, the spectrum is the addition of them properly weighted. For the sine BOC (BOCs) modulations (used in GPS L1CI, L1CQ, L1M, L2M, E1OS; and BeiDou-2 B1 future, and B1-C future signals), the spectrum is given by

$$S_{BOC_s(n,m)}(f) = \frac{f_r}{(\pi f)^2} \sin^2\left(\frac{\pi f}{f_r}\right) \tan^2\left(\frac{\pi f}{2f_b}\right), \tag{2.22}$$

or alternatively by

$$S_{BOC_s(n,m)}(f) = \frac{1}{f_r} \operatorname{sinc}^2\left(\frac{f}{f_r}\right) \tan^2\left(\frac{\pi f}{2f_b}\right), \tag{2.23}$$

where $f_r = m \cdot 1.023$ MHz and $f_b = n \cdot 1.023$ MHz. For the cosine BOC (BOCc) with m/n being an even number, the spectrum is

$$S_{BOC_c^e(n,m)}(f) = \frac{f_r}{(\pi f)^2} \left[\frac{2\sin\left(\frac{\pi f}{f_r}\right) \sin^2\left(\frac{\pi f}{4f_b}\right)}{\cos\left(\frac{\pi f}{2f_b}\right)}\right]^2, \tag{2.24}$$

or alternatively

$$S_{BOC_c^e(n,m)}(f) = \frac{1}{f_r} \left[\frac{2\operatorname{sinc}\left(\frac{f}{f_r}\right) \sin^2\left(\frac{\pi f}{4f_b}\right)}{\cos\left(\frac{\pi f}{2f_b}\right)}\right]^2. \tag{2.25}$$

If the ratio is odd, the spectrum changes to

$$S_{BOC_c^o(n,m)}(f) = \frac{f_r}{(\pi f)^2}\left[\frac{2\cos\left(\frac{\pi f}{f_r}\right)\sin^2\left(\frac{\pi f}{4f_b}\right)}{\cos\left(\frac{\pi f}{2f_b}\right)}\right]^2 \tag{2.26}$$

For the modified AltBOC with an odd rate (used in Galileo E5 and BeiDou-2 B2 future signals), the spectrum is given by

$$\begin{aligned} &S_{AltBOC(n,m)}(f) \\ &= \frac{f_r}{(\pi f)^2} 4\cos^2\left(\frac{\pi f}{f_r}\right)\frac{\cos^2\left(\frac{\pi f}{2f_b}\right) - \cos\left(\frac{\pi f}{2f_b}\right) - 2\cos\left(\frac{\pi f}{2f_b}\right)\cos\left(\frac{\pi f}{4f_b}\right) + 2}{\cos^2\left(\frac{\pi f}{2f_b}\right)}. \end{aligned} \tag{2.27}$$

Figure 2.21 shows the spectrum of each GNSS signal, together with the *composite* signal, defined as the addition of all the signals of a given system within a band. For example the composite GPS L1 signal of the old satellites is the addition of the C/A, P and M services, but for the new satellites, the composite signal also contains the C service. The spectra are weighted to a composite signals of 1 Watt. The power ratios between services are obtained from the ICDs [13–15, 19, 20] and summarized in Tables A.1 and A.2. Red dashed lines indicate the theoretical transmitted bandwidth given by the ICDs.

Note that the energy of the signals is allocated in the frequency domain so as to reduce the interference between other signals (see [8] for a detailed study in the GNSS-R scope). Figures 2.21n, 2.21o and 2.21p compares the composite signals of each signal (GPS, Galileo and BeiDou-2) in three different bands using the minimum expected power on the Earth's surface as given in the ICDs. The former figure also shows the DME carriers position, as they are critical in some GNSS-Rs techniques [9].

2.7 Conclusions

This chapter introduced PRNs and the modulations used in the GNSS signals. Detailed information can be found in the literature as well as in books such as [21–26]. The theory given here in used in Chapter 4 to find analytical expressions of the ACFs, in Chapter 5 to study the height precision of each signal. Finally, Chapter 8 shows possible architectures to generate the clean replicas in Field Programmable Gate Arrays (FPGAs).

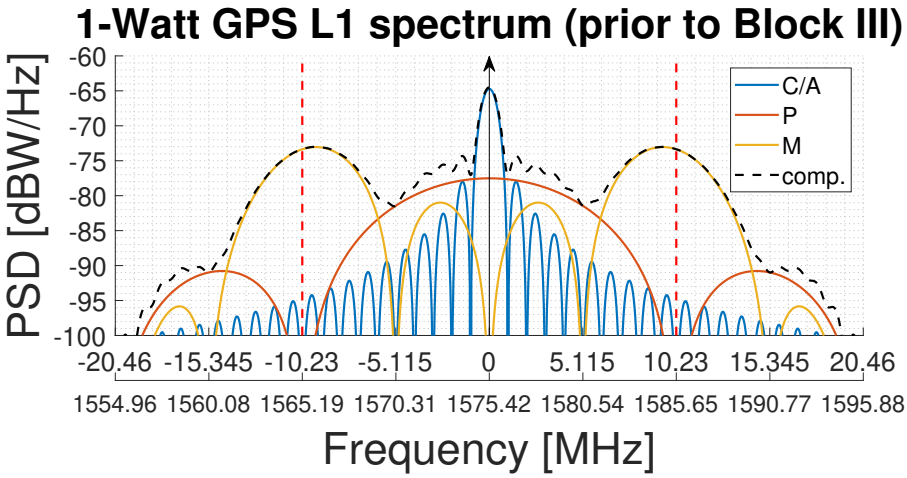
1-Watt GPS L1 spectrum (prior to Block III)
PSD [dBW/Hz]
-60
-65
-70
-75
-80
-85
-90
-95
-100
C/A
P
M
comp.
-20.46 -15.345 -10.23 -5.115 0 5.115 10.23 15.345 20.46
1554.96 1560.08 1565.19 1570.31 1575.42 1580.54 1585.65 1590.77 1595.88
Frequency [MHz]

(a)

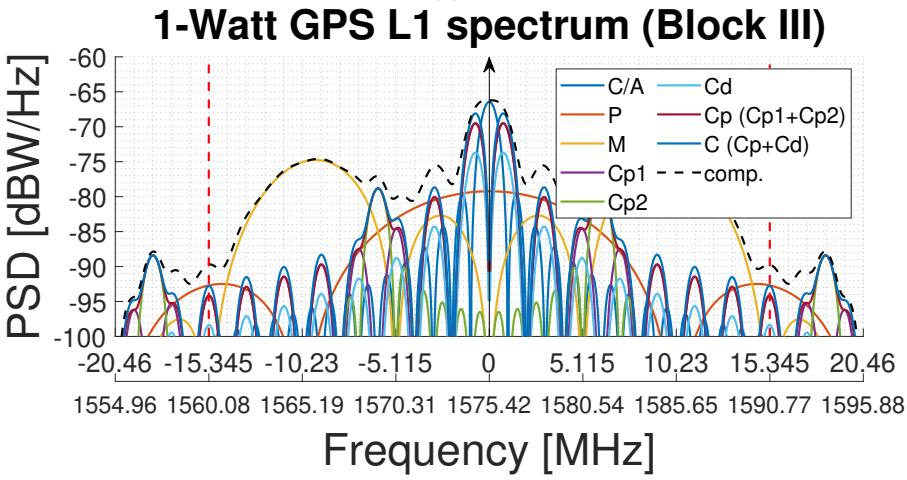
1-Watt GPS L1 spectrum (Block III)
PSD [dBW/Hz]
-60
-65
-70
-75
-80
-85
-90
-95
-100
C/A
P
M
Cp1
Cp2
Cd
Cp (Cp1+Cp2)
C (Cp+Cd)
comp.
-20.46 -15.345 -10.23 -5.115 0 5.115 10.23 15.345 20.46
1554.96 1560.08 1565.19 1570.31 1575.42 1580.54 1585.65 1590.77 1595.88
Frequency [MHz]

(b)

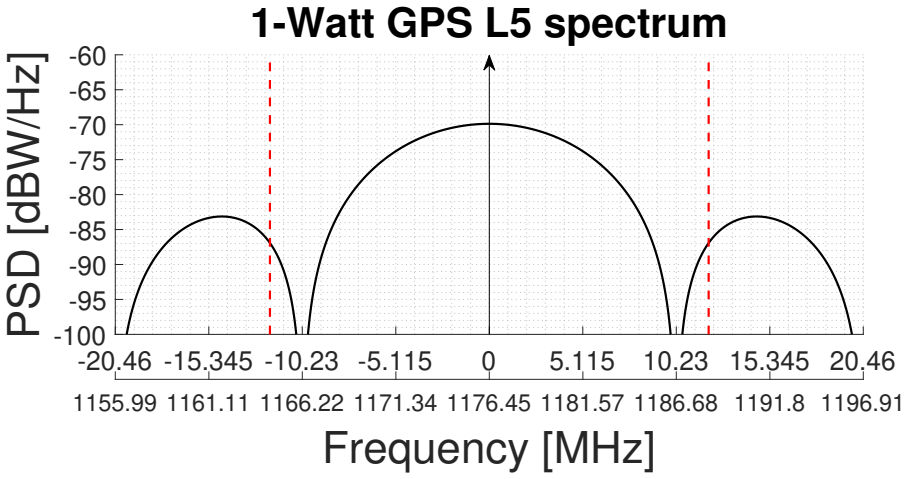
1-Watt GPS L5 spectrum
PSD [dBW/Hz]
-60
-65
-70
-75
-80
-85
-90
-95
-100
-20.46 -15.345 -10.23 -5.115 0 5.115 10.23 15.345 20.46
1155.99 1161.11 1166.22 1171.34 1176.45 1181.57 1186.68 1191.8 1196.91
Frequency [MHz]

(c)

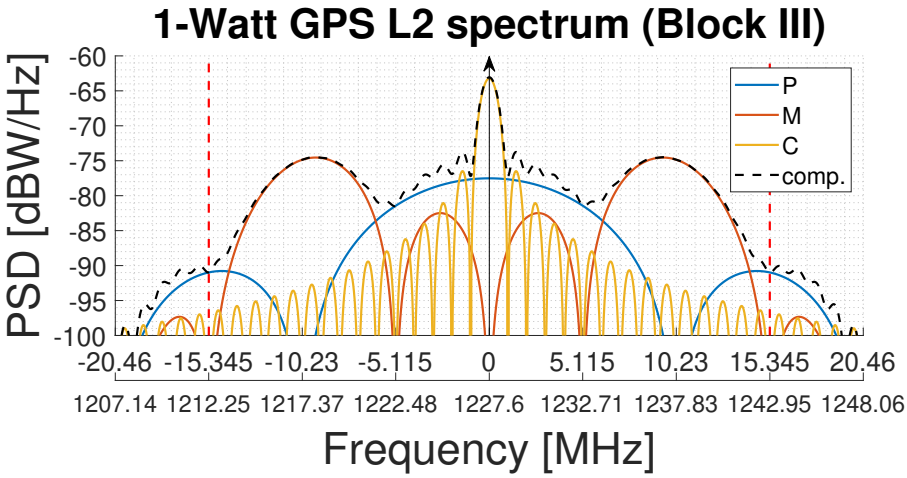
1-Watt GPS L2 spectrum (Block III)
PSD [dBW/Hz]
-60
-65
-70
-75
-80
-85
-90
-95
-100
P
M
C
comp.
-20.46 -15.345 -10.23 -5.115 0 5.115 10.23 15.345 20.46
1207.14 1212.25 1217.37 1222.48 1227.6 1232.71 1237.83 1242.95 1248.06
Frequency [MHz]

(d)

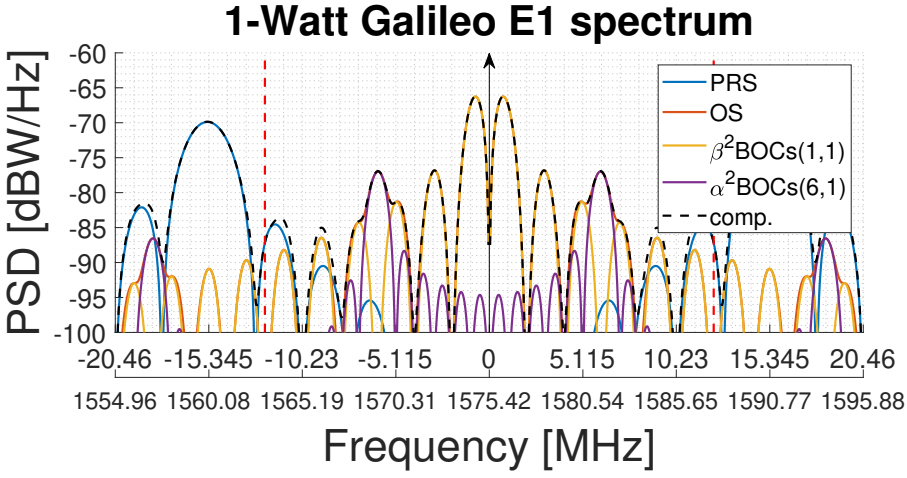
1-Watt Galileo E1 spectrum
PSD [dBW/Hz]
-60
-65
-70
-75
-80
-85
-90
-95
-100
PRS
OS
β^2BOCs(1,1)
α^2BOCs(6,1)
comp.
-20.46 -15.345 -10.23 -5.115 0 5.115 10.23 15.345 20.46
1554.96 1560.08 1565.19 1570.31 1575.42 1580.54 1585.65 1590.77 1595.88
Frequency [MHz]

(e)

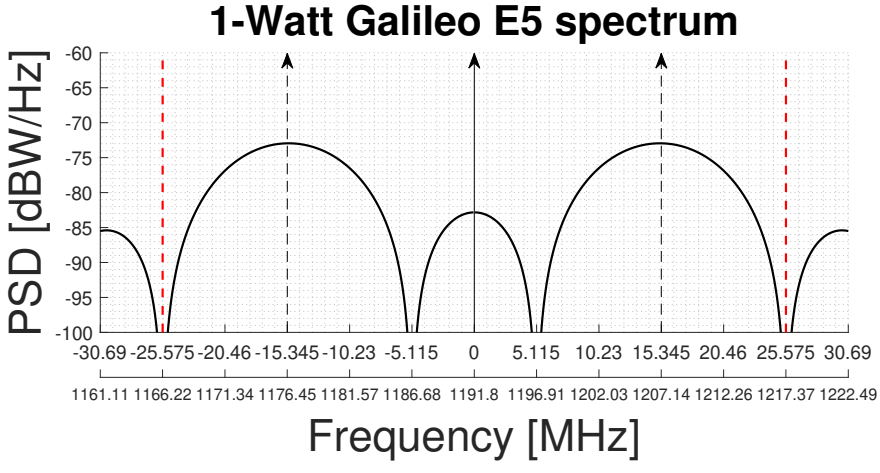
1-Watt Galileo E5 spectrum
PSD [dBW/Hz]
-60
-65
-70
-75
-80
-85
-90
-95
-100
-30.69 -25.575 -20.46 -15.345 -10.23 -5.115 0 5.115 10.23 15.345 20.46 25.575 30.69
1161.11 1166.22 1171.34 1176.45 1181.57 1186.68 1191.8 1196.91 1202.03 1207.14 1212.26 1217.37 1222.49
Frequency [MHz]

(f)

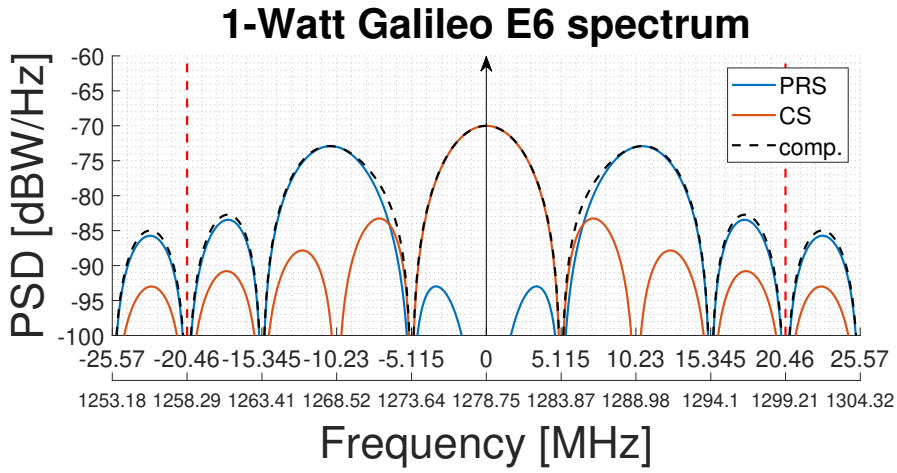
1-Watt Galileo E6 spectrum
PSD [dBW/Hz]
-60
-65
-70
-75
-80
-85
-90
-95
-100
PRS
CS
comp.
-25.57 -20.46 -15.345 -10.23 -5.115 0 5.115 10.23 15.345 20.46 25.57
1253.18 1258.29 1263.41 1268.52 1273.64 1278.75 1283.87 1288.98 1294.1 1299.21 1304.32
Frequency [MHz]

(g)

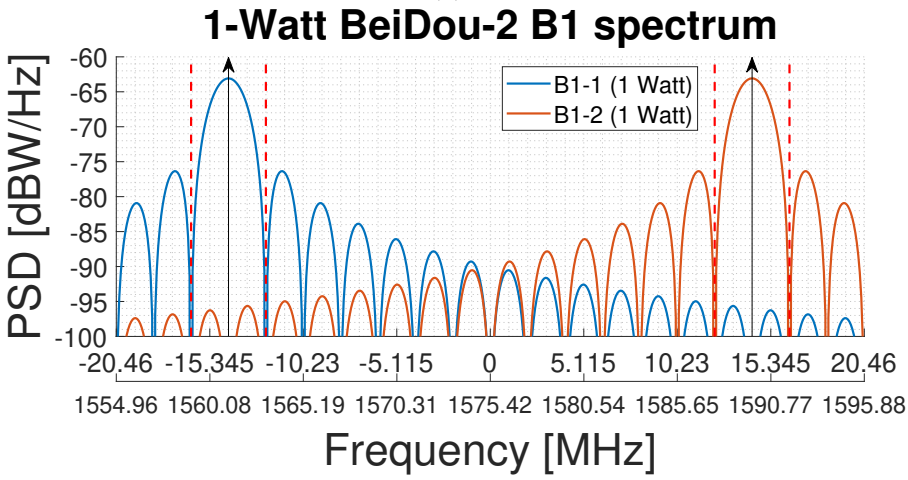
1-Watt BeiDou-2 B1 spectrum
PSD [dBW/Hz]
-60
-65
-70
-75
-80
-85
-90
-95
-100
B1-1 (1 Watt)
B1-2 (1 Watt)
-20.46 -15.345 -10.23 -5.115 0 5.115 10.23 15.345 20.46
1554.96 1560.08 1565.19 1570.31 1575.42 1580.54 1585.65 1590.77 1595.88
Frequency [MHz]

(h)

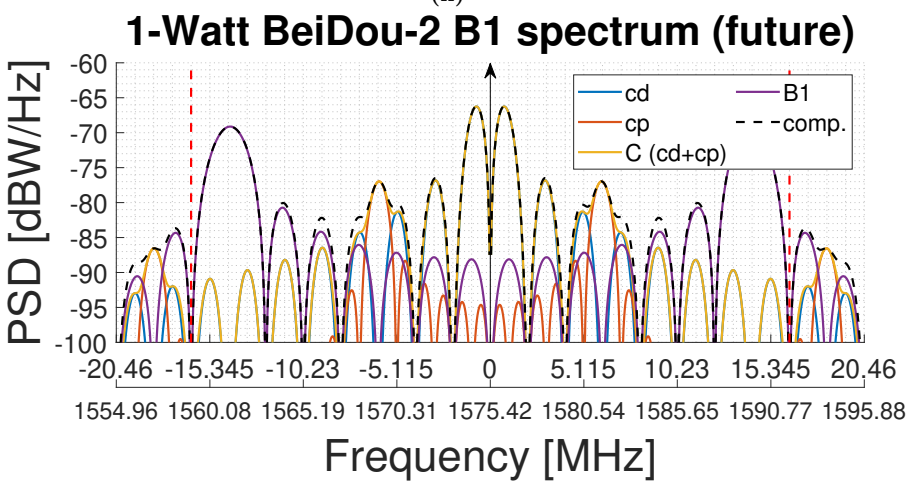
1-Watt BeiDou-2 B1 spectrum (future)
PSD [dBW/Hz]
-60
-65
-70
-75
-80
-85
-90
-95
-100
cd
cp
C (cd+cp)
B1
comp.
-20.46 -15.345 -10.23 -5.115 0 5.115 10.23 15.345 20.46
1554.96 1560.08 1565.19 1570.31 1575.42 1580.54 1585.65 1590.77 1595.88
Frequency [MHz]

(i)

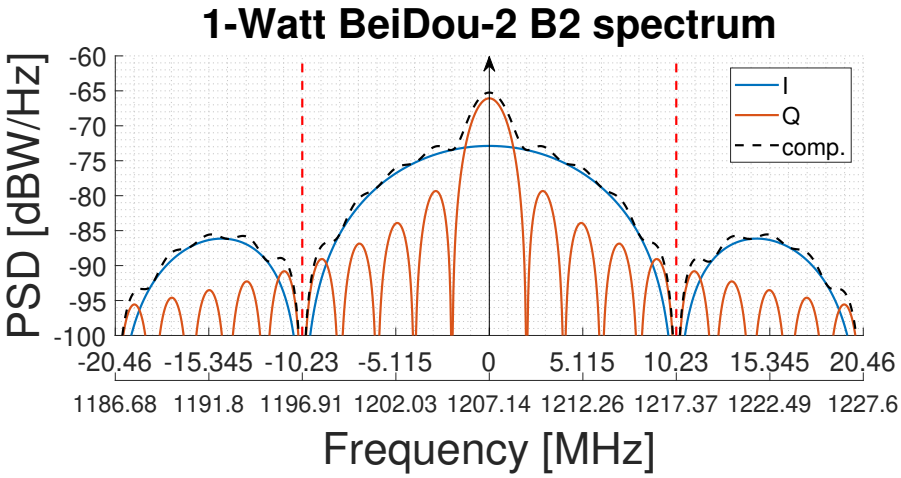
1-Watt BeiDou-2 B2 spectrum
PSD [dBW/Hz]
-60
-65
-70
-75
-80
-85
-90
-95
-100
I
Q
comp.
-20.46 -15.345 -10.23 -5.115 0 5.115 10.23 15.345 20.46
1186.68 1191.8 1196.91 1202.03 1207.14 1212.26 1217.37 1222.49 1227.6
Frequency [MHz]

(j)

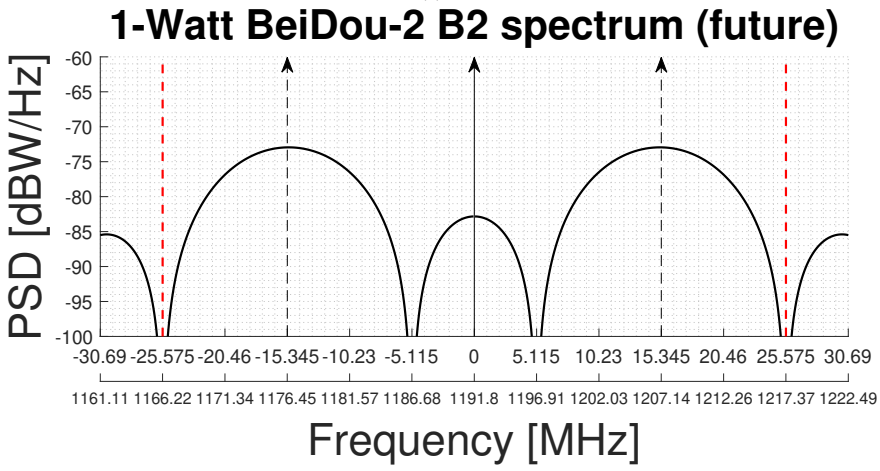
1-Watt BeiDou-2 B2 spectrum (future)
PSD [dBW/Hz]
-60
-65
-70
-75
-80
-85
-90
-95
-100
-30.69 -25.575 -20.46 -15.345 -10.23 -5.115 0 5.115 10.23 15.345 20.46 25.575 30.69
1161.11 1166.22 1171.34 1176.45 1181.57 1186.68 1191.8 1196.91 1202.03 1207.14 1212.26 1217.37 1222.49
Frequency [MHz]

(k)

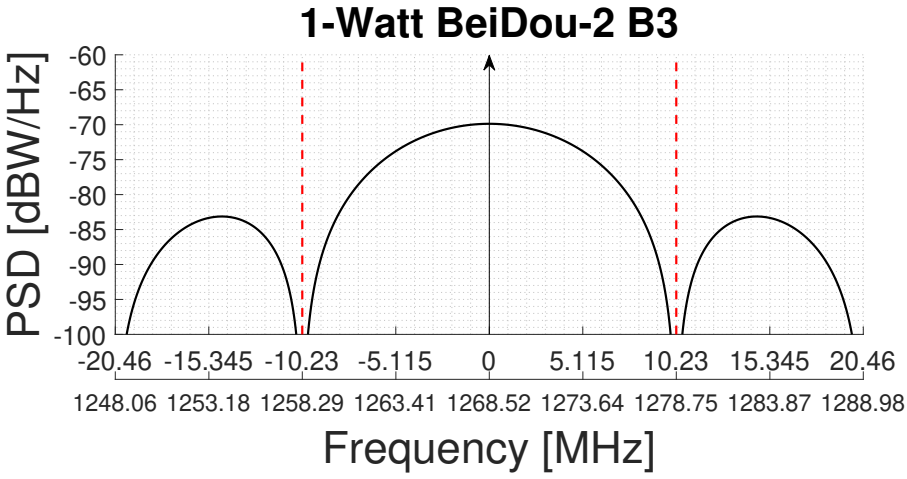
1-Watt BeiDou-2 B3
PSD [dBW/Hz]
-60
-65
-70
-75
-80
-85
-90
-95
-100
-20.46 -15.345 -10.23 -5.115 0 5.115 10.23 15.345 20.46
1248.06 1253.18 1258.29 1263.41 1268.52 1273.64 1278.75 1283.87 1288.98
Frequency [MHz]

(l)

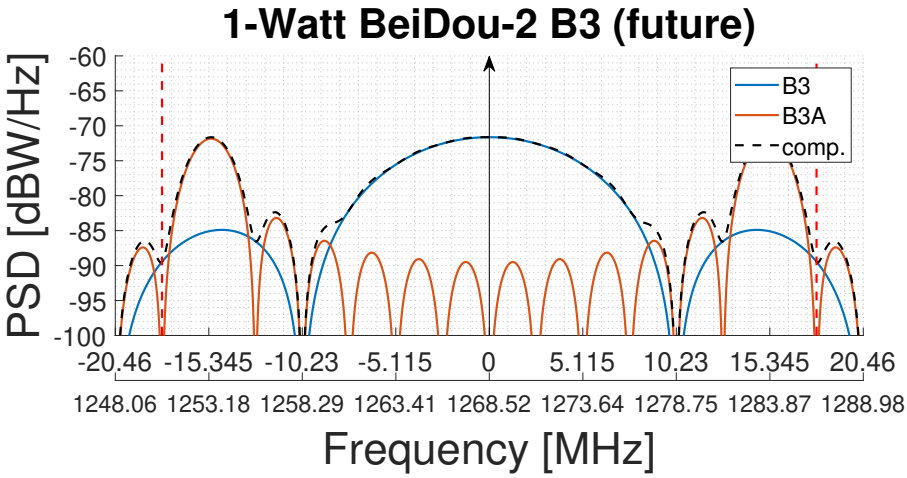
1-Watt BeiDou-2 B3 (future)
PSD [dBW/Hz]
-60
-65
-70
-75
-80
-85
-90
-95
-100
B3
B3A
comp.
-20.46 -15.345 -10.23 -5.115 0 5.115 10.23 15.345 20.46
1248.06 1253.18 1258.29 1263.41 1268.52 1273.64 1278.75 1283.87 1288.98
Frequency [MHz]

(m)

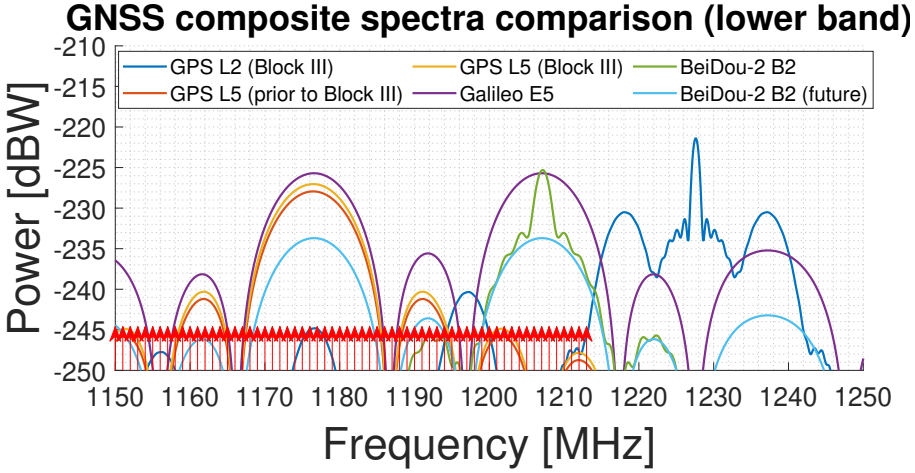
GNSS composite spectra comparison (lower band)
Power [dBW]
-210
-215
-220
-225
-230
-235
-240
-245
-250
GPS L2 (Block III)
GPS L5 (prior to Block III)
GPS L5 (Block III)
Galileo E5
BeiDou-2 B2
BeiDou-2 B2 (future)
1150 1160 1170 1180 1190 1200 1210 1220 1230 1240 1250
Frequency [MHz]

(n)

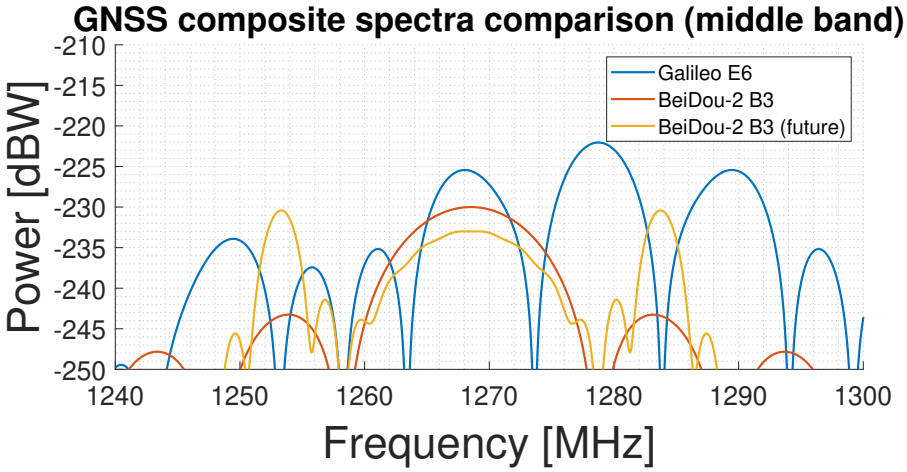
GNSS composite spectra comparison (middle band)
Power [dBW]
-210
-215
-220
-225
-230
-235
-240
-245
-250
Galileo E6
BeiDou-2 B3
BeiDou-2 B3 (future)
1240 1250 1260 1270 1280 1290 1300
Frequency [MHz]

(o)

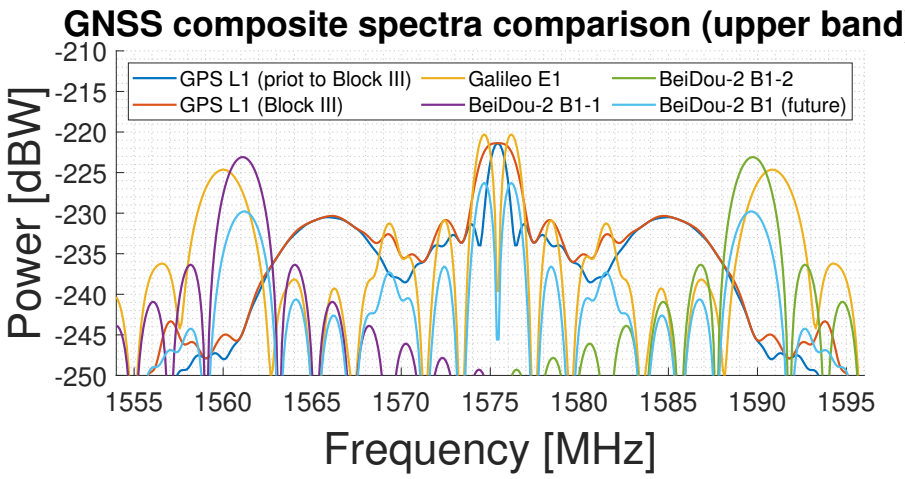

(p)

Figure 2.21: Power Spectral Density (PSD) of the GNSS signals normalized to a composite signal of 1 Watt: (a) GPS L1 band prior to Block III satellites, (b) GPS L1 band for Block III satellites, (c) GPS L5 band, (d) GPS L2 band, (e) Galileo E1 band, (f) Galileo E5 band, (g) Galileo E6 band, (h) BeiDou-2 B1 band, (i) BeiDou-2 future B1 band, (j) BeiDou-2 B2 band, (k) BeiDou-2 future B2 band, (l) BeiDou-2 B3 band, and (m) BeiDou-2 future B3 band; and comparison of GNSS composite spectra weighted by the minimum received powers of each signal: (n) lower band, (o) middle band, and (p) upper band. Red vertical lines indicate the theoretical transmitted bandwidth given by the ICDs. Red arrows show the DME carriers (powerless).

3

Chapter 3

Remote Sensing Using GNSS-R

The GNSS signals have been widely used as opportunity signals in other applications in addition to the original navigation purposes. In the remote sensing field, the refracted GNSS signals in the atmosphere, technique known as GNSS-Radio Occultation (GNSS-RO), or reflected over land and ocean, called GNSS-R, are subjects of topical interest. This chapter explains the latter, by giving background theory, different techniques to obtain the most common observables, examples of applications, and by describing past and existing instruments, focusing always on the ocean altimetry scope.

This chapter does not aim at being an introduction to GNSS-R, but at giving to the reader the minimum background needed to understand the following chapters. The books [26–28], and the article [29] are excellent sources of information with a detailed state-of-the-art of the research done so far in GNSS-R.

3.1 Introduction

The use of reflected GPS signals for scatterometry was first proposed in 1998 [1], and in 1991 a French military aircraft picked them up by accident while testing a GPS receiver [30]. In 1993 the use GNSS-R technique was proposed for ocean mesoscale altimetry in order to reduce the revisit time of satellite altimeters [2]. During the following 30 years, a big effort has been carried out to develop models for the observables, and the feasibility of the GNSS signals has been demonstrated not only for ocean altimetry, but also for sea surface wind speed and direction measurements, to improve the accuracy of sea salinity retrievals, and over land for soil moisture, canopy height, vegetation water content, and ice type and thickness among others.

The feasibility of different retrieval methods for mentioned applications has been demonstrated using signals from different GNSS constellations and bands, in a static position, airborne and balloon platforms, and even form space-borne vehicles. A review of GNSS-R applications, methods, instruments, field campaigns and missions can be found in the articles [29, 31–33], and in the books [26–28].

A GNSS-R instrument receives the signals transmitted by the navigation satellites reflected over a surface of interest, and in some configurations the direct signal as well (see Fig. 1.1a). This configuration is known in radar theory as a bistatic system (or multistatic if more than one transmitting satellite are used), and it is the basis for the reflection model used in GNSS-R. The traditional remote sensing instruments have a strong limitation in terms of the spatial and temporal coverage that the instrument can obtain, being unfeasible to measure a specific process with global coverage and with fast revisit time. On the other hand, an instrument receiving reflected GNSS signals, could track multiple reflection points at the same time, improving the mapping resolution and rate. In addition, GNSS-R technology does not require to build any transmitter, which

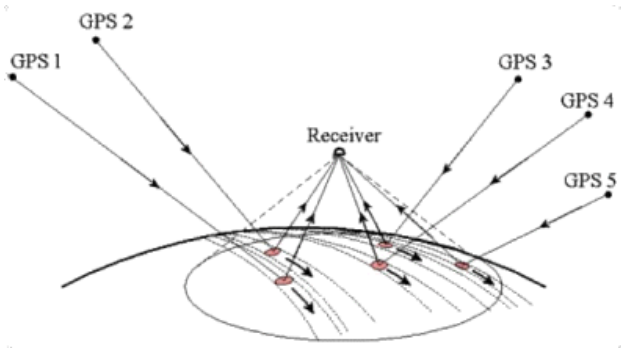

Figure 3.1: GNSS-R mulistastic concept [`http://www.altimetry.info/`]

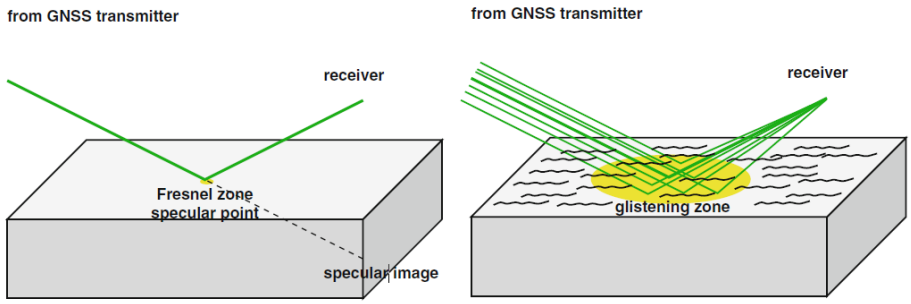

Figure 3.2: Concept of coherent (a) and diffuse (b) scattering. Obtained from [27]

significantly decreases the overall price. Even in some applications, a GNSS-R instrument can be as simple as a commercial GNSS receiver chip. By contrast, the GNSS signals are transmitted with low power and narrow bandwidth, as opposite of dedicated technology, and most of the remote sensing theory developed for each application has to be adjusted to fit with the GNSS-R reflection model.

3.2 Background on scattering theory

The scattering of microwave signals over a surface is a complex process which involves the permittivity, the topography and the roughness of the surface, and the frequency and the incident angle of the signal. General observations related to GNSS-R particularities are given here. Interested readers can continue their learning in books devoted to microwave scattering (e.g. [34, 35]), or in the references given in the aforementioned GNSS-R books.

Two different scattering processes are typically distinguished: specular and diffuse scattering, although in most scenarios, the total scattered power is a combination of the two processes. Both processes are shown in Fig. 3.2. The specular or coherent component dominates over smooth surfaces, while the diffuse or incoherent component dominates when the surface is rough. The simplest models characterize the roughness of a surface from the signal's wavelength and from its incident angle. Advanced models include other factors depending on the surface characteristics.

Before going into the details, it is worth to summarize in Table 3.1 some of the symbols that are used here. Most of the vector terms are referred to the Scattering Reference Frame coordinate system, defined as a 3D Cartesian coordinate system in which the *nominal* specular point lies at the center, and the Z-axis coincides with the geocentric radius vector and is positive onward. For nominal specular, it is understood that is the specular reflection point that can be computed based on the geometry of the system, which may differ a little from the real one, due for example, to the dynamics of the surface in ocean scenarios.

Table 3.1: List of main symbols related to GNSS-R geometry and scattering. See the List of Symbols section for more.

Symbol	Definition	Eq.
$\vec{S}$	Position vector of the specular point in ECEF coordinates.	e.g. [36]
$\vec{\rho}$	Position vector of a reflection point in SRF coordinates.	-
$\vec{T}, \vec{R}$	Position vector of the transmitter and receiver in ECEF or SRF coordinates (given if confusion is to be avoided).	-
$\hat{m}(\vec{\rho}), \hat{n}(\vec{\rho})$	Unitary vectors from a reflection point to the transmitter and to the receiver.	(3.9)
$\hat{q}(\vec{\rho})$	Scattering vector of a reflection point.	(3.15)
θ_e	GNSS satellite elevation angle as seen from the specular point or from another reflection point (depends on the context).	-
τ_{pk}	Delay of the direct signal	(6.1)
τ_r	Delay of the specular signal	(6.2)
$\tau_r(\vec{\rho})$	Delay of a reflected signal	(3.19)
$\tau(\vec{\rho})$	Delay a reglection point wrt specular	(3.7) (flat Earth approx.)
ν_d	Doppler shift of the direct	(6.3)
ν_r	Doppler shift of specular signal	(6.4)
$\nu_r(\vec{\rho})$	Doppler shift of a reflected signal	(3.20)
$f_d(\vec{\rho})$	Doppler shift point wrt specular	(3.8) (detailed in [27])
h_T, h_R	Altitudes of the transmitter and receiver.	e.g. [3]
R_{TS}, R_{SR}	Distance from the transmitter and from the receiver to the specular point	(3.2)
$R_{T\rho}, R_{\rho R}$	Distance from the transmitter and from the receiver to a reflection point.	(3.5)
T_{coh}	Coherent length, or time used to estimate the received power coherently.	Appendix A
λ, f_c	Nominal signal's wavelength and carrier frequency.	Appendix A
$\sigma^0_{pq}(\vec{\rho})$	Radar Cross Section (RCS) of a reflection point with an icident wave at polarization p, and reflecctd wave at polarization q.	KGO: (3.12)
$Y(\tau, \nu)$	Time domain cross-correlation between a signal of interest and a reference one for several Doppler frequencies. The function is called Cross-Ambiguity Function (CAF) if the signal of interest is the direct signal, and is called Delay Doppler Map (DDM) if is the reflected signal.	CAF: (2.3) DDM: (3.16) DDM power models: (3.18) (3.23)
$\chi(\tau, \nu)$	Auto Ambiguity-Function or Ambiguity Function (AF)	(2.5)
$\lvert\chi(\tau, \nu)\rvert^2$	Woodward Ambiguity Function (WAF).	(2.6)
$R_r(\tau)$	AutoCorrelation Function (ACF) of a time-domain function $r(t)$.	(2.7) and Chapter 4

3.2.1 Coherent scattering

In a pure specular reflection scenario, the incident wave is reflected in a single direction. This type of scattering happens over smooth surfaces compared to the signal's wavelength, which for the GNSS signals is around 20 cm (see Tables A.1 and A.2). The reflected wave is created from the contributions from a group of points surrounding the specular one. The basic models state that the points that contribute more to the reflected power, fall inside the area given by the projection of the first Fresnel zone. Although more complex areas are being investigated (e.g [37]).

The Fresnel zones are a series of confocal prolate ellipsoids in space, with the transmitter and mirror image of the receiver as focal points (see Fig. 3.3a). Let $\vec{T}$, $\vec{R}$ be the position vectors of the transmitter and receiver in a three-dimensional Cartesian coordinate system where the specular point S lies at its center. The projection of the Fresnel zones are ellipses with the specular point at the center, and with major and minor axes given by [37]

$$b = \sqrt{n\lambda \frac{R_{TS} R_{SR}}{R_{TS} + R_{SR}}}, \tag{3.1a}$$

$$a = \frac{b}{\sin \theta_e}, \tag{3.1b}$$

where n is the Fresnel zone order, λ is the signal's wavelength, and R_{TS} and R_{SR} are respectively the distances from the transmitter to the specular point, and from the latter to the receiver

$$R_{TS} = |\vec{T} - \vec{S}|, \tag{3.2a}$$

$$R_{SR} = |\vec{S} - \vec{R}|. \tag{3.2b}$$

In GNSS-R scenarios, the transmitter is at a much larger distance to the specular point than the receiver is. Then, the axis of the first Fresnel ellipse can be approximated by

$$b = \sqrt{\frac{\lambda h_R}{\sin \theta_e} + \left(\frac{\lambda}{2 \sin \theta_e} \right)^2}, \tag{3.3}$$

where h_R is the height of the receiver over the plane tangent to the specular point.

The size of the first Fresnel ellipse is a few tens of meters for aircrafts flying at a height below 5 km, and up to 100 meters for aircrafts flying at 10 km. In space-borne vehicles, the ellipse increases up to around 300 m at nadir, and up 1000 km at low elevation angles [27].

The spatial resolution of the coherent component may be larger than the first Fresnel ellipse, as additional power may be received from higher order Fresnel zones when the

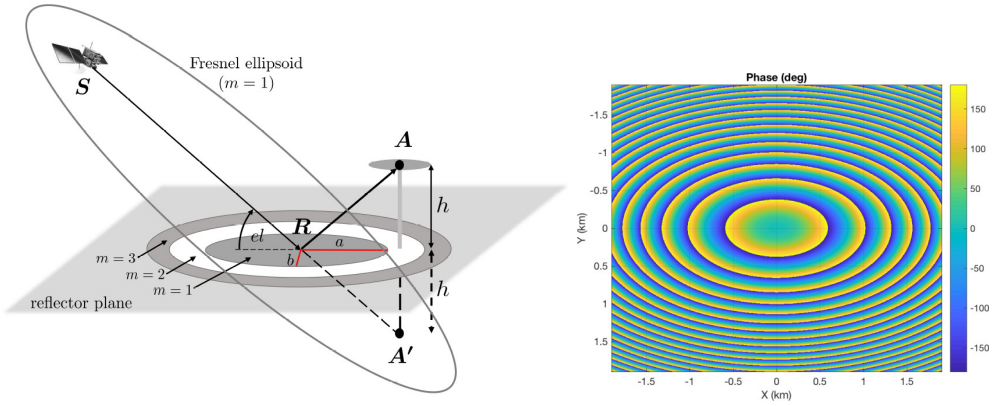

(a) **(b)**

Figure 3.3: (a) definition of the coherent scattering geometry, (b) phase of the reflected field over the surface of the Earth for a CYGNSS geometry with $\theta_e = 40°$. Obtained from [38] and [39] respectively.

scattering area and the antenna footprint are large enough. Higher order Fresnel projections are annular areas that surround the formers but excluding them (see the dark gray and white rings in Fig. 3.3a). The radius of each zone is the distance equivalent to a phase difference of 180° from the specular point (see Fig. 3.3b). The total received coherent power is the integration over these areas. This results in a fluctuation of the reflected coherent power as function of the scattering size because of the constructive or destructive contributions from the Fresnel rings.

Figure 3.4 shows an example of a reflected power evolution as function of the distance to the specular point for different incident angles. As the incident angle increases, the ellipses become larger, which means that the additional coherent energy contribution occurs from distances farther away from the specular reflection point.

A real scenario involves reflections over heterogeneous surfaces in terms of permittivity (see Fig. 3.5). Additionally, the received power is estimated in windows of a given duration (known as coherent length) and sometimes, further averaged in consecutive acquisitions (known as incoherent length). All these factors add additional power oscillations over time. As an anticipated result, Fig. 11.14 shows an example of these power fluctuations obtained from a field campaign. These oscillations must not be confused with those created from the speckle (explained in next section), although identifying the origin of them is not straightforward.

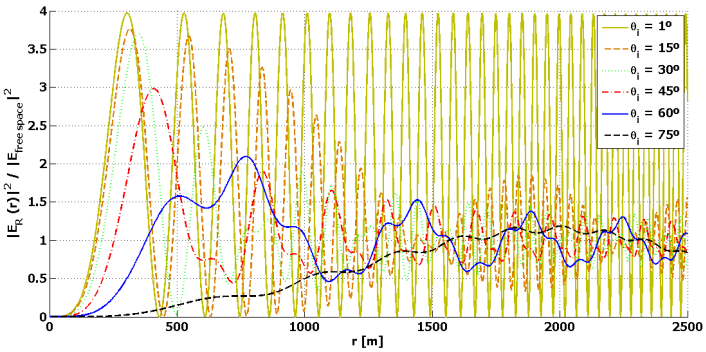

Figure 3.4: Evolution of the received coherent power as function of the distance to the specular point, normalized to the power received in free space and to the Fresnel reflection coefficient. From [37].

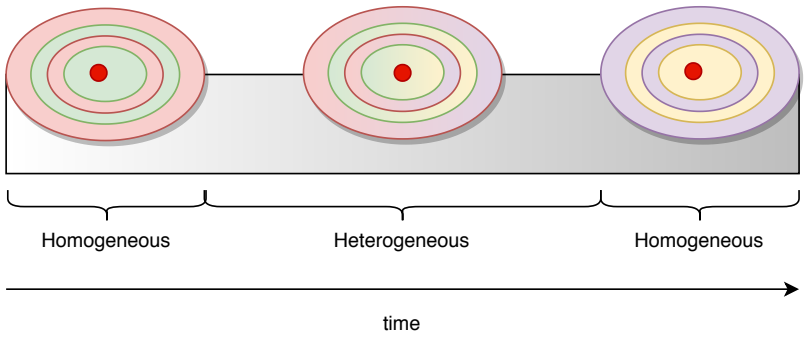

Figure 3.5: Example of the Fresnel zones over homogeneous and heterogeneous surfaces.

3.2.2 Incoherent scattering

In a diffuse scattering scenario, the incident wave is reflected in a broad range of directions. The wave is reflected over the so-called *facets*, which are surface patches whose size and curvature are of the order of signal's wavelength. The orientation of the facets with respect to the transmitter or receiver depends on the roughness of the surface. Only those facets with the proper orientation, will forward the incident wave to the receiver. The total received wave is the coherent addition of all the individual waves, each of which has a different phase. This is where the name of incoherent scattering comes from.

The dynamics of a GNSS-R scenario make that the orientation of the facets with respect the transmitter and receiver change in time randomly, which translates into power fluctuations of the aggregated wave. This effect is known as speckle (or signal fading in communications). Over land or ice surfaces, the change in the orientation of the facets is mainly due to the relative movement between the transmitter, the receiver and the

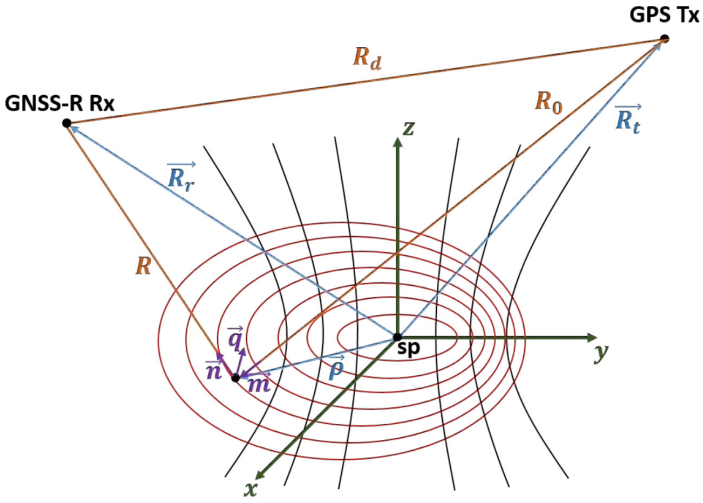

Figure 3.6: Configuration of glistening zone with the iso-Delay (in red), and the iso-Doppler (in black) contours. Note that these symbols are defined differently in the text: $R_0 = R_{T\rho}$, $R = R_{\rho R}$, $\vec{R_r} = \vec{R}$, $\vec{R_t} = \vec{T}$. From [40].

specular point. In the ocean, it is also due to the surface motion.

The area from where appropriate oriented facets exist above a given probability threshold is called the glistening zone. The larger the roughness of the surface, the larger the number of facets and in turn the glistening zone. Facets at a large distance from the specular point require a high slope in order to forward the incident wave to the receiver. Bear in mind, that the spatial resolution also depends on the antenna footprint, that is to say, the projection of the antenna radiation pattern over the surface.

Some glistening zone sizes are given in [27]. From an aircraft flying at 1 km, the size is about 24 m if the elevation angle is 60°, and about 55 m if the elevation angle 30°. For an aircraft at a height of 5 km, the area increases up to 50 m (60°) and 120 m (30°). For an aircraft at 10 km, the sizes are about 80 m (60°) and 170 m (60°). In a LEO satellite at 500 km, the area extends up to 500 m (60°) and 1200 km (30°).

Due to the bistatic geometry of GNSS-R, the wave received from each facet presents a different Doppler and delay. Thus, the glistening area can be divided into zones in which the reflected waves reach the receiver with a similar Doppler and delay. These zones are defined by the so-called iso-delay and iso-Doppler contours [41]. Figure 3.6 presents the geometry that defines the zones, and Fig. 3.7 shows examples of glistening areas for different scenarios.

Similarly to the geometry defined in the last section, let $\vec{T}$, $\vec{R}$ and $\vec{\rho}$ be the position vectors of the transmitter, receiver and reflection point in three-dimensional Cartesian

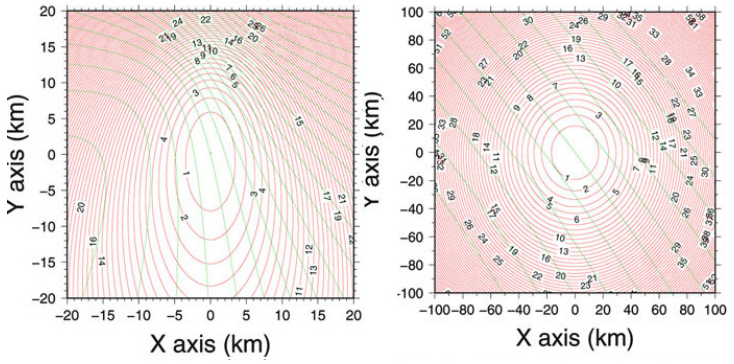

Figure 3.7: Simulated glistening zones for different scenarios: (left) aircraft at 10 km altitude flying at 250 m/s, and GNSS satellite seen with an elevation angle of 30°; (right) LEO satellite at 500 km altitude flying at 7 km/s, and GNSS satellite seen with an elevation angle of 60°. The iso-delay contours are separated by 1 C/A chips (≈300 m), the iso-Dopplers are at intervals of 100 Hz and 1 kHz respectively. The velocity vectors are 45° counter-clockwise from the X-axis. From [27].

coordinate system, where the specular point S lies at its center. The iso-delay contours are defined by the simple equation

$$\frac{R_{T\rho} + R_{\rho R}}{c} = const, \tag{3.4}$$

where c is the speed of light, $R_{T\rho}$ is distance from the transmitter to the point, and $R_{\rho R}$ is the distance from this point to the receiver

$$R_{T\rho} = |\vec{T} - \vec{\rho}|, \tag{3.5a}$$

$$R_{\rho R} = |\vec{\rho} - \vec{R}|. \tag{3.5b}$$

Under the flat Earth approximation, the iso-delay lines become ellipses over the plane in which the projection of the receiver and of the transmitter are the two foci, and specular point is the center. This approximation holds if the receiver has a much larger range than the distance between the reflection points and the specular one, and if the transmitter is at an even larger distance from those points than the receiver is. The major and minor axes of the ellipse passing through the points defined by $\vec{\rho}$, are approximated by [42].

$$a(\vec{\rho}) \approx \frac{\sqrt{2\tau(\vec{\rho})ch \sin\theta_e}}{\sin^2\theta_e}, \tag{3.6a}$$

$$b(\vec{\rho}) \approx \frac{\sqrt{2\tau(\vec{\rho})ch \sin\theta_e}}{\cos\sin_e}, \tag{3.6b}$$

where $\tau(\vec{\rho})$ is the total delay of the reflected signal with respect to specular delay

$$\tau(\vec{\rho}) \approx \frac{1}{c}\left[\sqrt{\rho_x^2 + (\rho_y + h_T \cot\theta_e)^2 + h_T^2} - \rho_y \cos\theta_e - \frac{h_R}{\cos\theta_e}\right], \tag{3.7}$$

where h_T and h_R are respectively the heights of the transmitter and receiver to the tangent plane, θ_e is the elevation angle seen from the specular point, and $\rho_z = 0$.

The iso-Doppler lines are curves of a higher order than hyperbola. In the particular case of a stationary (or quasi-stationary) target, the iso-Doppler curves referred to the Doppler at the specular point are given by

$$f_D(\vec{\rho}) = \frac{1}{\lambda}\left[\vec{T}_v \hat{m}(\vec{\rho}) - \vec{R}_v \hat{n}(\vec{\rho})\right], \tag{3.8}$$

where λ is the signal's wavelength, $\vec{T}_v$ and $\vec{R}_v$ are the velocity vectors of the transmitter and receiver respectively, and $\hat{m}(\vec{\rho})$ and $\hat{n}(\vec{\rho})$ are the unitary vectors from the reflection point to the transmitter and to receiver respectively

$$\hat{m}(\vec{\rho}) = \frac{\vec{\rho} - \vec{T}}{|\vec{\rho} - \vec{T}|}, \tag{3.9a}$$

$$\hat{n}(\vec{\rho}) = \frac{\vec{\rho} - \vec{R}}{|\vec{\rho} - \vec{R}|}. \tag{3.9b}$$

Due to the particularities of the GNSS-R processing (see Sec. 3.3), the Doppler areas are filtered by the sinc-exponential function [27]

$$\mathrm{sinc}(f_d T_{coh}) \exp^{-j\pi f_d T_{coh}}, \tag{3.10}$$

where T_{coh} is the coherent integration length. Thus, (3.8) should be rewritten as

$$f_D(\vec{\rho}) \pm \frac{1}{T_{coh}} = \frac{1}{\lambda}\left[\vec{T}_v \hat{m}(\vec{P}) - \vec{R}_v \hat{n}(\vec{P})\right]. \tag{3.11}$$

In [43], the impact of the Doppler of the target where analyzed using real space-borne data from the TDS-1 mission. For the flat Earth approximation, the iso-Doppler lines become hyperbolae. The equations are given in [27].

3.2.3 Scattering models

Tens of models have been developed in order to characterize the microwave scattering problem. Each model is valid under certain conditions involving the system geometry, the surface type and its time evolution, and the signal's wavelength, polarization and incident angle. Besides, the feasibility of using such models on actual research, depends on their computation requirements in terms of resources and time.

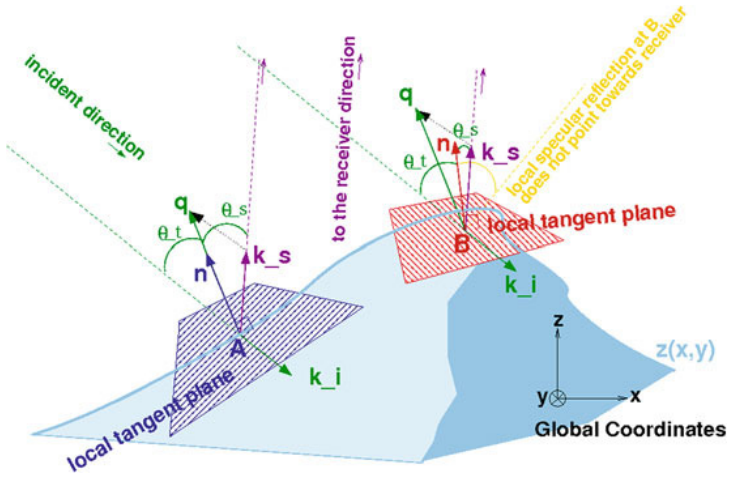

Figure 3.8: Concept of the KGO scattering model. Not that next symbols are defined differently in the text: $\mathbf{k_i} = -\hat{m}(\vec{\rho})$,$\mathbf{k_s} = \hat{n}(\vec{\rho})$. Not also that here, $\mathbf{n}$ is the normal vector of the plane tangent to a reflection point, which is not defined in the text. From [27]

Space-borne GNSS-R is a bistatic system in which the receiver is far away from the surface, in the so-called far zone. This means that the distance between the specular point and the receiver is much larger than the scattering area. The typical reflection model used in ocean GNSS-R scenarios is based on the Kirchhoff approximation. For land surfaces, the models are more complex, as there are more parameters involved (e.g. [44]). Some comments on these surfaces will be given in the course of this section.

In the general Kirchhoff approach, the reflection over each facet is considered to be locally specular, as it would happen if there was an plane tangent over the surface integration point. This means that the reflected wave depends only on the Fresnel coefficient of that point, and excludes local diffraction effects. This approximation is valid if the curvature of the facets is much larger than the signal's wavelength.

3.2.3.1 Kirchhoff Approach under Geometrical Optics model

In most of the GNSS-R literature, the Kirchhoff approach is further simplified with the stationary-Phase approximation, also known as Kirchhoff Approach under Geometrical Optics (KAGO) approximation or just KGO. This model assumes that the phase of the reflected wave is constant within the integration surface. Physically, this means that the only waves reaching the receiver, are those reflected in the facets in which the normal vector of the respective tangent plane, corresponds to the bisector angle between the incident and elevation angles. In other terms, the KGO holds when the incident and scattered angles are the same. Figure 3.8 shows the concept of the model.

The reflected power is expressed with the bistatic Radar Cross-Section (RCS). Under the KGO model, is given by

$$\sigma_{pq}^{0}\left(\vec{\rho}\right) = \pi k^2 |\Re_{pq}|^2 \frac{q^2}{q_z^2} P\left(Z_x, Z_y\right), \tag{3.12}$$

where

- $k = 2\pi/\lambda$ is the electromagnetic wave number.
- $\Re_{pq}$ is the Fresnel reflection coefficient for an incident wave with polarization q and a scattered wave with polarization p [41]

$$\Re_{RR} = \Re_{LL} = \frac{\Re_{VV} + \Re_{HH}}{2}, \tag{3.13a}$$

$$\Re_{RL} = \Re_{LR} = \frac{\Re_{VV} - \Re_{HH}}{2}, \tag{3.13b}$$

  where

$$\Re_{VV} = \frac{\epsilon_r \sin\left(\theta_e\right) - \sqrt{\epsilon_r - \cos^2\left(\theta_e\right)}}{\epsilon_r \sin\left(\theta_e\right) + \sqrt{\epsilon_r - \cos^2\left(\theta_e\right)}}, \tag{3.14a}$$

$$\Re_{HH} = \frac{\sin\left(\theta_e\right) - \sqrt{\epsilon_r - \cos^2\left(\theta_e\right)}}{\sin\left(\theta_e\right) + \sqrt{\epsilon_r - \cos^2\left(\theta_e\right)}}, \tag{3.14b}$$

  where the subscripts R, L, V, H denote respectively Right Hand Circular Polarization (RHCP), Left Hand Circular Polarization (LHCP), linear vertical polarization, and linear horizontal polarization; ϵ_r is the complex dielectric constant or permittivity of the medium relative to vacuum. Note that here, θ_e is the local elevation angle. Note also that these two latter equations hold when the incident and reflection angles are the same, as is one of the consequences of the KGO model.
- $q = |\vec{q}|$ is the modulus of the scattering vector

$$\vec{q}(\vec{\rho}) = k\left(\hat{n}\left(\vec{\rho}\right) - \hat{m}\left(\vec{\rho}\right)\right) \tag{3.15}$$

- $P\left(Z_x, Z_y\right)$ is the two-dimensional PDF of the large-scale (larger than several radio wavelengths) surface slopes. In [41] the PDF is assumed to be Gaussian. The slope variances and the correlation factor between them, depend on the wind speed among other parameters.

In essence, the RCS tells about the power of the scattered waves at a given direction for each polarization. The GNSS signals are transmitted at circular polarization, specifically RHCP, in order to avoid the ionospheric effects (i.e. Faraday rotation). Note that only

when the permittivity and the elevation angle are both small, most of the power is reflected in RHCP, while being mostly LHCP in any other configuration.

The permittivity depends on the physical properties of the medium, on the temperature, and on the frequency of the signal. In the literature, there are tens of empirical models for the permittivity of different types of medium (e.g. [34]). Although the KGO model was defined for ocean reflections, the models used for reflections in other type of surfaces, also include the medium permittivity in one way on another. Figure 3.9 shows the permittivity for some of these of surfaces. Bear in mind that the GNSS frequencies are transmitted at L-band, between 1.2 GHz and 1.5 GHz (see Tables A.1 and A.2).

The general idea is that the wetter the medium, the larger permittivity. For sea water, it depends on the salt concentration and on the temperature. The values at L-band, at typical sea surface temperatures, are between 60-70. These numbers are among the highest in natural occurring surfaces. In fact, the ocean reflections are mostly LHCP, even for low elevation angles. For ice surfaces, the permittivity depends on the ice age, and is around 3. For snow areas, the permittivity depends on the snow density, and the values are below 3. Over soils, it depends on the soil moisture, and it can be between 3 and 35. This large dynamic range allows the use of the GNSS-R signals for soil moisture estimation.

In a real scenario, the surfaces are heterogeneous, and thus the permittivity is a complex combination of different materials. As examples, the soil moisture in land surfaces can dramatically change between close points, and the foam on the sea surface has a permittivity different to that of the water.

3.2.3.2 Other models

The KAGO model fits well for forward scattering around the specular direction, when the polarization of the reflected wave is LHCP and when the incidence is much larger than the grazing angle. However, the model fails to predict the reflected power at other angles or at the RHCP (see for example an study on the polarimetric capabilities of GNSS-R over ocean in [45]). This latter consequence takes place because the diffraction effects have been neglected.

The Kirchhoff Model Under the Physical Optics Approximation (KPO), is another simplification of the general Kirchhoff approach. Unlike the KAGO, this model predicts a coherent component, but it can only be used for small slopes and sea roughness.

The Small Perturbation Method (SPM) or the Small Slope Approximation (SSA) models are the most appropriate models for polarimetric studies. The former can only be used when the surface correlation length is smaller than the signal's wavelength. The latter is only valid when the slopes of the roughness are small compared to the incidence and scattering angles [46].

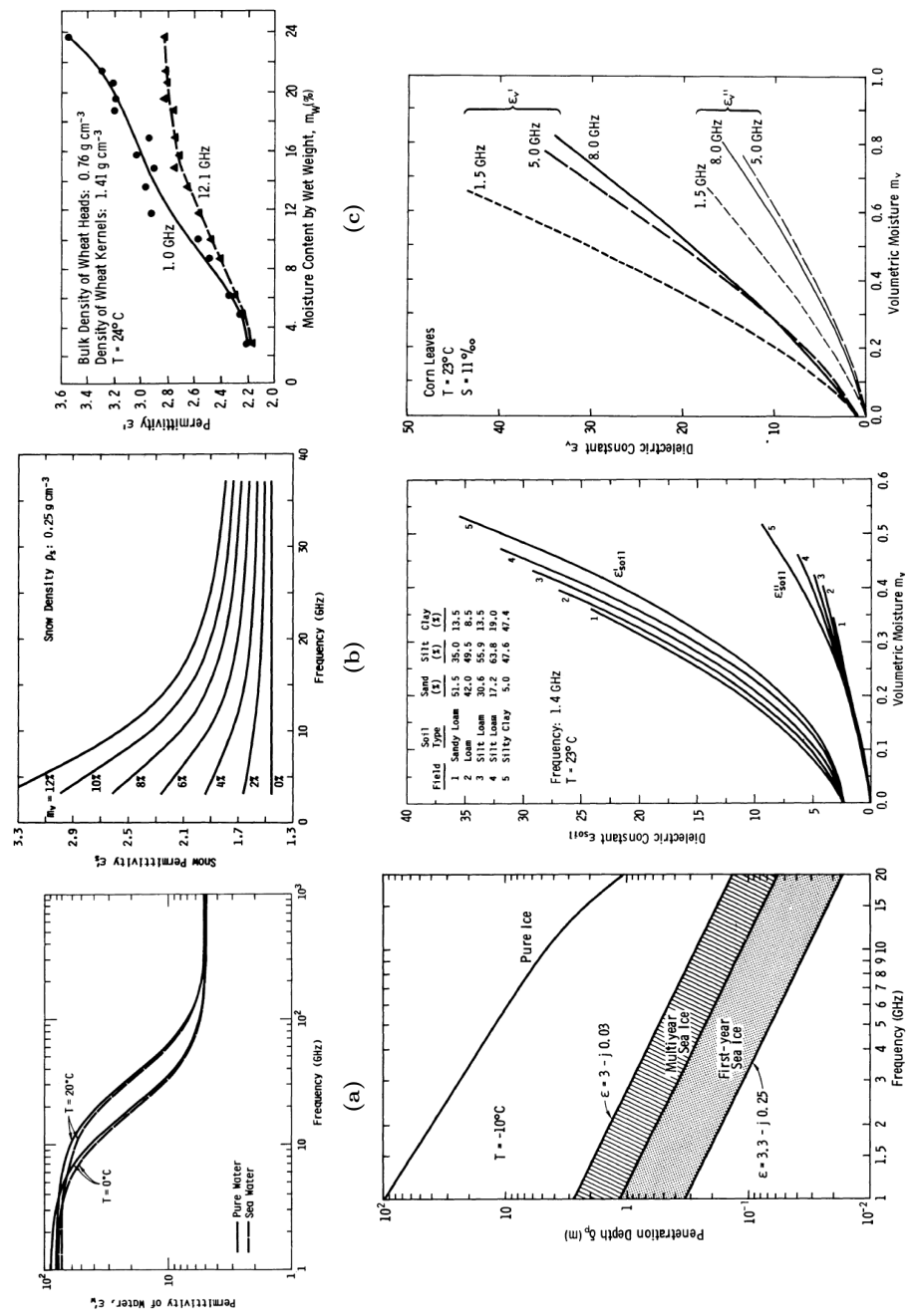

Figure 3.9: Permittivity for different type of mediums: (a) fresh and salt water (32.54‰); (b) wet snow with snow wetness as a parameter; (c) red winter wheat heads; (d) calculated penetration depth in ice; (e) soil with different moisture at 1.4 GHz; and (f) corn leaves. From [34]

3.3 The Delay Doppler Map

The Delay-Doppler Map (DDM) is the main observable in GNSS-R. It refers to the properties of a surface from the power of the scattered waves that reach the receiver. The term *map* comes from the fact that the waves coming from different reflection points are related (mapped) to delay/Doppler coordinates.

3.3.1 Definition

Let $x_r(t)$ be the complex baseband reflected signal after removing the carrier frequency and filtering out the high order components which appeared after the demodulation. Let also $r(t)$ be a *reference* signal. The coherent DDM is given by

$$Y(\tau,\nu) = \frac{1}{T_{coh}} \int_{T_{coh}} x_r(t)\, r^*(t-\tau)\, e^{j2\pi\nu t} dt, \tag{3.16}$$

where the overall losses and noise terms are omitted for clarity. This latter equation is similar to the CAF of the direct signal $x_d(t)$ in (2.3). However, the relationship between the AF of $r(t)$ with the DDM is not as simple as it is with the CAF (2.4). This relationship is given later.

Typically, the reflected signals have a low Signal-to-Noise Ratio (SNR), either because of the thermal noise or the speckle. For this reason, the DDM is often averaged incoherently

$$< |Y(\tau,\nu)|^2 >= \frac{1}{N_{in}} \sum_{n=1}^{N_{in}} |Y(t_n,\tau,\nu)|^2, \tag{3.17}$$

where N_{in} is the number of incoherent averages, and t_n denotes the time reference. In general, the averages are made with consecutive DDMs (i.e. $t_n \propto T_{coh}$). In any case, the coherent DDMs may first need to be repositioned (technique known as retracking) in the correlation plane. This is so, because the DDMs move inside the correlation plane as function of time. Bear in mind, that in the incoherent averaging process, the phase information is lost.

The location resolution of the scattered waves depends on the reference signal, and not on the scenario geometry or on the surface properties. In the delay/Doppler domain, this means that the estimated power is distorted by the AF of the reference signal, which in turn, impacts the measurements of any physical parameter. There are four main techniques depending on the reference signal: conventional GNSS-R (cGNSS-R), interferometric GNSS-R (iGNSS-R), reconstructed GNSS-R (rGNSS-R), and partial interferometric GNSS-R (piGNSS-R).

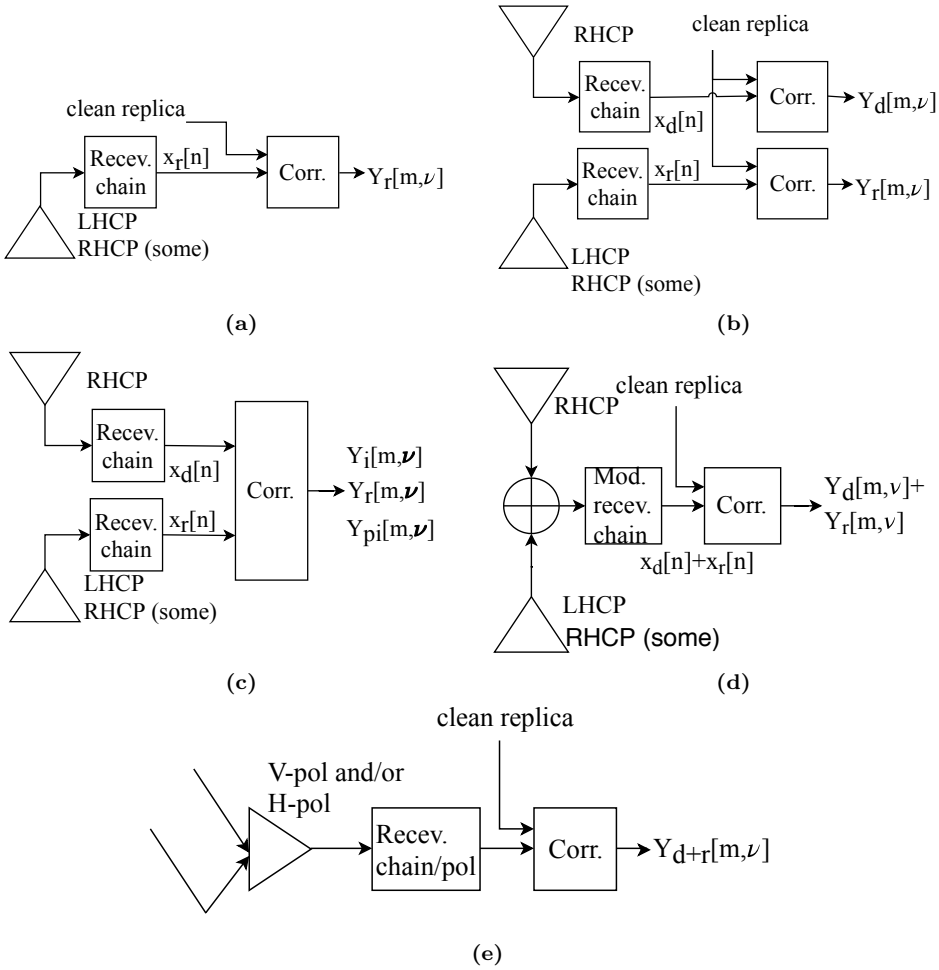

Figure 3.10: Some GNSS-R instrument configurations: (a) only the reflected signal is received and correlated with a clean replica (cGNSS-R); (b) like the former, but the direct signal is correlated as well with a clean replica and the result is used as reference (cGNSS-R); (c) the reflected signal is correlated with the direct (iGNSS-R), with a reconstructed component from the direct (rGNSS-R), or with extracted components from the direct (piGNSS-R); (d) both signals are combined in a shared correlator chain (cGNSS-R); (e) an antenna with linear (either vertical and/or horizontal) polarization pointing to the horizon receives the constructive/destructive pattern of the combined signal (cGNSS-R). Note that here the signals are defined as digital.

cGNSS-R

In cGNSS-R, the reference signal is a locally generated clean replica of the spreading sequence used in the transmitted signal (see Chapter 2). This method can only be performed with the public codes, which use narrow-band modulations that may not have enough bandwidth to achieve good accuracy measurements. Instrument configurations

using this technique are depicted in Figs. 3.10a, 3.10b, 3.10d and 3.10e. An example of a correlation architecture is given in Fig. 3.11a. Design principles for digital correlators are given in Chapter 8.

The configuration in Fig. 3.10d uses a shared correlation channel for the direct and reflected signals. The reason for doing this is not just to reduce the hardware requirements, but also since there are no different instrumental errors between the two signals, the system is self-calibrated. However, this configuration reduces the SNR as two noises are added.

The configuration in Fig. 3.10e, uses a single antenna with linear polarization that points to the horizon and picks the direct and reflected signals simultaneously. The reason behind this, is that the peak of the resulting DDM fluctuates due to the constructive and destructive addition of both signals. The fluctuation depends on the elevation angle of the GNSS satellite, on the receiver height, and on the surface parameters. The study of these fluctuations for remote sensing is called Interference Pattern Technique (IPT) (e.g. [47]).

iGNSS-R

The narrow-band drawback of the cGNSS-R is overcome in the iGNSS-R by using the direct signal as the reference, so as to take advantage of the wide-band restricted codes, but without actually knowing them [2]. Figure 3.10a shows an instrument configuration for iGNSS-R, and Fig. 3.11a shows an architecture for the correlator. The iGNSS-R technique presents three major drawbacks compared to cGNSS-R: the SNR is even lower, the cross-talk interference coming from undesired GNSS satellites, and the larger vulnerability to RFI signals. The impact of the first two problems can be reduced by using high directive antennas with beam steering in which only the desired satellite is tracked, and by a large incoherent averaging after the correlation process. Yet, residual interfering power from unwanted GNSS satellites may still be received. See Chapter 6 for a detailed study on the cross-talk phenomena. The RFI mitigation in GNSS-R systems, is one of the fields studied in [48].

rGNSS-R

This technique is applied to the composite GPS signal. It is based on the so-called semi-codeless techniques, which allows the tracking of the P(Y) signal without knowing the encrypting code Y. In rGNSS-R, the P(Y) code is reconstructed from the direct signal, which is then correlated with the reflected one. The advantage of this technique with respect to cGNSS-R, is that the large bandwidth of the P(Y) gives, in principle, a better range precision. However, the SNR is also reduced, as the estimated P(Y) signal contains errors. An instrument configuration for this technique is shown in Fig. 3.10c.

piGNSS-R

This technique is also applied to the composite GPS L1 signal. The P(Y) and M components are extracted from the direct signal by coherent demodulation, and are then correlated with the reflected (see Fig. 3.11b). The advantage of this technique with respect to the inteferometric, is an improved range resolution, but at expense of ab eveb larger reduction of the SNR. An instrument configuration for this technique is shown in Fig. 3.10c.

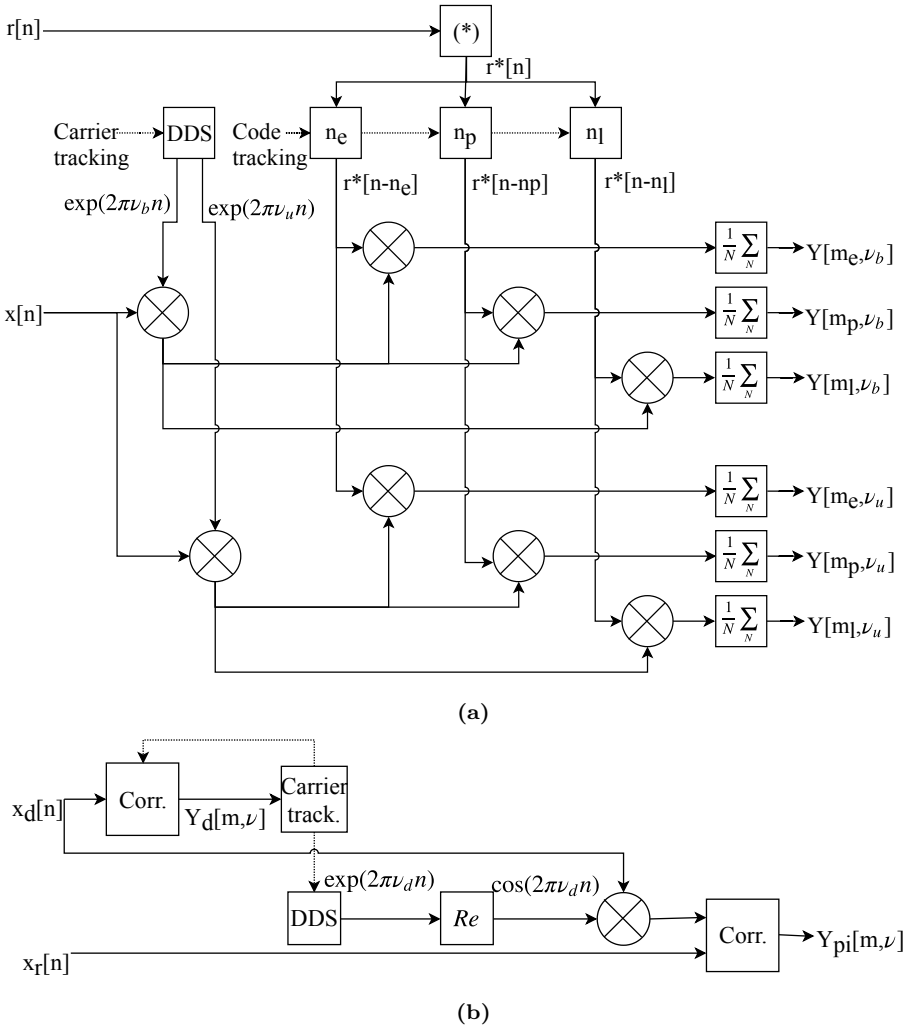

Figure 3.11: Correlator architectures: (a) example of classical correlator (with 3 delay lags and 2 Doppler bins) used in cGNSS-R ($r(t)$ is a clean replica) or in iGNSS-R ($r(t)$ is the direct signal); and (b) piGNSS-R correlator using the former block (from [49]). Note that here the signals are defined as digital, and N is the number of samples equivalent to T_{coh}.

3.3.2 The Zavorotny-Voronovich model

The most used DDM model for ocean reflections is the Zavorotny-Voronovich (ZV) model [41], which is based on the bistatic radar theory. Let $\vec{\rho}$ be the position vector of a reflection point in SRF coordinates lying at the plane tangent to the specular point ($\rho_z = 0$). The model predicts the power DDM as

$$< |Y(\tau,\nu)|^2 >= \frac{\lambda^2 T_{coh}^2}{(4\pi)^3} P_T \iint \frac{G_T(\vec{\rho})\, G_R(\vec{\rho})}{R_{T\rho}^2(\vec{\rho})\, R_{R\rho}^2(\vec{\rho})} |\chi(\tau - \tau_r(\vec{\rho}), \nu - \nu_r(\vec{\rho})|^2 \sigma_{pq}^0(\vec{\rho})\, d^2\vec{\rho}, \tag{3.18}$$

where

- P_T is the transmitted power.
- $G_T(\vec{\rho})$ and $G_R(\vec{\rho})$ are the transmitter's and the receiver's down-looking antenna gain when pointing at the reflection point.
- $\tau_r(\vec{\rho})$ is the delay made by the ray-path from the transmitter to the reflection point and from there to the receiver

$$\tau_r(\vec{\rho}) = \frac{R_{TS}(\vec{\rho})}{c} + \frac{R_{SR}(\vec{\rho})}{c}. \tag{3.19}$$

- $\nu_r(\vec{\rho})$ is the Doppler shift of the same ray-path described above with respect to the nominal carrier frequency

$$\nu_r(\vec{\rho}) = \frac{1}{\lambda}\left[\left(\vec{\rho_v}(\vec{\rho}) - \vec{T_v}(\vec{\rho})\right)\cdot(-\hat{m}(\vec{\rho})) + \left(\vec{R_v}(\vec{\rho}) - \vec{S_v}(\vec{r})\right)\cdot\hat{n}(\vec{\rho})\right], \tag{3.20}$$

  where $\vec{\rho_v}(\vec{\rho})$, $\vec{T_v}(\vec{\rho})$ and $\vec{R_v}(\vec{\rho})$ are the velocity vectors of the reflection point, the transmitter and the receiver, and $\cdot$ is the inner product.
- $|\chi(\tau,\nu)|^2$ is the WAF of the reference signal given in (2.6).
- $\sigma_{pq}^0(\vec{\rho})$ is the normalized bistatic RCS. Typically, the RCS under KGO approximation in (3.12) is used together with the ZV model.

Note that the distance $R_{T\rho}$ from (3.5) has been rewritten here as $R_{T\rho}(\vec{\rho})$ to denote that is an integral parameter. The same applies for $R_{\rho S}$ and for the velocity vectors.

The ZV model relates the power received from each point of the surface to a power in the delay and Doppler dimensions. However, this latter value is distorted by the WAF of the reference signal. In fact, the WAF can be understood as the impulse response from a single delay/Doppler cell in the glistening zone. The ideal WAF would be a 2D Dirac delta function, that is infinite at the origin and zero elsewhere. This WAF does not exist, as it could only be produced by an ideal white noise signal with infinite duration and infinite bandwidth. In fact, the term *ambiguity* comes, in classic radar theory, from the

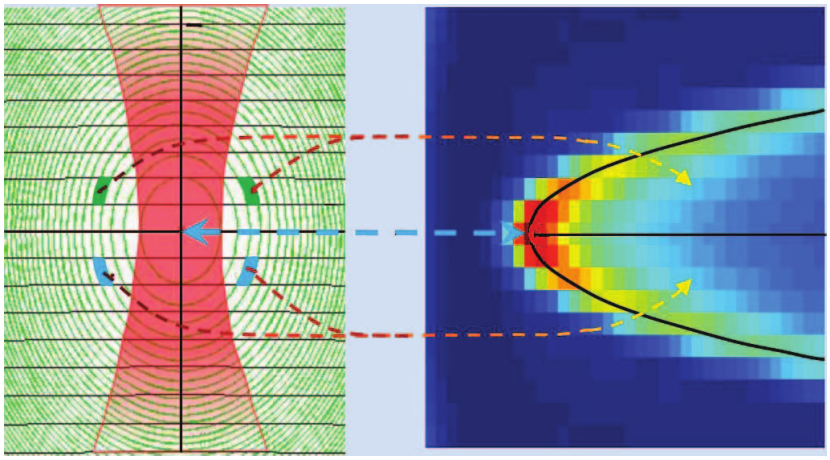

Figure 3.12: Mapping of pixels in the glistening zone to delay/Doppler coordinates. Obtained from [27].

fact that targets that are close to each other and have a similar velocity vector, cannot be easily distinguished.

Equation 3.18 can be expressed as a 2D convolution product [50]

$$< |Y(\tau,\nu)|^2 >= |\chi(\tau,\nu)|^2 ** \sum(\tau-\tau_r', \nu-\nu_r), \tag{3.21}$$

where $\sum(\tau,\nu)$ can be interpreted as a weighting factor to each delay/Doppler cell

$$\sum(\tau,\nu) = \frac{\lambda^2 T_{coh}^2}{(4\pi)^3} P_T \iint \frac{G_T(\vec{\rho})\, G_R(\vec{\rho})}{R_{T\rho}^2(\vec{\rho})\, R_{R\rho}^2(\vec{\rho})} |\delta(\tau-\tau_r(\vec{\rho}), \nu-\nu_r(\vec{\rho})|^2 \sigma^0(\vec{\rho})\, d^2\vec{\rho}, \tag{3.22}$$

where $\delta(\tau,\nu)$ is the 2D Dirac delta function.

One important consequence of (3.18), is that the points over the surface with the same delay and Doppler, are mapped into the same coordinates in the DDM plane. This is shown in Fig. 3.12, where the areas bounded by the iso-delay and iso-Doppler lines are mapped into the same DDM pixels. The specular point has no correspondence with any other point. There is then, an ambiguity in the DDM in order to locate the origin of the power arriving at each pixel. This ambiguity concept must not be confused with the one from the WAF described above.

There are several techniques to resolve the DDM ambiguity problem. One is to use DDMs from consecutive instants and/or from different satellites, which share part of the glistening zone. Another technique uses two beams as spatial filtering. By properly combining both beams, an ambiguous free zone can be created [51].

It is also worth commenting here, that the WAF is periodic in the delay dimension

due to the periodicity of the ranging codes. Mathematically, this can be expressed as $\tau_r' = \tau_r \ mod \ T_{coh}$. This could translate into an additional ambiguity in the delay dimension of the DDM from the points whose relative distances are multiples of the code periodicity. Luckily, this periodicity is around two orders of magnitude larger than the size in the delay dimension of a DDM from space.

3.3.3 Coherent model

The ZV equation assumes that the scattering is completely strong diffuse or incoherent. However, when the Rayleigh parameter is less than 1, or of order of 1, the regime of incoherent scattering is called *weak diffuse scattering*, and it is accompanied by the coherent component [52, 53]. In fact, the coherent scattering around the specular point may be noticeable or even dominant in some scenarios. This is the case in weak surface scenarios compared to the signal's wavelength, like calm sea, lakes and ice surfaces.

The DDM obtained from the coherent component can be expressed as [29, 54]

$$< |Y_{coh}(\tau,\nu)|^2 >= |Y_d(\tau,\nu)|^2 |\Re_{pq}|^2 \exp\left(-8\pi^2\sigma_h \sin^2(\theta)/\lambda^2\right), \tag{3.23}$$

where $|Y_d(\tau,\nu)|^2$ is the CAF of the direct signal given in (2.4) and σ is the Root Mean Square (RMS) height of the surface. This model is based on the KPO scattering model mentioned above and detailed in [55].

Strictly speaking, the equation above is applicable only for the case of the infinite plane surface, or, in practice, when the size of the reflecting surface is larger many times than the first Fresnel zone. If it is not the case, like for reflection from small lakes, one would need to calculate the Kirchhoff integral over that area numerically [56].

3.3.4 Derived observables and related applications

As mentioned before, the complex DDM is the main observable in GNSS-R and from where all the other observables are derived. Before introducing the new observables, is it worth understanding the impact of the scattered waves on the DDMs. In general, the power received from the specular point is the larger one. The contribution from the areas away from the specular point, add power at the trailing edges of the DDM. If the glistening zone is large enough, the DDM has a characteristic boomerang-like shape. The larger the roughness of the surface, the height of the receiver and the elevation angle of the GNSS satellite, the larger the glistening zone.

Figure 3.13 shows real DDMs obtained from an airborne campaign. Note first that the SNR (which can be qualitatively retrieved from the ratio between the peak and noise floor level) depends on the surface type. In this example, the reflection over land is noisier than over ocean, which in turn is noisier than over the calm waters of a harbour. Note also that the SNR improves with the incoherent averaging.

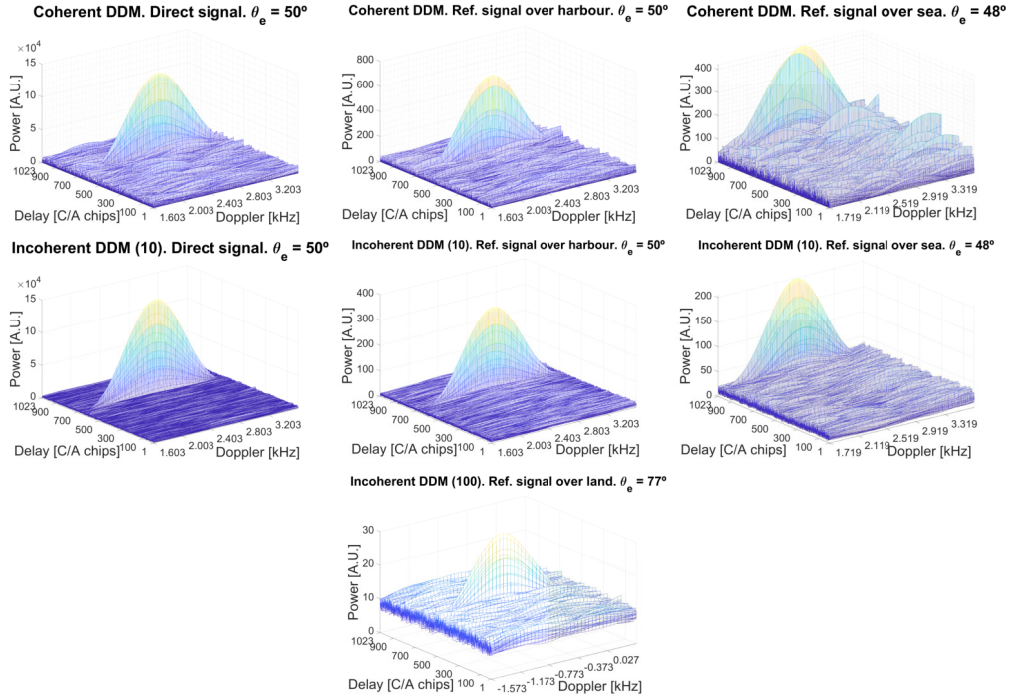

Figure 3.13: Example of L1 C/A cGNSS-R power DDMs obtained from an aircraft field campaign (see Chapter 10).

Figure 3.14 shows real DDMs obtained from different space-borne missions. The size of the space-borne DDMs over ocean depends on sea conditions, but it is approximately ten times larger in both delay and Doppler dimensions, than it is at airborne heights. As it can be appreciated in Fig. 3.14b, the wind speed direction, or more precisely, the direction with respect to the ground-track trajectory of the receiver, results in an asymmetric DDM. Finally, figure 3.14c compares a DDM over sea ice with a strong coherent component, with another DDM over sea, both in the Arctic region.

Some of the observables derived from the DDM are:

- The **altimetric delay** τ_r of the reflected signal, which is found at the maximum of the delay-derivative of the DDM [60]

$$[\tau_r, \nu_r] \stackrel{\triangle}{=} \arg\max_{\tau,\nu} \frac{\partial |Y(\tau,\nu)|^2}{\partial \tau}, \tag{3.24}$$

  As stated previously, this delay is actually the modulus of the true one with $Tcoh$, due to the delay periodicity of the WAF. The reason why the specular delay is found at the maximum of the delay-derivative, is because in principle, it is the instant that adds more power to the overall DDM. The model assumes that the

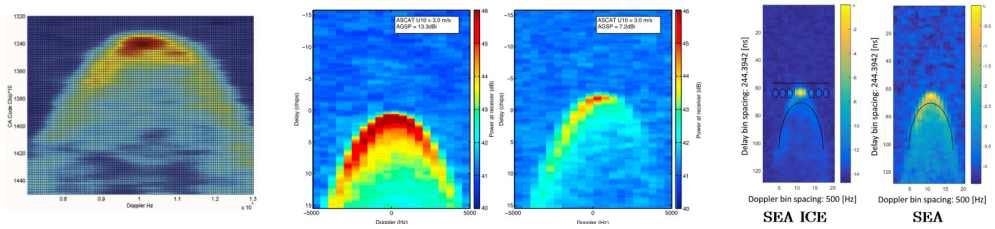

(a) (b) (c)

Figure 3.14: Example of power DDMs over ocean obtained with space-borne instruments using the cGNSS-R technique and L1 C/A signals. (a) UK-DMC-1 (h = 680 km); (b) comparison of two DDMS with same wind speeds but different wind direction with TDS-1 (h = 635 km); and (c) comparison of sea ice and sea reflections also with TDS-1. All DDMs are computed with a coherent correlation time of 1 ms and averaged 1000 times. From [57], [58], and [59].

power contribution from successive delays is monotonically decreasing. It is worth mentioning here, that recent findings in [61], have shown that if the coherent and incoherent components of the reflected signal are processed independently, the latter delay may not be found at the same position. This effect should be taken into account in altimetric retrievals.

This delay is used in altimetry measurements, together with the delay of the direct signal τ_{pk} given in (6.1) (see Fig. 3.15). Chapter 11 applies this theory in ocean altimetry and in land topography.

It is also important to state here, that this delay is a group delay, that is to say, the average delay of the signal within the received bandwidth. It can be also referred as code delay.

- A **waveform** is a delay profile of the DDM for a given Doppler frequency, usually passing through the specular delay

$$w(\tau) = |Y(\tau, \nu_r)|^2 . \tag{3.25}$$

Three regimes are typically identified in the waveforms. The noise floor, and the **leading and trailing edges**. While a sharp leading edge gives a better altimetric precision, the slope of the trailing edge is associated with the wind speed over ocean (see Fig. 3.16). Chapter 4 shows the impact of the receiver's bandwidth on the waveforms, and a detailed study of the achievable height precision is done in Chapter 5.

- The **covariance matrix of consecutive waveforms** in time was used in [62, 63] to study the noise statistics at different parts of the waveform and its impact on the altimetric retrievals.

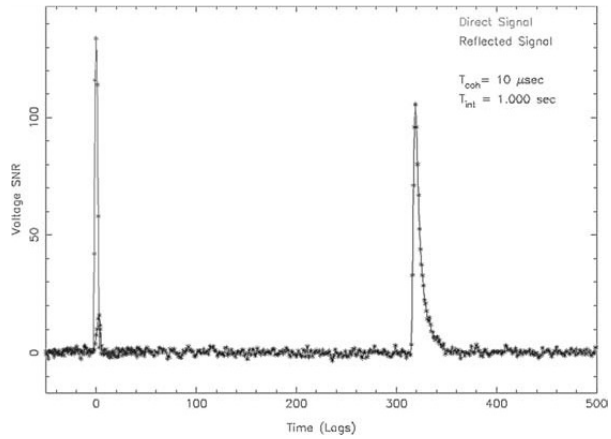

Figure 3.15: Example of a direct signal cross-correlation (left) and respective waveform (right). Note that the down-looking antenna also picked the direct signal. From [26].

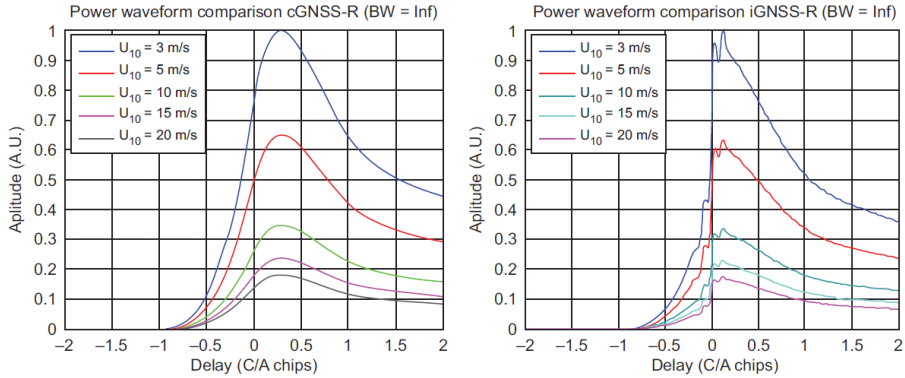

Figure 3.16: Comparison of simulated space-borne power waveforms over ocean for different wind speeds: (a) L1 C/A cGNSS-R and (b) L1 composite iGNSS-R. From [64].

- The **scatterometric delay** τ_{sc}, is the delay at the DDM peak

$$[\tau_{sc}, \nu_{sc}] \stackrel{\triangle}{=} \arg\max_{\tau,\nu} |Y(\tau, \nu)|^2. \tag{3.26}$$

  The term scatterometric comes from the fact that the peak value of the DDM is used as an estimator of the σ^0 of the surface. Sometimes in the literature, (3.26) is named as peak delay. In these cases, the scatterometric delay is then defined as the delay difference between the peak and the specular points (see Fig. 3.17).

- The **peak power ratio** of the reflected DDM and the direct CAF depends on the reflectivity of the surface, which in turn can be used as an estimator of the soil moisture (e.g. [40]). Chapter 11 uses this same idea to compare the soil moisture of an arid area before and after rains.

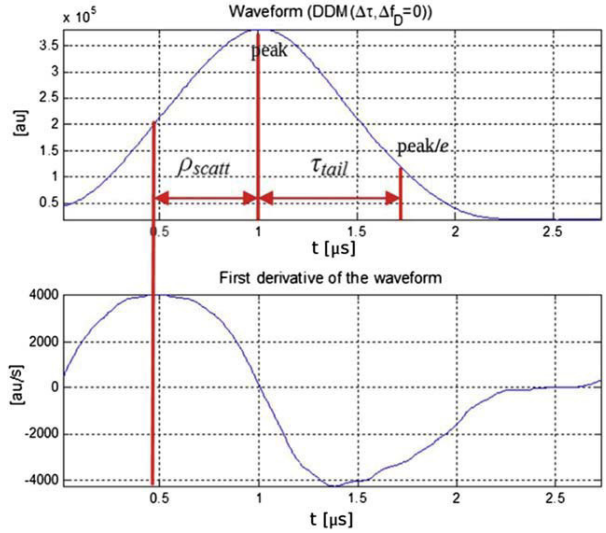

Figure 3.17: Example waveform showing the most distinctive points. From [65].

- The latter concept can be extended to the **polarimetric ratio** when dual-polarization antennas are used (either circular and/or linear). This is known to be highly sensitive to the permitivity of the surface for low elevation angles, which in turn can be used to estimate the soil moisture (e.g. [40]), or vegetation canopy (e.g. [66]) for example.
- Research has been done to separate the **coherent and incoherent contribution to the peak power**. In [67], the aim was to mitigate the interference from the direct signal into the reflected by estimating and substracting the former. In [61], a method was proposed to identify both components aiming at obtaining better precision measurements, as both components have a different spatial resolution (see Sec. 3.2).
- The **phase delay** or carrier-phase delay, is the specular delay obtained from the phase of the complex DDM. Needless to say, that in order to retrieve the carrier phase from reflected signals, the scattering must be mainly coherent. Phase delay gives an enhanced height precision, similar to what is done with high accurate GNSS receivers. Phase delay altimetry has been used over ice sheets even from space [68].
- The **time decorrelation of the complex peak** can be used to infer the sea coherence duration [69, 70]. Chapter 10 uses this concept for reflections over sea far from the coast and inside a harbour, and compares them using satellites with different elevation angles.
- The **IPT technique** introduced earlier, can obtain physical parameters from the power oscillations caused by the constructive and desctruvie addition of the direct

and reflected signals picked by an antenna with linear polarization (typically) pointing at the horizon (see Fig. 3.10). This technique has been used for soil moisture, vegetation height and snow thickness among others (e.g. [71]).

- The above technique can also be extended to the **polarimetric IPT** if an antenna with vertical and horizontal polarization is used [40].
- The **volume** and **area** of the DDM above certain threshold were originally suggested in [50] as metrics to infer the roughness of the surface. The volume has also been used in [70] in order to estimate the sea correlation time.
- The distance between the DDM peak with the **geometrical center** or with the **center of mass**, has been used to retrieve sea wind speed (e.g. [72]).
- The angle formed by the vector between different points of the DDM has been used as an indicator of the **DDM skewness** (see Fig. 3.18), which can be then used to estimate the sea wind direction (e.g. [73, 74]).
- The **DDM variance** and the **Allan DDM variance** have been used as wind speed estimators in [75]. Both observables aim at characterizing the speckle, which can then be related to the wind speed.
- In [76], a **linear combination of the DDM samples** was used to retrieve sea wind speed.

In general, these observables are related to the physical parameters by using empirical equations. Other approaches that have been developed recently, make use of Artificial Neural Networks (ANN) (e.g. [77–80]). The quality of any model is given by error metrics like the standard deviation, bias, Root Mean Square Error (RMSE), R-square, and the probability of false alarm and false detection when the estimated parameter is binary (for example the presence or not of ice).

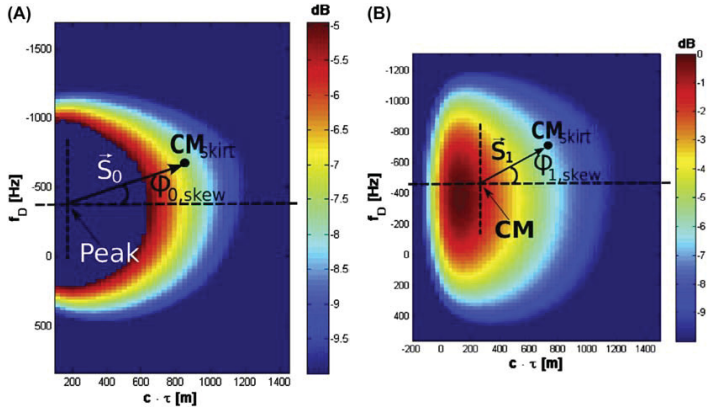

Figure 3.18: Definition of two different skewness angles. From [73].

Finally, it is worth commenting here the DDM deconvolution, also known as DDM inversion or GNSS-R imaging. This is not an observable, but a technique to retrieve the original radar cross-section over the glistening zone. This approach can be used in the applications mentioned above, but also offers a new set of research fields, such as ship and oil slick detection. The original deconvolution method was presented in [81].

3.4 Sea altimetry with GNSS-R

GNSS-R sea altimetry is the study of the Sea Surface Height (SSH) using reflected GNSS signals. The height is derived from the time difference between the direct and reflected signals. The time difference can be estimated using either the code or phase delay observables explained above.

The estimated sea height is actually the instantaneous height averaged over the antenna footprint from the points in the glistening zone. The Mean Sea Level (MSL) is the temporal average, which depends on short- and long-term variations due to the wind, currents, eddies and tides.

This section focuses on GNSS-R altimetry, but is worth stating here that the feasibility of GNSS-R has been demonstrated for other sea retrievals. These are wind speed modulus, usually defined at 10 meters above the sea surface (U_{10}); wind speed direction; Significant Wave Height (SWH); and sea salinity and temperature among others.

3.4.1 Comparison between radar and GNSS-R altimetry

Radar altimeters on board space vehicles have been used for remote sensing since the late 70s. The technology is well consolidated, and even the satellites of the missions to Mars carried altimeter instruments, as will the near-future missions to Jupiter and Venus. Since the early 90s, there has been a continuous succession of missions in order to map the Earth's oceans, most of them summarized in Table 3.2. Some basic concepts related to sea altimetry by using such instruments and their relationship with the GNSS-R technology are explained next. The web [`http://www.altimetry.info/`] and the respective pages of the missions are an excellent source of information for further details.

3.4.1.1 Coverage

The radar altimeters are nadir-looking (see Fig. 3.19), which limits its spatial and temporal resolution. There is in fact a trade-off between both parameters when designing the satellite orbit. The Poseidon/Jason series have a cycle-period of 10 days and a ground-track separation at the equator of 315 km. In contrast, the missions from ESA have a period of about 30 days and a ground-track separation as low as 75 km. Having said that, the orbits of successive missions from the same series are designed to work in tandem. By doing this, the ground-tracks of the satellites are interlaced in time, reducing the average temporal and spatial resolution.

Table 3.2: Satellite missions with radar altimeters. The cycle-period of the Cryosat-2 is a pseudo-cycle. Ground tracks separation are on the equator. Adapted and extended from `http://www.altimetry.info/` and from Table 4.2 in [82].

Satellite *Operator*	**Years**	**Cycle Track**	**Altimeter**	**Bands**	**Technology**				**Waveform**				**Error [cm]**
					Op.	**BW [MHz]**	**PRF [kHz]**	**Len. [us]**	**Gates**	**Width [ns]**	**Avg. [Hz]**	**Num avg.**	
ERS-1 *ESA*	91-00	35 d 80 km	RA	Ku	PC	330 (ocean) 82.5 (ice)	1.02	20	64	3.03	20	50	3
TOPEX/ Poseidon *NASA CNES*	92-06	10 d 315 km	TOPEX (aka NRA)	Ku	PC	320	4.5	102.4	128	3.125	10	456	2
				C		320/100	1.22	102.4/32			5	240	
			Poseidon-1 (aka SSALT)	Ku		320	1.718	105	60	3.125	20	86	
ERS-2 *ESA*	95-11	35 d 80 km	RA	Similar to ERS-1									
Jason-1 *NASA CNES*	01-13	10 d 315 km	Poseidon-2	Ku	PC	320	1.8	105	104	3.125	20	90	2
				C			0.3					15	
Envisat *ESA*	02-12	35 d 80 km	RA-2	Ku	PC	320/80/20	1.795	20	128	3.125	18	100	2
				S		160	0.449		64	6.25		25	
Jason-2 *CNES NASA NOA Eumetsat*	08-19	10 d 315 km	Poseidon-3	Similar to Poseidon-2									2.5
Cryosat-2 *ESA*	10-cur.	30* d 7.5 km	SIRAL-2	Ku	PC DDA	320	1.97 (LRM) 17.8 (SAR)	44.8	128/512		20		1.3 (ice chang.)
SARAL *ISRO CNES*	13-cur.	35 d 75 km	AltiKa	Ka	PC	500	3.8	110	128				
Sentinel-3 *ESA CNES*	16-cur.	27 d 104 km	SRAL	Ku	PC DDA	350	1.92	189.4	128	1.563	20	84/256	3
				C		320						14/8	
Jason-3 *NOAA Eumetsat*	16-cur.	10 d 315 km	Poseidon-3B	Similar to Poseidon-2									3.3

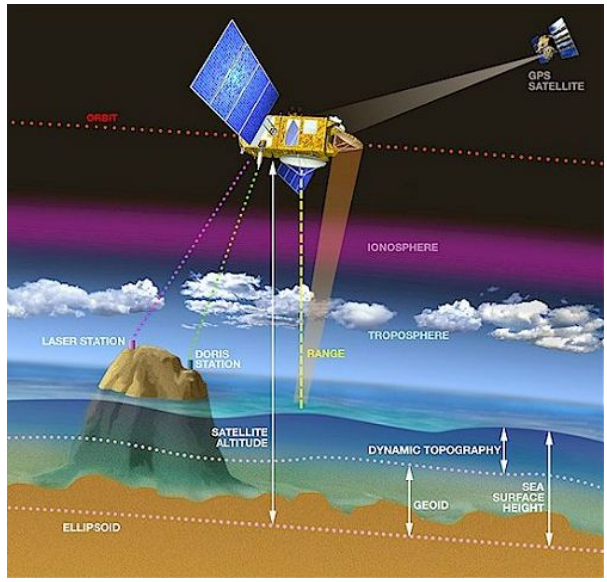

Figure 3.19: Artist view of a space-borne altimeter. From [`http://www.altimetry.info/`].

A single GNSS-R space-borne instrument could track tens of different reflection points simultaneously, depending on the hardware resources. The distance between those points must be such that they are not redundant and that there are not unmapped areas. The work in [83], proposed a constellation of GNSS-R satellites for early detection of tsunamis using the GPS, GLONASS and Galileo constellations. A configuration of 18 Low Earth Orbit (LEO) satellites in 3 planes would be enough to detect strong tsunamis within 15 minutes of their generation. For stronger tsunamis, 48 satellites in 8 planes would be needed. The range accuracy of the instruments should be at least 20 cm.

Although the number of satellites may seem high, it is far less than would be necessary if classical radar altimeters were used. With the appearance of the CubeSats, low cost, low weight and low consumption satellites, making a constellation like the one described feasible. The required range accuracy of 20 cm is 10 times worse even than that of the first altimeters. However, it is a reasonable value for a space-borne GNSS-R instrument.

The GNSS-R mission Cyclone Global Navigation Satellite System (CYGNSS) is devoted to measure the sea wind surface, in the scope of tropical cyclones forecasting. The orbit requirements for such mission are not as strict as they are for tsunami detection. The CYGNSS constellation is formed by 8 satellites with a mean revisit time of 7 hours. Each satellite has two down-looking antennas (one at both side of the ground-track), and it can measure 4 simultaneous reflections. This results in 32 wind measurements per second across the world with the full constellation.

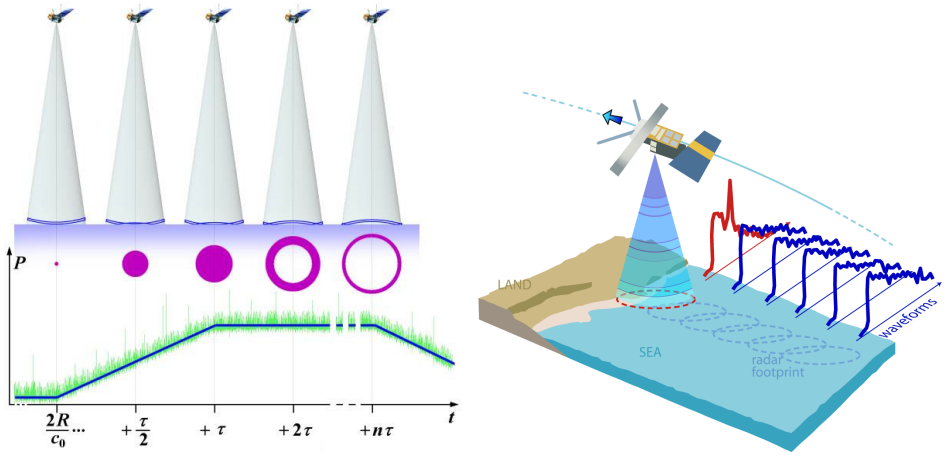

(a) (b)

Figure 3.20: Altimetry waveform formation concept: (a) step-by-step building, from [`https://www.radartutorial.eu/`]; (b) waveform contaminated by the coast-line, from [`http://www.altimetry.info/`]

3.4.1.2 Principle of operation

A radar altimeter measures the range of the satellite by estimating the round-trip time of a transmitted pulse. The return of the pulse is called echo. The power (or magnitude) of the echo with respect to the return time is named waveform. The sampled intervals are called delay *gates* or *lags*. From a flat surface or with little roughness, the pulse reaches first the nadir point (see Fig. 3.20a). As the pulse advances, the surface is illuminated forming annulus of same delay. The reflected area depends on the beamwidth of the antenna, which is typically about 1°. Similar to the GNSS-R waveforms, the radar waveforms can also be used to measure significant wave height, sea wind speed and the backscatter coefficient σ^0 of the reflecting surface. In land or coast scenarios, the radar waveform is also related to the vertical profile of the surface (see Fig. 3.20b). This includes for example topography and vegetation canopy.

Ideally, the pulse length should be smaller than the coherent length of the reflected surface. At the same time, high transmitted powers are required in order to achieve high precision measures. These two requirements together entails hardware difficulties in both the receiver and the transmitter. Radar altimeters overcome this problem by using a Pulse Compression (PC) technique called full-deramp technique or stretch processing (see Fig. 3.21). In this technique, the altimeter does not transmit a pulse, but a sequence of them at a given Pulse Repetition Frequency (PRF). Typical rates are between 1-2 kHz. Each pulse is frequency modulated (FM) within a given bandwidth, (named chirp). The compressed time resolution is inversely proportional to the bandwidth, whose common

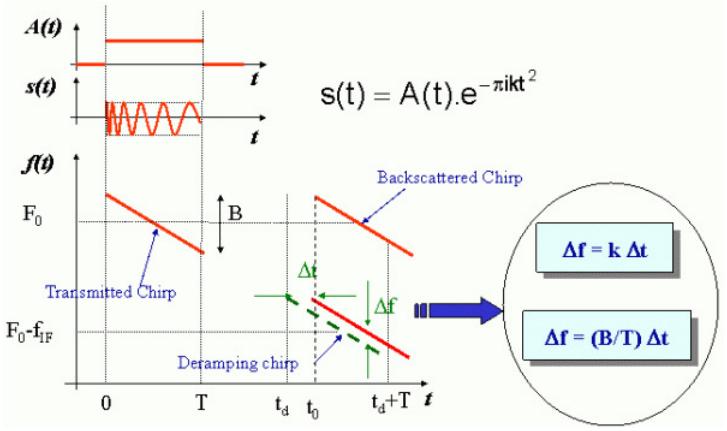

Figure 3.21: Deramping technique concept. From [`http://www.altimetry.info/`]

values are of the order of 300 MHz. The receiver combines the reflected signal with a clean replica of the transmitted chirp but with a slightly shifted central frequency (deramping chirp). The deramping mixer generates the frequency difference between both signals, but since they both have the same frequency rate, the resulting signal is a tone. The frequency of the tone depends on the phase of the incoming signal, which in turn depends on the delay. A space-borne deramping radar can give range resolutions of 2-3 cm. Alternative names for the deramping radar are pulse-compressed, pulse-limited, or just conventional.

Modern altimeters such as CryoSat-2 and Sentinel-3, use the Delay Doppler Altimetry (DDA) technique, also known as Synthetic Aperture Radar (SAR) altimetry, while using the conventional technique as Low Resolution Mode (LRM). A DDA radar exploits the Doppler effect caused by the satellite movement in the along-track direction, which increases the along-track resolution (see Fig 3.22). By way of an example, the along-track resolution of Sentinel-3 in LRM is about 1.64 km, which is reduced to about 300 m in the DDA processing.

The idea is that each reflected scatter reaches the receiver with a different Doppler shift that depends on their along-track location. By coherently processing a burst of consecutive pulses (and not just one as in classic altimetry), it is possible to discriminate the surface scatterers. Sentinel-3 uses 64 echoes within each burst, which equals an aperture duration of 3.5 ms. In DDA, the pulses are transmitted at a higher rate (≈10 times more) in order to have a relative constant phase between consecutive reflected pulses. This latter processing is actually called unfocused DDA. A full focused technique performs an inter-burst coherent integration, taking into account the phase evolution of the scatterers during the entire illuminaton time of a scatterer on the surface. With this technique, along-track resolutions of 16 cm could be achieved [84].

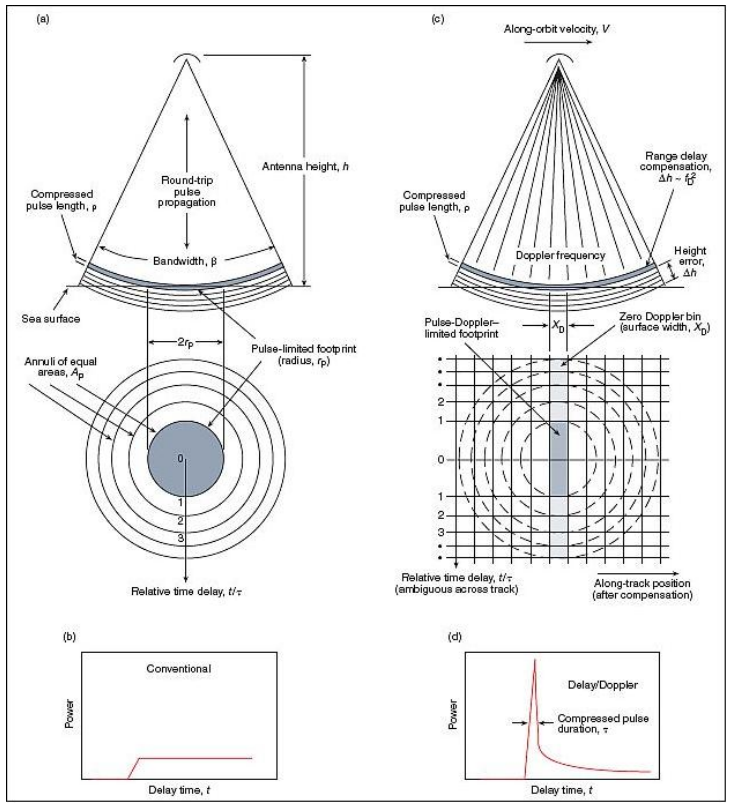

Figure 3.22: Comparison between pulse-limited alitmetry (left) and Delay Doppler Altimetry (right). From [`https://earth.esa.int/web/eoportal/satellite-missions/c-missions/cryosat-2`].

3.4.1.3 Tracking and re-tracking

The tracker system is the mechanism by which the reflected signal is kept within the altimeter analysis window. Two tracking models are used to predict the position of the echo. A close-loop tracker uses the position of the previous echoes as reference, applying for example a median filter. It is typically used over land. An open-loop tracker is based on the geometry of the system using for example Digital Elevation Models (DEMs). It is tipically used above the ocean, some land and in-land waters.

In order to improve the precision of the observations, the waveforms are reprocessed using a re-tracker. A re-tracker is an algorithm for determining the correction of the tracking bias. Each mission uses different retrackers for different types of surfaces (e.g. [82]). Two family of re-trackers exists. The first family of re-tracking algorithms tries to fit the waveform to a model that depends on the physics of the surface. Most of these models are based on the Brown model [85]. The second family of re-trackers are empirically-based

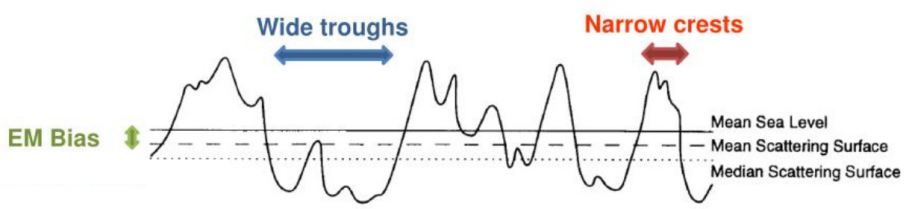

Figure 3.23: EM bias concept. From [89].

on the statitcs of the waveform and do not consider the reflecting surface.

Chapter 8 gives some comments for the delay and Doppler tracking in cGNSS-R and in iGNSS-R. The delay re-tracking in GNSS-R has been investigated in [36, 86, 87], and specifically for the CYGNSS mission in [88].

3.4.1.4 Source of errors

Aside from the instrumental errors and from the thermal and speckle noises, three main sources of error impact either the radar and the GNSS-R altimeters: the ionosphere, the troposphere and the ability to determine the position of the satellite.

The ionosphere introduces a delay to the signal that depends on its frequency. The error can be up to several meters. The dual-band radar altimeters reduce the impact of such error by combining the results from the two bands. Multi-band GNSS-R instruments can follow a similar approach by using the GNSS signals transmitted at the different bands. The larger the separation between the frequencies, the better the estimation of the ionospheric delay. Using several bands further improves the estimation.

The troposphere introduces delay that depends on the humidity. The error is below one meter, but is not dependent on the frequency and cannot be resolved by the latter means. Radar altimeters estimate this delay by using microwave radiometers, typically at 18,7 and 23,8 and/or 36,5 GHz. GNSS-R instruments could do the same as GNSS receivers, which predict the humidity by using models. These models depend on the season, the time of the day, and the location on the Earth.

The orbit of the satellite altimeters is precisely known by using a combination of high accurate GNSS receivers, laser trackers, and the DORIS system. In this system, a set of ground-based stations across the Earth, transmit a beacon signal which is picked up by the satellites. The satellites measure their movement from the Doppler shift of the signals.

Another source of error is the Electromagnetic bias (EM) bias. This error is the result from the non-symmetrical properties of the sea waves (see Fig. 3.23). More EM waves are reflected in the wide troughs, than in the narrow crests, resulting in negative

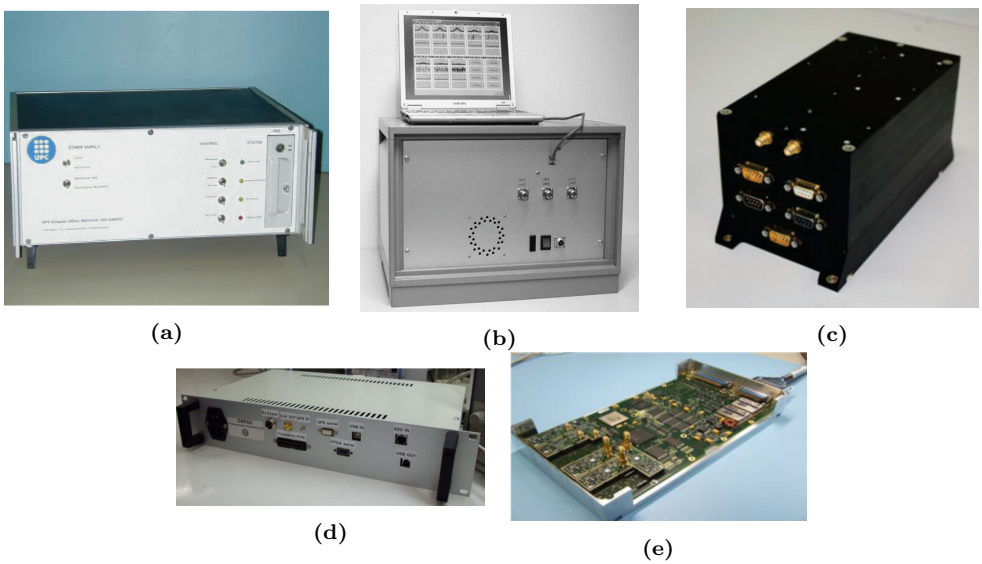

Figure 3.24: Some GNSS-R instruments: (a) DODEREC, (b) former GOLD-RTR, (c) PAU, (d) griPAU, and (e) SGR-ResSI used in TDS-1 . From [92], [93], [94], [95], and [96] respectively.

bias with respect to the mean sea level. Although this error is much smaller than that introduced by the atmosphere (typically few centimeters), it needs to be characterized as well. There is extensive literature on the EM bias for radar altimeters. However, the bistatic configuration of GNSS-R requires a specific model. Research on this latter issue can be found on [89–91].

3.4.2 GNSS-R instruments

Tables 3.3, 3.4, and 3.5 summarize the most relevant GNSS-R instruments with altimetric capabilities, and Figures 3.24 and 3.25 show pictures of some of them. The tables focus on the hardware, the correlation architectures, and on the results from altimetry campaigns. An instrument with altimetric capabilities is an instrument that either saves the raw sampled data or computes DDMs or waveforms in real-time. Thus, GNSS-R instruments devoted to scatterometry, in which the observable is the SNR or the CN0, are not shown here.

The listed instruments are those that presented a novelty in the time of their appearance, either by using new processing techniques, bands, constellations or highly dedicated hardware. With the popularization of the GNSS-R field, and with cost reduction of involved technology, many other instruments have appeared and can be found in the literature.

A review of instruments developed at the Remote Sensing Lab of the Universitat

Politècnica de Catalunya was published in [97]. Some of the instruments which by then were at preliminary stages, have been published in the Ph. D. thesis [5, 40, 48, 66], and the present one.

The first dedicated space-borne GNSS-R satellite was the UK-DMC-1 [98] followed by the TDS-1 [99]. Both missions demonstrated the feasibility of GNSS-R measurements from space. Shortly after, the CYGNSS mission was launched with 8 satellites for sea wind mapping [100]. The Universitat Politècnica de Catalunya launched a 6-unit Cubesat named 3Cat-2 conveying the PYCARO GNSS-R instrument. Sadly, the satellite did not reach the operational mode. Nevertheless, two missions are being prepared for the short-term: the 3Cat-4 satellite, and the FSSCAT mission which will have two federated cubesats, named 3Cat-5/A and 3Cat-5/B.

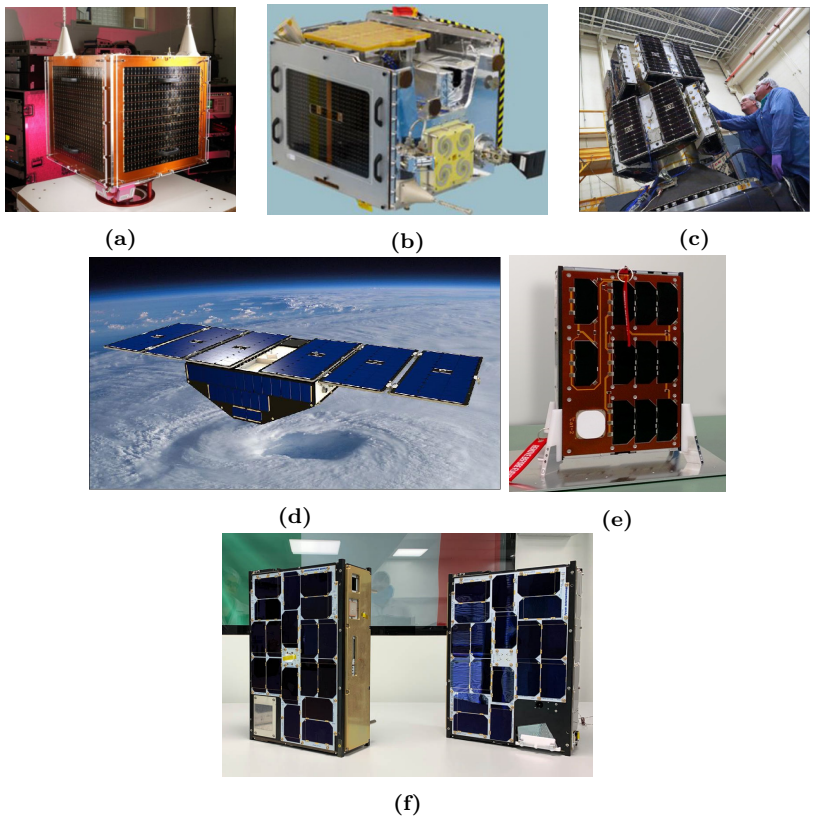

Figure 3.25: Some GNSS-R satellites: (a) UK-DMC-1 satellite from [`https://www.sstl.co.uk/space-portfolio/launched-missions/2000-2009/uk-dmc-1-launched-2003`]; (b) TDS-1 from [96]; (c) several CYGNSS satellites being tested, and (d) artist view of a CYGNSS satellite on space, both from [`https://directory.eoportal.org/web/eoportal/satellite-missions/c-missions/cygnss`]; (e) 3CAT-2 zenith side (courtesy of the Universitat Politècnica de Catalunya, NanoSat Lab.); and (f) 3CAT-5A and B from the FSSCAT mission (courtesy of Tyvak International).

Table 3.3: Summary of GNSS-R instruments with altimetric capabilities - Part I. Adapted and extended from Table 6.14 in [28, ch. 6] and from Table 4 in [29].

Team Instrument	Date	Instrument description									Featured campaigns								
		Hardware					Correlation			Bib.	Altimetry								Other
		Band	BW [MHz]	fs [MHz]	Reflected pol.	Comments	Mod	Comments	Rate		Technique	Signal	h [km]	Platform	Reflecting surface	σ [m]	Bib.	Bib.
NASA	1997			2	LHCP	Modified COTS GPS recv.	HW	Only C/N0 12 channels Delay lag sep.: 0.5 us Tcoh: 1ms Nincoh: 1000		[101]								[101]
NASA/JPL TurboRouge	2000	L1 L2		20.456	LHCP RHCP	Modified TurboRouge recv.	SW	RAW data: 1 bit 16 channels Delay lag sep.: 50 ns Tcoh: Multiple of 125 us	8 kHz	[102, 103]	cGNSS-R group delay	L1P L2P	1.5-3	airborne	ocean	1.7	[104]	[102]
											rGNSS-R group delay	L1P L2P	1.5-3	airborne	ocean	-	[105]	
											cGNSS-R phase delay	C/A	0.48	static	lake	0.02	[106]	
											cGNSS-R group delay	C/A L1P L2P	3	airborne	ocean	0.6	[107]	
ESA	2001	L1	20	6.25	LHCP	Modified GEC-Plessey recv.	SW	RAW data: 8 bits		[108]	cGNSS-R group delay	C/A	0.02	static	estuary	3.3	[108]	
											cGNSS-R phase delay	C/A	0.08	stattic	pond	0.003	[109]	
Starlab/ESA	2002	L1	20.456		LHCP	Modified TurboRouge recv.	SW	RAW data: 1 bit (only I) Tcoh: 10 ms		[110]	cGNSS-R group delay	C/A	1	airborne	ocean	1.5	[111]	
Starlab OCEANPAL	2002	L1			LHCP		SW			[112, 113]	cGNSS-R phase delay	C/A	0.02	static	estuary	0.031	[113]	[112, 113]
UPC/IEEC DODEREC	2002	L1		20.456	LHCP RHCP	PPS synchronism	SW	RAW data: 1 bit Tcoh: 10 ms		[92]	cGNSS-R group delay	C/A	0.1	static	coast		[92]	
SSTL SSTL SGR-10	2003	L1		5.71 (IF)	LHCP	On board UK-DMC [98] PPS synchronism	HW SW	RAW data: 2 bits (IF) Bursts of 40 s data		[98]	cGNSS-R group delay	C/A	700	space-borne			[57]	

Table 3.4: Summary of GNSS-R instruments with altimetric capabilities - Part II. Adapted and extended from Table 6.14 in [28, ch. 6] and from Table 4 in [29].

Team Instrument	Date	Instrument description									Featured campaigns							
		Hardware					Correlation			Bib.	Altimetry							Other
		Band	BW [MHz]	fs [MHz]	Reflected pol.	Comments	Mod	Comments	Rate		Technique	Signal	h [km]	Platform	Reflecting surface	σ [m]	Bib.	Bib.
GFZ	2004	L1			LHCP	Modified OpenSource GPS	HW	12 channels22 delays lags Delay lag sep.: 0.5 chips		[114]	interfer. phase	C/A	1	static	lake	0.02	[114]	
IEEC GOLD-RTR	2007	L1	8	40	LHCP	Aid by a commercial GPS recv. Freq. adjust. with GPSDO PPS syncrhonism Altera Stratix FPGA	HW	Either direct or reflected (not both) RAW data 1 bit 640 complex correlators of 14 bits DDM: 8 bits (8 MSB) 64 lags Delay lag sep. = 50 ns Tcoh = 1 ms Data rate: 1.6 MBps Has Timestamp	1 kHz	[93]	cGNSS-R group delay	C/A	3	airborne	ocean	1.4	[60]	PARIS tests: [115,116] Typhoon: [117,118] Others: [27,119]
											cGNSS-R group delay	C/A	3	airborne	ocean	1.2	[120]	
											iGNSS-R group delay	GPS L1	3	airborne	ocean	0.58		
											cGNSS-R phase delay	C/A	0.7	static	ice	0.6	[121]	
IEEC ASAP	2007	L1 L2	70 (IF)		LHCP RHCP	Based on GOLD-RTR Beamforming In-flight calibration with tones	HW	16 delay lags Delay lag sep.: progamable 320 complex correlators	1 kHz	[122]								
GFZ/DLR GORS	2007	L1 L2			LHCP RHCP	Comercial recv. JAVAD GeNeSiS-112	HW	72 channels	200 Hz	[123]	iGNSS-R phase delay	C/A	3.5	airborne	ocean	$\geq$0.8	[124,125]	[123]
											iGNSS-R* phase delay	GPS L1	0.7	static	ocean	0.5	[126,127]	
UPC PAU	2008	L1		16.384 (IF)	LHCP	Virtex-4 FPGA Includes Kurtosis RFI detector	HW	Relfected and direct path added before cross-correlation RAW data: 2 bits Delay lags: 4096 Delay lag sep: 0.25 C/A chips Doppler bin res.: 250 Hz Doppler bins: 16 Tcoh: 1ms Nincoh: 1000		[128–130]								[94,131]
UPC griPAU	2009	L1		5.745 (IF)	LHCP	Virtex-4 FPGA IF = 4.309 MHz	HW	RAW data: 8 bits Delay lags: 32 Delay lag sep.: 0.36/0.18/0.09 chips Doppler bins; 24 Dopper bin res.: 200 Hz Tcoh: 1ms (adjustable) Nincoh: 1000 (adjustable) Tracking refresh. period: 5 ms Data rate: 6.14 Mbps	1 kHz	[95]								Tests: [132] Sea coh. time: [70] Scatterometry: [133]

Table 3.5: Summary of GNSS-R instruments with altimetric capabilities - Part III. Adapted and extended from Table 6.14 in [28, ch. 6] and from Table 4 in [29].

Team Instrument	Date	Instrument description									Featured campaigns							
		Hardware					Correlation			Bib.	Altimetry							Other
		Band	BW [MHz]	fs [MHz]	Reflected pol.	Comments	Mod	Comments	Rate		Technique	Signal	h [km]	Platform	Reflecting surface	σ [m]	Bib.	Bib.
IEEC PIR/PIR-A	2010	L1	12	80	LHCP	Switch direct and reflected at 1 Hz Based on GOLD-RTR PPS synchronism	HW	Delay lags: 320 Delay lag sep.: 12.5ns Tcoh: 1ms	1 kHz	[115]								Tests: [115, 116, 134]
Uni. New South Wales	2011	L1		16.3676	LHCP	NordNav software recv.	SW	RAW Data: 1.5 bits Tcoh: 1ms Nincoh: 1000		[135]	cGNSS-R group delay	C/A	0.33	airborne	ocean	1	[135–137]	
UPC PYCARO	2012	L1 L2	20		LHCP	Used in 3cat2 and in Bexus.	HW		20 Hz	[138, 139]	cGNSS-R group delay	C/A	0.0476	static	ocean	0.45	[139]	Water channel: [140] Bexus: [141–144] 3CAT-2 [145–148]
											cGNSS-R group delay	C/A	0.65	static	pond	0.08		
											iGNSS-R group delay	GPS L1	0.18	static	estuary	0.08		
											rGNSS-R group delay	GPS L1	0.0476	static	ocean	0.2		
											rGNSS-R group delay	C/A	0.65	static	pond	0.04		
SSTL SSTL SGR-ReSI	2014	L1 L2			LHCP	On board TechDemoSat [99] Virtex-4	HW											
Shangai Ocean University	2015	B1		16;369	LHCP RHCP		SW	Uses BeiDou-2 Data rate: 16 MBps		[149]	cGNSS-R group delay	B1	0.05	static	lake	0.11 (GEO) 1.61 (IGSO)	[149]	
														static	coast	0.37 (GEO)		
											cGNSS-R phase delay			static	coast	0.331 (GEO)	[150]	
Deimos GRIP	2015	L1 E5	52	≤150	LHCP		HW	Uses also Galileo E5	1 Hz	[151]								[151]
NASA SSTL SGR-ReSI DMR	2016	L1				Used in CYGNSS mission [100] Based on SSTL SGR-ReSI 4 simultan. measur. per sat. per sec.	HW	Tcoh: 1ms Nincoh: 1000 Open-loop tracking		CYGNSS webpage								
UPC MIR	2019	L1 L5	32.736	32.736	RHCP	RAW Data: 1 bit Timestamp PPS syncrhonism In-flight calibration 19-elements hexagonal array Dual-band patch antennas Analog beamsteering 4 beams up and 4 down	SW	Uses also GPS L5 and Galileo E5A GPU correlators		This thesis and [5]	cGNSS-R group delay iGNSS-R group delay						This thesis and [5]	

Part II

Contributions to Theoretical Aspects of GNSS-R

4

Chapter 4

Simulation and Analysis of GNSS-R Composite Waveforms

NOWADAYS several GNSS services co-exist at L-band and some more will be available in the near future. These new signals were originally conceived to enhance the location accuracy, but they also offer a promising opportunity for improved GNSS-R retrievals. This chapter gives closed-form expressions for GNSS-R waveform simulation using the composite GPS L1 and L5 and Galileo E1, E5 and E6 signals as a function of the receiver bandwidth. The impact of the observation geometry and sea state on the waveform shape is studied in airborne and space-borne conditions. Finally, the altimetric height bias using the derivative method is analyzed as a function of the receiver's bandwidth.

The theory developed in this chapter was first published in [152] and extended in [153]. Figures and tables shown here are adapted from the latter references. The work done here has been used to upgrade the PAU/PARIS End-to-End Performance Simulator (P^2EPS) software [7, 44], which has been used in several GNSS-R related research such as the ones in [154–156]. More references can be found on the List of Publications. This work has also lead to a Matlab open-source code to generate GNSS signals [157].

4.1 Derivation of the autocorrelation functions

As explained in Chapter 3, the GNSS-R observables depend on the ACF of the GNSS-R signals. The classical BPSK has a well known ACF. The ACF BOC-based signals can be found in the literature (e.g. [17]), however they apply only to the ideal unfiltered case. This section describes their ACF as a function of the receiver bandwidth in such a way that allows efficient GNSS-R observables modeling for simulators.

4.1.1 Ideal autocorrelation functions

The exact expressions of the ACF of the GNSS signals are hard to derive. Additionally, each transmitted code is somewhat different from the rest of the same component, and many of them are restricted. Instead, a virtually closed-form approach of the ACF can be derived from the definition of the spectra. For the BPSK signals with a chip rate f_r the ACF is approximately given by the well-known triangle function

$$R_{BPSK}(\tau) = \Lambda\left(\tau/t_r\right) = \begin{cases} 1 - |\tau|/t_r, & |\tau| < t_r \\ 0, & \text{elsewhere} \end{cases} \tag{4.1}$$

where $t_r = 1/f_r$ is the chip period. For the sine-phased BOCs(n,m) signals, the ACF can be described as a sum of triangles [158]

$$\begin{aligned} R_{BOC_s}(\tau) = {} & \Lambda\left(\tau/t_b\right)(\tau) \\ & * \sum_{k=1-\alpha}^{\alpha-1} (\alpha - |k|)\left[2\delta\left(\tau - 2kt_b\right) - \delta\left(\tau - (2k-1)\,t_b\right) - \delta\left(\tau - (2k+1)\,t_c\right)\right], \end{aligned} \tag{4.2}$$

where $\alpha = n/m$ is the symbol ratio, $t_b = t_r/\alpha = 1/f_b$, and $\delta(\tau)$ is the Dirac delta function. The derivation of the ACF of the even cosine-phased BOC˙c(n,m) signals is given in Appendix B.1

$$\begin{aligned} R_{BOC_c}(\tau) = \Lambda\left(\tau/t_b\right) * \sum_{k=1-\alpha}^{\alpha-1} (\alpha - |k|)\left[6\delta\left(\tau - 2kt_b\right) - 4\delta\left(\tau - (2k-1/2)\,t_b\right)\right. \\ \left. + \delta\left(\tau - (2k-1)\,t_b\right) - 4\delta\left(\tau - (2k+1/2)\,t_b\right) + \delta\left(\tau - (2k+1)\,t_b\right)\right]. \end{aligned} \tag{4.3}$$

Little research has been done to find the ACF of the AltBOC modulations with constant envelope like E5. However, a very close approximation is provided as a general expression for the Complex Double Binary Offset Carrier (CDBOC) modulations [159]. This modulation is denoted by CDBOC(N_1,N_2,N_3,N_4) which matches an AltBOC(aN_1/2,a) for $N_1 > 1$, $N_2 = 2$, $N_3 = N_1$ and $N_4 = 1$. The generic expression for this ACF is

$$R_{AltBOC}(\tau) = R_1(\tau) + R_2(\tau), \tag{4.4}$$

Table 4.1: GNSS signals ACF summary. The restricted signals are marked with an asterisk. $t_r^{ca} = 1/1023$ ms. Power refers for a the typical minimum received power on Earth with a linear RHCP 3dBi direct antenna

GNSS	BAND	I/Q	SERVICE	COMPONENT	MODULATION		POWER [dBW]	EQ.	t_r	PARAMETERS
GPS	L1	I	P(Y)	DATA*	BPSK-R10		Typ: -158.5	4.1	$t_r^{ca}/10$	-
		Q	C/A	DATA	BPSK-R1		Typ: -155.5	4.1	t_r^{ca}	-
		I	M	N/A*	BOCs(10,5)		Typ: -154	4.2	$t_r^{ca}/5$	α= 2
	L5	I	SoL	DATA (L5I)	BPSK-R10		Typ: -154.9	4.1	$t_r^{ca}/10$	-
		Q		DATA (L5Q)	BPSK-R10		Typ: -154.9			
Galileo	E1	Q	PRS	DATA (E1A)*	BOCc(15,2.5)		Typ: -154	4.3	$2t_r^{ca}/5$	α= 6
		I	OS,SoL, CS	DATA (E1B)	CBOC(6,1,1/11)	BOCs(1,1)	Typ: -154	4.2	t_r^{ca}	α= 1
				PILOT (E1C)		BOCs(6,1)		4.2	t_r^{ca}	α= 6
	E6	Q	PRS	DATA (E6A)*	BOCc(10,5)		Typ: -152	4.3	$t_r^{ca}/5$	α= 2
		I	CS	DATA (E6B)*	BPSK-R5		Typ: -152	4.1		-
				PILOT (E6C)*	BPSK-R5					
	E5	I	OS	DATA (E5aI)	AltBOC(15,10) with constant envelope		Typ: -152	4.4-4.5b	$t_r^{ca}/10$	a = 10 N1 = 3 N2 = 2 N3 = 3 N4 = 1
		Q		PILOT (E5aQ)						
		I	OS,SoL, CS	DATA (E5bI)			Typ: -152			
		Q		PILOT (E5bQ)						

where $R_1(\tau)$ and $R_2(\tau)$ are

$$R_1(\tau) = \Lambda_{T_{B_{12}}}(\tau) * \sum_{i=0}^{N_1-1}\sum_{k=0}^{N_2-1}\sum_{i_1=0}^{N_1-1}\sum_{k_1=0}^{N_2-1}(-1)^{i+i_1+k+k_1}\cdot\delta\left[\tau-(i-i_1)\,T_{B_1}-(k-k_1)\,T_{B_{12}}\right], \tag{4.5a}$$

$$R_2(\tau) = \Lambda_{T_{B_{12}}}(\tau) * \sum_{l=0}^{N_3-1}\sum_{m=0}^{N_4-1}\sum_{l_1=0}^{N_3-1}\sum_{m_1=0}^{N_4-1}\sum_{p=0}^{N_r-1}\sum_{p_1=0}^{N_r-1}(-1)^{l+l_1+m+m_1}\delta\left[\tau-(l-l_1)\,T_{B_3}-(m-m_1)\,T_{B_{34}} - (p-p_1)\,T_{B_{12}}\right], \tag{4.5b}$$

with $T_{B_i} = {}^{Tc}/_{N_i}$, $T_{B_{ij}} = {}^{Tc}/_{N_iN_j}$ and $N_r = {}^{N_1N_2}/_{N_3N_4}$.

The last three columns in Table 4.1 relate the GNSS signals to the equations derived above. The chip periods t_r are referred to the period of a L1 C/A signal $t_r^{ca} = 1/1023$ ms. These equations are meaningful because they easily express the ACF of the GNSS signals with the convolution of the ACF of an ideal square pulse of a given length, with a sum of time-delayed delta functions. This will be very useful in the next section for band-limited pulses.

4.1.2 Band-limited autocorrelation functions

The expressions derived in last section fit only for infinite bandwidth signals. However, the filters used in the transmitting satellites and in the receiver, smooth the shape of

the ACF. The outcome of normalized band-limited pulse of length t_b from an ideal filter is [160, ch. 3]

$$u_B(t) = \frac{1}{\pi t_b}\left[\mathrm{Si}\left(2\pi B\left(t + t_b/2\right)\right) - \mathrm{Si}\left(2\pi B\left(t - t_b/2\right)\right)\right], \tag{4.6}$$

where $Si(x) = \int_0^x sin(x)/x dx$ is the sine integral function, and B is the baseband bandwidth of the filter. Assuming identical ideal square filters in the transmitter and in the receiver, the ACF of the last pulse is given in Appendix B.2 as

$$\begin{aligned} R_B(\tau) = &\frac{1}{\pi}(\tau + t_b)\,\mathrm{Si}\left(2\pi B\left(\tau + t_b\right)\right) + \frac{1}{2B\pi^2}\cos\left(2\pi B\left(\tau + t_b\right)\right) \\ &+ \frac{1}{\pi}(\tau - t_b)\,\mathrm{Si}\left(2\pi B\left(\tau - t_b\right)\right) + \frac{1}{2B\pi^2}\cos\left(2\pi B\left(\tau - t_b\right)\right) \\ &- \frac{2}{\pi}\tau\,\mathrm{Si}\left(2\pi B\tau\right) - \frac{1}{B\pi^2}\cos\left(2\pi B\tau\right). \end{aligned} \tag{4.7}$$

As explained in Chapter 3, the altimetric tracking point is related to the derivative of the ACF, which can be written as

$$R'_B(\tau) = \frac{1}{\pi}\left[\mathrm{Si}\left(2\pi B\left(\tau + t_b\right)\right) + \mathrm{Si}\left(2\pi B\left(\tau - t_b\right)\right) - 2\,\mathrm{Si}\left(2\pi B\tau\right)\right]. \tag{4.8}$$

To obtain the band-limited ACF for the GNSS signals, the ideal triangle function in (4.1)-(4.5b) should be substituted by the above expressions.

4.2 Instrumental bias

The retrieved specular delay explained in Chapter 3 is actually biased with respect to the true one [60]. This overall bias includes as well several instrumental ones, some of them are described experimentally in [134]. This section studies the bias produced by the receiver bandwidth, observation geometry and sea state state on the GPS and Galileo waveforms. The bandwidth bias was first evaluated in [60], and it has been observed in [161].

The P^{2}EPS software [154] has been used to generate ocean scenarios for several receiver heights h_r, sea surface wind speeds U_{10}, and elevation angles θ_e^r. The waveforms are then obtained using (3.25) with a coherent integration time of 1 ms. The elevation angle is defined as the angle between the surface tangent to the specular point on Earth and the line that passes through this point and the transmitter. Two main scenarios are considered. Airborne altitudes of 1-1.5 km, similar to those used in real flights campaigns, and also space-borne heights of 600 km (as intended for the PARIS IoD mission [3]) and 400 km (as proposed for the GEROS-ISS mission, which will receive the GNSS-R signals from the ISS [6]). The full scenario description is summarized in Table 4.2.

Table 4.2: Scenarios definition for different receiver height h_r, sea surface wind speed U_{10} and elevation angle θ_e^r.

Scenario	*1*	*2*	*3*	*4*	*5*	*6*	*7*	*8*
$\boldsymbol{h_r}$ **[km]**	1	1	1.5	1	600	600	400	600
$\boldsymbol{U_{10}}$ **[m/s]**	3	10	10	10	3	10	10	10
$\boldsymbol{\theta_e^r}$ **[°]**	90	90	90	60	90	90	90	60

4.2.1 Bandwidth impact

Figure 4.1 shows the effect of an ideal receiver filter on the waveform shape for different baseband bandwidths, and compares them to the unfiltered one, and to the ideal absolute square ACF. The zoomed section plots the waveform's leading edge around the specular delay (in circle). Note that the horizontal axes in all plots have delay units in C/A chips.

The waveforms are much more elongated in the delay domain than the ACFs are. Actually, the ACF can be understood as the waveform resulting from a specular reflection in a single reflection point from a perfectly flat surface. As the surface wind speed increases, the sea surface roughness increases as well, and has the effect of generating additional reflection points after the specular one. The obtained waveform is the addition of all the ACFs resulting from each scattered point. Additionally, as explained in Section 4.1.2, bandwidth filtering enlarges the ACF in the time domain, which results in a spreading of the band-limited waveforms over longer periods.

The waveform shape strongly depends on the bandwidth. The small bandwidth filters only allow to receive the narrow band modulations of the whole composite signal. When enlarging the bandwidth, the wideband modulations (i.e. BOC-based) are acquired and the waveform shape changes. This effect is primarily seen in the signals with a multi-peak ACF, as additional waveform peaks appear. It is noticed that the waveforms filtered with the transmitted bandwidth are a very close approximation of the ideal unfiltered ones.

Bandwidth filtering introduces a bias in the specular delay retrieval. This can be explained from the classical communications theory in which it is desired to measure the time of arrival of a single pulse (e.g. [160, ch. 9]). The rise time of the pulse is reduced as the bandwidth becomes larger. On the contrary, the filter flattens the rise step of the pulse, resulting in a negative bias for the arrival time, i.e. shifting towards early delays. The zoomed pictures in Fig. 4.1 clearly show that large bandwidth signals have a sharper leading edge, and that there is a negative bias in the specular point.

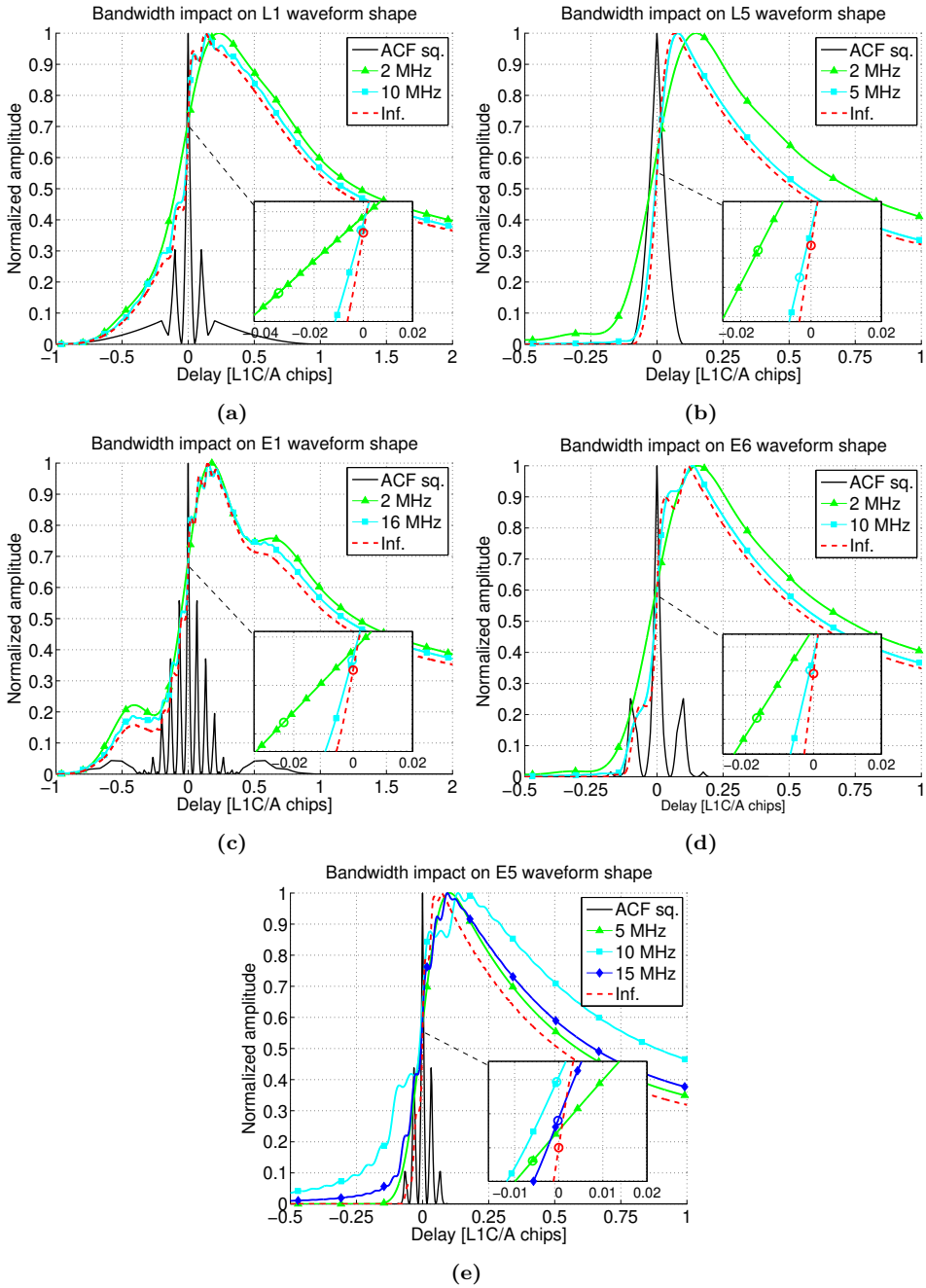

Figure 4.1: Ideal receiver bandwidth (baseband) impact on waveform shape and ideal squared ACF of the transmitted signal. Inside box: Zoom around the specular point delay (given by the circle). (a) L1, (b) L5, (c) E1, (d) E6, (e) E5. Simulation scenario #5 from Table 4.2.

In airborne conditions (flat Earth approximation), the time bias is converted into height bias by the following simple equation

$$bias_h = \frac{bias_\tau \cdot c}{2 \sin \theta_e^r}, \tag{4.9}$$

where c is the speed of light. Figure 4.2 shows the evolution of the height bias of all the composite signals as function of the bandwidth for scenario #1 (low altitude, airborne case, calm sea, and nadir reflection). The nonlinear behavior of the bias is due to the singular characteristics of the BOC signal's spectra. The BOC subcarriers spread the signal power towards further frequencies. When a new power lobe is collected by the receiver, the bias is reduced. The big difference between the signals (∼-1 cm for the E5 and ∼-170 cm for the L5 in their respective transmitted bandwidths) is related to the power containment factor, defined as the amount of signal power that falls within a certain bandwidth. The L5 signal requires a wider filter to receive the same percentage of power than the E5 signal. In other words, there is still significant power contribution at larger frequencies that reduce the bias.

Table 4.3 gives the retrieved bias for scenario #1, using different types of filters with the same bandwidth as the transmitted one. For the non-ideal filters the bandwidth is defined at -3 dB. Again, the power distribution of the signal has a large impact on the bias given by the different filters. See for example the region around the transmitted bandwidth of the GPS L5 signal (12.0 MHz), which has a large slope. Since the real filters receive certain power outside their cut-off frequency, they affect more the retrieved bias. On the other hand, the bias behavior of the Galileo E5 signal is almost flat when it reaches the transmitted bandwidth (25.6 MHz). Thus, the effect of the filter shape is negligible in this case.

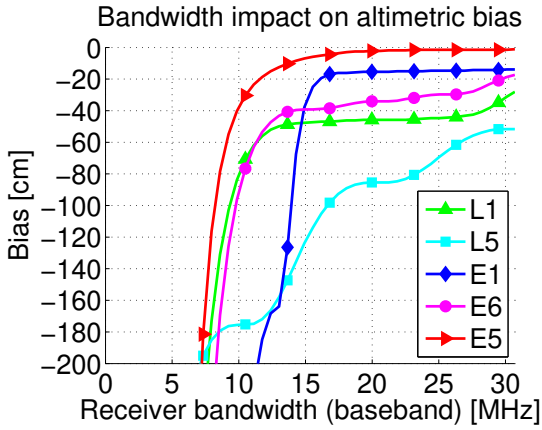

Figure 4.2: Altimetric bias produced by the receiver bandwidth. Scen. #1 from Table 4.2.

Table 4.3: Height bias [cm] produced by the receiver filter with the same bandwidth as the transmitter one (see Tables A.1 and A.2). Simulation scenario #1 from Table 4.2.

Filter Type	L1	L5	E1	E6	E5
Ideal	-47.3	-170.5	-20.5	-34.1	-1.4
3rd-order Butterworth	-49.1	-145.2	-22.4	-31.2	-1.4
5rd-order Butterworth	-48.4	-156.2	-22.4	-33.4	-1.4
5rd-order Chebyshev Type I	-48.0	-160.6	-17.6	-33.4	-1.4

4.2.2 Geometry and wind speed impact

Figure 4.3 shows several waveforms of the Galileo signals E6 and E1 ideally filtered with the same bandwidth as the transmitted one. In the airborne cases, one can intuitively see the shape of the original ACF. However, in the space-borne scenarios the waveforms are very similar aside their power. The idea is that the glistering zone, i.e. the surface area from where the reflections reach the receiver, viewed from a space-borne height is so large that the effect of the geometry and sea state is blurred. Thus, the waveforms for the airborne cases are much more sensitive to scenario parameters than in the space-borne case.

For low elevation angles and high altitudes, the waveform is spread in the delay domain because the glistering zone has also increased. Also, for large wind speeds, the waveform is extended because of the power coming from additional scatters. The relative magnitude of the secondary peaks residing at the trailing edge depends on the scenario, as well as the position of waveform's maximum peak (usually referred as scatterometric delay).

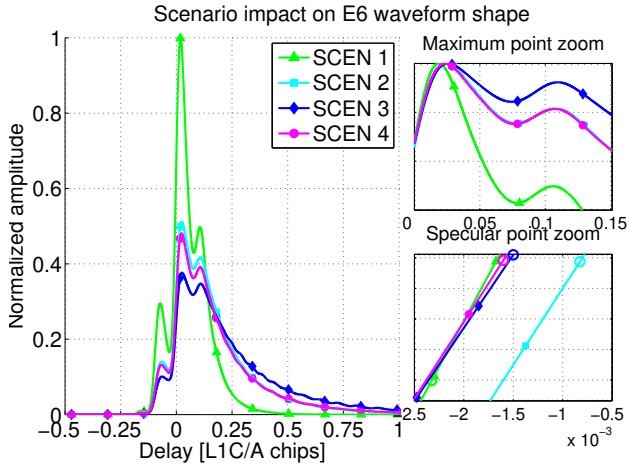

(a)

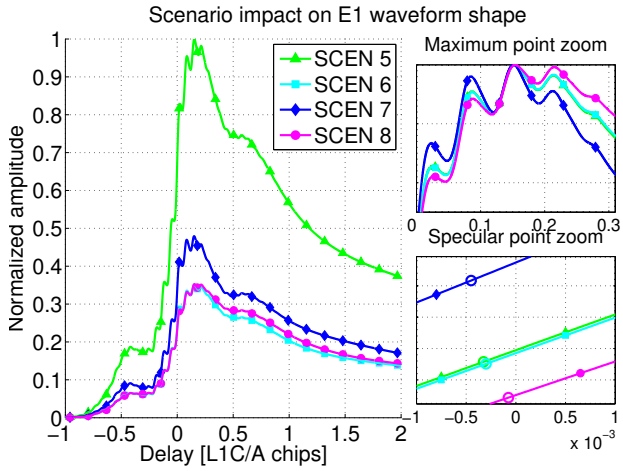

(b)

Figure 4.3: Waveform shape for different scenarios (see Table 4.2) using the transmitted bandwidths with an ideal filter. Top-right box: Zoom around the normalized maximum. Bottom-right box: Zoom around the specular delay (given by the circle). (a) E1, (b) E6.

The bandwidth bias does not only depend on the bandwidth itself, but also on the scenario parameters. Figure 4.4 illustrates this behavior using the GPS L1 and Galileo E1 with a fixed height and bandwidth, and changing the elevation angle and wind speed. It is observed that elevation angles higher than 65°have little impact on the bandwidth bias. However the bias is reduced as larger the wind speed is. Although this may seem counterintuitive, this bias is not a direct consequence of the sea state, but tells about the behavior of filtering at different wind speeds. Since the contribution of the specular reflection to the overall waveform is increased as smaller the wind speed is, the larger will be the impact of filtering and the larger will be the bias.

4.3 Conclusions

This chapter has provided closed-form expressions of the WAF of the GPS L1 and L5 and Galileo E1, E6 and E5 composite signals as a function of the receiver bandwidth. They are used to simulate waveforms for several airborne and space-borne scenarios.

The receiver bandwidth causes an instrumental bias that must be calibrated independently for each signal. However, this bias also depends on the observation geometry and the sea surface wind speed. The wind speed can be estimated from the relative position of the waveform maximum peak (or scatterometric delay) with respect to the altimetric delay, as well as from the relative power between the main peak and additional ones (if any). Once the wind speed is retrieved, the altimetric bias can be numerically computed.

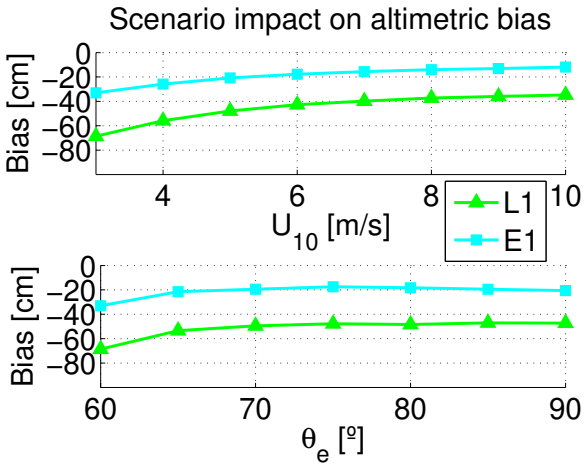

Figure 4.4: Wind speed (top) and elevation angle (bottom) impact on altimetric bias with a receiver height of 1 km.

5

Chapter 5

Precision Bounds in GNSS-R Altimetry

The GNSS signals offer a promising opportunity to perform mesoscale altimetry with worldwide coverage using small satellites. However, unlike the signals used in classical altimeters, the GNSS signals have smaller bandwidth and lower transmitted power. This chapter analyzes the achievable height precision of the GNSS-R altimeters based on the Cramér-Rao bound for time-delay estimation. Precision bounds for the composite signals GPS L1 and L5 and Galileo E1, E5 and E6 in a space-borne mission scenario are assessed, and the optimum receiver bandwidths which minimize them are obtained.

The theory developed in this chapter was first published in [152] and extended in [162]. Figures and tables shown here are adapted from the latter references.

5.1 Introduction

Classical radar altimeters define the waveforms with closed-form expressions based on the Brown model [85]. The parameters of these equations include the sea state as well as the height. The impact between them can be analyzed by different estimation methods. See for example [163, 164] using Maximum Likelihood Estimators (MLE), [165] for the Least Squares Method (LSM) or [166–169] for the generic case of Bayesian estimators. However, the Brown model cannot be applied to GNSS-R because of the bistatic configuration, and because the assumption of short transmitted pulses is not satisfied. At the moment, no closed-form expressions exist for the GNSS-R waveforms and the estimates are based on the model defined in (3.21).

The ultimately achievable GNSS-R altimetric precision is still under study. The first proposed technique used the tracking loop theory of GNSS receivers [170]. However, this method cannot actually be applied because the reflected signal has lost almost all the coherency, and the resulting cross-correlation is highly distorted. In [3] the waveform is linearized around the specular reflection point, and the height precision is found to be inversely proportional to the retrieved slope, similar to the estimate of the time of arrival of a single pulse in classical communications theory [160, ch. 3]. However, this method fits well only for high SNR and slowly varying waveforms. The Cramér-Rao bound (CRB) is a lower bound on the variance of any unbiased estimator of a deterministic parameter (e.g. [171]), and it is analyzed in [172] using only the L1CA signal and without deeply studying the effect of the sea state. The CRB is also applied in [173] to real GPS L1CA waveforms obtained from the UK-DMC space mission [57], which used the cGNSS-R technique. None of the methods mentioned evaluate the impact of the Doppler domain in the delay retrieval.

5.2 Cramér-Rao bound on GNSS-R signals

In principle, when estimating the time of arrival of a single pulse, the faster the rise time is, the less the system noise will affect the measurement. A perfect abrupt transition is more robust against noise, but if the rise time is reduced, the power threshold used to indicate the arrival of the pulse can lead to false or early detection [160]. The rise time is decreased by enlarging the signal's bandwidth. However, a wider bandwidth also increases the thermal noise, and eventually reduces the SNR and the delay accuracy estimation. Therefore, a trade-off exists in the bandwidth that one must use: smaller bandwidths lead to smoother pulses and very little thermal noise, while larger bandwidths lead to sharper pulses and more noise. The bandwidth that maximizes the SNR for different signals is already known in radar theory to evaluate the probability of detection [174, ch. 2]. For a

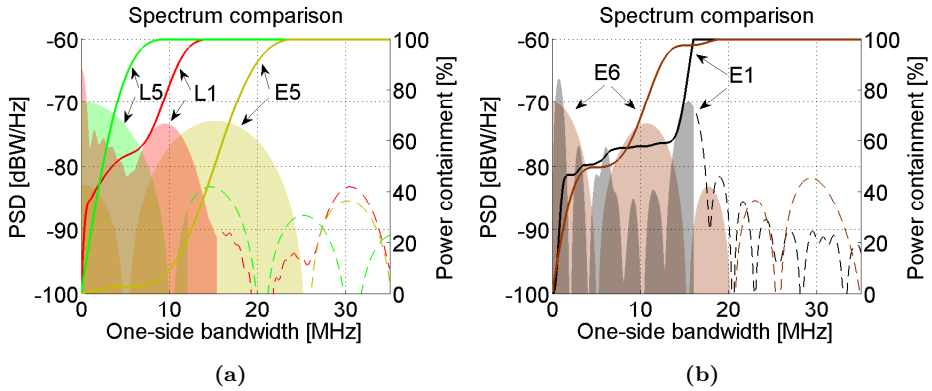

Figure 5.1: Power spectral density (PSD) (left ordinate axis) for 1-Watt power signals, and power containment factor (solid line, right ordinate axis) of the GNSS composite signals. Colored areas indicate the transmitted bandwidths and dashed lines represent their extension to further frequencies. (a) GPS L1 and L5 and Galileo E5, (b) Galileo E1 and E6.

rectangular pulse of duration t_b, the optimum bandwidth of an ideal filter is $\sim 0.7/t_b$. In this section, the bandwidth that minimizes the error variance for delay estimation using the reflected GPS and Galileo signals is studied.

GNSS signals are not simple pulses, but have BPSK and BOC modulations (re-read Chapter 2). Figure 5.1 plots the Power Spectral Densities (PSDs) of the composite signals and the power containment factor, defined as the amount of signal power that falls within the receiver bandwidth. Intuitively, the signals with higher frequency components, produce sharper edges, enabling more accurate altimetric estimations.

In the simplest case that the received signal consists of a single echo from a specular reflection, the DDM is an attenuated and noisy replica of the WAF of the transmitted signal. Similarly, the waveform has the same shape as the ACF squared. The theory in [171, ch. 10] uses the projection of the WAF around its peak over the delay-Doppler plane as a local bound. The term *around* refers to a cut of the WAF's main peak at a certain height for a given SNR. The resulting projection is an ellipse whose width in the delay domain gives the delay precision if the Doppler is known. If the Doppler is also unknown, the real delay precision is given by the projection of the ellipse over the delay-axis. This latter case happens when there is certain *coupling* between the two domains, as it is common in chirp signals [171, ch. 10]. These ellipses are actually the CRB ellipses, and express a lower bound on the variance of the delay for an unbiased estimator under AWGN noise [171, ch. 10].

This theory applies to the ideal case of a perfectly flat surface, which may happen in quiet lakes or under very low wind speed conditions. However, in a general ocean scenario, the reflected signal is not coming from a single path but a group of echos extended in

the delay and Doppler domains. These echoes come from multiple reflections around the specular point called the glistening zone (see Chapter 3. The scattering increases with the sea surface roughness (mainly linked to the sea surface wind speed), and the relative motion between the transmitter and the receiver. The $\sum(\tau,\nu)$ in (3.21) can be understood as the impulse response of a doubly-spread channel with time-selective (i.e. dispersion) and frequency-selective fadings. The resulting DDM is an expanded and distorted replica of WAF.

In the theoretical framework of GNSS-R, it is assumed that the impulse response starts with a specular reflection at τ_{sp} at a given Doppler ν_{sp} followed by a series of monotonically attenuated time-delayed deltas. This means that the time of arrival of the shortest range is no longer found at the maximum of the DDM, but at the maximum of its delay derivative [60]. The derivative can be expressed as

$$\frac{\partial\left|Y(\tau,\nu)\right|^2}{\partial\tau} = \left|\chi(\tau,\nu)\right|^2 ** \frac{\partial\sum(\tau,\nu)}{\partial\tau}. \tag{5.1}$$

Figures 5.2a and 5.2b show respectively the normalized RCS and its delay derivative for a given scenario obtained with the P^{2}EPS software [154]. The derivative highly reduces the area to be convolved with the WAF. The size of the RCS derivative is three orders of magnitude smaller than the WAF of any GNSS signal is (2 GPS L1C/A chips in the delay domain for the largest one [17], and 1 kHz in the Doppler domain for the typically case of $T_{coh} = 1$ms). Consequently, the DDM derivative around the specular point is almost the WAF. In other words, the specular delay precision can be studied from the WAF properties regardless of the sea state and observation geometry . This is found to be true for all signals and for any scenario simulated. Figure 5.2c compares both signals for the Galileo E1 signal as an example.

The valid area of such approximation depends on the signal and the receiver bandwidth. See for example Figs. 5.2d and 5.2e. Estimating a false center-Doppler frequency would result in an erroneous specular delay retrieval not predicted by the approximation. However, for the same SNR, the delay errors related to the Doppler domain are much smaller than the errors occurring exclusively in the delay domain. This result was previously shown in [175] and concludes that the approximation is valid for high enough SNRs, which are actually required for centimeter precision in the altimetric retrievals.

The projection of the WAF over the delay-Doppler plane is an ellipse with the axes parallel to the plane. Thus, the precision can be properly approximated from ACF properties. Figure 5.2f plots the ACF squared of the E1 signal for several bandwidths along with its respective waveform derivatives. Larger bandwidths produce sharper derivatives for which the effect of the noise would be smaller if the SNR was maintained. Hence, the CRB

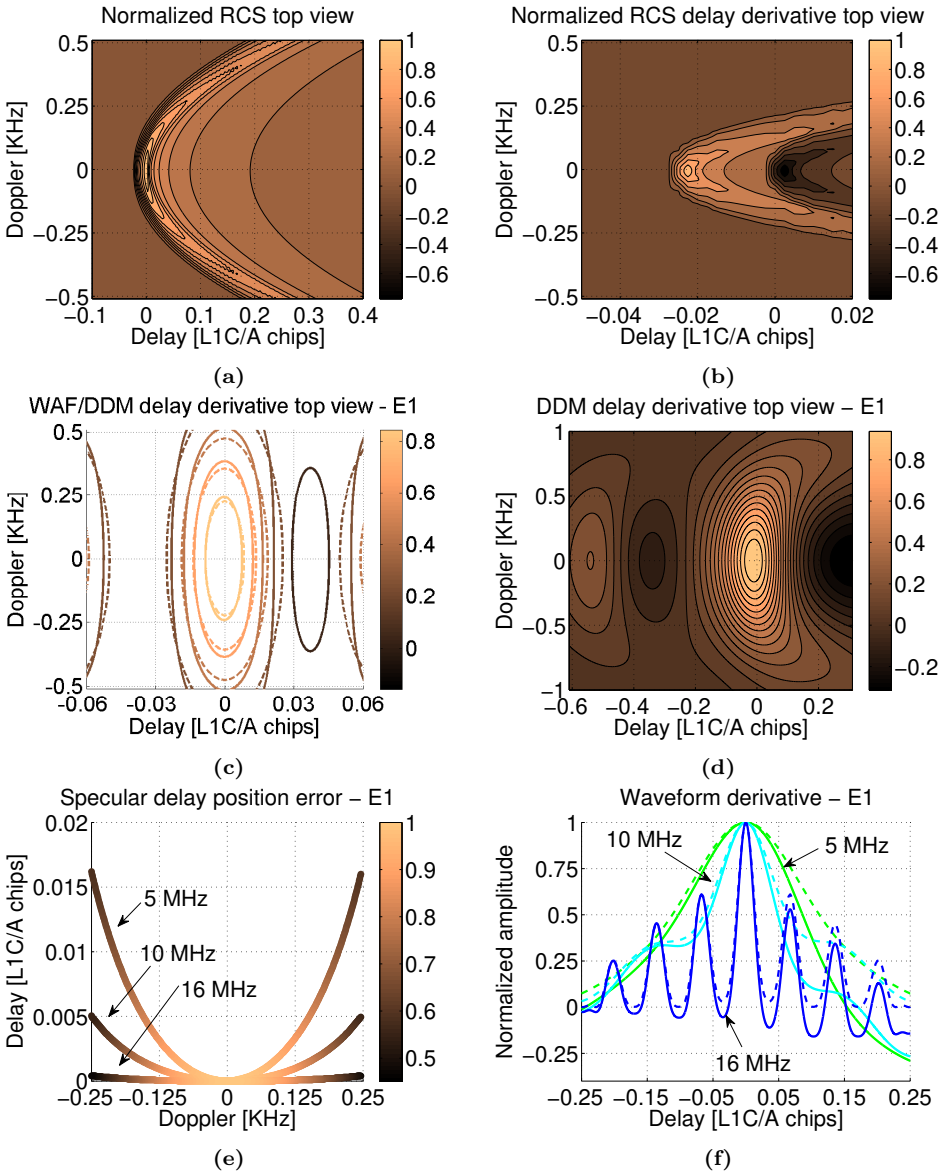

Figure 5.2: (a) RCS for a given scenario, (b) RCS delay derivative zoom, (c) WAF (dashed line) and DDM (solid line) comparison for B= 16 MHz, (d) DDM delay derivative for B= 5 MHz, (e) specular delay retrieval for each Doppler bin, and (f) receiver's bandwidth impact on the shape of the waveform derivative (solid line) and on the ACF squared (dashed line). All bandwidths are defined at baseband.

for time-delay estimation in the only presence of AWGN noise, is given by [171, ch. 10]

$$\sigma_\tau^2(B) \geq \frac{1}{SNR(B)} \cdot \frac{1}{(2\pi)^2 \beta^2(B)}, \tag{5.2}$$

where B is the receiver baseband bandwidth, and β is the so-called RMS bandwidth or Gabor bandwidth in [Hz] defined as (e.g. [171])

$$\beta^2(B) \triangleq \frac{\int_{-B}^{B} f^2 \left|H_{Tx}(f)\right|^2 \left|H_{Rx}(f)\right|^2 S_x(f)\, df}{\int_{-B}^{B} \left|H_{Tx}(f)\right|^2 \left|H_{Rx}(f)\right|^2 S_x(f)\, df}, \tag{5.3}$$

where $H_{Tx}(f)$ and $H_{Rx}(f)$ are respectively the transmitter and receiver normalized baseband filter transfer functions, and $S_x(f)$ is the power spectrum of the infinite bandwidth envelope of transmitted signal. The transmitted bandwidths are defined in the ICDs [13–15, 19, 20] and are summarized in Tables A.1 and A.2. The denominator is an energy normalization factor. Note that a modified definition has been used regarding the classical literature to ensure that no signal power is accumulated outside the transmitted band. The spectra of the signals where defined in Section 2.6.

The CRB states that the more the spectral energy is concentrated at the end of the band, the larger the RMS bandwidth is, and the more accurate the time delay measurement will be. In fact, the RMS bandwidth is the second moment of the band-limited signal's spectrum, or in the same respect, the maximum of the second derivative of its ACF. As any second derivative, it tells about the curvature of the original primitive. The flatter the ACF is, the more prone to delay errors it will be. In contrast, an ACF with high concavity will be less sensitive to delay errors.

The SNR in (5.2) is usually given in the literature by $2E/No$, where E is the signal's energy and $No/2$ is the two-sided noise PSD. Certainly, this is the best achievable SNR if a matched filter is used, and it is independent of the modulation. However, the GNSS-R receiver performs the correlation with the sampled signals after filtering. The number of effective samples to be coherently integrated $M_{coh} \leq f_s \cdot T_{coh}$, will depend on the ratio between the sampling frequency f_s and the bandwidth, as well as the number of bits [176]. Thus, the final SNR at the output of the interferometric cross-correlator is given by

$$SNR(B) = \frac{P_R(B)\, P_D(B) \cdot M_{coh} \cdot \sqrt{M_{in}}}{P_R(B)\, N_D(B) + P_D(B)\, N_R(B) + N_R(B)\, N_D(B)}, \tag{5.4}$$

where $P_R(B)$ and $P_D(B)$ are, respectively, the powers of the reflected and direct filtered signals at the input of the correlator, $N_R(B)$ and $N_D(B)$ are respectively the reflected and direct thermal noise levels for the given receiver bandwidth, and M_{in} is the number of incoherent averages. The signal power is

$$P_{R/D}(B) = \int_{-B}^{B} \left|H_{Tx}(f)\right|^2 \left|H_{Rx}(f)\right|^2 S_{R/D}(f)\, df, \tag{5.5}$$

where $S_{R/D}$ is the Fourier transform of the reflected or direct signal. The thermal noise power is $N_{R/D} = k_B T_{R/D} B_n$, where $T_{R/D}$ is the total noise temperature, $k_B = 1.38 \cdot$

$10^{-23} J/K$ is the Boltzmann's constant, and B_n is the equivalent noise bandwidth

$$B_n = \int_{-B}^{B} |H_{Rx}(f)|^2 \, df. \tag{5.6}$$

The system noise temperature is the addition of the antenna temperature and the system noise. If the two signals share the same receiver, only the antenna noise is different. The noise from the up-looking antenna placed in a satellite is typically 2.7 K at L-band, whereas the noise from the down-looking one depends on the sea brightness temperature, usually much higher. The interferometric processing results in a reduction of the post-correlation SNR as compared to the one that would be obtained if the transmitted code was known. In the cGNSS-R case, $N_D(B)$ is zero, and $SNR(B) = P_R(B)/N_R(B) \cdot M_{coh} \cdot \sqrt{M_{in}}$.

Equation (5.4) was already known for delay estimation (e.g. [177]) and matches Eq. 4 in [3] after some rearrangements

$$SNR(B) = \frac{SNR_R(B)\, SNR_D(B) \cdot M_{coh} \cdot \sqrt{M_{in}}}{1 + SNR_R(B) + SNR_D(B)}, \tag{5.7}$$

where $SNR_R(B)$ and $SNR_D(B)$ are respectively the reflected and direct thermal SNRs at the input of the correlator: $SNR_{R/D}(B) = P_{R/D}/N_{R/D}$. If the reflected signal power is well below the thermal noise, and $SNR_D(B)$ is high enough, the post correlation SNR has a similar behavior than the thermal one.

5.3 Range precision

The RMS bandwidths of the GNSS composite signals obtained using (5.3) with ideal filters are shown in Fig. 5.3a. The power distribution among its components is based on the values given in the Tables A.1 and A.2. As it is seen, they do not increase uniformly with the receiver's bandwidth, but in some regions they rise more steeply because of the irregularities in their respective PSDs. In order to compare the performance of the GNSS signals, and to show the effect of an excessive bandwidth, a common SNR is used. This reference $\mathrm{SNR}_{\mathrm{ref}}$ is defined as the one that would be obtained if the signals with more power (either Galileo E6 or E5) are received with a 35 MHz ideal baseband filter (larger than any transmitted bandwidth). Figure 5.3b shows the obtained SNRs using (5.4) with ideal filters. For the signals with BOC components, the SNR has a non-monotonic behavior because of the uneven power distribution of their spectra and presents some local maxima.

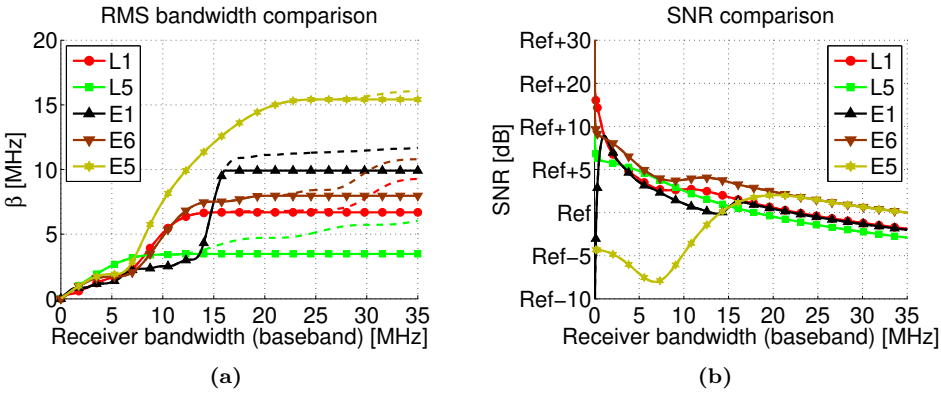

Figure 5.3: (a) RMS bandwidth comparison of the ideal band-limited transmitted signals (solid line), and of the infinite bandwidth signals (dashed line). (b) Relative SNR evolution as function of the bandwidth for the ideal band-limited transmitted signals.

Assuming a flat Earth, the delay precision defined in (5.2), is converted into height precision by the simple equation:

$$\sigma_h = \frac{\sigma_\tau c}{2 \sin \theta_e}, \tag{5.8}$$

where c is the speed of light, and θ_e^r is the elevation angle, defined as the angle between the surface tangential to the specular point on Earth and the line that passes trough these point and the transmitter. Figure 5.4 shows the evolution of the height precision of the GNSS signals as a function of the receiver's bandwidth. The curves are plotted along

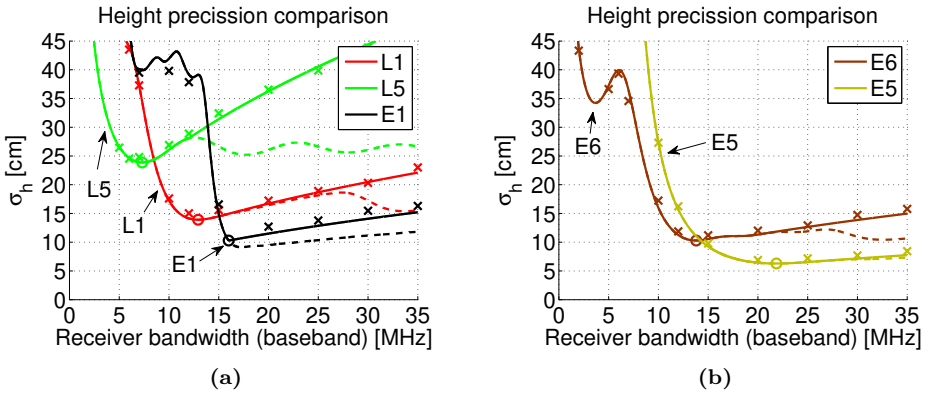

Figure 5.4: Analytical height std. for the ideal band-limited transmitted signals (solid line), and for the infinite bandwidth signals (dashed line) as function of the receiver's bandwidth at baseband. The circles indicate the position of minimum error, and the crosses are the simulation results after 1000 Monte Carlo iterations. (a) GPS L1 and L5 and Galileo E1, (b) Galileo E6 and E5.

Table 5.1: Optimum parameters for best altimetric precision using different type of filters. All parameters are referred to the whole composite signals and not to its individual components. Simulations done with a reference SNR_{ref} of 20 dB.

SIGNAL	PARAM.	IDEAL	BUTT. 3rd	BUTT. 5rd	CHEB. I 5rd
L1	β [MHz]	6.52	6.23	6.37	6.38
	ΔSNR [dB]	3.10	1.80	2.09	2.48
	B_{opt} [MHz]	25.86	26.77	26.56	24.66
	σ_h [cm]	13.91	15.56	14.72	14.09
L5	β [MHz]	3.23	3.08	3.15	3.22
	ΔSNR [dB]	4.72	3.69	3.76	3.77
	B_{opt} [MHz]	14.58	13.59	14.16	13.80
	σ_h [cm]	23.87	25.35	24.53	24.00
E1	β [MHz]	9.92	9.42	9.61	9.85
	ΔSNR [dB]	1.30	0.03	0.45	1.39
	B_{opt} [MHz]	32.00	39.45	37.49	32.09
	σ_h [cm]	10.28	12.68	11.83	10.36
E6	fi [MHz]	7.42	7.30	7.35	7.42
	ΔSNR [dB]	4.41	3.09	3.44	3.91
	B_{opt} [MHz]	27.60	30.34	29.43	26.28
	σ_h [cm]	10.30	11.46	10.93	10.45
E5	fi [MHz]	15.18	14.94	15.00	15.08
	ΔSNR [dB]	2.31	1.20	1.56	1.92
	B_{opt} [MHz]	43.72	45.83	44.50	41.62
	σ_h [cm]	6.29	6.96	6.64	6.34

with the simulation results after 1000 Monte Carlo iterations using the P^{2}EPS software. An interesting result is that the error curves present a minimum at a given bandwidth B_{opt} which is smaller than the nominal signal's bandwidth (last column in the Tables A.1 and A.2). Enlarging the bandwidth beyond the transmitted one will reduce the precision because more noise will be added into the system, compared to the additional signal power. However, except for the Galileo E1, the optimum bandwidths are found below the transmitted ones. Actually, they are very close to the main lobe bandwidth or *modulation bandwidth* of the wider component of their respective signals. They are also located close to a local maximum of the SNR, similarly to what was previously stated for the single pulse example. The complete results are summarized in Table 5.1 using an ideal filter, a Butterworth of 3rd- and 5th-order, and a Chebyshev of 5th-order. The reference SNR_{ref} is 20 dB and the ΔSNR is defined as the SNR increment at the optimum bandwidth over the reference one.

The signal with the best performance is the Galileo E5 ($\sigma_h = 6.34$ cm with 5th-order Chebyshev filter) since it has the widest spectrum and the highest transmitted power. The signal with the worst precision is the GPS L5 ($\sigma_h = 24.00$ cm with 5th-order Chebyshev filter). Although this reference SNR may seem very large, it already includes the incoherent averaging and is in accordance with the value expected for the PARIS

IoD space mission scenario (17.7 s incoherent averaging, corresponding to ≈120 km dwell line) [3] after adjusting for the new receiver bandwidth and by using the Galileo E5/E6 signal power as a reference instead of the GPS L1.

Some issues concerning the CRB bounds given in this section should be mentioned. Firstly, the CRB is an asymptotic bound in terms of SNR, which means that it predicts the best achievable measurements up to a certain SNR. The threshold SNR depends on the signal characteristics and is more severe for signals with multi-peak ACF. Simulations show that the SNRs required for centimeter resolution are much higher than the threshold ones. These high SNRs can be achieved using high directivity antennas and large incohering integration times. Secondly, it is assumed that the precision is only limited for the AWGN receiver noise, and speckle (i.e. multiplicative noise) is not included in these derivations. And thirdly, all the bias are assumed to be known.

5.4 Conclusions

In this chapter the optimum altimetric performance of the GNSS-R using the composite GPS and Galileo signals in-space has been evaluated using the CRB. The height precision strongly depends on the signal bandwidth or more specifically, on the power distribution within this bandwidth. The optimum receiver bandwidths which minimize the error variances of each signal have been found to be slightly below the transmitted ones. As a result, a trade-off exists for multi-band altimeters such as the PARIS IoD sharing the same receiver chain, specially in the low band (i.e. GPS L5 and Galileo E5). For these receivers, an individual digital filter must be added after sampling for each type of signal, since a single analog filter covering the whole band will not be optimum.

The influence of Doppler errors on the delay estimation is found to be negligible compared to the errors occurring exclusively in the delay dimension. The wind speed and the scenario geometry have no impact on the precision curves except, indeed, for the received power, as these parameters affect more the trailing edge of the waveform, than in the leading edge.

The Galileo E5 signal exhibits the best performance, whereas the GPS L5 has the worst. However, the ultimate performance will depend on the real transmitted powers by the GNSS satellites, which can differ up to 6 dB from their nominal values during their lifetime. The transmission of the GPS L1M signal is selectable, and not all the satellites may contain it, which will decrease the expected precision of the GPS L1 composite signal.

6

Chapter 6

Cross-talk Interference Study

This chapter presents a statistical analysis of the cross-talk phenomenon in interferometric GNSS-R (iGNSS-R). Cross-talk occurs when the Delay-Doppler Map (DDM) of a tracked satellite overlaps others from undesired satellites. This study is performed for ground-based and airborne receivers, and for a receiver on board the International Space Station (ISS) such as the GEROS-ISS experiment proposal. Its impact on ocean altimetry retrievals is analyzed using different antenna arrays. Results show that for elevation angles higher than 60 degrees, cross-talk can be present almost all the time from ground, up to 61% from airborne receivers at 2 km height, and up to ∼10% at the ISS height. Cross-talk can only be mitigated using highly directive antennas with narrow beamwidths. Cross-talk impact using a 7-element hexagonal array still induces large errors on ground, but reduces to centimeter level on airborne receivers, and are negligible from the ISS.

The theory developed in this chapter was first published in [178] and extended in [179]. Figures and tables shown here are adapted from the latter references.

6.1 Introduction

The interferometric DDM given in (3.16) is actually not a single DDM, but one DDM for each satellite in view. It may happen that unwanted DDMs fall close to the desired one. This effect is known as cross-talk, and to the knowledge of the author, although it has been previously stated, it had not been properly formulated until [179]. Cross-talk can introduce critical errors in altimetry, scatterometry, and SAR-like imaging, as well as in defining the correlation window location [62, 86]. Figure 6.1 shows a sketch of multiple DDMs found in delay-Doppler after the correlation process. If the desired satellite to be tracked is #1, there would be overlapping with the DDMs from satellites #2 and #4, while satellites #3 and #5 would have no impact, although they are also in view.

In order to study the cross-talk probability, it is important to understand the nature of the DDM correlation. Two close DDMs do not necessary imply that their respective pairs of transmitter/specular points are also close and vice-versa. On one hand, the Doppler depends on the relative velocity vectors between the transmitter and the receiver. Satellites with different trajectories can have the same Doppler if their radial velocity with respect to the receiver is the same. On the other hand, the delay dimension is limited by the minimum between the correlation length T_{coh}, and the duration of the codes, which can range from 1 ms to more than a week. However in GNSS-R, the correlation length is often set to $T_{coh} = 1$ ms (e.g. [58]), to ensure sea state coherence. This means that all the interferometric delays multiple of T_{coh}, fall in the same delay lag (see the DDM #2 in Fig. 6.1).

As introduced in Chapter 3, the DDM extends the WAF in both domains mainly because of the geometry, but also because of the sea state. The size of the WAF in the delay domain is the maximum ACF length of all the signals inside the same band τ_{Λ}^{max}, given in the second row of Table 6.1. The size in the Doppler domain does not depend on the signal, but on the inverse of the correlation length $\approx 1/T_{coh} = 1$ kHz. The DDMs are simulated using the P^{2}EPS [154] software, and trimmed within rectangles where their amplitude decays below a threshold value. A satellite has cross-talk if the circumscribed rectangle of its DDM is overlapped with another one or more. It is worth saying that other effects as multipath in the direct and/or the reflected signals [67], or cross-polarization interference, can also result in DDM overlapping. These cases are not considered in this work.

In this study, satellite orbits have been propagated using the STK software [180], using their actual ephemeris data. For those satellites that are not launched yet, their nominal ephemeris have been used. The GEO and GSO satellites have not been simulated because their antennas point just to specific regions. It has been assumed that all the satellites transmit in all their available bands, despite their current version, as will eventually

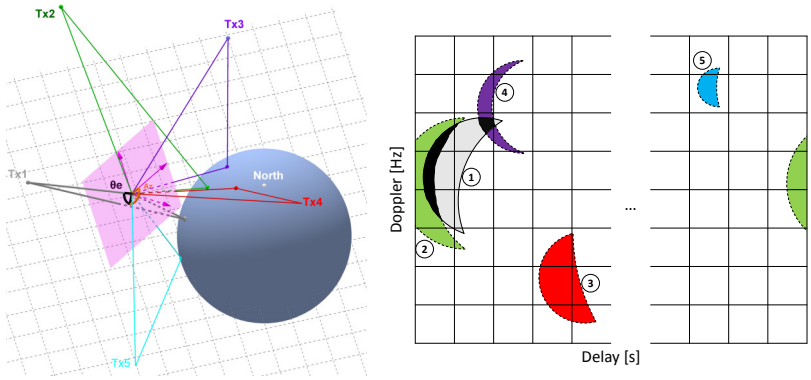

Figure 6.1: Cross-talk phenomenon example with 5 satellites in view (a), and their respective DDMs in the delay/Doppler plane (b). If the receiver is tracking satellite #1, there would be overlapping (black areas) with satellites #2 and #4.

happen when the constellations get upgraded. A total of 83 satellites (32 GPS, 27 Galileo, and 24 BeiDou-2) have been simulated. The properties of these constellations were given in Table 2.1, and their spectra allocation was shown in Fig. 2.1.

Most of the GNSS signals are actually the aggregate of several codes. In this section, the DDMs are obtained from the whole composite signals, although new techniques to remove specific codes are being investigated [49]. The receiver is simulated to be tuned to each carrier frequency, and with the same bandwidth as the transmitted one. The interfering signals may come from other satellites of the same constellation, and from other constellations if they share the same band. The third row of Table 6.1 summarizes the overlapped bands in which cross-talk may happen. If for example the desired signal is a GPS L1 or Galileo E1, the interfering signals may be these two, but also the BeiDou-2 B1 and B1-2. However if the desired signal is a BeiDou-2 B1 or B1-2, it would have interference only with its own constellation. This is because if the receiver is designed to receive only this specific signal, very little power would be received from the GPS L1 or Galileo E1 (see Chapter 4).

6.2 Definition

Let $\vec{T}$, $\vec{R}$ and $\vec{S}$ denote respectively the positions of a GNSS transmitting satellite, a receiver, and their related specular point on the Earth's surface (i.e. the point in which the reflected path is shortest). Their respective velocity vectors are $\vec{T_v}$, $\vec{R_v}$ and $\vec{S_v}$. The direct signal arrives to the receiver with a delay τ_{pk} and Doppler ν_d, and the specular

reflected signal with τ_r and ν_r

$$\tau_{pk} = \frac{\left|\vec{T} - \vec{R}\right|}{c}, \tag{6.1}$$

$$\tau_r = \frac{\left|\vec{T} - \vec{S}\right|}{c} + \frac{\left|\vec{S} - \vec{R}\right|}{c}, \tag{6.2}$$

$$\nu_d = \left[\left(\vec{R_v} - \vec{T_v}\right) \cdot \frac{\left(\vec{T} - \vec{R}\right)}{\left|\vec{T} - \vec{R}\right|}\right] \frac{f_c}{c}, \tag{6.3}$$

$$\nu_r = \left[\left(\vec{S_v} - \vec{T_v}\right) \cdot \frac{\left(\vec{T} - \vec{S}\right)}{\left|\vec{T} - \vec{S}\right|} + \left(\vec{R_v} - \vec{S_v}\right) \cdot \frac{\left(\vec{S} - \vec{R}\right)}{\left|\vec{S} - \vec{R}\right|}\right] \frac{f_c}{c}, \tag{6.4}$$

where c is the speed of light and f_c is the carrier frequency of the transmitted signal. The interferometric Doppler ν_{sp}, and the interferometric delay τ_{sp} inside a correlation window of length T_{coh}, are defined as

$$\nu_{sp} = \nu_d - \nu_r, \tag{6.5}$$

$$\tau_{sp} = (\tau_{pk} - \tau_r) \bmod T_{coh}, \tag{6.6}$$

where mod is the modulus operation (remainder of the division).

For the sake of simplicity, it is assumed that the DDMs are symmetrical in the Doppler axis at ν_{sp}, although the wind speed direction can produce a skewness [73]. The spread in the Doppler domain is then defined as $\nu_{sp} \pm \gamma_\nu$, which results in a width

$$W_\nu = 2\gamma_\nu. \tag{6.7}$$

In the delay domain, the DDM spans from half the ACF's length $\tau_\Lambda^{max}/2$ *before* τ_{sp}, to γ_τ units *after* τ_{sp}. The true position of these limits are not necessary *before* or *after* because of the circular properties of the delay domain. The geometric delay center τ_{sc}, and width W_τ are

$$\tau_{sc} = \left(\tau_{sp} + \frac{\gamma_\tau - \tau_\Lambda^{max}/2}{2}\right) \bmod T_{coh}, \tag{6.8}$$

$$W_\tau = t_c/2 + \gamma_\tau. \tag{6.9}$$

The size of a typical DDM from ground or airborne heights, is similar to the WAF of the transmitted signal: $\gamma_\tau \approx \tau_\Lambda^{max}/2$, and $\gamma_\nu \approx 1$ kHz. From the ISS, the DDMs obtained with [154] shows $\gamma_\tau \approx 6$ C/A chips and $\gamma_\nu \approx 2$ kHz where the amplitude decay by $1/e$.

Consider now two satellites i and j. The distance between their interferometric Doppler centers is

$$\Delta\nu_{ij} = |\nu_i - \nu_j|. \tag{6.10}$$

In the circular delay space, two distances can be defined between the delay center of their DDMs

$$d_{ij} = \left(\tau_{sci} - \tau_{scj}\right) \bmod T_{coh}, \tag{6.11}$$

$$d_{ji} = \left(\tau_{scj} - \tau_{sci}\right) \bmod T_{coh}. \tag{6.12}$$

The true delay distance is defined as the minimum of them

$$\Delta\tau_{ij} = min\{d_{ij}, d_{ji}\}. \tag{6.13}$$

The two satellites have their DDMs overlapped if their interferometric distances are smaller than the defined thresholds

$$C_{ij} = \begin{cases} 1 & \text{if } \Delta\tau_{ij} \leq \left(W_{\tau i} + W_{\tau j}\right)/2, \Delta\nu_{ij} \leq \left(W_{\nu i} + W_{\nu j}\right)/2 \\ 0 & \text{else} \end{cases} \tag{6.14}$$

The number of interfering satellites on satellite i is

$$K_i = \sum_{j \neq i} C_{ij}. \tag{6.15}$$

6.3 Statistics

This section presents several figures of merit to statistically study the cross-talk behavior. These figures are obtained by averaging the individual statistics of each satellite with all of the same constellation for a specific band. For example, the statistics of the GPS L5 refer to any GPS satellite when the signal of interest is the GPS L5. In this case, the interfering signals may be other GPS L5 signals, but also the Galileo E5A from the Galileo satellites. The statistics are the result of simulating 4 days of satellite positions sampled every second, and are repeated for some receiver altitudes, speeds and locations over the Earth, as well as on-board ISS.

6.3.1 DDM distribution in the delay/Doppler plane

The study starts with the one-to-one joint PDF of the interferometric delay and Doppler differences between the tracked satellite and the others in view sharing the same band

$$P\left(\Delta\tau_{ij}, \Delta\nu_{ij}\right) \ \forall i \neq j. \tag{6.16}$$

This PDF gives the distribution in the delay/Doppler plane of the distance between the centers of the desired DDM and the others in view. As an example, Fig. 6.2 shows the PDF when the tracked satellite is a BeiDou-2, whereas the others may also be Galileo,

Table 6.1: Cross-talk statistics and impact summary when tracking a satellite with $\theta_e^d > 60°$. Abbrevations are τ_Λ^{max}: composite signal ACF's maxim length, $\bar{P}_{cs}^{60}$: cross-talk probability, $\bar{N}_{sat}^{60}$: average number of interfering satellites, τ_{cs}: 90th percentile cross-talk duration, τ_{ncs}: 90th percentile cross-talk free duration, $\bar{T}^{60}$: percentile at which SIR is larger than 10 dB, $\bar{\epsilon}^{60}$: altimetric average error, and $\bar{S}^{60}$: percentile at which the error is smaller than 10 cm. Impact results on non-averaged waveforms using a 7 element hexagonal array.

		Band	**GPS L5**	**Galileo E5A**	**Galileo E5B**	**BeiDou-2 B2**	**Galileo E5**	**GPS L2**	**Galileo E6**	**BeiDou-2 B3**	**GPS L1**	**Galileo E1**	**BeiDou-2 B1/B1-2**
		τ_Λ^{max} **[ms]**	0.2	0.2	0.2	1	0.2	2	0.4	0.2	2	2	1
		Interferent	GPS L5 Galileo E5A	GPS L5 Galileo E5A	Galileo E5B BeiDou-2 B2	Galileo E5B BeiDou-2 B2	Galileo E5 GPS L5 BeiDou-2 B2	GPS L2	Galileo E6 BeiDou-2 B3	Galileo E6 BeiDou-2 B3	GPS L1 Galileo E1 BeiDou-2 B1 BeiDou-2 B1-2	GPS L1 Galileo E1 BeiDou-2 B1 BeiDou-2 B1-2	BeiDou-2 B1/B1-2
Ground (250 m)	**Statistics**	$\bar{P}_{cs}^{60}$ *[%]*	30.1	29.4	73.5	86.2	80.3	19.0	51.6	50.8	>99.9	>99.9	25.7
		$\bar{N}_{sat}^{60}$	0.65	0.63	1.58	2.03	1.92	0.39	1.10	1.06	6.04	6.00	0.54
		τ_{cs} *[s]*	282	278	1194	1827	1102	342	543	485	10805	12702	923
		τ_{ncs} *[s]*	553	536	436	300	275	1571	510	473	98	38	4181
		$\bar{T}^{60}$ *[%]*	81.0	71.5	56.2	36.7	58.5	83.0	69.3	44.0	32.9	6.2	94.2
	Impact	$\bar{\epsilon}^{60}$ *[cm]*	1.98	<0.01	<0.01	73.76	<0.01	1.34	<0.01	99.00	6.40	10.70	4.93
		$\bar{S}^{60}$ *[%]*	53.7	13.4	92.0	23.0	92.1	92.0	90.6	25.6	93.3	75.9	80.9
Airborne (2 km)	**Statistics**	$\bar{P}_{cs}^{60}$ *[%]*	3.6	3.6	20.3	24.0	22.7	2.0	12.7	13.1	44.7	61.0	2.1
		$\bar{N}_{sat}^{60}$	0.07	0.07	0.41	0.49	0.46	0.04	0.25	0.26	1.06	1.40	0.04
		τ_{cs} *[s]*	152	154	805	855	578	189	424	430	2038	2891	320
		τ_{ncs} *[s]*	3948	4233	3551	3500	2191	6455	3425	3356	3186	2392	10509
		$\bar{T}^{60}$ *[%]*	86.6	79.0	64.5	60.4	69.8	90.0	76.0	49.5	84.1	58.2	98.5
	Impact	$\bar{\epsilon}^{60}$ *[cm]*	0.14	<0.01	<0.01	74.30	<0.01	<0.01	<0.01	122.92	0.95	2.00	<0.01
		$\bar{S}^{60}$ *[%]*	68.2	20.0	95.3	12.2	94.6	98.2	94.6	11.4	94.6	87.5	49.0
Space-borne (400 km)	**Statistics**	$\bar{P}_{cs}^{60}$ *[%]*	5.4	5.2	6.9	7.2	9.7	2.3	6.9	7.2	8.2	9.7	1.7
		$\bar{N}_{sat}^{60}$	0.11	0.11	0.14	0.14	0.20	0.05	0.14	0.14	0.17	0.20	0.03
		τ_{cs} *[s]*	13	15	22	21	18	13	22	21	14	18	13
		τ_{ncs} *[s]*	257	278	326	321	205	493	326	321	188	205	638
		$\bar{T}^{60}$ *[%]*	82.8	78.0	64.6	48.7	70.4	82.0	68.3	48.7	89.9	66.2	90.0
	Impact	$\bar{\epsilon}^{60}$ *[cm]*	0.02	0.01	0.02	1.40	0.14	0.04	0.02	1.40	0.02	0.25	0.10
		$\bar{S}^{60}$ *[%]*	54.0	39.1	95.9	93.1	95.3	93.2	95.9	95.6	94.7	95.2	93.1

as it would happen when receiving a BeiDou-2 B2 signal. For low receiver altitudes, the direct and reflected paths are almost equal, which translates in a compensation of the interferometric delay and Doppler. Thus, the interferometric differences are found around the origin of the delay/Doppler plane. As the altitude increases, the direct and reflected paths increase their difference, and the interferometric point move away from the origin. No differences are found for typical vehicle speeds (up to 300 km/h) or locations on Earth. In the ISS case, the delay difference is almost uniform in the delay domain, and the Doppler difference can be up to 10 kHz because of its high speed.

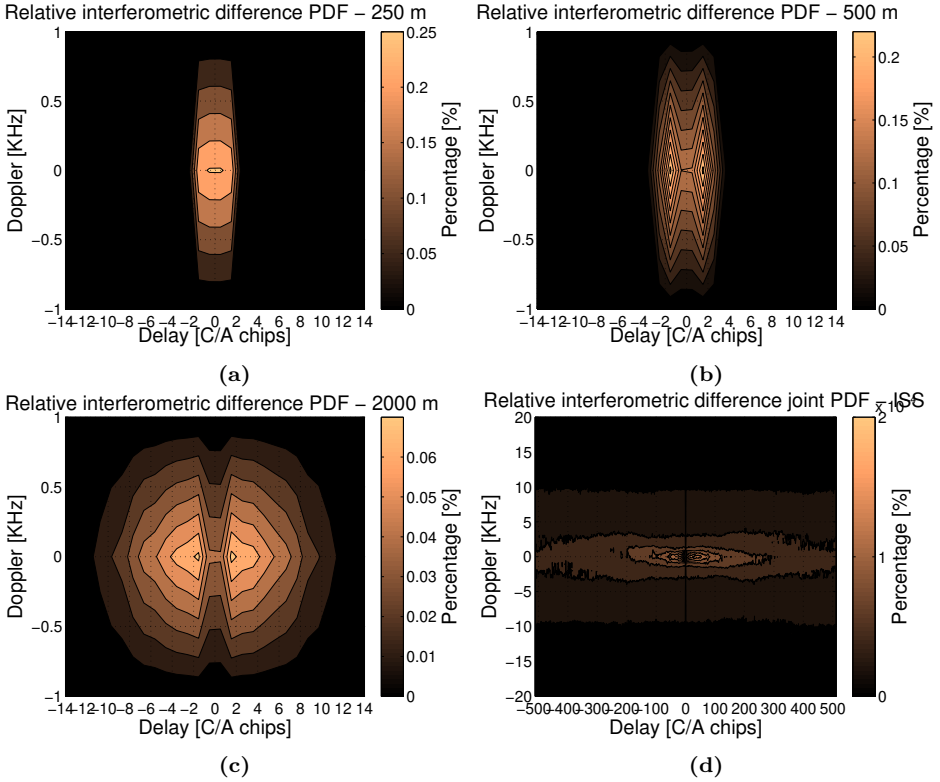

Figure 6.2: One-to-one joint PDF of the interferometric difference position for the BeiDou-2 B2 signal at (a) 250 m, (b) 500 m, (c) 2 km, and (d) ISS's orbit (400 km).

6.3.2 Cross-talk probability

Going into a more detailed analysis, it is interesting to study the probability of cross-talk as function of the elevation angle of the tracked satellite

$$P_{cs}\left(\theta_e^d\right) = \frac{1}{C}\sum_{i=1}^{C} P\{K_i > 0 | \theta_{e\,i}^d = \theta_e^d\}. \tag{6.17}$$

where C is the number of satellites of the constellation. The elevation angle θ_e^d is defined from the receiver's horizontal plane to the GNSS satellite (direct signal elevation angle), unlike in most GNSS-R literature, where the reference point is the specular one. These two angles are almost the same for ground-based and airborne altitudes, but may be different for space-borne receivers. Figure 6.3 shows this probability for different receiver altitudes and signals. As a general rule, the probability decreases with the elevation angle. The reason is that most cross-talk happens with satellites with similar elevation angle than the tracked one because their interferometric delay and Doppler differences are similar.

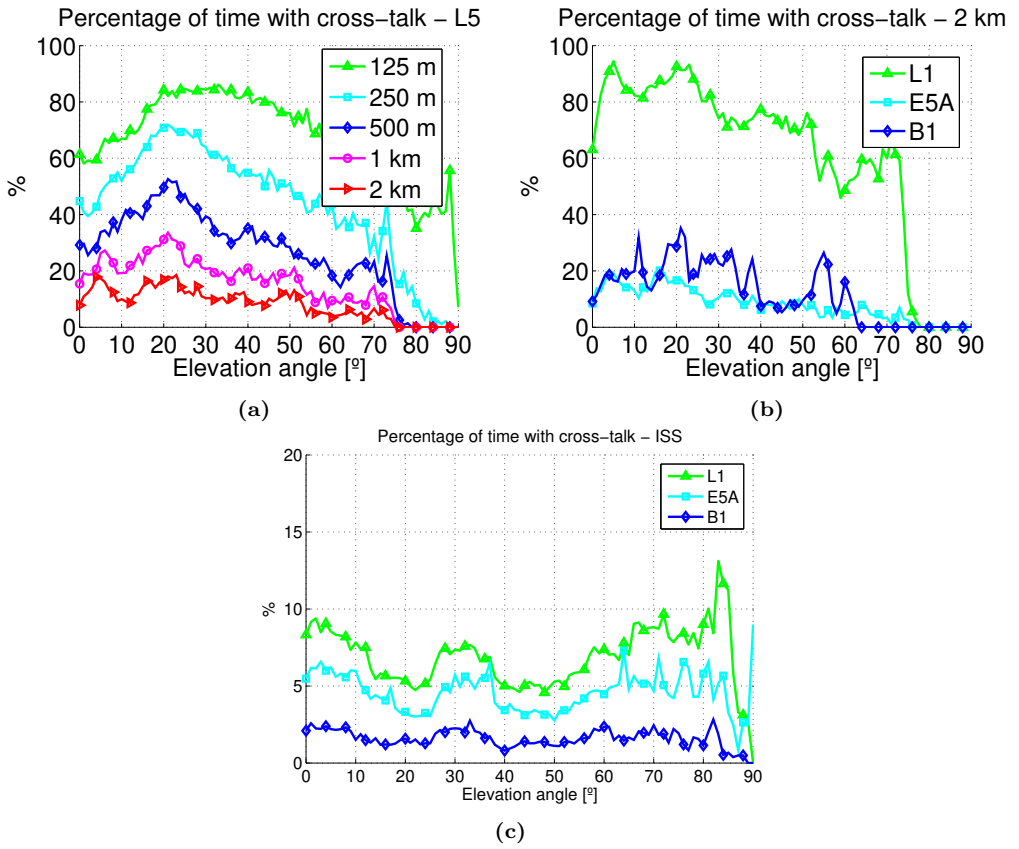

Figure 6.3: Percentage of time with cross-talk as function of the elevation angle of the tracked GNSS satellite. (a) At different receiver altitudes for the GPS L5 band, (b) for the GPS L1, Galileo E5A, and BeiDou-2 B1/B1-2 bands at 2 km altitude, and (c) at the ISS (400 km).

As the GNSS constellations were designed, it is not common to have many satellites with high elevation angles. On the other hand, and as previously stated, increasing the receiver altitude also reduces cross-talk. From almost constant cross-talk at ground altitudes, to almost zero at airborne scenarios when the elevation angle is high enough ($\theta_e^d \approx 65°$). The cross-talk probability also depends on the signal. For example, since the GPS L1 shares the band with the three constellations, it presents more cross-talk probability than the Galileo E5A or BeiDou-2 B1/B1-2, which can only be interfered by two and one constellations respectively. However the Galileo E5A has less cross-talk than the BeiDou-2 B1/B1-2 because the latter has a wider DDM, and thus more chances of overlapping. No differences are observed for different receiver speeds or locations on Earth, except for the fact that the observed elevation angles are limited by the receiver's latitude. The ISS has slow varying percentages with 13% as the worst case.

Most GNSS-R experiments and missions are usually designed to work with satellites with high elevation angles (e.g. [6] up to 35 degrees incidence angles). The first proposed figure of merit is the average cross-talk probability when the elevation angle of the tracked satellite is larger than 60 degrees (but allowing all the angles of the interfering satellites), and averaged over all the satellites of the same constellation

$$\bar{P}_{cs}^{60} = \frac{1}{C}\sum_{i=1}^{C}\int_{60^\circ}^{90^\circ}\frac{P\{K_i > 0|\theta_{e\,i}^d = \theta_e^d\}}{P\{\theta_{e\,i}^d \geq 60^\circ\}}d\theta_e^d. \tag{6.18}$$

The results at 250 m, 2 km, and at the ISS are summarized in Table 6.1. On ground, the percentage of time with cross-talk is almost 100% for the GPS L1 or Galileo E1 signals, but 19% for the GPS L2 signal. At 2 km, the largest percentage is also for the Galileo E1 with 61% of time, whereas for the GPS L2, it is reduced to 2%. At the ISS, the probabilities are a bit higher than in an airborne case because the DDMs are wider. The Galileo E1 has cross-talk 9.7% of time and the BeiDou-2 B1 just 1.7%.

6.3.3 Average number of interfering satellites

The cross-talk can be further analyzed with the number of satellites which are interfering. Let $N_{sat}^i\left(\theta_e^d, K\right)$ be a family of PDFs (on the variable K, given in (6.15)) for each elevation angle θ_e^d of the tracked satellite i. Figure 6.4 plots its mode, and 90% confidence interval for the Galileo E1 and GPS L1 signals at several receiver altitudes. When the altitude is very low, almost all the satellites in view (∼25) produce cross-talk, but they are reduced to almost zero when the altitude is over 2 km, and the elevation angle is larger than 60 degrees. At the ISS the cross-talk is mainly produced by a single interfering satellite.

The second figure of merit is the average number of satellites when the elevation angle is larger than 60 degrees, and averaged over all the satellites of the same constellation

$$\bar{N}_{sat}^{60} = \frac{1}{C}\sum_{i=1}^{C}\sum_{k=1}^{C+O-1}\int_{60^\circ}^{90^\circ}\frac{P\{K_i = k|\theta_{e\,i}^d = \theta_e^d\}\cdot k}{P\{\theta_{e\,i}^d \geq 60^\circ\}}d\theta_e, \tag{6.19}$$

where O is the number of satellites of other constellations that may interfere. Results are shown in Table 6.1. At 250 m, the signals GPS L1 and Galileo E1 have an average of 6 interfering satellites, whereas the GPS L2 signal just 0.4. At 2 km, the GPS L1 and Galileo E1 signals have 1 and 1.4 receptively, while the other signals have less than 0.5. Finally at the ISS, the maximum average interfering satellites is 0.2.

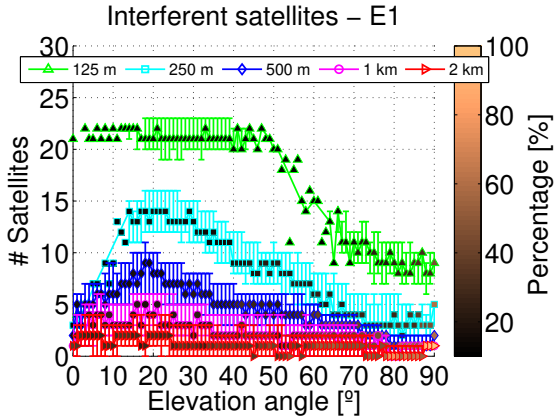

(a)

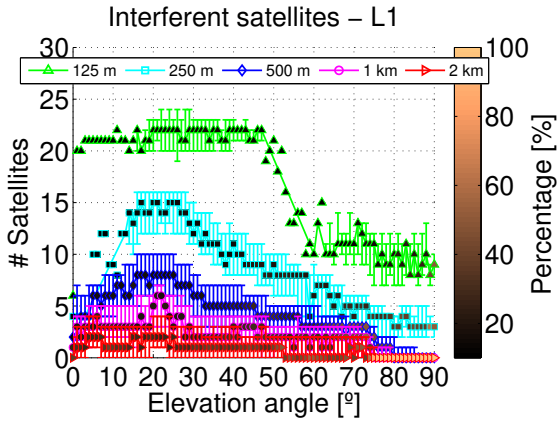

(b)

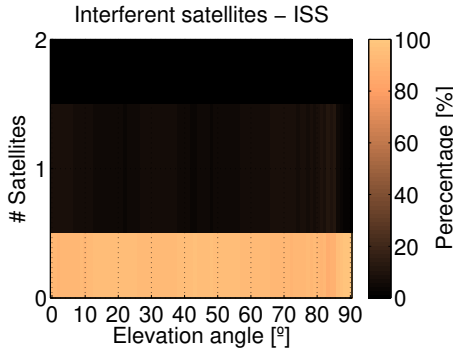

(c)

Figure 6.4: Number of interfering satellites (symbols are the mode, and error bars are the 90% confidence interval) as function of the elevation angle of the tracked GNSS satellite for different receiver altitudes (a) Galileo E1 and (b) GPS L2, and (c) histogram for the GPS L1 at ISS.

6.3.4 Cross-talk duration statistics

Another interesting parameter is how the cross-talk is distributed over time. Let $\bar{D}^{60}_{\tau_{cs}}(\tau)$, $\bar{D}^{60}_{\tau_{ncs}}(\tau)$ and $\bar{D}^{60}_{\tau_a}(\tau)$, be the duration CDFs of the cross-talk, cross-talk free, and total access when the elevation angle of the tracked satellite is larger than 60 degrees. The total access duration depends on the constellation and not on the individual signals. The CDFs for some bands at 2 km and on the ISS are plotted in Fig. 6.5. At these altitudes, in general the cross-talk free duration bursts are longer than the cross-talk ones are, except the GPS L1 at 2 km which both have a similar behavior. At the ISS, all the cross-talk free bursts are almost the same.

The third and fourth proposed figures of merit are the 90th percentiles τ_{cs} and τ_{ncs} of those CDFs

$$\bar{D}^{60}_{\tau_{cs}}(\tau_{cs}) = 90\%, \tag{6.20}$$

$$\bar{D}^{60}_{\tau_{ncs}}(\tau_{ncs}) = 90\%. \tag{6.21}$$

Results are summarized in Table 6.1. For ground-based and airborne receivers, the cross-talk burst duration can be very large, specially for the Galileo E1 signal with 12702 seconds and 2891 seconds respectively, while the largest cross-talk free burst is 1571 seconds for the GPS L2 signal. At the ISS, the cross-talk bursts are reduced to less than 20 seconds, and the cross-talk free are larger than 200 seconds for all the signals. These parameters are useful to define the optimum incoherent averaging duration of the waveforms.

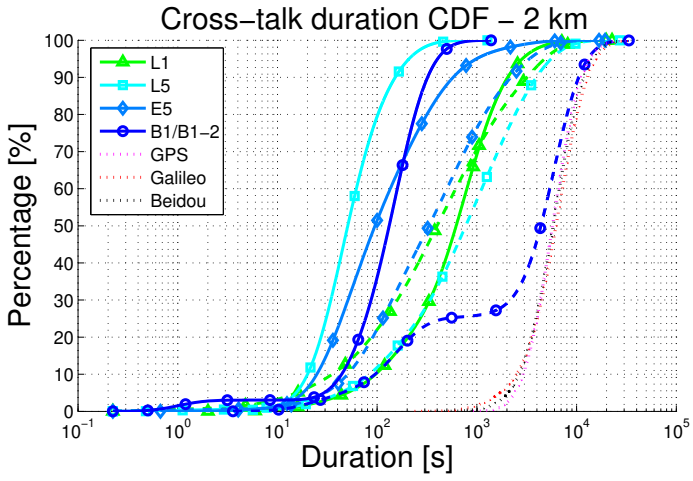

(a)

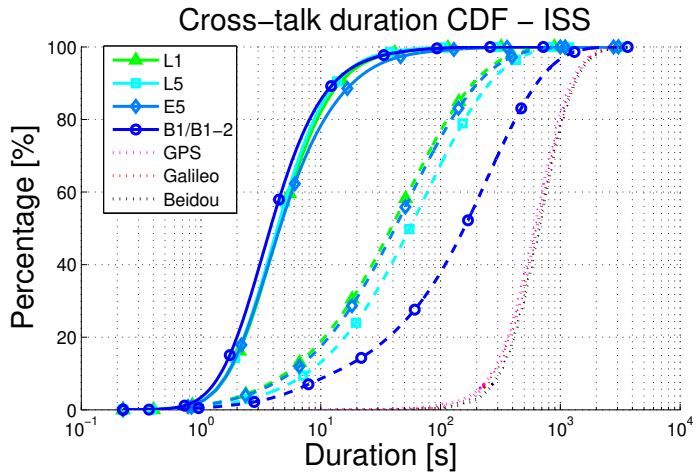

(b)

Figure 6.5: CDFs of the duration of the cross-talk (solid line with marks), cross-talk free (dashed line), and total access (dotted line) when tracking a satellite with $\theta_e^d > 60^{\mathrm{o}}$ for the GPS L1 and L5, Galileo E5 and BeiDou-2 B1/B1-2 signals (a) at 2 km, and (b) at the ISS (400 km).

6.3.5 Interfering power

In order to mitigate the cross-talk impact, antenna arrays with beamsteering capabilities and good relative sidelobe levels are needed. Let $G^i(\theta_e^d, \rho)$ be a family of CDFs (given by ρ) of the Signal-to-Interference Ratio (SIR) between the power of the direct signal of the desired satellite i over all the interfering j after the receiver's up-looking antenna. The SIR for a given realization of a desired satellite is

$$\rho = \frac{P^i \cdot D(\theta_{e\,i}^d, \phi_a^i, \theta_{e\,i}^d, \phi_a^i)}{\sum_{j \neq i} \rho_{ij}} \cdot \left(\frac{\lambda}{4\pi |\vec{T^i} - \vec{R^i}|} \right)^2, \tag{6.22}$$

where

$$\rho_{ij} = \begin{cases} P^j \cdot D\left(\theta_{e\,i}^d, \phi_a^i, \theta_{e\,j}^d, \phi_a^j\right) \cdot \left(\dfrac{\lambda}{4\pi |\vec{T^j} - \vec{R^j}|} \right)^2 & C_{ij} = 1, \\ 0 & \text{otherwise}, \end{cases} \tag{6.23}$$

where P is the transmitted power, ϕ_a is the azimuth angle, $D(\theta_{e\,i}^d, \phi_{a_i}, \theta_{e\,j}^d, \phi_j)$ is the receiver's antenna directivity at $[\theta_e^d j, \phi_{a_j}]$ when pointing at $[\theta_{e\,i}^d, \phi_{a_i}]$, and λ is the signal wavelength. The performance of different antennas is evaluated by computing the averaged percentile at which the SIR is larger than 10 dB over all the satellites of the same

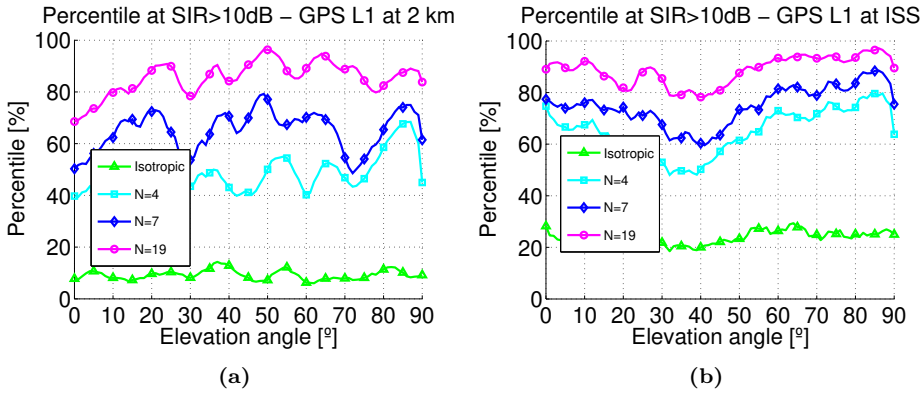

Figure 6.6: Percentile at which SIR>10 dB for different antenna arrays for the GPS L1 signal (a) at 2 km, and (b) at the ISS (400 km).

constellation

$$\bar{T}\left(\theta_e^d\right) = \frac{1}{C}\sum_{i=1}^{C} G^i(\theta_e^d, \rho = 10 \text{ dB}). \tag{6.24}$$

Figure 6.6 plots the results for an isotropic antenna; a 4 elements rectangular array; and a 7, and 19 elements hexagonal arrays, all with a element spacing of 0.93λ. The isotropic antenna gives a constant poor performance, because it does not mitigate any interfering power, while the antenna arrays improve the SIR by up to 10 dB at ground, or up to 3 dB at the ISS. The non-linearity of the array plots, comes from the side lobes which are picking interfering power of satellites with low elevation angles. Similar results are obtained with a spacing of 0.575λ to avoid grating lobes in the hexagonal arrays (not shown in the figures).

The next figure of merit is the average of the percentile over an elevation angle higher than 60 degrees

$$\bar{T}^{60} = \frac{1}{C}\sum_{i=1}^{C}\int_{60^\circ}^{90^\circ} G^i\left(\theta_e^d, \rho = 10 \text{ dB}\right)\frac{P\{\theta_{e\,i}^d = \theta_e^d\}}{P\{\theta_{e\,i}^d \geq 60^\circ\}} d\theta_e^d. \tag{6.25}$$

Results for the 7 element array are summarized in Table 6.1. At ground, the percentile for the Galileo E1 is just a 6.2%, while the best one is 94.2% for the BeiDou-2 B1 or B1-2 signals. For an airborne receiver, the former improves to a 58.2%, and to 66.2% at the ISS.

6.4 Impact

The cross-talk impact on coherent waveforms (i.e. non-averaged) is evaluated at the point of maximum derivative, as it is a bias of the true altimetry height [60]. The specular point is searched within a narrow window of +/-100 meters with respect to the theoretical one, as is the largest error between the WGS84, and the geoid over the ocean. Similar to the last section, this study is done statistically and repeated using the same scenarios, and for the different antenna arrays. It is assumed that the desired satellite is ideally pointed by the antennas, and that its DDM is perfectly tracked in the correlation plane.

Figure 6.7 shows the impact of cross-talk on GPS L1 waveforms, and how the different antenna arrays reduce the interfering waveforms. An isotropic or a single patch antenna would produce indistinguishable corrupted waveforms from which any parameter would be difficult to retrieve. The corrupted waveform at 250 meters, reassembles to a real corrupted one obtained at the TIGRIS experiment [67] at a similar height.

Let $E^i\left(\theta_e, \epsilon\right)$ and $R^i\left(\theta_e, \epsilon\right)$ be the PDFs and CDFs of the error ϵ between the correct specular point and the estimated one of the tracked satellite i

$$\epsilon = |\hat{\tau} - \tau|. \tag{6.26}$$

The average errors are

$$\bar{\epsilon}^i\left(\theta_e\right) = \int \epsilon E^i\left(\theta_e, \epsilon\right) d\epsilon, \tag{6.27}$$

and the percentiles at which the error is smaller than 10 cm are

$$S^i\left(\theta_e\right) = 1 - R^i\left(\theta_e, \epsilon = 10 \text{ cm}\right). \tag{6.28}$$

The last figures or merit are again obtained from the average over an elevation angle larger than 60 degrees

$$\bar{\epsilon}^{60} = \frac{1}{C} \sum_{i=1}^{C} \int_{60^\circ}^{90^\circ} \bar{\epsilon}^i\left(\theta_e^d\right) \frac{P\{\theta_{e\,i}^d = \theta_e^d\}}{P\{\theta_{e\,i}^d \geq 60\check{z}\}} d\theta_e^d, \tag{6.29}$$

$$\bar{S}^{60} = \frac{1}{C} \sum_{i=1}^{C} \int_{60^\circ}^{90^\circ} S^i\left(\theta_e^d\right) \frac{P\{\theta_{e\,i}^d = \theta_e^d\}}{P\{\theta_{e\,i}^d \geq 60^\circ\}} d\theta_e^d. \tag{6.30}$$

Results are presented in Table 6.1 when using the hexagonal antenna array of 7 elements. The average error at 250 meters can range from 99 cm for the BeiDou-2 B3 signals to almost zero for the Galileo E5/E5A/E5B signals. The GPS L1 and Galileo E1 have an error of 6.4 and 10.7 cm respectively. At 2 km, they are reduced to 1 and 2 cm respectively, while for the other signals the cross-talk has almost disappeared, except for the BeiDou-2 B2 and B3 signals which still has large errors. At the ISS, all errors are below 0.05 cm.

The percentiles that ensure an error smaller than 10 cm, are found between 13.4% and 93.3% at ground for the Galileo E5A and GPS L1 signals respectively. At 2 km they are between 49.5% and 98.5% for the BeiDou-2 B3 and BeiDou-2 B1 signals respectively. Although some percentiles may seem to have no improvement with increasing the height, they actually refer to the percentage of time in which there is cross-talk, and it is by joining the two factors, that one can observe the enhancement. At the ISS, they are larger than 95% for all the signals.

The results presented here are very good as would be expected from the probabilities given in last section. This is because the window used to estimate the specular delay is much smaller than the one defined for the cross-talk overlapping (3 times at ground or airborne, and 21 times at ISS). Searching in the full waveform (e.g. in Fig. 6.7), produces artificially larger errors.

6.5 Conclusions

Cross-talk can be a severe problem in iGNSS-R when all the GNSS constellations will be fully deployed. In order to mitigate it, three requisites should be considered. First, use directive antenna arrays with beamforming capabilities tracking the target satellite and its reflected point on the surface. Second, know the position of the desired DDM in the delay domain within a window of +/- 100 m. Third, track satellites with elevation angles larger than 60 degrees only.

A 7 element hexagonal array is enough to ensure errors below 2 cm at 2 km height when tracking satellites with elevation angle larger than 60 degrees. At ground, this antenna still can produce 10 cm errors, and a larger one, such as a 19 element hexagonal array is recommended.

One could expect that the cross-talk impact from the ISS should be worse, because the statistics shown in Section 6.3.2 give a cross-talk probability up to 10%. The reason for this difference is because the overlapping probability was computed within a window of [-300, 1800] meters around the specular point, much larger than the window of [-100, 100] meters. Figure 6.2d shows an almost empty area of [-270, 270] meters, this tells that actually the interfering DDMs are already quite far from the desired one. In other words, the interfering DDMs overlapp the tracked one with just their tails, instead of with their peak. This principle can also be seen in Fig. 6.7c. The analysis done in this chapter reinforces the GEROS-ISS experiment feasibility.

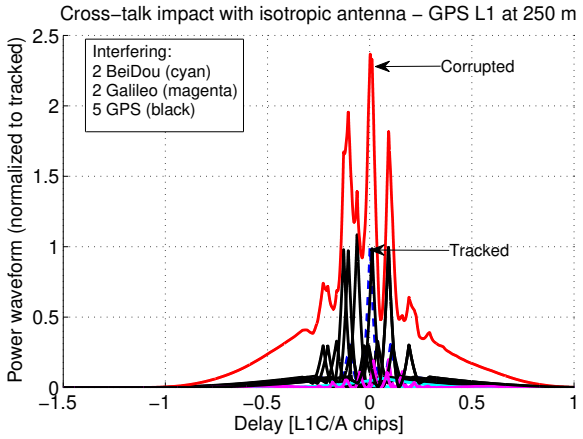
Cross−talk impact with isotropic antenna − GPS L1 at 250 m
Interfering:
2 BeiDou (cyan)
2 Galileo (magenta)
5 GPS (black)
Corrupted
Tracked
Power waveform (normalized to tracked)
Delay [L1C/A chips]

(a)

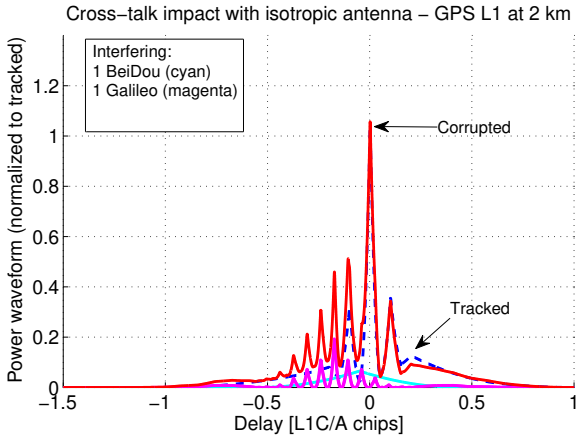
Cross−talk impact with isotropic antenna − GPS L1 at 2 km
Interfering:
1 BeiDou (cyan)
1 Galileo (magenta)
Corrupted
Tracked
Power waveform (normalized to tracked)
Delay [L1C/A chips]

(b)

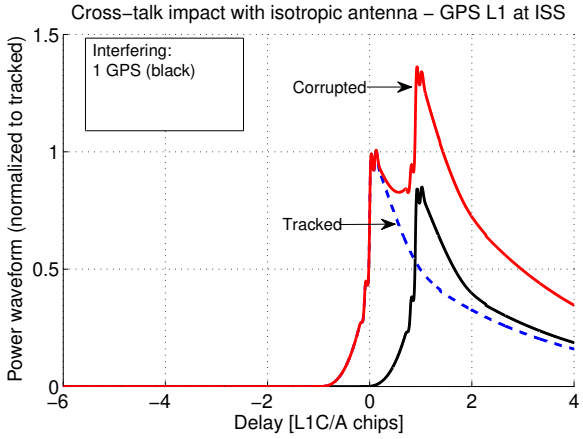
Cross−talk impact with isotropic antenna − GPS L1 at ISS
Interfering:
1 GPS (black)
Corrupted
Tracked
Power waveform (normalized to tracked)
Delay [L1C/A chips]

(c)

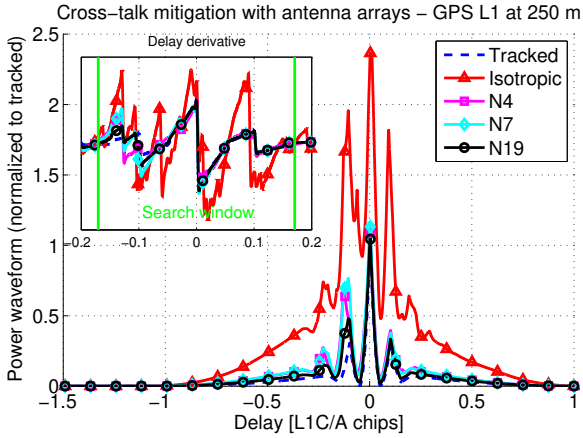

(d)

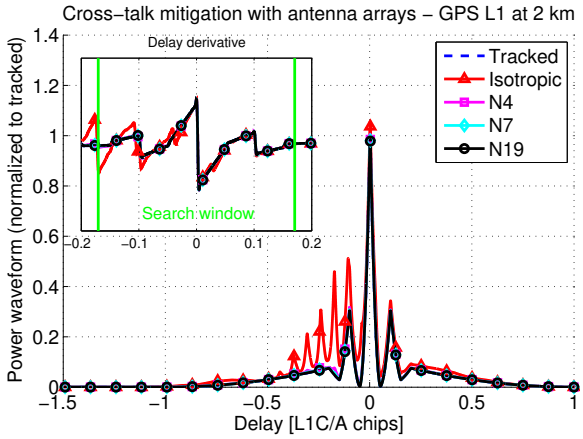

(e)

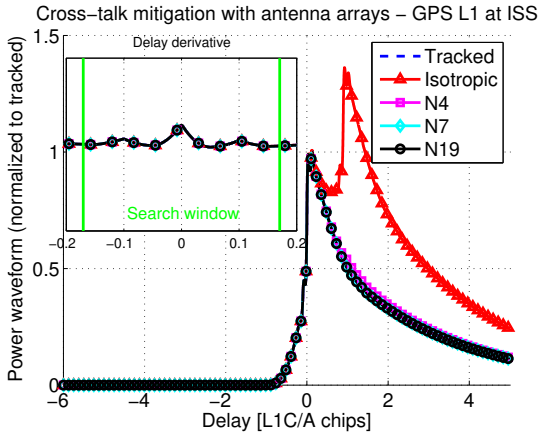

(f)

Figure 6.7: Sample cross-talk impact on GPS L1 waveforms. (a)-(c) interfering waveforms and corrupted one obtained with an isotropic antenna at 250 m, 2 km, and at the ISS (400 km), and (d)-(f) cross-talk mitigation by using symmetrical antenna arrays of 4, 7 and 19 elements.

7

Chapter 7

Stochastic Properties and Metrics of Quantized GNSS-R Signals

This chapter first investigates the impact of the ADC quantization on the power and variance of a sampled GNSS-R signal. It then gives the stochastic description of the most common DDM observables for the 2-level quantized signal and for ideal analog one. These observables are the peak amplitude, phase, power and averaged power, and the noise power and averaged power. Analytic expressions of the PDF, mean and variance are given when possible, and references to the literature for approximations when not. The equations given here can be used in simulators when aiming to studying the impact of the noise at each observable.

This chapter also studies and compares the different definitions of SNRs typically used in the GNSS-R literature. Finally, the peak detectability of noisy waveforms is revised as well.

7.1 Introduction

The stochastic properties of the coherent and incoherent scattering of the reflected microwave signals is a subject of study vast enough to have complete books devoted to it (e.g. [34,35,181,182]). The scattering of the GNSS signals in a bistatic configuration has been studied in [41,52,69,183–185] among others. All these latter works are focused on the coherent and incoherent power statistics. In this chapter, this theory is applied to the quantized signals, with special emphasis on 2-level quantization. Additionally, the stochastic properties are analyzed not only for the peak power but also for the amplitude, magnitude and phase.

7.2 Analog signal model

Let $s(t)$ be either a received direct or reflected complex baseband GNSS signal contaminated with complex zero-mean Additive White Gaussian Noise (AWGN) $n(t)$:

$$s\left(t\right)=\sqrt{P\left(t\right)}e^{j\theta(t)}+\frac{\sigma_n}{\sqrt{2}}n\left(t\right), \tag{7.1}$$

where $P(t)$ and $\theta(t)$ are respectively the power and phase of the noiseless signal, and σ_n^2 is the noise power. The latter term is actually the addition of the thermal noise generated by the instrument with the one received by the antenna. For the sake of simplicity, it is assumed that all terms are stationary during the correlation process, and thus the t dependency will be removed from now on. Under this assumption, it is assumed that the Doppler shift is compensated, and that the clean replica is aligned with the data bits and secondary code transitions. In the case of the reflected signal, it is also assumed that the stationary duration of the reflected surface is larger than the correlation length.

7.2.1 Direct signal

The direct signal can be modeled as a bivariate normal random variable with the in-phase and quadrature components I and Q

$$s\sim\mathcal{N}\left(\mu_I,\mu_Q,\sigma_I,\sigma_Q\right) \tag{7.2}$$

where $\mu_I=\sqrt{P}\cos\theta$ and $\mu_Q=\sqrt{P}\sin\theta$ are the mean of amplitudes components, and the $\sigma_I=\sigma_Q=\sigma_n/\sqrt{2}$ are their standard deviations. Both components may be correlated due to a leakage between instrument chains and/or to unbalanced demodulators. However, as explained in Appendix C.1, two correlated random variables can become uncorrelated by applying a simple transformation.

The relationships between the physical magnitudes and the PDFs that will be used in the course of this chapter are summarized in Fig. 7.1. The magnitude $r=\sqrt{P}=$

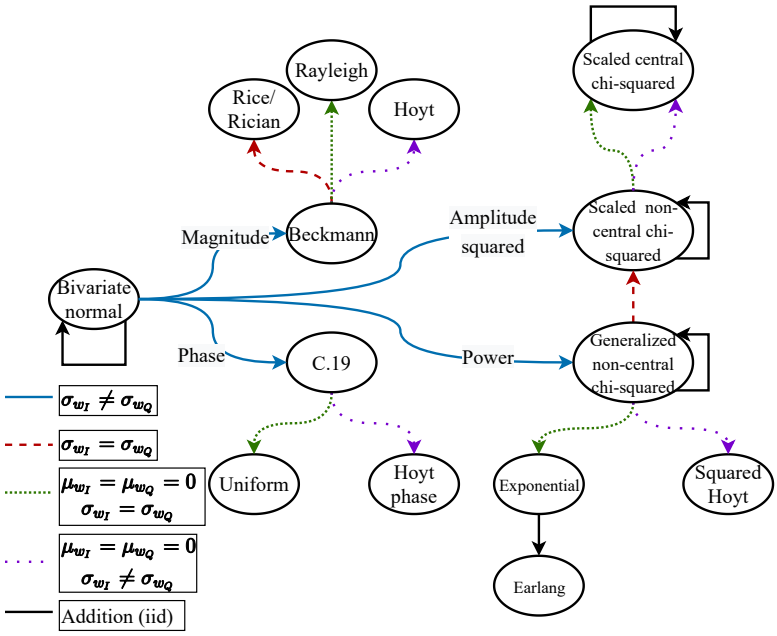

Figure 7.1: Relationships among the physical magnitudes of a complex signal w and their respective random variables. Solid black arrow indicates the addition independent and identically distributed (iid) random variables. Amplitude square refers to the squaring of each amplitude component (i.e. I^2 and Q^2).

$\sqrt{I^2 + Q^2}$ follows a Rice (also known as Rician) distribution $r \sim \text{Rice}(P, \sigma_n)$. The PDF, mean and standard deviation are given in Section C.4. The PDF of the power $P = I^2 + Q^2$ follows a scaled non-central chi-squared distribution with two degrees of freedom. The term *scaled* comes from the fact the variances are not unitary. The term *non-central* comes the fact that the means μ_I and μ_Q are not necessary zero. The PDF, mean and standard deviation are given in Section C.9. Finally, the PDF of the phase is given in (C.15).

In contrast, the PDF of the magnitude of the noise follows a Rayleigh distribution (Section C.6), and the PDF of the power σ_n^2 follows an exponential distribution, which is in fact the same as the scaled chi-squared distribution with two degrees of freedom. The PDF and the moments are given in Section C.8.

The analog SNR, this is, the SNR immediately before the Analog-to-Digital Converter (ADC) is defined as

$$SNR_s = \frac{\mu_I^2 + \mu_Q^2}{\sigma_I^2 + \sigma_Q^2} = \frac{P}{\sigma_s^2}. \tag{7.3}$$

This definition can be understood as the ratio between the signal power of an ideal

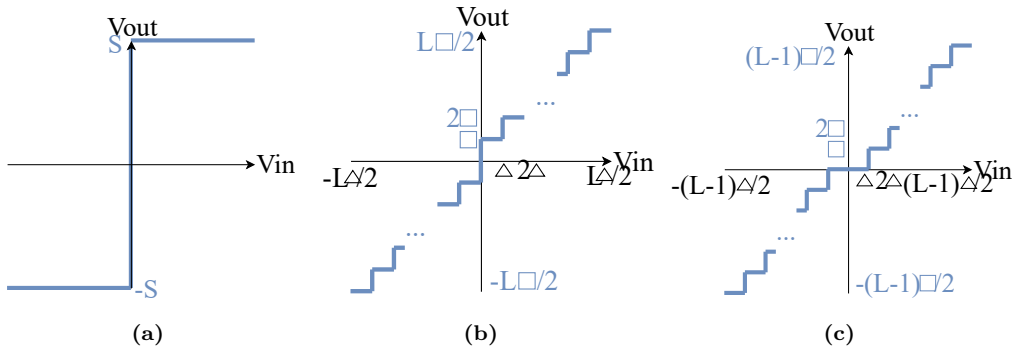

Figure 7.2: ADC uniform coding schemes: (a) 2-level, (b) mid-riser (L even), and (c) mid-tread (L odd). △ is the quantization step size, and □ is the encoding step size.

noiseless signal and the noise power. Although this concept may seem obvious here, this definition will be used in the future to define the SNR in not so obvious contexts.

It is appropriate to comment here that the statistical moments that will be given in the course of this chapter are the theoretical ones, also known as *raw* moments. In reality, the moments are estimated from a finite number of observations. These estimates are called *sample* moments, and they can also be characterized by a a given distribution. An estimator is unbiased if the expected value of the sample moment is equal to the raw moment. It is well beyond the scope of this Ph. D. thesis to go into further details, but extensive theory can be found in the literature (e.g. [186]).

7.2.2 Reflected signal

The PDF of the magnitude of the noiseless reflected signal also follows a Rice distribution. It is modeled as $r \sim \text{Rice}(\nu_{coh}, \sigma_{inc})$, where ν_{coh}^2 denotes the coherent power and σ_{inc}^2 is the contribution of all the remaining paths [35]. It can be shown that the complex signal can also be modeled as in (7.2) but with $\mu_I = \nu_{coh}\cos\theta$, $\mu_Q = \nu_{coh}\sin\theta$ and with $\sigma_s^2 = \sigma_{inc}^2 + \sigma_n^2$. The analog SNR of the reflected signal can be expressed as

$$SNR_s = \frac{\nu_{coh}^2}{\sigma_s^2} = \frac{\nu_{coh}^2}{\sigma_{inc}^2 + \sigma_n^2}. \tag{7.4}$$

However, in the literature another definition can also be found, which is the ratio between the total signal power (coherent and incoherent) over the noise power

$$SNR_s = \frac{\nu_{coh}^2 + \sigma_{inc}^2}{\sigma_n^2}. \tag{7.5}$$

The ratio $\nu_{coh}^2/\sigma_{inc}^2$ has also been used as a metric in other studies (e.g [61, 185]).

7.3 Sampled signal model

The impact of the 2-level sampling is well known in the GNSS literature (e.g. [21–23]). In the scope of GNSS-R, it was initially formalized in [187]. Similar theory was developed for microwave correlation radiometers in [176]. This theory is revised here and expanded to multi-level sampling.

7.3.1 2-levels

Let x_I and x_Q be the sampled analog signals I and Q respectively. From now on, they will be written as $x_{\{I,Q\}}$. The simplest ADC has only 2-levels, and has the decision threshold at zero as depicted in Fig. 7.2a. Mathematically, this is expressed as

$$x_{\{I,Q\}} = \begin{cases} -S & \{I,Q\} < 0 \\ S & \{I,Q\} \geq 0 \end{cases} \tag{7.6}$$

where S is the digital output value.

The probability that an analog input value is encoded correctly is

$$P_{ok} = P\left(x_{\{I,Q\}} = S | \{I,Q\} \geq 0\right) = 1 - \Phi\left(\frac{0 - \mu_{\{I,Q\}}}{\sigma_{\{I,Q\}}}\right) = \frac{1}{2}\left[1 + \operatorname{erf}\left(\frac{\mu_{\{I,Q\}}}{\sqrt{2}\sigma_{\{I,Q\}}}\right)\right], \tag{7.7}$$

where $\Phi(z) = \frac{1}{\sqrt{2\pi}} \int_{-\infty}^{z} e^{-t^2/2} dt$ is the CDF of the normal standard random variable z, and $\operatorname{erf}(z) = \frac{2}{\sqrt{\pi}} \int_0^z e^{-t^2} dt$ is the error function. The argument inside the error function in (7.7) can be expressed in terms of the analog SNR: $\frac{\mu_I}{\sqrt{2}\sigma_I} = \sqrt{SNR_s}\cos\theta$ and $\frac{\mu_Q}{\sqrt{2}\sigma_Q} = \sqrt{SNR_s}\sin\theta$.

The moments of $x_{\{I,Q\}}$ are found as

$$E\left[x_{\{I,Q\}}^r\right] = S^r P_{ok} + (-S)^r \left(1 - P_{ok}\right). \tag{7.8}$$

Note that the even moments are equal to S^r. The mean and variance of the amplitude components are

$$\mu_{x_{\{I,Q\}}} = E\left[x_{\{I,Q\}}\right] = S \operatorname{erf}\left(\sqrt{SNR_s}\{\cos\theta, \sin\theta\}\right), \tag{7.9a}$$

$$\sigma^2_{x_{\{I,Q\}}} = E[x^2_{\{I,Q\}}] - \mu^2_{x_{\{I,Q\}}} = S^2\left[1 - \operatorname{erf}^2\left(\sqrt{SNR_s}\{\cos\theta, \sin\theta\}\right)\right]. \tag{7.9b}$$

These equations are important because state that both the mean and the variance of the sampled signal do not depend on the respective values of the analog signal, but on

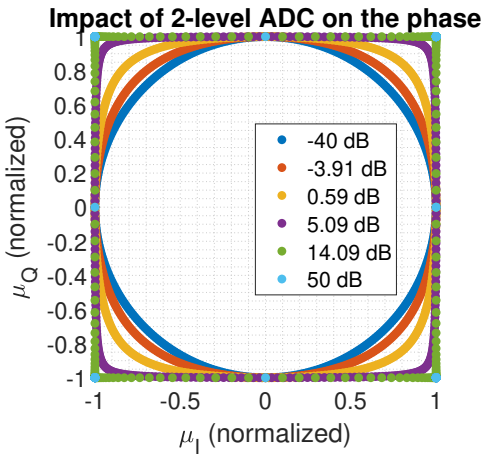

Figure 7.3: Impact of a 2-level ADC on the phase of the sampled signal for different analog SNRs.

the latter SNR and phase. In fact, both moments could be used as estimators of the analog SNR. However, it must be taken into account that the error function converges to 1 for large arguments, and to 0 for small and positive arguments. This means that the moments will saturate in this two extreme conditions.

The I/Q polar diagram of the sampled signal estimated with $\text{atan}(\mu_{x_Q}/\mu_{x_I})$ is shown in Fig. 7.3. As it can be seen, the phase evolution is distorted and eventually lost for large SNRs. The reason for that is that the erf function is more or less linear for small positive arguments, but it saturates to 1 when the argument is large. Nevertheless, the phase jumps of 180° due to data bit transitions can still be detected because the erf function is an odd function (i.e. $\text{erf}(-z) = -\text{erf}(z)$). In fact, most commercial GNSS receivers use 2-level ADCs (e.g. [24]).

The power, variance and SNR are given by

$$P_x = \mu_{x_I}^2 + \mu_{x_Q}^2 = \text{erf}^2\left(\sqrt{SNR_s}\cos\theta\right) + \text{erf}^2\left(\sqrt{SNR_s}\sin\theta\right), \tag{7.10}$$

$$\sigma_x^2 = \sigma_{x_I}^2 + \sigma_{x_Q}^2 = 2 - \text{erf}^2\left(\sqrt{SNR_s}\cos\theta\right) - \text{erf}^2\left(\sqrt{SNR_s}\sin\theta\right), \tag{7.11}$$

$$SNR_x = \frac{P_x}{\sigma_x^2} = \frac{\text{erf}^2\left(\sqrt{SNR_s}\cos\theta\right) + \text{erf}^2\left(\sqrt{SNR_s}\sin\theta\right)}{2 - \text{erf}^2\left(\sqrt{SNR_s}\cos\theta\right) - \text{erf}^2\left(\sqrt{SNR_s}\sin\theta\right)}. \tag{7.12}$$

As seen in Fig. 7.4, the SNR of the sampled signal decreases by ≈2 dB for small analog SNRs. For large analog SNRs, the digital one saturates to ≈-2 dB if the phase is a

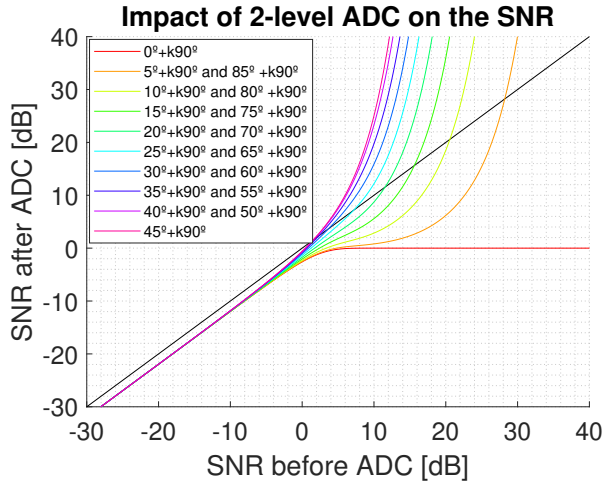

Figure 7.4: Impact of a 2-level ADC on the SNR of the sampled signal for different phases of the analog signal.

multiple of 90° or to infinite for any other phase. The idea behind this is that, if the analog SNR is very large, the sampled signal looses the variance information, and thus the SNR of the sampled signal tends to infinite.

The main conclusion of this section, is that a 2-level ADC can be used in GNSS-R if the analog SNR is low (as it will be generally the case) at the expense of reducing the SNR to about 2 dB. However, these ADCs should not be used for scatterometry or for phase altimetry if the analog SNR is large.

7.3.2 Multi-level

The theory for multi-level ADCs is extensive. The general idea is that the analog signal is first quantified within partition levels and then encoded with the so-called code-book. Given a number of levels L, the Lloyd algorithm finds the optimum partition thresholds and associated code-book that minimizes the distortion of the quantized PDF [188]. If a GNSS-R instrument uses the Lloyd or other encoding algorithms, the partition thresholds and the code-book should be saved as meta-data information.

In general, the ADCs have fixed partition levels and code-book values (either uniform or optimized for Gaussian signals). Also in general, the ADCs are used in combination with an Automatic Gain Control (AGC) which expands or compresses the analog signal into the Dynamic Range (DR) of the ADC. If this latter configuration is used in an GNSS-R instrument, the AGC gain should be continuously monitored and saved as meta-data. If an AGC is not used, the number of levels and the dynamic range of the ADC should be large enough so as to be sensitive to changes of the signal power and variance. In fact, both parameters are codependent. Using a large dynamic range and few number of levels

would produce a signal similar to what a 2-level ADC would produce.

This latter strategy is studied here by using two types of uniform ADCs. The mid-riser ADC, which as has an even number of levels (Fig. 7.2b), and the mid-tread ADC, which as an odd number of levels (Fig. 7.2c). Note that the mid-tread ADC includes the zero output value. In the figure, $\triangle$ is the quantization step size, and $\square$ is the encoding step size. For L even, $\triangle = DR/L$ and $\square = 2S/L$. For L odd, $\triangle = DR/(L-1)$ and $\square = 2S/(L-1)$. The quantized signal is given by

$$x_{\{I,Q\}} = \begin{cases} -S & \{I,Q\} \leq -DR/2 \\ \square k & -DR/2 < \{I,Q\} < DR/2 \\ S & \{I,Q\} \geq DR/2 \end{cases} \tag{7.13}$$

where k is quantization index

$$k = \begin{cases} \lfloor s/\triangle \rfloor + 1 & L \text{ even} \\ \lfloor s/\triangle \rfloor & L \text{ odd} \end{cases} \tag{7.14}$$

and where $\lfloor \cdot \rfloor$ depicts the floor function.

Following a similar approach as done in (7.8), the moments of $x_{\{I,Q\}}$ are found as

$$\begin{aligned} E\left[x_{\{I,Q\}}^r\right] = {} & \frac{S^r}{2}\left[1 - \operatorname{erf}\left(\frac{DR - \mu_{\{I,Q\}}}{\sqrt{2}\sigma_{\{I,Q\}}}\right)\right] \\ & + \frac{\square^r}{2}\sum_{i=0}^{\omega}(i+\varphi)^r\left[\operatorname{erf}\left(\frac{A - \mu_{\{I,Q\}}}{\sqrt{2}\sigma_{\{I,Q\}}}\right) - \operatorname{erf}\left(\frac{B - \mu_{\{I,Q\}}}{\sqrt{2}\sigma_{\{I,Q\}}}\right)\right] \\ & + \frac{(-\square)^r}{2}\sum_{i=0}^{\omega}(i+\varphi)^r\left[\operatorname{erf}\left(\frac{-B - \mu_{\{I,Q\}}}{\sqrt{2}\sigma_{\{I,Q\}}}\right) - \operatorname{erf}\left(\frac{-A - \mu_{\{I,Q\}}}{\sqrt{2}\sigma_{\{I,Q\}}}\right)\right] \\ & + \frac{(-S)^r}{2}\left[1 + \operatorname{erf}\left(\frac{-DR - \mu_{\{I,Q\}}}{\sqrt{2}\sigma_{\{I,Q\}}}\right)\right], \end{aligned} \tag{7.15}$$

where $A = \triangle(i+1)$, $B = \triangle i$; $w = (L-2)/2$ if L is even or $w = (L-3)/2$ if L is odd; and $\varphi = 1$ if L is even or $\varphi = 0$ if L is odd. The power, variance and SNR are then obtained with (7.10), (7.10) and (7.10) respectively. Note that the latter equation holds only for those signals modulated with 2 symbols (such as GPS L1 C/A and L5). The Galileo E1OS and the E5 have 2 and 3 different symbols respectively. However, as it will be shown in Chapter 8, they can be demodulated using 2 symbols with little impact on the ACF. The extension of (7.15) for multi-symbol signals is left for further work.

In GNSS-R, both the average signal power and the variance can be used as observables of the physical parameters of the reflecting surface. Ideally, a change of the analog average

power should produce a proportional change in the average power of the digital signal, and not affect the variance of the latter. Similarly, a change of the analog power variance should produce a proportional change in the variance of the digital signal, and not affect the latter average power. However, as it can be inferred from (7.15), the average power and variance of the sampled signal are both affected by changes of the analog average power and variance. The dynamic range and the number of levels of ADC can be optimized for a given dynamic range of signal power and variance by using the partial derivatives of (7.15). These derivatives can be analytically found by knowing that $\frac{d}{dz}\operatorname{erf}(z) = \frac{2}{\sqrt{\pi}}\exp(-z^2)$, and by applying the chain rule.

The above concept is better illustrated in Figs. 7.5, 7.6, and 7.7. They show the impact of the number of levels and dynamic range on the sampled signal power, variance and SNR respectively for different analog signal powers and variances. Ideally, the average power of the sampled signal should follow equally spaced vertical lines, and the variance should follow equally spaced horizontal lines. Similarly, the SNR should follow equally spaced diagonal lines with unitary slope. However, the three metrics saturate when either the combination of the analog signal power and variance is larger than the dynamic range of the ADC, or when it is smaller than the lowest partition threshold. In order to give context to the reader, the ADC used in the MIR instrument (see Chapter 9) uses 14 bits, equivalent to 16384 levels.

7.4 Waveform model

7.4.1 Conventional waveform

Let $w = w_I + jw_Q$ be the complex cross-correlation between either the direct or the reflected sampled signal with the clean replica. For the sake of simplicity, it is assumed that the Doppler shift has been removed and that the signal is aligned with the reference one. It is simply given by

$$w_{\{I,Q\}} = \frac{1}{N}\sum_{N} x_{\{I,Q\}}, \tag{7.16}$$

where N is the coherent length in number of samples. The power waveform is

$$Y = |w|^2 = ww^* = w_I + w_Q, \tag{7.17}$$

and the averaged power waveform of equally weighted power waveforms is

$$Z = \frac{1}{M}\sum_{M} Y, \tag{7.18}$$

where M is the number of incoherent averages. Tables 7.1 and 7.2 summarizes the statistics of the waveform observables, which are next analyzed.

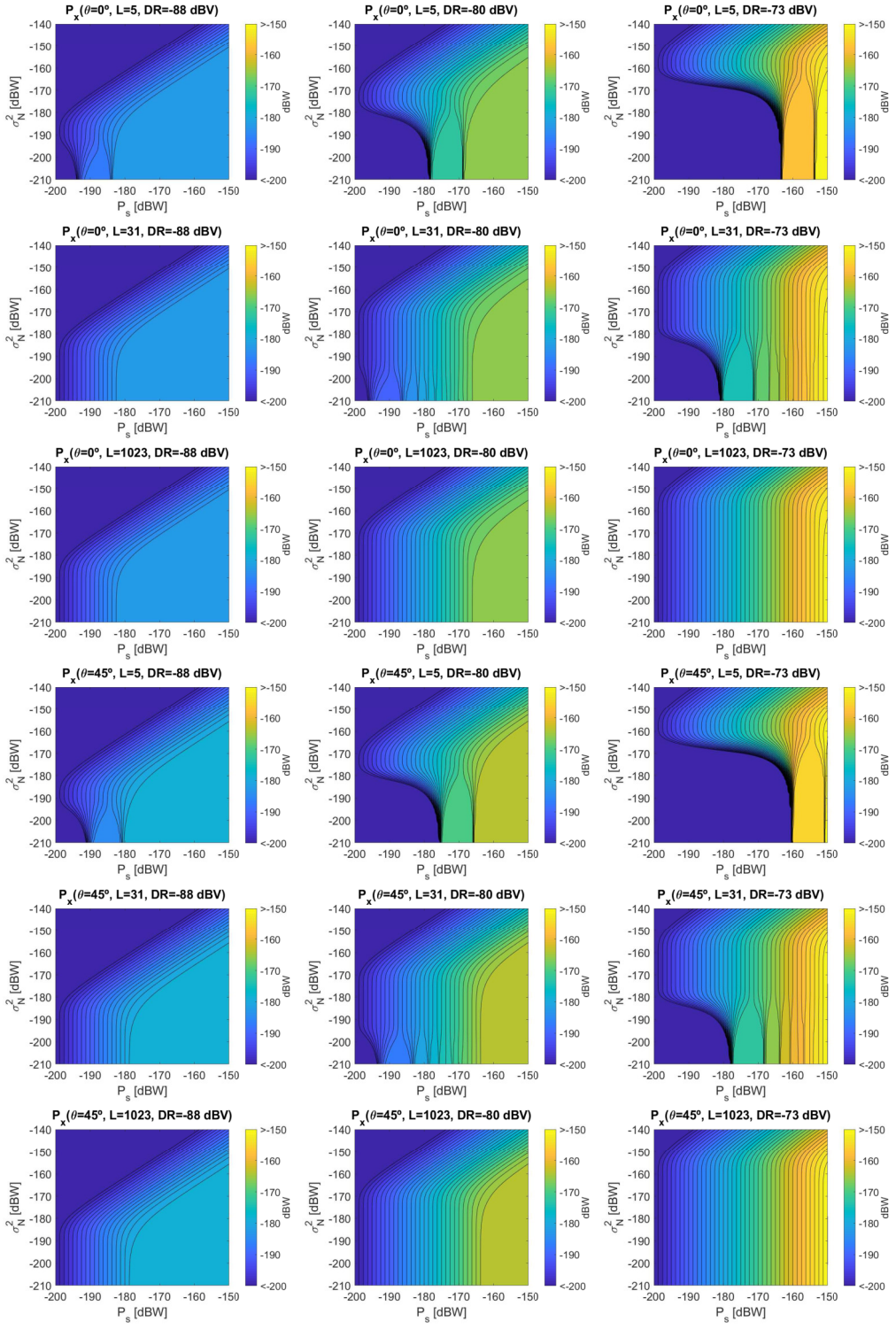

Figure 7.5: Impact of the number of levels and dynamic range on the sampled signal power. Lines are separated by 1.25 dBW.

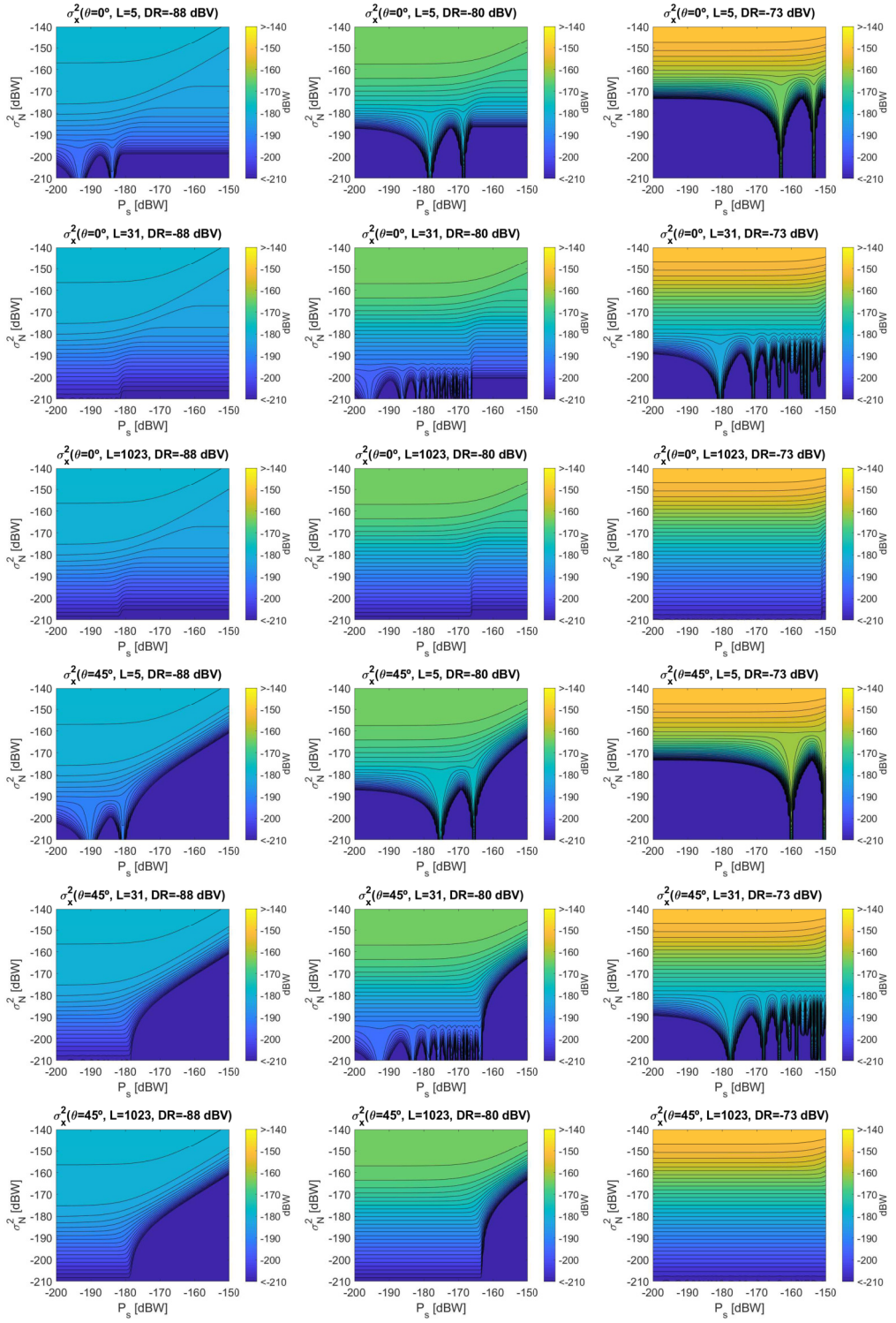

Figure 7.6: Impact of the number of levels and dynamic range on the sampled signal variance. Lines are separated by 1.75 dBW.

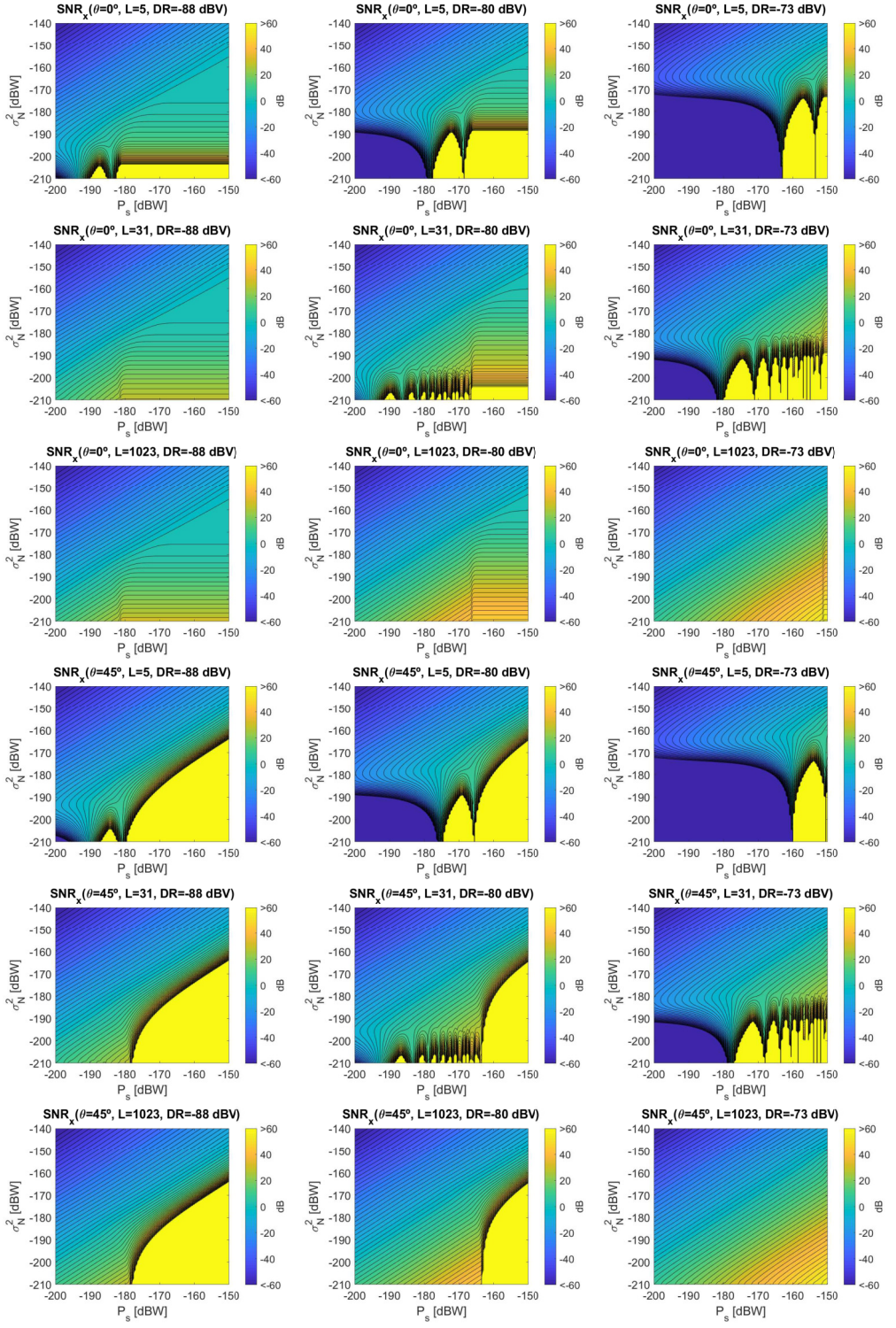

Figure 7.7: Impact of the number of levels and dynamic range on the sampled signal SNR. Lines are separated by 2 dB.

7.4.1.1 Peak statistics

A - Amplitude, magnitude and phase

According to the central limit theorem, the waveform peak is described as a bivariate normal random variable with the next mean and variance

$$\mu_{w_{\{I,Q\}}} = \mathrm{E}\left[\frac{1}{N}\sum_{N} x_{\{I,Q\}}\right] = \frac{1}{N}\,\mathrm{E}\left[\sum_{N} x_{\{I,Q\}}\right] = \frac{1}{N}\sum_{N}\mu_{x_{\{I,Q\}}} = \mu_{x_{\{I,Q\}}}, \tag{7.19a}$$

$$\sigma^2_{w_{\{I,Q\}}} = \mathrm{V}\left[\frac{1}{N}\sum_{N} x_{\{I,Q\}}\right] = \frac{1}{N^2}\,\mathrm{V}\left[\sum_{N} x_{\{I,Q\}}\right] = \frac{1}{N^2}\sum_{N}\sigma^2_{x_{\{I,Q\}}} = \frac{1}{N}\sigma^2_{x_{\{I,Q\}}} \tag{7.19b}$$

If the number of levels of the ADC is large, the variances of the two components would be almost the same. However, as seen in (7.11) and in (7.15), the phase of the analog signal produces different sampled amplitude variances when the number of ADC levels is small. This means that the peak magnitude $r = |w|$ is no longer characterized by the Rice PDF but by the Beckmann. There is not a simplified closed-form expression for the Beckmann PDF and for its statistical moments (see Section C.3).

The phase is characterized by the PDF given in (C.15). To the knowledge of the author, there are not closed-form expressions for the mean and the variance. However, they have been obtained numerically from the definition of the PDF and plotted in Fig. 7.8 against the SNR after the cross-correlation. This SNR will be defined later, but the

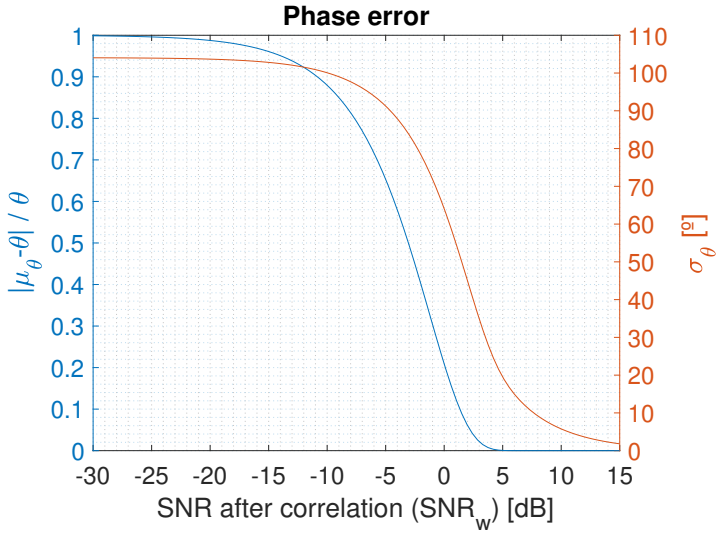

Figure 7.8: Magnitude of the relative error (left axis) and standard deviation (right axis) of the waveform peak phase.

idea behind this figure is that the PDF of the noise converges to the uniform one for low SNRs. This means that the variance of the analog signal not only introduces a variance on the phase, but also a bias that depends on both the true value of the phase and on the SNR.

B - Power

The fact that the variances of the amplitudes are different, also means that the peak power $Y = r^2$ is no longer given by the scaled non-central chi-squared distribution but by its generalized form. There is not a closed-form expression for its PDF, but approximations can be found in the literature (e.g. [189]). However, the mean and the power are given by

Table 7.1: Scholastic characterization of the waveform magnitudes.

RV		Peak		Noise floor $\mu_{x_I} = \mu_{x_Q} = 0$	
		No quantification $\sigma^2_{x_I} = \sigma^2_{x_Q} = \sigma^2_s/2$	ADC $\sigma^2_{x_I} \neq \sigma^2_{x_Q}$	No quantification $\sigma^2_{x_I} = \sigma^2_{x_Q} = \sigma^2_s/2$	ADC $\sigma^2_{x_I} \neq \sigma^2_{x_Q}$
Amplitude w	PDF	Bivariate normal (C.2)			
	Param.	$\mu_{\{x,y\}} = \mu_{\{x_I,x_Q\}}$ $\sigma^2_{\{x,y\}} = \sigma^2_{\{x_I,x_Q\}}/N$	$\mu_{\{x,y\}} = \mu_{\{x_I,x_Q\}}$ $\sigma^2_{\{x,y\}} = \sigma^2_{\{x_I,x_Q\}}/N$	$\mu_{\{x,y\}} = 0$ $\sigma^2_{\{x,y\}} = \sigma^2_{\{x_I,x_Q\}}/N$	$\mu_{\{x,y\}} = 0$ $\sigma^2_{\{x,y\}} = \sigma^2_{\{x_I,x_Q\}}/N$
	$\mu_{\{w_I,w_Q\}}$	$\mu_{\{x,y\}}$			
	$\sigma^2_{\{w_I,w_Q\}}$	$\sigma^2_{\{x,y\}}$			
Magntiude $r = \lvert w \rvert$	PDF	Rice (C.7)(C.9)	Beckmann (C.5)(C.6)	Rayleigh (C.13)	Hoyt (C.11)
	Param.	$\nu = \mu^2_{w_I} + \mu^2_{w_Q}$ $\sigma^2 = \sigma^2_{w_I} = \sigma^2_{w_Q}$	$\mu_{\{x,y\}} = \mu_{\{w_I,w_Q\}}$ $\sigma^2_{\{x,y\}} = \sigma^2_{\{w_I,w_Q\}}$	$\sigma^2 = \sigma^2_{w_I} = \sigma^2_{w_Q}$	$q = \frac{max\{\sigma_{w_I}, \sigma_{w_Q}\}}{min\{\sigma_{w_I}, \sigma_{w_Q}\}}$ $w = \sigma^2_{w_I} + \sigma^2_{w_Q}$
	μ_r	(C.8a)(C.10a)	NA	(C.14a)	(C.12a)
	σ^2_r	(C.8b)(C.10b)	NA	(C.14b)	(C.12b)
Phase $\theta = \angle w$	PDF	(C.15)		Uniform (C.17)	Hoyt phase (C.16)
	Param.	$\mu_{\{x,y\}} = \mu_{\{w_I,w_Q\}}$ $\sigma^2_{\{x,y\}} = \sigma^2_{\{w_I,w_Q\}}$		$[0,2\pi)$	$b = \frac{\sigma^2_{w_I} - \sigma^2_{w_Q}}{\sigma^2_{w_I} + \sigma^2_{w_Q}}$
	μ_θ	NA		(C.18a)	see Section C.7
	σ^2_θ			(C.18b)	
Amplitude squared $g = w^2$	PDF	Scaled non central chi squared (C.23)		Scaled central chi squared (C.19)	
	Param.	$k = 1$ $\sigma = \sigma_{w_I} = \sigma_{w_Q}$	$k = 1$ $\sigma = \{\sigma_{w_I}, \sigma_{w_Q}\}$	$k = 1$ $\sigma = \sigma_{w_I} = \sigma_{w_Q}$	$k = 1$ $\sigma = \{\sigma_{w_I}, \sigma_{w_Q}\}$
	$\mu_{\{g_I,g_Q\}}$	(C.24a)		(C.20a)	
	$\sigma^2_{\{g_I,g_Q\}}$	(C.24b)		(C.20b)	
Power $Y = r^2$	PDF	Scaled non central chi squared (C.23)	Generalized chi squared [189]	Exponential (C.27)	Squared Hoyt (C.25)
	Param.	$k = 2$ $\lambda = \mu^2_{w_I} + \mu^2_{w_Q}$ $\sigma = \sigma_{w_I} = \sigma_{w_Q}$	-	$\lambda = 1/\mu_r$	$q = \frac{max\{\sigma_{w_I}, \sigma_{w_Q}\}}{min\{\sigma_{w_I}, \sigma_{w_Q}\}}$ $w = \sigma^2_{w_I} + \sigma^2_{w_Q}$
	μ_Z	(C.24a)	(7.20a)	(C.28a)	(C.26a)
	σ^2_Z	(C.24b)	(7.20b)	(C.28b)	(C.26b)

Table 7.2: Scholastic characterization of the waveform averaged magnitudes.

RV		Peak		Noise floor $\mu_{x_I} = \mu_{x_Q} = 0$	
		No quantification $\sigma^2_{x_I} = \sigma^2_{x_Q} = \sigma^2_s/2$	ADC $\sigma^2_{x_I} \neq \sigma^2_{x_Q}$	No quantification $\sigma^2_{x_I} = \sigma^2_{x_Q} = \sigma^2_s/2$	ADC $\sigma^2_{x_I} \neq \sigma^2_{x_Q}$
Averaged amplitude $\overline{w} = \frac{1}{M}\sum_1^M w$	PDF	Bivariate normal (C.2)			
	Param.	$\mu_{\{x,y\}} = \mu_{\{w_I,w_Q\}}$ $\sigma^2_{\{x,y\}} = \sigma^2_{\{w_I,w_Q\}}/M$	$\mu_{\{x,y\}} = \mu_{\{w_I,w_Q\}}$ $\sigma^2_{\{x,y\}} = \sigma^2_{\{w_I,w_Q\}}/M$	$\mu_{\{x,y\}} = 0$ $\sigma^2_{\{x,y\}} = \sigma^2_{\{w_I,w_Q\}}/M$	$\mu_{\{x,y\}} = 0$ $\sigma^2_{\{x,y\}} = \sigma^2_{\{w_I,w_Q\}}/M$
	$\mu_{\{\overline{w}_I,\overline{w}_Q\}}$	$\mu_{\{x,y\}}$			
	$\sigma^2_{\{\overline{w}_I,\overline{w}_Q\}}$	$\sigma^2_{\{x,y\}}$			
Averaged magnitude $\overline{r} = \frac{1}{M}\sum_1^M r$	PDF	Closed approximations [190, 191]	NA	Closed approximations [192]	Closed approximations [193]
	$\mu_{\overline{r}}$	[194]			
	$\sigma^2_{\overline{r}}$	[194]			
Aaveraged amplitude squared $\overline{g} = \frac{1}{M}\sum_1^M g$	PDF	Scaled non central chi squared (C.23)		Scaled central chi squared (C.19)	
	Param.	$k = M$ $\sigma = \sigma_{w_{I_i}} = \sigma_{w_{Q_i}} \forall i$	$k = M$ $\sigma = \{\sigma_{w_I}, \sigma_{w_Q}\}$	$k = M$ $\sigma = \sigma_{w_{I_i}} = \sigma_{w_{Q_i}} \forall i$	$k = M$ $\sigma = \{\sigma_{w_I}, \sigma_{w_Q}\}$!!
	$\mu_{\{\overline{g}_I,\overline{g}_Q\}}$	(C.24a)		(C.20a)	
	$\sigma^2_{\{\overline{g}_I,\overline{g}_Q\}}$	(C.24b)		(C.20b)	
Averaged power $Z = \frac{1}{M}\sum_1^M Y$	PDF	Scaled non central chi squared (C.23)	Generalized chi squared [189]	Erlang (C.29)	NA
	Param.	$k = 2M$ $\lambda = \sum_1^M \mu^2_{w_{I_i}} + \mu^2_{w_{Q_i}}$ $\sigma = \sigma_{w_{I_i}} = \sigma_{w_{Q_i}} \forall i$	-	$k = M$ $\lambda = 1/\mu_p$	-
	μ_z	(C.24a)	(7.23a)	(C.30a)	(7.23a)
	σ^2_Z	(C.24b)	(7.23b) or (7.24)	(C.30b)	(7.23b) or (7.24)

$$\mu_Y = \mathrm{E}[Y] = \mathrm{E}\left[w_I^2\right] + \mathrm{E}\left[w_Q^2\right] = \mu^2_{w_I} + \mu^2_{w_Q} + \sigma^2_{w_I} + \sigma^2_{w_Q}, \tag{7.20a}$$

$$\sigma^2_Y = \mathrm{V}[Y] = \mathrm{V}\left[w_I^2\right] + \mathrm{V}\left[w_Q^2\right] = 2\sigma^2_{w_I}\left(2\mu^2_{w_I} + \sigma^2_{w_I}\right) + 2\sigma^2_{w_Q}\left(2\mu^2_{w_Q} + \sigma^2_{w_Q}\right), \tag{7.20b}$$

where the next identities have been used

$$\mu_{w^2_{\{I,Q\}}} = \mathrm{E}\left[w^2_{\{I,Q\}}\right] = \sigma^2_{w_{\{I,Q\}}} + \mu^2_{w_{\{I,Q\}}}, \tag{7.21a}$$

$$\sigma^2_{w^2_{\{I,Q\}}} = \mathrm{V}\left[w^2_{\{I,Q\}}\right] = \mathrm{E}\left[w^4_{\{I,Q\}}\right] - \mu_{w^2_{\{I,Q\}}} \tag{7.21b}$$

$$\mathrm{E}\left[w^4_{\{I,Q\}}\right] = \mu^4_{w_{\{I,Q\}}} + 6\mu^2_{w_{\{I,Q\}}}\sigma^2_{w_{\{I,Q\}}} + 3\sigma^4_{w_{\{I,Q\}}}. \tag{7.21c}$$

Note that the latter equation holds under the assumption that the amplitudes $w_{\{I,Q\}}$ are Gaussian random variables. Equations (7.20a) and (7.20b) are important because they show that the mean of the power waveform peak is biased by the noise power. Similarly, the variance of the power waveform peak has a multiplicative term coming from the original signal power. In the ideal analog case (or if the number of ADC levels is large),

$\mu_{w_{\{I,Q\}}} = \mu_{s_{\{I,Q\}}}$ and $\sigma^2_{w_I} = \sigma^2_{w_Q} = \sigma^2_s/2N$. Then (7.20a) and (7.20b) are rewritten as

$$\mu_Y = P + \sigma^2_s/N, \tag{7.22a}$$

$$\sigma^2_Y = \left(2P + \sigma^2_s/N\right)\sigma^2_s/N, \tag{7.22b}$$

which are the well-known expressions for power statistics under AWGN noise (e.g. [34]).

C - Average power

The PDF of the average peak power $Z = \sum_M Y/M$ also follows a generalized chi-square distribution, but with $2M$ degrees of freedom. If M is large enough, and the waveforms are uncorrelated, the distribution converges to a Gaussian under the central limit theorem. If the power waveforms are independent and identically distributed (iid), and also are equally weighted in the averaging process, the mean and the variance of the averaged peak power are given by

$$\mu_Z = \mathrm{E}\left[Z\right] = \mathrm{E}\left[\frac{1}{M}\sum_M Y\right] = \frac{1}{M}\,\mathrm{E}\left[\sum_M Y\right] = \frac{1}{M}\sum_M \mu_Y = \mu_Y, \tag{7.23a}$$

$$\sigma^2_Z = \mathrm{V}\left[Z\right] = \mathrm{V}\left[\frac{1}{M}\sum_M Y\right] = \frac{1}{M^2}\,\mathrm{V}\left[\sum_M Y\right] = \frac{1}{M^2}\sum_M \sigma^2_Y = \frac{1}{M}\sigma^2_Y. \tag{7.23b}$$

One important thing to state here is that although the averaging does indeed reduce the peak variance, it is not able to remove the noise terms of the mean in (7.20a). In fact, these terms can only be reduced by using a larger coherent integration length. This issue does not affect the SNR after the correlation, but as it will be explained later, affects the detectability of the peak from the noise floor.

The assumption that consecutive reflected waveforms are uncorrelated has been experimentally proven to be not valid [118, 195]. This correlation is the result of the time dynamics (such as the sea waves) and/or pattern distributions (such as crop fields) of the reflecting surface. As a result of the correlation, the central limit theorem does no longer apply. However, it can be extended to *sufficiently weakly correlated* variables under certain circumstances. It is well beyond the scope of this Ph. D. thesis to enter into the details, and more information can be found in the literature (e.g. [196]). The mean of the

averaged peak is also given by (7.23a). However, the variance changes to

$$\begin{aligned}\sigma_Z^2 = \mathrm{V}\left[Z\right] = \mathrm{V}\left[\frac{1}{M}\sum_i^M Y_i\right] = \frac{1}{M^2}\,\mathrm{V}\left[\sum_i^M Y_i\right] = \frac{1}{M^2}\left(\sum_i^M \mathrm{V}\left[Y_i\right] + 2\sum_{i\neq j}^M \mathrm{Cov}\left[Y_i, Y_j\right]\right) \\ = \frac{1}{M^2}\left(M\sigma_Y^2 + 2\sum_{i\neq j}^M \rho_{Y_iY_j}\sigma_{Y_i}\sigma_{Y_j}\right) = \frac{1}{M^2}\left(M\sigma_Y^2 + 2\sigma_Y^2\sum_{i\neq j}^M \rho_{Y_iY_j}\right) \\ = \frac{1}{M^2}\left(M\sigma_Y^2 + \sigma_Y^2\left(M-1\right)\hat{\rho}\right) = \frac{1}{M}\sigma_Y^2 + \frac{M-1}{M}\hat{\rho}\sigma_Y^2,\end{aligned} \tag{7.24}$$

where $\mathrm{Cov}(x, y)$ denotes the covariance between the random variables x and y; ρ_{xy} is their correlation coefficient, and $\hat{\rho}$ is the average correlation coefficient among all the waveforms. Note that a different notation has been used with respect to the previous equations in order to facilitate the readability. Note also than when the waveforms are weakly correlated ($\hat{\rho} \approx 0$), the above equation converges to (7.23b). In contrast, when the waveforms are highly correlated ($\hat{\rho} \to 1$), the variance above tends to $\sigma_Z^2 \to \sigma_Y^2$.

7.4.1.2 Noise floor statistics

A - Amplitude, magnitude and phase

The waveform samples from the noise floor also are also described as a bivariate normal random variable. In principle, the original samples $x_{\{I,Q\}}$ can be correlated if a digital filter with a large number of taps is used, but this is omitted here for the sake of simplicity. The variance $\sigma_{w_{\{I,Q\}}}$ is the same as the variance of the peak given in (7.19b). The mean $\mu_{w_{\{I,Q\}}}$ is ideally zero. However, the fact that the PRN codes are not totally random and that the correlation length is finite, produces secondary spurious peaks. These peaks are actually very small (see for example Fig. 2.13). In the case of a GPS L1 C/A, the power of the strongest spurious peak is $(65/1023)^2 \approx 0.004 = -23.97$dB below the true peak [21]. These spurious peaks are deterministic, and strictly speaking, they have the same stochastic properties as the peak but with a reduced power. However, if the analog SNR is low, the spurious peaks are well below the noise floor, and thus it can be assumed that $\mu_{w_{\{I,Q\}}} = 0$ along the noise floor. This assumption may no longer be valid after the incoherent averaging, and further comments on that will be given later.

Again, since the variances of the amplitude components are different, the magnitude of the noise floor samples is not longer a Rayleigh random variable, but Hoyt (see Section C.5). The PDF of the phase of the noise floor samples follows the Hoyt phase distribution given in (C.16). This phase has no physical meaning, but it is given here for the sake of completeness.

B - Power

Similarly, the power of the noise samples are no longer characterized by an exponential random variable but by the squared Hoyt given in Section C.10. The mean μ_Y and variance σ_Y^2 are also found following the same derivation as done for (7.20b) and (7.20a)

$$\mu_Y = \mathrm{E}\left[Y\right] = \mathrm{E}\left[w_I^2\right] + \mathrm{E}\left[w_Q^2\right] = \sigma_{w_I}^2 + \sigma_{w_Q}^2, \tag{7.25a}$$

$$\sigma_Y^2 = \mathrm{V}\left[Y\right] = \mathrm{V}\left[w_I^2\right] + \mathrm{V}\left[w_Q^2\right] = 2\sigma_{w_I}^4 + 2\sigma_{w_Q}^4. \tag{7.25b}$$

In general, the variance of the noise floor power is used as an estimator of the variance of the peak power. This method allows the estimation of the peak statistics by using a single waveform. However, as seen from (7.25b) and (7.20b) both variances are different, and this estimator is only valid for low post correlation SNRs. Additionally, if the SNR is high, the power of the spurious peaks may be above the true noise floor. Under these circumstances, the estimator will not be computing a variance but the average power of the spurious peaks. The post-correlation SNRs at which this estimator saturates are: $\approx$ 27.8dB (C/A), $\approx$ 38.6dB (E1OS), $\approx$ 40.2dB (L5), and $\approx$ 45.8dB (E5).

In the ideal analog case (or if the number of ADC levels is large), the noise power can be characterized by the exponential distribution. The mean and variance are then simplified to

$$\mu_Y = \sigma_s^2/N, \tag{7.26a}$$

$$\sigma_Y^2 = \sigma_s^4/N^2. \tag{7.26b}$$

Note that under the exponential random variable assumption, $\mu_Y = \sigma_Y^2$, and the noise floor can be either estimated from the mean or from the variance. However, doing so from the mean would require a smaller number of observations in order to have a better estimation.

C - Average power

No closed-form expressions exists for the addition of iid squared Hoyt random variables. However, approximations can be found on [193], and the central limit theorem can be also applied if the number of averages is large enough.

The addition of iid exponential random variables is an Erlang random variable (see Section C.12), which is a particularization of the Gamma random variable in which the shape parameter k can only be a positive integer. Similarly to the exponential distribution, the mean and variance of the Earlang are related with $\mu_Z^2 = \sigma_Z^2$, which means that both moments can be also used as an estimate of the averaged noise floor.

Regardless of the distribution, the mean μ_z and the variance σ_z^2 are given by (7.23a) and (7.23b) respectively.

7.4.2 Interferometric waveform

Let $x^D = x_I^D + jx_Q^D$ and $x^R = x_I^R + jx_Q^R$ be the complex baseband digital direct and reflected signals respectively. The interferometric waveform $w = w_I + jw_Q$ is modeled here as

$$w = \sum_N \left(x_I^D + jx_Q^D\right)\left(x_I^R + jx_Q^R\right) \tag{7.27}$$

which produces the amplitude components

$$w_I = \frac{1}{N}\sum_N x_I^D x_I^R + x_Q^D x_Q^R, \tag{7.28a}$$

$$w_Q = \frac{1}{N}\sum_N -x_I^D x_Q^R + x_Q^D x_I^R. \tag{7.28b}$$

7.4.2.1 Peak statistics

All the magnitudes have the same stochastic characteristics than in the conventional case, but with new different moments.

A - Amplitude, magnitude and phase
The mean of amplitudes are found as

$$\mu_{w_I} = \mu_{x_I^D}\mu_{x_I^R} + \mu_{x_Q^D}\mu_{x_Q^R}, \tag{7.29a}$$

$$\mu_{w_Q} = -\mu_{x_I^D}\mu_{x_Q^R} + \mu_{x_Q^D}\mu_{x_I^R}, \tag{7.29b}$$

where the equality $\mathrm{E}[ab] = \mu_a\mu_b$ has been used. The variances are

$$\begin{aligned}\sigma_{w_I}^2 &= \frac{1}{N}\left[\left(\sigma_{x_I^D}^2 + \mu_{x_I^D}^2\right)\left(\sigma_{x_I^R}^2 + \mu_{x_I^R}^2\right) - \mu_{x_I^D}^2\mu_{x_I^R}^2\right] \\ &\quad + \frac{1}{N}\left[\left(\sigma_{x_Q^D}^2 + \mu_{x_Q^D}^2\right)\left(\sigma_{x_Q^R}^2 + \mu_{x_Q^R}^2\right) - \mu_{x_Q^D}^2\mu_{x_Q^R}^2\right] \\ &= \frac{1}{N}\left[\sigma_{x_I^D}^2\sigma_{x_I^R}^2 + \sigma_{x_Q^D}^2\sigma_{x_Q^R}^2 + \sigma_{x_I^D}^2\mu_{x_I^R}^2 + \sigma_{x_Q^D}^2\mu_{x_Q^R}^2 + \sigma_{x_I^R}^2\mu_{x_I^D}^2 + \sigma_{x_Q^R}^2\mu_{x_Q^D}^2\right],\end{aligned} \tag{7.30a}$$

$$\begin{aligned}\sigma_{w_Q}^2 &= \dots \\ &= \frac{1}{N}\left[\sigma_{x_I^D}^2\sigma_{x_Q^R}^2 + \sigma_{x_Q^D}^2\sigma_{x_I^R}^2 + \sigma_{x_I^D}^2\mu_{x_Q^R}^2 + \sigma_{x_Q^D}^2\mu_{x_I^R}^2 + \sigma_{x_Q^R}^2\mu_{x_I^D}^2 + \sigma_{x_I^R}^2\mu_{x_Q^D}^2\right],\end{aligned} \tag{7.30b}$$

where the equality $\sigma^2(ab) = (\sigma_a^2 + \mu_a^2)(\sigma_b^2 + \mu_b^2) - \mu_a^2\mu_a^2$ has been used.

In the analog ideal case or by using an ADC with a large number of levels, the means are rewritten as

$$\mu_{w_I} = \sqrt{P_D}\cos(\theta_D)\sqrt{P_R}\cos(\theta_R) + \sqrt{P_D}\sin(\theta_D)\sqrt{P_R}\sin(\theta_R) = \sqrt{P_D P_R}\cos(\theta_D - \theta_R), \tag{7.31a}$$

$$\mu_{w_Q} = \ldots = \sqrt{P_D P_R}\sin(\theta_D - \theta_R), \tag{7.31b}$$

where P_D and P_R are the analog direct and reflected signal powers respectively; θ_D and θ_R are their phases; and where the next equalities have been used $\cos(a-b) = \cos(a)\cos(b) + \sin(a)\sin(b)$ and $\sin(a-b) = \sin(a)\cos(b) + \cos(a)\sin(b)$. Note that the waveform peak phase is indeed the relative phase between the direct and reflected signals: $\text{atan}(\mu_{w_Q}/\mu_{w_I}) = \theta_D - \theta_R$.

Also in the ideal case, the variances are equal and simplified to

$$\sigma^2_{w_I} = \sigma^2_{w_Q} = \frac{1}{N}\left(\frac{\sigma^2_D\sigma^2_R}{2} + \frac{\sigma^2_D}{2}P_R + \frac{\sigma^2_R}{2}P_D\right), \tag{7.32}$$

where σ^2_D and σ^2_R are the analog signal variances respectively.

B - Power

The power statistics are obtained also using (7.20a) and (7.20b). In the ideal case, they are simplified to

$$\mu_Y = P_D P_R + P_R\frac{\sigma^2_D}{N} + P_D\frac{\sigma^2_R}{N} + \frac{\sigma^2_D\sigma^2_R}{N}, \tag{7.33a}$$

$$\sigma^2_Y = \frac{1}{N^2}\left(P_D\sigma^2_R + \sigma^2_D\left(P_R + \sigma^2_R\right)\right)\left(\sigma^2_D\left(P_R + \sigma^2_R\right) + P_D\left(2NP_R + \sigma^2_R\right)\right). \tag{7.33b}$$

Note that the equations above converge respectively to (7.22a) and (7.22b) when $P_D \to 1$ and $\sigma^2_D \to 0$.

C - Average power

The mean of the averaged power is obtained as in (7.23a). The variance is obtained with (7.23b) if the consecutive waveforms are not correlated, or with (7.24) if they are. However, it should be kept in mind that the correlation between inteferometric waveforms may not be the result only from the stationary properties of the reflecting surface, but also from those of the direct signal.

7.4.2.2 Noise floor statistics

A - Amplitude, magnitude and phase

Similar to the conventional case, it is also assumed that the mean amplitudes from the noise floor are $\mu_{w_I} = \mu_{w_Q} = 0$. The variances are obtained as in (7.30a) and (7.30b)

$$\sigma^2_{w_I} = \frac{1}{N}\left[\sigma^2_{x^D_I}\sigma^2_{x^R_I} + \sigma^2_{x^D_Q}\sigma^2_{x^R_Q}\right], \tag{7.34a}$$

$$\sigma^2_{w_Q} = \frac{1}{N}\left[\sigma^2_{x^D_I}\sigma^2_{x^R_Q} + \sigma^2_{x^D_Q}\sigma^2_{x^R_I}\right]. \tag{7.34b}$$

In the ideal analog case, they are equal and simplified to

$$\sigma^2_{w_I} = \sigma^2_{w_Q} = \frac{1}{N}\frac{\sigma^2_D\sigma^2_R}{2}. \tag{7.35}$$

B - Power

The power statistics are also obtained using (7.25a) and (7.25b). In the ideal case, they are simplified to

$$\mu_Y = \frac{1}{N}\sigma^2_D\sigma^2_R, \tag{7.36a}$$

$$\sigma^2_Y = \frac{1}{N^2}\sigma^4_D\sigma^4_R. \tag{7.36b}$$

C - Average power

The mean of the averaged power is given by (7.23a) and the variance by (7.23b).

7.5 Metrics

7.5.1 Peak detection

Detection theory is a means to measure the ability to differentiate between a signal of interest from the noise or RFI. Detection theory is well studied in the radar (e.g. [171,174]) and GNSS (e.g. [24]) fields. Regarding GNSS-R, in [185] the term *detectability criterion* was used based only on the SNR after the correlation and not on the signal statistics, as is done in the radar theory. Here, this latter theory is used.

In radar theory, the presence or not of the reflected echo is treated as a statistical problem. An arbitrary threshold (in general in power units) is used to differentiate between the returning echo from any undesired signal. For a given threshold γ, there is an associated probability of detection P_D and a probability of false alarm P_{FA}. These values depend on the threshold and on the PDFs of the reflected echo and of the undesired components. In this chapter, only the components with the statistics derived in the previous section are considered. The impact of other distributions commonly found on RFI on the GNSS-R reflections is studied in [48].

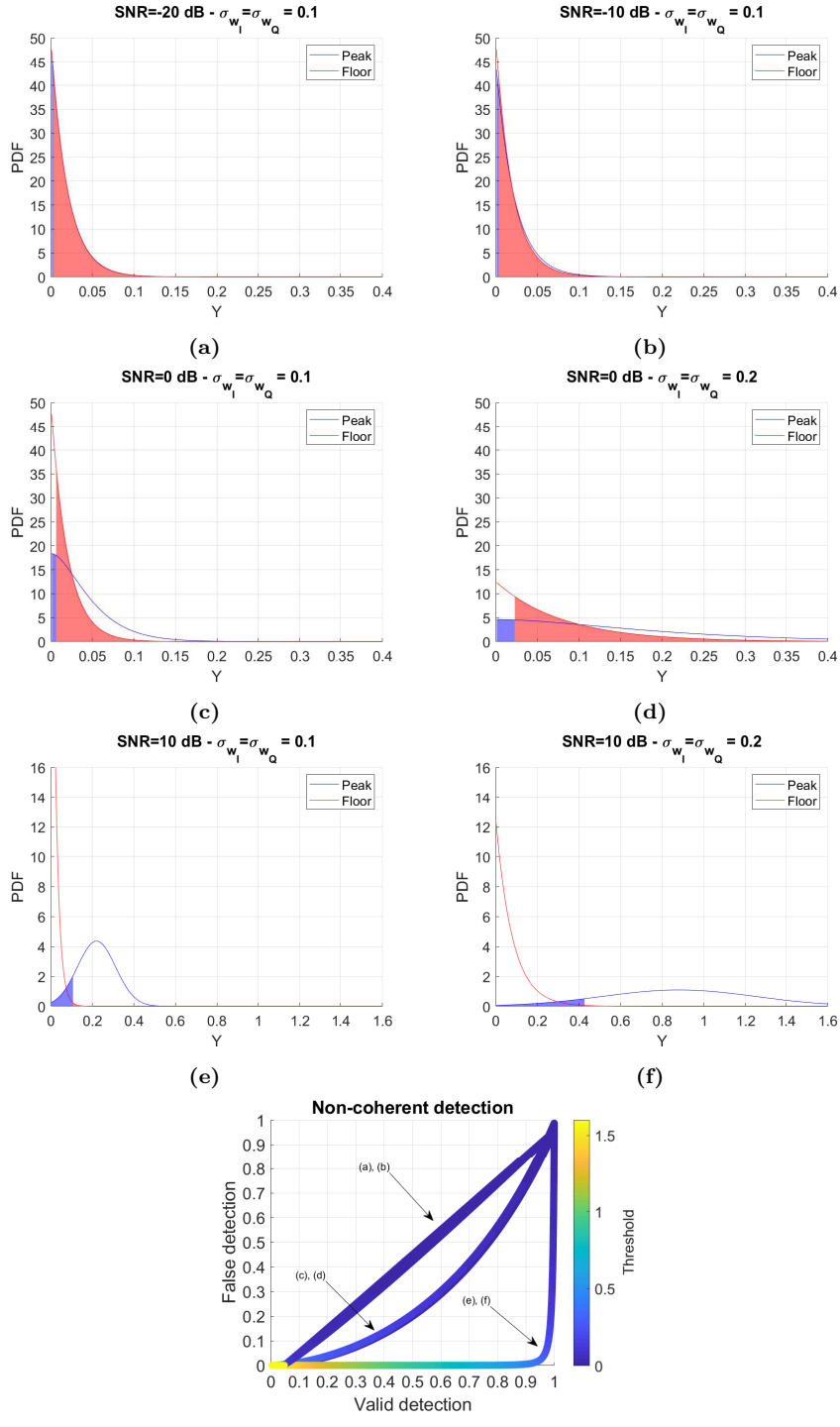

Figure 7.9: Peak detectability with no averages: (a)-(f) PDFs of the peak power (blue) and of the noise floor (red); and (g) false detection vs valid detection diagram as function of the threshold.

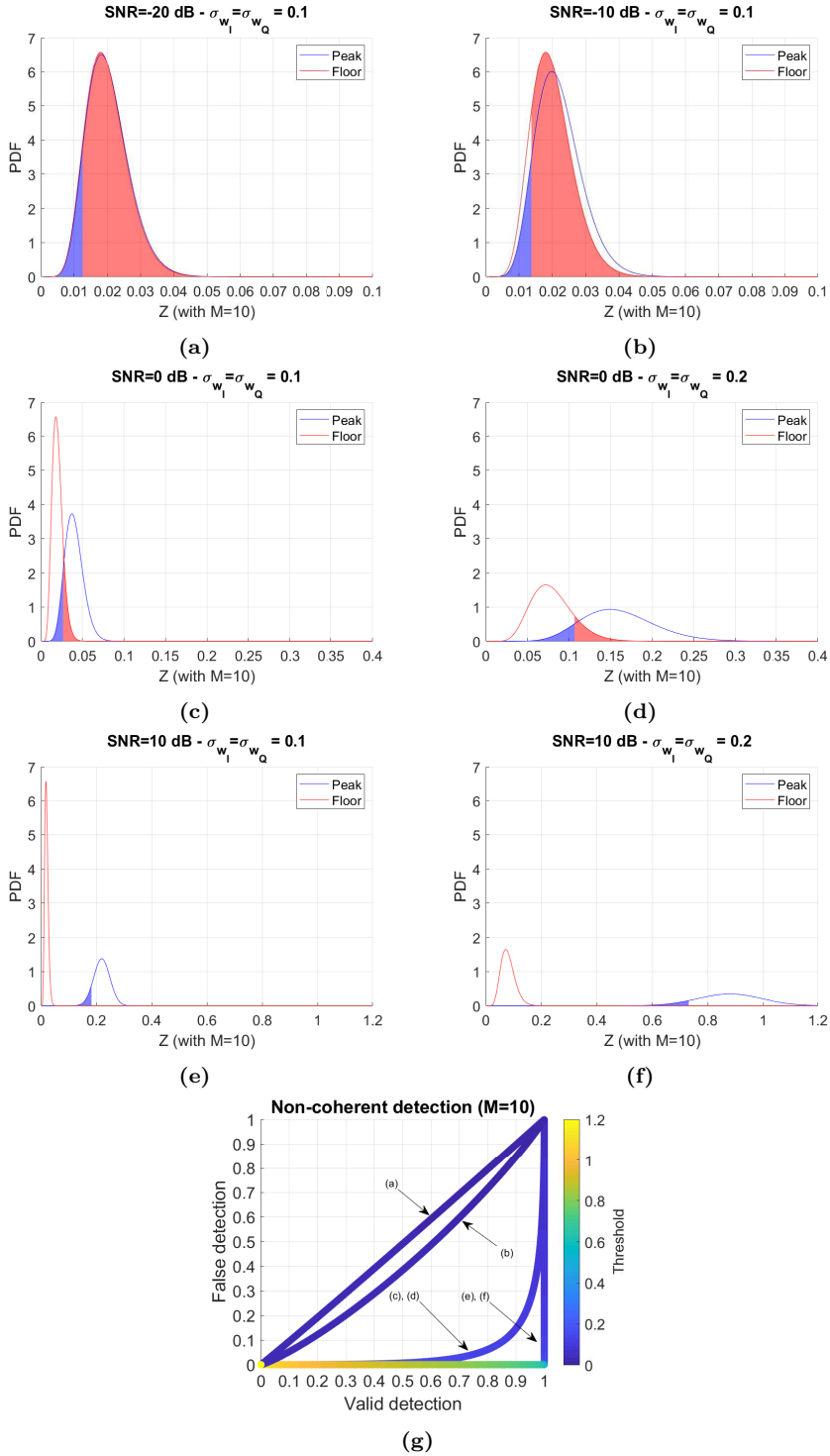

Figure 7.10: Peak detectability with 10 averages: (a)-(f) PDFs of the peak power (blue) and of the noise floor (red); and (g) false detection vs valid detection diagram as function of the threshold.

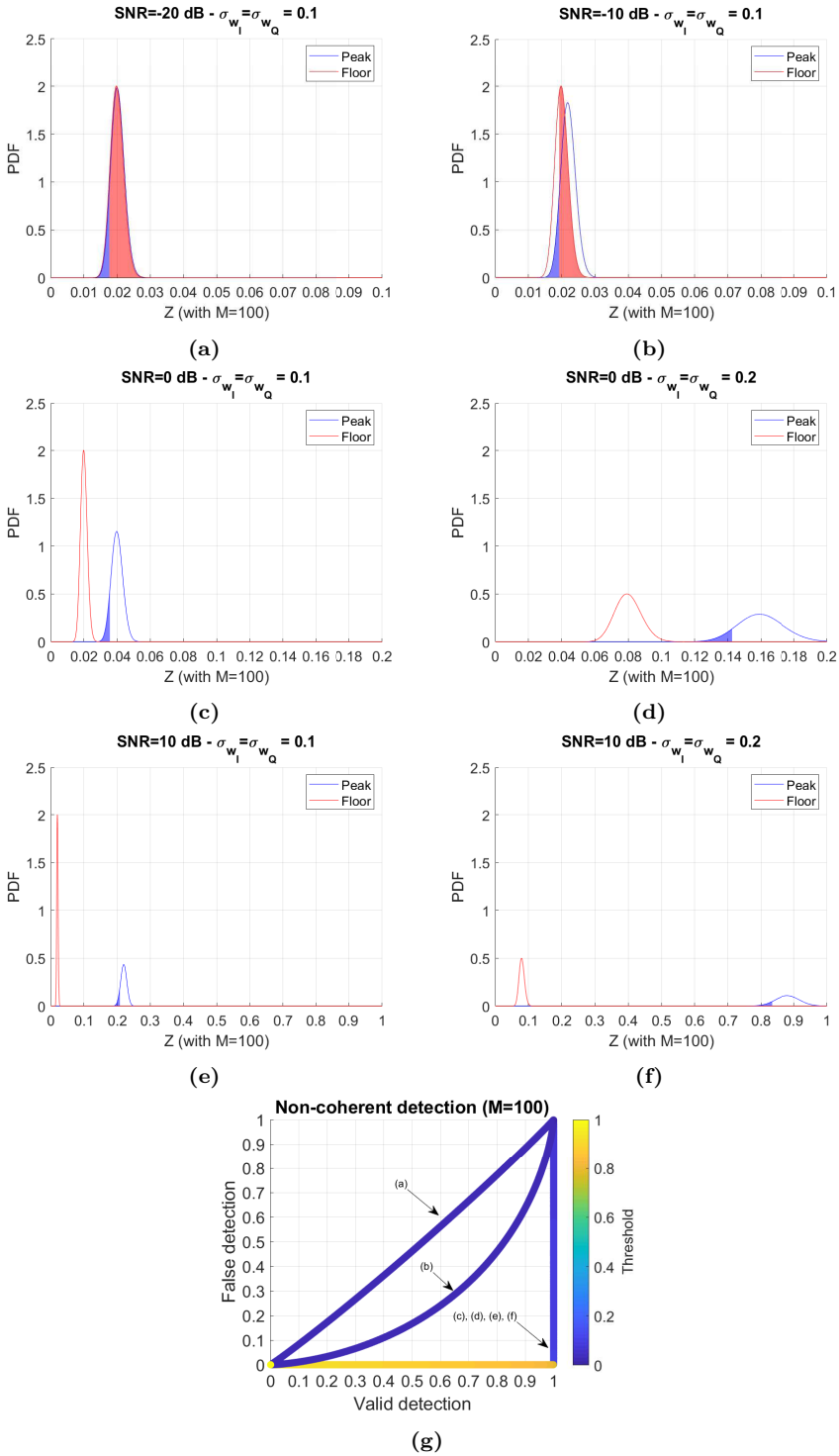

Figure 7.11: Peak detectability with 100 averages: (a)-(f) PDFs of the peak power (blue) and of the noise floor (red); and (g) false detection vs valid detection diagram as function of the threshold.

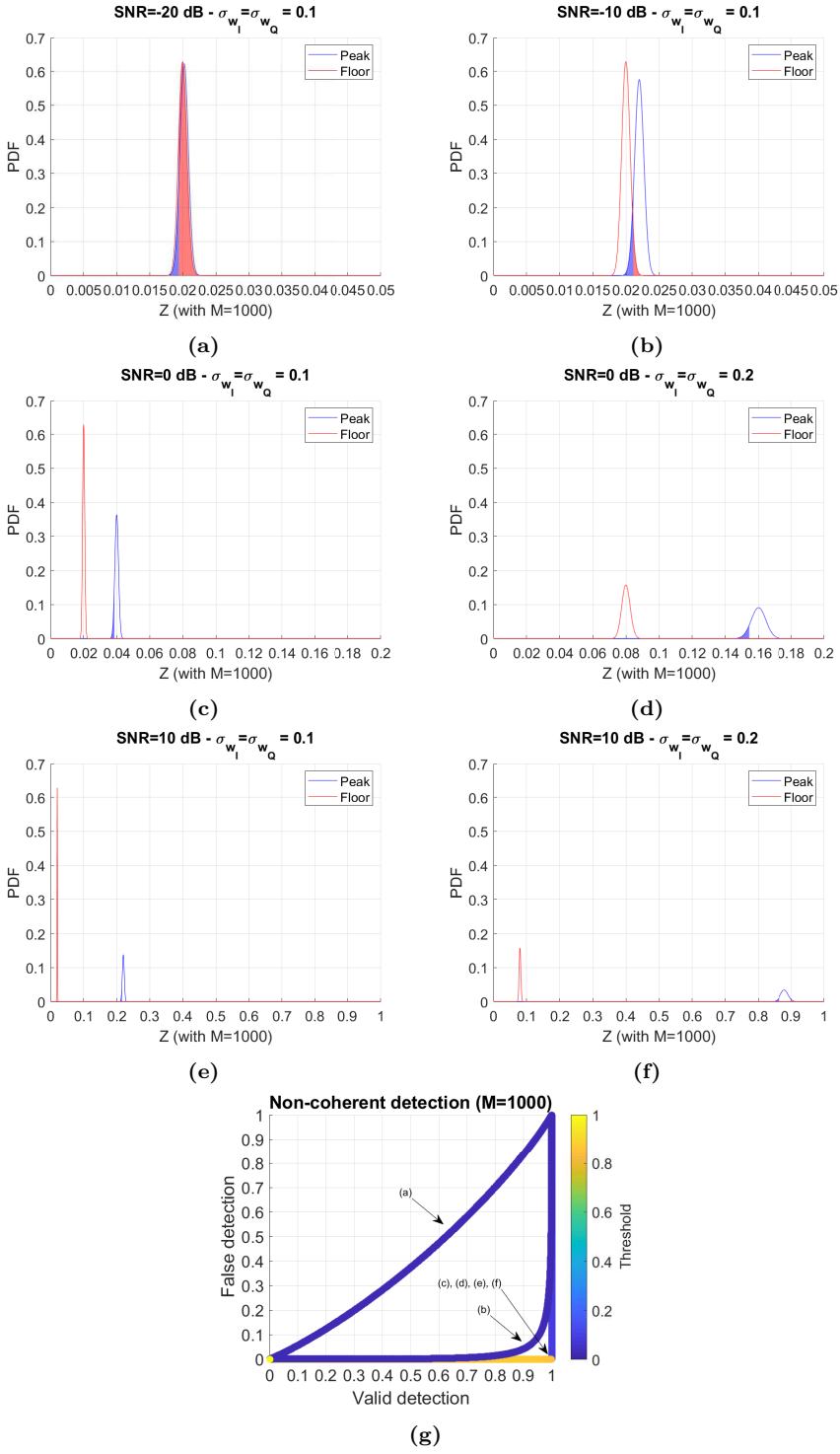

Figure 7.12: Peak detectability with 1000 averages: (a)-(f) PDFs of the peak power (blue) and of the noise floor (red); and (g) false detection vs valid detection diagram as function of the threshold.

The false alarm and detection probabilities of a waveform peak power Y_s (or averaged Z_s) contaminated with a noise signal with power Y_n (or averaged Z_n) are

$$P_{FA} = P(Y_n \geq \gamma) = \int_{\gamma}^{\infty} f_{Y_n}(y_n) \tag{7.37a}$$

$$P_D = 1 - P(Y_s \leq \gamma) = 1 - \int_{-\infty}^{\gamma} f_{Y_s}(y_s) \tag{7.37b}$$

where $f_{Y_n}(y_n)$ and $f_{Y_s}(y_s)$ are the PDFs of the noise and the noiseless signal respectively. They were derived through the last section and summarized in Tables 7.1 and 7.2. Figures 7.9, 7.10, 7.11, and 7.12 show those PDFs for different post-correlation non-coherent SNRs and for different number of averages, and their associated P_{FA} and P_D for an arbitrary threshold. As it can be seen, there is a trade-off in the threshold value. A large threshold produces a small probability of false alarm, but it also reduces the probability of detection. In contrast, a small threshold produces a high detection probability, but it also increases the probability of false alarm. As the incoherent averaging increases, the PDFs get narrower (under the Gaussian assumption, around their mean). This allows the detection of the peak even if the original post-correlation SNR was very small. For instance, compare (7.20a) with (7.25a). If the variances (7.20b) and (7.25b) are well reduced after the incoherent averaging, the term $\mu_{w_I}^2 + \mu_{w_Q}^2$ would be distinguished from $\sigma_{w_I}^2 + \sigma_{w_Q}^2$. However, the number of required averages may be too large, which would in turn reduce the spatial and temporal resolution of the observable.

7.5.2 Peak SNR

Different SNRs definitions exist in the GNSS-R literature. They are studied here and generalized for the sampled signals in which the variances of its amplitude components signal are different. Derivations follow and results using a GPS L1 C/A signal are shown in Fig. 7.13.

7.5.2.1 Coherent

The coherent SNR after the correlation is defined as

$$SNR_w = \frac{\mu_{w_I}^2 + \mu_{w_Q}^2}{\sigma_{w_I}^2 + \sigma_{w_Q}^2}. \tag{7.38}$$

Conventional

In the conventional case, the coherent SNR is obtained using (7.20a) and (7.20b), which yields to

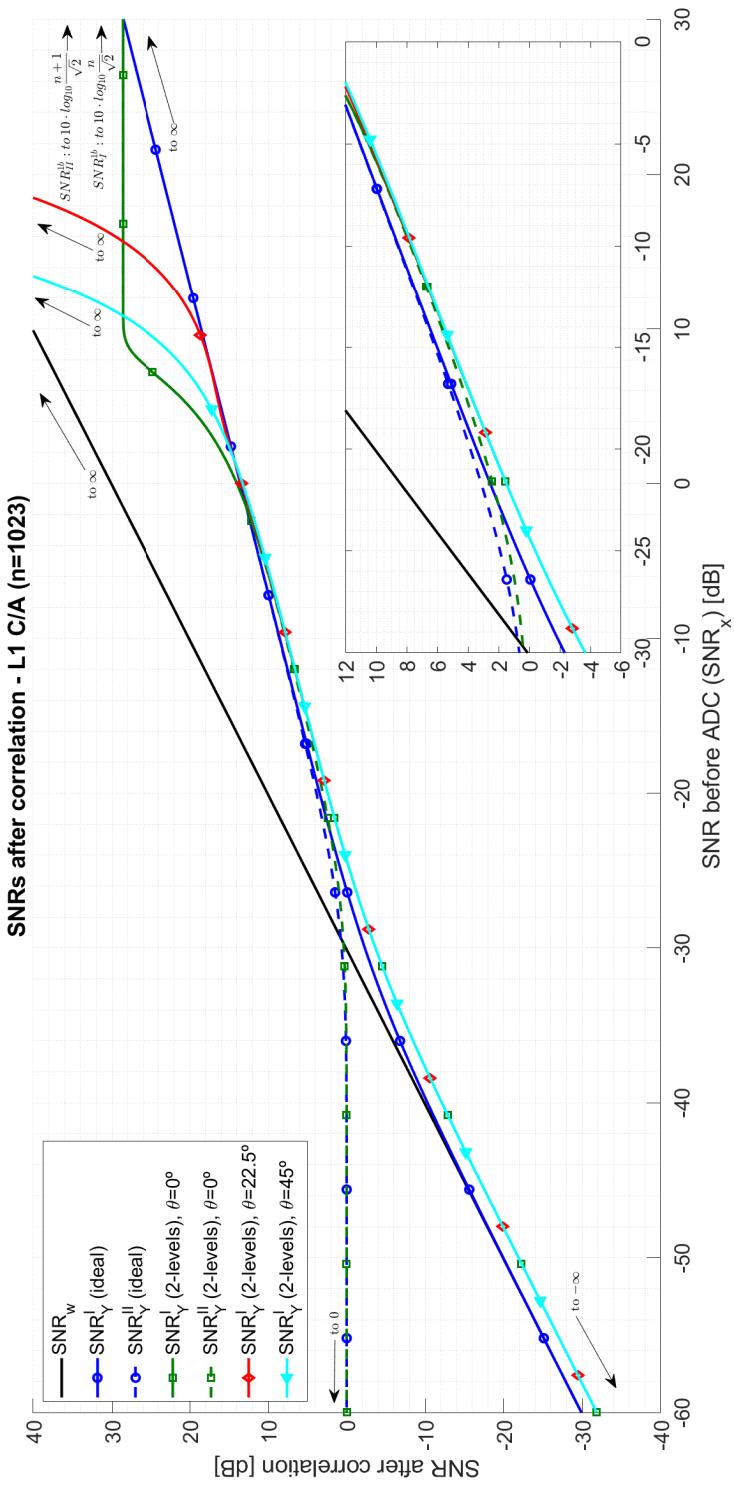

Figure 7.13: Comparison between different post-correlation SNR definitions

$$SNR_w = \frac{\mu_{x_I}^2 + \mu_{x_Q}^2}{\sigma_{x_I/N}^2 + \sigma_{x_Q/N}^2} = NSNR_x, \tag{7.39}$$

where the term $10log_{10}(N)$ is typically known as the correlation or processing gain with respect to the SNR after the ADC SNR_x. This gain can be easy seen in Fig 7.13.

Interferometric

The coherent SNR of the interferometric peak is obtained using (7.29a), (7.29b), (7.30a) and (7.30b). After a tedious but straightforward manipulation, the next equalities are derived

$$\begin{aligned} SNR_w &= N\frac{\left(\mu_{x_I^D}^2 + \mu_{x_Q^D}^2\right)\left(\mu_{x_I^R}^2 + \mu_{x_Q^R}^2\right)}{\left(\mu_{x_I^D}^2 + \mu_{x_Q^D}^2\right)\left(\sigma_{x_I^R}^2 + \sigma_{x_Q^R}^2\right) + \left(\sigma_{x_I^D}^2 + \sigma_{x_Q^D}^2\right)\left(\mu_{x_I^R}^2 + \mu_{x_Q^R}^2 + \sigma_{x_I^R}^2 + \sigma_{x_Q^R}^2\right)} \\ &= N\frac{SNR_{w_R}}{1 + \frac{SNR_{w_R}+1}{SNR_{w_D}}} \\ &= N\frac{SNR_{w_D}SNR_{w_R}}{1 + SNR_{w_D} + SNR_{w_R}}, \end{aligned} \tag{7.40}$$

where SNR_{w_D} and SNR_{w_R} are the conventional coherent SNR of the direct and reflected signals respectively. The equality in the middle is the well known expression derived in [3]. The last equality is the same expression found in the literature for the time delay estimation between two noisy signals (e.g. [177]). These equations shows the degradation of the interfermoetric processing with respect to the conventional. Note that when SNR_{w_D} is large, this SNR_w tends to the one in (7.39).

7.5.2.2 Non-coherent

In general, the coherent SNR is not large enough to provide good estimates, and the waveform must be incoherently averaged. Two different non-coherent SNR are typically found in the literature, here named as SNR_Y^I and SNR_Y^{II}. They are defined as

$$SNR_Y^I = \frac{\mu_Y - \mu_Y|_{P=0}}{\sigma_Y}, \tag{7.41a}$$

$$SNR_Y^{II} = \frac{\mu_Y}{\sigma_Y}. \tag{7.41b}$$

The first definition is in fact conceptually equivalent to the analog SNR given in (7.3). Sometimes in the literature, σ_Y^2 is used in denominator instead of σ_Y [197]. Equivalent SNRs can also defined for the magnitude $r = \sqrt{Y}$ in [194].

The derivations below are aimed at relating SNR_Y with SNR_w, and thus, the results are the same for both the conventional and interferometric techniques. However, the former is used as reference. Starting with the ideal analog case (or when the number of ADC levels is large), the SNR_Y^I is obtained using (7.22a) and (7.22b). After an easy manipulation, next equation is obtained

$$SNR_Y^I = \frac{SNR_w}{\sqrt{2SNR_w + 1}}. \tag{7.42}$$

This equation is important because it shows that the non-coherent SNR has decreased with respect to the coherent. This is well known in the GNSS literature and referred to as *squaring loss* (e.g. [197]). Although this may seem counter-intuitive, the explanation is simple. The estimation of a power is more prone to errors than estimating two uncorrelated amplitudes is (e.g. [171]). However, this loss is recovered in the incoherent averaging. See in Fig. 7.13, that SNR_Y^I tends to SNR_w for low analog SNRs, and to $SNR_w/\sqrt{2}$ for high analog SNRs.

Also in the ideal case, the second definition of SNR is given by

$$SNR_Y^{II} = \frac{SNR_w + 1}{\sqrt{2SNR_w + 1}}. \tag{7.43}$$

Note from Fig. 7.13 and that for high analog SNRs, this SNR converges to SNR_Y^{II}. However for low analog SNR, it rapidly converges to 0dB.

If the number of ADC levels is low, the above equations are no longer valid as they do not consider the impact of the analog phase. In this case, (7.20b) and (7.20a) must be used. After some tedious, but straightforward manipulations, the next expressions are obtained

$$SNR_Y^I = \frac{SNR_w}{\sqrt{2}\sqrt{\frac{(1+q^4)}{(1+q^2)^2} + 2\frac{1+q^2r^2}{(1+q^2)(1+r^2)}SNR_w}}, \tag{7.44a}$$

$$SNR_Y^{II} = \frac{SNR_w + 1}{\sqrt{2}\sqrt{\frac{(1+q^4)}{(1+q^2)^2} + 2\frac{1+q^2r^2}{(1+q^2)(1+r^2)}SNR_w}}, \tag{7.44b}$$

where

$$r^2 = \frac{\mu_{w_I}^2}{\mu_{w_Q}^2} \tag{7.45a}$$

$$q^2 = \frac{\sigma_{w_I}^2}{\sigma_{w_Q}^2} \tag{7.45b}$$

Note that when $\sigma_{w_Q}^2 = \sigma_{w_I}^2$, $q = 1$, and both SNRs tend to ideal ones. The SNRs of signals with different phases sampled using a 2-level ADC are shown in Fig. 7.13. As it

can be seen, they all converge when the analog SNR is low. However, when the analog SNR is large, the phase impacts them in a different manner. For a phase of 0°, the SNR saturates, and for other phases it tends to infinite. Nevertheless, the reduction of SNR by using a 2-levels ADC with respect to the ideal one, is about 2 dB for typical analog SNR values.

7.5.2.3 Incoherent averaging

The SNRs SNR_Z^I and SNR_Z^{II} of the averaged power peak are simply obtained by using (7.23a) and (7.23b) (if the waveforms are not correlated) or (7.24) (if they are correlated). In the former case

$$SNR_Z^I = \frac{\mu_Z - \mu_Z|_{P=0}}{\sigma_Z} = \sqrt{M} SNR_Y^I, \tag{7.46a}$$

$$SNR_Z^{II} = \frac{\mu_Z}{\sigma_Z} = \sqrt{M} SNR_Y^{II}. \tag{7.46b}$$

In the latter case

$$SNR_Z^I = \frac{\sqrt{M}}{\sqrt{\hat{\rho}(M-1)+1}} SNR_Y^I, \tag{7.47a}$$

$$SNR_Z^{II} = \frac{\sqrt{M}}{\sqrt{\hat{\rho}(M-1)+1}} SNR_Y^{II}. \tag{7.47b}$$

The term $\frac{M}{\hat{\rho}(M-1)+1}$ was actually named *effective* incoherent averaging term in [195].

7.6 Conclusions

In this chapter, the stochastic characterization of the amplitude, phase, magnitude, power and averaged power of the waveform peak and of the noise samples has been studied in detail. This is of special utility in simulators, when aiming to studying the impact of the noise at each observable.

The generic expressions of the coherent, non-coherent and non-coherent averaged SNRs have been obtained. In this generic form, the variance of the amplitude components of the sampled signal are not necessary equal, as happens when the ADC has a low number of levels. Using a 2-levels ADC reduces the coherent SNR for about 2 dB if the analog SNR is low (as it is typically the case). For high analog SNRs, the 2-levels ADC losses the sensitivity to changes in the analog signal power and phase, and noise power. Under these cases, an ADC with a larger number of levels may be used.

Finally, this chapter has also studied the ability to detect the waveform peak from the noise floor by using their stochastic properties. Results show that the peak can be detected even if the coherent SNR is very low if a large number of incoherent averages are performed, at expense of reducing the temporal and spatial resolution of the observations.

8

Chapter 8

Design Considerations for Real-time GNSS-R Back-end Receivers

This chapter first describes hardware architectures to create GNSS signals and real-time correlators in FPGA and in Graphics Processing Unit (GPU) devices. The impact of the sampling frequency, Fast Fourier Transform (FFT) quantification errors and of other configuration parameters on the cross-correlations is also analyzed. Finally, tracking considerations in ground, airborne and space-borne scenarios is investigated for the cGNSS-R and iGNSS-R techniques.

Some of the work presented here has been published in [198–200] and in the BSc. thesis [201].

8.1 Introduction

This chapter arises from the need to create real-time correlators for the GNSS signals in FPGAs to be used in the MIR instrument (see Chapter 9). To do so, a way to efficiently generate the GNSS signals was obtained, and different real-time cross-correlation architectures were investigated as well, even leading a to method to obtain sample-to-sample correlations. The impact of the secondary codes on the correlation is given here as well.

The actual version of the MIR instrument does not compute real-time correlations, but stores the raw data. The DDMs are obtained a posteriori with GPU platforms. However, as it will be shown, these platforms also allow real-time processing, with the advantage that they are more versatile and easier to program than the FPGAs.

8.2 GNSS signals generation in FPGAs

This section explains the generation of the GNSS signals intended to be used in the MIR instrument. They are the GPS L1 C/A and L5, and Galileo E1OS and E5.

8.2.1 Primary codes

The generation of the primary codes (typically referred as PRN) was given in Section 2.4.1. The codes used in the GPS L1 C/A and L5 and in the Galileo E5 signals can be generated with LFSRs. However, the Galileo E1OS codes are memory codes that can only be previously saved in the internal memories of the FPGA. Figure 8.1 shows the block diagram of a generic LFSR, and Appendix D gives a code implementation. Note that this structure assumes that the clock rate is a multiple of the fundamental PRN rate.

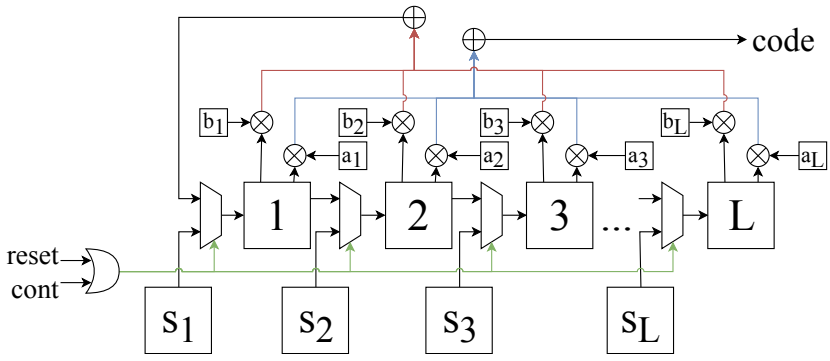

Figure 8.1: Block diagram for a generic LFSR with L registers. b_i are the *taps* used to update the value of the first register, a_i are the taps used to generate a new output, and s_i are the *seed* or initial state of the registers. The LFSR may be restarted before its natural end with the counter *cont*.

Table 8.1: Phase look-up table to generate a E5 signal as $x_{E5}(t) = exp(jk(t)\pi/4)$.

		-1	**-1**	**-1**	**-1**	**-1**	**-1**	**-1**	**-1**	**1**	**1**	**1**	**1**	**1**	**1**	**1**	**1**	**E5aI**
		-1	**-1**	**-1**	**-1**	**1**	**1**	**1**	**1**	**-1**	**-1**	**-1**	**-1**	**1**	**1**	**1**	**1**	**E5bI**
		-1	**-1**	**1**	**1**	**-1**	**-1**	**1**	**1**	**-1**	**-1**	**1**	**1**	**-1**	**-1**	**1**	**1**	**E5aQ**
		-1	**1**	**-1**	**1**	**-1**	**1**	**-1**	**1**	**-1**	**1**	**-1**	**1**	**-1**	**1**	**-1**	**1**	**E5bQ**
t	**0**	5	4	4	3	6	3	1	2	6	5	7	2	7	8	8	1	
	1	5	4	8	3	2	3	1	2	6	5	7	6	7	4	8	1	
	2	1	4	8	7	2	3	1	2	6	5	7	6	3	4	8	5	
	3	1	8	8	7	2	3	1	6	2	5	7	6	3	4	4	5	
	4	1	8	8	7	2	7	5	6	2	1	3	6	3	4	4	5	
	5	1	8	4	7	6	7	5	6	2	1	3	2	3	8	4	5	
	6	5	8	4	3	6	7	5	6	2	1	3	2	7	8	4	1	
	7	5	4	4	3	6	7	5	2	6	1	3	2	7	8	8	1	

8.2.2 BOC signals

The BOC signals were explained in Section 2.5. The block diagrams given there could be implemented, however there are easier approaches based on phase LookUp Tables (LUTs). In fact, the Galileo ICD [15] already suggests implementing the Galileo E5 signal with the LUT given in Table 8.1. The top 4 rows show the value of the 16 possible combinations of the 4 primary codes, generated with a rate of $10 \cdot 1.023 = 10.23$ MHz. The t-sequence circularly shifts from 0 to 7 with a rate of $120 \cdot 1.023 = 122.76$ MHz and must be synchronized with the primary codes. At each instant, the value of the internal matrix is the phase $k(t)$ in $x(t) = \exp(jk(t)\pi/4)$.

An equivalent table for the E1OS signal is not given in the ICD, but it can be easily obtained using (2.14). The amplitude evolution is given in Table 8.2. In this case, the rate of the primary codes is 1.023 MHz, and the rate of the t -sequence is $12 \cdot 1.023 = 12.276$ MHz. As given in (2.12), the E1OS signal may be considered as a complex signal. In this case, the amplitude evolution is as given in Table 8.3.

In the above tables, it is assumed that the rate of the t-sequence is its nominal one. In other words, it moves one step at each period. If other sampling rates are desired (either smaller or larger), the t-sequence would have to *jump* across its domain. The generation of the t-sequence for rates multiple of 1.023 MHz can be obtained as follows.

The involved parameters are:

- N: Desired sampling frequency in multiples of 1.023 MHz.
- M: Fundamental frequency of the modulation in multiples of 1.023 MHz. This is 120 for E5 signal and 12 for E1OS signal.

- X: Fundamental frequency of the PRNs in multiples of 1.023 MHz. This is 10 for E5 signal and 1 for E1OS signal.
- L_x: Length of the PRN in PRN chips. This is 10230 for the E5 signal and 4092 for E1OS signal.
- L_0: Length of the fundamental t-sequence in t-sequence chips. This is 8 for E5 signal and 12 for E1OS signal.
- L_M: Length of the sampled t-sequence in samples.
- L_N: Length of the sampled t-sequence in t-sequence sampled chips.
- TT: Number of un-sampled PRN chips required to synchronize the PRN signal and the t-sequence.
- PP: Number of sampled t-sequences required to synchronize the PRN signal and the t-sequence.
- TTT: Number of un-sampled PRN chips required to synchronize the PRN chips and the t-sequence chips
- PPP: Number of sampled t-sequence chips required to synchronize the PRN chips and the sampled t-sequence chips.

The M/N is the ratio between the fundamental rate and the desired one. Its irreducible fraction T/P can be found as

$$T = \frac{M}{\gcd(M,N)}, \tag{8.1a}$$

$$P = \frac{N}{\gcd(M,N)}, \tag{8.1b}$$

Table 8.2: Look-up table to generate a E1OS signal assuming is real. Where $\alpha = \sqrt{10/11} + \sqrt{1/11}$ and $\beta = \sqrt{10/11} - \sqrt{1/11}$.

		1	**1**	**-1**	**-1**	**E1B**
		1	**-1**	**1**	**-1**	**E1C**
t	**0**	2β	2α	-2α	-2β	
	1	-2β	2α	-2α	2β	
	2	2β	2α	-2α	-2β	
	3	-2β	2α	-2α	2β	
	4	2β	2α	-2α	-2β	
	5	-2β	2α	-2α	2β	
	6	2β	-2α	2α	-2β	
	7	-2β	-2α	2α	2β	
	8	2β	-2α	2α	-2β	
	9	-2β	-2α	2α	2β	
	10	2β	-2α	2α	-2β	
	11	-2β	-2α	2α	2β	

Table 8.3: Look-up table to generate a E1OS signal assuming is complex. Where $\alpha = \sqrt{10/11} + \sqrt{1/11}$ and $\beta = \sqrt{10/11} - \sqrt{1/11}$.

		1		**1**		**-1**		**-1**		**E1B**
		1		**-1**		**1**		**-1**		**E1C**
		Real	Imag	Real	Imag	Real	Imag	Real	Imag	
t	**0**	$(\alpha+\beta)$	$-(\alpha-\beta)$	$(\alpha+\beta)$	$(\alpha-\beta)$	$-(\alpha+\beta)$	$-(\alpha-\beta)$	$-(\alpha+\beta)$	$(\alpha-\beta)$	
	1	$(\alpha-\beta)$	$-(\alpha+\beta)$	$(\alpha-\beta)$	$(\alpha+\beta)$	$-(\alpha-\beta)$	$-(\alpha+\beta)$	$-(\alpha-\beta)$	$(\alpha+\beta)$	
	2	$(\alpha+\beta)$	$-(\alpha-\beta)$	$(\alpha+\beta)$	$(\alpha-\beta)$	$-(\alpha+\beta)$	$-(\alpha-\beta)$	$-(\alpha+\beta)$	$(\alpha-\beta)$	
	3	$(\alpha-\beta)$	$-(\alpha+\beta)$	$(\alpha-\beta)$	$(\alpha+\beta)$	$-(\alpha-\beta)$	$-(\alpha+\beta)$	$-(\alpha-\beta)$	$(\alpha+\beta)$	
	4	$(\alpha+\beta)$	$-(\alpha-\beta)$	$(\alpha+\beta)$	$(\alpha-\beta)$	$-(\alpha+\beta)$	$-(\alpha-\beta)$	$-(\alpha+\beta)$	$(\alpha-\beta)$	
	5	$(\alpha-\beta)$	$-(\alpha+\beta)$	$(\alpha-\beta)$	$(\alpha+\beta)$	$-(\alpha-\beta)$	$-(\alpha+\beta)$	$-(\alpha-\beta)$	$(\alpha+\beta)$	
	6	$-(\alpha-\beta)$	$(\alpha+\beta)$	$-(\alpha-\beta)$	$-(\alpha+\beta)$	$(\alpha-\beta)$	$(\alpha+\beta)$	$(\alpha-\beta)$	$-(\alpha+\beta)$	
	7	$-(\alpha+\beta)$	$(\alpha-\beta)$	$-(\alpha+\beta)$	$-(\alpha-\beta)$	$(\alpha+\beta)$	$(\alpha-\beta)$	$(\alpha+\beta)$	$-(\alpha-\beta)$	
	8	$-(\alpha-\beta)$	$(\alpha+\beta)$	$-(\alpha-\beta)$	$-(\alpha+\beta)$	$(\alpha-\beta)$	$(\alpha+\beta)$	$(\alpha-\beta)$	$-(\alpha+\beta)$	
	9	$-(\alpha+\beta)$	$(\alpha-\beta)$	$-(\alpha+\beta)$	$-(\alpha-\beta)$	$(\alpha+\beta)$	$(\alpha-\beta)$	$(\alpha+\beta)$	$-(\alpha-\beta)$	
	10	$-(\alpha-\beta)$	$(\alpha+\beta)$	$-(\alpha-\beta)$	$-(\alpha+\beta)$	$(\alpha-\beta)$	$(\alpha+\beta)$	$(\alpha-\beta)$	$-(\alpha+\beta)$	
	11	$-(\alpha+\beta)$	$(\alpha-\beta)$	$-(\alpha+\beta)$	$-(\alpha-\beta)$	$(\alpha+\beta)$	$(\alpha-\beta)$	$(\alpha+\beta)$	$-(\alpha-\beta)$	

where $\gcd(M, N)$ is the greatest common divisor between M and N. The length of the sampled t-sequence in sample units is

$$L_M = \mathrm{lcm}(T, L_0), \tag{8.2}$$

where $\mathrm{lcm}(T, L_0)$ is the least common multiple between T and L_0. Equivalently, the same length can be expressed in units of sampled t-sequence chips as

$$L_N = L_M \frac{P}{T}. \tag{8.3}$$

Finally, the sampled t-sequence can be computed as

$$t(indx) = \mathrm{mod}(\lfloor \frac{M}{N} \cdot i \rfloor, L_0) \quad indx = 0, 1, ..., L_N - 1 \tag{8.4}$$

where *mod* is the modulus operator. This new sequence can in turn be saved in a LUT of length L_N and read at the desired sampling frequency N. The output is then fed to the LUTs in Tables 8.1, 8.2 or 8.3. Note that the equation above holds for $N \geq 1$ in the E1OS sampled signals, and for $N \geq 10$ in the E5 sampled signals, as their respective PRNs have to be generated at their nominal rate. The sampled t-sequence of the E1OS signal for different sampling rates is given in Table 8.4. For the E5 signal, it is given in the second column of Table 8.5.

In the t-sequence given in (8.4) it is assumed that the sequence starts synchronized with the PRNs. However, the rate of the sequence is larger (or equal) to the rate of the PRN. This means that during the duration of one PRN, the t-sequence may change. It

Table 8.4: Generation of the E1 t-sequence with different sampling rates.

N	t-sequence
2	0 6
4	0 3 6 9
6	0 2 4 6 8 10
8	0 1 3 4 6 7 9 10
10	0 1 2 3 4 6 7 8 9 10
12	0 1 2 3 4 5 6 7 8 9 10 11
14	0 0 1 2 3 4 5 6 6 7 8 9 10 11
16	0 0 1 2 3 3 4 5 6 6 7 8 9 9 10 11
18	0 0 1 2 2 3 4 4 5 6 6 7 8 8 9 10 10 11
20	0 0 1 1 2 3 3 4 4 5 6 6 7 7 8 9 9 10 10 11
22	0 0 1 1 2 2 3 3 4 4 5 6 6 7 7 8 8 9 9 10 10 11
24	0 0 1 1 2 2 3 3 4 4 5 5 6 6 7 7 8 8 9 9 10 10 11 11
26	0 0 0 1 1 2 2 3 3 4 4 5 5 6 6 6 7 7 8 8 9 9 10 10 11 11
28	0 0 0 1 1 2 2 3 3 3 4 4 5 5 6 6 6 7 7 8 8 9 9 9 10 10 11 11
30	0 0 0 1 1 2 2 2 3 3 4 4 4 5 5 6 6 6 7 7 8 8 8 9 9 10 10 10 11 11
32	0 0 0 1 1 1 2 2 3 3 3 4 4 4 5 5 6 6 6 7 7 7 8 8 9 9 9 10 10 10 11 11

is then important to be able to synchronize both signals. This is in fact necessary when generating the PRN not from the origin, but from a given chip, as it may be done in the tracking system.

This synchronization between the t-sequence and the PRNs for the E1OS and E5 signals is shown in Figs. 8.2a and 8.2b respectively. The top row indicates the PRN index (0 to 4091 for E1OS and 0 to 10229 for E5). The rows below indicate the index of the t-sequence for different sampling rates. Note that in the E1OS signal, there is a complete t-sequence in each PRN chip, despite the sampling frequency. This means that the t-sequence is generated always from the origin for any PRN chip and sampling frequency. However this is not the case in the E5 signal. For example, the t-sequence and the PRN signal are synchronized every 2 PRN chips or 3 t-sequences if the sampling frequency is $120 \cdot 1.023$ MHz, and every 10 PRN chips or 1 t-sequence if the sampling frequency is $32 \cdot 1.023$ MHz. Results for other sampling frequencies are summarized in columns 5 and 7 of Table 8.5. Both numbers are found as

$$TT = X/gcd(M/L_M, X), \tag{8.5a}$$

$$PP = M/(L_M \cdot gcd(M/L_M, X)), \tag{8.5b}$$

The latter paragraph described the synchronization between the t-sequence and the PRN chips. In order to generate the t-sequence is also necessary to study the synchro-

Table 8.5: Generation of the E5 t-sequence with different sampling rates.

		t-seq. length		t-seq. sync			t-seq. chip sync		
N	**t-sequence**	**chips**	**#PRN**	**#t**	**chips**	**#PRN**	**chips**	**#PRN**	**index**
10	0 4	2	2	1	2	2	1	1	0 1
15	0	1	2/3	3	3	2	3	2	0
20	0 6 4 2	4	2	1	4	2	2	1	0 2
24	0 5 2 7 4 1 6 3	8	10/3	3	24	10	12	5	0 4
30	0 4	2	2/3	3	6	2	3	1	0 1
32	0 3 7 3 7 2 6 2 6 1 5 1 5 0 4 0 4 7 3 7 3 6 2 6 2 5 1 5 1 4 0 4	32	10	1	32	10	16	5	0 16
40	0 3 6 1 4 7 2 5	8	2	1	8	2	4	1	0 4
50	0 2 4 7 1 4 6 0 3 5	10	2	1	10	2	5	1	0 5
60	0 2 4 6	4	2/3	3	12	2	6	1	0 2
70	0 1 3 5 6 0 2 4 5 7 1 2 4 6	14	2	1	14	2	7	1	0 7
80	0 1 3 4 6 7 1 2 4 5 7 0 2 3 5 6	16	2	1	16	2	8	1	0 8
90	0 1 2 4 5 6	6	2/3	3	18	2	9	1	0 3
100	0 1 2 3 4 6 7 0 1 2 4 5 6 7 0 2 3 4 5 6	20	2	1	20	2	10	1	0 10
110	0 1 2 3 4 5 6 7 0 1 2 4 5 6 7 0 1 2 3 4 5 6	22	2	1	22	2	11	1	0 11
120	0 1 2 3 4 5 6 7	8	2/3	3	24	2	12	1	0 4

nization between the t-sequence chips and the PRN chips. For example, if a sampling frequency of $32 \cdot 1.023$ MHz is used, there are 16 t-sequence chips in 5 PRN chips. The ratios for other sampling frequencies are summarized in columns 8 and 9 of Table 8.5. They can be found as

$$PPP = N/gcd(N, X) \tag{8.6a}$$

$$TTT = X/gcd(N, X) \tag{8.6b}$$

Finally, the *indx*-sequence, that is, the sequence that describes the position of the index of the t-sequence as function of the PRN chip, is given in the last column of Table 8.5. As an example, if the sampling rate is $32 \cdot 1.023$ MHz, the index 0 in the t-sequence corresponds also to 0, while the index 16 corresponds to 4. The index sequence is described as

$$\begin{aligned} indx(0) &= 0 \\ indx(1) &= L_N/2. \end{aligned} \tag{8.7}$$

A word of caution should be given regarding the theory developed here. Sampling the GNSS signals at a multiple of 1.023 MHz (the so-called commensurate sampling) can lead to a loss of the DLL tracking the correlation peak (e.g. [202]). However, many commercial GNSS receivers, such as LabSat [203], use a commensurate sampling frequency. Nevertheless, this issue is believed not to have an impact here, as such type of tracking is not used.

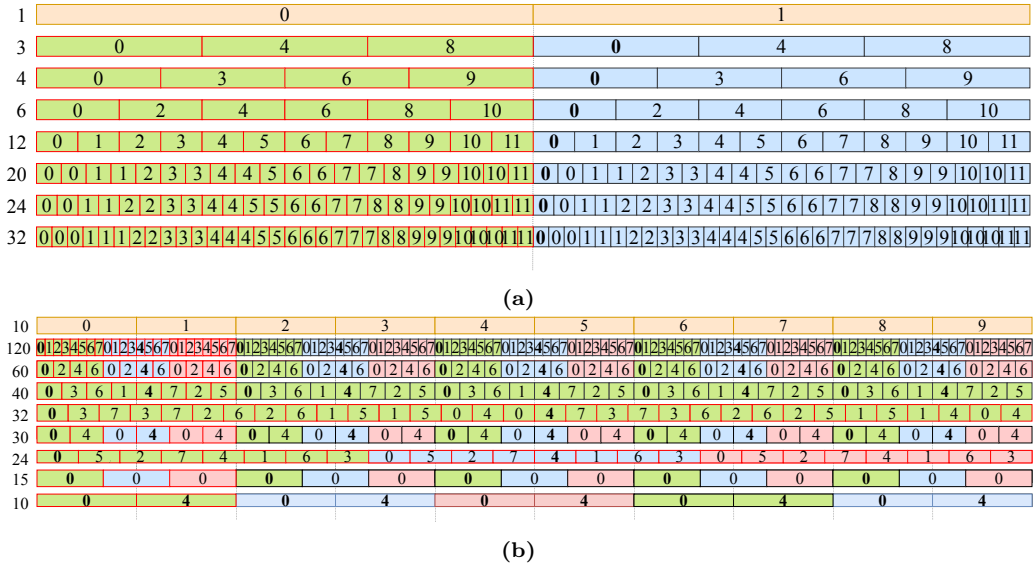

Figure 8.2: Synchronization between the (a) E1OS and (b) E5 t-sequence sampled at different rates with their respective PRNs running at their fundamental rates (1.023 MHz and 10.23 MHz respectively). Numbers indicate indexes of the unsampled t-sequence. Colors indicate a full t-sequence. Red boxes indicate synchronicity between the sampled t-sequence and the PRN chips. Bold indexes indicate synchronicity between the sampled t-sequence chips and PRN chips.

8.2.3 Impact of the quantization and sampling

The impact of quanitzation on the Galileo E1OS and E5 ACF is shown in Fig. 8.3. The signals are quantified using a different number of bits, but with integer values. Although both the E1OS and E5 signals have 4 and 5 levels respectively (E5 contains the 0 level), 2 or 3 bits will still produce distortion because the relationship between the levels is not an integer number (see Section 2.5). Nevertheless, the distortion observed in the ACF is small. Using two levels may be a good trade off to relax hardware complexity.

The impact of sampling frequency is given in Fig. 8.4. A sampling frequency of 2.046 MHz for the E1OS signal and of 30.69 MHz for the E5 signal produces an ACF similar to the ideal one, as most of the power is concentrated around these frequencies. Still, there is an additional power reduction not shown in the figures, and thus the range precision may be reduced if the sampling frequency is not large enough. At the same time, enlarging the sampling frequency also introduces more noise, which eventually leads to a degradation in the range precision. This latter issue was studied in Chapter 5.

8.2.4 Impact of the secondary codes

The secondary codes allow the use of longer coherent integration time while allowing at the same time the use of the original code length. Their lengths are 20 ms (L5) and

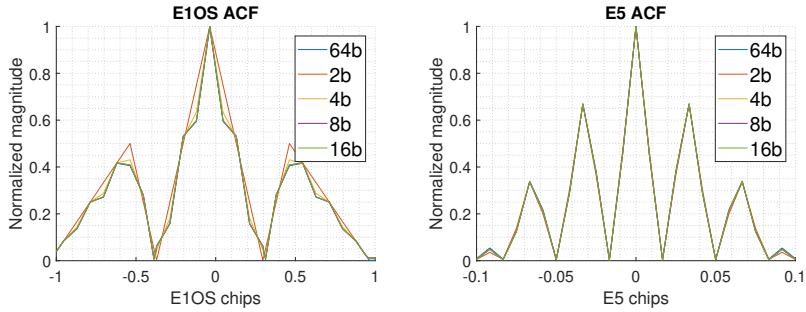

Figure 8.3: Impact of quantization on the ACF of Galileo E1OS (left) and E5 (right) signals using different number of bits.

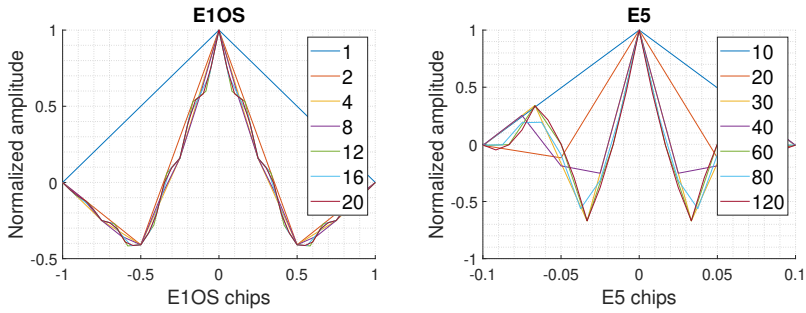

Figure 8.4: Impact of sampling frequency on Galileo E1OS (left) and E5 (right) signals. The rates shown in the legends are in multiples of 1.023 MHz.

100 ms (E1OS and E5) (see Section 2.4.2). In order to give context to the reader, the work in [69] showed a coherence time below 5 ms in open ocean. However, in shore calm waters, the coherence time can be as large as 200 ms [70]. Similar values were obtained in Chapter 10.

The secondary codes require a more complex acquisition and tracking techniques. A typical approach to synchronizing with the secondary codes is by using the circular correlation with an FFT length twice the period of the primary code. The second half of the FFT of reference signal is padded with zeros. By doing this, one of the two peaks of the resulting ACF is not affected by the secondary code.

The impact of not synchronizing with the secondary codes, is similar to not doing so with the data bits transitions. However, the rate of the secondary codes is much larger than the data rate. The effects on the ACF are peak power variability and Doppler artifacts (see for example Fig. 10.5). The peak position is not affected. The impact on the ACF peak magnitude is shown in Fig. 8.5, and on the phase in the left column of Fig. 8.5. The magnitude impact is studied at each coherent peak (X axis) and at different delays (Y axis). The peak power is maximum when either the sequences are perfectly

aligned, or when the secondary codes are in such a way that they produce a constructive correlation. In the opposite case, when each peak is added destructively, the peak power deceases to zero. The phase is affected with errors multiple of 90°.

It is also interesting to study the impact of the secondary codes on the incoherent peak power. This is shown in the right column of Fig. 8.5. The average peak power is similar to the coherent one: 0.45 (L5), 0.6 (E1OS), and 0.27 (E5), however the standard deviation has considerably decreased (by ≈100).

8.3 Linear correlation

The linear cross-correlation between the sampled signals $x[n]$ and $y[n]$ is given by

$$R_{xy}[m] = \frac{1}{N}\sum_{n=0}^{N-1} x[n]\, y^*[n+m], \tag{8.8}$$

where N is the correlation length in number of samples. This equation produces one correlation value every N samples. However, over high dynamic surfaces, it may be interesting to analyze overlapped cross-correlations [62]. For example, this information could be used to study the speckle noise. The time evolution of the cross-correlation can be expressed as

$$R_{xy}[m,k] = \frac{1}{N}\sum_{n=k}^{k+N-1} x[n]\, y^*[n+m], \tag{8.9}$$

where k is the index of the first sample from which the correlation is computed. By changing the index k to $k+1$, one can obtain

$$\begin{aligned} R_{xy}[m,k+1] &= \frac{1}{N}\sum_{n=k+1}^{k+N} x[n]\, y^*[n+m] \\ &= R_{xy}[m,k] + \frac{1}{N}x[k+N]\, y^*[k+N+m] - \frac{1}{N}x[k]\, y^*[k+m]. \end{aligned} \tag{8.10}$$

This equation is important because it allows the calculation of a new cross-correlation value every sample instead of every N samples, by using two additional complex products and one additional complex addition. This correlator was named as sample-to-sample correlator in [62], but to author's knowledge, this is the first time that it is simplified in such a way that it can be efficiently implemented in real-time instruments. The added value of such correlator depends on the user's need to characterize the time-dynamics of the surface under study, but is strongly limited by the bandwidth of the transmission system with the host computer, and by the hard disk space of the latter. A simple counter can be used to save the results at a specific rate rather than for every sample.

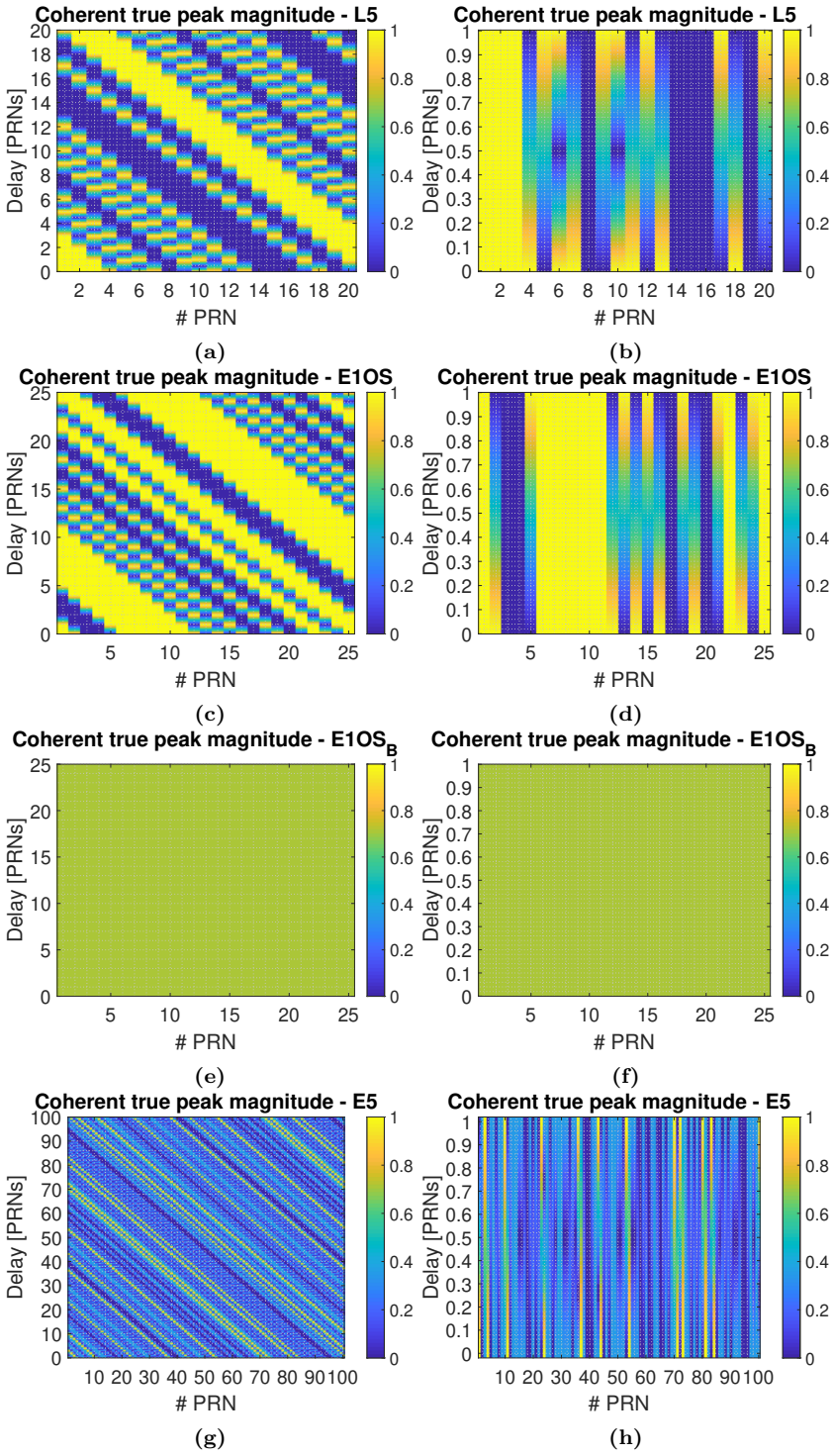

Figure 8.5: Impact of non-removed secondary codes on ACF peak magnitude. Second column shows a zoom of the first one for small delays

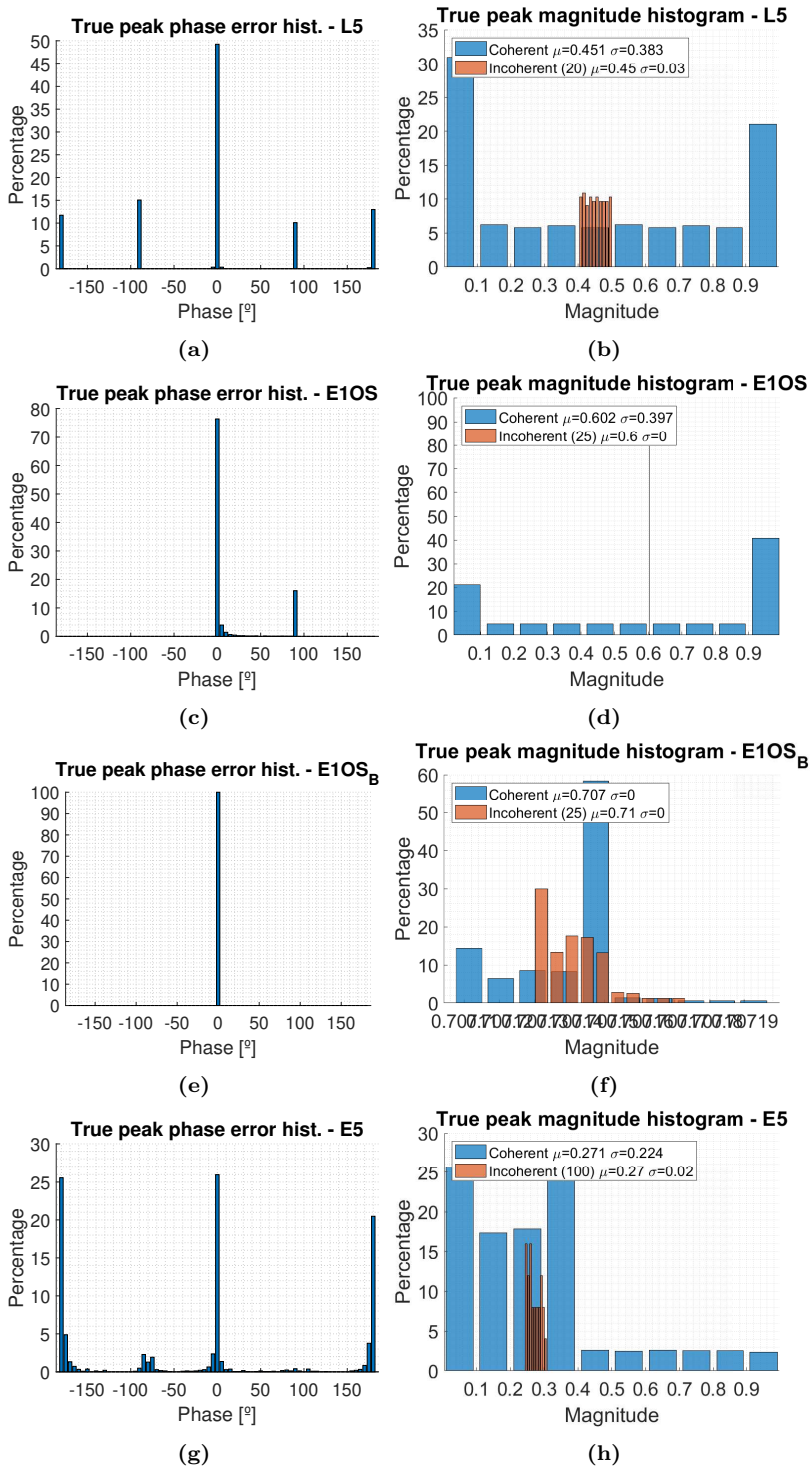

Figure 8.6: Impact of non-removed secondary codes on ACF true peak phase.

In the conventional case, and if N is a multiple of the clean replica (namely $y[n]$) period, the sample-to-sample correlation can be further simplified to

$$\begin{aligned} R_{xy}[m, k+1] &= \frac{1}{N} \sum_{n=k+1}^{k+N} x[n]\, y^*[n+m] \\ &= R_{xy}[m, k] + \frac{1}{N} \left(x[k+N] - x[k]\right) y^*\left[mod\left(k+m, N\right)\right], \end{aligned} \tag{8.11}$$

where *mod* is the modulus operator. This correlator requires only one additional complex product and one additional complex addition.

A typical GNSS receiver performs the linear cross-correlation at only three delay lags, namely early, prompt and late. The prompt gate follows the peak, while the other two are used to estimate the error between the prompt and the true delay of the incoming signal. This error is then used to adjust the position of the three correlators. In GNSS-R, much more lags are needed because the reflected signal is spread in the time and in the Doppler domains. However, the lags can be unequally spaced in order to reduce the hardware, software and transmission bandwidth resources. As an example, there may be several lags around the peak with a spacing between them equal to the original sampling period. Additional lags could be placed at larger delays and Dopplers but with a distance between them just large enough so that the DDM or waveform trailing edge can be fitted a posteriori.

8.3.1 Implementation in FPGAs

Examples of implementation of GNSS signals correlators in FPGAs can be found in the literature (e.g. [204–206]). However, the actual implementation depends on the instrument needs and is highly conditioned to the FPGA resources. Some approaches and general context are given here, together with an implementation of the sample-to-sample correlator described above.

Before going into detail, it is worth giving first a brief comment about the type of resources that an FPGA has. Broadly speaking, there are 4 types of resources. Slice registers (also known as Flip-Flop registers), LUTs, RAM memories and DSP objects. A slice register is a single-bit memory cell used to hold a state. A LUT is an entity that combines several inputs using logic gates to create one or more outputs. RAM memories typically come with a given finite size (16kb/18kb/36kb,...), but their width and bit depth can be adjusted. Finally, a DSP block is an Arithmetic Logic Unit (ALU), which is able to add, substract, and multiply up to three inputs. The slice registers and the LUTs are referred to as *fabric* elements.

Table 8.6: Available resources of the Xilinx FPGA xc7k410t-2ffg900 (USRP X310) before and after the Ettus utilization.

	Available	**Available after Ettus 3.8.5**
Slice Registers	508,400	447,577
Slice LUTs	254,200	191,764
RAMB36E1	795	391
RAMB18E1	1,590	1,574
DSP48E1s	1,540	1,453

Table 8.7: Available resources of the Xilinx FPGA xc3sd3400 (USRP N210) before and after the Ettus utilization.

	Available	**Available after Ettus 3.8.5**
Slice Flip Flops	47,744	27,735
4 input LUTs	47,744	15,252
RAMB16BWERs	126	85
DSP48As	126	95

The routines that the FPGA has to perform, are usually *described* with either VHSIC Hardware Description Language (VHDL) or Verilog. The conversion from the behavioral description to the actual implementation in the FPGA with the aforementioned entities, is done by optimizing the number of resources, while guaranteeing that the clock signal arrives synchronously to all of them. Some operations can be either done with the fabric objects, while others can only be implemented with DSPs. For illustration purposes, Tables 8.6 and 8.7 show the available resources of the two FPGA devices used in the MIR instrument (see Chapter 9). The former is a Xilinx Kintex7-410T used to process the GNSS signals. The latter is a much simpler FPGA, the Xilinx Spartan 3A-DSP 3400, used to generate the calibration signal of the instrument. The final user available resources are a little bit more reduced because of the original circuity implemented in the USRPs (in the tables, for the code version 3.8.5).

The FPGA developer can make use of the so-called Intellectual Property (IP) cores, which are licensed reusable units of logic that can be configured. The resources used for the most common IP cores are given in the Tables 8.8, 8.9, 8.10, and 8.11. These numbers will be used as an estimation of the resources needed to implement the correlations, although as stated, the actual number is the result of an optimization process that takes into account the overall program.

In the linear correlation given in (8.8), there are N complex products and N complex additions for each delay lag. This means 4 real products and $2N$ real additions. Needless to say that implement the correlation in parallel would unnecessarily overuse all the available resources. The proper way to address this is by using an structure similar to the one in Fig. 8.7a. This block can be implemented with 4 Real Signed Multiplier+Accumulator

Table 8.8: Resource utilization for Xilinx Real Signed Multiplier IP for different input (A,B) widths with a Kintex7-410T.

	Fabric					**DSP**			
A	**2**	**4**	**8**	**16**	**32**	**4**	**8**	**16**	**32**
B	**2**	**4**	**8**	**16**	**32**	**4**	**8**	**16**	**32**
Slice Registers	4	8	16	32	64	0	0	0	34
Slice LUTs	4	18	72	281	1,093	0	0	0	6
RAMB36E1	0	0	0	0	0	0	0	0	0
RAMB18E1	0	0	0	0	0	0	0	0	0
DSP48E1s	0	0	0	0	0	1	1	1	4

Table 8.9: Resource utilization for Xilinx Complex Signed Multiplier IP for different input (A,B) widths with a Kintex7-410T.

	Fabric			**DSP**		
A	**8**	**16**	**32**	**8**	**16**	**32**
B	**8**	**16**	**32**	**8**	**16**	**32**
Slice Registers	330	1,079	3,693	32	64	458
Slice LUTs	382	1,179	4,009	36	72	355
RAMB36E1	0	0	0	0	0	0
RAMB18E1	0	0	0	0	0	0
DSP48E1s	0	0	0	3	3	12

cores (Table 8.11) and 2 Real Signed Adders (Table 8.10). The former IP core uses at least one DSP object. This means that a single delay gate will use 4 DSP objects. This would be reasonable if few delay gates were to be computed, for example the early, prompt and late gates mentioned before. However, using these IP cores to compute a full DDM may not be feasible. There are 1543 available DSP objects in the USRP X310 (Table 8.6). This represents that 363 correlators would have to be shared between all the delay lags and Doppler bins, and for the direct and reflected signals (and eventually the intefero-metric as well). The same correlator can be *reused* if the ratio between the data rate and the clock is large enough. This is in fact a typical strategy done in FPGA programming. However, it also requires complex synchronization mechanisms.

The resources used in the last architecture can be drastically reduced if 2-level signals are used. As shown in Fig. 8.7b, the reference signal can be used as the control signal of the accumulator to add or subtract the incoming signal with the accumulated previous value. This is the strategy done in the griPAU instrument [95]. This architecture can be used with the GPS L1 and L5 signals, as they have only two values (i.e ± 1). However, as shown in last section, it could be also used for the Galileo E1OS and E5 signals with a little loss of power. The resources required for the accumulator can be further reduced if the received signal is also quantified with two levels. This is in fact the approach followed by most GNSS receivers. The impact of this was found to be a reduction of the

Table 8.10: Resource utilization for Xilinx Real Adder IP for different input (A,B) widths with a Kintex7-410T.

	Signed																
	Fabric									**DSP**							
A	**2**	**2**	**2**	**2**	**2**	**4**	**8**	**16**	**32**	**2**	**2**	**2**	**2**	**2**	**4**	**8**	**16**	**32**
B	**2**	**4**	**8**	**16**	**32**	**4**	**8**	**16**	**32**	**2**	**4**	**8**	**16**	**32**	**4**	**8**	**16**	**32**
Slice Registers	3	5	9	17	33	5	9	17	33	0	0	0	0	0	0	0	0	0
Slice LUTs	3	5	9	17	33	5	9	17	33	0	0	0	0	0	0	0	0	0
RAMB36E1	0	0	0	0	0	0	0	0	0	0	0	0	0	0	0	0	0	0
RAMB18E1	0	0	0	0	0	0	0	0	0	0	0	0	0	0	0	0	0	0
DSP48E1s	0	0	0	0	0	0	0	0	0	1	1	1	1	1	1	1	1	1
	Unsigned																
	Fabric									**DSP**							
A	**2**	**2**	**2**	**2**	**2**	**4**	**8**	**16**	**32**	**2**	**2**	**2**	**2**	**2**	**4**	**8**	**16**	**32**
B	**2**	**4**	**8**	**16**	**32**	**4**	**8**	**16**	**32**	**2**	**4**	**8**	**16**	**32**	**4**	**8**	**16**	**32**
Slice Registers	3	5	9	17	33	5	9	17	33	0	0	0	0	0	0	0	0	0
Slice LUTs	3	5	9	17	33	5	9	17	33	0	0	0	0	0	0	0	0	0
RAMB36E1	0	0	0	0	0	0	0	0	0	0	0	0	0	0	0	0	0	0
RAMB18E1	0	0	0	0	0	0	0	0	0	0	0	0	0	0	0	0	0	0
DSP48E1s	0	0	0	0	0	0	0	0	0	1	1	1	1	1	1	1	1	1

Table 8.11: Resource utilization for Xilinx Real Signed Multiplier+Accumulator IP for different input (A,B,C) widths with a Kintex7-410T.

A	**2**	**2**	**2**	**2**	**2**	**4**	**8**	**16**	**32**
B	**2**	**4**	**8**	**16**	**32**	**4**	**8**	**16**	**32**
C	**2**	**4**	**8**	**16**	**32**	**4**	**8**	**16**	**32**
Slice Registers	0	0	0	0	17	0	0	0	242
Slice LUTs	0	0	0	0	1	0	0	0	224
RAMB36E1	0	0	0	0	0	0	0	0	0
RAMB18E1	0	0	0	0	0	0	0	0	0
DSP48E1s	1	1	1	1	3	1	1	1	4

SNR of about 3 dB (see Chapter 7). This block can be implemented either with DSP objects, or with few fabric elements. A signal quantized with 2 bits, sampled at 32.736 MSps and correlated during 1 ms, would require an accumulator able to store up to 16 bits. These represents only around 20-30 LUTs and slice registers, meaning that up to $\approx$ 15k correlators could be implemented. Obviously, this number would be reduced, as the resources would be used for other tasks, but it gives an idea on the efficiency of this architecture.

Figure 8.8a shows the architecture for the sample-to-sample correlator given in (8.11). The core correlator can be any of the two described above, but it also requires a First In First Out (FIFO) entity (implemented with a RAM memory block) and a complex signed addition (using 2 Real Signed Adders). In this architecture, the accumulator does not

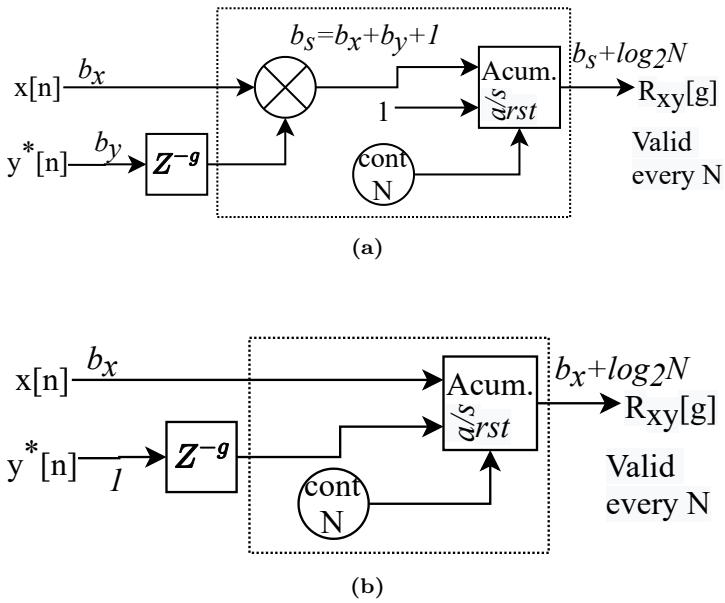

Figure 8.7: Implementation of linear correlators in FPGAs (only one delay gate): (a) classic, (b) one of the signals is quantified with 1 bit.

have to be restarted. However, an overflow control mechanism must be implemented.

Finally, Fig. 8.8b shows the implementation of the iGNSS-R sample-to-sample correlator in (8.10). This structure uses an additional FIFO with respect to the cGNSS-R case.

During the correlation process, the number of bits per value has increased with respect to the original bits per sample. Additionally, the data rate has also changed. In the classic correlators, the average data rate has changed by $f_s' = f_s \cdot L/N$, where L is the total number of delay lags and Doppler bins. In the sample-to-sample correlators, the data rate has changed by $f_s' = f_s \cdot L/R$, where $R \leq N$ is the number of saved correlation values. The combination of the new bit depth and the data rate may not be supported by either the transmission channel bandwidth or by the host hard drive storage. Several strategies can be used in order to decrease the number of bits. They are truncation, different rounding modes, and scaling.

- Truncation drops the Least Significant Bits (LSBs). Rounding modes include rounding towards the nearest higher integer, towards the nearest smaller integer, towards zero, away from zero, towards positive infinitive, towards negative infinite or towards the nearest integer (either positive or negative). This latter mode is called convergent because it produced unbiased samples.

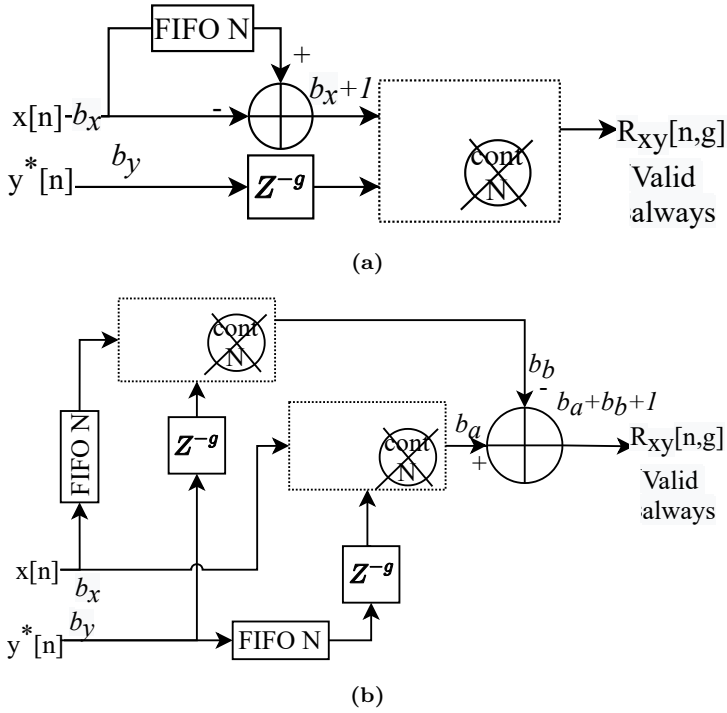

Figure 8.8: Implementation of sample-to-sample linear correlators in FPGAs (only one delay gate): (a) cGNSS-R, (b) iGNSS-R. The core correlators of Fig. can be the ones in Fig. 8.7 but without resetting the adder.

- Scaling is a variation of the truncation mode which consists on using as a reference level an intermediate bit with meaningful information, instead of the Most Significant Bit (MSB) of the data bus. This is in fact the principle of operation of an AGC, in which the data is compressed (or expanded) into a given bit depth. The first bit with meaningful information can be found with a priority encoder (see Appendix D). However, if the signal is noisy or under the presence of RFI (especially in iGNSS-R), this could overestimate the signal amplitude. An alternative is to use a moving mean or mode, or the percentile-50. See Appendix D for possible implementations.

If the data rate is still too large, the complex correlation may be converted into power. This would require 2 Real Signed Multipliers (Table 8.8) and 1 Real Unsigned Adder (Table 8.10). Finally, the data rate can be further decreased by averaging the power with an additional Real Signed Accumulator (see Appendix D).

8.4 Circular correlation

The circular correlation obtained with FFT algorithms is an efficient way to compute the cross-correlation (see Fig. 8.9). These algorithms manage to decrease the complexity of computing the Discrete Fourier Transform (DFT) from $O(N^2)$ to $O(NlogN)$ (e.g. [207,208]). This means that although the circular correlation requires calculating 3 FFTs, the overall computing complexity is smaller than that of the linear correlation, even if few delay lags are computed.

The FFT algorithms are variants of the Cooley–Tukey FFT algorithm, which consist of computing the DFT of size N by dividing the data into smaller subsets N_1 and N_2 such that $N = N_1 N_2$. Specifically, the algorithm performs N_1 DFTs of size N_2. These results are combined recursively in structures known as *butterflies*. Finally, it performs N_2 DFTs of size N_1. The N_1 is called the *radix*. The most typical FFT implementations use $N_1 = 2$ (radix-2) or $N_1 = 4$ (radix-4). The split-radix algorithm is a combination of both.

8.4.1 Implementation in FPGAs

Although it is true that the FFT algorithms use less number of products than the DFT, their implementation in FPGAs also require RAM memory. Additionally, the IP FFTs blocks of the Xilinx family, require data lengths that are a power of 2. Table 8.12 summarizes the resources needed to implement an FFT of different lengths, data bit widths and configuration options. The impact of these parameters on the FFT are analyzed next.

8.4.1.1 Modes of operation

The Xilinx IP core has two modes of operation: pipelined and burst. Figure 8.10 shows a time diagram example of both. The pipelined mode allows continuous data processing. The burst mode computes the FFTs by *frames*. It first loads the data into the RAM memories and processes them sequentially by reusing the butterfly structures. While the

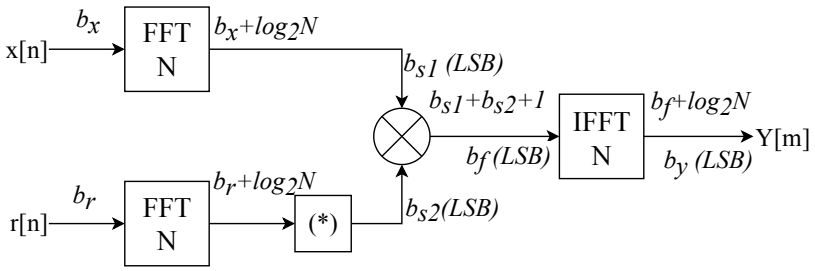

Figure 8.9: Block diagram for the circular correlation.

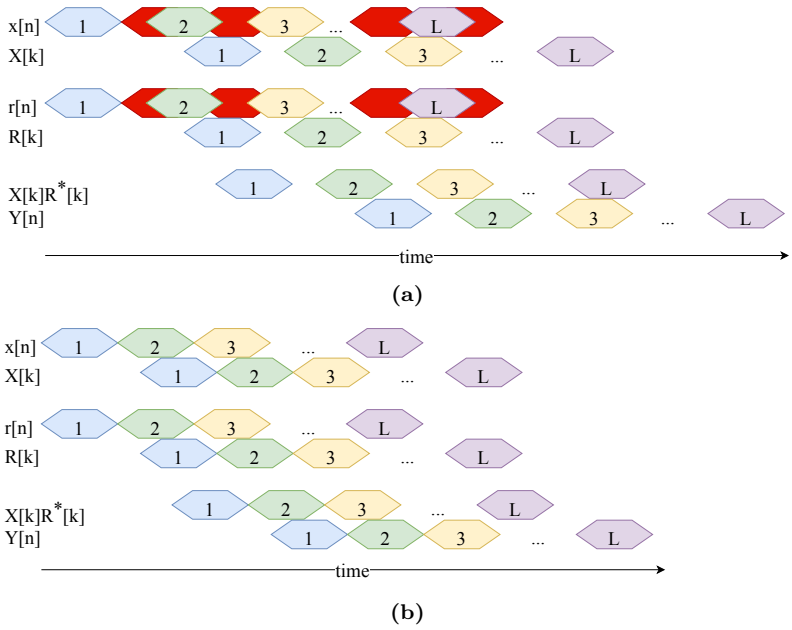

Figure 8.10: Circular correlation implemented with the Xilinx FFT IP core and using two architecture options: (a) burst I/O, and (b) pipelined streaming. Red hexagons mean data that would be lost if introduced to the core before it finishes processing a frame.

FFT core is running, the data input ports are disabled until the whole frame is processed. It is a task of the developer to handle the data rate so as that it is not lost. When the processing is done, the result is burst at the clock rate. Have in mind that the pipeline mode may also output the data in bursts, although obviously, the average output rate is the same as the input. The burst mode (either in radix-2 or radix-4) uses much fewer resources than the pipeline mode. The reduction can be as much as twice the resources (see Table 8.12).

Table 8.12: Resource utilization of the Xilinx FFT IP core v8.0 with a Kintex7-410T.

Length	**1024**	**1024**	**1024**	**1024**	**1024**	**4096**
Width	**8**	**8**	**8**	**8**	**16**	**8**
Scaled/Unscaled	**S**	**S**	**S**	**S**	**S**	**S**
Fabric/DSP	**F**	**F**	**F**	**D**	**F**	**F**
Pipelined/Radix4/Radix2	**P**	**R4**	**R2**	**P**	**P**	**P**
Slice Registers	3,111	2,227	2,227	2,788	4,299	4,069
Slice LUTs	2,299	1,575	1,575	1,851	3,046	3,360
RAMB36E1	0	0	0	0	0	0
RAMB18E1	7	11	11	7	8	14
DSP48E1s	12	9	9	36	13	15

The burst mode can be used to compute circular correlations assuming that some data will be lost. In other words, it will produce cross-correlation values that are not continuous in time, but the peak position would not be affected if the 3 FFTs are properly synchronized. This idea can be used for example as an initial acquisition scheme in order to find the peak position.

8.4.1.2 Scaling and rounding modes

The resources of the FFT core can be reduced if the data is scaled and/or rounded after each butterfly structure, at the expense of increasing the quantification noise. Figures 8.11, 8.12, 8.13 show the impact of the scaling and rounding schemes on a GPS L1 C/A signal, on its ACF, and on the cross-correlation with another PRN respectively. The analysis is done for different signal powers.

Note from Fig. 8.11, that when a signal with low amplitude is scaled, then it cannot be reconstructed. Bear in mind that the IFFT operation has been performed with Matlab. Doing it again with an FPGA core would distort the signal even more due to the quantization effects. One conclusion of these results, is that the reference PRN cannot be generated using only 2 bits (± 1) as stated in the linear correlation architecture. The impact of the quantization noise is best observed in the ACFs in Fig. 8.12. Again, the IFFT has been obtained with Matlab. The quantization of the PRN with 8 bits (± 127) is resilient to the scaling and rounding, but the 4 bits (± 7) case still shows an increase of the noise floor.

Another interesting result is observed in Fig. 8.13. As it can be seen, the cross-correlation between different PRNs produces a correlation peak if the signal power is low and if scaling is used. This intriguing result may mean that the combination of scaling and rounding for those kind of signals, produces a deterministic signal common in all of them. This behavior could lead to problems when acquiring satellites and deciding if they are present or not.

8.4.1.3 FFT length

As previously stated, Xilinx FFT IP cores are designed to have a length multiple of a power of 2. In principle, this means that the received signal has to be sampled (or re-sampled) to match this criteria. Similarly, the PRNs generated with a sampling frequency multiple of their fundamental chip rate (as proposed in Section 8.2), have to be re-sampled as well.

However, as it will be shown here, data rates that are multiple of 1.023 MHz can be used together with FFTs lengths multiple of a power of 2, if a reduction of the SNR up to 3 dB could be acceptable. This could be the case for example of the tracking system, which finds the peak position. Then, the linear correlation could be used in the delay lags around the peak.

Using an FFT length larger than the period of the PRN, produces as many correlation peaks as codes fit into the correlation window. The power of the secondary peaks depends on the number of additional samples. As an example, Fig. 8.14 shows the cross-correlation of a delayed L1 C/A sampled at 1.023 MSps using FFT lengths of 1024. The period of the C/A signal is 1 ms or 1023 samples. This means that there is only one additional sample (actually one chip) in the correlation window. The second peak is therefore very small, even more than the cross-terms produced in the correlation. However, the power of the main peak depends on the delay. The power is maximum when the delay is zero, and decreases to half its maximum value when delay is 0.5 ms. The reason for this is that in the circular correlation it is assumed that the signal has a period equal to the FFT length, which is not true here.

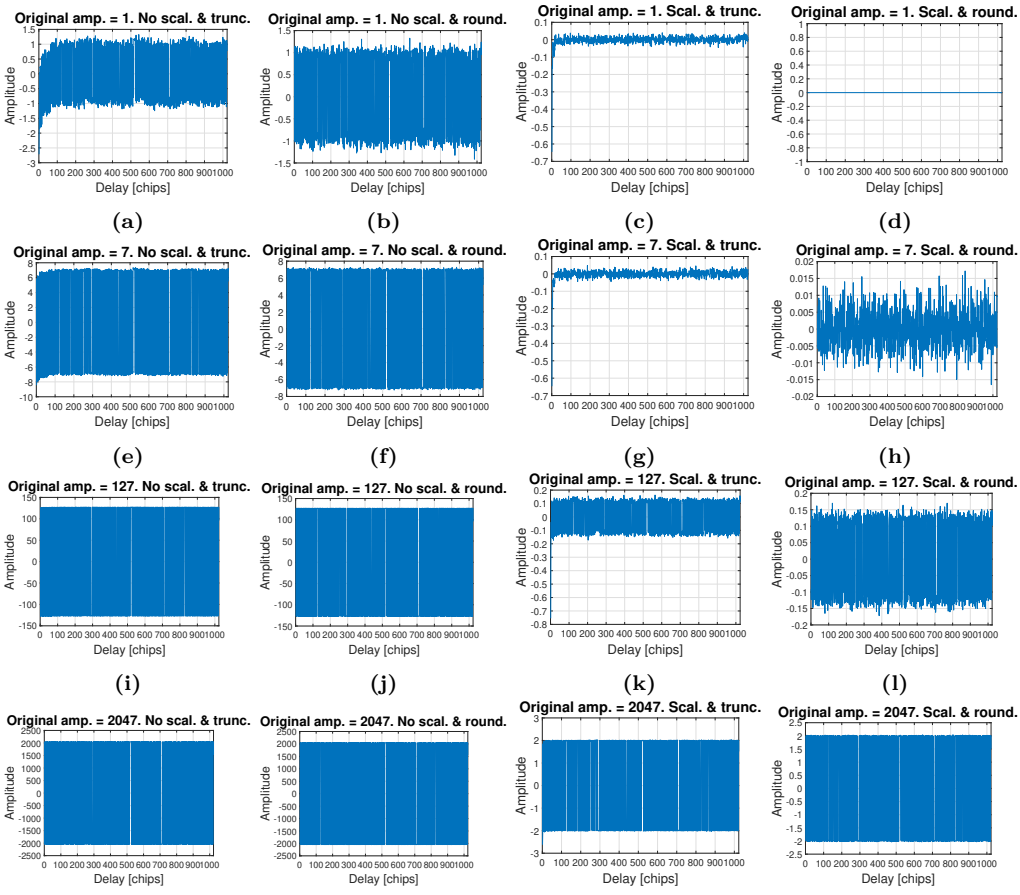

Figure 8.11: Impact of Xilinx FFT on a C/A signal using different FFT configurations and signal powers. The IFFTs are computed with Matlab.

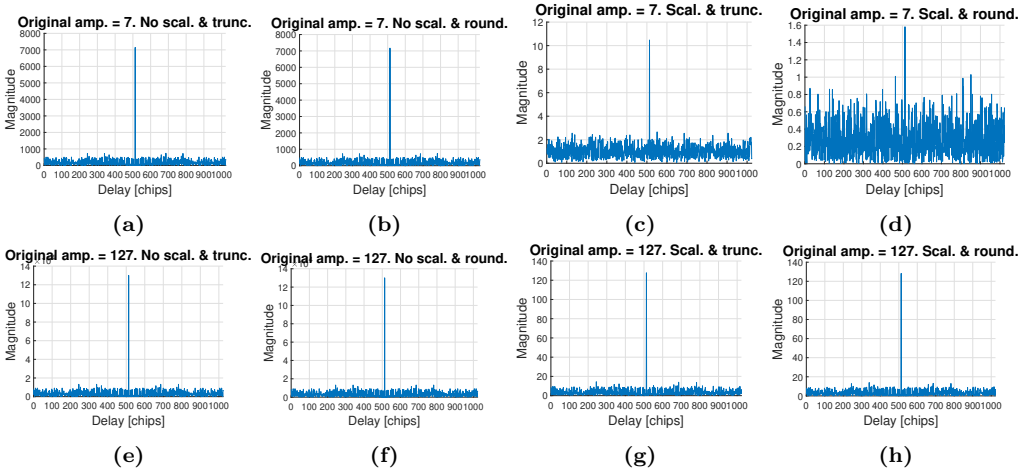

Figure 8.12: ACF of a C/A signal using Xilinx's FFT and Matlab's IFFT.

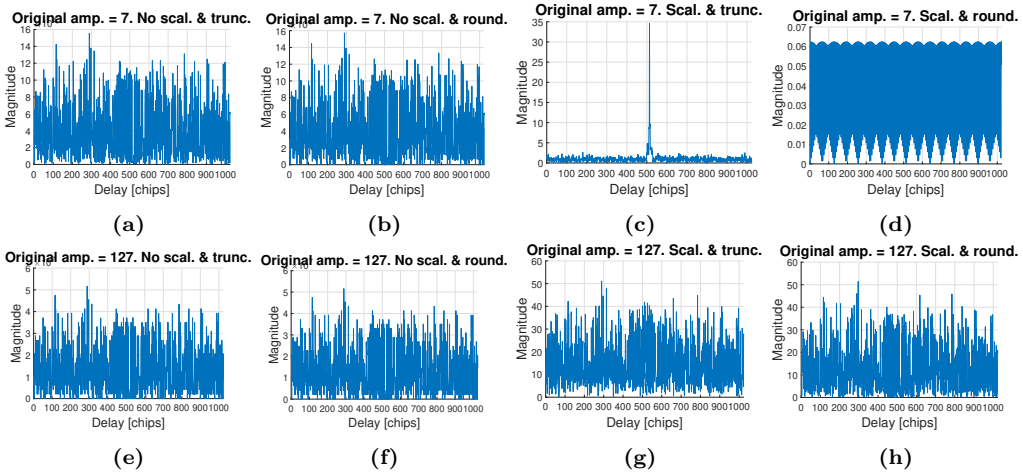

Figure 8.13: Impact of Xilinx FFT on the XCF between different C/A signals XCF using different FFT configurations and signal powers. The XCFs are computed with Matlab.

An example with a larger difference between the FFT length and the number of samples in the PRN period is shown in Fig. 8.15. In this case, the FFT has a length of 16384, and the sampling frequency is 10.23 MSps. Now, 1 ms is equal to 10230 samples, wich means that there are 6155 additional samples. In this case, the two additional peaks can be clearly seen at a delay of 6155 and 10230 samples from the main one. Their power is reduced to $(10230/16384)^2 \approx 0.39$. It is interesting to note here, that the power of the secondary peak is larger than the true one when the delay is larger than 0.5 ms. The reason for that is, as its name indicates, the circular correlation *circularly shifts* the secondary peaks back to the origin. By understanding this behavior one should be able

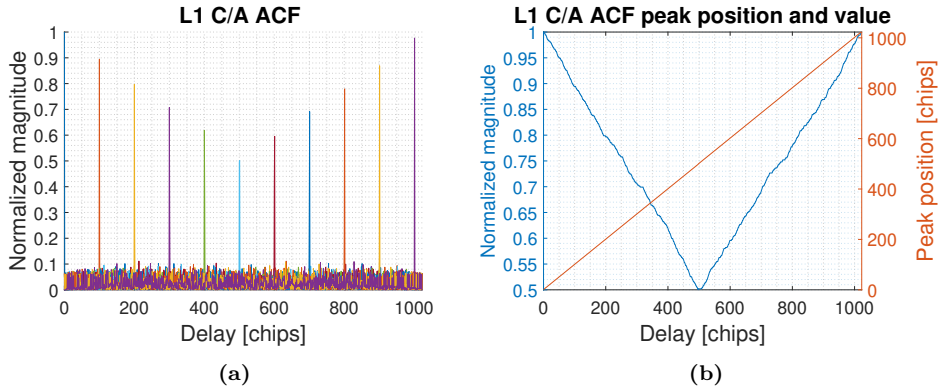

Figure 8.14: Impact of a 1024-FFT on the circular ACF peak magnitude and position of a C/A PRN sampled with 1.023 MHz (1023 samples). (a) Result for different delays (different colors); (b) peak magnitude and position.

to track the correct peak, however that would increases the complexity unnecessarily.

The conclusion is that the number of samples in a PRN period should be as close as possible to the FFT length. For example, in the latter case, using an $f_s = 16 \cdot 1.023 = 16.368$ MSps, would represent only 16 additional samples, and the behavior would be very similar to the one in Fig. 8.14.

8.4.1.4 Bit width

As shown in Fig. 8.9, each block in the circular correlation adds additional bits to the data bus. This is similar to what happened in the linear correlation, but in this case the bit growth is even larger. As an example, if the data signal and reference PRN are quantified with 8 bits and the FFT length is 16384, the input of the IFFT would be of 45 bits. This is an extremely large number, that would use most of the resources of the FPGA, if it had to be implemented. Thus, bit reduction strategies similar to the ones proposed in the linear correlation should be applied.

The maximum value of the FFT depends on the signal modulation. One limiting case is a tone, in which all the power is concentrated in the same frequency, and thus using the whole dynamic range of the FFT. Another extreme case is AWGN, in which the power is spread equally within all the frequency range. An example using a GPS L1 C/A PRN is depicted in Fig. 8.16. The MSB is analyzed for different input signal powers (ranging from 1 to 16), for two different FFT lengths, and by using different scaling and rounding modes. Even the non scaled modes are smaller than the theoretical bit width growth (10 and 14 for a FFTs length of 1024 and 16384 respectively). If the scaling is enabled, the reduction is even larger.

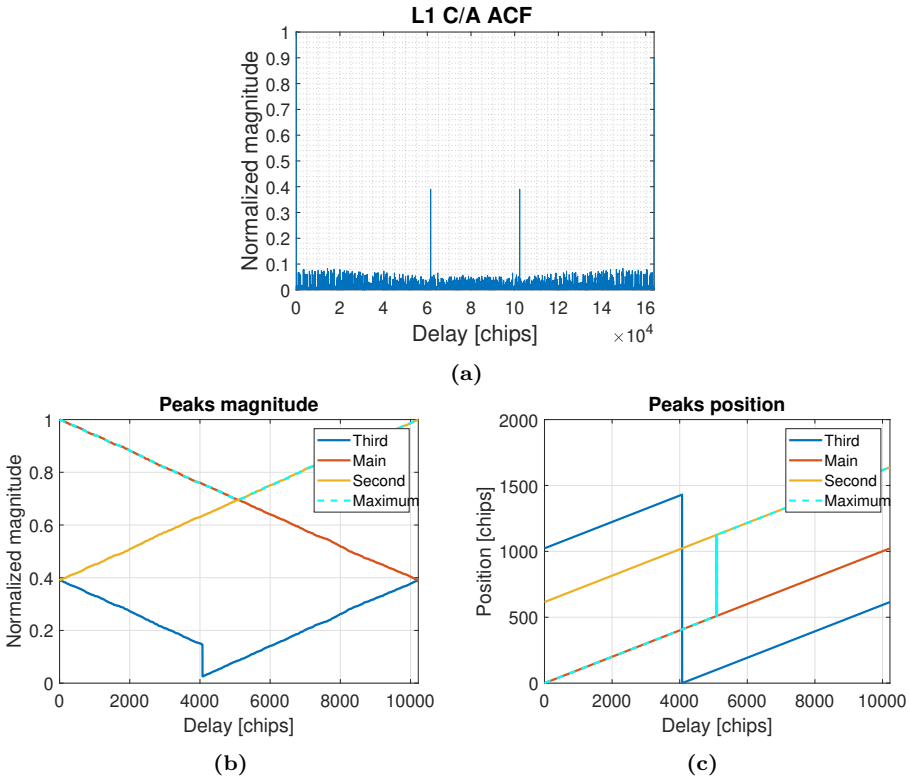

Figure 8.15: Impact of a 16384-FFT on the circular ACF peak magnitude and position of a C/A PRN sampled with 10.23 MHz (10230 samples). (a) Result for a single delay; (b) peaks magnitude; and (c) peaks position. Tracked refferes to the largest one, main to the true one.

8.4.2 Implementation in CPUs and GPUs

As seen in last sections, building either a linear or a circular correlator in FPGAs is challenging and gives little flexibility. However, nowadays there are other alternatives based on software, such as the GPUs or even Central Processing Units (CPUs), that can run fast enough to produce real-time correlations.

The software platforms discussed here are the Matlab 2018b with the Signal Processing Toolbox, the open-source C/C++ library FFTW 3.3.5 [209], and the free GPU CUDA library for NVIDIA platforms 10.0 [210]. They have been tested to process the data of the MIR instrument (see Part III). The time and memory performance of each software depends on the ability of the programmer to build an efficient program. However, in the opinion of the author, programming circular correlations with the mentioned programs is not intrinsically complex. There are however two issues that should be stated here. Firstly, Matlab uses multi-threading on most of the functions involved in the correlation,

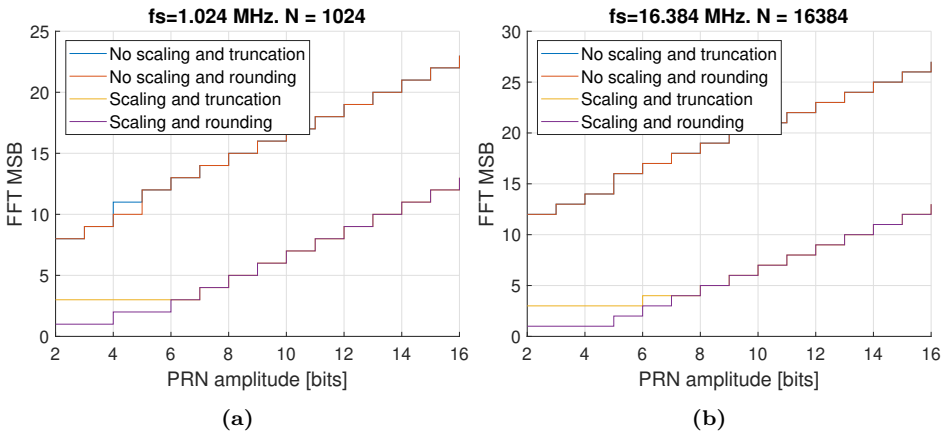

Figure 8.16: MSB resulting from the FFT of C/A PRN using Xilinx IP core v8.0 as function of the ower and using different FFT configurations. (a) Signal sampled at 1.024 MHz (1024 samples) and FFT size of 1024; (b) signal sampled at 16.384 MHz (16384 samples) and FFT size of 16384. Blue and red are almost overlapped.

if the machine is multi-core. Multi-threading in the C/C++ program is in principle also possible. However, this latter program has been built using a single-thread for simplicity. The second issue involves the memory sharing between the operating system and the GPU. In principle, the GPU cannot access the memory of the operating system, and thus, a buffer between both must be implemented. This increases the amount of time of the overall operation. Although there are mechanisms to share the memory between both devices, this has not been implemented here and is given for further improvements.

The aforementioned libraries allow more flexibility than the IP cores of the FPGA devices. For instance, the FFT length does not need to be a power of 2, and they also allow the calculation of multi-dimensional and overlapped FFTs. Although an FFT length multiple of a power of 2 is the most efficient implementation, the FFTW library also handles efficiently lengths of the form $2^A \cdot 3^B \cdot 5^C \cdot 7^D \cdot 11^E \cdot 13^F$, where $E + F$ is either 0 or 1. In general, the smaller the prime factors, the better the performance. The same applies with the Matlab *fft* function, as it is based on the FFTW library. As for the CUDA library, the algorithms are optimized for the lengths that can be written in the form $2^A \cdot 3^B \cdot 5^C \cdot 7^D$. To illustrate this, if the sampling frequency is 10.23 MSps, 1 ms of data would be equal to 10230 samples. The closest power of 2 towards infinite is 16384, which represents 6154 additional samples or 60.2% of overhead. In this case, it is clear that it is not worth using the closest power of 2. However, a length of $2^{11} \cdot 5^1 = 10240$, would be more reasonable. This would represent only 10 additional samples, or just 0.1% of overhead.

In MIR, 1 ms of data corresponds to 32736 samples. The closest power of 2 towards

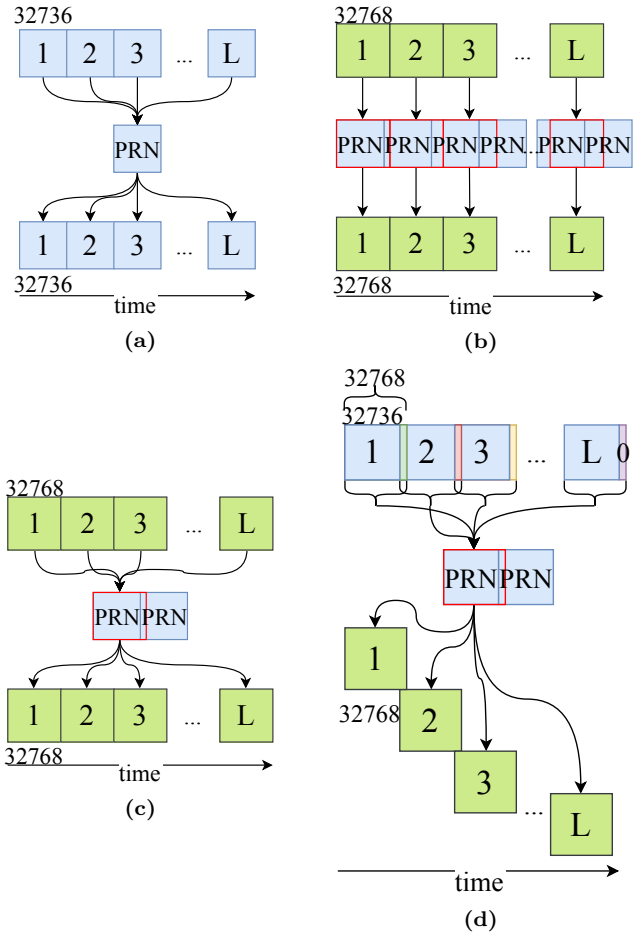

Figure 8.17: Proposed circular correlation architectures to process the MIR data (see Part III) using cGNSS-R. Here, 32736 samples are 1 ms at a fs=32,736 MSps, and 32768 is the nearest power of 2.

infinite is 32768, which represents 32 additional samples, or just 0.1% of overhead. Similarly, 4 ms of data equal to 130944 samples. The closest power of 2 towards infinite is 131072, which represents 128 additional samples, or also just 0.1% of overhead. These numbers are small enough so as not to consider other alternatives.

The aforementioned programs do not only compute circular correlations, but also read the raw data from the hard drive, and save a portion of the DDM around its peak and associated metadata such as the SNR. The main problem when reading the MIR data is that the samples are stored with 2 bits. However, the functions to load binary data handle only multiples of 8 bits. This means that a masking function that iterates over the raw data steam is required. As it will be shown, this mask function takes substantial

run-time. Although the FPGAs in MIR organizes the data bit stream in such a way that it allows the use of an efficient mask (see Chapter 9), the author believes that there is still space for improvement in the masking function.

The software programs have been tested by using two different computers:

- Configuration 1
  - Laptop Intel i7 (4th gen) at 2.20 GHz
  - 16 GB RAM
  - NVIDIA GeForce GT 750M (384 cores at 967 MHz with 4 GB RAM)
  - Windows 8 64b
- Configuration 2
  - Tower Intel i7 (8th gen) at 3.20 GHz
  - 32 GB RAM
  - NVIDIA RTX 2080 (2944 cores at 1472 MHz with 8 GB RAM)
  - Windows 10 64b

The above programs and computers have been used to compare the correlation architectures depicted in Fig. 8.17. The simplest option is shown in Fig. 8.17a, in which consecutive data blocks of 1 ms or 32736 samples are cross-correlated with the same reference PRN block, which needs to be computed only once. However, and as stated previously, block sizes multiple of a power of 2 are more efficiently handled. Three different options have been considered for such cases. In Fig. 8.17b, data blocks of 32768 samples or 1,000977517106549 ms are correlated with circularly shifted replicas of the reference PRN. Although this scheme uses efficient FFT lengths, it also requires twice the number of FFTs, and thus, probably reducing the overall performance in terms of time and resources. Figure 8.17c shows a similar approach but with a fixed reference. This results in a correlation loss and in a peak drift of 32 samples after each correlation. Although the loss is negligible (32/32768 = 0.098%), this system requires a re-tracking mechanism after each correlation. Finally, Fig. 8.17d takes advantage of the overlapping option of the FFT libraries, by reusing the last 32 samples of each 32768 block to produce a new correlation block. This architecture creates overlapped cross-correlations, but it allows the use of a single reference block.

The run-time results of the functions involved in the circular correlation using the different software platforms and computers are shown in Figs. 8.18, 8.21, 8.20, 8.19 and 8.22. Table 8.13 summarizes the memory resources. All results are discussed next.

8.4.2.1 Run-time comparison

Figure 8.18 shows the overall run-time of the different software platforms to process one incoherent cGNSS-R waveform with a coherent length of 1 ms (32736 and 32768 samples)

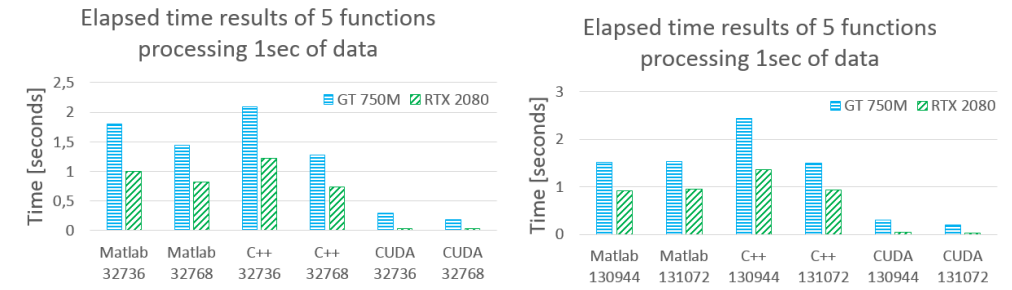

Figure 8.18: Overall run-time of different software platforms to process one incoherent cGNSS-R waveform, using different FFT lengths. Left: N_{in}=1000, FFT lengh=32736 or 32768. Right: N_{in}=250, FFT length=130944 or 131072. Blue and green refer to configurations #1 and #2 respectively. In the CUDA platforms, the 1000 coherent waveforms are obtained in parallel. From [201]

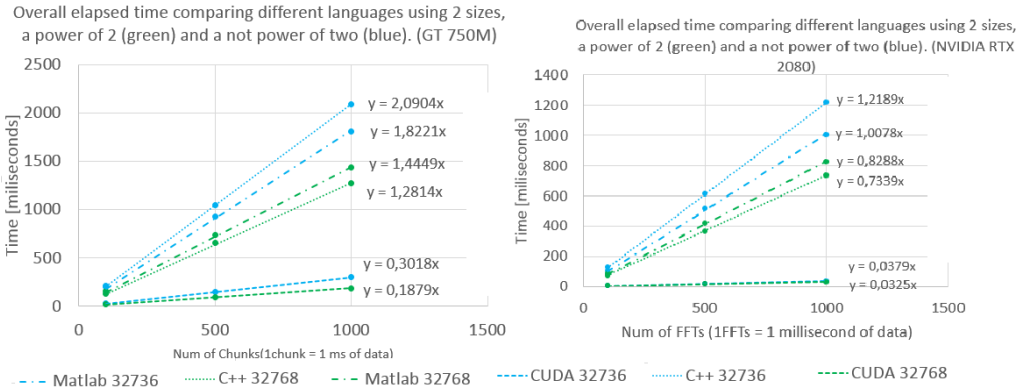

Figure 8.19: Overall run-time of different software platforms to process one incoherent cGNSS-R waveforms (N_{in}=1000) with different FFT lengths (32736, 32768) with respect to the number of coherent waveforms processed in parallel (100, 500, 1000). Left: conf. #1, right: conf #2. From [201].

or 4 ms (139044 and 131072 samples) and with 1000 averages. The results are obtained using the two computers. The architecture in Fig. 8.17a is used with the original block size (i.e. 32736 and 139044), and the architecture in Fig. 8.17d is used with the blocks whose size is a power of two (i.e. 32768 and 131072).

Only those configurations with an overall run-time below 1 second are in principle suitable for real-time processing. The following conclusions can be drawn. Firstly, the GPUs outperform the CPUs in all the configurations. The time improvement is about 90% with respect to the C++ program. Secondly, the programs handling with data blocks whose length is a power of 2, improve the run-time by about 15%-20%, except the Matlab code dealing with the 130944 and 131072 samples, which both show a similar performance.

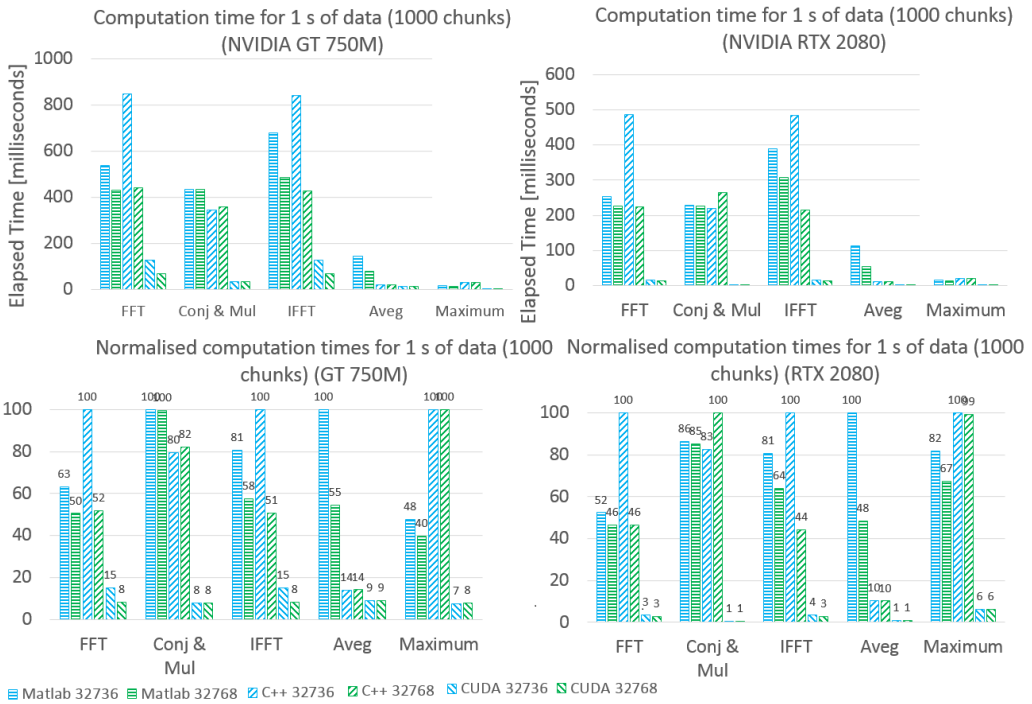

Figure 8.20: Top row shows the run-time of each function used to obtain one incoherent cGNSS-R waveform (N_{in}=1000) using different software platforms, FFT lengths (32736, 32768), and with configuration #1 (left) and #2 (right). Bottom row shows the same results but normalized to the slowest software. In the CUDA platforms, the 1000 coherent waveforms are obtained in parallel. From [201].

Finally, Matlab is slightly faster than the C++ code when processing the original sample sizes. However, both have a similar performance when handling the blocks with a length multiple of a power 2.

The last figure showed the time required to process 1000 coherent waveforms. Figure 8.19 shows the derived time slope by using different incoherent averages (100, 500 and 1000). Although not shown in the figure, averages of 5000 also had the same slope. Only CUDA running in the GPU, and the Matlab software using the computer labeled as #1 could be used in real-time.

The last time estimates only take into account the run-time to compute the cross-correlations and omit the time required to read the raw data, find the peak, compute the SNR, and save the results. As seen in Figs. 8.20 and 8.21, these extra functions can take up to 19% (GT750M) and up to 34% (RTX2080) of the overall run-time. However, as seen in Fig. 8.22, they do not prevent the GPU platforms from working in real-time.

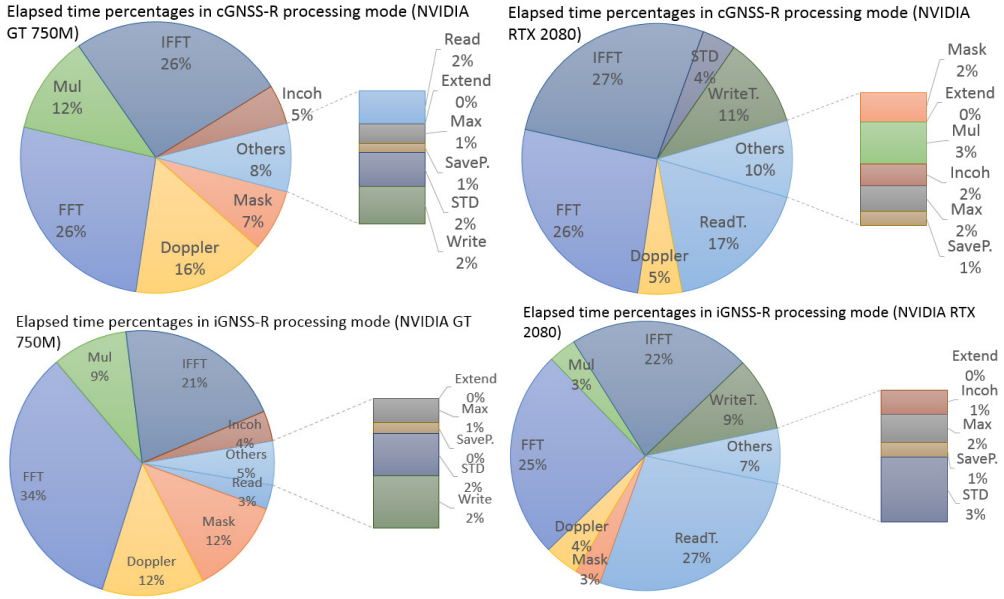

Figure 8.21: Execution time percentage of the CUDA functions to read the raw data; obtain one incoherent waveform (N_{in}=1000, FFT lenght =32768), peak and noise std.; and save the results. Top row: cGNSS-R; bottom row: iGNSS-R; left column: conf. #1; right column: conf. #2. The 1000 coherent waveforms are obtained in parallel. From [201].

8.4.2.2 CUDA overall memory use

Table 8.13 shows the overall memory use the CUDA programs using the NVIDIA card GT750M (4 GB RAM) when processing data blocks of 32768 samples. The analysis is performed by using different number of incoherent averages, and of Doppler bins. All the observables are processed simultaneously. This means that those DDMs in which the combination of the number of averages and number bins requires too much memory, will have to be computed sequentially. That would increase the overall run-time estimates given in the previous section.

Note first that, as expected, the memory use when computing an interferometric waveform increases linearly with the number of averages. For this specific waveform length and card, the maximum number of coherent waveforms that can be computed in parallel is about 5000. For the conventional case, a linear extrapolation suggests that the maximum is about 7600.

When computing full DDMs, there is a trade-off between the number of Doppler bins and the number of averages that can be computed in parallel. The 4 analyzed configurations require to compute around 5000 coherent waveforms. However, differences of about 30% of memory resources are found between them. The reason is that large

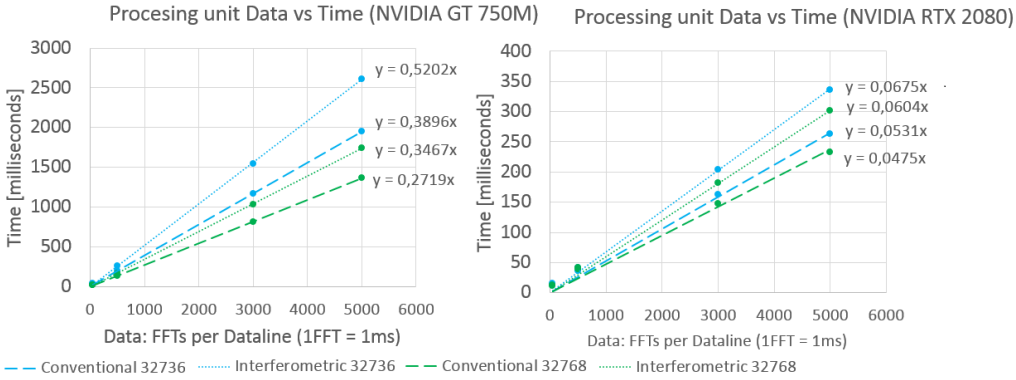

Figure 8.22: Overall run-time of the CUDA functions to read the raw data; obtain one incoherent waveform (cGNSS-R and iGNSS-R, with N_{in}=1000) with different FFT lengths (32768, 32768), the peak and noise std.; and save the results, as function of the number of coherent waveforms processed in parallel (500, 3000, 5000). From [201].

Table 8.13: Overall memory use of the CUDA programs with the GT750M card. Top row shows the results obtained when computing an incoherent waveform of 32768 samples for different number of averages (50, 500, 3000 and 5000). Bottom row shows the results for an incoherent DDM also of 32768 samples and with different number of Doppler bins (51, 11 and 1) and for a different number of averages (100, 500, 1000, 5000). Left column is for cGNSS-R and right column for iGNSS-R. From [201].

Chunks of data	50	500	3000	5000
cuFFT Buffer	0,31%	3,05%	18,31%	30,52%
Variables declared	0,35%	3,49%	20,89%	34,82%
Total memory used	0,66%	6,54%	39,20%	65,34%

Data configurations	100*51	500*11	1000*5	5000*1
cuFFT Buffer	0,61%	3,05%	6,10%	30,52%
Variables declared	34,27%	37,06%	33,82%	34,82%
Total memory used	34,88%	40,11%	39,93%	65,34%

Chunks of data	50	500	3000	5000
cuFFT Buffer	0,31%	3,05%	18,31%	30,52%
Variables declared	0,65%	6,53%	39,20%	65,33%
Total memory used	0,96%	9,58%	57,51%	95,85%

Data configurations	100*51	500*11	1000*5	5000*1
cuFFT Buffer	0,61%	3,05%	6,10%	30,52%
Variables declared	65,39%	70,62%	64,34%	65,33%
Total memory used	66,00%	73,67%	70,44%	95,85%

incoherent averages are more memory consuming than the number of bins are, as the former needs to load more raw data into memory.

8.4.2.3 Initial processing results

The results of the MIR data processed with the CUDA program are explained in Chapter 11. As anticipated results, Fig. 8.23 shows an example of a direct and reflected GPS and Galileo power waveforms. The reflected signal is stronger than the direct signal because there is an additional power amplifier in the respective hardware receiver chain. Figure 8.24 shows the peak position of a GPS direct and reflected signals over time. The change of slope is due to a change of sign of the Doppler of the incoming signals. This happens when the transmitter is first moving towards the receiver and then moving away (or vice versa).

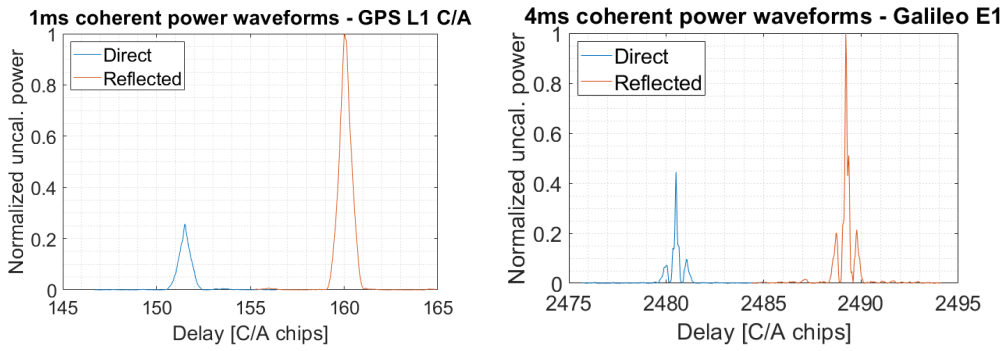

(a) (b)

Figure 8.23: Comparison between reflected and direct power waveforms: (a) GPS L1 C/A, (b) Galileo E1OS. Note that reflected signal is stronger because of the larger gain of the respective receiver chain (see Chapter 9).

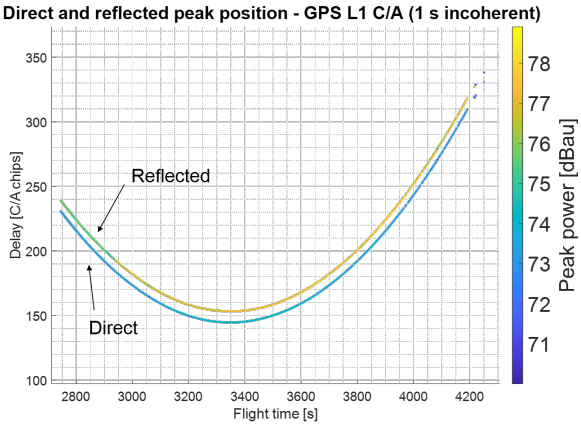

Figure 8.24: Delay and reflected peak position of a GPS L1 C/A signal.

8.5 Window tracking considerations

GNSS receivers continuously track the peak of the cross-correlation in the delay-Doppler plane using closed tracking loops (e.g. [206]). While the code tracking is typically implemented using DLLs, the carrier tracking can be designed to follow either the phase of the signal using with PLLs, the Doppler frequency of the signal using Frequency Lock Loops (FLLs), or with a combination of both. These architectures implicitly assume that the incoming signal is coherent, which, is not necessarily true for the reflected signals [61,67]. Although there is vast literature on non-coherent discriminators, they are not easy to implement, and therefore are not considered in this Ph. D. thesis.

As an easier alternative, the tracking of the peak in the delay-Doppler plane can be

implemented by using a number of delay lags and Doppler bins large enough to ensure that the peak is present in one of them. The position of the correlator lags and of the Doppler bins is then refreshed at a given period. The number of lags and bins, and the refresh rate depend on the vehicle height and dynamics, and on the GNSS-R technique (i.e. cGNSS-R or iGNSS-R). There is in fact a trade-off between the number of correlators and the refresh period. While a large number of correlators would require a low refresh period, they would produce a large amount of data to be handled. In the opposite case, a small number of correlators would require a large refresh period, increasing the synchronicity complexity between the hardware and/or software sub-systems.

Investigation on the GNSS-R tracking windows has been previously performed in [36, 86, 87], and specifically for the CYGNSS mission in [88]. This section further investigates this issue with the new GNSS constellations and for the iGNSS-R technique. The nominal orbits of the GPS, Galileo, Glonass and BeiDou-2 constellations have been simulated over a three day period using the STK software [180]. The delays and the Dopplers frequencies of the direct and reflected signals have been computed at two latitudes on the Earth (equator and 70°), at two different heights (125 m and 2 km), in a static position and with a speed of 200 km/h, and at the ISS (≈400 km. ≈7.5 km/s). Results are shown in Figs. 8.25, 8.26, 8.27, 8.28 and 8.29, and are analyzed in the next paragraphs.

8.5.1 Doppler range

Figure 8.25 shows the Doppler shift of the direct and reflected signals, and the subtraction of both (labeled as interferometric), for ground and airborne scenarios. The results for the ISS are depicted in the top row of Fig. 8.28. The shift is referenced to the L1 carrier frequency. Conversion to the carrier frequencies of the other bands is easily obtained by applying the ratio between each of them and L1 (see Tables A.1 and A.2)

The Doppler is positive when the satellite is approaching the receiver and negative when moving away. At the same time, the higher the elevation angle, the lower the Doppler. The observed groups of lines of each constellation are caused by the satellites within the same constellation plane (see Chapter 2). Note also that the GLONASS satellites can be seen at higher elevation angles at the 70° latitude scenario because their orbital inclination (65°) is larger than that of the GPS (55°) or Galileo (56°) satellites.

The Doppler range for either the direct and the reflected signals is between ±5 kHz at ground and airborne scenarios. The range decreases downto ±3 kHz for elevation angles larger than 40°. At these same scenarios, the interferometric Doppler range is much smaller, of the order of few Hz. However, differences are observed between different latitudes, heights and speeds. The range increases by ≈10 units from 125 m to 2 km at given latitude. At the same time, it increases by ≈5 units from a latitude of 0° to a

latitude of 70°, at the two considered heights. The big jumps observed in the scenario where the receiver is moving, are caused because the aircraft trajectory was simulated with very sharp turns. In a real scenario, the turns would be smoother, however the window of an interferometric correlator should anyway have range of ±50 Hz to prevent losing the lock.

At the ISS, the Doppler range is much higher, up to ±40 kHz for low elevation angles, and up to ±30 kHz for angles larger than 40°. The interferometric Doppler range is slightly smaller, about ±15 kHz for angles larger than 40°.

8.5.2 Doppler rate

Figure 8.26 shows the Doppler rate at ground and airborne scenarios, and the middle row of 8.28 for the ISS. The Doppler rates are smaller than ±1 Hz/s for all the ground and airborne scenarios, except again, during the aircraft sharp turns. The interferometric Doppler rate decrease downto ±2 mHz/s in the static cases.

A rate of 1 Hz/s translates into an accumulated phase of 0.36° during a typical correlation length of 1 ms. This is an acceptable error for a typical receiver without a continuous Doppler tracking. A correlator with a Doppler width of 2 kHz, would require to be refreshed at a rate of 1e-3 mHz, or 1e6 coherent correlations. However, at the ISS, the Doppler rates can be as high as 100 Hz/s, which translates into an accumulated phase of 36° in 1 ms. High-performance PLLs in combination with Kalman filters and with IMU data are required to overcome this problem.

8.5.3 Delay rate

Figure 8.27 shows the delay rate in C/A chips (≈300 m) per second at ground and airborne scenarios, and the bottom row of Fig. 8.28 at the ISS. Indeed, the shapes of the curves are similar to those of the Doppler, as the latter depends on the relative radial velocity between the transmitter and the receiver. Delay rates up to ±3 C/A chips/s are observed for ground- and airborne-based scenarios. For these same scenarios, the interferometric delay rate decreases by ±100 units.

In order to give context to the reader, a tracking window with length of 10 C/A chips, should have a refresh period of 1.33 Hz, on in other words every 1333 coherent correlations. However, at the ISS, the rate delay can be as high as 20 C/A chips/s for elevation angles larger than 40°. In the interferometric cases it decreases downto to 2 C/A chips/s.

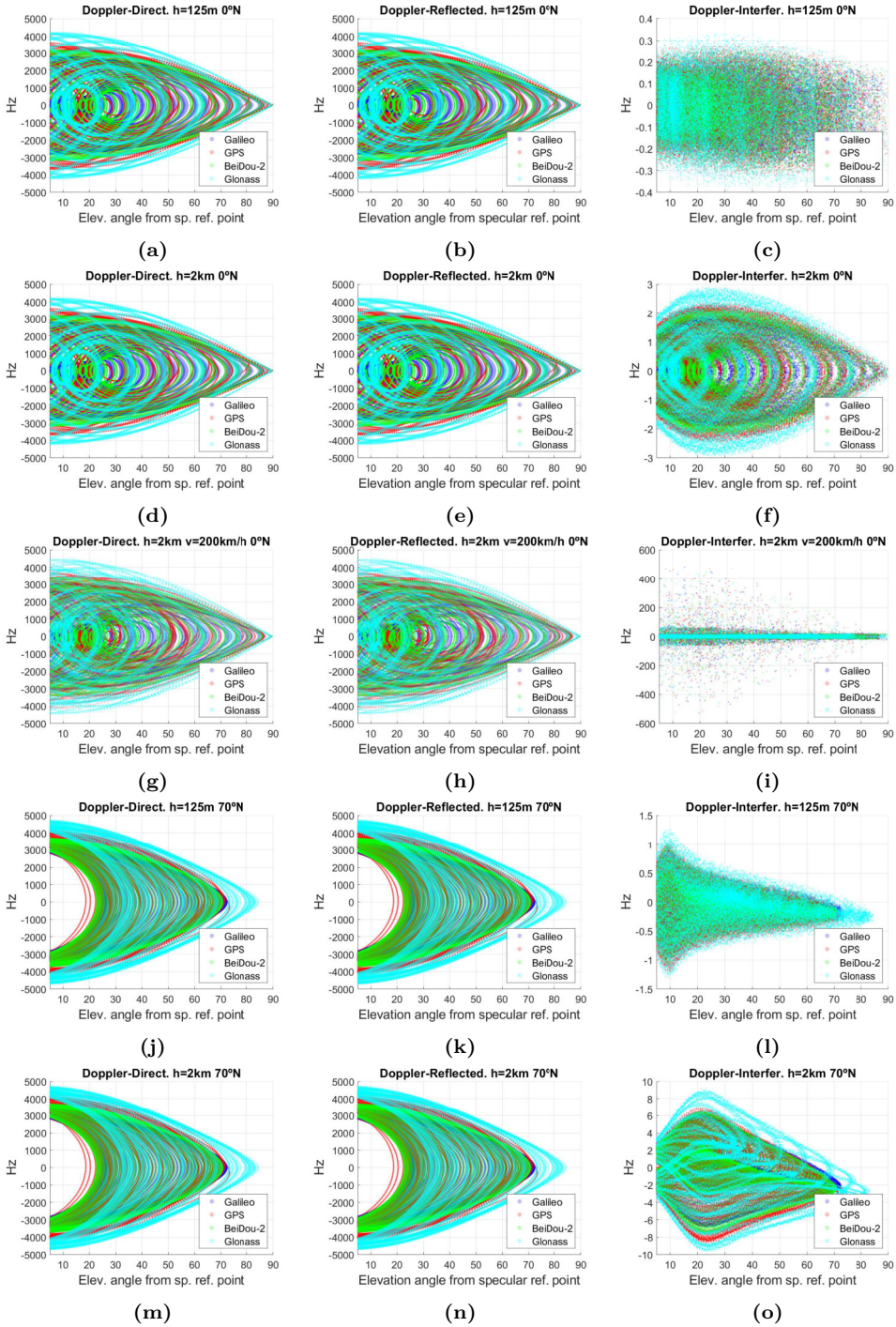

Figure 8.25: Received Doppler at L1 as function of the satellite elevation angle from airborne scenarios for the direct (left column) and reflected signals (middle column), and the substraction of both (right column). Simulations for different receiver latitudes, heights and speeds.

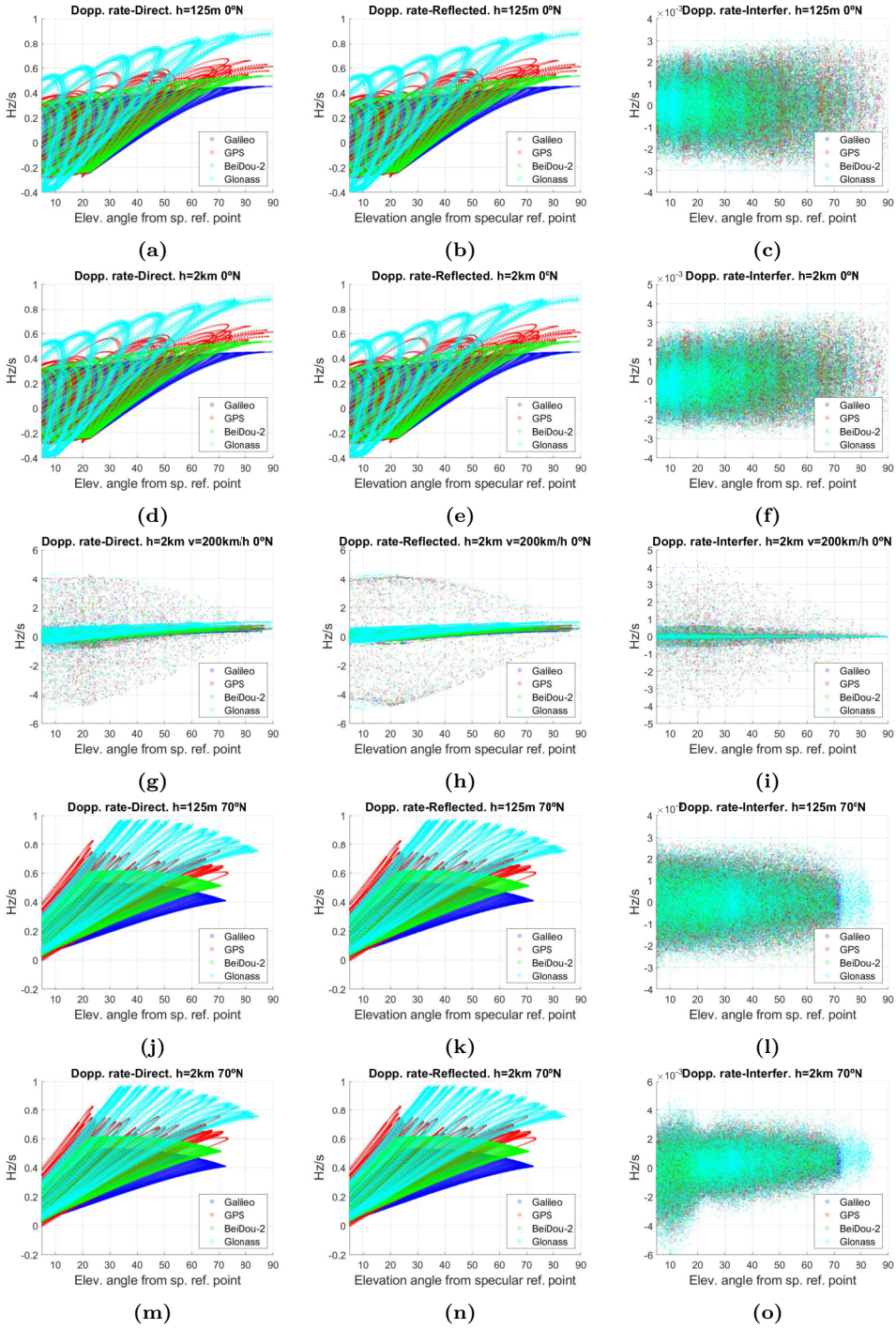

Figure 8.26: Doppler rate at L1 as function of the elevation angle from airborne scenarios for the direct (left column) and reflected signals (middle column), and the substraction of both (right column). Simulations for different receiver latitudes, heights and speeds.

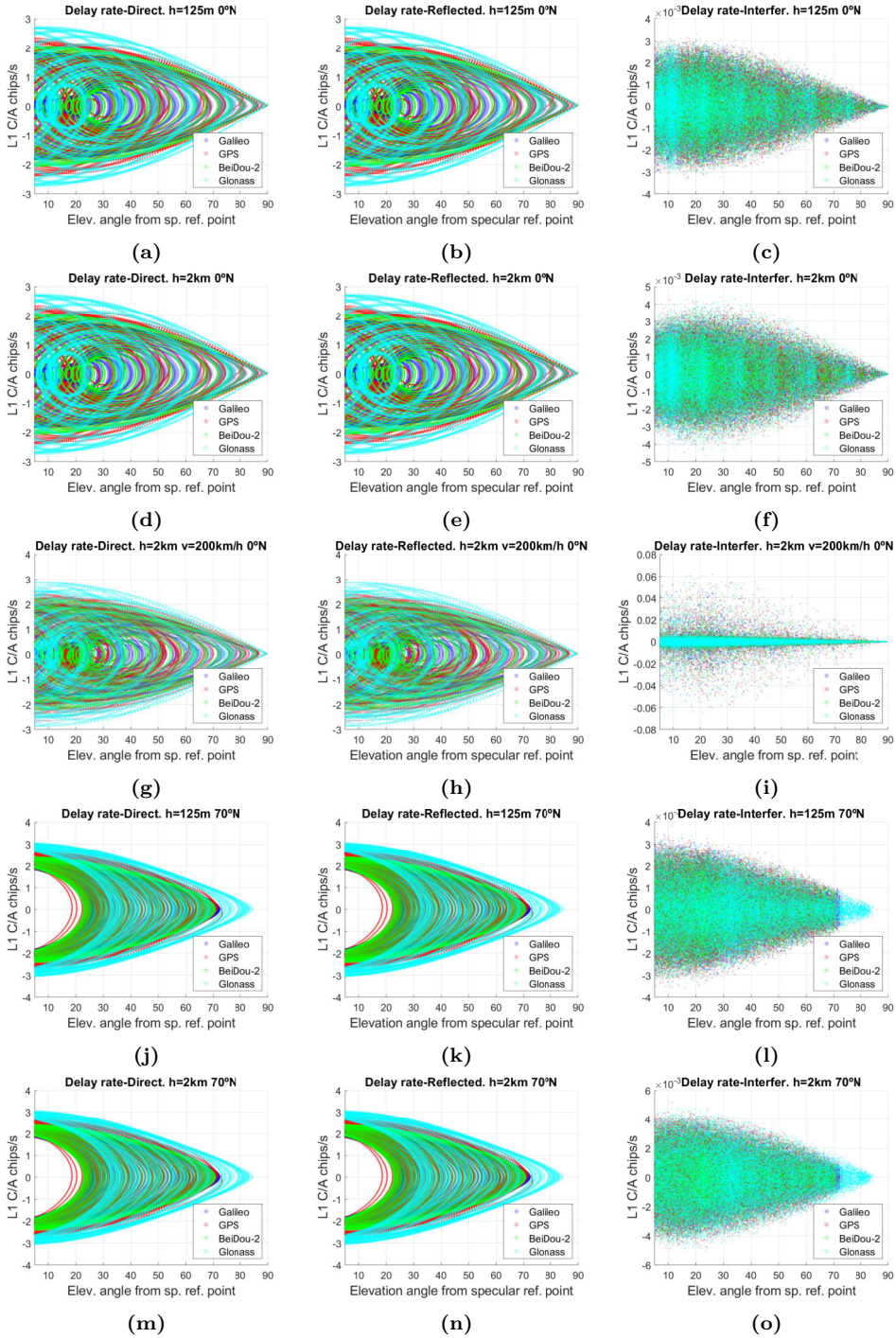

Figure 8.27: Range rate as function of the elevation angle from airborne scenarios for the direct (left column) and reflected signals (middle column), and the substraction of both (right column). Simulations for different receiver latitudes, heights and speeds.

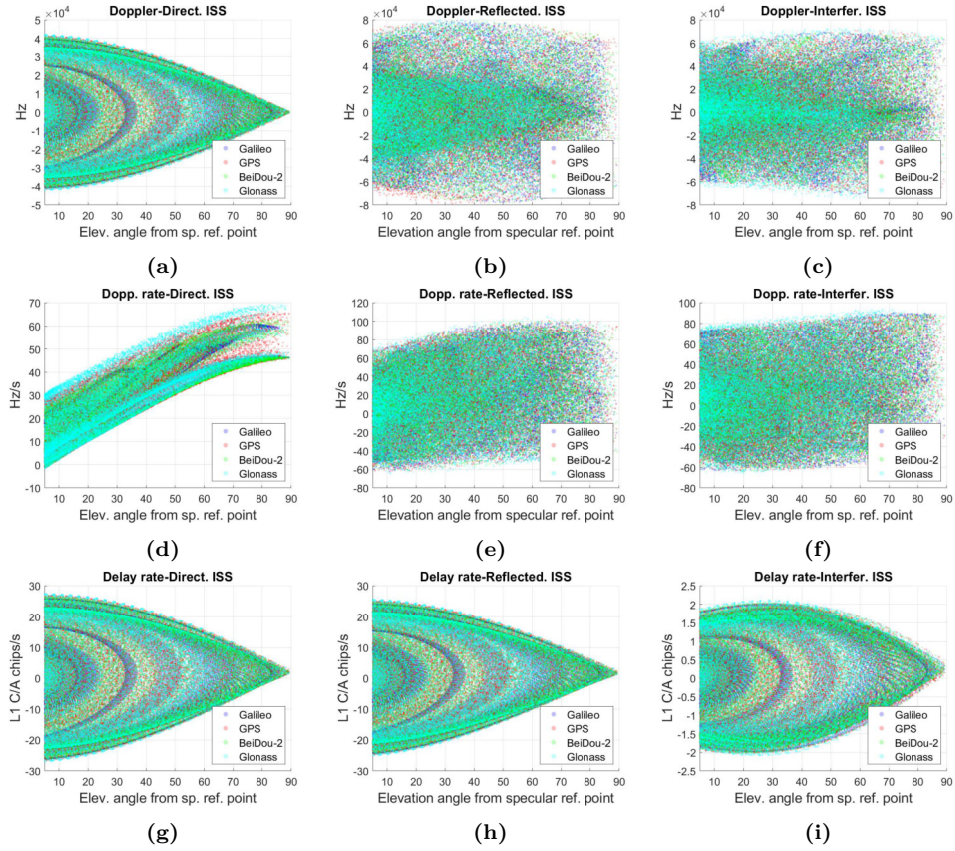

Figure 8.28: Doppler, Doppler rate and range rate from the ISS.

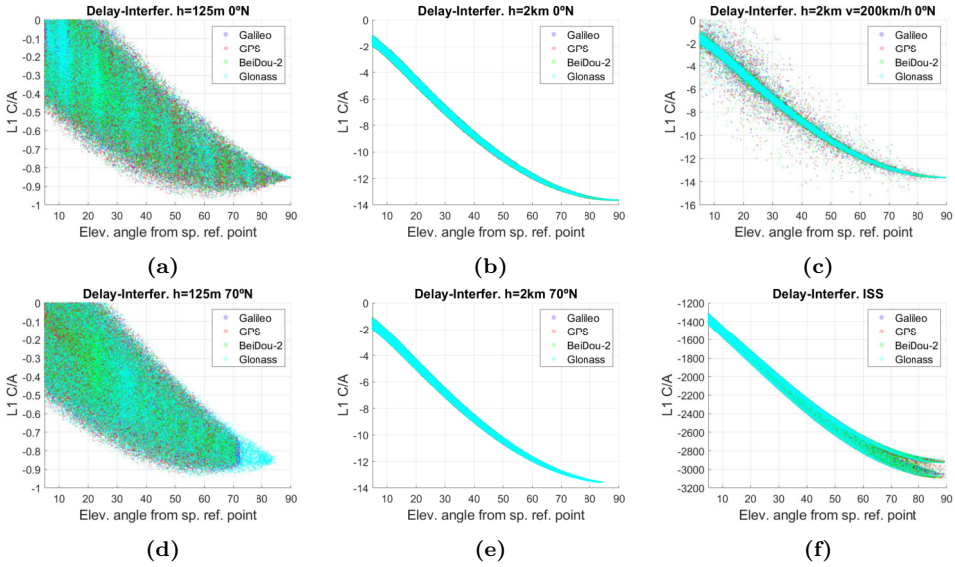

Figure 8.29: Interferometric range distance.

8.5.4 Interferometric delay range

Figure 8.29 shows the interferometric range for all the scenarios. Ideally, a real-time receiver would first have to delay the direct signal by an estimation of the inteferometric delay before correlating it with the reflected signal. A simpler approach can be done in ground and airborne scenarios by using a correlation window large enough that guarantees that most of both signals are received. For example, a receiver flying at 2 km height would need a window of 14 C/A chips, and would the uncorrelated samples would be up to $14/1023 \approx 1.37\%$.

8.6 Full acquisition implementation on FPGAs

The FPGA architecture originally considered for MIR is given in Fig. 8.30. It first performs a *coarse* circular correlation between the direct signal after removing the Doppler with the reference PRN. By coarse, it is understood that the signal is downsampled and compressed (i.e. less bits per sample). See again Figs. 8.3 and 8.4 for the impact that this has on the ACF. The reference Doppler and the PRN number are given by an external commercial GNSS receiver (see Chapter 9). The PRN is generated as explained in Section 8.2 and saved into a dual-port RAM. This RAM has two independent bus address and two outputs, which means that it can be shared simultaneously by the circular and linear correlators. Then, the linear correlation for a given number of delay lags and for different number of Doppler bins is performed around the peak. The refresh period of the delay lags and Doppler bins is obtained after the results in Section 8.5. Optionally, the DDM is incoherently averaged (see Appendix D), and finally the results are sent to a host computer via Ethernet. This is a similar approach as done in [95] for the griPAU GNSS-R instrument.

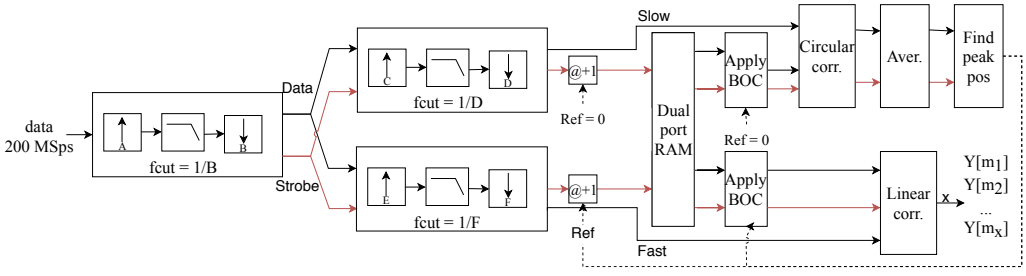

Figure 8.30: Proposed configuration to track the ACF peak in a window of X lags. The same PRN is generated simultaneously at 2 different rates. The one with lower rate is circularly correlated with the received signal in order to find the peak position. The one with higher rate is linearly correlated with the same signal only around the peak position. The synchronicity adaption of the signals is not shown.

Table 8.14: Resources required to downsample a signal from 200 MHz to 1.023 MHz by cascading 2 Xilinx IP FIR compilers v6.3 with a FPGA Kintex7 XC7K410T.

1.023										
First resampler			Second resampler		Resources first		Resources second		Total resources	
I	D	Throug.	I	D	DSP	18K RAM	DSP	18K RAM	DSP	18K RAM
3	400	1.5	341	500	2	3	2	3	4	6
3	500	1.2	341	400	2	3	2	3	4	6
11	400	5.5	93	500	2	3	2	3	4	6
11	500	4.4	93	400	2	3	2	3	4	6
31	400	15.5	33	500	2	3	2	3	4	6
31	500	12.4	33	400	2	3	2	3	4	6
341	500	136.4	3	400	2	3	2	3	4	6
341	400	170.5	3	500	2	3	2	3	4	6
93	500	37.2	11	400	2	3	2	3	4	6
93	400	46.5	11	500	2	3	2	3	4	6
33	500	13.2	31	400	2	3	2	3	4	6
33	400	16.5	31	500	2	3	2	3	4	6

Since the circular correlation is used only to find the peak, the burst mode given in Fig. 8.10a is used in order to use less FPGA resources. The linear correlation is the one given in Fig. 8.7b and with $b_x = 8$ bits. The sampling frequencies are $50 \cdot 1.023 = 51.15$ MSps for the linear correlations and 1.023 MSps for the circular one. The MIR front-end samples the data at 200 MSps, this means that fractional downsampling is required in order to achieve the desired rates. This can be efficiently implemented with polyphase filters (e.g. [208]). However, the ratios are too large to implemented in a single IP core, and thus, two consecutive polyphase filters must be used.

The downsamping ratios and the required resources are summarized in Tables 8.14 and 8.15. Note that the order of the two re-samplers impacts on the required resources. One strategy is to use the combination that uses less resources. However, it is also interesting to see that since both frequencies are multiples of each other, the first re-sampler can be shared. Figure 8.16 shows the two possible combinations that allow this configuration. Although for this particular case, this strategy uses more resources than using 4 polyphase filters, it may relax the synchronization complexities between them.

8.7 Conclusions

This chapter studied the feasibility of different CPU and GPU architectures to obtain DDMs in real-time. They have been compared in terms of run-time and memory resources. Results show that mass market GPUs can be used for said task. A run-time slope as low as 0.03 was obtained using an affordable GPU to process 1ms incoherent waveforms. The slope increased up to 1.21 when using a C program running over a modern CPU.

Table 8.15: Resources required to downsample a signal from 200 MHz to 51.15 MHz by cascading 2 Xilinx IP FIR compilers v6.3 with a FPGA Kintex7 XC7K410T. Green filled rows show the configurations that use less resources.

51.15										
First resampler			Second resampler		Resources first		Resources second		Total resources	
I	D	Throug.	I	D	DSP	18K RAM	DSP	18K RAM	DSP	18K RAM
3	8	75	341	500	38	4	2	3	40	7
3	10	60	341	400	32	4	2	3	34	7
11	16	137.5	93	250	26	4	2	3	28	7
11	20	110	93	200	18	4	2	3	20	7
11	25	88	93	160	14	4	2	3	16	7
11	32	68.75	93	125	12	4	2	3	14	7
11	40	55	93	100	10	4	2	3	12	7
31	32	193.75	33	125	12	4	6	5	18	9
31	40	155	33	100	12	4	6	5	18	9
31	100	62	33	40	6	5	6	5	12	10
31	50	124	33	80	8	4	6	5	14	9
31	80	77.5	33	50	6	5	6	5	12	10
341	500	136.4	3	8	2	3	28	4	30	7
341	400	170.5	3	10	2	3	28	4	30	7
93	250	74.4	11	16	2	3	10	4	12	7
93	200	93	11	20	2	3	10	4	12	7
93	160	116.25	11	25	2	3	10	4	12	7
93	125	148.8	11	32	6	5	10	4	16	9
93	100	186	11	40	6	5	10	4	16	9
33	125	52.8	31	32	6	5	6	5	12	10
33	100	66	31	40	6	5	6	5	12	10
33	40	165	31	100	10	4	6	5	16	9
33	80	82.5	31	50	6	5	6	5	12	10
33	50	132	31	80	8	5	6	5	14	10

This chapter has also given FPGA architectures to create the GNSS PRNs and the BOC sub-carriers for the modern signals. By using LUT tables, these signals can be easily generated and synchronized with the respective PRNs if the sampling frequency is multiple of the fundamental rate 1.023 MHz.

The FPGA resources has been deeply studied for different linear and circular correlators. Additionally, a new efficient architecture for a sample-to-sample correlator (either for the conventional or interferometric processing) has been assessed. The impact of quantization, sampling frequency and other configuration parameters have been also analyzed. If a circular correlation is used, the sampling frequency should be such that the number of samples in one PRN is as close as possible to the FFT length, in order not to reduce the peak power.

Finally, an acquisition and window tracking architecture has been proposed. First the circular correlation is performed between the clean replica with a downsampled and

compressed version of the incoming signal in order to find the peak position. Then, the linear correlator is performed around the desired delay lags and Doppler bins. The relationship between the refresh rate in both the delay and Doppler dimensions, and the DDM area has been simulated for the conventional and interferometric cases.

There are two issues here that have been let for future improvement. First, to explore secondary codes alignment architectures that can be used in real-time. Second, to investigate shared memory strategies between GPU and operating systems, in order to further increase the run-time performance.

Table 8.16: Common interpolator (A) and decimator (B) to downsample a signal from 200 MHz to 1.023 (further interpolate with C and downsample with D) and to 51.15 MHz (further interpolate with E and downsample with F). See Fig. 8.30. Green filled rows show the configurations that use less resources.

51.15 & 1.023							
A	**B**	**C**	**D**	**E**	**F**	**DSP**	**18K RAM**
341	500	3	400	3	8	42	10
341	400	3	500	3	10	36	10

Part III

MIR Instrument: Description and Results from the Field Campaigns

9

Chapter 9
MIR Instrument Description

This chapter describes the MIR instrument, and its precursor Multi-band Airborne L-band reflectometrY with GNSS (MALYGNSS). MIR is an airborne GNSS-R instrument with 4 pairs of beams with analog beamsteering capabilities, that samples direct and reflected GNSS signals at the L1/E1 and L5/E5A bands for remote sensing applications. The author's contribution to the instrument is focused on the back-end, which down-converts and samples the signals in order to obtain the GNSS-R observables a posteriori. The hardware of the instrument is the main goal of the Ph. D. thesis of Dr. Raul Onrubia [5], but is briefly summarized here for the sake of completeness. The bachelor thesis in [211, 212] have also contributed to this work.

The instrument progress has been successively published in [198, 213–219]. The full description was finally published in [220].

9.1 Introduction

The purpose of MIR was to state and face the problems of designing a GNSS-R space-borne instrument similar to the PARIS IoD or the GEROSS-ISS payload [6]. Although the development of these latter instruments was finally canceled, at least by now, other space missions that require similar technology may come in the next years. Two main goals were conceived in order to study the challenges of such instruments. The first goal was to design array antennas with large directivity beams and with beamsteering capabilities to be used to spatial filter undesired satellites. That would allow, in principle, to take advantage of the iGNSS-R technique by mitigating the cross-talk effects (see Chapter 6). The design of these arrays inherently requires a proper calibration method. The second goal was to implement real-time conventional and interferometric DDMs, and delay/Doppler peak tracking architectures. That would reduce the amount of data to be sent and stored in a host computer. Although this last problem is not a big issue for an airborne instrument, it is indeed for space-borne ones, where the available transmission bandwidth is critical. Bear in mind that from space-borne scenarios, only around 1% of a waveform has useful information.

The development of MIR has been a joint task between the author and Dr. Onrubia during the course of his Ph. D., and with the occasional contribution of few undergraduate students. The main task of the author was to develop the DSP part, and the main task of Dr. Onrubia was to design and develop the hardware, although both tasks are mutually dependent, especially in the calibration system and in the communication between devices.

The initial design of MIR considered a complex system formed by two dual-band antenna arrays (one up- and one down-looking), 4 Software Defined Radio (SDR) devices with FPGAs, an embedded system, a commercial GNSS receiver and other attitude determination elements. All the subsystems had to be controlled by a host computer. The arrays would be able to analog track up to 4 different pairs of satellites/reflection points at the GPSs L1/Galileo E1 and GPSs L5/Galileo E5a bands (2 beams per band), and the beams would be sampled with the SDRs. The embedded computer would combine the data from GNSS receiver with the angular information to choose the desired satellites to be tracked, and would resolve the pointing angles of the arrays. The embedded computer would also tell the SDR devices the PRNs to correlate with, and an estimation of the Doppler. The computation of the DDMs was intended to be done in real-time in the FPGAs, which would finally send just the area around the peak to the host, thus on-board computation of DDMs would allow continuous mapping of the Earth.

The hardware was successfully implemented. However, several problems encountered during the development of the correlators, limited the expected performance of the real-time processing (see Chapter 8). Real-time correlators were tested satisfactorily with real

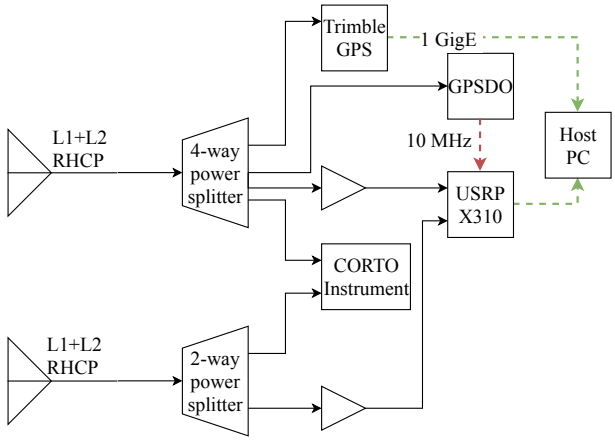

Figure 9.1: Block diagram of MALYGNSS.

GPS L1 C/A signals and even with synthetic Galileo pilot signals (i.e. signals without secondary codes and data components generated with a laboratory equipment). However, the reliability of correlation and tracking architectures was reduced when acquiring the true signals with secondary codes. Additionally, although the SDR brochure stated that they were user configurable, it was especially difficult to adapt the communications with the host computer to meet the instrument requirements. For these reasons, the SDR part was simplified to just sample the beams with 1 bit complex samples in order not to fill the host hard drive and to be able to perform field campaigns of several hours. As stated in Chapter 7 sampling with 1 bit does not substantially reduce the SNR. Although the second main goal of the instrument was not accomplished per se, the work done has revealed some issues that should be considered for future designs, and solutions are proposed in Chapter 8, and some FPGA example codes are given in Appendix D.

The MIR rackmount and antenna sizes, and the power consumption were designed to fit the requirements of a specific aircraft that would be used in field campaign tests in Australia together with Monash University. However, a chance to fly MIR as an opportunity sensor in the HUMIT project from the Institut Cartográfic i Geológic de Catalunya (ICGC) appeared in fall 2017. By then, MIR was not fully finished, and in fact, the antenna arrays would not have fitted in aircraft sensor apertures. A simplified version of MIR using comercial antennas and only 1 SDR instead of 4 was designed and named MALYGNSS. Results of the flight are presented in Chapter 10. The complete MIR finally flew on 4 occasions in Australia in spring 2018, one near the coastline of Melbourne, one at the Bass Strait, and two times over Yanco (NSW) fields, one before and one after the rainy season. Initial results are shown in Chapter 11. This chapter

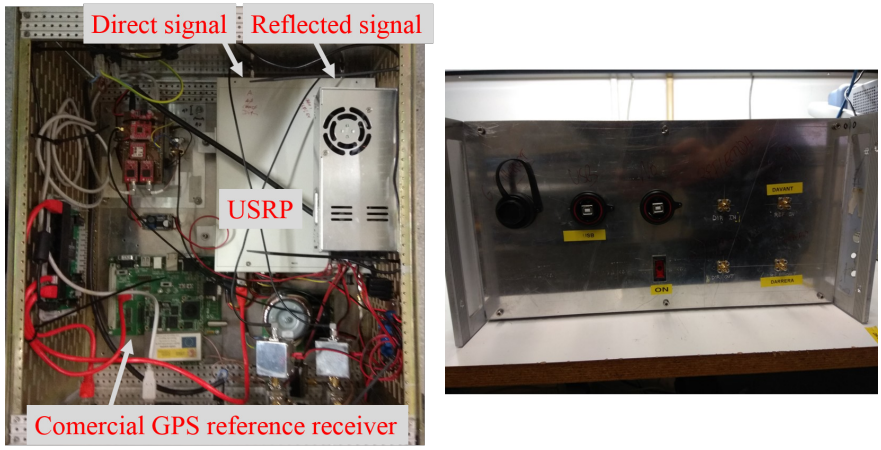

(a) **(b)**

Figure 9.2: MALYGNSS pictures: (a) some parts including the USRP X310 dual-channel receiver, two power amplifiers and the reference GPS receiver; and (b) rackmount.

continues with the details of MALYGNSS and MIR instruments, with special focus on the calibration and DSP of the latter.

9.2 MALYGNSS general overview

MALYGNSS is a dual-band GNSS-R instrument at the GPS L1/L2 bands that samples the direct and reflected signals at 8.184 MSps with 16 bits complex samples. The back-end is a dual-channel Ettus Universal Software Radio Peripheral (USRP) X310 with a GPS disciplined oscillator (GPSDO) that provides precise time-stamping and a high accuracy reference clock. Since just one USRP was used, it was possible to receive only one band at a time. Thus, consecutive acquisitions of 60 seconds were taken at each band with a gap of $\sim$ 1 second between them. MALYGNSS also flew together with the CORTO instrument [221], that has a commercial GPS receiver and compares the SNR of the direct and reflected signals so as to get the reflectivity of the terrain. A block diagram of the instrument is sketched in Fig. 9.1 and photos are shown in Fig. 9.2. Next paragraphs briefly explain the different parts of the instrument.

9.2.1 Front-end

The up- and down-looking antennas are commercial antennas at RHCP and LHCP respectively. The up-looking antenna is from Sensor Systems Inc., and has a bandwidth at -10 dB of 20 MHz at L1 and of 20 MHz at L2. The down-looking one is from Antcom Corporation with a bandwidth at -14 dB of 24 MHz for both bands. Both antennas are

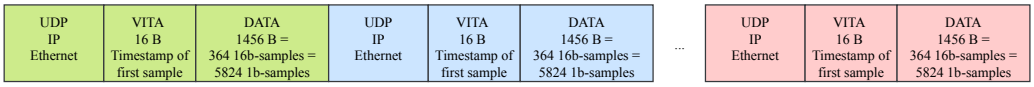

Figure 9.3: Ettus packet structure over IP/UDP.

active with an approximately gain of 40 dB. One amplifier for each branch gives an extra 20 dB gain. Detailed information of the front-end can be found in [222].

9.2.2 Back-end receiver

The Ettus USRP family devices are versatile SDRs highly used in research in a wide range of different applications. Ettus refers to the USRPs as *motherboards*, and they can be either receivers and/or transmitters depending on the *daughterboards* placed in their available slots. Different daughterboards allow to transmit and/or receive at different bands. In an USRP used as a receiver, the daughterboards amplify and down-convert the signals, which are then sampled in the motheboard with an ADC, and followed by a FPGA, which frames the samples in User Datagram Protocol (UDP) packets, and sends them to a host computer via Ethernet. These UDP packets also have an extra header for time-stamping (see Fig. 9.3). The FPGA comes with some elementary DSP, and with an embedded CPU that configures and controls all the elements of the USRP, such as the RF filters, amplifiers, down-converters, or the reference clock selection via Serial Peripheral Interface (SPI) or General Purpose Input/Output (GPIO) ports. The USRPs are configured and controlled via the host computer with the USRP Hardware Driver (UHD). These drivers, the FPGA source code, and the *firmware* (i.e. the code running inside the CPU) are all open-source.

The USRPs can use either an internal or an external 10 MHz reference clock, and Pulse-Per-Second (PPS) signals. The reference clock can be internally generated with the motheboard Crystal-Controlled Oscillator (XCO), externally injected, or also internally generated with a GPSDO. The PPS is an optional external used for time synchronization between devices or for a high accuracy time-stamping.

The USRP used for MALYGNSS is a dual-channel x310 with two single-channel DB-SRX2 receiver daughterboards (see a simplified block diagram in Fig. 9.4). The DBSRX2 boards can receive signals in the 800 MHz-2.3 GHz band with a RF bandwidth up to 60 MHz. The ADC of the motherboard samples the signals at 200 MSps with 14 bits complex samples. The FPGA is a Xilinx Kintex7 XC7K410T. The USRP is programmed to use an internal GPSDO with the current GPS time. The GPSDO provides a reference signal with a frequency stability of <1 parts-per billion (ppb), and PPS signal with an accuracy of 50 ns.

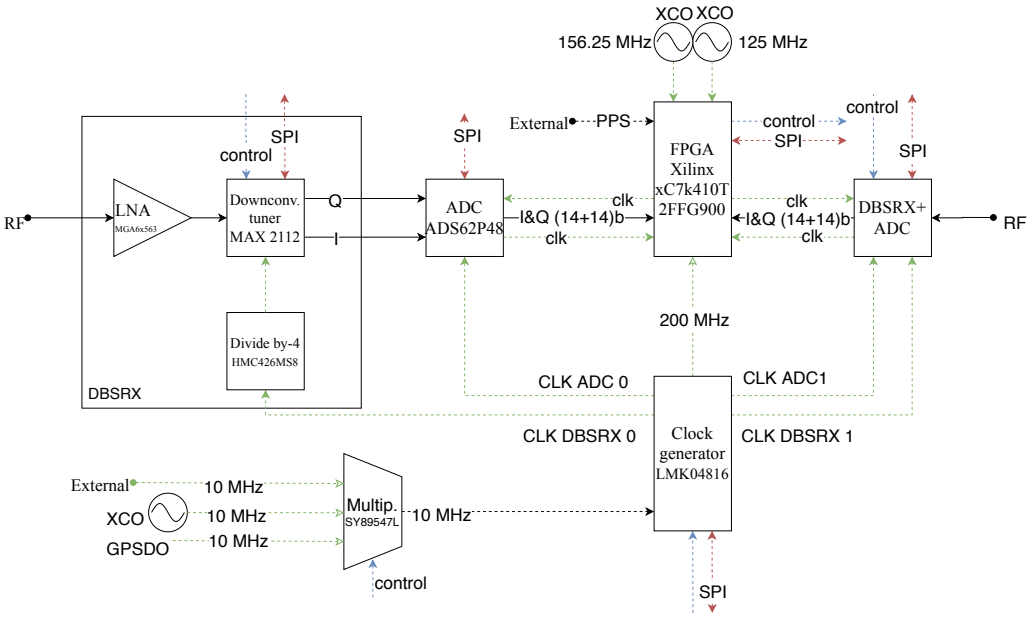

Figure 9.4: Simplified block diagram of the USRP X310 when used as a receiver.

9.2.3 DSP

The original Ettus DSP allows, in principle, to set the sampling rate from the host via the UHD drivers. However, the configuration is limited to rates that are divisors of the FPGA main 200 MHz clock. Since the original idea of MIR was to generate the PRNs internally, the DSP was modified to downsample the signal from 200 MSps to 8.184 MSps (8·1.023 MSps) with 16 bits complex samples. This rate was used because, as stated in Chapter 8, rates that are multiple of the fundamental rate 1.023 MHz, allow to efficiently generate the PRNs. The downsampling is done by cascading the interpolators and decimators as shown in Fig. 9.5, since it is the configuration that uses less FPGA resources (see Section 8.6). The simultaneous sampling of the direct and reflected signals, utilizes around 65% of the bandwidth of the Gigabit Ethernet channel.

9.2.4 Attitude and positioning determination

The CORTO instrument has a low-cost IMU with a data-logger that stores the attitude of the aircraft. Additionally, the aircraft is also equipped with a professional IMU which is the one actually used for flying. Both data are available for a proper processing of recorded GNSS signals.

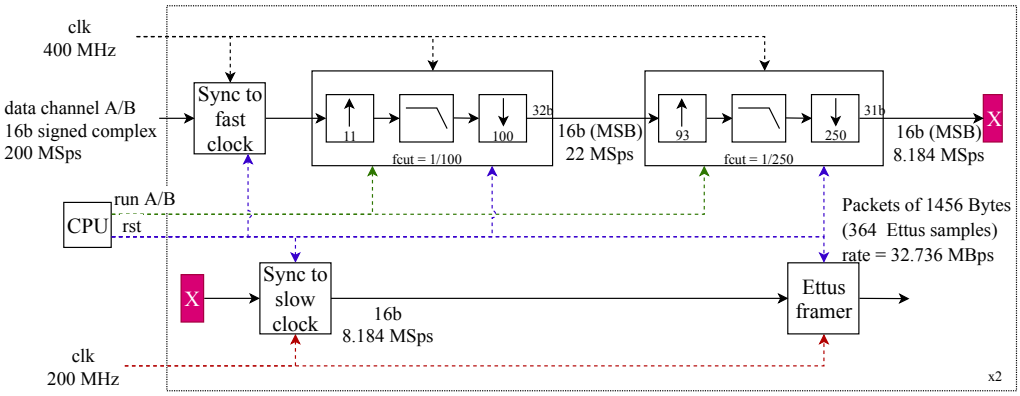

Figure 9.5: Block diagram of the DSP of MALYGNSS.

9.2.5 Software

The software running on the host computer is very similar to the one used for MIR. It is described in Section 9.4.

9.3 MIR hardware overview

This section summarizes the work done by Dr. Onrubia in his thesis [5]. The design of each board, most of the manufacturing, and the whole integration, including the rack has been done in the laboratory facilities by him. The antenna and front-end were formerly introduced in [213] and detailed in [215, 216]. An overall description of the instrument can be found in [220], and in [5].

MIR has an up- and down-looking antenna arrays centered at the GPS L1/Galileo E1 and GPS L5/Galileo E5a bands. Each antenna can steer two beams per band using analog beamformers, thus up to 4 different transmitters and 4 reflected points can be received at the same time. The beamsteering is controlled by an embedded system Wandboard Quad [**?**] that chooses the satellites to be tracked based on an algorithm that tries to select satellites from different constellations if their elevation angle is high enough. The selected satellites are updated approximately every 10 minutes. The steering angles are obtained from the position given by a commercial GPS Trimble BD982 receiver, and from the attitude inferred with an IMU and with an inclinometer. Each beam is continuously sampled at 32.736 MSps with 1 bit complex samples using 4 dual-channel USRPs X310 and stored in a host computer via Gigabit Ethernet. A common clock and a time synchronization signal is used among devices. An overall block diagram of the instrument is presented in Fig. 9.6, and pictures are shown in Figs. 9.11 and 9.12.

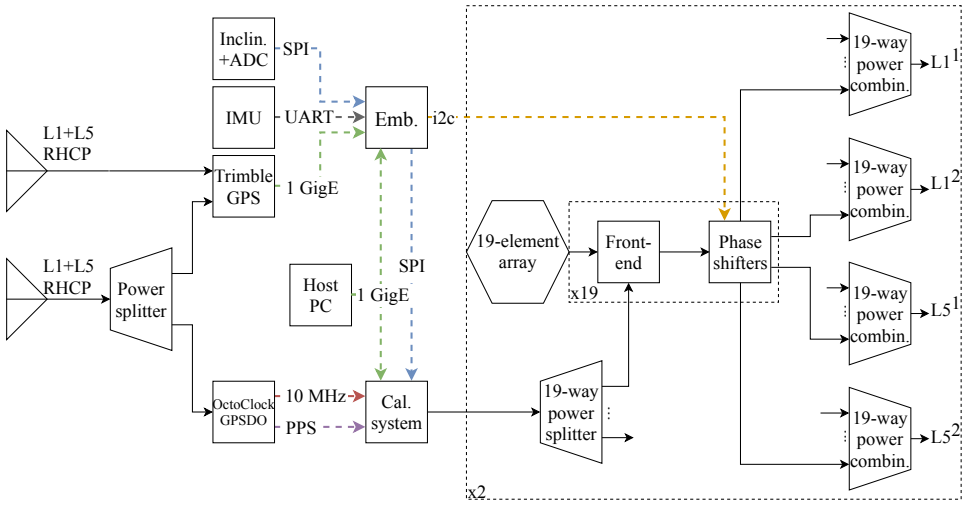

Figure 9.6: Block diagram of MIR.

The amplitude and phase calibration of all the RF channels is done by injecting a known PRN signal to each one of the elements that form the arrays. This signal is generated with an USRPs N210 at intermediate frequency and further up-converted to the the L1 and L5/E5a bands. The cables used in the calibration system were characterized in the laboratory. A detailed description of the calibration procedure is presented in [220], and it is summarized in section 9.6. Next paragraphs further explain the hardware parts and subsystems of MIR.

9.3.1 Antennas

The up- and a down-looking antennas are both 19 element symmetrical hexagonal arrays. The polarization is RHCP for the up-looking antenna and LHCP for the the down-looking. The antenna elements are dual-layer patches centered at the GPS L1/Galileo E1 (1.57542 GHz) and at the GPS L5/Galileo E5a (1.17645 GHz) bands with a bandwidth at -10 dB of 21 MHz at the L1/E1 band, and of 34 MHz at L5/E5a band. These patches were specifically designed for the instrument and were patented in [223]. The element spacing is $0.752\lambda_{L1}$ or $0.561\lambda_{L5}$, and if the array is fed with an uniform current distribution, the directivity at boresight is 20.3 dB for the L1/E1 band, and 18.2 dB for the L5/E5 band. The secondary lobes when pointing at boresight are -15 dB for both bands. These values were measured in the anechoic chamber of the Antenna Lab. at UPC [224].

Figures 9.11a and 9.11b show respectively a photo of one patch and the up-looking antenna. The size of the arrays with the ground plane are 800x800x60 mm for the up-looking and 929.64x929.64x60 mm for the down-looking. The down-looking antenna is

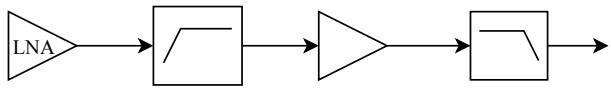

Figure 9.7: Block diagram of the patch antenna front-end.

larger because MIR was originally designed to fit into a specific airplane. While the down-looking antenna was made to be placed at the belly of the plane, the up-looking was designed to fit in the rear part of the cabin (see Section 11.1.1 for pictures). The fuselage of the aircraft is made of carbon fibers, thus not blocking the reception of the GNSS signals. The down-looking array was wrapped with vinyl fiber to protect it from humidity, rain and wind.

9.3.2 Patches front-end

The signal coming from each patch is amplified with a Low-Noise Amplifier (LNA) of 15 dB at L1 and filtered to remove out-of-band RF signals using a high-pass filter with a bandwidth at -3dB of 880 MHz (see Fig. 9.7). The signal is further amplified again with 22 dB at L1 and low-pass filtered with a bandwidth at of 1825 MHz -3dB. The gain of the amplifiers at L5 is a little bit larger. The LNAs are located immediately after the patches, inside the arrays (see Fig. 9.11c).

9.3.3 Beamformers

After the frond-end, each signal is split into two branches, one band-passes the L1/E1 signals, and the other branch band-passes the L5/E5a signals (see Fig. 9.8). The filters bandwidth at -3dB are 75 MHz at L1/E1, and 60 MHz at L5/E5a. After filtering, the signals are divided again by two so as to generate two beams per band. The beam steering is performed with I/Q vector modulators driven by Digital Analog Converters (DACs). Their value is programmed by the embedded system via an Inter-Integrated Circuit (I^2C) network at 3 Hz. The vector modulators allow the control of the phase up to 4.9° error and the magntiude up to 0.03 dB error after calibration. The impact of these errors on the array directivity is less than 0.1 dB. Note that the signals have been pre-amplified with 17 dB at L1 because the vector modulators are very noisy. Finally, the 19 signals of each array are combined to create the beams. A picture of the a phase shifter board is shown in Fig. 9.11d, and a picture of one combiner is shown in Fig. 9.11e.

The four beams of each array are mounted in the same structure (see Figs. 9.11g and 9.11f). Since these structures can warm up to 50°C, holes were made on the top and on one side, and fans were installed in order to remove the heat (not shown in the pictures).

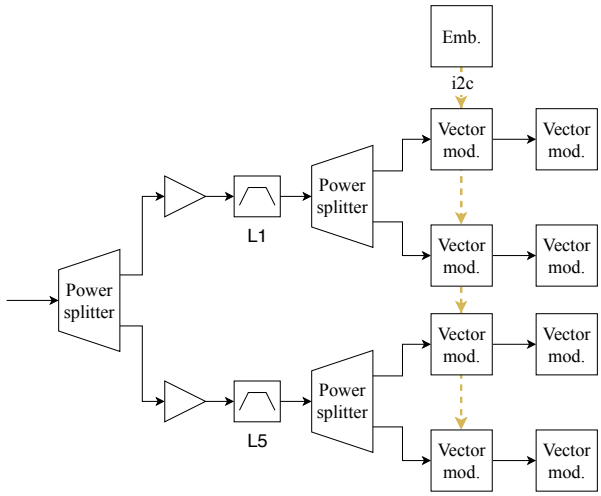

Figure 9.8: Block diagram of a phase shifter.

9.3.4 Calibration system

The calibration system is presented in Fig. 9.9 and a photo in Fig. 9.11h. The USRP N210 generates a BPSK signal of 50 MHz centered at 100 MHz. The signal is then split into two branches and low-pass filtered to remove the replicas produced by the USRP N210 (see Section 9.5.1 for details). The bandwidth of this filter at -3dB is 158 MHz. The signals are then up-converted to the GPS L1/Galileo E1 and to the GPS L5/Galileo E5 bands and filtered again with a bandwith of 100 MHz at -3dB in order to remove any spurious signals and up-conversion replicas. The up-conversion tones are generated with a programmable fractional frequency synthesizers with less than 0.1 Hz error via a SPI. Finally, the up-converted signals are combined together and injected to each front-end with two 19-way power splitters (one for each array). These latter combiners are placed inside the array structures.

The calibration system is controlled by the host computer and by the embedded. The former tells to the latter, to the USRP N210, and to the USRPs X310 to start or to stop the calibration mode. The embedded activates or deactivates the synthesizers.

9.3.5 USRPs X310 frame

The 8 beams are connected by pairs of respective direct and reflected signals to the 4 USRPs X310 (see Fig. 9.10). The down-looking beams are further amplified with 35 dB at L1 because the USRPs are noisy and have low sensibility (see Section 9.6.4 for details).

The USRPs down-convert the signals to baseband and sample them at 32.736 MSps

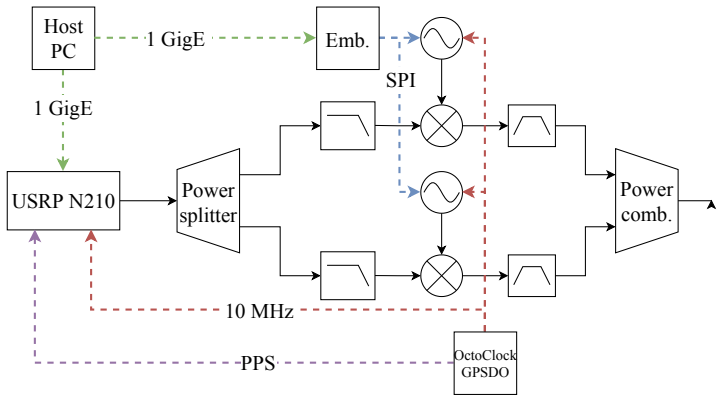

Figure 9.9: Block diagram of MIR calibration system.

with 1 bit complex samples. The samples are framed in UDP packets of 5824 samples and are sent to the host computer via Gigabit Ethernet. Each USRP channel uses a different port. This sample rate uses an overall Ethernet bandwidth at only 52.3% of its capability. This value was selected because several problems were encountered during the test stages that seriously limited the reliability of the transmission and/or storing of the data. Either the Ethernet switch, board and cables, and the hard drive write speed (even with a solid state one) are a serious bottleneck for continuous sampling at the required rates.

9.3.6 Reference frequency and time synchronization

The USRPs and the synthesizers of the calibration system have a common 10 MHz reference clock. The USRPs also share the same time synchronization PPS. Both reference signals are generated with a 8-port OctoClock. The OctoClock has a GPSDO that gives a frequency accuracy of less than 1 ppb if a GPS antenna is connected and a navigation solution is available, or 25 ppb otherwise. The PPS has an accuracy of 50 ns.

9.3.7 RF cables

MIR has 268 RF semi-flexible cables with SubMiniature version A (SMA) connectors of different lengths grouped in bundles of 19. The maximum measured phase error within these bunches is 2° at L1.

9.3.8 Power supply

MIR has three power supplies. One of 12 V for the 4 USRP X310; one of 7.5 V for the beamformers and the arrays; and one of 5 V for the additional amplifiers of the reflected beams, the whole calibration system, the Trimble GPS, the inclinometer, the IMU and the embedded. The host computer has its own power line. The overall power consumption

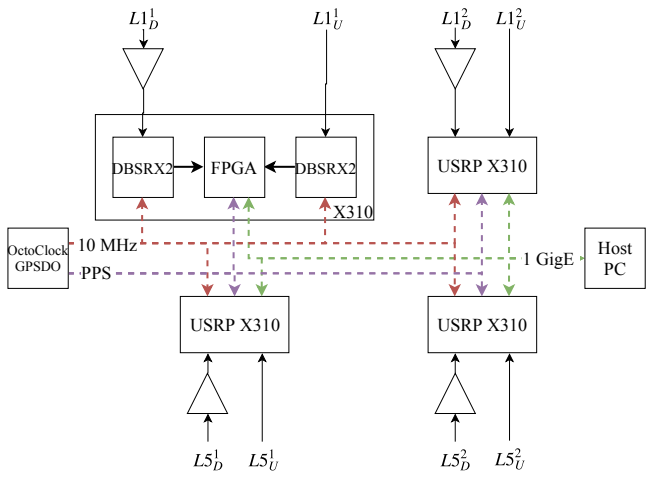

Figure 9.10: Block diagram of MIR back-end.

without the laptop is 470 W.

9.3.9 Rackmount

All the MIR elements except the arrays are assembled in a rackmount structure of 570x500x470 mm made with standard aluminum profiles of 30x30 mm. Some modifications have been done with respect to the pictures in Fig. 9.12 to fit the requirements of the test measurements and for the anechoic chamber characterization. The overall weight of MIR including the antennas is 110 kg.

9.3.10 Position and attitude determination

The user position and the ephemeris from the satellites are obtained with the Trimble receiver using the same commercial multi-band Antcom GNSS antenna used for MALYGNSS (see Section 9.2). The receiver is connected to the host, which logs all the data via Gigabit Ethernet.

The attitude is derived from a 9 Degrees of Freedom (DoF) Razor IMU and from a Seika NG-4 inclinometer sampled with an ADC. The IMU is connected to the embedded computer via a Universal Asynchronous Receiver-Transmitter (UART), and the ADC via SPI. The average sampling rate for both devices and for the Trimble is 10 Hz. Since the IMU sometimes fail to respond, an additional GNSS antenna was connected to the Trimble receiver. Both antennas are located in the same ZX plane, which allows the inference of the heading by properly combining the two navigation solutions.

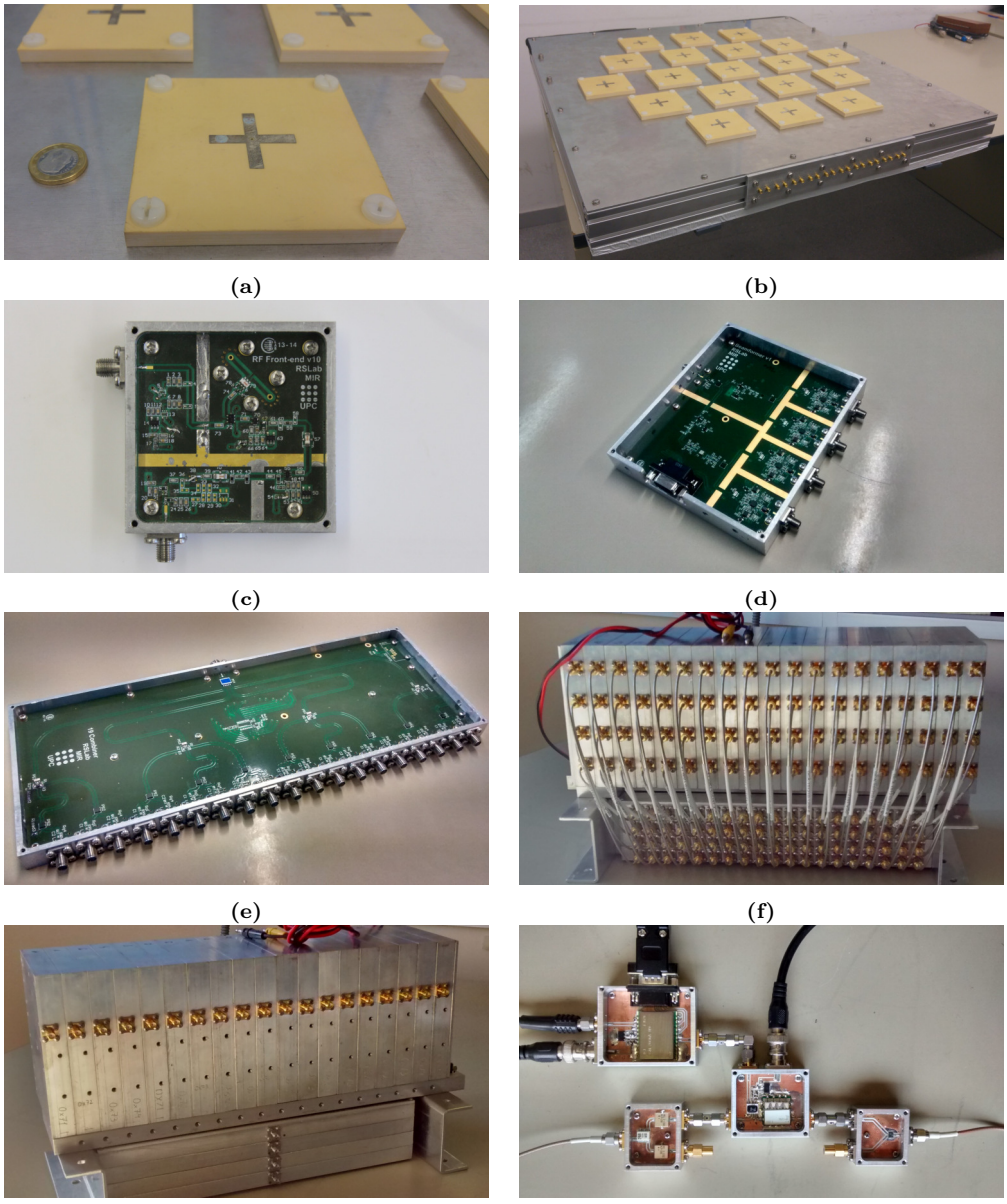

Figure 9.11: Pictures of some the MIR parts: (a) L1/L5 dual-band patch antenna, (b) up-looking 19-elements hexagonal array, (c) front-end (rear of the patch), (d) 4 channels phase-shifter box, (e) 19-way power combiner, (f) 4 beams analog beamformer containing 19 phase-shifter boxes and 4 19-way power combiners, (g) previous picture seen from the other side, and (h) calibration signal up-converter. From [5].

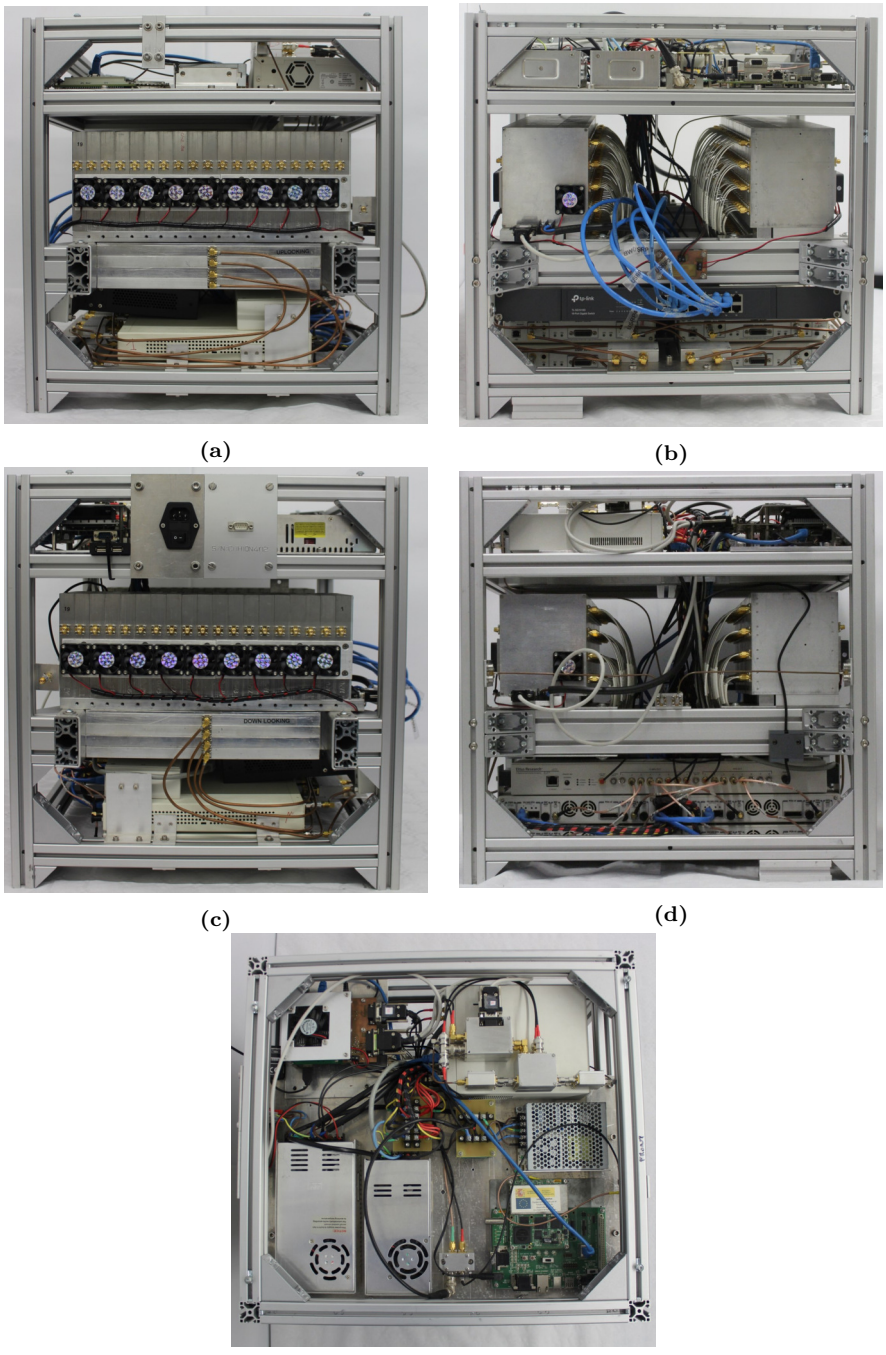

Figure 9.12: Photos of the MIR rack. Top level contains the power supplies, the embedded, the Trimble GPS receiver, and the full calibration system. Middle level contains the 8 beamformers. Bottom level contains the 4 USRPs x310, the OctoClock, the Ethernet switch, and the additional amplifiers used in the down-looking beams.

9.4 MIR Software

There are five different software programs running simultaneously in MIR. The first operates in the embedded and controls all the MIR systems except the USRPs. The second is executed on the host computer and sets up the embedded computer. The third also runs on the host, controls all the USRPs and stores the raw data. The last two, are firmware programs running in ZPU microprocessors embedded in the FPGAs of the USRPs. The firmware set up the chips inside the USRPs.

9.4.1 Embedded and host-embedded software

The software that runs on the embedded computer and the one that controls the latter on the host computer, are part of the work done in [5]. This section briefly describes the first program. The second is a simple program that wakes up or switches off the embedded computer.

The embedded program is a C application over Linux. The fact that the embedded computer has four cores, allows the use of multiple threads. This helps to reduce the time needed to configure all the subsystems. The program runs either in normal mode or in calibration mode.

9.4.1.1 Normal mode

In normal mode, the program continuously configures the 8 beams to point to a specific satellite or reflection point. In order to do so, it manages the vector modulators via two I^2C links. The pointing angles are derived from the the data obtained from different sensors and from the calibration parameters. Those sensors are the Trimble GNSS receiver, the IMU, and the inclinometer.

The embedded computer is connected to the Trimble receiver via TCP/IP and via USB. From the TCP/IP link, the embedded computer receives the GPS time, the vehicle position, the clock errors, the aircraft attitude, and the azimuth, elevation and SNR of the GNSS satellites in view. The update rate from all these values is either 1 Hz or 10 Hz. From the USB link, the embedded gets the Doppler and the SNR of the same satellites, at 1 Hz rate.

The embedded computer is connected to the IMU via USB, from where it gets an other estimation of the attitude of the aircraft at a rate of 10 Hz. Finally, the connection to the inclinometer is done through SPI, and the data rate is on demand. All this information is combined, and the desired satellites to be tracked are computed with the algorithm introduced earlier in this chapter. Note that some information obtained from different

sensors is redundant. This is so because it was observed that some data packets were malformed. Some sensor data is also stored in a Secure Digital (SD) card for later post-processing and debugging.

9.4.1.2 Calibration mode

In calibration mode, the program deactivates all the vector modulators and switches off the switches of all the front-end, except those corresponding to the central element of the array. It then enables the up-converters and mixers of the calibration system via SPI. The process is repeated iteratively for the 8 beams.

9.4.2 Host-USRP software and FPGAs firmware

The program running over the host, is a C++ program that controls all the USRPs by using the 3.8.5 UHD drivers. The firmware are the original Ettus versions. They manage the Ethernet port; and the clock generators, donw-converters, up-converters, ADCs, DACs, and any other chip via SPIs or dedicated lines. This section explains the host program.

Before explaining the tasks for the program, it is worth giving some comments here regarding the UHD drivers. These drivers are open-source, and the use of their functions is well documented. The functions provide top level user instructions to set up the USRPs. However, to the opinion of the author, there is a lack of documentation on how these instructions are translated into the final commands sent to the USRPs. The next examples may help to understand the problems faced when developing this software.

The drivers generate the down-conversion frequency first by configuring the analog down-converter to its closest possible frequency, and then by removing the residual frequency digitally in the FPGA. However, this latter digital block is generic, and some residual error may still be present. A user willing to generate a specific frequency, has to build a dedicated DSP, but bearing in mind the down-conversion factor already performed by the analog chip. A similar issue happens when setting the gain and the filter bandwidth. Both values are achieved by configuring different elements, either analog or digitally, at different stages.

Another difficulty associated with the drivers is the setting the sampling frequency. The ADC of the USRPs X310 is fixed to 200 MSps. The frequency set with the drivers is achieved digitally by using a generic DSP block. However, not all the resampling frequencies can be synthesized. A user building a dedicated digital downsampler will have to bear in mind that other blocks in the FPGA may be expecting to handle data at a different rate.

One extra obstacle is that there is no friendly way to communicate user instructions to the USRPs X310, as there is for the USRP N210, which has a dedicated user register. Sending specific commands to the USRPs X310 is needed in order to change between the calibration and normal modes. This issue has been solved by using the registers reserved to set the sampling frequency, as this value has been hard-coded in the DSPs. In order to do so, the drivers have been modified, and an additional register control block has been implemented in the FPGAs.

Moreover, the DBSRX2 daughterboards, which are the boards mounted in the USRPs X310, that down-convert the signals, were not originally supported by the drivers, even though in the commercial brochure it stated that they were. On top of all that, some DBSRX2 boards functioned abnormally. A similar problem was encountered in the USRP N210, which could not generate the calibration signal at the desired carrier frequency, even though in theory it was supposed to be possible. All these issues were solved by modifying the drivers, and were reported to the Ettus company. The changes are given in Annex E.

Besides, there were three issues that caused high TCP/IP packet losses. The first issue involved the Ethernet bus. Although this bus was Gigabit Ethernet (GigE), a data rate of 1 Gbps was only supported as peak speed, but not sustained in time. In fact, during the instrument tests, it was observed that some Ethernet boards functioned better than others in terms of packet losses. The second issue involved the hard disk drive. The original disk planned for the instrument had a write speed of about 100 MBps. However, this value was again, a peak speed. Finally, the third issue involved the Windows 10 operating system. By default, Windows 10 has a file indexer and an anti-virus that run as background processes. This slowed down the writing of the files, and caused the data in the buffers to be lost.

By using a modern Ethernet board, a high speed Solid-State Drive (SSD), and by deactivating the Windows background processes, a sustained speed of 80 MBps was achieved with almost no packet loss. This is the rate in the calibration mode (2 channels transmitting 16 bit samples at 10 MSps), which is in fact, a burst transmission. However, in the normal mode, a rate of 65.472 MBps (8 channels transmitting 1 bit complex samples at 32.736 MBps) was used in order to have a larger safety margin. The reason will be further understood in next paragraphs, but the idea is that the samples are framed in packets of 1456 bytes, and sent to the Ethernet bus at the clock speed. This means that the 65.472 MBps or 32.736 MBps are in fact, average speeds, but not the actual ones. The Ethernet bandwidth used by all the other transmissions is negligible (i.e. the data sent by the sensors and all the low level protocol instructions sent by and to the host).

The last problem of the UHD drivers given here, concerns the function used to request the data from the receivers. This function allows the specification of the number of desired

Table 9.1: RF channel assignment table. Asterisks indicate malfunctioning boards (see text).

					Chan A:0				Chan B:0			
	IP	**Band**	**Beam**	**Serial n.**	**Serial n.**	**RF Port.**	**Signal**	**UHD chan.**	**Serial n.**	**RF Port.**	**Signal**	**UHD chan.**
USRP 1	192.168.2.11	L1	2	F4DF17F4E689	EFR1ET6D2	B	Ref.	0	EFR1ETED2*	A	Dir.	1
USRP 2	192.168.2.12	L1	1	F4DEE9F4E692	E3R27R2D2	B	Ref.	2	E4R2AQ6D2	A	Dir.	3
USRP 3	192.168.2.13	L5	1	F4DF01F4E356	EFQ29QDD2	B	Dir.	4	E6R2AQCD2	A	Ref.	5
USRP 4	192.168.2.14	L5	2	F4DF18F4E67F	E1R2AQ6D2*	B	Dir.	6	EER29QCD2*	A	Ref.	7

of samples. However, it was noticed that the first received samples in successive calls to the function, belonged to the previous acquisition. Not only that, but the number of old samples was not constant. That happened because the buffers inside the FPGAs were not reset properly before starting a new acquisition. This problem was overcome by building a flushing mechanism that kept asking samples to the USRPs after deactivating their acquisition blocks.

Returning to the topic of this section, the host software has three operating modes: initialization, normal and calibration. They are explained next.

9.4.2.1 Initialization mode

The tasks of this mode are to create and configure the so-called USRP *objects*, which are a collection of functions and variables that define the USRPs. The workflow is as follows.

1. Configures the USRPs X310.
   (a) Creates the USRP object that will manage all the USRPs X310, with the IP addresses given in Table 9.1.
   (b) Maps the 8 RF channels (labeled as *A:0* and *B:0* in the Table 9.1) to UHDs channels.
   (c) Sets the PPS signal and the clock reference as external signals across all the USRPs X310. Waits for 1 second to allow the changes to be done.
   (d) Sets the corresponding RF frequency to each channel. Waits for 1 second. As aforementioned, the resolution of the analog frequency synthesizers is limited. This translated into the next errors when aiming to generate the GNSS carrier frequencies: -2 Hz at L1, +2 Hz at L5/E5A, +3 Hz at E5, +5 Hz at E5B, and +2 Hz at L2.
   (e) Checks that the 8 Local Oscillators (LOs) are locked. As previously stated, the LOs of some DBSRX2 boards would not lock if it was not for the changes applied to the drivers.

Table 9.2: IP assignment table.

	IP
Host	192.168.2.1
Trimble	192.168.2.4
Embedded	192.168.2.5
N210	192.168.2.10
X310	192.168.11-14

(f) Sets a gain of 30 dB and a filter bandwidth of 40 MHz to the 8 channels.

(g) Sets a sampling frequency of 1 MSps across all the USRPs X310. Waits for 1 second. This sampling frequency is not the true one, as it is hard-coded in the FPGAs. However, this call is needed in order to launch other functions associated with the acquisition. As explained above, the sampling frequency register is used to switch the USRPs X310 between modes. The 1 MSps value used here is in fact arbitrary. The DSPs blocks developed for MIRs will tell the original ones to not stream data to the host when receiving this sampling frequency.

2. Configures the USRP N210.

   (a) Creates the USRP object that will manage the USRP N210, with the IP address given in Table 9.2.

   (b) Sets the PPS signal and the clock reference as external. Waits for 1 second.

   (c) Sets the transmission Intermediate Frequency (IF) to 100 MHz. Waits for 1 second. The original drivers do not translate this value into the correct USRP instruction. Instead, the drivers have been modified and hard-coded to do so.

9.4.2.2 Calibration and normal modes

The software operation during the normal and calibration modes is similar. Typically, before each field campaign, the user will first run the calibration mode, and then the normal mode. The step-by-step procedure is as follows.

1. Issues a start command to the USRP N210 in the calibration or a halt command in the normal mode. In this latter mode, the USRP N210 should have been already halted, but the command is sent for good measure.

2. Configures the streaming parameters.

(a) Creates and initialize the *stream args* object. This object defines the data format sent by the USRPs X310, the desired data format to be stored in the host computer, and enables or disables the UHD channels previously mapped in the USRP object. The data formats are both configured as complex 16 bit integer, but the channels enabled depend on the mode.

- In the normal mode, the 8 channels are enabled.
- In the calibration mode, just the 2 channels of a given USRP X310 are enabled.

(b) Creates a *rx streamer* object from the *stream args* object.

(c) Tells the enabled channels to switch either to the normal or calibration mode.

(d) Creates and initializes a *stream cmd* struct. This struct defines how the devices send the samples to the host, and when to start or stop streaming. Configuring this struct is essential in order to time-align the packets of the enabled channels.

i. Sets the stream method as continuous, also in the calibration mode. This is so, because it was observed that the drivers timed out when asking the number of samples desired for the calibration, probably because of an internal overflow.

ii. Gets the current Unix time from the operative system, and converts it to GPS time. A recent synchronization of the system time with an internet server is desirable. However, MIR was not designed to have internet access during the field campaigns. Instead, the operative system was configured to get the time from the Trimble GPS onboard MIR via Network Time Protocol (NTP).

iii. Sets this latter time to the time register of all the USRP X310. Waits for 1 second. The drivers synchronize all the channels by using the PPS signal.

iv. Sets the *stream cmd* struct to start the transmission 3 seconds after issuing the command. This value was found by trial-and-error.

(e) Issues the streaming command using the *rx streamer* object.

3. Creates one binary file to store the metadata, and as many other files as enabled channels (2 in the calibration mode and 8 in the normal).

4. Receives and stores the data continuously until either halt command is issued (normal mode) or a certain amount of samples have been received (calibration mode).

(a) Receives 1456 bytes (364 complex samples of 16 bits) for each channel, and associated metadata. The metadata refers to all channels. It contains the

timestamp of the first sample in GPS time format, and other error flags (if any).

(b) Saves the timestamp in the log file as double (8 bytes).

(c) Saves the raw data in the respective files as 16 bit complex integers.

- In the normal mode, the size of the files is 268,435,440 bytes, which corresponds to 1,073,741,760 MIR samples (1 bit complex), or about 32.8 seconds (at 32.736 MSps). Once this amount of samples is received, the program creates a new set of files, whose names include an index which increases at each iteration.
- In the calibration mode, the size of the files is 235,698,736 bytes, which corresponds to 58,924,684 calibration samples (16 bit complex), or about 5.9 seconds (at 10 MSps).

(d) The streaming stops until the following circumstances occur:

- In normal mode, the only way to stop the streaming is to abort the whole program by using an operating system command (i.e. Control+C). Bear in mind, that the size of the last files will depend on when the user has issued the abort command.
- In calibration mode, the program keeps asking for samples until it has received the 58,924,684 samples mentioned above.

5. Flushes the samples in the FPGA buffers that were not streamed to the host (only in the calibration mode).

   (a) Tells the devices to end the continuous streaming as soon as possible.

   (b) Keeps receiving samples, but without storing them, until the metadata flag that indicates the end of burst is received.

6. In the calibration mode, the program goes back to point 2, until the 4 USRPs have been calibrated.

7. Once all the USRPs X310 have been calibrated, the program issues a halt command to the USRP N210, and goes back to point 1.

9.5 MIR DSP on the FPGAs

The FPGAs inside the USRPs are described either in Verilog or in VHDL. The original Ettus code is open-source, and includes the blocks required to synchronize the devices

with the PPS signal, to configure the chips in the USRPs (see Fig. 9.4), and to manage all the communications ports, including the Ethernet. The Ettus code also includes some DSP blocks to up-convert, down-convert and resample the signals from the ADCs or to the DACs. The modifications of the FPGA codes done for MIR are in order to generate the calibration signal in the USRP N210, and to resample the signals from the beams in the USRPs X310.

To the experience of the author, there is a lack of documentation on how the overall original code is organized. Understanding the purpose of a Verilog/VHDL code is much more complex than doing so with typical programming languages, as the former languages are low level hardware instructions. Three main issues involving the original Ettus code have been addressed.

The first problem involves the time-stamping in the USRPs X310. The time-stamp refers to the time in which the first sample of an Ethernet packet is framed. However, this is not the actual time of the sample, since all the blocks previous to the framing add a latency. This would have been a subject of characterization in the original plan for MIR, which would have used many DSP objects and introduced a large latency. However, for this version of MIR, it was observed that the latency was negligible.

The second issue concerns the reset of the internal buffers inside the FPGAs between consecutive acquisitions in the USRPs X310, or transmissions in the USRP N210. Additional reset lines have implemented in order to properly restart the buffers.

The last issue regards the construction of the Ethernet packets in the USRP X310. The Ettus codes in the FPGA, firmware and drivers, expects an Ethernet packet with 364 complex samples of 16 bit width. That corresponds to 1456 bytes, which is the available user data of the Maximum Transmission Unit (MTU) in TCP/IP. Modifying the length of the packets or the samples width, would require heavy changes in all the codes. Instead, a re-framing block has been build prior the one of Ettus.

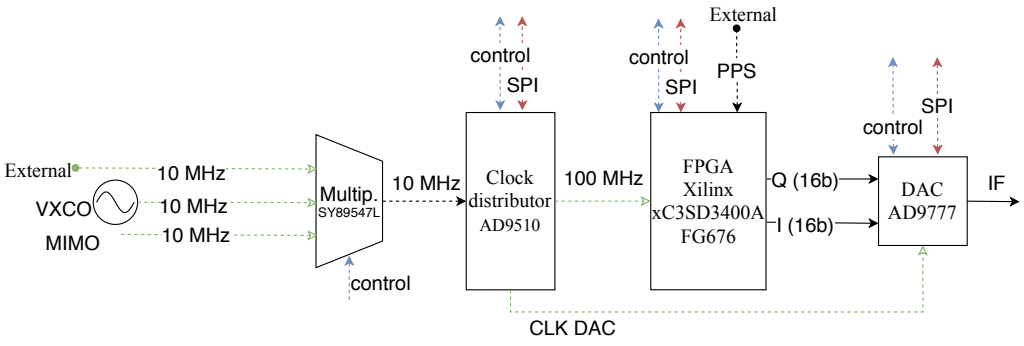

Figure 9.13: Simplified block diagram of the USRP N210 when used as a transmitter.

9.5.1 USRP N210

The USRP N210 is used to generate the calibration signal. Figure 9.13 shows a block diagram of the elements of the USRP involved in the transmission of a signal. The FPGA is a Xilinx Spartan 3A-DSP 3400.

Instrument calibration with tones, pulses or noise injection is well-known in radar and microwave radiometers (e.g. [34]). The first considered calibration signals for MIR were two tones at the GPS L1 and L5 frequencies. However, it was observed that the DBSRX2 boards have a Direct Current (DC) filter (see Fig. 9.14) that would filter out the tones. For this reason, a signal with a large bandwidth was finally implemented. As opposed to the tone calibration, this kind of signal would allow to infer the overall transfer function of the channel and the group delay from the slope of the phase response. The methodology to do so is given in Section 9.6.

The work in [225] proposed to use PRN sequences for the calibration of interferometric radiometers. The motivation of this work was to remove the distribution network complexities when using a common noise source. PRN sequences have similar properties to those of Gaussian noise. They have a sharp autocorrelation function and a flat spectrum over the desired bandwidth depending on the chip rate. Additionally, they are repeated cyclically, which allows averaging at the receiver.

The calibration signal for MIR is obtained by concatenating the GPS L5Q PRNs 33 to 42. However, the chipping rate is set to 10 MHz instead of 10.23 MHz. Furthermore,

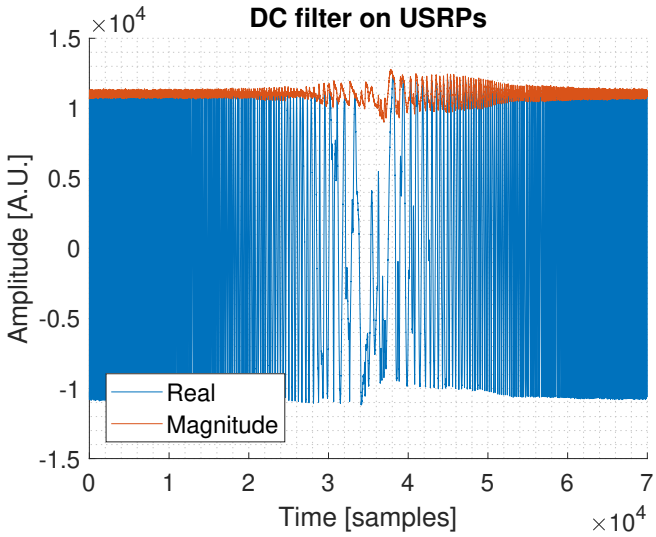

Figure 9.14: DC filtering on the USRPs X310 observed when injecting a chirp signal. Note the ripples of the transient state.

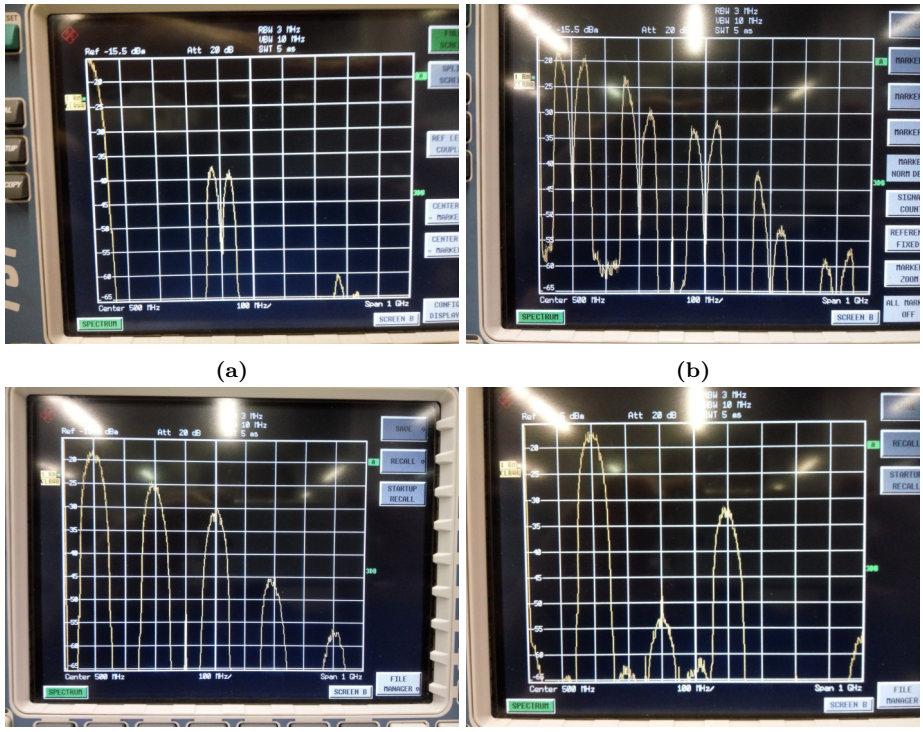

Figure 9.15: 4 modes of up-conversion by using DAC filter images. (a) No interpolation; and interpolation by 2 (b), 4 (c), and 8 (d).

the last 2300 chips are removed, thus the length of the signal is 100000 chips or 10 ms. The signal transmitted by the USRP has an IF of 100 MHz. This frequency was chosen in order to facilitate the use of comercial analog up-converters to the L1 and L5 carrier frequencies (see Section 9.3).

The 10 MHz rate is below the Nyquist bandwidth used to sample in the normal mode (32.736 MSps). This is so because of the way the signal is up-converted to 100 MHz. The signal is placed at such IF not by multiplying its baseband version with a tone, but by taking advantage of the DAC filter images. By configuring the DAC clock and its *mode*, the signal can be up-converted to different frequencies. Figure 9.15 shows the generated analog signal with the 4 modes of operation when using as digital signal the calibration signal, but with a chipping rate of 25 MHz instead of 10 MHz. Note that the analog signal will need to be further filtered in order to get the desired lobe. Other IFs can be obtained by up-converting first the digital signal. However, the DAC mode, and the digital signal IF and bandwidth, need to be chosen properly so as to avoid overlapping between the alias. For this reason, a chipping rate of 10 MHz used. Note finally the sinc

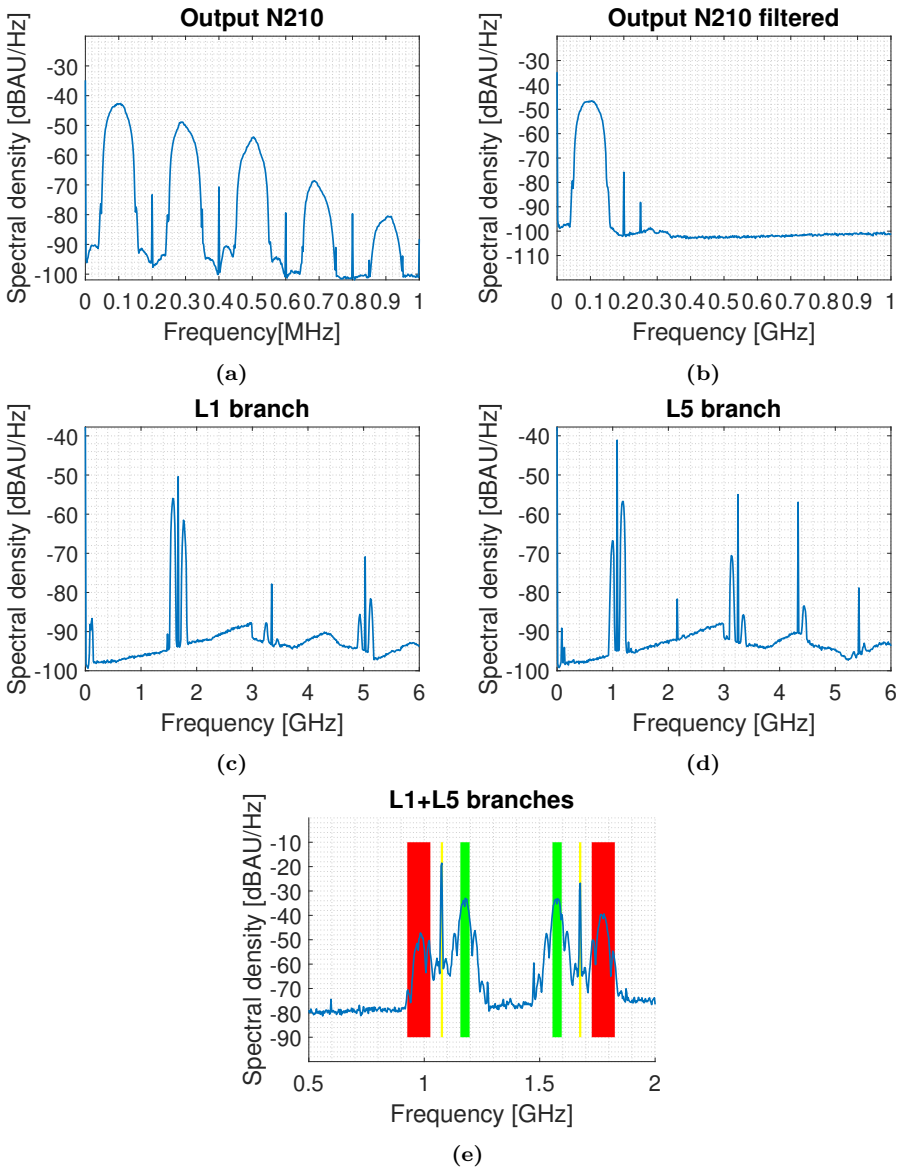

Figure 9.16: Spectrum of the calibration signal at each stage: (a) Output of N210, (b) after High Pass Filter (HPF) to remove DAC alias, (c) L1 after branch up-converstion, (d) L5 branch after up-conversion, and (e) the two branches filtered and added. In green, the region of the spectrum that will be used for calibration. In red, the spectral replicas. From [5]

power envelope of the alias, which limits the generation of powerful lobes at large IFs.

The IF signals are then up-converted to the L1/L5 bands as previously explained in Section 9.3 and sketched in Fig. 9.9. The spectrum of the signal at each point of the

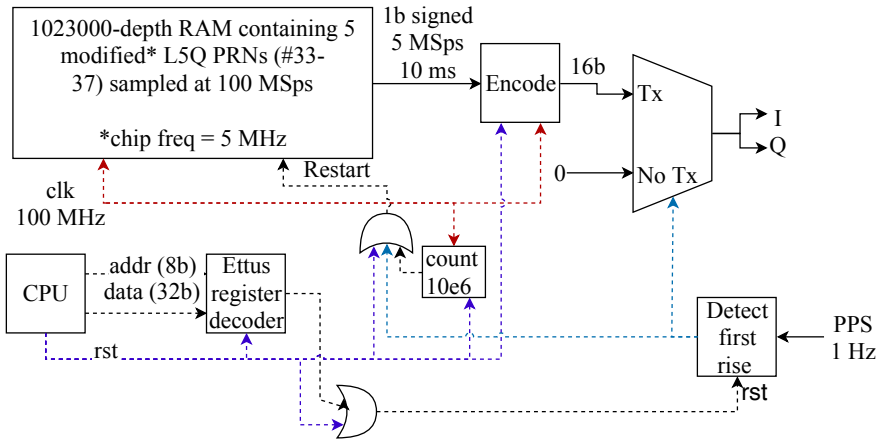

Figure 9.17: Block diagram of the DSP inside USRP N210 FPGA.

calibration system can be seen in Fig. 9.16.

Returning to the topic of how the PRNs are generated, those are in fact stored in distributed RAM in the FPGA. However, they have been previously resampled at 100 MSps, as this is the internal clock frequency of the FPGA. Figure 9.17 shows a block diagram of the blocks inside the FPGA, and the workflow is explained next:

1. Waits until the user register tells to start transmitting.
2. Wait for the next rise of the PPS signal. Then, it performs three tasks in parallel:
   - Continuously generates the baseband calibration signal starting from the first chip. This signal is shown in Fig. 9.18. Note first that the signal is cyclically repeated between consecutive PPS. Note also the short latency between the PPS and the calibration signal.
   - Continuously generates a digital tone starting with zero phase using a CORDIC algorithm. As aforementioned, in order to generate the analog frequency at an IF 100 MHz, the digital signal must be generated at baseband. Thus, this block does not generate a tone, but a constant. However, the block is kept in case it is needed in future developments.
   - Up-converts the signal with the tone by with a Digital Up-Converter (DUC).
3. Keeps transmitting the signal until the user register tells to stop.

It is worth mentioning here two potential issues concerning the way a rise of the PPS signal is detected. A positive change of the PPS is retrieved by comparing its current value

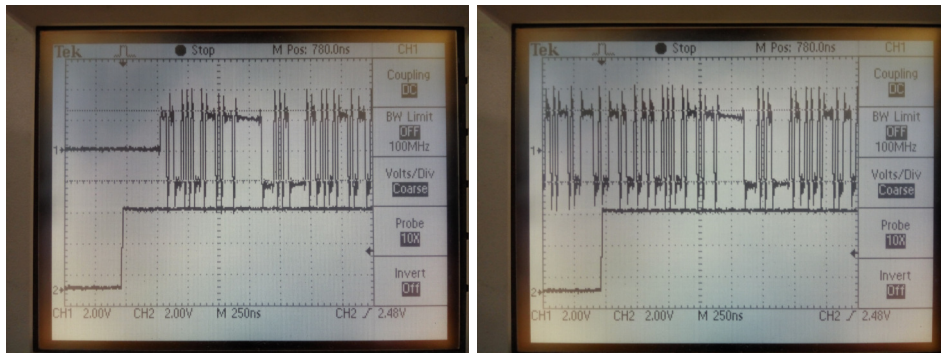

(a) **(b)**

Figure 9.18: Baseband version of the calibration signal transmitted by the USRP N210 (top) shown along with the PPS signal (bottom) seen with an oscilloscope. (a) Transmission after first PPS pulse arrival, (b) transmission in successive PPS.

with the previous one in the last clock. The rate of this clock is 100 MHz, which means that the estimation of the PPS rise time has a precision of 5 ns. As it will be detailed in next section, the USRPs X310 use the same PPS signal in order to start recording the calibration signal. Although their clock frequency is 200 MHz, and thus, the precision is 2.5 ns. Both clock frequencies can be increased in order to have a better precision.

Another problem affecting the precision of the PPS rise time estimate, is the precision of the CMOS technology when converting voltage values to *high* or *low* states. It can happen, that during the transition stage, the digital PPS changes its state multiple times. This problem can be solved by comparing the current PPS state not only with the previous one, but with several of them. Nevertheless, these two latter issues do not have a big impact on the current version of MIR, as there is no inter-calibration between the 19 elements of the arrays (see Section 9.6). However, the suggested changes could be considered in future MIR versions or in similar instruments.

9.5.2 USRPs X310

The USRPs X310 are used to stream to the host the GNSS signals in the normal mode, and the calibration signals in the calibration mode. Figure 9.4 showed the block diagram of the elements of the USRP involved in the sampling of the signals. The FPGA is a Xilinx Kintex-7 XC7410T.

The sampling frequency of the ADC is fixed to 200 MSps. The DSP developed here down-converts the signals and frames the samples into Ethernet packets to be sent to the host computer. The DSP blocks are shown in Fig. 9.19 and its workflow is explained next.

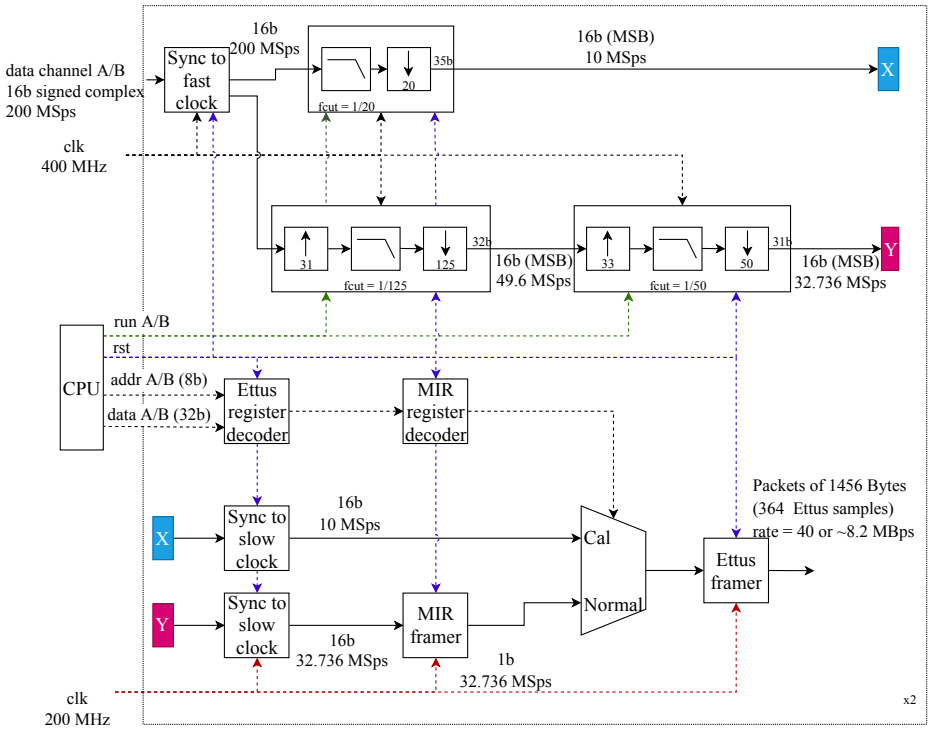

Figure 9.19: Block diagram of the DSP inside USRP X310 FPGA.

1. Decodes the register originally intended for configuring the sampling frequency. Here, this register is used to issue user commands from the host to the USRPs X310, as these USRPs do not have a user register, as USRP N210 does (see Section 9.4.2). The USRP X310 will then switch to the normal or to the calibration mode.

2. Downsamples the signals.

   - In the calibration mode, the signal is downsampled from the original rate of 200 MSps to 10 MSps by decimating by 20. The anti-aliasing filter is a Hamming window with 256 coefficients quantized with 16 bits. Those kind of filters have a Finite Impulse Response (FIR) and have a linear phase. The filtered signal is truncated back to 16 bits, but a convergent rounding method is suggested in future versions so as to reduce any associated DC bias.

     Figure 9.20 presents the transfer function of this filter in blue. The red and yellow plots aim at showing the filter cut-off frequency. They have been obtained by generating the calibration signal 10 MHz above/below the true IF.

   - In the normal mode, the signal is downsampled from the original rate of 200 MSps to 32.768 MSps. Then, the signal is requantized to 1 bit (MSB). The

downsampling is performed in two stages. The first, resamples the signal to 49.6 MSps and the second resamples it to the desired 32.768 MSps. The truncation method and the antialasing filter types are the same as in the calibration mode except, of course, for the cut-off frequency.

3. Frames the samples into structures of 16 bits. The reason behind this, is that the original Ettus FPGA blocks, firmware and drivers, expect 16 bit complex samples. Significant changes on all the codes should be made in order to use a different data format. Additionally, the writing and reading of files in the host computer is performed in multiples of 8 bits. These issues do not involve the calibration mode, as the signal is already sampled using 16 bits. However, in the normal mode the samples are sorted as shown in Fig. 9.21. The host program will then write the data to the files as int16 with little-endian mode. By reading then the files as int8, and also with little-endian mode, the samples will appear in the correct order. However, masking will be needed in order to convert the samples to 8 bits variables.

9.6 MIR calibration and characterization

The goal of any calibration is to relate the measurements made by an instrument with reference measurements with a known accuracy. In order to do so, each one of the elements of the instrument must be first characterized. In MIR, each subsystem needs a specific characterization method. The passive elements, that is to say, the RF cables, power combiners and splitters, switches, and filters, may be characterized only once. On the

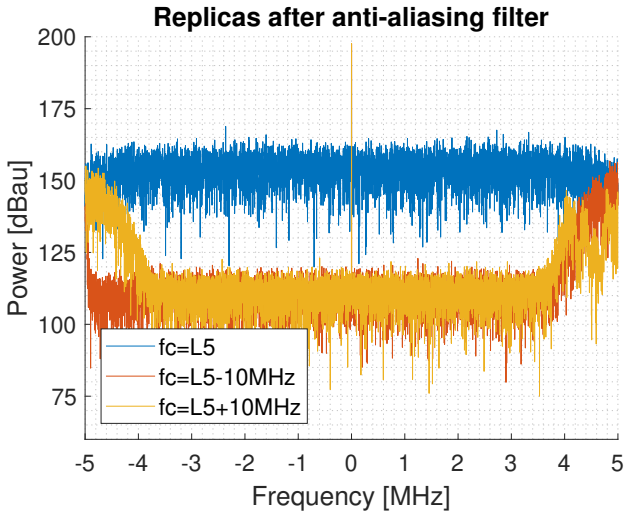

Figure 9.20: Study of the anti-aliasing filter used used in the calibration branch. The right part of the yellow spectrum shows an artifact produced by the signal generator, and is also observed with an spectrum analyzer.

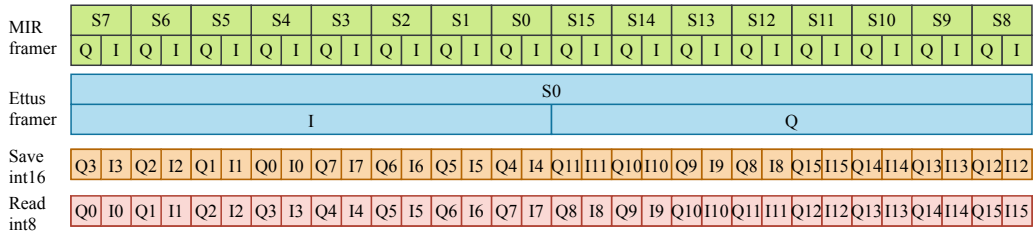

Figure 9.21: Framing of MIR 1 bit samples to be further read as int8.

other hand, the amplifiers, vector modulators, and LOs, are active elements which require a periodic calibration. Some of the characterization results have to be applied during the flight. Those are the ones involving the formation and the steering of the beams. In contrast, other parameters can be applied a posteriori to the sampled data.

Although in MIR there are many elements that affect the measurements, this thesis will focus on five. Firstly, the vector modulator unbalances, and the delay and attenuation of the RF cables. Secondly, the change in the magnitude, phase and delay of the signals when passing through the channels. Thirdly, the antenna arrays directivity as function of the steering angle. Fourthly, the overall thermal noise of channels. Fifthly, the behavior of the cross-correlation peak power as function of the signal power at the USRP ports. The calibration of the first three elements is one of the goals of the thesis in [5], but is briefly described here for the sake of completeness.

Aside from these latter factors, there are others that have been also investigated, such as: the leakage between channels, the USRPs sensitivity, the DC offsets, the DC filtering, or the cross-polar power of the arrays. Some comments on those latter issues are presented through-out the course of this chapter, and others are explained in [5].

The elements explained in this Ph. D. thesis are summarized in Table 9.3, showing how often they need to be characterized (columns), and when the results are applied (rows). In the table, "once" does not mean that these elements have to be characterized a single

Table 9.3: Characterization periodicity of the main parameters.

		Obtain	
		Once	*Periodically*
Apply	*In-flight*	Vector modulators unbalance RF cables delay and atten.	Channels delay, phase and power
	Posteriori	Arrays directivity Channels noise SNR mapping	-

Table 9.4: Characterization methods of the main parameters.

Parameter	Method	Needed for	Ref.
Vector modulator unbalances	Network analyzer	Beamforming and steering	Sec. 9.6.1 (and [5])
RF cables delay and atten.	Network analyzer	Beamforming and steering	Sec. 9.6.1 (and [5])
Channels delay, phase and power	MIR Calibration system	Comparing channels in cGNSS-R Always in iGNSS-R	Sec. 9.6.2 (and [5])
Arrays directivity	Anechoic chamber	Comparing channels in cGNSS-R Always in iGNSS-R	Sec. 9.6.3 (and [5])
Channels noise	Dedicated DSP	Sensitivity analysis	Sec. 9.6.4
SNR mapping	Signal generator	Sensitivity analysis	Sec. 9.6.5

time in their lifetime, as aging has in impact on them. Those elements were characterized some weeks before the Australian campaigns. The elements marked as "periodically", have drifts mainly because changes of temperature affect their behavior. Those elements were characterized immediately before the start of the field campaigns. MIR was switched on about 100 minutes before starting the characterization so as to allow the beamformers to reach the thermal equilibrium [5]. It is worth stating here that all the oscillators in MIR are continuously disciplined with the same GPSDO, and thus not requiring further characterization during a typical flight duration.

Table 9.4 shows the characterization method of the latter elements and to which parameters the results are applied to. The following sections address the characterization of each parameter.

9.6.1 Beamfoming calibration

Analog beamforming is performed by introducing phase differences between the channels of each element of the array. It is therefore critical to characterize the RF cables length and the vector modulators in order to form and steer the beams. Each cable introduces a slightly different delay. Similarly, the vector modulators have non idealities, that is to say, I/Q unbalances and offsets.

Those elements have been characterized with a network analyzer [5]. The results have been stored in the embedded and are applied during the flight. As an example, Fig. 9.22 shows the phasor of the 19 vector modulators that form an L5 beam when they are all set to introduce no phase. Note that there are differences of up to 45°, but that on average, they are compensated. Nevertheless, this residual error still has an impact on the radiation patterns. Figure 9.23 plots them before and after calibration. Note that the effect on the main lobe is small, but on the secondary lobes it is more substantial.

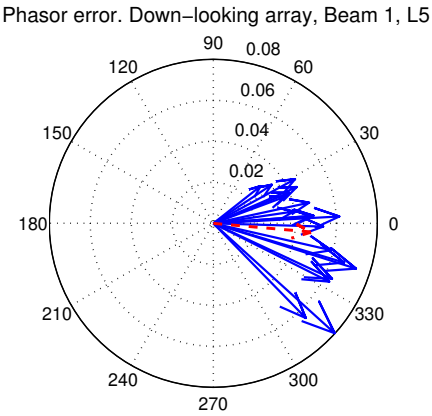

Figure 9.22: Phasors of the 19 channels that form an L5 beam (solid line blue), and resulting normalized phasor (dashed line red).

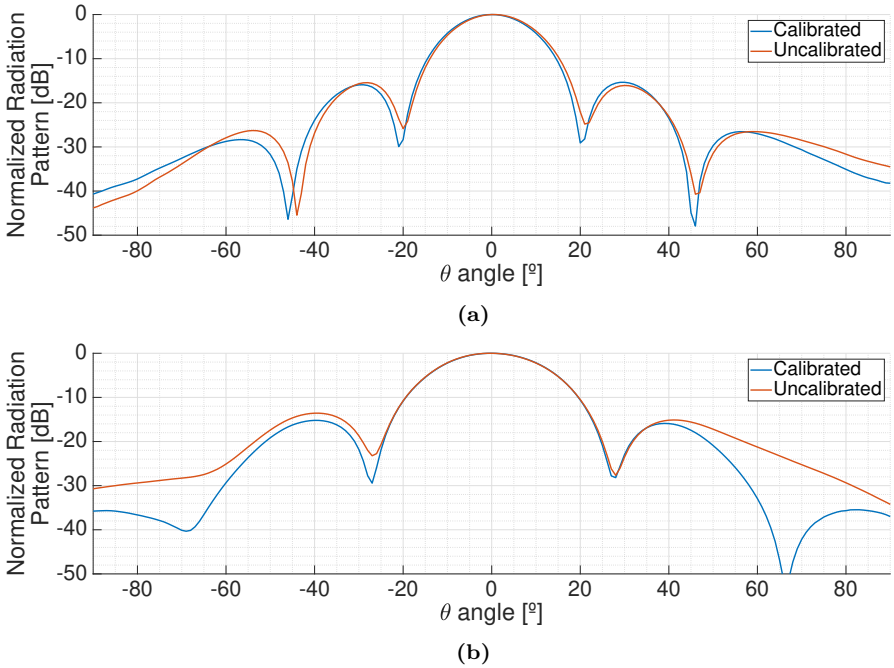

Figure 9.23: Antenna arrays radiation patterns pointing at boresight before and after calibration: L1 (a) and L5 (b). From [5].

9.6.2 Channel impulse response and phase

These parameters are important in order to compare observables obtained with different beams in cGNSS-R. In iGNSS-R they are necessary in order to obtain the observables.

The characterization principle and some comments on its use in the MIR instruments are described below.

9.6.2.1 Methodology

This method is based on the work done in [225] to calibrate radiometers by using PRN sequences (see Section 9.5.1). The goal is to retrieve the channel gain, phase and group delay from its transfer function $H(f)$ and phase response. Let $x(t)$ be a PRN signal passing through a channel with impulse response $h(t)$, which adds a Gaussian noise term $w(t)$. Let also $y(t)$ be the received signal: $y(t) = x(t) * h(t) + w(t)$. The characterization procedure is the following. The first step is to perform the cross-correlation with a local generated replica of $x(t)$:

$$R_{xy}(t) = y(t) * x^*(-t) = R_{xx}(t) * h(t) + n(t), \tag{9.1}$$

where $n(t) = R_{xw}(t)$. The second step is to compute the Fourier transform of the cross-correlation:

$$S_{xy}(f) = \mathcal{F}\{R_{xy}(t)\} = |X(f)|^2 \cdot H(f) + N(f). \tag{9.2}$$

The transfer function can then be estimated by dividing the latter equation by the signal spectrum:

$$\hat{H}(f) = \frac{S_{xy}(f)}{|X(f)|^2}. \tag{9.3}$$

Finally, the impulse response function is found with the inverse Fourier transform:

$$\hat{h}(t) = \mathcal{F}^{-1}\left\{\hat{H}(f)\right\}. \tag{9.4}$$

This method takes advantage of the noise reduction of the correlation, which translates into a better channel estimation instead of estimating directly from $y(t)$. The spectrum of the PRN should be as flat as possible inside the receiver bandwidth so as to avoid any divisions by zero or by small numbers. An easy method to avoid this latter problem is by comparing the denominator in (9.3) with an arbitrary tolerance: $\max(|X(f)|^2, \text{tol})$.

Assuming that the channel has a linear phase response, the magnitude, phase and group delay of $\hat{h}(t)$ can be found as:

$$a = |\hat{h}(t_m)|, \tag{9.5a}$$

$$\theta = \hat{\varphi}(t_m), \tag{9.5b}$$

$$\tau_g = -\frac{\delta\hat{\varphi}(f)}{\delta f}, \tag{9.5c}$$

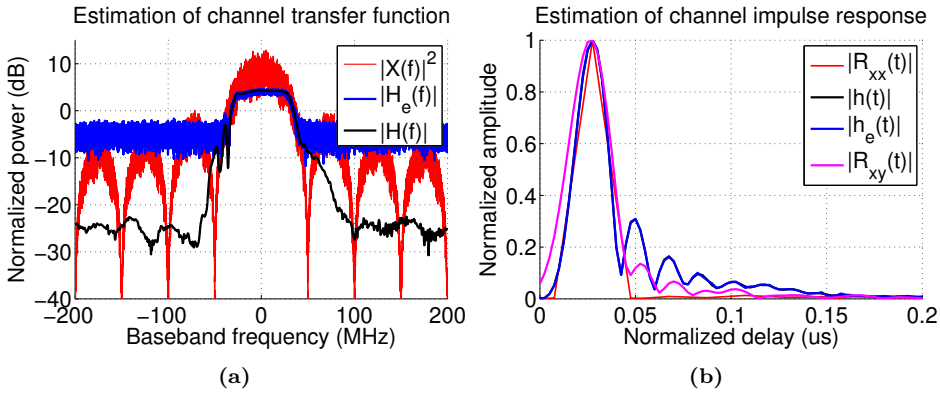

(a) (b)

Figure 9.24: Calibration method procedure using the channel transfer function of one of the MIR L5/E5 channels. The estimated channel is almost overlapped with the one obtained with the vector analyzer (in black).

where $t_m = \arg\max_t |\hat{h}(t)|$, and $\hat{\varphi}(t) = \angle\hat{h}(t)$. In order to find accurate values, the estimated impulse function can be averaged and interpolated with polynomial functions around the maximum, as is done in classical GNSS processing.

As an example, Fig. 9.24a shows the transfers functions of a MIR channel obtained by the method described above, but using a PRN with a chip frequency of 50 MHz instead of 10 MHz. The responses were also obtained with a vector analyzer and taken as reference functions (shown in black). It can be observed that the frequency response is well estimated inside the 50 MHz bandwidth, and that outside this, it is just noise. Figure 9.24b compares the estimated and reference time responses of the channel, the autocorrelation of the PRN, and the cross-correlation of the latter with the received signal. The estimated and reference impulse responses are almost the same, despite just the center part of the transfer function having been recovered.

9.6.2.2 Application to the MIR instrument

The characterization of the MIR channels is not as easy as the procedure described above. The channel $h(t)$ is in fact the combination of multiple channels (see Fig. 9.6) [5]. Some part of the channel is shared between the different elements of MIR, while other parts are specific for each element. Bear in mind that the calibration network also needs to be characterized. All these uncertainties create a complex system of equations that require multiple measurements by activating/deactivating the vector modulators and the switches in the front-ends.

For the campaigns in Australia, it was decided to characterize only the central element of the arrays for each of the 8 beams. Then, the pre-calibration results (see Section 9.6.1)

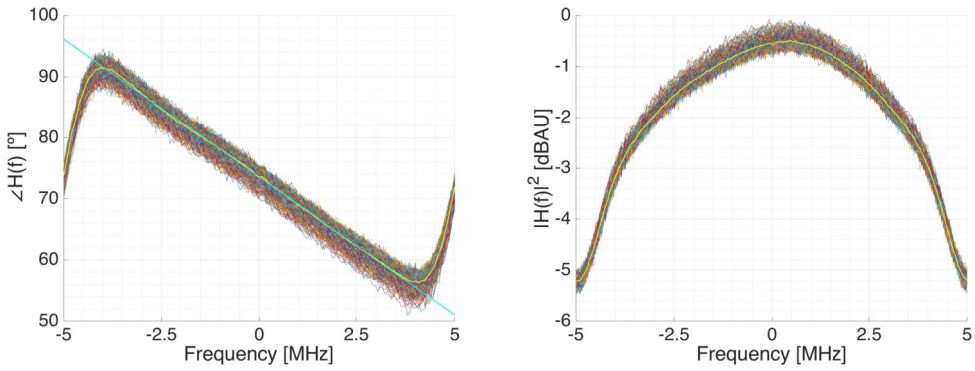

(a) **(b)**

Figure 9.25: Estimated channel transfer function (a) and phase (b), obtained by averaging multiple realizations. From [5].

are used to relatively calibrate the other elements. Figure 9.25 presents the transfer function and the phase response of an actual MIR channel. The group delays obtained in the Australian campaigns were between -2.0 ns and 3.9 ns, and the gain factors were between 31.5 dB and 38.8 dB. Of course, the phase followed a uniform distribution.

9.6.3 Array characterization

Characterizing the directivity of the array antennas is important to be able to compare the observables obtained from satellites with different elevation angles. This characterization was done in an anechoic chamber at UPC [5]. Results from the down-looking array are given in Fig. 9.26. Note that directivity differences of up to 8 dB are obtained within 60° and 90° angles.

The work done in [5], shows the results from the cross-polar characterization of the front part of the arrays. Be aware that the up-looking array has RHCP polarization. However, depending on the scenario, a reflected signal (mainly LHCP, at least in reflections over water) can be picked up as well, if the cross-polarization is not small enough. Similarly, the down-looking array has LHCP polarization, but can receive direct signals for the same reason. The results showed an attenuation of about 15 dB at L1 and 20 dB at L5 within 60° and 90° angles. Although these numbers may not seem large enough, bear in mind that cross-polarization interference would come mainly from reflections in the aircraft structure, and from surface waves along the fuselage. By the way the antenna arrays were positioned in the aircraft, these issues were not a problem.

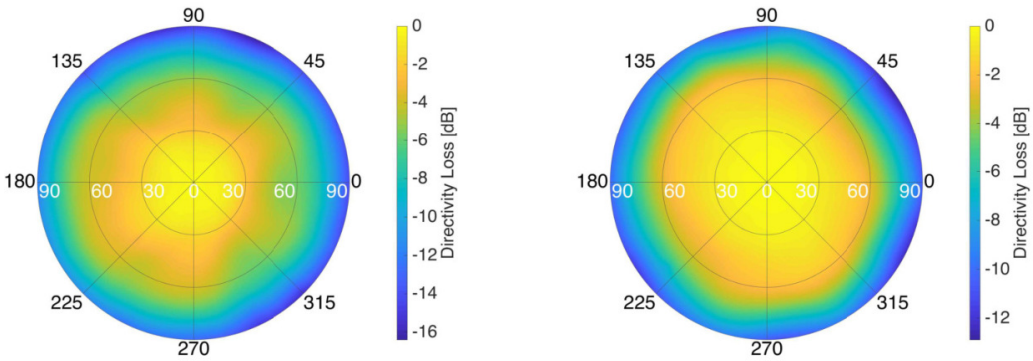

Figure 9.26: Directivity loss of the down-looking array as a function of the pointing direction at L1/E1 (left), and L5/E5A (right) frequency bands. From [5].

9.6.4 Thermal noise characterization

The noise characterization is needed for two main reasons. Firstly, to have an idea of the variance of the measurements due to the thermal noise, although the antenna noise temperature, which depends on the scenario, will further increase this variance. Secondly, to infer the sensitivity of the ADCs, and of the 1-bit coherent cross-correlation.

This characterization studied the noise introduced by each of the elements in MIR: the USRPs with a matched load, the amplifiers, the beamformers, and the arrays (measured inside the anechoic chamber). The characterization was done by pairs of reflected/direct channels. The DSP of the USRPs X310 was modified in order to sample the signals with 8 bits at 20 MSps, so as to be able to measure the power, which would not have been possible to do with just 1-level samples. The results are shown in Figs. 9.27, 9.28 and 9.29.

This characterization was done after the field campaigns in Australia. Unfortunately, it was observed that the samples presented a large DC offset. This offset is larger in the direct signals (Fig. 9.27) than in the reflected ones (Fig. 9.28), because the latter are noiser. Although this effect would not have been a problem if 8 bit samples had been used, it could have been in the 1-level sampling used in the field campaigns. This is so, because in the latter case the DC can not be removed after the sampling.

Further investigation, concluded that the offset was caused by the down-converter in the DBRX2 boards (see Fig. 9.4). In fact, the original Ettus code in the FPGA included a DC-removal block. Sadly, this block was bypassed when modifying the codes for MIR. However, activating it again for future versions of MIR, should be straightforward.

The power values shown in the legend of Fig. 9.29 are stored and used later for the sensitivity analysis, together with the results from the next section.

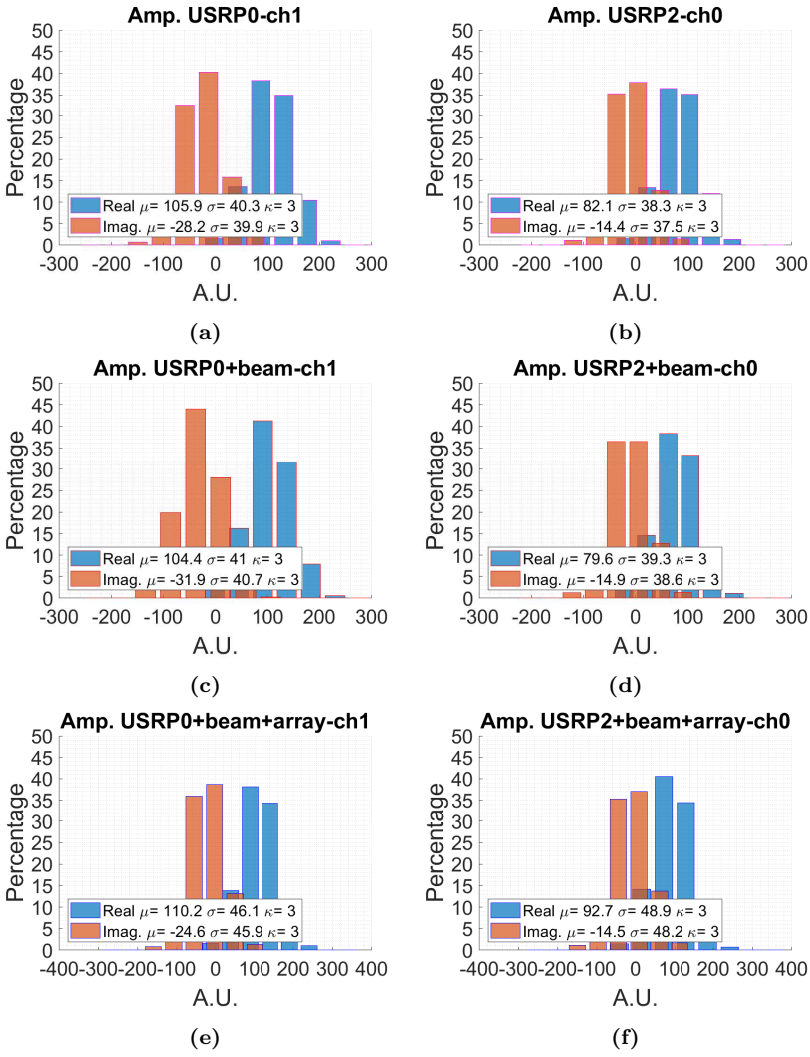

Figure 9.27: I/Q amplitude histograms of 2 direct channels. The left column is an L1 channel and the right column is an L5 channel. Top row shows the USRPs alone, middle row shows with the beamformers, and bottom row shows with the beamformers and the direct array in the anechoic chamber. κ in legend means kurtosis. Note that different acquisitions may produce a different DC offset.

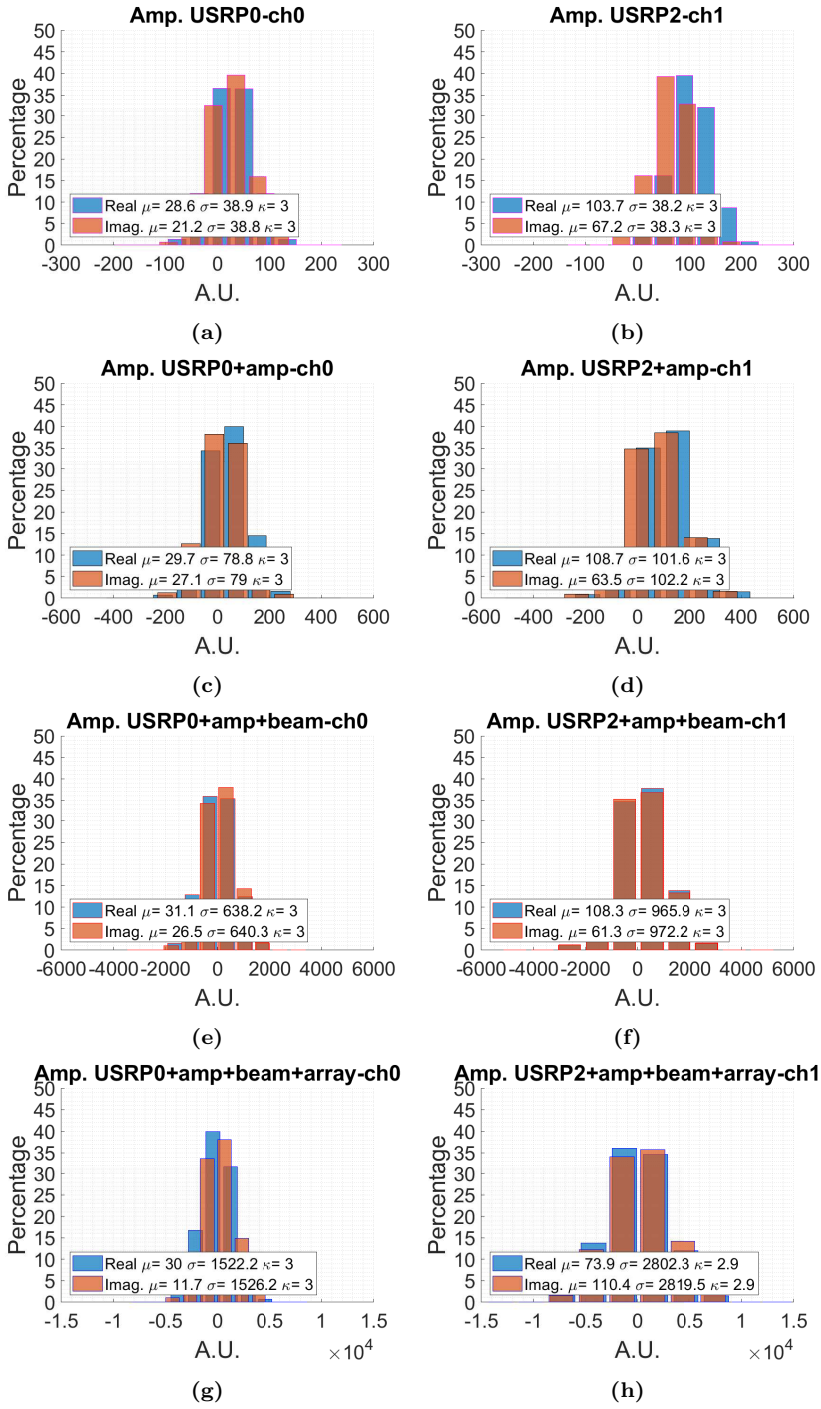

Figure 9.28: I/Q amplitude hist. of 2 reflected channels. The left column is an L1 channel, and the right column is an L5. The upper row shows the USRPs alone, second row shows with the amplifiers, third row shows with the amplifiers and beamformers, and bottom row shows with the amplifiers, beamformers and the array. The array has a different mean because it was obtained in another capture.

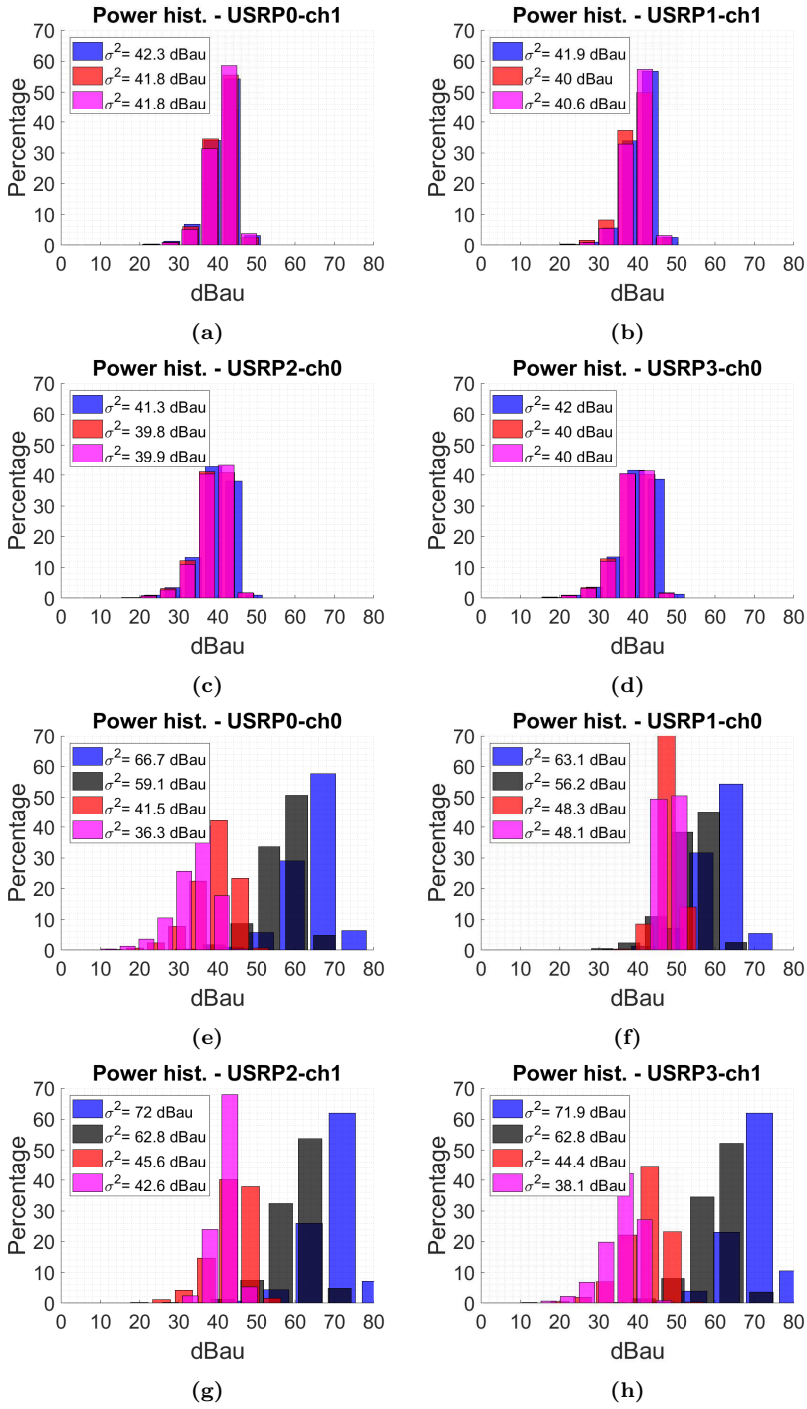

Figure 9.29: Power histograms of the MIR channels. The 2 upper rows show the 4 direct channels, the 2 bottom rows show the 4 reflected channels. Colors are: blue (USRPs alone), black (with amplifier in the reflected channels), red (with beamformers), and pink (with the arrays).

9.6.5 DDM peak power characterization

The analysis given here is done after the findings in Chapter 7. In that chapter it was shown that the peak of a DDM obtained from 1-level samples, does not depend on the input signal power but on the latter SNR. In order to study this behavior on the MIR measurements, a signal generator SMU200A [226] was used to transmit synthetic GNSS signals with different SNRs, and injected into the USRP ports. The signals were generated without data bits or secondary codes.

The signal generator was first calibrated relatively to MIR as follows. The whole MIR instrument was started, but the signal at the input port of the USRP was instead connected to a spectrum analyzer. The power of this signal within a bandwidth of 32.736 MHz was computed. The signal generator was then used to generate a AWGN signal with a bandwidth of 32.736 MHz and the power was measured again with the spectrum analyzer. The signal strength was adjusted to be the same as the measured one with the USRP. Finally, synthetic GNSS signals were created also with the signal generator, and added to the AWGN noise at baseband. By changing the power ratio between both signals, different SNRs could be obtained. The overall process was repeated for the 8 beams. Figure 9.30 shows a block diagram of the above description.

Figure 9.31 shows the results for the 8 beams. The sensitivity of the DDM peak power to SNR changes has the same behavior given in Chapter 7. In the case of the up-looking channels, the saturation point for low SNRs of the Galileo E1OS signas, is around 40 dB lower than for the GPS L1 C/A because of the larger coherent integration time. For the down-looking channels, the saturation point for high SNRs is around 30 dB higher than for the up-looking channels, for all the signals.

In the down-looking channels, where the noise level is much higher, the peak power saturates for a much higher input power, displacing the curves towards the right. The down-looking channels are noisier because they have an extra amplifier. However, these results suggest that the amplifiers were not actually needed, and that this increase of noise might even degrade the instrument performance.

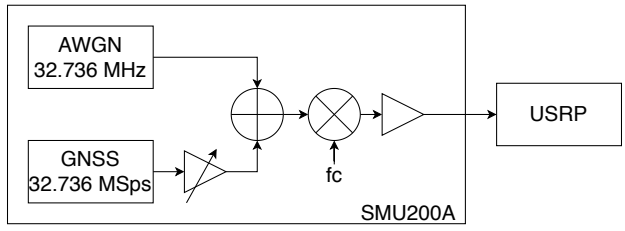

Figure 9.30: Block diagram of the system used to characterize DDM peak power.

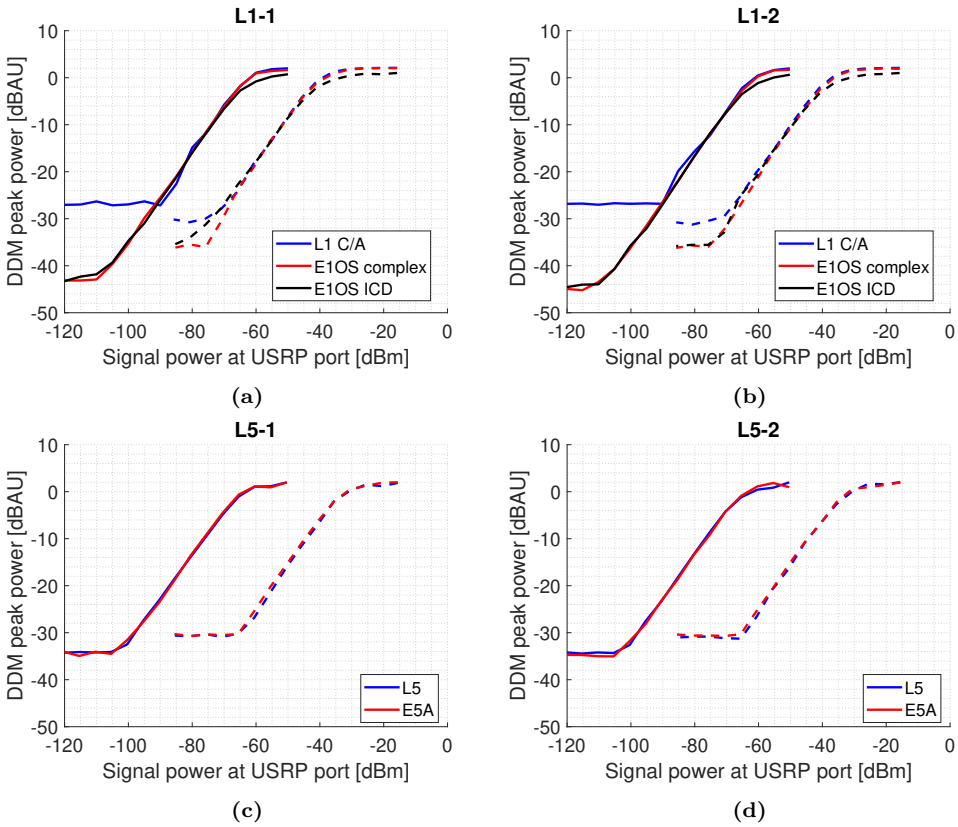

Figure 9.31: Relationship between conventional DDM peak power and SNR at the USRPs input ports. Solid lines are the for up-looking channels, and dashed lines and for the down-looking channels

9.7 Conclusions

This chapter has described the hardware, software, and FPGA codes of MIR, as well as the characterization and calibration procedure of its basic elements.

The MIR instrument is composed of 1 up-looking and 1 down-looking dual-band (L1/L5) 19-element hexagonal arrays. Up to 4 pairs of up/down-looking analog beams can be created, 2 at L1, and 2 at L5. Their directivity is 20.3 dB and 18.2 dB respectively. The beams are analogically steered towards the satellites by using vector modulators, which are controlled with an embedded computer that uses the position of the vehicle and the ephemeris of the GNSS satellites (both parameters obtained with a high precision GNSS) and the attitude of the vehicle (obtained with an IMU). The tracked satellites are updates every 10 minutes.

The beams are sampled synchronously and by pairs using 4 SDRs at 32.736 MSps

and with 1 bit complex samples. The sampled data is then sent via Ethernet to a host computer.

The calibration of the vector modulators is performed by injecting a reference signal to the antennas. This signal has a baseband bandwidth of 10 MHz and is generated with a dedicated SDR. This transmitter and the 4 receivers are time-aligned with a common PPS signal.

Regarding the FPGA coding, two issues are suggested for future improvements. Firstly, to remove the DC offset generated by the down-converter in the USRPs X310. A simple moving average calculator should be a feasible method. Secondly, to improve the detection of a PPS pulse rise by comparing the actual value not only with the previous one but with several more. Hardware improvements are suggested in [5].

10

Chapter 10

Results from the HUMIT Campaign

This chapter assesses the feasibility to estimate the sea coherence time at L-band from an airborne vehicle using GNSS-R signals. The MALYGNSS instrument (see Section 9.2) is used to acquire direct and reflected signals over open sea waters and over a harbour. The direct signals are used as a reference to retrieve the Doppler frequency and any phase jumps due to data bits transitions. This information is applied to the reflected signals, and the sea correlation time is studied from the complex cross-correlation between consecutive reflected DDMs peaks. Results show that the estimation depends on the satellite elevation angle, and that is highly influenced by the aircraft dynamics if they are not properly removed.

The theory developed in this chapter was initially investigated in [227], but more detailed and new results are presented here.

10.1 Introduction

The phase of a reflected GNSS signal over the sea, or more precisely, its stability over time, tells us about the sea state. The more agitated the sea, the shorter the coherence of the reflected signal. If the phase stability is too short or if it evolves in such a way that produces a destructive phase interference during the correlation process, the integration may be unable to produce any correlation gain. The work done in [69] from an airbone platform over open waters, and in [70] from a static position in a coastline, studied the coherence of the reflected signal from the time decorrelation of consecutive DDM peaks. This length was then related to the wind speed. A similar methodology is repeated here with data recorded from an aircraft at two different sea scenarios, open waters and inside a harbour, and with a detailed study of the impact of the satellite elevation angle, and of the aircraft dynamics on the estimates.

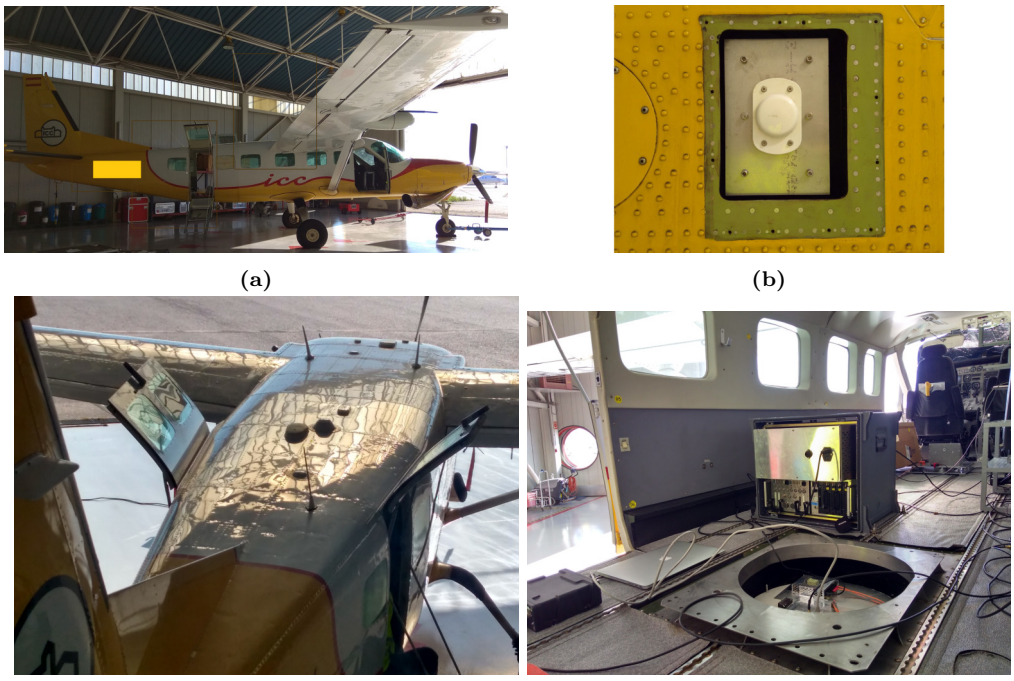

(a) **(b)**

(c) **(d)**

Figure 10.1: Photos of MALYGNSS being assembled in the aircraft: (a) side view of the aircraft in the hangar, (b) down-looking antenna on the aircraft belly, (c) up-looking antenna on the aircraft top fuselage, and (d) box in witch MALGYGNSS rackmount is mounted inside of the aircraft.

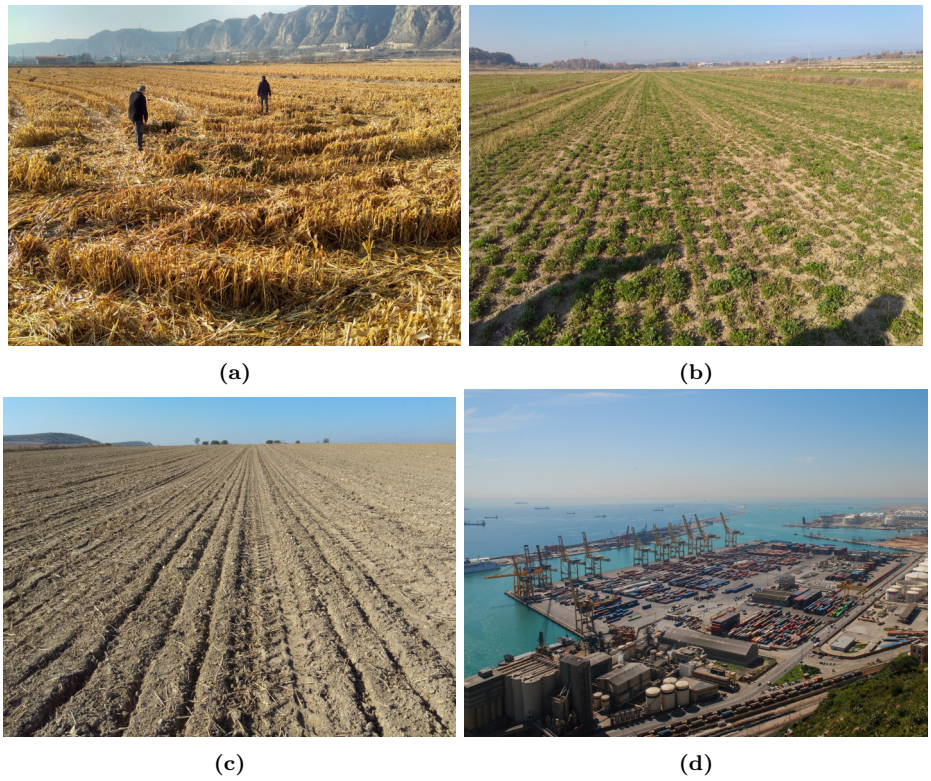

Figure 10.2: Pictures of some of the areas overflowed during the MALGYNSS campaign: (a) HUMIT point #5 (41.83022°, 0.81071°), (b) HUMIT point #6 (41.78725°, 0.84502°), (c) HUMIT point #9 (41.79822°, 0.87326°), and (d) Barcelona harbour. Pictures (a)-(c) are actual pictures, and picture (d). From `https://en.wikipedia.org/wiki/Port_of_Barcelona`.

10.2 Field campaign description

The MALYGNSS instrument flew as an opportunity sensor in the HUMIT project from the Catalan Cartographic and Geologic Institute, known in Catalan by the initials ICGC, in fall 2017. The aim of this project was to retrieve soil moisture from small satellites with multispectral sensors [221]. Besides MALYGNSS and the optical sensors, a radiometer named ARIEL and the COmpact Reflectometer for Terrain Observations (CORTO) GNSS reflectometer were also mounted as opportunity instruments [221]. Figure 10.1 shows the aircraft and the assembly of the MALYGNSS rackmount and antennas. The CORTO instrument was mounted in the same rackmount, and the radiometer was placed in the hole shown in Fig. 10.1d. The attitude information could be obtained either from the low-cost IMU of the CORTO instrument, or from the one on board the aircraft. More information about the assembly and the antennas characteristics can be found on [5].

The mentioned flight was done as a feasibility study close to Balaguer, Spain, where

the ICGC has a network of soil sensors. Actual photos of different types of the fields overflowed are presented in Fig. 10.2, and the aircraft groudtracks while MALYGNSS was capturing signals, and the location of the sensors are shown in Fig. 10.3a. Preliminary results of the MALYGNSS instrument for soil moisture estimation were presented in [222], and in [228] those signals were used to study different types of RFI mitigation techniques.

When approaching Barcelona airport, the aircraft overflew the sea close to the Barcelona coastline and also the city cargo harbour. Although it was not planned as a flight route, the aircraft groundtracks were close to buoys and tide gauges from the SIMAR network, managed by the Spanish state-owned enterprise Puertos del Estado. The time series data of those sensors are free and available through the website [`http://www.puertos.es/`] and will be used later as a reference data. A picture of the harbour is shown in Fig.

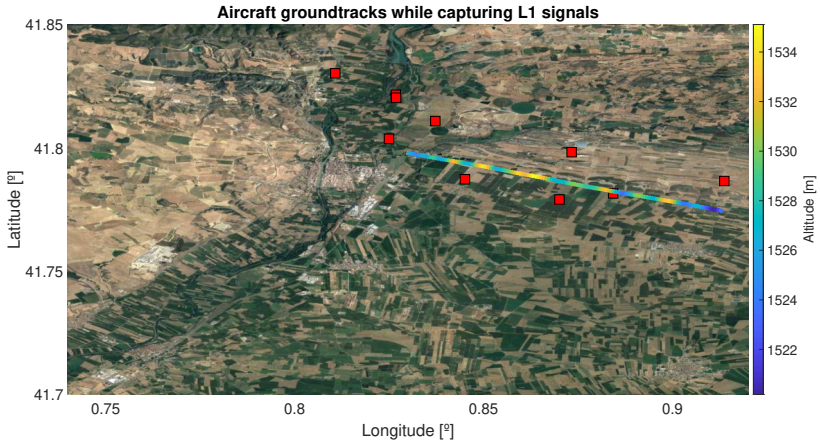

(a)

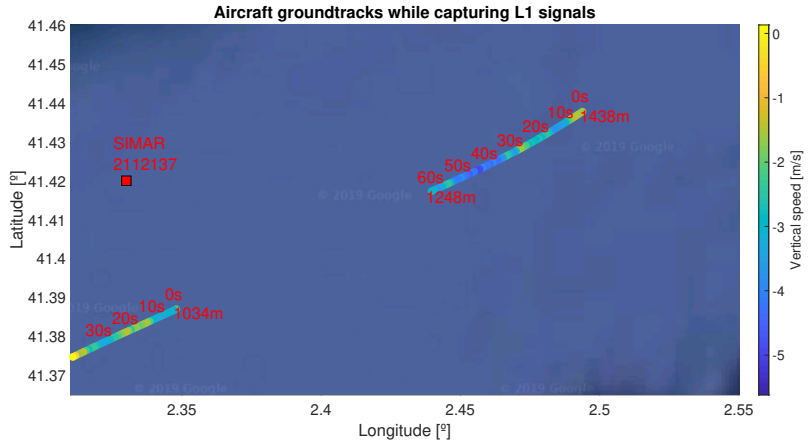

(b)

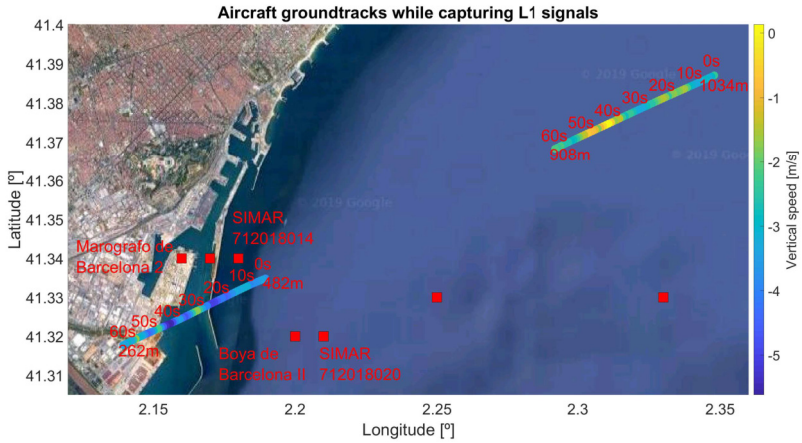

(c)

Figure 10.3: Aircraft groundtracks while recording L1 signals. Colorscale shows the flight altitude in the land map, and the descending speed in the sea maps. Square markers show the position of HUMIT base stations in the land map, and buoys or tide gauges in sea maps.

10.2d, and the aircraft groundtracks and the SIMAR points are presented in Fig. 10.3.

Due to the limited capacity of the MALYGNSS hardrive, the instrument was only activated when overflying the areas of interest in consecutive acquisitions of 60 seconds at GPS L1 and L2 bands with a gap of ~ 1 second between them. This resulted in just one L1 and one L2 captures over the HUMIT sensors, and three L1 and one L2 captures over the sea. The L2 captures are not shown in Fig. 10.3 because they have not been used in this thesis. Although the software developed in [157], was used to acquire L2C signals, and initial results with those signals were presented in [222].

The distance of the groundtracks to the coastline in the three sea captures were about 13 km, 7 km and 400 m respectively. The aircraft speed was roughly constant at 310 km/h in the first two captures, and at 250 km/h during the third one. The aircraft descended from 1438 m to 262 m during the three captures with a descending speed up to 6 m/s. Figure 10.4 shows the skyplot of the satellites in view during the captures.

10.3 Time decorrelation of the DDM peak

The DDM was first defined in (3.16), but is rewritten here for the sake of completeness. A DDM is the delay cross-correlation of a received signal $x(t)$ (either direct or reflected) with a reference one $r(t)$ at different Doppler frequencies ν over a coherent integration time T_{coh}

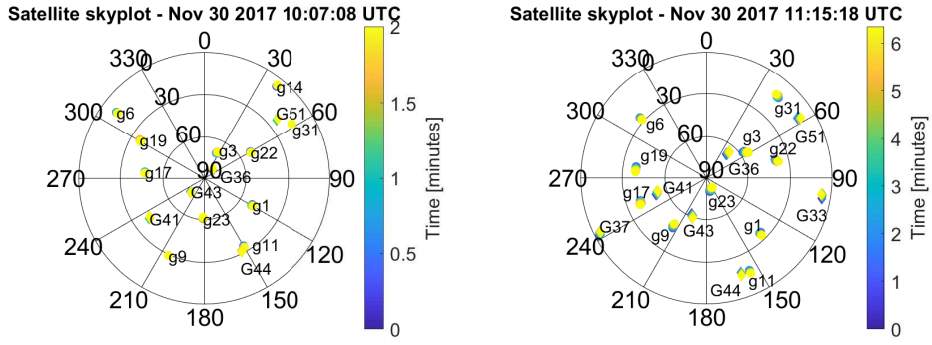

(a) **(b)**

Figure 10.4: Skyplot of the satellites in view in the HUMIT campaign while capturing L1 signals: (a) over land and (b) over sea. Lowercase g stands for GPS and uppercase G stands for Galileo.

$$Y(\tau,\nu) = \frac{1}{T_{coh}} \int_{T_{coh}} x(t)\, r^*(t-\tau)\, e^{-j2\pi\nu t} dt. \tag{10.1}$$

The reference signal is a locally generated clean replica of one or all the components that conform the received signal. This equation is the one usually given in the literature, but for the theory developed hereafter, it is useful to introduce the time dependency as

$$Y(\tau,\nu,t) = \frac{1}{T_{coh}} \int_{t}^{t+T_{coh}} x(t)\, r^*(t-\tau)\, e^{-j2\pi\nu t} dt. \tag{10.2}$$

In general, the coherent integration time T_{coh} is set to the duration of the reference signal T_c, and consecutive DDMs are computed with $t = N \cdot T_{coh}$, where N is an integer. However, the integration length can be reduced or enlarged, and consecutive DDMs can be separated by any amount or they can be overlapped if the reference signal is properly generated and aligned with the received one.

The power and the phase of the direct signal can be estimated from the peak of the DDM

$$[\tau_{pk}, \nu_{pk}] = \arg\max_{\tau,\nu} |Y_d(\tau,\nu,t)|^2. \tag{10.3}$$

As for the reflected signal, the reference power and phase are also obtained from the DDM peak

$$[\tau_{sc}, \nu_{sc}] = \arg\max_{\tau,\nu} |Y_r(\tau,\nu,t)|^2. \tag{10.4}$$

This latter point is usually denoted as *scatterometric* in order to distinguish it from the *specular* one, found where the delay derivative of the reflected DDM is maximum (see

Chapter 3). Needless to say that reference Dopplers and delays are also time dependent, but the time symbols have been omitted for the sake of simplicity.

The phase of the received signal changes over time due to the Doppler effect, but also due to any transition of the data bits. To ensure a coherent integration, the signal should preserve its phase during the correlation process. The Doppler has to be estimated and compensated, and the phase jumps have to be detected and removed. In this work, the reference delay and Doppler are estimated from the direct signal as it is less noisy than the reflected one, and then used to reconstruct both signals taking into account the scenario geometry. The delays are estimated using non-overlapped periods of $T_{coh} = 1$ ms, and the Dopplers are the average of the estimates over 1 second periods, also non-overlapped. It is also important to state here, that the stability of the oscillator used to synthesize the LOs and the sampling frequency is critical to derive the phase of the signal. The oscillator used in MALYGNSSs has a frequency accuracy of < 1 ppb. In order to give the reader context, the oscillator accuracy of commercial GNSSs receivers can be as low as 50 ppm. Those receivers overcome this drawback by using PLLs, which continuously correct the down-conversion and chipping rate frequencies.

The signal coherence length is obtained from the time ACF of the complex DDM value at the reference points given previously. The ACF of the direct signal is used as a reference and is given by

$$R_d(\tau) = \frac{1}{MT_{coh}} \int_{t}^{t+NT_{coh}} Y_d(\tau_{pk}, \nu_{pk}, t)\, Y_d^*(\tau_{pk}, \nu_{pk}, t-\tau)\, dt, \tag{10.5}$$

and the ACF of the reflected signal is given by

$$R_r(\tau) = \frac{1}{MT_{coh}} \int_{t}^{t+NT_{coh}} Y_r(\tau_{sc}, \nu_{sc}, t)\, Y_r^*(\tau_{sc}, \nu_{sc}, t-\tau)\, dt. \tag{10.6}$$

where M must be large enough to ensure that the decorrelation can be observed. A value of $N = 1000$ (equal to 1 second) was shown to be sufficient. The decorrelation times τ_d and τ_r ate defined as at the time the magnitude of their respective ACF decreases from the maximum by a factor $1/e$ [70]

$$|R_d(\tau_d)| = \frac{1}{e}|R_d(0)|, \tag{10.7}$$

and

$$|R_r(\tau_r)| = \frac{1}{e}|R_r(0)|. \tag{10.8}$$

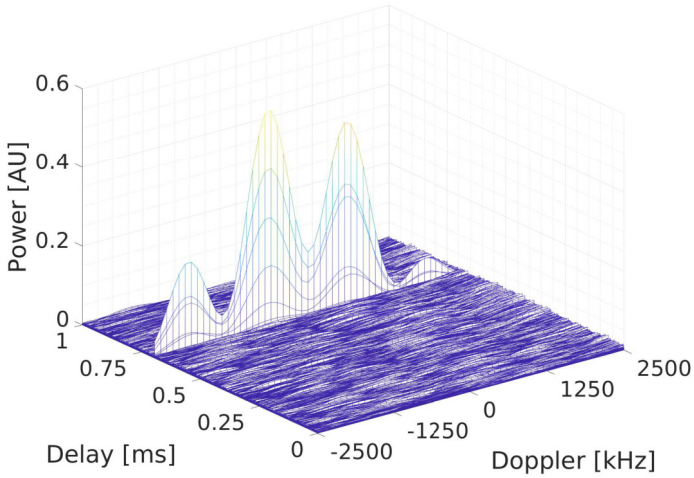

Figure 10.5: Impact of a GPS L5 secondary code chip transition during the correlation process on the DDM. From [5].

10.3.1 Impact of navigation bits and secondary codes transitions

As explained in Chapter 2, the GNSS signals are formed by combining different components. In general, they carry low rate data streams modulated by the PRN sequences at a much faster rate. By contrast, the so-called pilot signals are data-less. In these signals, the PRNs do not modulate any data, but cyclic repeated sequences known as secondary codes, usually with a period of several times the one of the PRNs. This allows large coherent integration correlations without concerning for unexpected phase transitions due to data signals. The fact that the fundamental PRN is also present in the pilot signals, also allows the performance of correlations with the duration of just one PRN period.

These new signals add more complexity to the acquisition scheme, as it is necessary to synchronize not only to the PRN but also to the secondary codes. A phase transition during the coherent integration produces a correlation loss and distorts the DDM in the Doppler domain. In the worst case, if the transition happens exactly at half of the correlation, the result will be zero. As an example, Fig. 10.5 shows a DDM of a Galileo E1OS direct signal in which the secondary code has changed of phase during the correlation process, producing two additional peaks in the Doppler domain.

A typical GNSS receiver performs the synchronization with the secondary codes and with the Doppler using PLLs. This configuration is needed for real-time receivers and is not straightforward to implement. In this work, the Doppler and any phase jumps are estimated and compensated in an iterative way until they are removed up to a certain

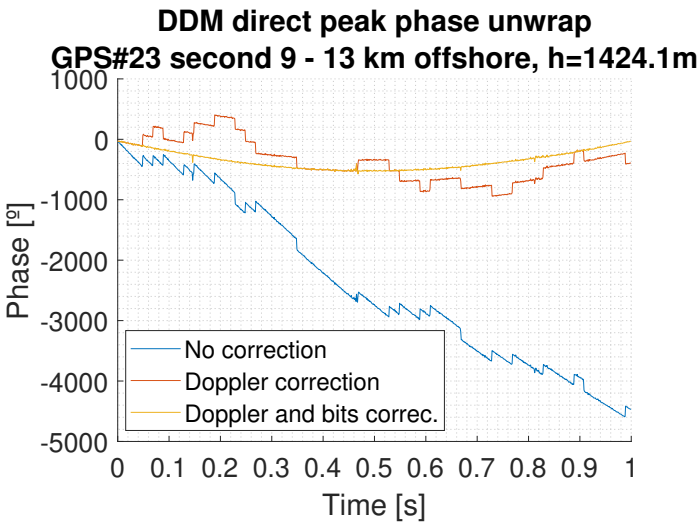

Figure 10.6: Phase evolution of a direct GPS L1 C/A signal after and before removing the Doppler frequency and the data bits transitions. Adapted from [227].

convergence tolerance. Figure 10.6 shows the phase evolution of a GPS L1 C/A direct signal before and after the Doppler and the navigation bit corrections.

The available signals from the HUMIT campaign are the GPS L1 C/A and L2C, and the Galileo E1OS. However, only the former has been used in the present work. The reason why will be further explained, but the characteristics of all of them in terms of phase discontinuities are explained next for the sake of completeness.

The GPS L1 C/A signal is formed by a single PRN with a rate of 1.023 MHz and a length of 1023 chips, with a data stream at a rate of 50 Hz. The phase transitions are only due to a data bit change which produces a transition of $\phi = 180°$.

The GPS L2C signal is also a real signal obtained from the time multiplex of two PRNs named L2CM and L2CL. Both PRNs are generated at 511.5 kHz. The former has a length of 10230 chips and the latter 767250 chips, resulting in a duration of 20 ms and 1.5 s respectively. The time multiplex is performed chip by chip, resulting in a composite signal of 1.023 MHz. The L2CM contains a data stream at a rate of 50 Hz, and the L2CL is a pilot signal with a secondary code. The L2CM is sensitive to data bits transitions, which produce also phase jumps of $\phi = 180°$. On the other side, the L2CL is not sensitive to the data bits, and allows a very large coherent integration.

The Galileo E1OS signal is, as well, a real signal obtained by applying the CBOC modulation on two different PRNs named E1B and E1C. Both PRNs have a chipping rate of 1.023 MHz and a length is of 4092 chips, resulting in a duration of 4 ms. The data bits are sent only over the E1B component and have also a duration of 4 ms. Additionally,

the E1C chain carries a secondary code of 25 chips, also at a rate of 250 Hz, resulting in a duration of 100 ms. The Galileo E1B is sensitive only to the data bit changes, and E1C is sensitive only the secondary code changes, both with phase transitions of $\phi = 180°$. The E1C component allows a larger integration time, but unlike L2C, it does include a secondary code, which make a shorter integration time more complex.

10.3.2 Impact of vehicle dynamics

During the data acquisitions over the sea, the aircraft was approaching Barcelona airport and therefore was constantly adjusting is attitude, velocity vector and speed. This translated into a continuous and non-linear change of the Doppler. Although this change rate is small as compared to the duration of the GNSS codes, and thus not affecting the performance of a typical GNSS receiver, it impacts on the phase coherence for longer times.

In this work, an average Doppler was obtained in periods of 1 second and removed from the direct and reflected signals. However, a residual Doppler was still present at some instants. The phase evolution of the direct and reflected signals and their respective ACF at three distinctive moments are shown in Fig. 10.7. The titles tell the second of the capture, from which an idea of the aircraft dynamics can be obtained from the vertical speed at that second in Fig. 10.3.

A stable instant in open waters is shown in Fig. 10.7a. The phase of the direct signal is pretty much steady, and its respective ACF is almost flat during the whole second. Nevertheless, the phase stability of the reflected signal is too short to be seen in these figures and will be analyzed later. By contrast, Fig. 10.7c presents an instant with a residual Doppler, which in fact changes sign in the middle of the second. Although the change of phase is small in the whole second, it severely impacts the ACF of the direct signal. Again, the coherence of the reflected signal is too short to be influenced by this residual Doppler. Finally, Fig. 10.7e shows a similar moment in terms of the aircraft dynamics, but over the harbour. In this case, the residual Doppler affects the ACF of both signals. Although the coherence of the reflected signal due to the sea state is below the coherence due to the residual Doppler, the latter impacts on any estimation of the former. Figure 10.8 presents a zoom of the latter instant showing that in fact the phase of the reflected signal has a similar trend to that of the direct one while the sea is coherent.

Keeping in mind that the latter figures do not show the phase evolution but the phase unrwrap obtained with Matlab default algorithm. If the phase is very noisy, as in the case of the reflected signals, the algorithm may fail to fix the phase discontinuities.

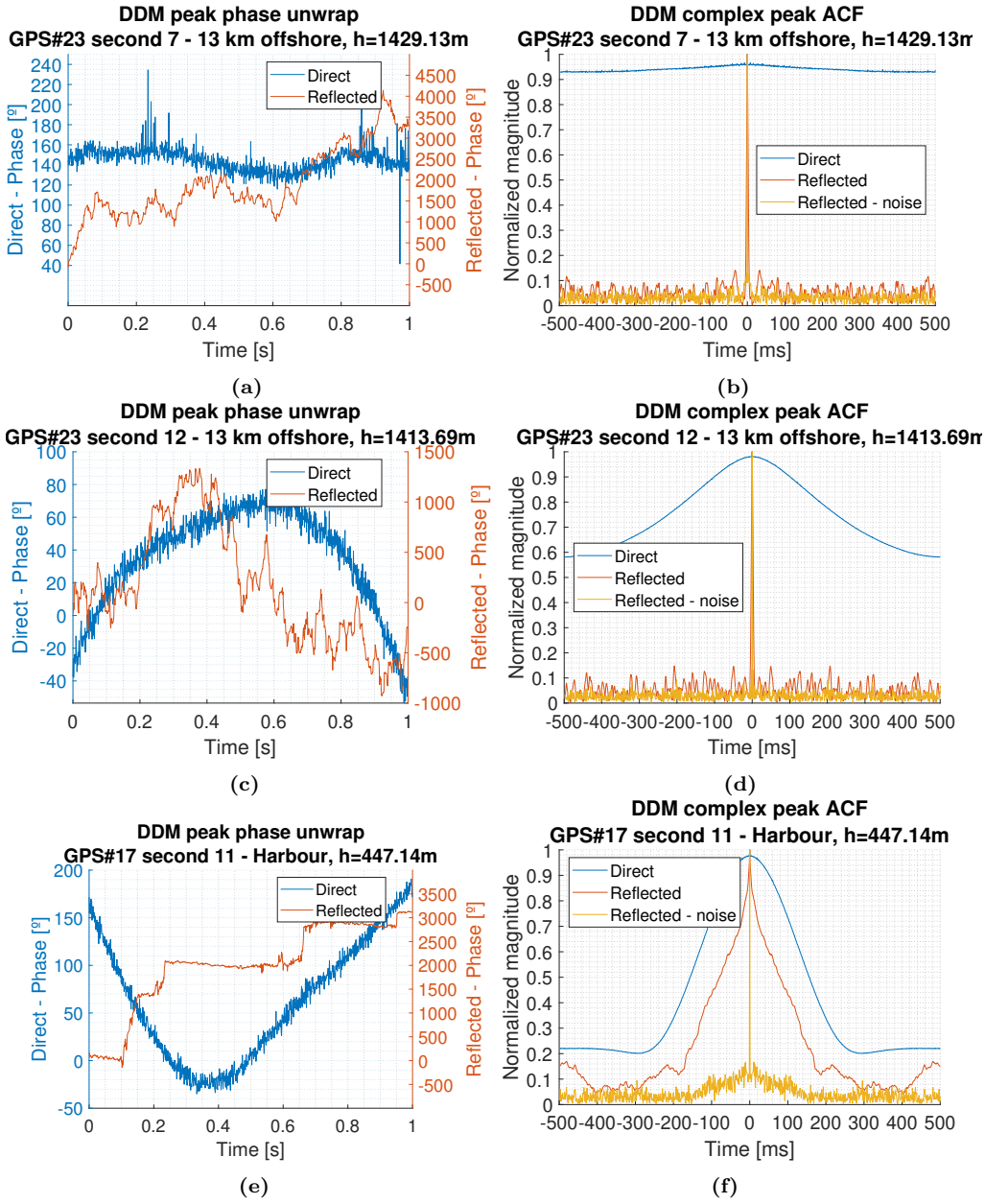

Figure 10.7: Phase evolution (left column) and DDM complex peak ACF (right column) of direct and reflected signals for different scenarios and aircraft dynamics (see Fig. 10.3).

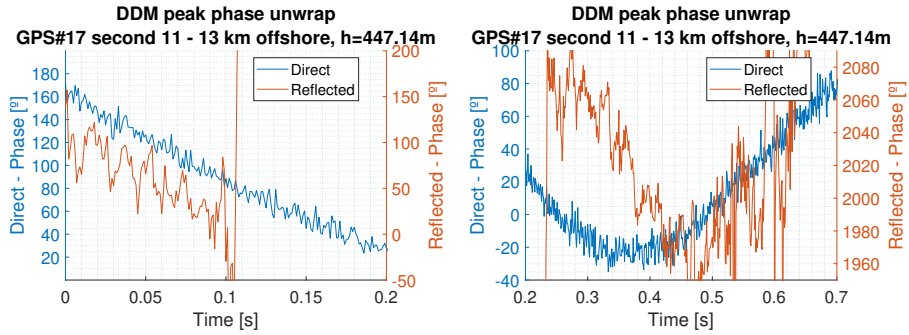

Figure 10.8: Impact of aircraft dynamics on a reflected signal phase (zooms of Fig. 10.7e).

10.4 Results

Four GPS satellites with good SNR and different elevation angles have been selected to study the sea state: #17 (40°), #9 (47°), #3 (57°), and #23 (80°). The ACFs of their DDM complex peaks over 1 second are plotted in Fig. 10.9. For the acquisition over the harbour, only the reflections in the inner waters have been used. It would have been interesting to compare the sea correlation time inside and nearby the harbour, since the altitude of the flight was similar in both cases, but the sea was calmer in the first instance. However, the number of reflections outisde the harbour was not enough to get statistically representative results.

Due to the low height of the flight, the reflection locations of the 4 satellites were very close to each other, and it is safe to assume that sea state was similar for all of them at a given instant. However, it can be observed that sensitivity to the sea state depends on the satellite elevation angle. The larger the elevation angle, the smaller the ACF correlation length. This information should be included in any model used to relate the sea correlation length with the ACF one. Unfortunately, no model has been derived in this thesis because only a few seconds of data were available.

The ACF correlation length of each satellite is similar in the first two captures: 3.2 ms (80°), 3.9 ms (57°), 4.5 ms (47°), and 5.9 ms (40°). These values are well below the duration of the aircraft dynamics. There are few results in the harbour capture, but it can already be seen that the duration of coherent component is much more larger than in the previous scenarios. In fact, it is large enough to be influenced by the aircraft dynamics. To make things worse, the aircraft maneuvers at that moment where much more prominent as it was less than 5 km to the airport runway. Nevertheless, results show also a dependence on the elevation angle: 22.2 ms (82°), 42.4 ms (56°), 44.9 ms (50°), and 94.8 ms (39°).

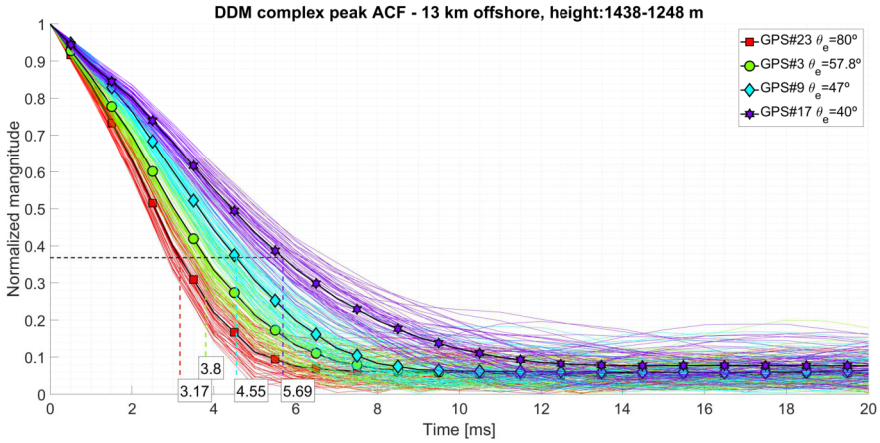

(a)

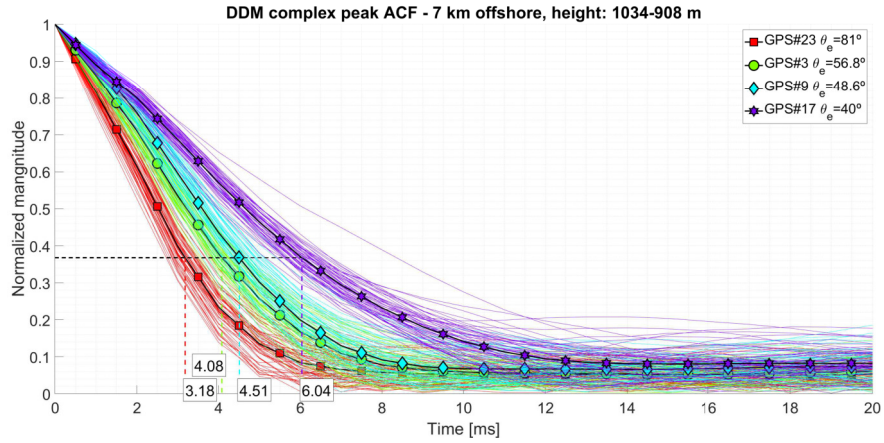

(b)

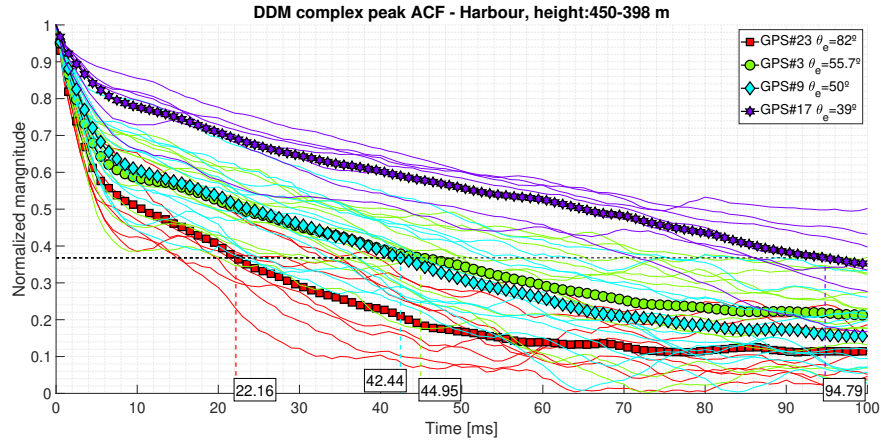

(c)

Figure 10.9: Sea coherence time estimated from the DDM complex peak 1-second ACF of the reflected signals for different scenarios and satellite elevation angles.

The correlation lengths in the open sea captures are above the code duration of the GPS L1 C/A signals, but similar to those of the Galileo E1OS signals (4 ms), and below the ones of the signals GPS L1C (10 ms), BeiDou-2 B1C (20 ms), GPS L2C (20 ms the short code and 1.5 s the large one), just to name a few. This reduces the expected performance of the latter signals in terms of coherent SNR.

10.5 Discussion

The latter results are analyzed here with the data obtained from the SIMAR sensors, and are compared with the ones presented in the similar experiments [70] and [69], performed from a static position and from an aircraft respectively.

The wind speed and the Significant Wave Height (SWH) measured by the SIMAR

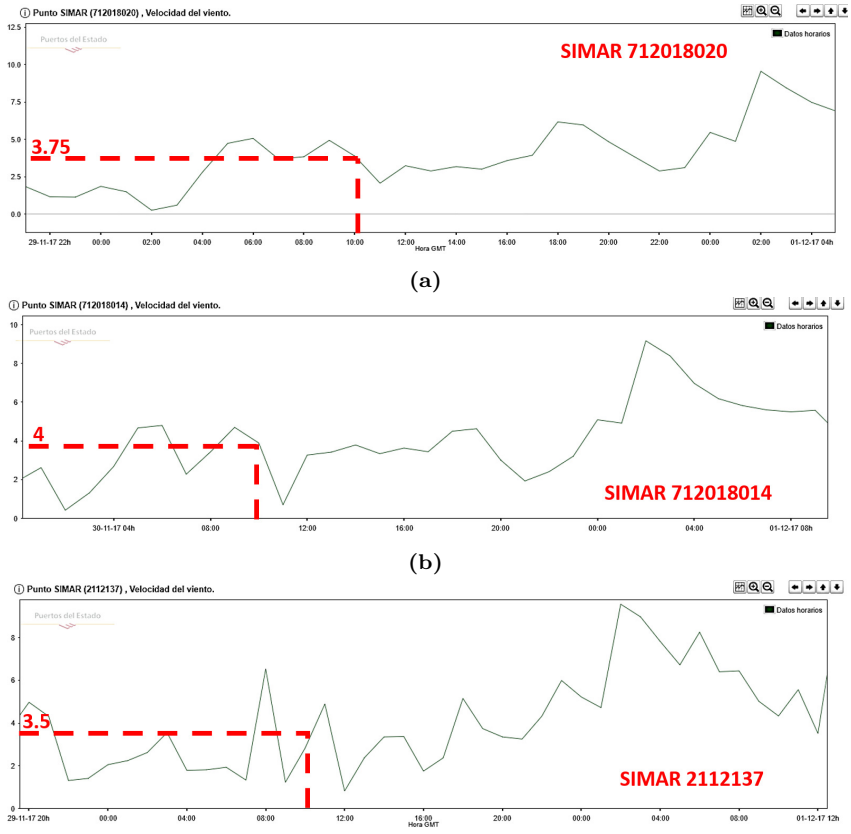

Figure 10.10: Wind speed in m/s measured by the SIMAR sensors close to the aircraft groundtracks. Time scale is in GMT format. The three sea tracks from Fig. 10.3 were taken respectively at 10.07, 10:09 and 10:11 on 30 Nov. 2017 UTC. From [`http://www.puertos.es`].

sensors are presented in Figs. 10.10 and 10.11 respectively. The SWH was about 0.6 meters in open water and only 0.05 meters inside the harbour. The wind speed was around 5 m/s in open water and around 2 m/s nearby the harbour. The values for the harbour scenario indicate very calm waters with almost no waves. This scenario behaves like a mirror for reflections at L band, and in fact, some navigation bit transitions could be seen in the reflected signal phase.

The experiment in [70] was done from a static position in a 383 meters cliff above the sea. The reference data was obtained from a buoy at a distance of 18 km. Due to the geometry of the set up, only satellites with elevation angles between 14° and 30° could be acquired. The obtained results do not discern by elevation angle and show a 100 ms correlation length for wind speeds of 5 m/s and up to 200 ms for wind speeds of 2 m/s. It is not straightforward to compare these results with the ones obtained in the harbour, as the satellite elevation angles were different and the aircraft dynamics contaminated the ACF. Although as shown in Fig. 10.4 there were satellites with lower elevation angles,

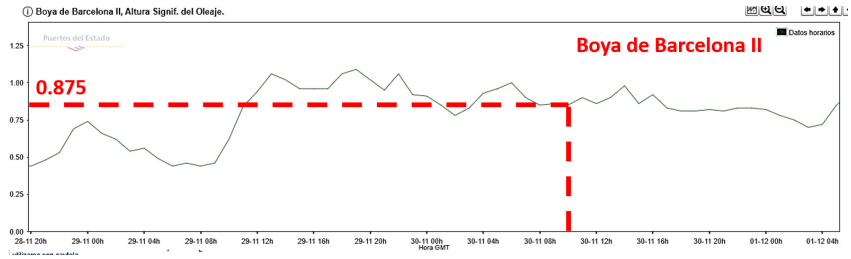

(a)

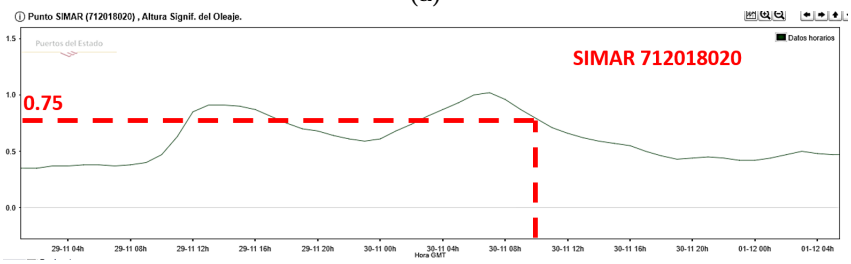

(b)

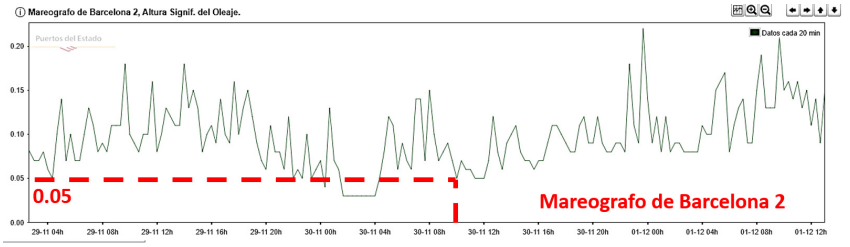

(c)

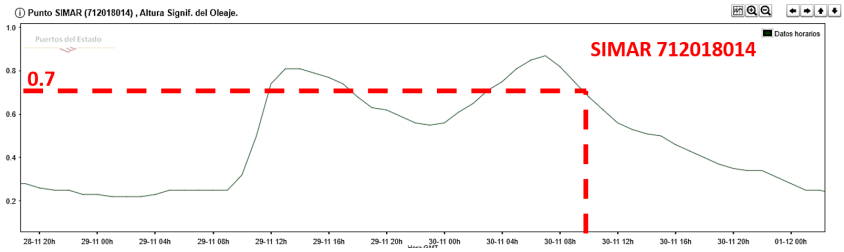

(d)

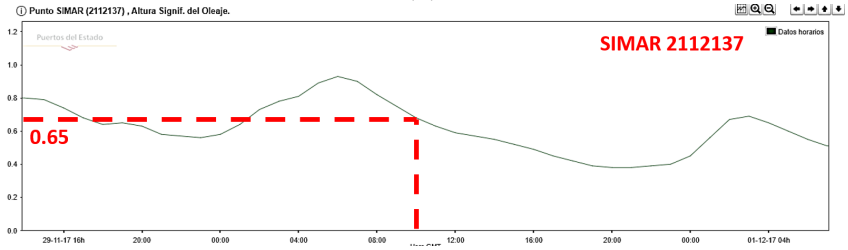

(e)

Figure 10.11: SWH in meters measured by the buoys close to the aircraft groundtracks. Time scale is in GMT format. The three sea tracks from Fig. 10.3 were taken respectively at 10.07, 10:09 and 10:11 on 30 Nov. 2017 UTC. From `http://www.puertos.es`.

their SNR was too low to get satisfactory results. The reason why in [70] it was possible to use satellites with those angles, but not here, may be because the former experiment used an array antenna pointing to that area of the sky, whereas the present experiment used a commercial antenna pointing to the aircraft nadir and with a limited field of view.

The experiment in [69] was performed from an aircraft flying at an altitude of 3200 m. There was no reference data, but a wind speed of 6.2 m/s was derived from a model. The obtained correlation lengths were 4.56 ms (58.64°), 5 ms (51.61°), 4.5 ms (50.87°), and 6.3 ms (29.9°). These values are well in accordance with the previous findings in the open waters, although the flight height was between two and three times lower.

To conclude the discussion, it is interesting to see that although the difference in terms of ACF correlation length are clear between satellites and scenarios, it is not in terms of reflected power. In Fig. 10.13 the reflected DDM peak power is plotted for each satellite at the reflection point, along with the combined histograms for all the satellites and for each scenario. No big differences are observed in the power statistics, except for those reflections outside the water.

10.6 Conclusions

This chapter shown that the sea correlation time can be estimated from the time decorrelation of the reflected DDM peak, after compensating the Doppler and by removing the phase jumps due to a navigation bit or a secondary code chip transition. However, the window length in which this time can be estimated, depends on the user ability to compensate for the motion of the receiver. If the receiver dynamics and the peak decorrelation time are within the same order of magnitude, the Doppler and any oscillator offset and drift, must be estimated more frequently. Although this may not be a problem in open sea scenarios, it is in calm waters, as in harbours, in which the the sea coherence can last for a few hundreds of milliseconds.

Results show that the correlation time increases for low elevation angles. In open sea, it can be also seen that the correlation time increases with decreasing the receiver height. This may be explained from the fact that the fewer the number of Fresnel zones which contribute to reflected signal, the less noisy is its phase [37]. Correlation times between 3.17 ms and 6.04 ms are obtained at heights from 1438 to 908 m and with elevation angles between 80° and 40° respectively. These values are increased to 22.16 ms and 44.95 ms in a harbour scenario. Although there is few data available to derive a model, these results are in accordance to the ones obtained in [69] in open waters, and in [70] close to the shore.

The results in open sea are also important because they state that the maximum coherent integration time in such scenarios is similar or even smaller than the code duration of the new GNSS signals. Thus, the expected improvement of such signals with respect to the GPS L1 C/A one in terms of coherent SNR is reduced. For this reason, although

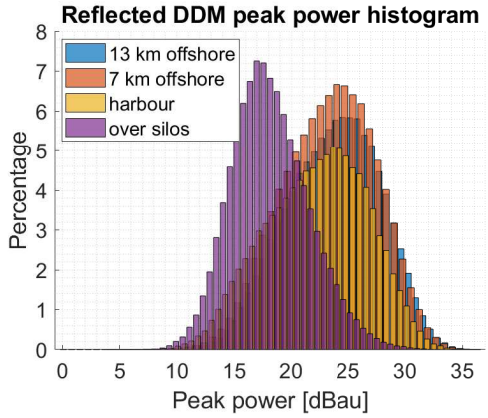

Figure 10.12: Combined DDM peak power histogram for all the PRNs and for each scenario.

the GPS L2C and the Galileo E1OS signals were also recorded in this experiment, only the L1 C/A ones were used. However, as future research, it would be interesting to use as well the GPS L2C signals, because they are transmitted at a different frequency ($\lambda_{L2} \approx 1.284\lambda_{L1}$), which may be useful for the development of a more accurate model.

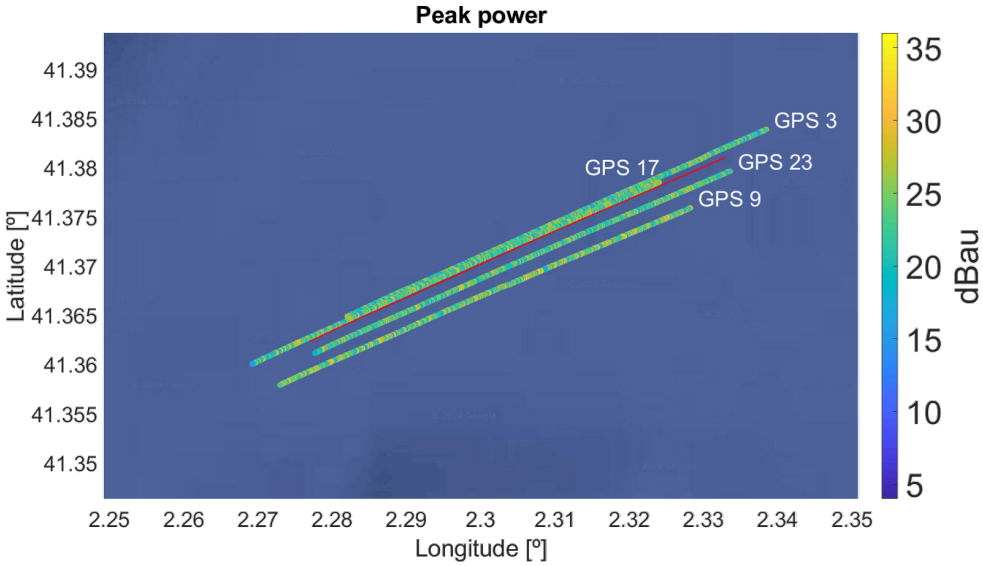

(a)

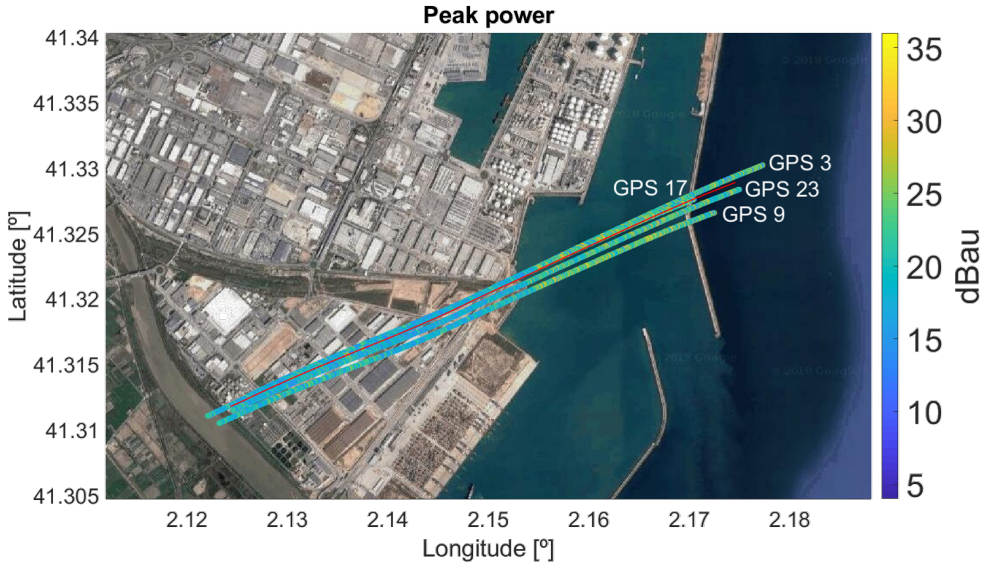

(b)

Figure 10.13: Reflected DDM peak power at (a) 7 km offshore and (b) in the harbour. Adapted from [227].

11

Chapter 11

Results from the Australian Campaigns

This chapter gives the results from the MIR campaigns in Australia for a variety of different applications. These are: detection of water-land transitions, soil moisture estimation, sea state and altimetry, and land topography. In addition, a brief analysis has been done on the cross-talk phenomenon and on the impact of GNSS secondary codes on the retrievals when they are not properly aligned during the correlation process.

Preliminary results were first presented in [229], and a detailed cross-talk study was published in [230].

11.1 Introduction

The MIR instrument flew four times over South Eastern Australia during the southern hemisphere autumn of 2018. The experiments were designed and performed together with Prof. Jeff Walker from Monash University. The first flight was planned as a test and was conducted over the entrance of the Port Phillip Bay (VIC), where a buoy and a tide gauge would be used later as ground-truth data. Two flights where designed over the Yanco (NSW) area, where the Monash University has a network of soil moisture sensors for hydrological monitoring named Oznet [231]. The main goal of these latter experiments, was to state the feasibility of the GNSS-R technology for soil moisture estimation from airborne instruments. The first flight was performed at the very beginning of autumn, and the second one after the first heavy rains. Finally, one flight was conducted over the Bass Strait, which separates Australia from Tasmania, departing from Mallacoota (VIC). The main goal of this flight was to study the altimetric capabilities of the new GNSS signals by using the cGNSS-R and iGNSS-R techniques. Figure 11.1 shows actual pictures of the areas overflowed during those flights, and Fig. 11.2 shows the aircraft groundtracks.

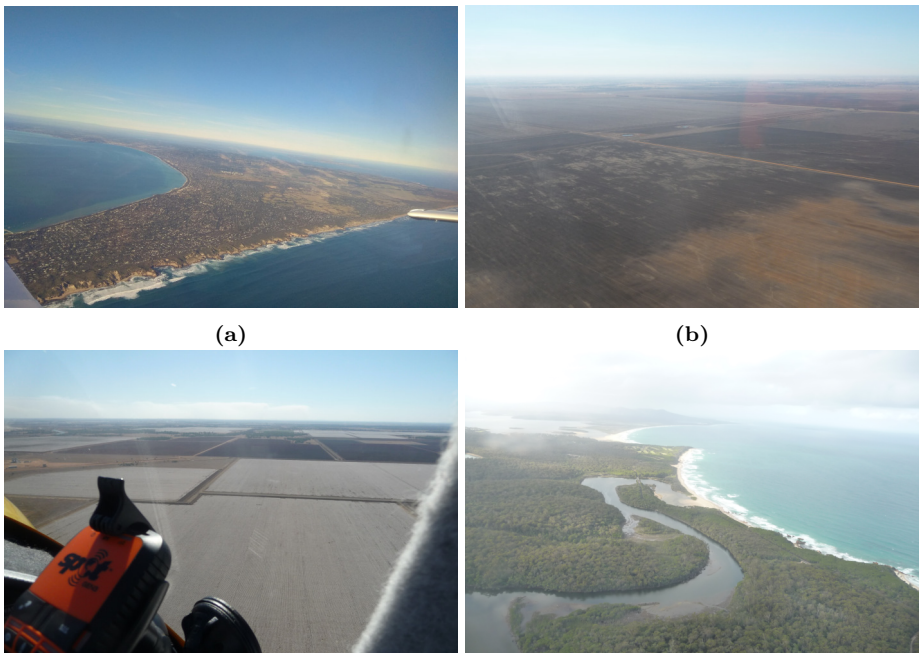

Figure 11.1: Actual photos of some areas overflown during the MIR campaigns: (a) Port Phillip Bay as seen from the Mornington peninsula, (b) fields and (c) cultivated fields in Yanco, and (d) Croajingolong National Park near Mallacoota.

11.1.1 Field campaigns design

The aircraft was a piloted by Jon Johanson [232], a well-known aviator in the Australian aviation community. In fact, MIR was designed in order to fit the constraints of Johanson's aircraft. The size of the antenna arrays, the overall power consumption or the RF cables length, were among the issues that needed to be planned and agreed in advance. The rackmount was placed in the rear part of the aircraft, with the up-looking antenna on top of it. The down-looking antenna was placed in the aircraft belly. The size of up-looking ground plane was smaller than the down-looking one, so as to fit it inside the cabin (see Section 9.3 for details).

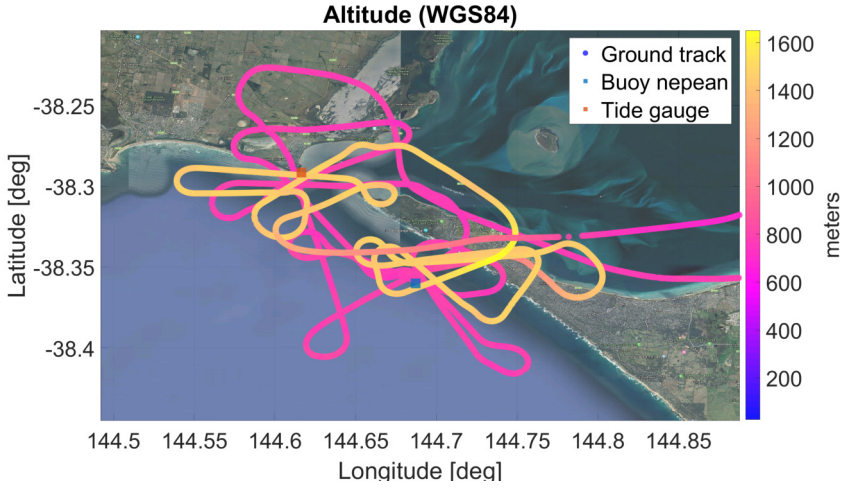

(a)

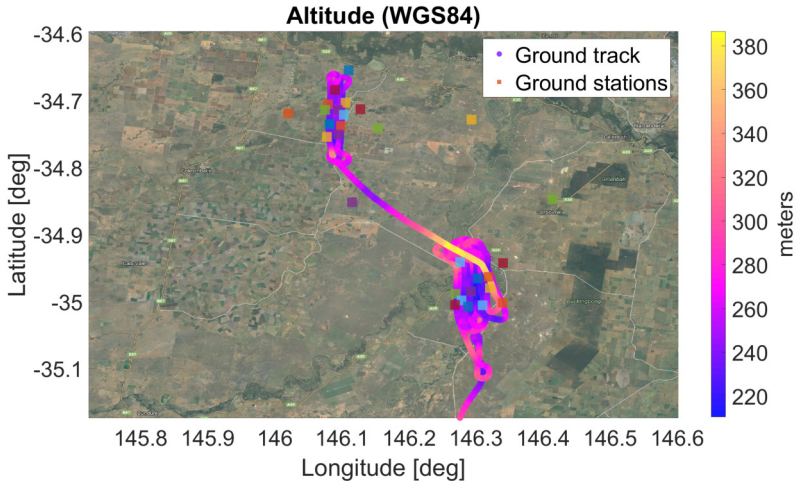

(b)

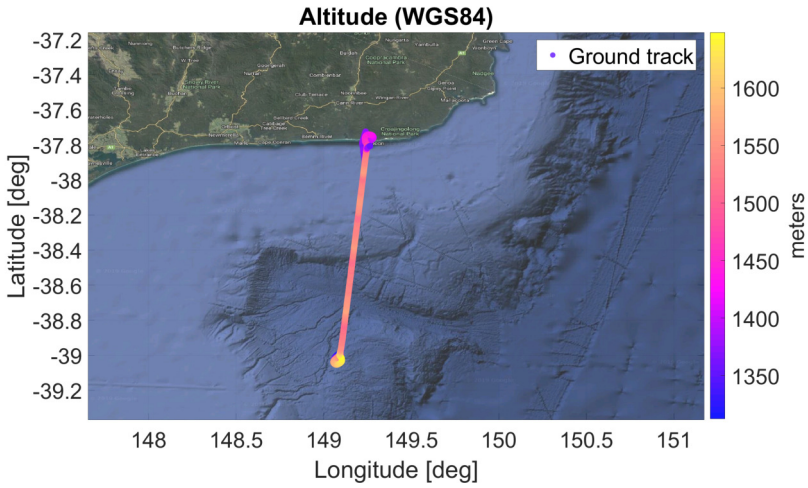

(c)

Figure 11.2: Flight altitude maps of the MIR campaigns: (a) over Port Philip bay, (b) over Yanco, and (c) over Bass Strait.

The assembly was not straightforward and took several weeks of dedicated work, as there where many hidden details that where not taken into account during the design process. To name a few, the rackmount fasteners had to guarantee that the instrument would not move during the maneuvers, the screws and washers had to be vibration-resistant, and the down-looking antenna was further wrapped with a vinyl layer to protect it against humidity and to block the screw holes against the wind. Figure 11.3 shows the assembly process, and detailed AutoCAD schematics can be found in [5].

The author and Dr. Onrubia accompanied the pilot by turns. During the flights, the companion had to control and monitor the MIR instrument, as well as support the pilot and clarify any doubts about the planned route. The design of the flight waitpoints was supervised by Prof. Jeff Walker. From a scientific point of view, the flights were designed to fly over ground sensors in the Port Philip Bay and Yanco flights, and to follow a Cryosat-2 groundtrack in the Bass Strait flight. In the former cases, the aircraft turns had to be planned in order to give the pilot enough space for heading between consecutive sensors. Besides the scientific considerations, many other factors regarding safety issues where taken into account. In order give the reader context, the design difficulties of the Bass Strait flight may help as an example. The Cryosat-2 passes over that area are not daily but weekly or fortnightly. Among the pilot requirements, was to fly during light hours, in good meteorological conditions, and to go no further than a given distance from the closest airfield. In order to meet all these requirements, several flights where designed spanning over a couple of months. Figure 11.4 shows some of them.

Figure 11.3: Photos of the MIR assembly in the aircraft: (a) side view of the aircraft, (b) MIR rackmount inside the aircraft, (c) up-looking array placed over the rackmount, (d) down-looking array being mounted on the aircraft belly, (e) view of the cables from the down-looking array to the rackmount, and (f) aircraft flight showing the down-looking array.

11.1.2 Specular reflection point calculation

Before going through this section, it is worth clarifying first some basic concepts. GNSS receivers give the user location over a reference ellipsoid called geodetic datum. The

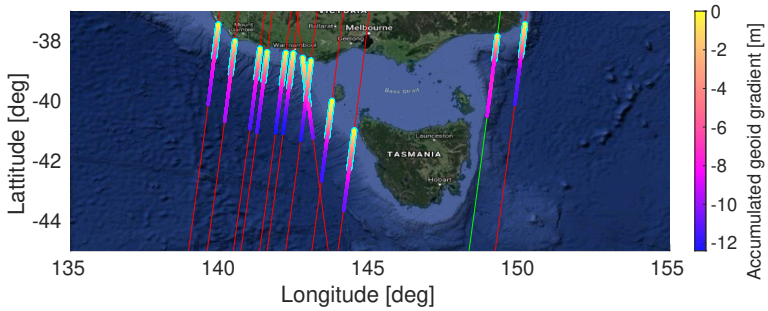

Figure 11.4: Accumulated geoid gradient over Cryosat groundtracks. Considered tracks are marked in red, and final one in green. Obtained from [5].

ellipsoid is an object that approximates the geoid, either locally or globally, using simple mathematical models. The most common one is the World Geodetic System 84 (WGS84), which is global and geocentric. The geoid is the shape that the ocean surface would take under perfect calm conditions, without tides, waves or currents. Unlike the datums, the geoid surface is irregular (up to 200 m) due to the uneven distribution of mass on the Earth. The Earth Gravitational Model 96 (EGM96) is the reference geoid commonly used together with the WGS84 datum. The last published version is from 2008. The shape of land surfaces (topography) and of the underwater depth (bathymetry) is further given by DEMs. Global models are obtained by dedicated radar and lidar satellite and airplane missions. Some models represent only the bare ground, while others also include buildings, trees and other features. The one used in this thesis is Shuttle Radar Topography Mission 3 (SRTM3) v2.1 which has a resolution of 3 arc-seconds, or about 90 m at the equator.

On top of the latter definitions, there is the surface roughness over the land, and the waves, tides and currents over the ocean. The surface roughness is defined by local deviations of a surface from the ideal (flat) one. The impact of those features on the GNSS reflections depends on the signal frequency band and on the incident angle. In water bodies, the waves are fluctuations around the mean sea level caused by the wind. The wave height is defined from the trough to crest, and can range from the few centimeters of the surface ripples to the several meters of the swells. As there is certain amount of randomness between consecutive waves, their height is typically given by the SWH or by the RMS. A tide is a periodic rise and fall of the mean sea level caused by the combined effect of the gravity forces of the Sun and the Moon, and the rotation of the Earth.

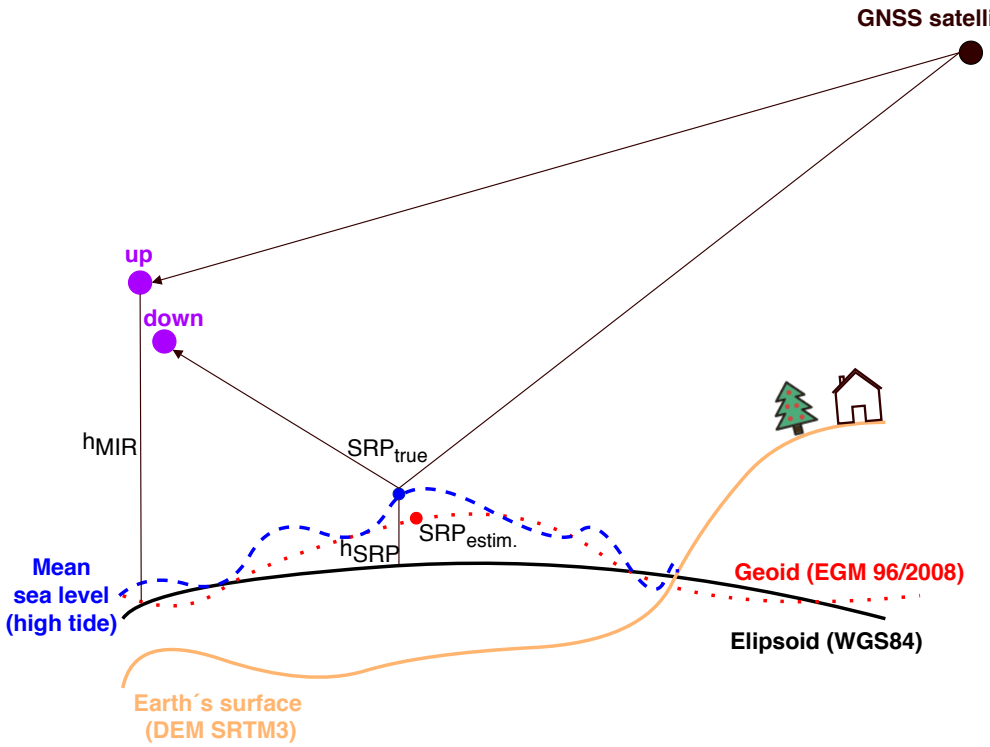

Figure 11.5: Example of a MIR reflection scenario.

Figure 11.5 shows a diagram of the above descriptions using a MIR scenario, that is, with the transmitter and the receiver at different positions. The picture has been exaggerated in order to show the distinct features. Note first that this is a side view of 3D scenario. Note also that the paths from the satellite to the up-looking antenna and to the Specular Reflection Point (SRP) should be almost parallel, with virtually identical incident angles, and that the ellipsoidal heights should be orthogonal to the ellipsoid.

The SRP calculation method used in this thesis is explained in [5]. The points are found using the EGM96/2008 geoid and following the conditions defined in [26]: the normal vector to the SRP is in the plane defined by the receiving antenna, the transmitting satellite and the SRP; the local incident angle and the local reflection angle are equal; and the distance from the satellite to the SRP, and from the latter to the receiving antenna, must be the shortest path. On the land reflections, these conditions are further modified in order to use as well the SRTM3 model. These conditions do not give a closed-form expression to find the SRP, but allow finding it iteratively up to a certain degree of tolerance error.

The true SRP differs from the estimated one because of the tides; the errors in the

models propagated in the derivation process; the mismatches between RF chains; and the so-called EM. The calibration of the RF components has been carried out in [5] at the same time of writing this chapter. The EM bias is the error introduced due to the non-symmetric properties of the sea waves. Their shape does not reassemble a sine wave, but the crests may be sharper on one side than the other. Work on this latter issue and regarding GNSS signals can be found on [90, 91].

Figure 11.6 shows the specular reflection points in the Port Philip bay flight. The marker inner color shows the elevation angle of the tracked satellite, and the contour color indicates the satellite constellation and PRN. The satellite selection algorithm was based on the elevation angle, while aiming to track satellites from different constellations.

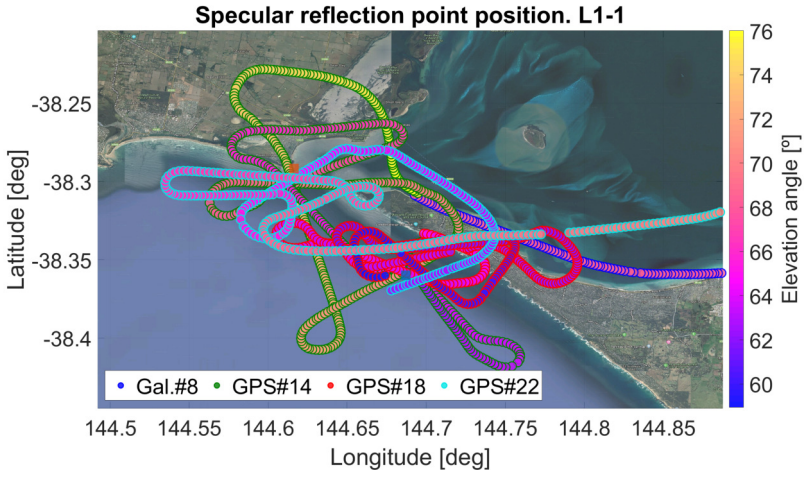

(a)

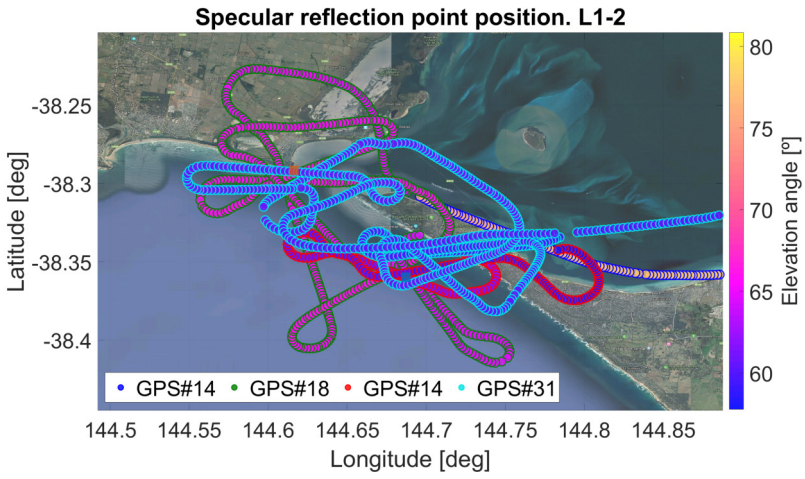

(b)

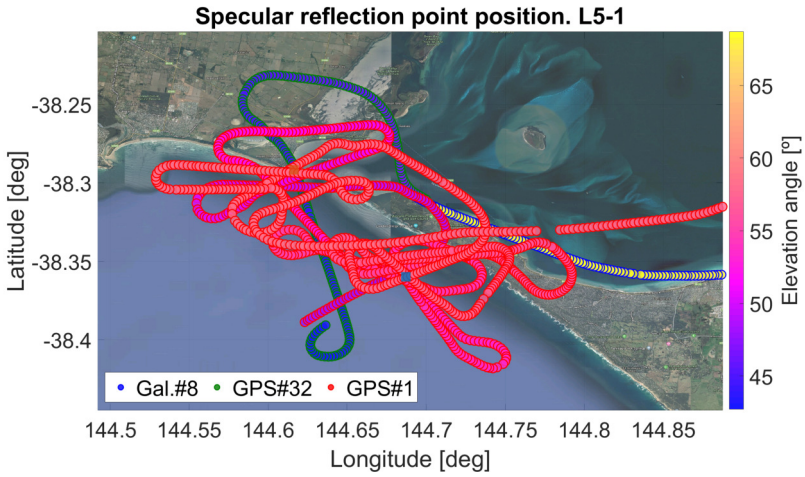

(c)

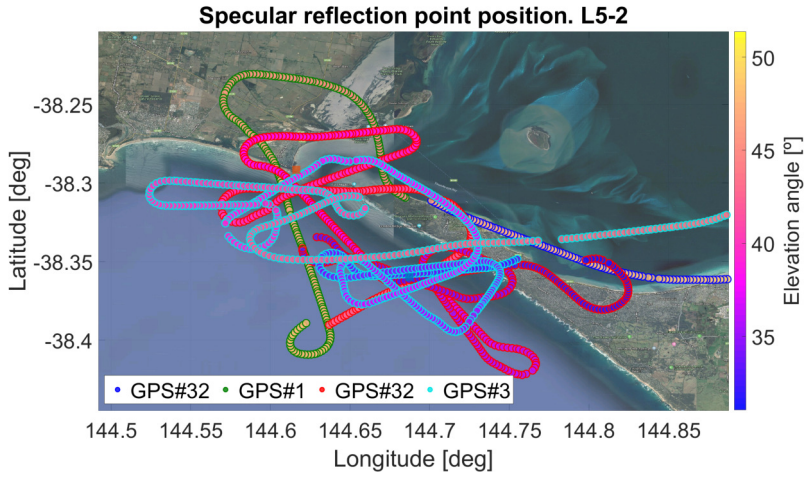

(d)

Figure 11.6: Specular reflection points position during the Port Philip bay flight: (a) Beam L1 #1 , (b) beam L1 #2, (c) beam L5 #1, and (d) beam L5 #2.

The satellite change was roughly every 10 minutes. It can be noticed that GPS #14 and #18 were swapped between the two L1 beams. That happened because the algorithm first allocates the L1-1 beam, without checking if that satellite was already tracked by the other beam. A similar behavior can be seen in the two L5 beams. Finally, it can also be noticed that only the Galileo PRN #8 was simultaneously tracked by L1 and L5 beams. The reason is that the algorithm was independent of the band, as by then, there were few GPS satellites in view transmitting at L5 with a high elevation angle.

11.1.3 Notes on beamsteering

The steering angles were obtained by combining the position of the aircraft and of the satellites, with the attitude of the former, and taking also into account the position of the antennas inside the vehicle. The aircraft principal axes, named yaw, pitch and roll, were obtained with an IMU and are shown in Fig. 11.7. The satellite elevation and azimuth, and the steering angles of the up- and down-looking beams are shown in Fig. 11.8. Note that it is not straightforward to find the axis of symmetry between both beams, as it depends on the satellite position in the skyplot and on the aircraft attitude.

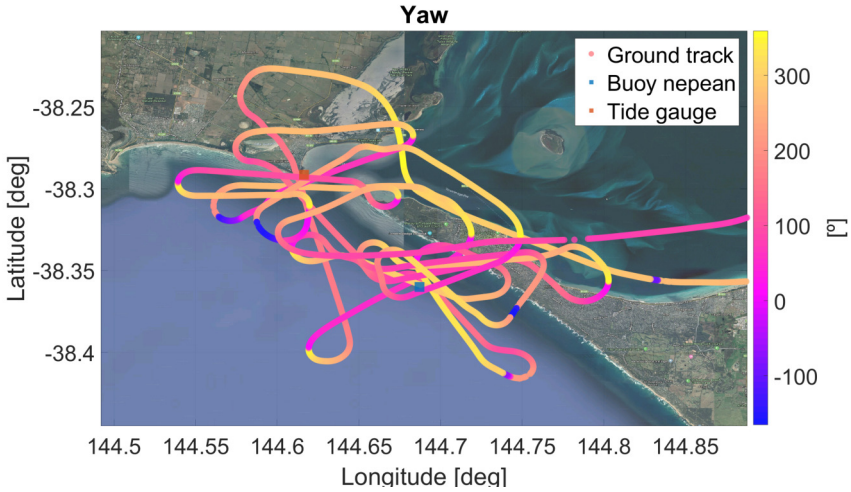

(a)

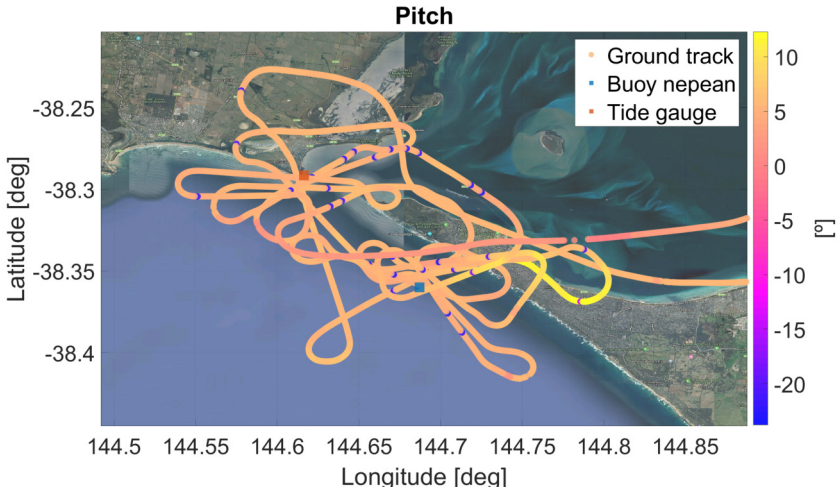

(b)

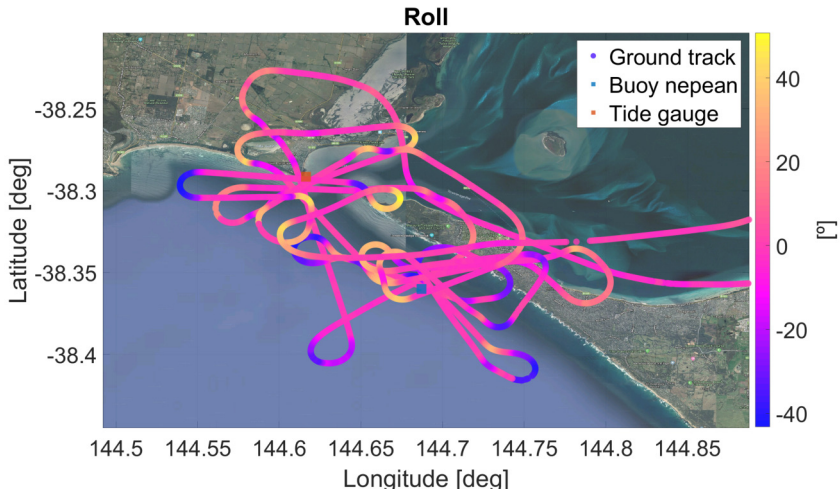

(c)

Figure 11.7: Aircraft principal axes during the Port Philip bay flight: (a) Yaw, (b) pitch, and (c) roll.

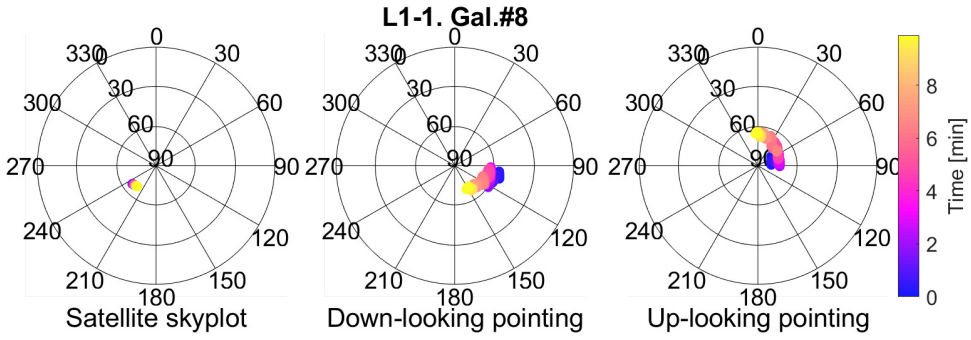

(a)

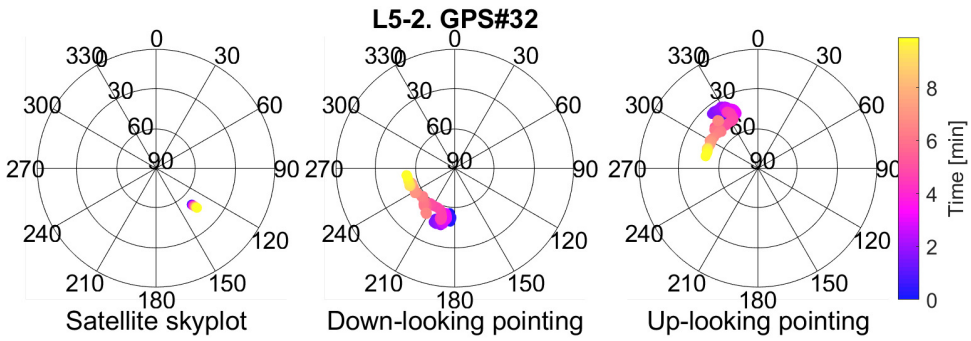

(b)

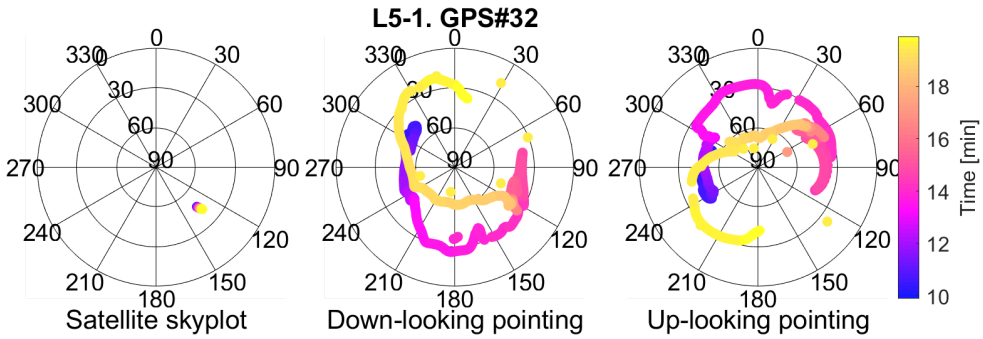

(c)

Figure 11.8: Examples of pointing angles during the Port Philip bay flight: (a) Beam L1 #1 tracking Galileo satellite #8, (b) beam L5 #2 tracking GPS satellite #32, and (c) beam L5 #1 tracking GPS satellite #32.

11.2 Water-body transitions

The first flight was done over the Port Philip bay on 30 April 2018, taking off from Tyabb airfield at Mornington Peninsula. The goal of this fight was to test the instrument aboard the aircraft. Nevertheless, the route was already designed to fly over two maritime buoys, which eventually could be used as a reference ground truth data. The two buoys were overflown several times at two different heights (see Fig. 11.2a) so as to be able to compare its impact on the DDMs. The average ground speed was about 65 m/s.

Figure 11.9: Queenscliff village in Bellarine Penisula, showing inner calm (left) and sea (right) waters. From [`https://en.wikipedia.org/wiki/Queenscliff,_Victoria`]

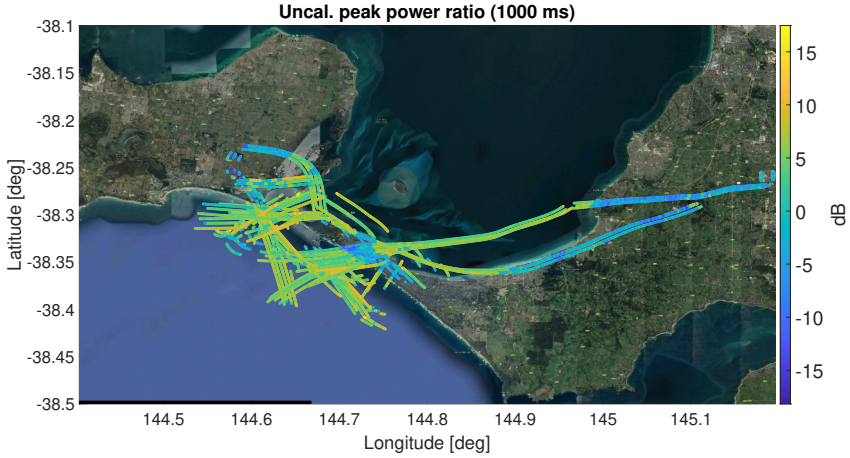

Figure 11.10: Uncalibrated direct/reflected DDMs peak power ratio in the Port Philip bay flight map.

Although the buoys data have not finally been used in this thesis, the flight allowed the study of the transition between water bodies and land by analyzing the reflectivity of the surface. Different types of water bodies were overflown during the flight: small irrigation ponds, sea waters, inner bay waters, and low depth calm ones. These two latter surfaces can be observed on the two sides of the Bellarine Peninsula in Fig. 11.9.

Figure 11.10 shows the DDM peak power ratio of the 4 pair of up-/down-looking beams. Each scatter is obtained by using as a coherent integration time, the duration of the respective code (1 ms for GPS C/A and L5 and Galileo E5, and 4 ms for the Galileo E1OS). The incoherent averaging corresponds to 1 second averages (1000 for the 1 ms signals and 250 for the 4 ms ones). Bear in mind that these values do not represent the reflectivity, as the impact of the elevation angle and of the roughness of the land surfaces should be removed. Additionally, the antennae directivity and the cable losses should also be taken into account [5]. Nevertheless, the land and sea surfaces can already be easily distinguished due to the latter having a much stronger peak power ratio. Note also that there are gaps of data with respect to the tracks shown in Fig. 11.2a. These points have been removed because during the processing, it was observed that the beams were not pointing correctly during the aircraft sharp turns.

Figure 11.11 shows the combined histogram of the above peak power ratios. One can easily identify that there are two combined distributions. A Gaussian fitting mixture model inferred that water surfaces have a mean of 5.7 dB and a variance of 4.4 dB, while land surfaces have a mean of -2.7 dB and a variance of 21.3 dB. These values should be taken as qualitative preliminary study, as there are many other parameters that

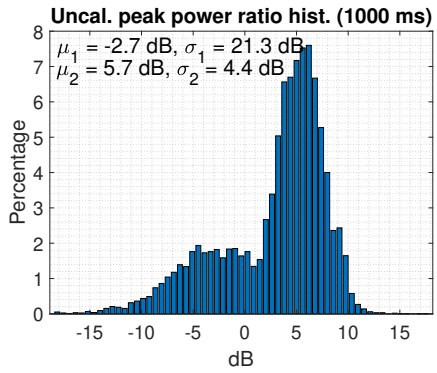

Figure 11.11: Uncalibrated direct/reflected DDMs peak power ratio histogram in the Port Philip bay flight. Combined results for all the bands, signals and satellites.

affect these estimations. For example, the spatial resolution depends on the coherent and incoherent integration lengths, and on the satellite elevation angle. Certain configurations may blur small areas like shorelines or residential neighborhoods, creating *artificial* values. Additionally, in land areas, there are points with high reflectivity, such as roads and building rooftops. Some of these characteristic features are shown next.

The top maps in Fig. 11.12 zoom in on the map of Fig. 11.10 around certain areas. The markers correspond also to 1 second averages. The bottom pictures show the respective temporal series of the beam L1-1 only, using different incoherent averages. Note first in Fig. 11.12a, that the scatters have a small mapping bias. This error may come from non-accurate reference coordinates in the base map, as it was downloaded from Google Maps using a free software tool [233].

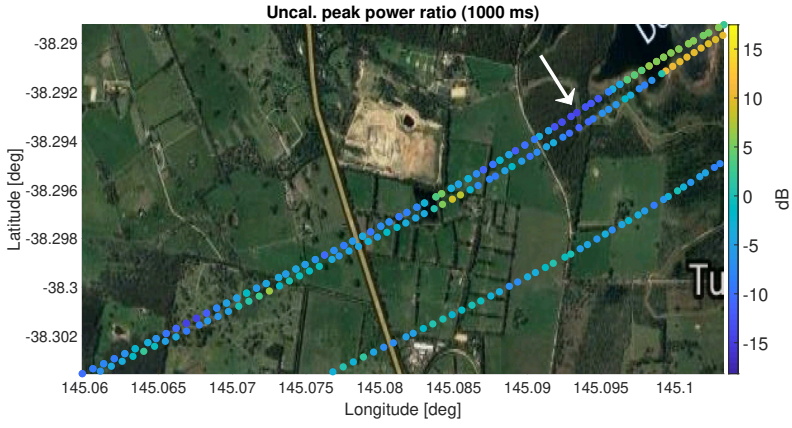

(a)

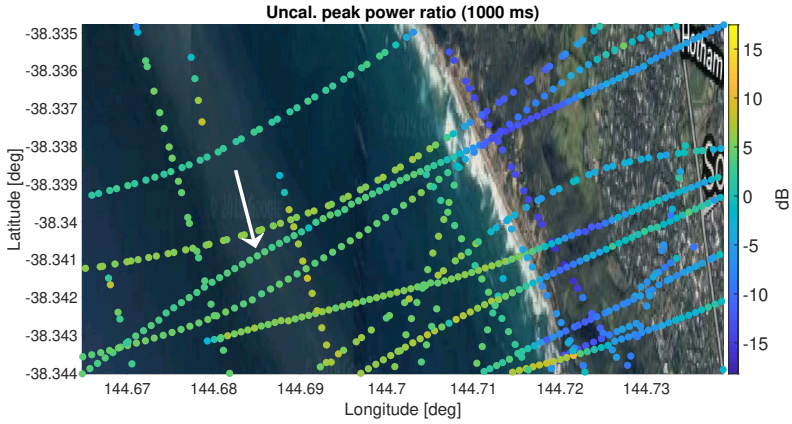
Uncal. peak power ratio (1000 ms)
Latitude [deg]
-38.335
-38.336
-38.337
-38.338
-38.339
-38.34
-38.341
-38.342
-38.343
-38.344
144.67
144.68
144.69
144.7
144.71
144.72
144.73
Longitude [deg]
dB
15
10
5
0
-5
-10
-15

(b)

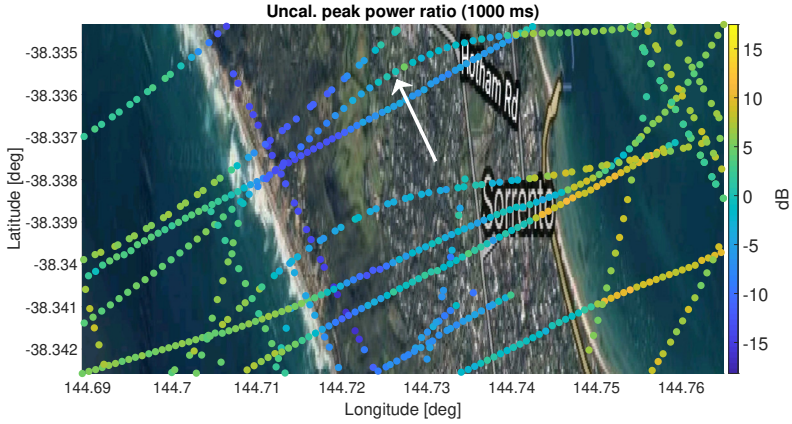
Uncal. peak power ratio (1000 ms)
Latitude [deg]
-38.335
-38.336
-38.337
-38.338
-38.339
-38.34
-38.341
-38.342
144.69
144.7
144.71
144.72
144.73
144.74
144.75
144.76
Longitude [deg]
dB
15
10
5
0
-5
-10
-15

(c)

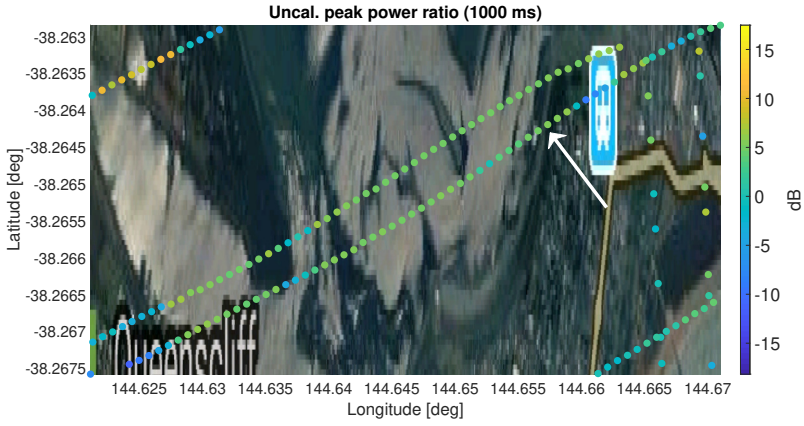
Uncal. peak power ratio (1000 ms)
Latitude [deg]
-38.263
-38.2635
-38.264
-38.2645
-38.265
-38.2655
-38.266
-38.2665
-38.267
-38.2675
144.625
144.63
144.635
144.64
144.645
144.65
144.655
144.66
144.665
144.67
Longitude [deg]
dB
15
10
5
0
-5
-10
-15

(d)

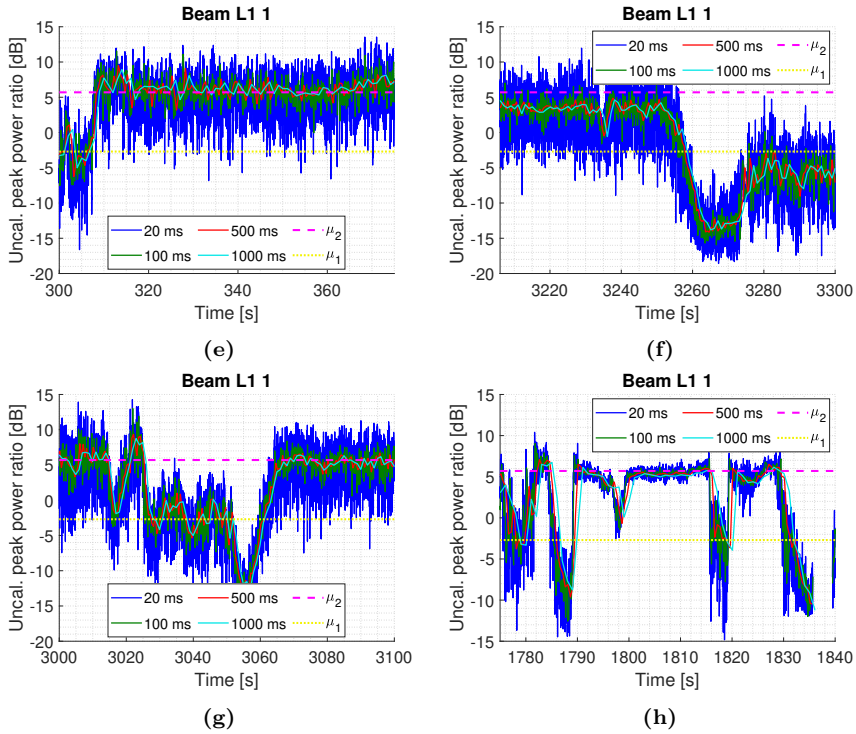

Figure 11.12: Peak power ratio in the Port Philip bay flight: detailed maps (above), and respective time plots (bottom). Time plots are sorted as left-right and top-bottom.

In Figs. 11.12f and 11.12g, it can be seen that the smaller the averaging is, the larger the variance of the measurements is. In contrast to that, small averaging values allow the discerning of different types of surfaces and the appearance of transition areas like the shorelines. See also in Fig 11.12c, the difference between urban and country or forest areas. Some urban reflections can be as bright as the ones over sea. Note also in Fig 11.12c, the two kinds of reflection over sea. The open sea shore on the right is rougher than the inner bay on the left, which translates into a noisier and smaller reflectivity. This effect is much more noticeably in the quiet waters of Fig. 11.12d as previously shown in Fig. 11.9. Not only the variance is smaller, but also the leading edges are sharper.

The latter figures show the interesting feature that reflectivity follows an interference pattern in the transitions between water bodies and land. As stated in [37], this behavior may be the result of the Fresnel zones passing from one medium to another when the coherent component dominates. This can be confirmed in Fig. 11.13, where the reflectivity of the L1 and L5 bands of the same GPS satellite are shown overlapped. The vertical lines indicate where both oscillations have the peaks aligned. Note that the oscillations have a 4:3 rate, the same between L1 and L5 carrier frequencies. See also in Fig. 11.14 that small incoherent lengths allow the detection of smaller areas.

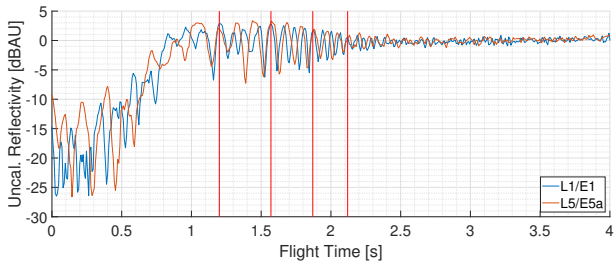

Figure 11.13: Comparison of L1 and L5 reflectivities when changing from a land to a water surface. From [5].

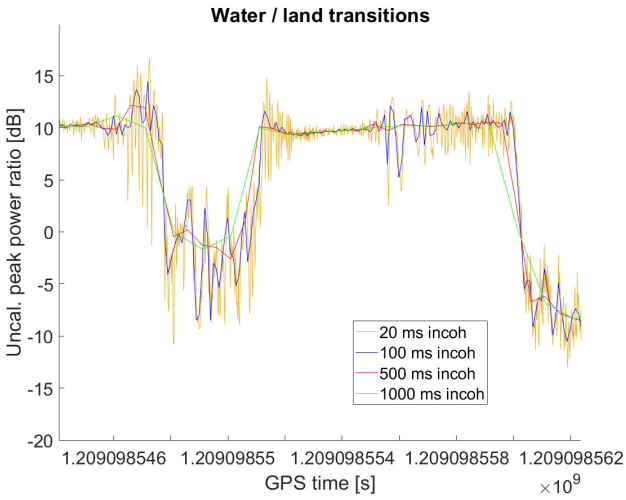

Figure 11.14: Impact of the averaging on the power ratio when changing of surface type.

11.3 Soil moisture

The second and fourth flights were done on 1 May 2018 and on 18 June 2018 respectively. The altitude was between 300-400 m, and the ground speed was between 50 and 70 m/s. The flights departed from Yanco (NSW) and flew over the sensors from the Oznet hydrological monitoring network [231]. The first flight, named *dry*, was carried out after 15 days without any rain event, and with only 9.2 mm accumulated rainfall in the previous 89 days. The second one, named *wet*, was performed with 8.2 mm accumulated rainfall from the previous day and with 24.6 mm accumulated rainfall in the previous 9 days (see Fig. 11.15).

The DDM peak power ratios of both fights are shown in Figs. 11.16 and 11.17. The square markers show the position of Oznet sensors, whose depth is 5 cm underneath. The average soil moisture in the dry flight was about 5.7%, which was increased up

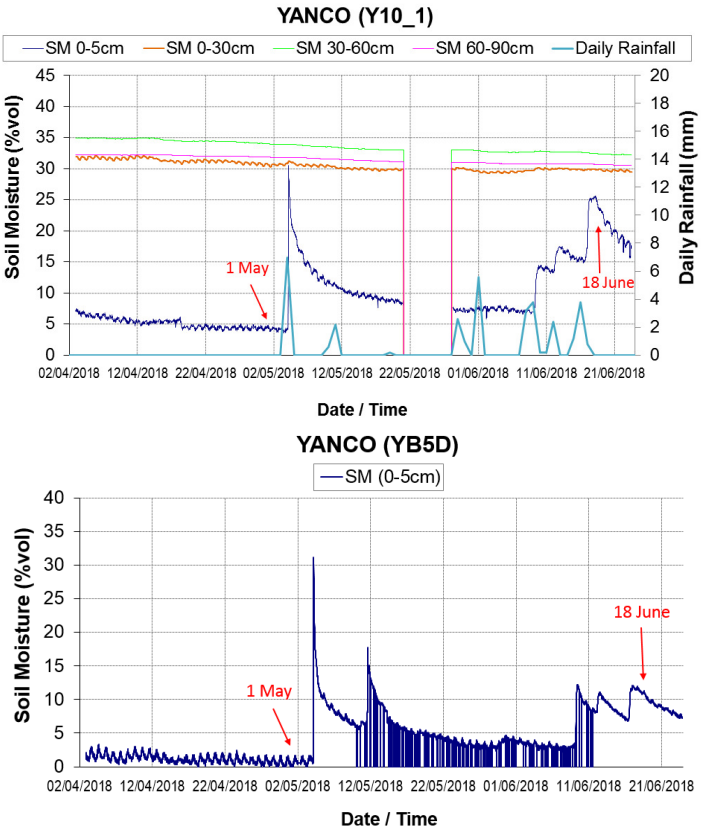

Figure 11.15: Soil moisture time evolution at two Yanco ground sensors.

to 19.1% in the wet one. Note that in the wet flight, there is a large dynamic range on the soil moisture values, even between adjacent sensors. The stantard deviation of this flight was about 8.8%, while in the dry flight was about 3%. The data from the sensors is well in accordance with the power ratios obtained with MIR. However, bear in mind that as stated previously, these values are not reflectivity values, as the impact of the satellite elevation angle and of the surface roughness should be removed, as well mismatches between hardware chains should be calibrated [5].

The power ratio histograms are presented in Fig. 11.18. They are obtained by combining all the results from all the signals and bands. Both present a similar standard deviation of about 3.5 dB, but the average is shifted from −5.1 dB in the dry flight to 0.7 dB in the wet one. A further analysis should be done by isolating different fields based on the cultivation type and state (see Figs. 11.1b and 11.1c). Additionally, there are outlayers that should be removed from the analysis. As examples, the Yanco Creek that meanders through the lands, and the farm silos, produce high reflectivity values.

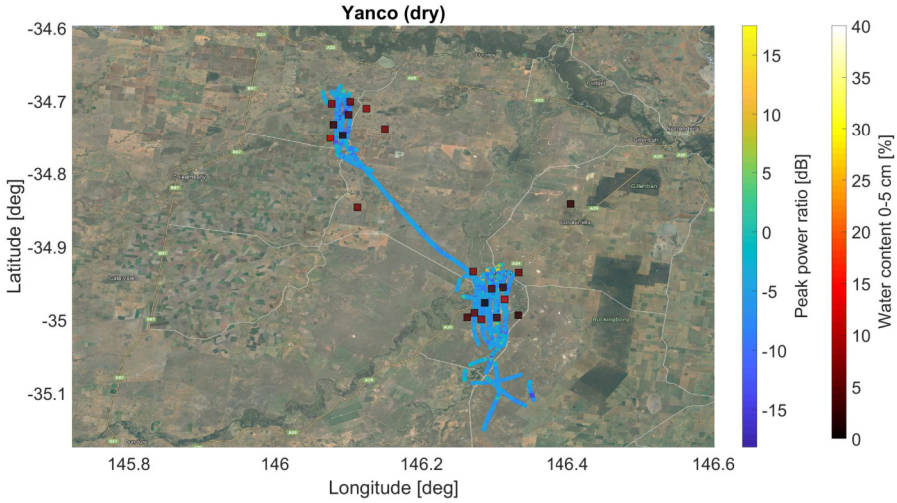

(a)

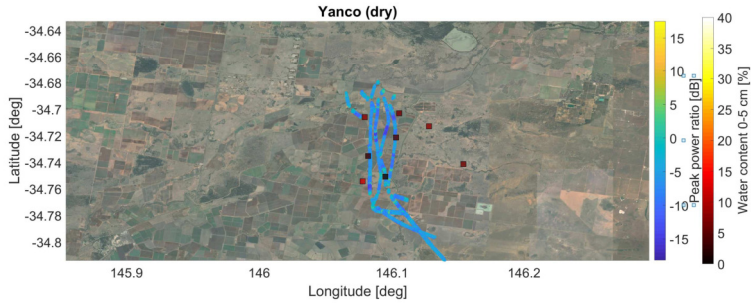

(b)

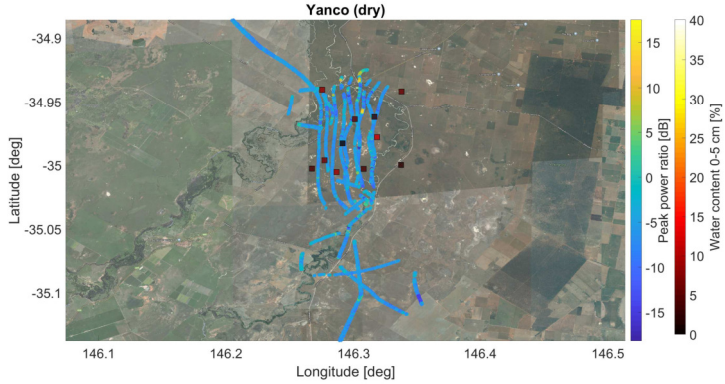

(c)

Figure 11.16: Uncalibrated direct/reflected DDMs peak power ratio map in the Yanco flight during the dry season: (a) overall map, (b) zoom in the northern fields, and (c) zoom in the southern fields. Incoherent averages of 1 second.

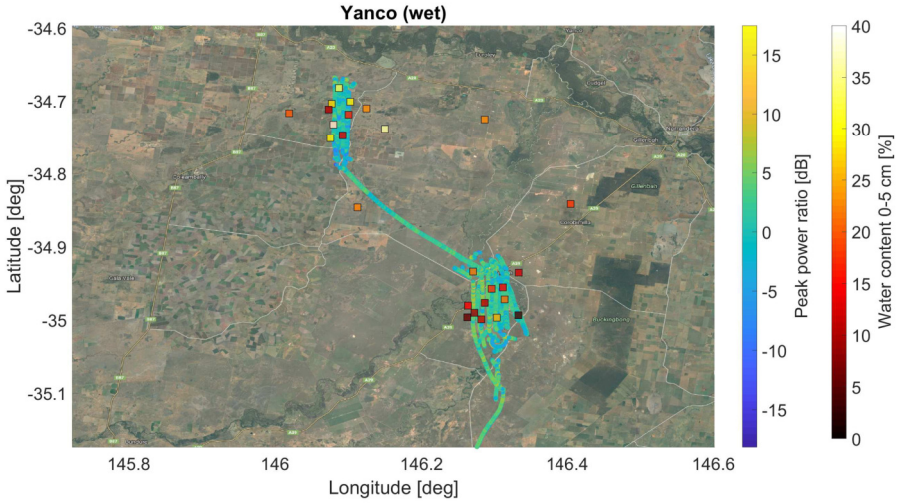

(a)

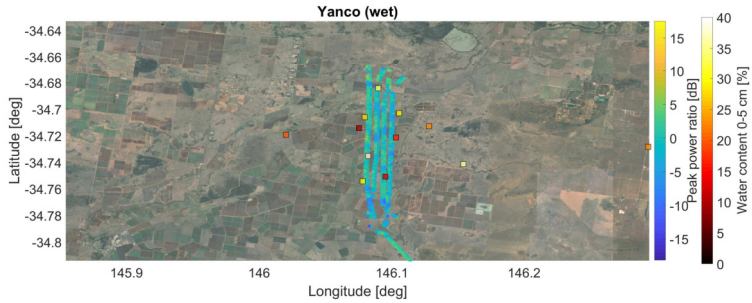

(b)

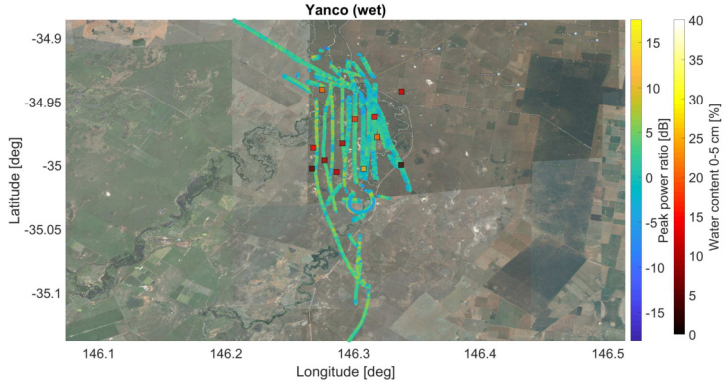

(c)

Figure 11.17: Uncalibrated direct/reflected DDMs peak power ratio map in the Yanco flight during the rain season: (a) overall map, (b) zoom in the northern fields, and (c) zoom in the southern fields.. Incoherent averages of 1 second.

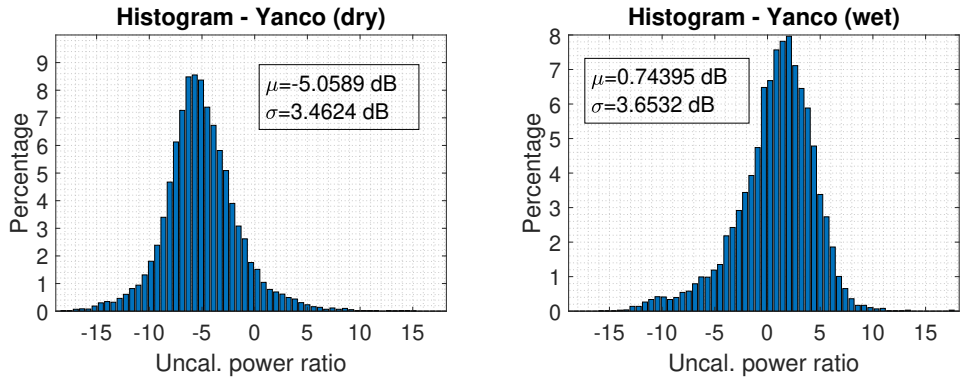

(a) (b)

Figure 11.18: Uncalibrated direct/reflected DDMs peak power ratio histograms in the Yanco flights: (a) dry season and (b) rain season. Combined results from all the bands, signals and satellites. Incoherent averages of 1 second.

11.4 Sea altimetry

The third flight was done on 6 June 2018 departing from Mallacoota (VIC) following a Cryosat-2 ground track to a distance of 125 km offshore in the Bass Strait (see Fig. 11.4). The ground track was flown over 4 times in 2 round trips. The ground speed was between 75-80 m/s when flying from the coast, and between 60-70 m/s when flying back. The altitude was about 1400 m in the first round trip, and about 1600 m in the second one. The Cryosat-2 flew over that area in between the two round trips, and it took less than 2 minutes, in contrast to 30 minutes needed for the aircraft.

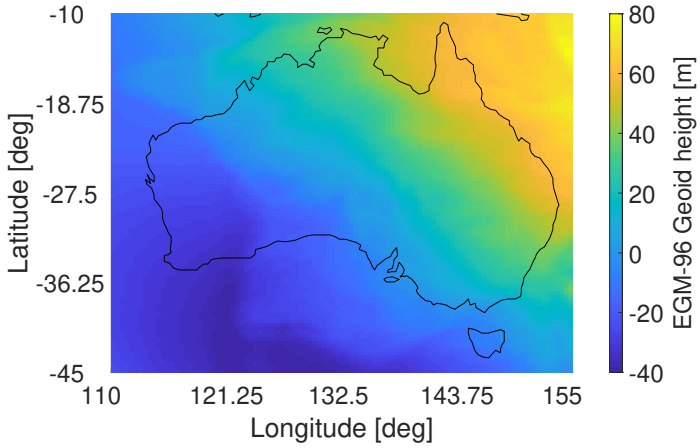

Figure 11.19: EGM-96 geoid height in Australia. From [5].

The goal of this flight was to study the feasibility of MIR for sea altimetry retrievals by using the Cryosat-2 data as a reference data. To give the reader historical context, MIR was initially developed to mimic the features of an eventual instrument in the PARIS IoD mission [3]. In rough outlines, these are the interferometric processing and the analog multi-beamsteering capabilities. The reason why the Bass Strait area was chosen can be seen in Fig. 11.19. This area allows shows a significant change in the geoid height without having to fly far the from the shore.

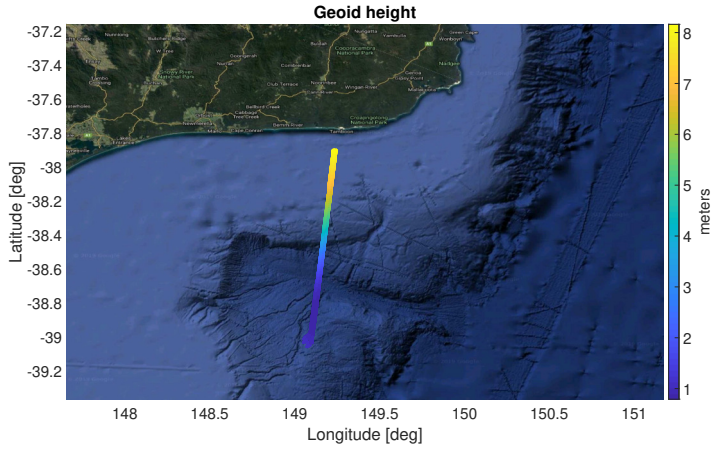

(a)

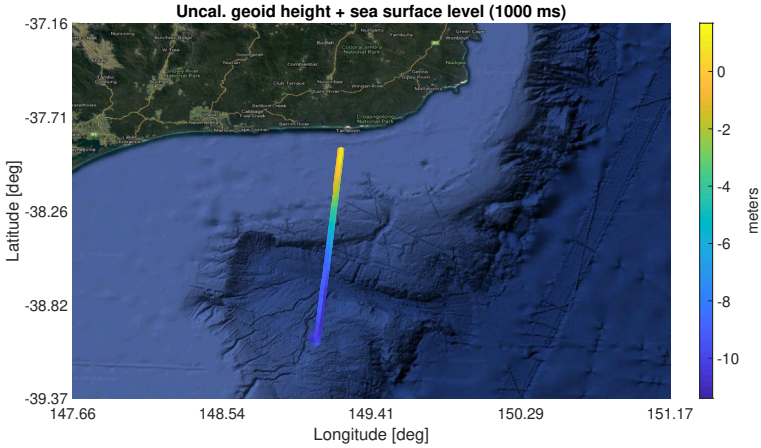

(b)

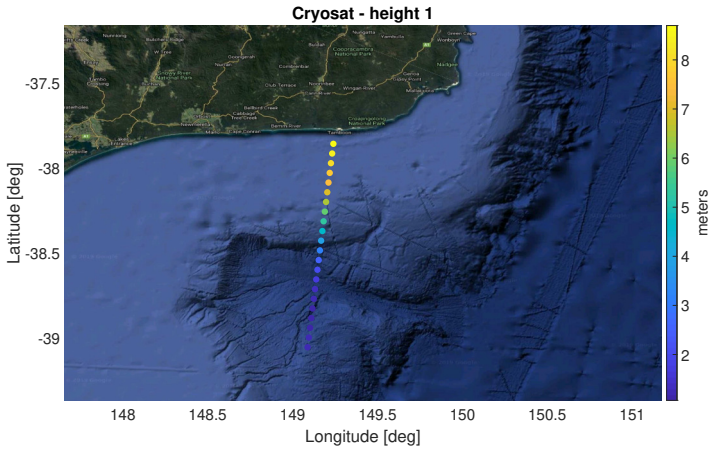

(c)

Figure 11.20: Comparison between the EGM96 geoid (a), the estimated sea height with the MIR instrument (b), and the height given by Cryosat-2 (c) over the Bass strait.

Figures in 11.20 shows respectively the geoid at the flight groundtracks, the altimetry data obtained with MIR applying a moving average, and the height given by Cryosat-2. Note that again, these are the overlapped results for all the bands, signals and beams in the 2 round-trips. One should also consider, that the huge structures seen in the pictures which resemble a mountain chain, are actually bathymetry data. That is to say, the sea floor height. All results correlate well, although the MIR data includes not only the geoid, but also the sea state and the tides, which may have changed during the round trips. The large bias with respect to the true geoid, may be produced because the calibration results are not applied (see [5]), and because the moving average introduces an artificial bias.

11.5 Land topography

When analyzing the data from the Bass Strait flight, it was observed that when overflying the coast, it was possible to correlate the altimetry results with land topography. Figure 11.21 shows these results for some relevant segments, together with Google Earth imagery. Segments 1 and 10 were mostly over a dense forest (see Fig. 11.1d), while segments 4 and 12 where partially over sand dunes.

A qualitative analysis can be seen in Fig. 11.22. Top figures show the topography of these segments as obtained with the DEM of Google Earth. Bottom figures show the height obtained with MIR and the EGM96 geoid on such segments. Note that the fly direction in segments 1 and 10 was off coast, and vice versa in segments 4 and 12.

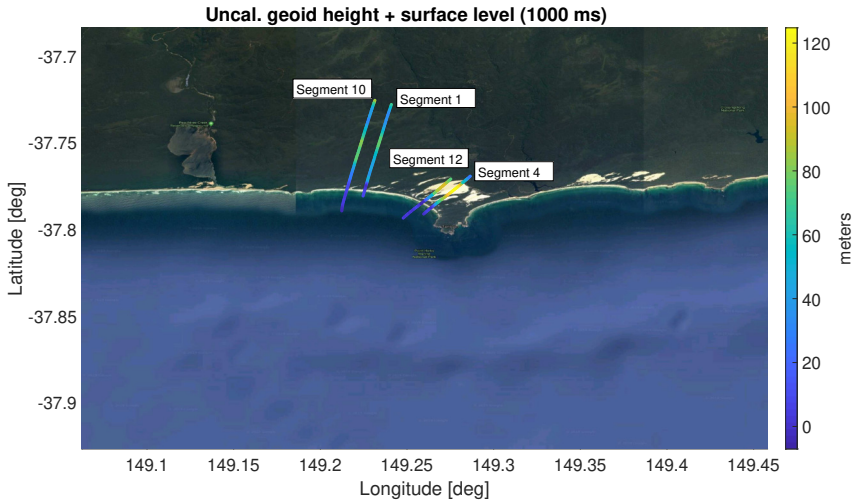

(a)

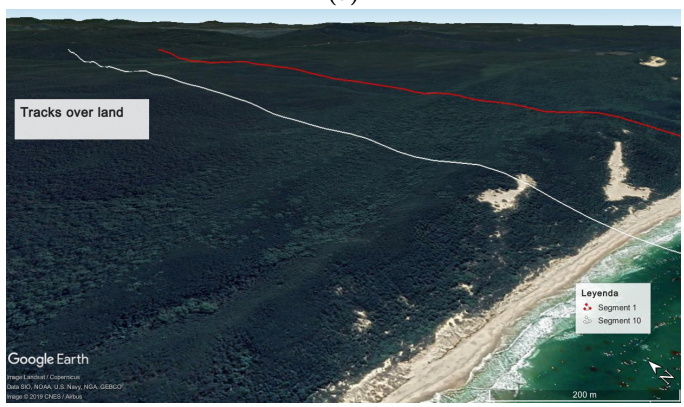

(b)

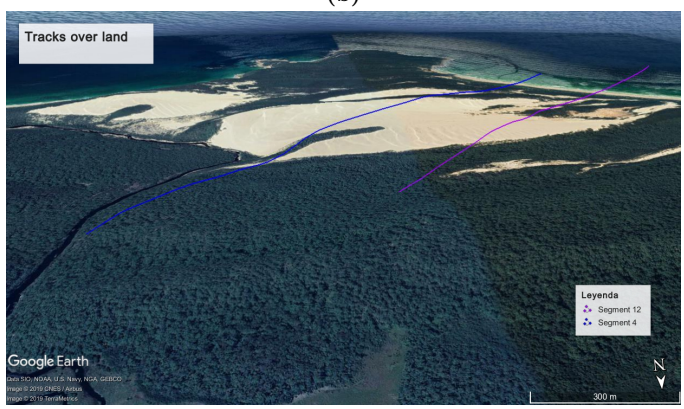

(c)

Figure 11.21: Maps showing some reflection point tracks over land during the Bass strait flight: (a) estimated height with the MIR instrument, and (b) and (c) 3D plots of the tracks obtained with Google Earth.

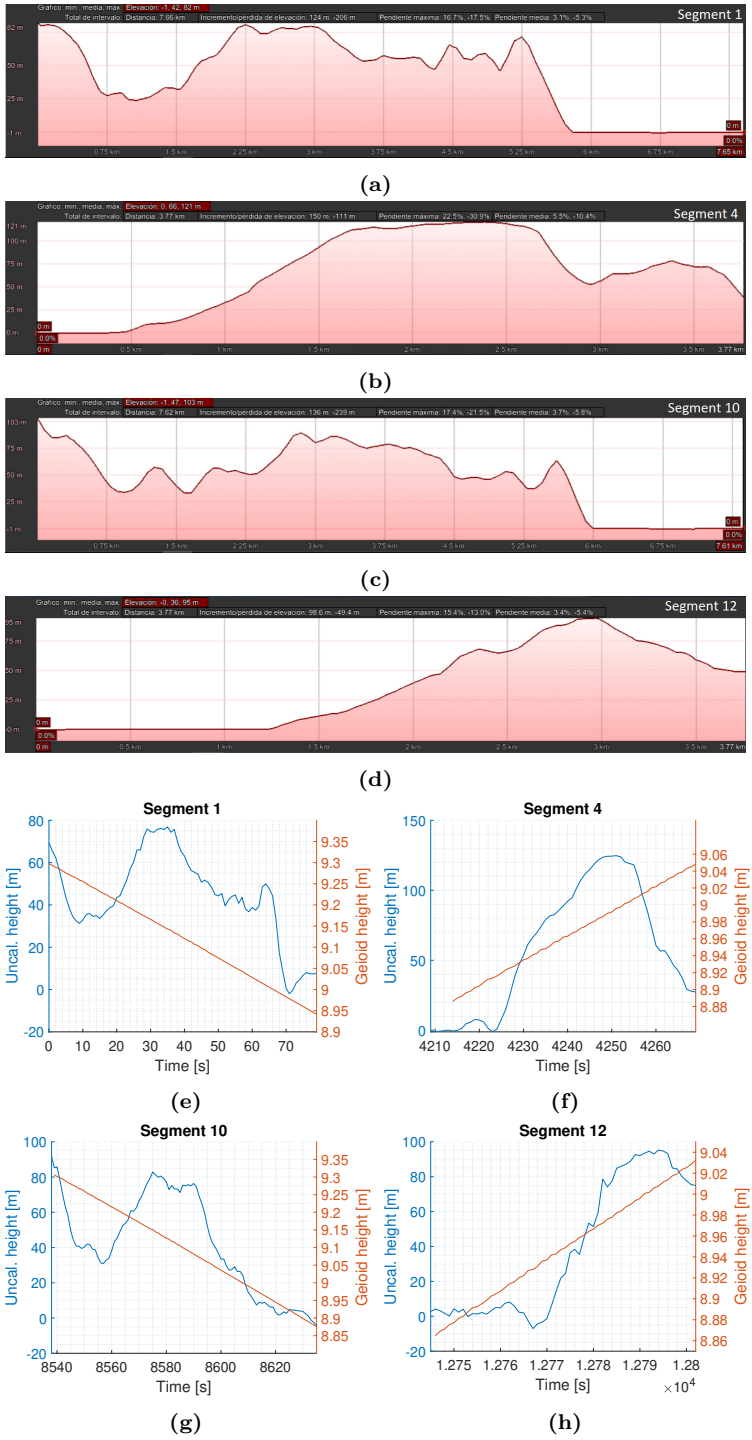

Figure 11.22: Comparison between the topography of land tracks from the Bass strait flight (a)-(d) and the estimated height with the MIR instrument (e)-(h). Topography obtained with Google Earth.

11.6 Cross-talk impact

Among the goals of the MIR campaigns, was to evaluate the feasibility of the interferometric processing and compare it with the conventional one, especially in the altimetry retrievals. Although this work has not been done yet, a brief analysis on the cross-talk phenomenon is given here. A detailed study can be found in [5] or in [230].

Figure 11.23 shows the direct path SIR of the *worst* interfering satellite (red text) over the tracked one (green text) as function of their elevation angles. For *worst* it is understood that is the interfering satellite that on average has the largest SIR during the tracking of the desired one. The figure combines the results from the 4 flights, for all bands, beams and signals. As it can be observed, even with the 19 element hexagonal arrays used in MIR, the average SIR is 10 dB, and can be up to 30 dB. Furthermore, there may be other satellites interfering simultaneously, although with a lower SIR. The interference value does not only depend on the relative position of the satellites in the skyplot, but also on the attitude of the plane, as the sidelobes of the beams may be pointing to the non desired ones (see Fig. 11.6). For this same reason, the SIR of the reflected signals may be different to the respective direct ones.

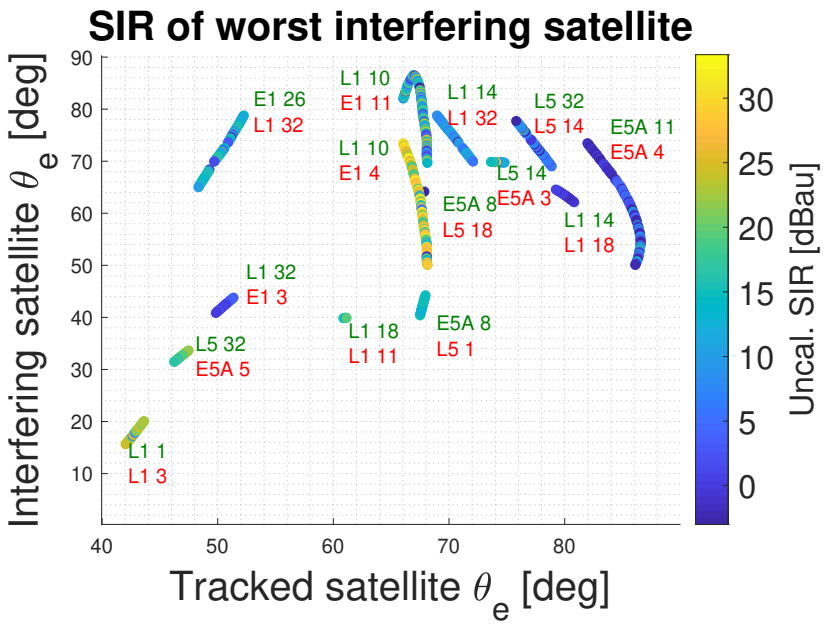

(a)

Figure 11.23: SIR of the worst interfering satellite (red annotations) over the tracked one (green annotations) for all the MIR campaigns, bands, beams, signals and satellites.

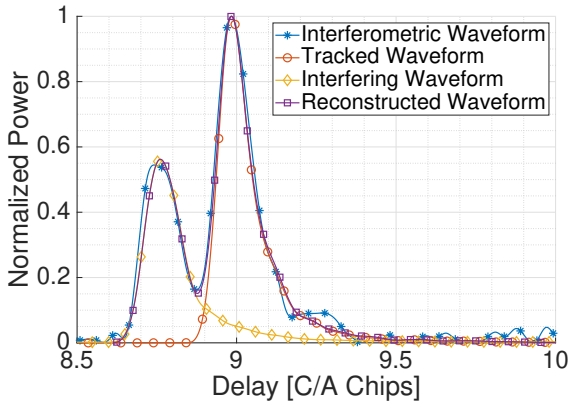

Figure 11.24: Impact of an interfering satellite on an interferometric waveform. From [5].

A large SIR does not necessary translate into a high degradation in the altimetric precision. As seen in Fig. 11.24, although the interfering waveform has a power of almost 60% of the desired one, it does not overlap with the latter leading edge. In [230] it is shown that the cross-talk probability was up to 10%, being larger in the L5 signals than in the L1 signals. Although the L5 beams are narrower than those of the L1, the fact that there were few GPS satellites transmitting at L5, forced MIR to choose some with a low elevation angle. As stated in Chapter 6, satellites with low elevation are more susceptible to cross-talk interference, especially at airborne heights. The same latter reference also shows an increase of the standard deviation of 18 cm and a bias up to 7 cm.

11.7 Considerations on the new GNSS signals

As stated in Chapter 9, the original plan for MIR was to compute conventional and interferometric DDMs in real time. Although this objective was fulfilled for the GPS L1 C/A signals, the secondary codes present in the other signals made the acquisition and tracking blocks fail. These new signals require a more complex tracking system in order to synchronize with transitions on the secondary codes. Strictly speaking, the L1 C/A should also be synchronized with the data bit transitions, which may happen in multiples of 20 ms (20 times the ranging code period). This represents that on average, 2.5% of 1 ms coherent DDMs may be corrupted. Nevertheless, the incoherent averaging should reduce the distortion.

As given in Section 2.4.2, the secondary codes transitions for GPS L5 and Galileo E5, and for the Galileo E1OS, happen in multiples of 1 ms and 4 ms respectively, the same as the periodicity of the respective ranging codes. On top of that, the data symbol rates are

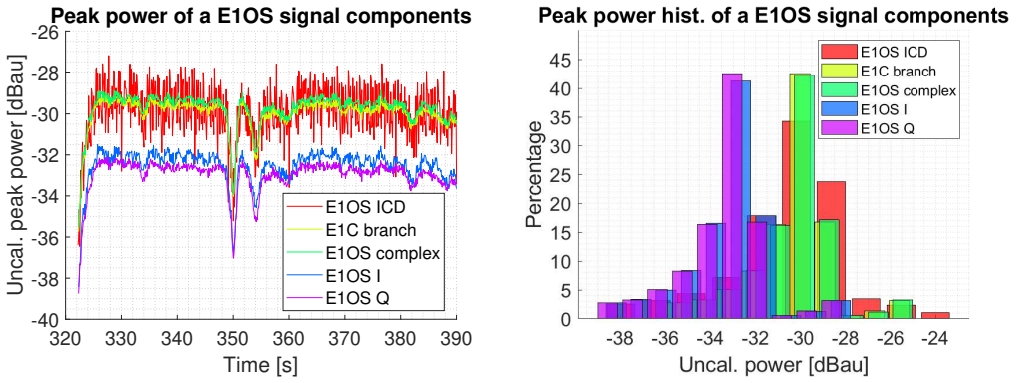

Figure 11.25: Comparison between the peak power of the direct signal using different E1OS demodulators (Yanco dry flight). See text for the definition of the legend terms.

100 sps for the L5, and 250 sps for the E1OS and E5 signals (see Table A.1). These means that even the incoherent averaging may not help to reduce the DDMs distortion. In [5], a simple method was given to find bit transitions. It consists of enlarging the coherent integration length to twice the period of the ranging code, and to use zero-padding on the second half of the clean replica. In this way, two cross-correlation peaks appear and one of them is never affected by a secondary code bit change.

An example, a L5 distorted DDM was given in Fig. 10.5. Note that the delay dimension is not affected, and thus it should not impact the altimetric performance in terms of bias. However, the reduction of SNR will indeed impact the precision. For the very same reason, the scatterometric retrievals will be affected. Bear in mind that this issue may not be a problem in interferometric processing at airborne heights, as the delay between the direct and reflected signals may translate only into few chips.

Figure 11.25 shows the impact of lack of syncronization with E1OS secondary codes on the DDMs peak power. Different E1OS components have been studied (see Fig. 2.15). For *E1OS* it is understood the definition given in the ICD [15] (see Eq. 2.12), in contrast to *E1OS complex*, which assumes that the modulation is actually complex, as stated in [18] (see Eq. 2.14). The *E1OS I* and *E1OS Q* terms denotes the in-phase and quadrature components on the complex case. Finally, *E1C* denote the dataless (i.e. pilot) E1C branch in Fig. 2.15. Correlating with either the complex version or with the E1C branch, produces less variance on the measured peak with respect to the ICD version. As expected, the correlation with only E1OS I or E1OS Q, reduces the power by about -3 dB, as only half of the signal is used.

11.8 Conclusions

This chapter has given the first results obtained from the MIR campaigns in Australia. The feasibility of MIR has been demonstrated for diverse remote sensing applications. Those are soil moisture, land topography, sea state and altimetry, and land-water bodies transition.

There is however more work to be done. The first step may be to apply the calibration parameters, recently obtained in [5], to all the above measurements. This would, in principle, reduce the variance of the estimates and improve the correlation with the ground truth data sets. Later on, the specular reflection model should be improved to include a DEM with more resolution. This would reduce the mapping error, and consequently help to relate the sensor data from the Yanco fields with the measured one, or reduce the topography bias in the land segments in the Bass Strait flight.

From then on, a myriad of new investigations could be done. Some of those that could be applied to all the flights are: evaluate the impact of different coherent and incoherent averages on the precision of the estimates and on their spatial resolution; analyze the different signals and bands individually; filter the results by satellite elevation angle; and study the impact of the aircraft speed and height on the glistening zone size.

New work that could be specifically done with the data on each individual flight is:

In the Port Philip bay, it would be interesting to classify land areas by urban or country, and the sea areas by shoreline, inner bay waters or open sea ones. Additionally, the study done in Chapter 10 for sea state determination based on the time decorrelation of DDM peak phase, could be reproduced. This would in turn, give the chance to evaluate the feasibility of phase-based estimations when sampling with 1 level. The data from the buoy and from the tide-gauge could be used as reference data of the sea state.

In the Yanco flights, the author suggests separating the land areas between different types of crop, and between different harvest status. Furthermore, the outlayers caused by reflections on buildings or over the Yanco Creek, should be removed.

In the Bass Strait flight, it would be first interesting to apply the tides motion (if any) on the results. After this, interferometric processing should be performed and compared to the conventional one. Similarly to the Port Philip bay, sea state determination based on phase measurements could be analyzed.

Part IV

Conclusions and Future Research Lines

12

Chapter 12

Conclusions and Future Work

This chapter first presents the conclusions and the main contributions of this thesis. It then provides few ideas for the possible continuation of this work.

12.1 Conclusions

This Ph. D. thesis has gone through different stages. The first part was devoted to theory development. The second part was committed to contributing to the development of an airborne GNSS-R instrument named MIR, including its testing and calibration. The last part was dedicated to the designing of a set of field campaigns and to the processing of the obtained data.

In the first stage, to the knowledge of the author, this work has been the first to analyze in depth two different issues. First, the cross-talk phenomenon by giving statistics of its occurrence and of its impact on altimetry and scatteromety. Second, the impact of 1-level sampling on the GNSS-R observables in terms of precision and sensitivity. Aside from this two subjects, three others have been addressed. The first, has been to apply the well-known precision bounds theory of GNSS signals to the GNSS-R scope in order to find the optimum receiver bandwidth. The second, has been to derive analytic expressions of the ACF of the GNSS signals in order to be used in GNSS-R reflection simulators. The third, has been to give real-time correlation and tracking architectures for FPGAs in order to obtain GNSS-R observables.

Regarding the second part, this thesis has contributed to two main issues. Firstly, to develop the signal processing blocks in the FPGAs of the back-end receivers and of the transmitter used to generate the calibration signal, and to build the host software that controls all of them. Secondly, to build a software running over GPUs that obtains DDMs at high speed from raw sampled data. The software can perform the conventional and interferometric techniques.

Concerning the last part, the work carried out in this thesis can be separated into two issues. Firstly, the design of five airborne field campaigns for MIR, one on the Catalonia coast, and four at several places in South West Australia. Each field campaign was aimed at studying different kinds of surfaces. The second issue has been to process the data from the latter campaigns with the GPU software mentioned above. The data has been applied to the following scenarios: sea altimetry, sea state, water bodies detection, soil moisture estimation and topography retrieval. Although the data has not been fully processed, it shows promising results. This work is currently being carried out by the Ph. D. student Juan Francisco Muñoz.

The work done in this thesis resulted in three articles in peer-reviewed journals and in five conference proceedings, all of them as first author. At the time or writing this chapter, two more journal articles have been submitted. Furthermore, topics derived from this thesis have contributed to eighteen journal articles, of which four are as second author and three are as third author; in thirty-three conference articles, of which six

are as second author, and thirteen are as third author; and in twenty abstract papers in related workshops with different authorship order. Finally, the author has co-directed two bachelor's thesis, one belonging to a five-year degree and the other to a three-year degree. The complete list of publications can be found at the end of this Ph. D. thesis.

12.2 Future Research Lines

This Section provides a few ideas for the possible continuation of the work done in this thesis. Some of them have been already given at the end of each chapter.

Some ideas refer to topics that the author believes may be interesting as future research by using the data from the MIR and MALYGNSS field campaigns. Those are:

- Apply the calibration parameters, the antenna directivity at a given pointing angle, and the SNR mapping to the GNSS-R observables obtained with MIR. This would reduce the variance of the measurements.
- Filter the observables by satellite elevation angle, signal, band, and beam. Infer relationships if any, and derive individual statistics.
- Relate the observables with the available ground-truth data. Find instrument bias, precision and sensitivity to different physical magnitudes.
- Improve the reflection point calculation method in land by using a DEM model with a smaller spatial resolution. This would improve the correlation between the observables and the ground-truth data.
- Process the BeiDou-2 B1 signals from the MIR and MALYGNNS campaigns, and the GPS L2C from the latter. Compare with the existing signals.
- Improve the GPU software in order to deal with secondary codes transitions. This would help to reduce the variance of the estimates.
- Process the MIR data using the interferometric technique, and compare it with the conventional one.
- Evaluate the performance of the MIR arrays by obtaining the DDMs of the untracked satellites that are in view.
- Obtain observables using different coherent and incoherent times. Infer the instrument spatial resolution. Analyze the DDM peak and noise floor variace reduction.

Other ideas refer to issues that the author encourages in order to ameliorate the parts of the MIR instrument developed in this thesis. Those are:

- Remove the DC offset of the USRPs X310 by embedding an adaptive block in their FPGAs. A simple mean calculator should be a feasible method.
- Investigate shared memory strategies between GPUs and operating systems. This would allow the generation of DDM observables in real-time by using GPUs.
- Explore secondary codes alignment architectures for real-time correlators, either in FPGAs or in GPUs.
- Integrate a real-time RFI mitigation algorithm in the FPGAs. The one developed in [48] should be suitable as it used a similar hardware.
- Update the Ettus drivers if this helps to improve the transmission of orders from the host computer.
- Consider other satellite selection algorithms aiming to reduce the cross-talk interference.
- Improve the the time synchronization between the USRP N210 and the USRPs X310 by using an up-sampled version of the PPS rise.

Part V

Appendices

A

Appendix A

GNSS Summary Tables

THIS appendix presents summary tables of the GNSS systems and signals. This information is only valid for the MEO constellations. The signals transmitted by the augmentation systems (SBAS), regional systems (RNSS), and GEO or GSO satellites, may have different properties. The data is mainly obtained from the official ICDs, but some information of the restricted signals has been found on other sources (references are given in the tables), and likely assumptions have been done on some bandwidth and power values (indicated when it proceeds). All the bandwidths are referred to RF (i.e. double-sideband). Footnotes are:

[1] Bandwidths for a commercial receiver. The ICD does not tell the transmitted bandwidths for the restricted signals. Note for example that the nominal bandwidth of the modulation used by E1 PRS is 35.806 MHz, much larger than the given 24.552 MHz, which is only useful for receiving the open signals.

[2] Reserved bands for the BeiDou-2 system referred to a central frequency of 1575.42 MHz for the B1/B1-2, 1191.795 MHz for the B2, and 1268.52 MHz for the B3.

[3]Bandwidth at -1 dB. At -3 dB is 16.368 MHz for the B1/B1-2 and 36.828 for the B2.

[4] Assumed likely values.

[5] Referred to a central frequency of 1189 MHz.

[6] Minimum received power on Earth using an ideally matched RHCP antenna with a gain of 3 dBi (GPS) or 0 dBi (Galileo). Values are valid for elevations between the ones listed in column θ_e and 90 degrees. Nominal and maximum values can be up to 6 dB larger.

[7] The bandwidth of the BOC signals is defined between the outer nulls of their largest spectral lobes.

Table A.1: Summary of GNSS signals - Part I. Restricted services are marked with an asterisk.

Sys.	Band	f_c [MHz]	λ [cm]	Tx. BW [MHz]	ITU BW [MHz] [17]	SERVICES	I/Q	COMPONENT	MODULATION	Main lob. BW [MHz][7]	1st code			2nd code			BOC	Data rate [bps/sps]	Min. rec. power [dBW][6]	Relative power	θ_e [deg]
											f_T [MHz]	family	Lenght [chips/ms]	f_T [MHz]	Lenght [chips/ms]		f_b [MHz]				
GPS	L1	1575.42	19.04	former 20.46 III: also 30.69	24	P(Y)*	I	DATA	BPSK-R10	20.460	10.23	short-cycled + m-Sequence	6.9E12/ 1 week				-	50/50	-161.5	1	5
						C/A [13]	Q	DATA	BPSK-R1	2.046	1.023	Gold	1023/1				-	50/50	-158.5	1	5
						L1C [19]	I	DATA (L1D)	TMBOC(6,1,4/33)	4.092	1.023	Weil	10230/10				1.023	50/100	III: -157	3/4	5
							Q	PILOT (L1p)		14.322							1800	1.023 & 6.138		1/4	
	L2	1227.6	24.43	former 20.46 III: also 30.69	24	M*	I	N/A	BOC(10,5)	30.690	5.115	N/A	N/A				N/A	10.23	-157 [3]	1	N/A
						P(Y)*	I	DATA	BPSK-R10	20.460	10.23	short-cycled + m-Sequence	6.9E12/ 1 week				-	50/50	IIA/IIR: -164.5 IIR-M/IIF: -161.5	1	5
						L2C [13]	Q	DATA (L2CM)	BPSK-R1 (mux 2 @ 511.5 kHz)	2.046	0.5115	m-Sequence	10230/20				-	50/50	IIF: 50/50 IIR-M: also 25/50	1/2	5
								PILOT (L2CL)					767250/1500							1/2	
	L5	1176.45	25.50	24.00	25	M*	I	N/A	BOC(10,5)	30.690	5.115	N/A	N/A				N/A	10.23	N/A	1	N/A
						S&L [14]	I	DATA (L5I)	BPSK-R10	20.460	10.23	short-cycled + m-Sequence	10230/1		10		-	50/100	IIF: -157.9 III: -157.0	1	5
							Q	PILOT (L5Q)	BPSK-R10						20				IIF: -157.9 III: -157.0	1	
Galileo [15]	E1	1575.42	19.04	24.552[1]	32.0	PRS*	Q	DATA (E1A)	BOCc(15,2.5)	35.805	25.575	-	N/A		N/A		15.345	50/100	-157 [17]	1	N/A
						OS, SoL, CS	I	DATA (E1B)	CBOC(6,1,1/11)	4.092	1.023	Random	4092/4		-	1.023 & 6.138		125/250	-157 [17]	10/11	10
								PILOT (E1C)		14.322					25			-		1/11	
	E6	1278.75	23.46	40.92[1]	40	PRS*	Q	DATA (E6A)	BOCc(10,5)	30.690	5.115	N/A	N/A		N/A		10.23	50/100	-155 [17]	1	N/A
						CS*	I	DATA (E6B)	BPSK-R5	10.230	5.115	Memory	5115/1		-		-	500/1000	-155	1/4	10
								PILOT (E6C)	BPSK-R5		5.115				100		-	-		1/4	
	E5	E5: 1191.795 E5A: 1176.45 E5B: 1207.14	E5: 25.17 E5A: = 25.50 E5B = 24.85	E5: 51.15[1] E5A: 20.46[1] E5B: 20.46[1]	50[5]	OS, CS	I	DATA (E5aI)	AltBOC(8,15,10) with constant envelope	51.150	10.23	short-cycled + m-Sequence	10230/1		20		15.345	25/50	-155	1/4	10
							Q	PILOT (E5aQ)							100			-		1/4	
						OS, SoL, CS	I	DATA (E5bI)							4			125/250	-155	1/4	
							Q	PILOT (E5bQ)							100			-		1/4	

Table A.2: Summary of GNSS signals - Part II. Restricted services are marked with an asterisk.

Sys.	Band	fc [MHz]	λ [cm]	Tx BW [MHz]	ITU BW [MHz] [17]	SERVICES	I/Q	COMPONENT	MODULATION	Main lob. BW [MHz][7]	1st code			2nd code		BOC	Data rate [bps/sps]	Min. rec. power [dBW][6]	Relative power	θ_e [deg]
											fr [MHz]	family	Lenght [chips/ms]	fr [MHz]	Lenght [chips/ms]	fb [MHz]				
BeiDou-2 (current) [20, 234]	B1	FcB1 : 1561.098 FcB1-2 :1589.742	λ_{B1}: 19.22 λ_{B1-2} : 18.87	B1: 32.736[2] B1-1: 4.092[3] B1-2: 4.092[3]	DNF	B1(Q)*	Q	DNF	QPSK-R2	4.092	2.046	DNF	DNF/¿400		-	-	-	-163[4]	1	5[4]
						B1(I)	I	DATA				Gold	2046/1		20/20	-	DNF/50	-163[4]	1	5[4]
						B1-2(Q)*	Q	DNF	QPSK-R2	4.092	2.046	DNF	DNF/¿400		-	-	-	-163[4]	1	5[4]
						B1-2(I)	I	DATA				Gold	2046/1		20/20	-	DNF/50	-163[4]	1	5[4]
	B2	1207.14	24.85	B2: 51.15[2] B2: 20.46[3]	DNF	B2-Q*	Q	DNF	BPSK-R10	20.460	10.23	DNF	DNF/¿160		-	-	-	-163[4]	1	5[4]
						B2-I	I	DATA	BPSK-R2	4.092	2.046	DNF	2046/1		20/20	-	DNF/50	-163[4]	1	5[4]
	B3	1268.52	23.65	B3: 35.805[2] B3: 20.46[4]	DNF	B3*	Q	DNF	QPSK-R10	20.460	10.23	DNF	DNF/¿160		-	-	-	-163[4]	1	5[4]
							I	DATA				DNF	10230/1		20/20	-	DNF/50	-163[4]	1	5[4]
BeiDou-2 (future) [235]	B1	1575.42	19.04	32.736	DNF	B1-CD	I	DATA	MBOC(6,1,1/11)	4.092	1.023	DNF	DNF		DNF	1.023	50/100	DNF	10/11	DNF
						B1-CP		PILOT		14.322		DNF	DNF		DNF	6.138	-		1/11	DNF
						B1*	I	DATA	BOCs(14,2)	32.736	2.046	DNF	DNF		DNF	14.322	50/100	DNF	0.5	DNF
								DNF									-		0.5	
	B2	B2: 1191.795 B2A: 1176.45 B2B: 1207.14	25.17	51.15	DNF	B2aD	I	DATA	AltBOCs(15,10)	51.150	10.23	DNF	DNF		DNF	15.345	25/50	DNF	0.25	DNF
						B2aP	Q	PILOT				DNF	DNF		DNF		-		0.25	DNF
						B2bD	I	DATA				DNF	DNF		DNF		50/100		0.25	DNF
						B2bP	Q	PILOT				DNF	DNF		DNF		-		0.25	DNF
	B3	1268.52	23.65	35.805	DNF	B3*	I	DNF	QPSK-R10	20.460	10.23	DNF	DNF		DNF	-	500/-	DNF	0.5	DNF
							Q	DNF				DNF	DNF		DNF				0.5	DNF
						B3-AD*	I	DATA	BOCs(15,2.5)	35.805	2.5575	DNF	DNF		DNF	15.345	50/100	DNF	0.5	DNF
						B3-AP*		PILOT				DNF	DNF		DNF		-	DNF	0.5	DNF

B

Appendix B

Derivation of the GNSS Autocorrelation functions

THIS appendix includes the derivation of the ACF of a generic $BOC_c(n,m)$ signal, and the band-limited expressions of the ACF and its derivative of a single pulse.

B.1 Autocorrelation function of BOC_c(n,m) signals

This derivation follows a similar approach done in [158] for the BOC_s(n,m) modulations. The BOC_c(n,m) symbol can be described as:

$$s(t) = \begin{cases} 1, & t \in [(2k-\alpha)t_c, (2k-\alpha+1/2)t_c] \\ -1, & t \in [(2k-\alpha+1/2)t_c, (2k-\alpha+3/2)t_c] \\ 1, & t \in [(2k-\alpha+3/2)t_c, (2k-\alpha+2)t_c] \end{cases} \qquad k = 0...n-1 \tag{B.1}$$

where $\alpha = n/m$ is the number of BOCc symbols inside a chip of duration T_c, and $t_c = T_c/\alpha$ is the length of the BOCc symbol. The Fourier transform of this signal is

$$\begin{aligned} S(w) &= \mathscr{F}\{s(t)\} \\ &= \sum_{k=0}^{\alpha-1} \left(\int_{(2k-\alpha)t_c}^{(2k-\alpha+1/2)t_c} e^{-jwt} \mathrm{d}t - \int_{(2k-\alpha+1/2)t_c}^{(2k-\alpha+3/2)t_c} e^{-jwt} \mathrm{d}t + \int_{(2k-\alpha+3/2)t_c}^{(2k-\alpha+2)t_c} e^{-jwt} \mathrm{d}t \right) \\ &= \frac{i}{w} \left(\sum_{k=0}^{\alpha-1} e^{-jwt_c 2k} \right) \cdot e^{-jwt_c(1-\alpha)} \cdot \left(2e^{jwt_c/2} - 2e^{-jwt_c/2} - e^{jwt_c} + e^{-jwt_c} \right), \end{aligned} \tag{B.2}$$

and the spectrum is then

$$\begin{aligned} P(w) = |S(w)|^2 = S(w)S(w)^* &= \frac{1}{w^2} \left(\sum_{k=1-\alpha}^{\alpha-1} (\alpha - |k|) \, e^{j2wkt_c} \right) \cdot \\ &\Big[10 - 4\left(e^{jwt_c} + e^{-jwt_c}\right) \\ &\qquad - 4\left(e^{jwt_c/2} + e^{-jwt_c/2}\right) - e^{-j2wt_c} - e^{-j2wt_c} + 4\left(e^{j3wt_c/2} + e^{-j3wt_c/2}\right) \Big] \\ &= \frac{1}{w^2} \left(\sum_{k=1-\alpha}^{\alpha-1} (\alpha - |k|) \, e^{j2wkt_c} \right) \cdot 16 \sin^2(wt_c/2) \cdot \left[2 - \sin^2(wt_c/2) - 2\cos(wt_c/2) \right] \\ &= \frac{\sin^2(wt_c/2)}{(wt_c/2)^2} (t_c/2)^2 \cdot \\ &\sum_{k=1-\alpha}^{\alpha-1} \left[(\alpha - |k|) \, 6e^{j2wkt_c} + e^{j(2k-1)wt_c} + e^{j(2k+1)wt_c} - 4e^{j(2k+1/2)wt_c} - 4e^{j(2k-1/2)wt_c} \right]. \end{aligned} \tag{B.3}$$

The first element of last equation is the spectrum of a pulse of duration t_c, while the summation is the effect of the BOC subcarrier. Finally, the ACF is given by

$$\begin{aligned} R_{BOC_c}(\tau) = \mathscr{F}^{-1}\{P(w)\} = \Lambda_{t_c}(\tau) * \\ \sum_{k=1-\alpha}^{\alpha-1} (\alpha - |k|) \left[6\delta\left(\tau - 2kt_c\right) - 4\delta\left(\tau - (2k-1/2)\, t_c\right) + \delta\left(\tau - (2k-1)\, t_c\right)\right. \\ \left. - 4\delta\left(\tau - (2k+1/2)\, t_c\right) + \delta\left(\tau - (2k+1)\, t_c\right)\right]. \end{aligned} \tag{B.4}$$

B.2 Band-limited autocorrelation function and derivative of a pulse

Since the ideal ACF of the GNSS signals can be expressed as the convolution between the ACF of an ideal pulse with a train of deltas, their band-limited equations can be derived from the filtered pulse. Let $u_B(t)$ be a pulse of duration t_c filtered with an ideal filter of baseband bandwidth B [160, ch. 3]

$$u_B(t) = \frac{1}{\pi t_c}\left[Si\left(2\pi B\left(t + t_c/2\right)\right) - Si\left(2\pi B\left(t - t_c/2\right)\right)\right], \tag{B.5}$$

where $Si(x) = \int_0^x sin(x)/x dx$ is the sine integral function. The ACF is given by

$$\begin{aligned} R_B(\tau) = \int u_B(t) u_B(t-\tau) \mathrm{d}t = \int_{\tau - t_c/2}^{\tau + t_c/2} u_B(t) \mathrm{d}t = \frac{1}{\pi}(\tau + t_c) Si\left(2\pi B\left(\tau + t_c\right)\right) \\ + \frac{1}{2B\pi^2}\cos\left(2\pi B\left(\tau + t_c\right)\right) + \frac{1}{\pi}(\tau - t_c) Si\left(2\pi B\left(\tau - t_c\right)\right) \\ + \frac{1}{2B\pi^2}\cos\left(2\pi B\left(\tau - t_c\right)\right) - \frac{2}{\pi}\tau Si\left(2\pi B\tau\right) - \frac{1}{B\pi^2}\cos\left(2\pi B\tau\right) \end{aligned} \tag{B.6}$$

where the next two relations have been used

$$\int Si\left(b + ax\right) \mathrm{d}x = \frac{\cos\left(b + ax\right) + \left(b + ax\right) Si\left(b + ax\right)}{a}, \tag{B.7}$$

$$Si(-x) = -Si(x). \tag{B.8}$$

Finally, the ACF derivative is found by using $\mathrm{d}Si(x)/\mathrm{d}x = sin(x)/x$

$$R'_B(\tau) = \frac{1}{\pi}\left[Si\left(2\pi B\left(\tau + t_c\right)\right) + Si\left(2\pi B\left(\tau - t_c\right)\right) - 2Si\left(2\pi B\tau\right)\right]. \tag{B.9}$$

C

Appendix C

Probability Density Functions of some Random Variables

THIS appendix first gives the orthogonal transformation to convert two correlated random variables to uncorrelated. This may be required in instruments in where there is a leakage between the receiver chains or where unbalance demodulators are used.

The appendix then gives the PDFs, mean and variance of the random variables involved in the different magnitudes of the GNSS-R waveform samples. They are the amplitude, phase, complex magnitude or envelope, and power. The stochastic definition of the addition iid of each of these magnitudes is given as well.

C.1 Orthogonal transformation to correlated random variables

As given in [236], two correlated random variables x and y can be transformed to uncorrelated by applying the transformation

$$x' = x\cos\phi + y\sin\phi \tag{C.1a}$$
$$y' = -x\sin\phi + y\cos\phi \tag{C.1b}$$

where $\phi = \frac{1}{2}\tan^{-1}\left(\frac{2\rho\sigma_x\sigma_y}{\sigma_x^2 - \sigma_y^2}\right)$. The new means and variances are then

$$\mu_{x'} = \mu_x\cos\phi + \mu_y$$
$$\mu_{y'} = \mu_y\sin\phi + \mu_x$$

$${\sigma_{x'}}^2 = \sigma_x^2\cos^2\phi + \sigma_y^2\sin^2\phi + \rho\sigma_x\sigma_y\sin 2\phi$$
$${\sigma_{y'}}^2 = \sigma_x^2\sin^2\phi + \sigma_y^2\cos^2\phi + \rho\sigma_x\sigma_y\sin 2\phi$$

Note that if x and y are both Gaussian random variables, their transformations are Gaussian as well.

C.2 Bivariate normal distribution

The bivariate normal distribution is denoted by $\mathcal{N}\left(\mu_x, \mu_y, \sigma_x^2, \sigma_y^2\right)$. Its PDF given by

$$f(x,y) = \frac{1}{2\pi\sigma_x\sigma_y\sqrt{1-\rho^2}}e^{-\frac{v}{2(1-\rho^2)}} \tag{C.2}$$

where

$$v \triangleq \frac{(x-\mu_x)^2}{\sigma_x^2} - \frac{2\rho\,(x-\mu_x)\,(y-\mu_y)}{\sigma_x\sigma_y} + \frac{(y-\mu_y)^2}{\sigma_y^2} \tag{C.3}$$

and

$$\rho \triangleq \frac{Cov_{xy}}{\sigma_x\sigma_y}$$

is the correlation coefficient between x and y.

In order to facilitate the understanding of the PDFs that will follow, it is interesting to express (C.2) in the polar form $f(r,\theta)$, where $r = \sqrt{x^2+y^2}$, $\theta \triangleq \operatorname{atan} y/x$ and

$$v = \frac{(r\cos\theta - \mu_x)^2}{2\sigma_x^2} - \frac{2\rho\,(r\cos\theta - \mu_x)\,(r\sin\theta - \mu_y)}{\sigma_x\sigma_y} + \frac{(r\sin\theta - \mu_y)^2}{2\sigma_y^2}. \tag{C.4}$$

C.3 Beckmann distribution

The magnitude of a complex Normal random variable follows a generalized Beckmann distribution [237]. Its PDF is obtained by integrating (C.2) over θ

$$f_R(r) = \frac{r}{2\pi\sigma_x\sigma_y\sqrt{1-\rho^2}} \int_0^{2\pi} e^{-\frac{v}{2(1-\rho^2)}} d\theta. \tag{C.5}$$

Last equation cannot be further simplified, however [238] gives a closed-form bound expression. If the in-phase and quadrature components are uncorrelated, the PDF can also be expressed with summations [236]

$$\begin{aligned} f_R(r) = {} & \frac{r}{2\sigma_x\sigma_y} \exp\left[-\frac{1}{2}\left(\frac{\mu_x^2}{\sigma_x^2} + \frac{\mu_y^2}{\sigma_y^2} + \frac{r^2}{2\sigma_x^2} + \frac{r^2}{2\sigma_y^2}\right)\right] \\ & \sum_{n=0}^{\infty} \frac{\varepsilon_n I_n \frac{r^2}{4}\left(\frac{1}{\sigma_y^2} - \frac{1}{\sigma_x^2}\right)}{\left[\left(\frac{r\mu_x}{\sigma_x^2}\right)^2 - \left(\frac{r\mu_y}{\sigma_y^2}\right)^2\right]^n} I_{2n}\left(\sqrt{\left(\frac{r\mu_x}{\sigma_x^2}\right)^2 + \left(\frac{r\mu_y}{\sigma_y^2}\right)^2}\right) \\ & \sum_{k=0}^{n} \delta_k C_k^n \left[\left(\frac{r\mu_x}{\sigma_x^2}\right)^2 - \left(\frac{r\mu_y}{\sigma_y^2}\right)^2\right]^{n-k} \left(2\frac{r^2\mu_x\mu_y}{\sigma_x^2\sigma_y^2}\right)^k \end{aligned} \tag{C.6}$$

where $I_n(\cdot)$ is the modified Bessel function of the first kind with order n, $C_k^n = n!/k!\,(n-k)!$ and

$$\delta_k = \begin{cases} 0 & \text{for } k: \text{odd} \\ 2(-1)^{k/2} & \text{for } k: \text{even} \end{cases}$$

The advantage of this expression is that in can be computed numerically up to a desired accuracy.

To the known of the author, there are not closed-form expressions for the mean and variance.

C.4 Rice distribution

The magnitude of a complex normal random variable follows a Rice distribution if the in-phase and quadrature components are uncorrelated, have equal variances and arbitrary means. Its PDF is given by

$$f_R(r) = \frac{r}{\sigma^2} e^{\frac{-\left(r^2+\nu^2\right)}{2\sigma^2}} I_0\left(\frac{r\nu}{\sigma^2}\right) \tag{C.7}$$

where $\sigma = \sigma_x^2 = \sigma_y^2$ is the scale parameter, and $\nu = \mu_x^2 + \mu_y^2$ is the non centrality parameter. The mean and variance are

$$\mu_r = \sigma\sqrt{\pi/2}L_{1/2}\left(\frac{-\nu^2}{2\sigma^2}\right) \tag{C.8a}$$

$$\sigma_r = 2\sigma^2 + \nu^2 - \frac{\pi\sigma^2}{2}L_{1/2}^2\left(\frac{-\nu^2}{2\sigma^2}\right) \tag{C.8b}$$

where $L_n(\cdot)$ is the Laguerre polynomial of order n.

Equivalently, a Rice random variable can be characterized with a shape parameter $K = \nu^2/2\sigma^2$ and a new scale parameter $\Omega = \nu^2 + 2\sigma^2$

$$f_R(r) = \frac{2\left(K+1\right)r}{\Omega}e^{-K-\frac{\left(K+1\right)r^2}{\Omega}} \times I_0\left(2\sqrt{\frac{K\left(K+1\right)}{\Omega}}r\right). \tag{C.9}$$

The mean and variances are then rewritten as

$$\mu_r = \sqrt{\frac{\Omega}{2\left(K+1\right)}}\sqrt{\pi/2}L_{1/2}\left(-K\right) \tag{C.10a}$$

$$\sigma_r = \Omega - \frac{\pi}{2}\frac{\Omega}{2\left(K+1\right)}L_{1/2}^2\left(-K\right). \tag{C.10b}$$

Approximations of the PDF of the addition of iid Rice random variables is given in [190, 191].

C.5 Hoyt distribution

The magnitude of a complex normal random variable follows a Hoyt distribution if the in-phase and quadrature components are uncorrelated, have equal means and arbitrary variances. The PDF is parameterized with a shape parameter $q = max\{\sigma_x, \sigma_y\}/min\{\sigma_x, \sigma_y\}$ and a spread parameter $w = \sigma_x^2 + \sigma_y^2$

$$f_R(r) = \frac{r\left(1+q^2\right)}{qw}\exp\left[-\frac{\left(1+q^2\right)^2r^2}{4q^2w}\right]I_0\left(\frac{\left(1-q^4\right)r^2}{4q^2w}\right). \tag{C.11}$$

The mean and variance are

$$\mu_r = \sqrt{\frac{2}{\pi}}\sqrt{\frac{w}{q^2+1}}E\left(1-q^2\right) \tag{C.12a}$$

$$\sigma_r^2 = w\left(1 - \frac{2E\left(1+q^2\right)^2}{\pi\left(q^2+1\right)^2}\right). \tag{C.12b}$$

where $E(\cdot)$ is the complete elliptic integral of the second kind.

The addition of iid Hoyt random variables is studied in [193].

C.6 Rayleigh distribution

The magnitude of a complex normal random variable follows a Rayleigh distribution if the in-phase and quadrature components are uncorrelated, have equal variances and zero means. Its PDF is given by

$$f_R(r) = \frac{r}{\sigma^2} e^{\frac{-r^2}{2\sigma^2}} \tag{C.13}$$

where $\sigma = \sigma_x = \sigma_y$ is the scale parameter. The mean and variance are

$$\mu_r = \sigma\sqrt{\pi/2} \tag{C.14a}$$

$$\sigma_r^2 = \frac{4-\pi}{2}\sigma^2. \tag{C.14b}$$

The addition of iid Rayleigh variables is studied in [192].

C.7 Phase distributions

The PDF of the phase of a complex normal random variable is obtained by integrating (C.2) with respect to r [236]

$$\begin{aligned} f_\Theta(\theta) = &\frac{1}{2\pi\sigma_x\sigma_y\sqrt{1-\rho^2}} \times \exp\left[-\frac{\mu_x^2}{2\sigma_x^2\left(1-\rho^2\right)} - \frac{\mu_y^2}{2\sigma_y^2\left(1-\rho^2\right)} + \frac{\rho\mu_x\mu_y}{\sigma_x\sigma_y\left(1-\rho^2\right)}\right] \\ &\times \frac{1}{2\mathcal{A}\left(\theta\right)}\left[1 + \frac{\sqrt{\pi}\mathcal{B}\left(\theta\right)}{2\sqrt{\mathcal{A}\left(\theta\right)}} \exp\left(\frac{\mathcal{B}^2\left(\theta\right)}{4\mathcal{A}\left(\theta\right)}\right) \operatorname{erfc}\left(\frac{-\mathcal{B}\left(\theta\right)}{2\sqrt{\mathcal{A}\left(\theta\right)}}\right)\right] \end{aligned} \tag{C.15}$$

where

$$\begin{aligned} \mathcal{A}\left(\theta\right) &\triangleq \frac{\cos^2\theta}{2\sigma_x^2\left(1-\rho^2\right)} + \frac{\sin^2\theta}{2\sigma_y^2\left(1-\rho^2\right)} - \frac{\rho\sin\theta\cos\theta}{\sigma_x\sigma_y\left(1-\rho^2\right)} \\ \mathcal{B}\left(\theta\right) &\triangleq \frac{1}{\sigma_x\left(1-\rho^2\right)}\left(\frac{\mu_x}{\sigma_x} - \frac{\rho\mu_y}{\sigma_y}\right)\cos\theta + \frac{1}{\sigma_y\left(1-\rho^2\right)}\left(\frac{\mu_y}{\sigma_y} - \frac{\rho\mu_x}{\sigma_x}\right)\sin\theta. \end{aligned}$$

To the known of the author, there are not closed-form expressions for the mean and variance.

If the in-phase and quadrature components are uncorrelated, have zero means and arbitrarily variances, (C.15) transforms into a Hoyt phase distribution [239]

$$f_\Theta(\theta) = \frac{\sqrt{1-b^2}}{2\pi\left(1-b\cos\left(2\theta\right)\right)} \tag{C.16}$$

where $b = \left(\sigma_x^2 - \sigma_y^2\right) / \left(\sigma_x^2 + \sigma_y^2\right)$ is the Hoyt fading parameter. The mean and variance have complicated closed form expressions which can be obtained by using for example symbolic software such as Wolfram Alpha.

If the in-phase and quadrature components are uncorrelated, have zero means and equal variances, (C.15) transforms into a uniform distribution over the domain $[0, 2\pi)$

$$f_\Theta(\theta) = \frac{1}{2\pi} \tag{C.17}$$

with mean and variance

$$\mu_\theta = \pi \tag{C.18a}$$

$$\sigma_\theta^2 = \pi^2/12. \tag{C.18b}$$

C.8 Scaled chi-squared distribution

The addition of k squared uncorrelated normally distributed random variables with unit variance and zero mean follows a chi-squared distribution. If the variances are not unitary but are the same, the PDF can be expressed in its *scaled* form

$$f_G(g) = \frac{1}{2^{k/2}\Gamma\left(k/2\right)} \left(\sigma^2 g\right)^{k/2-1} e^{-g/2\sigma^2} \tag{C.19}$$

where k is the degrees of freedom, $\sigma = \sigma_i \ \forall i$ and $\Gamma(\cdot)$ is the Gamma function. The mean and variance are

$$\mu_g = k\sigma^2 \tag{C.20a}$$

$$\sigma_g^2 = 2k\sigma^4. \tag{C.20b}$$

If $k = 1$, then

$$f_G(g) = \frac{1}{\sigma\sqrt{2\pi}\sqrt{g}} e^{-g/2\sigma^2}. \tag{C.21}$$

and

$$\mu_g = \sigma^2 \tag{C.22a}$$

$$\sigma_g^2 = 2\sigma^4. \tag{C.22b}$$

If the normal random variables are correlated or their variances are different, the distribution is a *generalized chi squared*, which does not have a known PDF.

C.9 Scaled non-central chi-squared distribution

The addition k squared uncorrelated normally distributed random variables with unit variance and arbitrary mean follows a non central Chi-squared distribution. If the variances are not unitary, but are the same, the PDF can be expressed in its *scaled* form (based on [240])

$$f_P(p) = \frac{1}{2}\frac{1}{\sigma^{k/2+1}} e^{-\frac{p+\lambda}{2\sigma^2}} \left(\frac{p}{\lambda}\right)^{k/4-1/2} I_{k/2-1}\left(\frac{\sqrt{p\lambda}}{\sigma}\right) \tag{C.23}$$

where k is the degrees of freedom, $\lambda = \sum_{i=1}^{k} \mu_{x_i}^2$ is the non-centrality parameter, and $\sigma = \sigma_i \ \forall i$. The mean and variance are

$$\mu_p = k\sigma^2 + \lambda \tag{C.24a}$$

$$\sigma_p^2 = 2\sigma^2\left(k\sigma^2 + 2\lambda\right). \tag{C.24b}$$

If the variances of the normal random variables are different, the distribution is a *generalized non central chi squared* which does not have a known PDF.

C.10 Squared Hoyt

The addition 2 squared uncorrelated normally distributed random variables with zero means and arbitrary variances, follows a Squared Hoyt distribution. Its PDF is given by

$$f_P(p) = \frac{1+q^2}{2qw} \exp\left[-\frac{\left(1+q^2\right)^2 p}{4q^2 w}\right] I_0\left(\frac{\left(1-q^4\right)p}{4q^2 w}\right) \tag{C.25}$$

where $q = max\{\sigma_x, \sigma_y\}/min\{\sigma_x, \sigma_y\}$ is the shape parameter and $w = \sigma_x^2 + \sigma_y^2$ is the spread parameter. The mean and variance are

$$\mu_p = w \tag{C.26a}$$

$$\sigma_p^2 = 2\frac{w^2\left(1+q^4\right)}{\left(1+q^2\right)^2}. \tag{C.26b}$$

C.11 Exponential distribution

The addition 2 squared uncorrelated normally distributed random variables with zero means and equal variances, follows an exponential distribution. Its PDF is given by

$$f_P(p) = \lambda e^{-\lambda p} \tag{C.27}$$

where $\lambda =$ is the rate parameter. The mean and variance are

$$\mu_p = 1/\lambda \tag{C.28a}$$
$$\sigma_p = 1/\lambda^2. \tag{C.28b}$$

C.12 Erlang distribution

The addition of k uncorrelated exponential random variables with the same λ, follows an Erlang distribution. Its PDF is given by

$$f_Z(z) = \frac{\lambda^k z^{k-1} e^{-\lambda z}}{(k-1)\,!}. \tag{C.29}$$

The mean and variance are

$$\mu_z = k/\lambda \tag{C.30a}$$
$$\sigma_z = k/\lambda^2. \tag{C.30b}$$

D

Appendix D

VHDL

This appendix describes VHDL implementations for the LFSR and AGC blocks and required low-level entities. They have been designed in such a way that can be implemented in hierarchical and cascaded formats. This allows the use of fast clocks at the expense of an increased latency.

D.1 LFSR

```
entity LFSR_generator is
  GENERIC(WIDTH : integer := 10;
    WIDTH_CMP : integer := 0);
  Port (clk : in STD_LOGIC;
    rst : in STD_LOGIC;                          reset
    seed  : in STD_LOGIC_VECTOR (WIDTH-1 downto 0);     initial state
    tap : in STD_LOGIC_VECTOR (WIDTH-1 downto 0);     XOR taps for input
    RESET : in STD_LOGIC_VECTOR (WIDTH-1 downto 0);     reset at this state
    output : in STD_LOGIC_VECTOR (WIDTH-1 downto 0);    phase selector taps
    SEQ : out STD_LOGIC;                        1 bit output
    count_cmp : in STD_LOGIC_VECTOR (WIDTH_CMP-1 downto 0);     reset
    ENABLE : in STD_LOGIC;                         Enable high (to freeze the LSFR)
    valid : out STD_LOGIC);
end LFSR_generator;

architecture Behavioral of LFSR_generator is

  signal reg: std_logic_vector(WIDTH-1 downto 0);
  signal tap_mem: std_logic_vector(WIDTH-1 downto 0);
  signal RESET_mem: std_logic_vector(WIDTH-1 downto 0);
  signal output_mem: std_logic_vector(WIDTH-1 downto 0);
  signal seed_mem: std_logic_vector(WIDTH-1 downto 0);
  signal count_cmp_mem : std_logic_vector(WIDTH_CMP-1 downto 0);
  signal count : std_logic_vector(WIDTH_CMP-1 downto 0);
    Debugging (these lines will be removed when synthesizing)
  signal epoch : STD_LOGIC;
  signal all_ones: std_logic_vector(WIDTH-1 downto 0);
  signal epoch_ones : STD_LOGIC;

  begin
    proc: process(clk)

      variable xor_result_1 : std_logic;    taps
      variable xor_result_2 : std_logic;    phases

      begin
        if (rising_edge(clk)) then
          if (rst = '1') then
              LSFR
            reg <=  (others => '0');
            xor_result_1 :=  '0';
            xor_result_2 :=  '0';
            SEQ <= '0';
            valid <= '0';
            count <= (others => '0');
               These values must be already valid when reseting.
            tap_mem <= tap;
            RESET_mem <= RESET;
            output_mem <= output;
            seed_mem <= seed;
            reg <= seed;
            count_cmp_mem <= count_cmp;
               Debugging
            all_ones <= (others => '1');
```

```
55              epoch <= '0';
                epoch_ones <= '0';
57            else

59              if (ENABLE = '0') then     Freeze everything
                  valid <= '0';
61              else

63                valid <= '1';
    Shift the register
65  reg(WIDTH-1 downto 1) <= reg(WIDTH-2 downto 0);

67                    First register update
                  xor_result_1 := reg (0) and tap_mem(0);
69                for i in 1 to WIDTH-1 loop
                    xor_result_1 := (xor_result_1 xor (reg (i) and tap_mem(i)) );
71                end loop;
                  reg(0) <= xor_result_1;
73                   LSFR output
                  xor_result_2 := reg(0) and output_mem(0);
75                for i in 1 to WIDTH-1 loop
                    xor_result_2 := (xor_result_2 xor (reg (i) and output_mem(i)) );

77  end loop;
                  SEQ<= xor_result_2;
79                   Force original seed when reaching RESET_mem state
                  if (reg = RESET_mem) then
81                  reg <= seed_mem;
                  end if;
83                   Force original seed after count_cmp_mem clocks
                  if count_cmp_mem > 0 then
85                  if count = count_cmp_mem then
                      reg <= seed_mem;
87                    count <= (others => '0');
                    else
89                    count <= count +1;
                    end if;
91                end if;
                     Debugging
93                if (reg = seed) then
                    epoch <= '1';
95                else
                    epoch <= '0';
97                end if;
                  if reg = all_ones then
99                  epoch_ones <= '1';
                  else
101                 epoch_ones <= '0';
                  end if;
103             end if;    enable
              end if;      reset
105         end if;        clock
      end process proc;
107 end Behavioral;
```

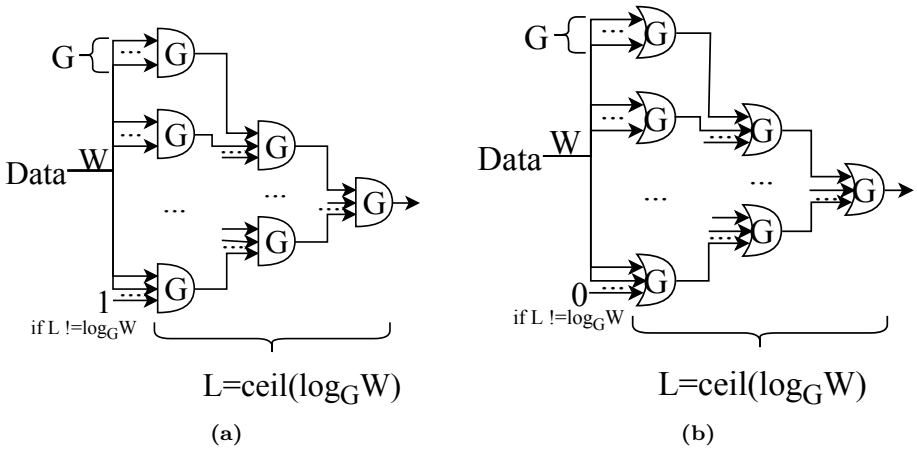

Figure D.1: Implementation of synchronous logic gates with an arbitrary length W using smaller gates of size G: (a) AND, and (b) OR.

D.2 Synchronous logic gates

D.2.1 AND gate

```
1  library IEEE;
   use IEEE.STD_LOGIC_1164.ALL;
3  use IEEE.math_real.all;          maths

5  entity AND_sync is
     GENERIC(WIDTH : integer := 14;
7         L : integer := 8);
     PORT(clk : in STD_LOGIC;
9         rst : in STD_LOGIC;
          x_in : in STD_LOGIC_VECTOR(WIDTH 1 downto 0);
11        x_out : out STD_LOGIC_VECTOR(WIDTH 1 downto 0);
          result : out STD_LOGIC);
13 end AND_sync;

15 architecture Behavioral of AND_sync is

17   constant A : integer := integer(ceil(log(real(WIDTH))/log(real(L))));
     constant B : integer := integer(L**A);
19
     type array_AND is array (0 to A) of STD_LOGIC_VECTOR(B 1 downto 0);
21   signal aux : array_AND;

23   type array_signal is array (0 to A) of STD_LOGIC_VECTOR(WIDTH 1 downto 0);
     signal signal_delayed : array_signal;
25
     function function_AND (X : STD_LOGIC_VECTOR(L 1 downto 0)) return STD_LOGIC is
27     begin
         for j in 0 to L 1 loop
29         if X(j) = '0' then
```

```
          return '0';
        end if;
      end loop;
      return '1';
  end function_AND;

  begin

    result <= aux(A)(0);
    x_out <= signal_delayed(A)(WIDTH-1 downto 0);

    process (clk)
      begin
        if (rising_edge(clk)) then
          if (rst = '1') then
            aux(0)(WIDTH-1 downto 0) <= (others => '0');
            aux(0)(B-1 downto WIDTH) <= (others => '1');
            for M in 1 to A loop
              aux(M)(WIDTH-1 downto 0) <= (others => '0');
            end loop;

            signal_delayed <= ((others=>(others=>'0')));
          else
            aux(0)(WIDTH-1 downto 0) <= x_in;
            signal_delayed(0)(WIDTH-1 downto 0) <= x_in;

            for J in 1 to A loop
              for K in 0 to ((L**(A-J))-1) loop
                aux(J)(K) <= function_AND(aux(J-1)((K+1)*L-1 downto K*L));
              end loop;
            end loop;

            for I in 1 to A loop
              signal_delayed(I)(WIDTH-1 downto 0) <= signal_delayed(I-1)(WIDTH-1
     downto 0);
            end loop;
          end if;
        end if;
    end process;
end Behavioral;
```

D.2.2 OR gate

```
library IEEE;
use IEEE.STD_LOGIC_1164.ALL;
use IEEE.math_real.all;          maths

entity OR_sync is
  GENERIC(WIDTH : integer := 14;
       L : integer := 3);
  PORT(clk : in STD_LOGIC;
       rst : in STD_LOGIC;
       x_in : in STD_LOGIC_VECTOR(WIDTH-1 downto 0);
       x_out : out STD_LOGIC_VECTOR(WIDTH-1 downto 0);
       result : out STD_LOGIC);
```

```
end OR_sync;

architecture Behavioral of OR_sync is

  constant A : integer := integer(ceil(log(real(WIDTH))/log(real(L))));
  constant B : integer := integer(L**A);

  type array_OR is array (0 to A) of STD_LOGIC_VECTOR(B-1 downto 0);
  signal aux : array_OR;

  type array_signal is array (0 to A) of STD_LOGIC_VECTOR(WIDTH-1 downto 0);
  signal signal_delayed : array_signal;

  function function_OR (X : STD_LOGIC_VECTOR(L-1 downto 0)) return STD_LOGIC is
    begin
      for j in 0 to L-1 loop
        if X(j) = '1' then
          return '1';
        end if;
      end loop;
      return '0';
  end function_OR;

  begin

    result <= aux(A)(0);
    x_out <= signal_delayed(A)(WIDTH-1 downto 0);

    process (clk)
      begin
        if (rising_edge(clk)) then
          if (rst = '1') then
            aux <= ((others=>(others=>'0')));
            signal_delayed <= ((others=>(others=>'0')));
          else
            aux(0)(WIDTH-1 downto 0) <= x_in;
            signal_delayed(0)(WIDTH-1 downto 0) <= x_in;

            for J in 1 to A loop
              for K in 0 to ((L**(A-J))-1) loop
                aux(J)(K) <= function_OR(aux(J-1)((K+1)*L-1 downto K*L));
              end loop;
            end loop;

            for I in 1 to A loop
              signal_delayed(I)(WIDTH-1 downto 0) <= signal_delayed(I-1)(WIDTH-1
     downto 0);
            end loop;
          end if;
        end if;
    end process;
end Behavioral;
```

Table D.1: Truth table of the encoders.

(a) 4:2 encoder.

Input	Encoder	Valid
0000	XX	0
0001	00	1
0010	01	1
0011	XX	0
0100	10	1
0101	XX	0
0110	XX	0
0111	XX	0
1000	11	1
1001	XX	0
1010	XX	0
1011	XX	0
1100	XX	0
1101	XX	0
1110	XX	0
1111	XX	0

(b) 8:3 priority encoder.

En. in	Input	Out	Val.	En. out
0	xxxxxxxx	000	0	0
1	00000000	000	0	1
1	00000001	000	1	0
1	0000001x	001	1	0
1	000001xx	010	1	0
1	00001xxx	011	1	0
1	0001xxxx	100	1	0
1	001xxxxx	101	1	0
1	01xxxxxx	110	1	0
1	1xxxxxxx	111	1	0

D.3 Encoders

D.3.1 Normal encoder

```
entity priority_encoder is
  Generic (WIDTH_IN : integer := 8;          pow of 2
        WIDTH_OUT : integer := 3);        log2(WIDTH_IN)
  Port (input_signal : in std_logic_vector(WIDTH_IN 1 downto 0);      unsigned
      output_signal : out STD_LOGIC_vector(WIDTH_OUT 1 downto 0);     unsigned
      enable_out : out std_logic;        used for nesting
      enable_in : in std_logic;          used for nesting
      valid_out : out std_logic;         used for nesting
      strobe_out : out std_logic;
      clock : in std_logic;
      reset : in std_logic;
      strobe_in : in std_logic;
      output_MSB : out std_logic_vector(WIDTH_IN 1 downto 0));      unsigned
end priority_encoder;

architecture Behavioral of priority_encoder is

  function find_MSB(input_signal : STD_LOGIC_vector) return integer is

    variable var : integer;

    begin
      var := (2**WIDTH_OUT) 1;
      for j in WIDTH_IN 1 downto 0 loop
```

```
25          if input_signal(j) = '1' then
              return var;
27          else
              var := var 1;
29          end if;
        end loop;
31      return var;      zero
    end find_MSB;
33

35  function find_MSB_vector(input_signal : STD_LOGIC_vector) return
      STD_LOGIC_vector is

37    variable var : std_logic_vector(WIDTH_IN 1 downto 0) := (others => '0');

39    begin
        for j in WIDTH_IN 1 downto 0 loop
41        if input_signal(j) = '1' then
            var(j) := '1';
43          return var;
          end if;
45      end loop;
        return var;      zero
47  end find_MSB_vector;

49  begin
      process(clock)
51      begin
          if (rising_edge(clock)) then
53          if (reset = '1') then
              enable_out <= '0';
55            valid_out <= '0';
              output_signal <= (others => '0');
57            strobe_out <= '0';
              output_MSB <= (others => '0');
59          else

61              sync outputs with strobe_in
              enable_out <= '0';
63            valid_out <= '0';
              strobe_out <= '0';
65

              if (enable_in = '1') then
67              if strobe_in = '1' then
                  if (input_signal = 0) then
69                  enable_out <= '1';
                    valid_out <= '0';
71                  output_signal <= (others => '0');
                    strobe_out <= '1';
73                  output_MSB <= (others => '0');
                  else
75                  enable_out <= '0';
                    valid_out <= '1';
77                  output_signal <= std_logic_vector(to_unsigned(find_MSB(
    input_signal), output_signal'length));
                    output_MSB <= find_MSB_vector(input_signal);
```

```
79
                    strobe_out <= '1';
81                end if;     input_signal = 0
              end if;     strobe_in
83          else      enable_in
              enable_out <= '0';
85            valid_out <= '0';
              output_signal <= (others => '0');
87          end if;     enable_in
          end if;     rst
89      end if;     clck
    end process;
91 end Behavioral;
```

D.3.2 Priority encoder

```
1  entity priority_encoder_nested is
     Generic (WIDTH_IN : integer := 32;            pow of 2
3            WIDTH_OUT : integer := 5;           log2(WIDTH_IN)
             WEI : integer := 8);      size of the encoders (pow of 2)
5    Port (input_signal : in std_logic_vector(WIDTH_IN-1 downto 0);      unsigned
          output_signal : out STD_LOGIC_vector(WIDTH_OUT-1 downto 0);    unsigned
7         enable_in : in std_logic;          used for nesting
          valid_out : out std_logic;      used for nesting
9         clock : in std_logic;
          reset : in std_logic;
11        strobe_in : in std_logic;
          strobe_out : out std_logic);
13 end priority_encoder_nested;

15 architecture Behavioral of priority_encoder_nested is

17   constant N : integer := integer(real(WIDTH_IN)/real(WEI));
     constant WEO : integer := integer(log2(real(WEI)));
19   constant NLOG : integer := integer(log2(real(N)));
     constant LATENCY : integer := N+3;
21
     type ARRAY_2_N is array (0 to 2) of std_logic_vector(N-1 downto 0);
23   type ARRAY_N_WEI is array (0 to N-1) of std_logic_vector(WEI-1 downto 0);
     type ARRAY_N_N_WEI is array (0 to N-1) of ARRAY_N_WEI;
25   type ARRAY_N_WEO is array (0 to N-1) of std_logic_vector(WEO-1 downto 0);
     type ARRAY_2_N_WEO is array (0 to 2) of ARRAY_N_WEO;
27   type ARRAY_N_NLOG is array (0 to N-1) of std_logic_vector(NLOG-1 downto 0);
     type ARRAY_2_N_NLOG is array (0 to 2) of ARRAY_N_NLOG;
29
     signal enable_vector : std_logic_vector(N-1+1 downto 0);
31   signal valid_vector : std_logic_vector(N-1 downto 0);
     signal strobe_in_vector : std_logic_vector(N-1 downto 0);
33   signal strobe_out_vector : std_logic_vector(LATENCY-1 downto 0);

35   signal input_matrix : ARRAY_N_WEI;
     signal input_matrix_delayed : ARRAY_N_N_WEI;
37   signal valid_encoders_matrix : ARRAY_2_N;
     signal mask : ARRAY_N_NLOG;
39   signal valid_encoders_matrix_AND_mask : ARRAY_N_NLOG;
```

```
  signal MSB_matrix : ARRAY_2_N_NLOG;
41 signal output_encoders : ARRAY_N_WEO;
  signal LSB_matrix : ARRAY_2_N_WEO;
43
  component priority_encoder is
45   Generic (WIDTH_IN : integer := 8;
         WIDTH_OUT : integer := 3);
47   Port (input_signal : in std_logic_vector(WIDTH_IN-1 downto 0);
       output_signal : out STD_LOGIC_vector(WIDTH_OUT-1 downto 0);
49       enable_out : out std_logic;
         enable_in : in std_logic;
51       valid_out : out std_logic;
         strobe_out : out std_logic;
53       clock : in std_logic;
         reset : in std_logic;
55       strobe_in : in std_logic;
         output_MSB : out std_logic_vector(WIDTH_IN-1 downto 0));
57 end component;

59 begin

61   pe_chain : for i in 0 to N-1 generate
       pe : priority_encoder
63       Generic map (WIDTH_IN => WEI,
                WIDTH_OUT => WEO)
65       Port map (input_signal => input_matrix_delayed(0)(i)(WEI-1 downto 0),
              output_signal => output_encoders(i)(WEO-1 downto 0),
67            enable_out =>  enable_vector(i),
              enable_in => enable_vector(i+1),
69            valid_out => valid_vector(i),
              strobe_out => open,
71            clock => clock,
              reset => reset,
73            strobe_in => strobe_in_vector(i),
                output_MSB => output_MSB_matrix(i)(WEI-1 downto 0)
75            output_MSB => open
              );
77   end generate pe_chain;

79      input_signal to input_matrix
     fill_input_matrix : for i in 0 to N-1 generate
81     input_matrix(i)(WEI-1 downto 0) <= input_signal((i+1)*WEI-1 downto i*WEI);
     end generate fill_input_matrix;
83
        Create mask
85   fill_mask : for i in 0  to N-1 generate
       mask(i)(NLOG-1 downto 0) <= std_logic_vector(to_unsigned(i,NLOG));
87   end generate fill_mask;

89      Multiply mask by valid vector
     rows : for i in 0 to N-1 generate
91     columns : for k in 0 to NLOG-1 generate
         valid_encoders_matrix_AND_mask(i)(k) <= valid_vector(i) and mask(i)(k)
     ;
93     end generate columns;
   end generate rows;
```

```
95
        Outputs
97      valid_out <= valid_encoders_matrix(1)(0);

99      MSB : for k in WIDTH_OUT-1 downto WEO generate
          output_signal(k)<= MSB_matrix(1)(0)(k-WEO);
101     end generate MSB;

103     LSB : for k in WEO-1 downto 0 generate
          output_signal(k) <= LSB_matrix(1)(0)(k);
105     end generate LSB;

107     strobe_out <= strobe_out_vector(LATENCY-1);

109       AUX : for k in N-1 downto 0
            output_MSB_out(k* downto ) <= output_MSB_matrix(k)(WEI-1 downto 0);
111       end generate AUX;

113     process(clock)
          begin
115         if (rising_edge(clock)) then
              if (reset = '1') then
117
                valid_encoders_matrix <= (others=>(others=>'0'));
119             LSB_matrix <= (others=>(others=>(others=>'0')));
                input_matrix_delayed <= (others=>(others=>(others=>'0')));
121
                MSB_matrix <= (others=>(others=>(others=>'0')));
123
                enable_vector(N-1+1) <= '0';
125             strobe_in_vector(N-1 downto 0) <= (others=>'0');

127             strobe_out_vector <= (others=>'0');

129           else
                  Delay strobe_out
131             strobe_out_vector(0) <= strobe_in;
                strobe_out_vector(LATENCY-1 downto 1) <= strobe_out_vector(LATENCY-2
      downto 0);
133
                  Delay enable
135             enable_vector(N-1+1) <= enable_in;

137               Delay strobe_in
                strobe_in_vector(N-1)<=strobe_in;
139             for i in 1 to N-1 loop
                  strobe_in_vector(N-1-i) <= strobe_in_vector(N-1-i+1);
141             end loop;

143               Delay input
                for i in N-1 downto 0 loop
145               input_matrix_delayed(i)(N-1-i)(WEI-1 downto 0) <= input_matrix(N-
      1-i)(WEI-1 downto 0 );
                end loop;
147
                for j in N-2 downto 0 loop
```

```
149                 for tt in (N j 1) downto 1 loop
                      input_matrix_delayed(tt 1)(j)(WEI 1 downto 0) <=
    input_matrix_delayed(tt)(j)(WEI 1 downto 0);
151                 end loop;
                  end loop;
153
                    Valid signal
155               valid_encoders_matrix(0)(N 1 downto 0) <= valid_vector;

157               valid_encoders_matrix(1)(N 1) <= valid_encoders_matrix(0)(N 1);

159               for i in N 1 downto 1 loop
                    valid_encoders_matrix(1)(i 1) <= valid_encoders_matrix(1)(i) or
    valid_encoders_matrix(0)(i 1) ;
161               end loop;

163                 MSB
                  for k in NLOG 1 downto 0 loop
165
                    MSB_matrix(1)(N 1)(k) <= MSB_matrix(0)(N 1)(k);
167
                    for i in N 1 downto 0 loop
169                   MSB_matrix(0)(i)(k) <= valid_encoders_matrix_AND_mask(i)(k);
                    end loop;
171               end loop;

173               for k in NLOG 1 downto 0 loop
                    for i in N 2 downto 0 loop
175                   MSB_matrix(1)(i)(k) <= MSB_matrix(1)(i+1)(k) or MSB_matrix(0)(i)
    (k);
                    end loop;
177               end loop;

179                 LSB
                  for k in WEO 1 downto 0 loop
181
                    LSB_matrix(1)(N 1 )(k) <= LSB_matrix(0)(N 1 )(k);
183
                    for i in N 1 downto 0 loop
185                   LSB_matrix(0)(i)(k) <= output_encoders(i)(k);
                    end loop;
187               end loop;

189               for k in WEO 1 downto 0 loop
                    for i in N 2 downto 0 loop
191                   LSB_matrix(1)(i)(k) <= LSB_matrix(1)(i+1)(k) or LSB_matrix(0)(i)
    (k);
                    end loop;
193               end loop;

195             end if;     rst
              end if;     clck
197       end process;
  end Behavioral;
```

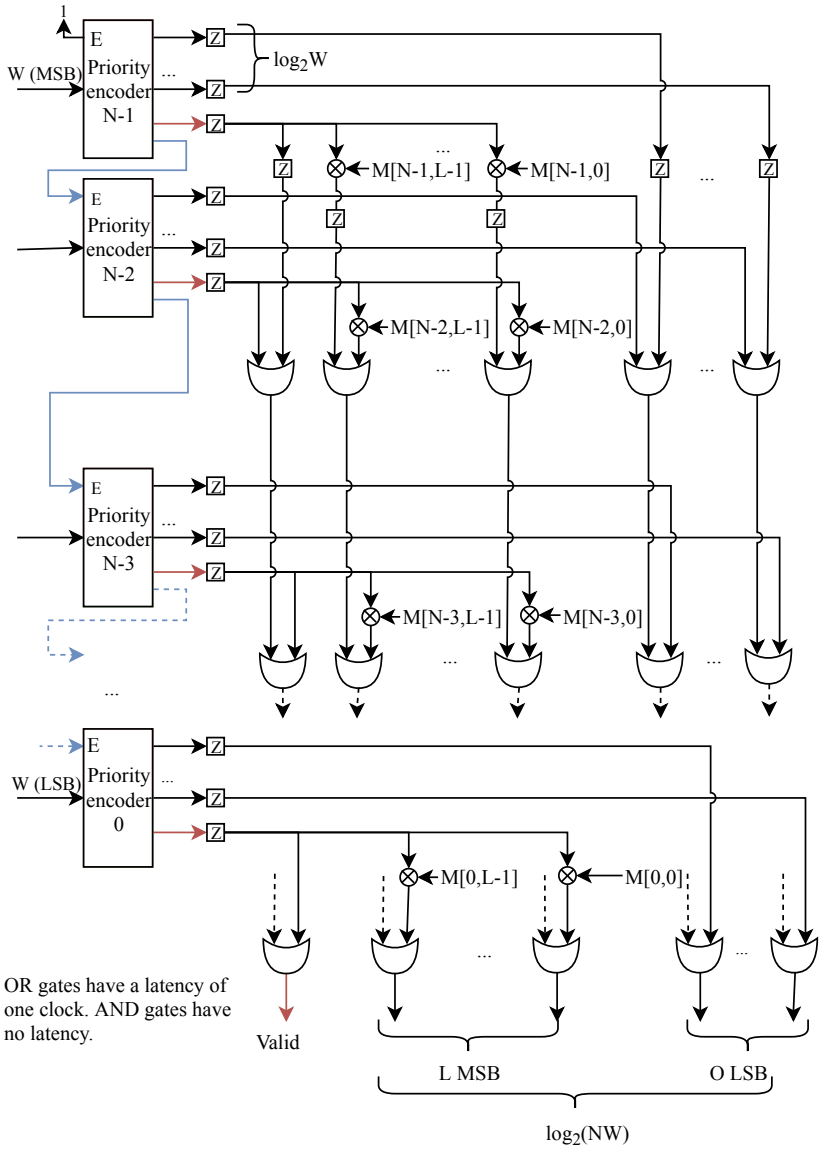

Figure D.2: Implementation of a synchronous priority encoder with an arbitrary length NW by nesting N smaller ones of size W.

D.4 AGC

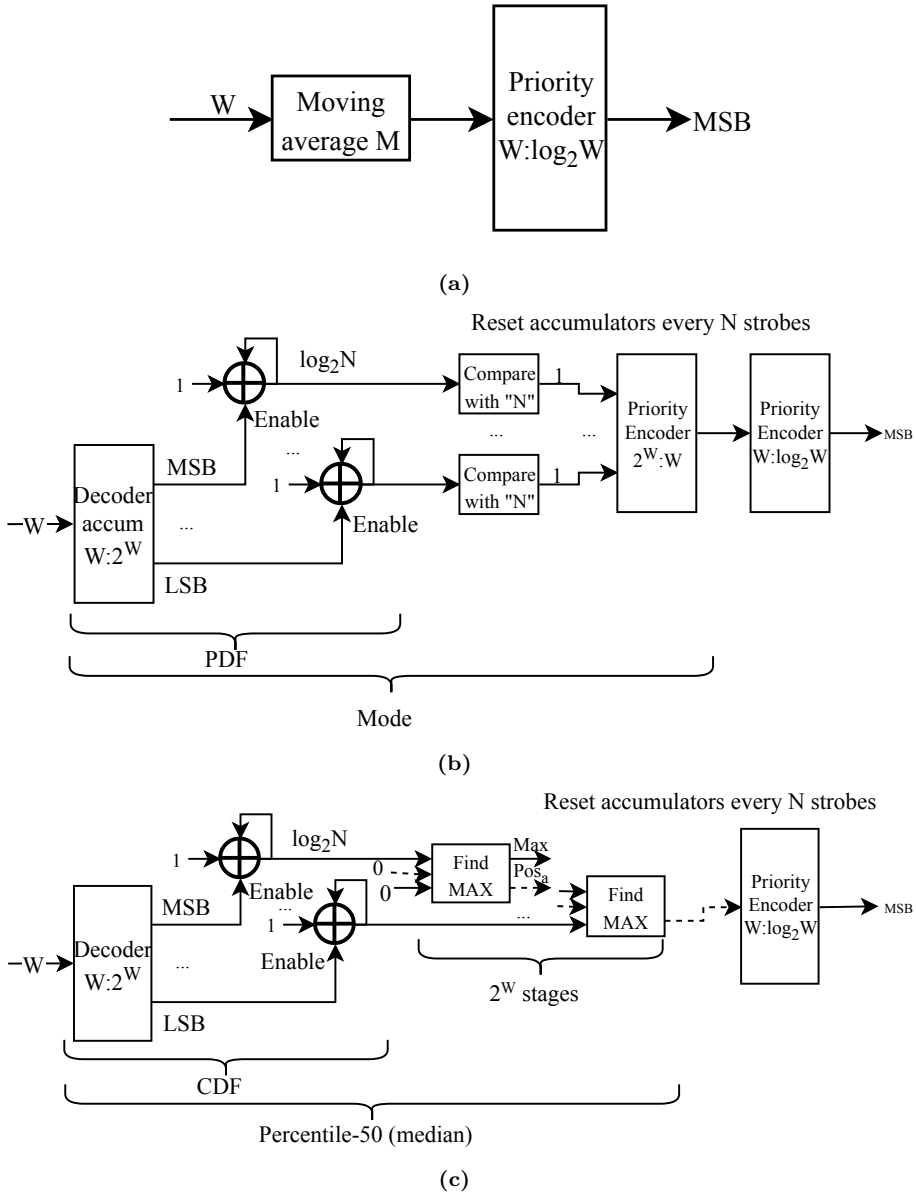

Figure D.3: Implementation of AGCs using different signal metrics without sliding window: (a) based on mean, (b) based on mode, and (c) based on median. The truth table of the decoders is given in Table D.2. An hierarchical implementation is given in Fig. D.4

Table D.2: Truth table for two different 8:3 decoders.

Enable in	Input	Decoder	Acum decoder
0	xxx	00000000	00000000
1	000	00000001	00000001
1	001	00000010	00000011
1	010	00000100	00000111
1	011	00001000	00001111
1	100	00010000	00011111
1	101	00100000	00111111
1	110	01000000	01111111
1	111	10000000	11111111

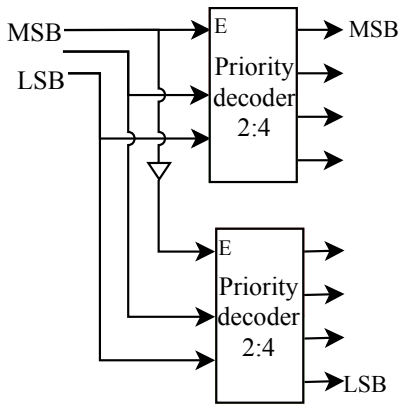

Figure D.4: Implementation of a synchronous 3:8 decoder using two 2:4 decoders. The same idea can be used to implement larger decoders.

D.5 Other entities

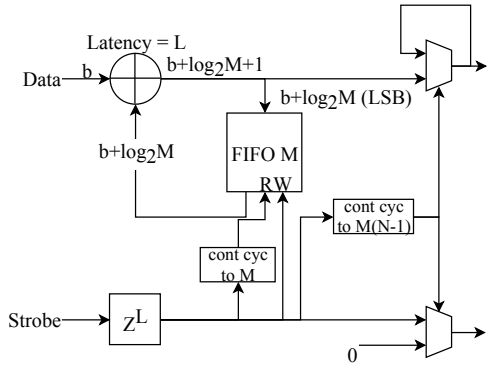

Figure D.5: Implementation of M averages of a vector of b bits without sliding window.

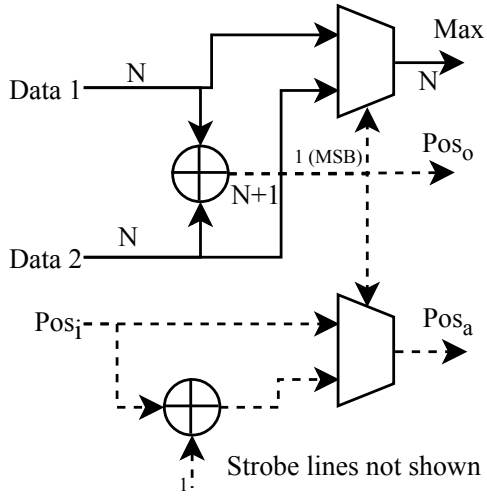

Figure D.6: Implementation to find the maximum between two signals of N bits.

E

Appendix E

Changes made in the Ettus Drivers UHD 3.8.5

THE version of the UHD drivers in MIR are the 3.8.5, which at the time of building the host program, were already a bit old. However, this version was used because the drivers are only compatible with a specific firmware version and FPGA image. Later versions of the drivers, required to use FPGA images that could only be build with a software for which the university did not have licenses.

This appendix give two bugs found in the drivers, and describes a method to create a user register in the USRP X310.

E.1 Changes involving the USRPs X310

- Change the clock frequency of the DBSRX2 boards, so that their LOs can lock to the desired RF frequencies.

  – In *host/lib/usrp/x300/x300_clock_ctrl.cpp*, change

  ```
  static const double X300_DEFAULT_DBOARD_CLK_RATE = 50e6;
  ```

  to

  ```
  static const double X300_DEFAULT_DBOARD_CLK_RATE = 100e6;
  ```

- Create a user register in order to sent commands to the USRP. This register will then be called with *usrp_object->set_user_register_MIR*. The address of this register is the same as that of the register used to set the sampling frequency, as this value has been hard-coded in the FPGA. Thus, a VHDL entity has been build in the FPGA in order to filter out this command to the rest of the original FPGA entities.

  – In *host/include/uhd/usrp/multi_usrp.hpp*, add next line at the end of the *Mboard methods* section.

  ```
  virtual void set_user_register_MIR(double mir_reg, size_t chan =
      ALL_CHANS) = 0;
  ```

  – In *host/lib/usrp/multi_usrp.cpp*, add next code at the end of the *Mboard methods* section.

  ```
  void set_user_register_MIR(double mir_reg, size_t chan){
    _tree->access<double>(rx_dsp_root(chan) / "mir_reg" / "value").set(
      mir_reg);
    return;
  }
  ```

  – In *host/lib/usrp/multi_usrp.cpp*, add next line at the end of the file.

  ```
  virtual double set_mir(const double mir_reg) = 0;
  ```

  – In *host/lib/usrp/cores/rx_dsp˙core_3000.cpp*, add next line immediately before the "set˙host˙rate" function function.

  ```
  double set_mir(const double mir_reg){
    _iface->poke32(REG_DSP_RX_DECIM,  mir_reg);
    return 0;
  }
  ```

  – In *host/lib/usrp/x300/x300_impl.cpp*, add the code below immediately before this line

  tree->create<double>(rx_dsp_path / "rate" / "value")

  ```
  _tree->create<double>(rx_dsp_path / "mir_reg" / "value")
  .coerce(boost::bind(&rx_dsp_core_3000::set_mir, perif.ddc, _1))
  .subscribe(boost::bind(&x300_impl::update_mir, this, boost::ref(mb),
      radio_index, _1))
  .set(0);
  ```

  - In *host/lib/usrp/x300/x300˙impl.hpp*, add next line immediately before *update˙rx˙samp˙rate*.

    ```
    void update_mir(mboard_members_t&, const size_t , const double);
    ```

  - In *host/lib/usrp/x300/x300˙io˙impl.cpp*, add the code below immediately before this line
    void x300_impl::update_rx_samp_rate(mboard_members_t &mb, const size_t dspno, const double rate).

    ```
    void update_mir(mboard_members_t&, const size_t , const double);
    ```

E.2 Changes involving the USRP N210

- Configure the USRP N210 to generate the calibration signal with an IF of 100 MHz.

  - In the function "*set_tx_mod_mode*" in *host/lib/usrp/usrp2/codec_ctrl.cpp*, force *mod_mode* as indicated:

    ```
    void set_tx_mod_mode(int mod_mode){
      mod_mode = 4;
      ...
    }
    ```

Part VI

Bibliography and List of Publications

Bibliography

[1] C. D. Hall and R. A. Cordey, "Multistatic scatterometry," in *International Geoscience and Remote Sensing Symposium (IGARSS)*. IEEE, 1988, pp. 561–562. (Cited on pages 4 and 46.)

[2] M. Martin-Neira, "A passive reflectometry and interferometry system (PARIS): application to ocean altimetry," *ESA Journal*, vol. 17, no. 4, pp. 331–355, 1993. (Cited on pages 4, 46, and 61.)

[3] M. Martin-Neira, S. D'Addio, C. Buck, N. Floury, and R. Prieto-Cerdeira, "The PARIS Ocean Altimeter In-Orbit Demonstrator," *IEEE Transactions on Geoscience and Remote Sensing*, vol. 49, no. 6, pp. 2209–2237, jun 2011. (Cited on pages 6, 48, 88, 96, 101, 104, 150, 280, and 298.)

[4] E. Valencia, "Ocean Monitoring Using L-band Microwave Radiometry and GNSS-R," Ph.D. dissertation, Universitat Politècnica de Catalunya, 2012. (Cited on page 7.)

[5] R. Onrubia, "Advanced GNSS-R Instruments for Altimetry and Scatterometry," Ph.D. dissertation, Universitat Politècnica de Catalunya, 2020. (Cited on pages 7, 8, 79, 82, 199, 205, 211, 213, 223, 228, 229, 230, 232, 233, 234, 240, 243, 248, 262, 264, 265, 266, 271, 275, 276, 279, 281, 284, 285, 286, and 287.)

[6] J. Wickert, O. Andersen, G. Beyerle, E. Cardellach, B. Chapron, and C. Förste, "GEROS-ISS : GNSS Reflectometry , Radio Occultation and Scatterometry Onboard the International Space Station," in *Living planet symposium (ESA)*, no. 1, 2013, pp. 2–4. (Cited on pages 7, 88, 113, and 200.)

[7] H. Park, A. Camps, D. Pascual, Y. Kang, R. Onrubia, J. Querol, and A. Alonso-Arroyo, "A Generic Level 1 Simulator for Spaceborne GNSS-R Missions and Application to GEROS-ISS Ocean Reflectometry," *IEEE Journal of Selected Topics in Applied Earth Observations and Remote Sensing*, vol. 10, no. 10, pp. 4645–4659, 2017. (Cited on pages 7, 8, and 85.)

[8] J. Querol, A. Alonso-Arroyo, R. Onrubia, D. Pascual, H. Park, and A. Camps, "SNR Degradation in GNSS-R Measurements under the Effects of Radio-Frequency Interference," *IEEE Journal of Selected Topics in Applied Earth Observations and Remote Sensing*, vol. 9, no. 10, pp. 4865–4878, oct 2016. (Cited on pages 14 and 38.)

[9] R. Onrubia, J. Querol, D. Pascual, A. Alonso-Arroyo, H. Park, and A. Camps, "DME/TACAN impact analysis on GNSS reflectometry," *IEEE Journal of Selected Topics in Applied Earth Observations and Remote Sensing*, vol. 9, no. 10, pp. 4611–4620, oct 2016. (Cited on pages 14 and 38.)

[10] J. Walker, "Some circular orbit patterns providing continuous whole Earth coverage," *Journal of the British Interplanetary Society*, vol. 24, pp. 369–384, 1971. (Cited on page 14.)

[11] A. W. Rihaczek, *Principles of high-resolution radar*. New York, NY: Wiley, 1969. (Cited on page 23.)

[12] G. Jourdain and J. P. Henrioux, "Use of large bandwidth-duration binary phase shift keying signals in target delay Doppler measurements," *The Journal of the Acoustical Society of America*, vol. 90, no. 1, pp. 299–309, 1991. (Cited on page 23.)

[13] "IS-GPS-200F Navstar GPS Space Segment/User Segment Interfaces." [Online]. Available: http://www.gps.gov/technical/icwg/ (Cited on pages 25, 38, 100, and 298.)

[14] "ICD-GPS-705 Navstar GPS Space Segment/User Segment Interfaces." [Online]. Available: http://www.gps.gov/technical/icwg/ (Cited on pages 25, 38, 100, and 298.)

[15] "European GNSS (Galileo) open service signal in space interface control document (OS SIS ICD) issue 1.1." [Online]. Available: https://www.gsc-europa.eu/ (Cited on pages 26, 32, 38, 100, 155, 286, and 298.)

[16] J. W. Betz, "Binary offset carrier modulations for radionavigation," *NAVIGATION: Journal of the Institute of Navigation*, vol. 48, no. 4, pp. 227–246, dec 2001. (Cited on pages 28 and 37.)

[17] J. Á. Ávila-Rodríguez, "On Generalized Signal Waveforms for Satellite Navigation," Ph.D. dissertation, Universität der Bundeswehr, München, Neubiberg, 2008. (Cited on pages 29, 86, 98, 298, and 299.)

[18] J.-A. Avila-Rodriguez, G. W. Hein, S. Wallner, J.-L. Issler, L. Res, L. Lestarquit, A. de Latour, J. Godet, F. Bastide, T. Patt, and J. Owen, "The MBOC Modulation: The Final Touch to the Galileo Frequency and Signal Plan," *Navigation*, vol. 55, no. 1, pp. 15–28, mar 2008. (Cited on pages 32 and 286.)

[19] "IS-GPS-800B Navstar GPS Space Segment/User Segment L1C Interface." [Online]. Available: http://www.gps.gov/technical/icwg/ (Cited on pages 38, 100, and 298.)

[20] "BeiDou Navigation Satellite System Signal in Space Interface Control Document - Open Service Signal (Version 2.0)." (Cited on pages 38, 100, and 299.)

[21] J. Bao-Yen, *Fundamentals of Global Positioning System Receivers. A software approach*, 2nd ed. Wiley-Interscience, 2005. (Cited on pages 38, 127, and 139.)

[22] C. J. Kaplan, Elliott D., Hegarty, *Understading GPS. Principles and Applications*, 2nd ed. Artech House, 2006. (Cited on pages 38 and 127.)

[23] E. Hofmann-Wellenhof Bernhard; Lichtenegger, Herbert; Wasle, *GNSS - Global Navigation Satellite Systems. GPS, GLONASS, Galileo and more.* Springer Wien New York, 2008. (Cited on pages 38 and 127.)

[24] F. V. Diggelen, *A-GPS. Assisted GPS, GNSS, and SBAS.* Artech House, 2009. (Cited on pages 38, 128, and 143.)

[25] N. I. Ziedan, *GNSS Receivers for Weak Signals.* Artech House, 2006. (Cited on page 38.)

[26] D. Gleason, Scott; Gebre-Egziabher, *GNSS Applications and Methods.* Artech House, 2009. (Cited on pages 38, 45, 46, 68, and 265.)

[27] F. Jin, Shuanggen; Cardellach, Estel; Xie, *GNSS Remote Sensing. Theory, Methods and Applications.* Springer, 2014. (Cited on pages 45, 46, 47, 48, 49, 52, 53, 54, 55, 64, and 81.)

[28] W. Emery and A. Camps, *Introduction to Satellite Remote Sensing. Atmosphere, Ocean, Land and Cryosphere Applications.* Elsevier Inc., 2017. (Cited on pages 45, 46, 80, 81, and 82.)

[29] V. U. Zavorotny, S. Gleason, E. Cardellach, and A. Camps, "Tutorial on Remote Sensing Using GNSS Bistatic Radar of Opportunity," *Geoscience and Remote Sensing Magazine, IEEE*, vol. 2, no. 4, pp. 8–45, dec 2014. (Cited on pages 45, 46, 65, 80, 81, and 82.)

[30] J. C. Auber, A. Bibaut, and J. M. Rigal, "Characterization of multipath on land and sea at GPS frequencies," in *Proceedings of ION GPS*, vol. 2, 1994, pp. 1155–1171. (Cited on page 46.)

[31] S. Jin and A. Komjathy, "GNSS reflectometry and remote sensing: New objectives and results," *Advances in Space Research*, vol. 46, no. 2, pp. 111–117, jul 2010. (Cited on page 46.)

[32] S. Jin, G. P. Feng, and S. Gleason, "Remote sensing using GNSS signals: Current status and future directions," *Advances in Space Research*, vol. 47, no. 10, pp. 1645–1653, may 2011. (Cited on page 46.)

[33] K. Yu, C. Rizos, D. Burrage, A. G. Dempster, K. Zhang, and M. Markgraf, "An overview of GNSS remote sensing," *EURASIP Journal on Advances in Signal Processing*, dec 2014. (Cited on page 46.)

[34] F. T. Ulaby, R. K. Moore, and A. K. Fung, *Microwave Remote Sensing: Active and Passive, vols.I-III.* Noorwood, MA: Artech House, Inc., 1981. (Cited on pages 47, 57, 58, 124, 138, and 221.)

[35] P. Beckmann, *The Scattering of Electromagnetic Waves from Rough Surfaces.* Artech House, 1963. (Cited on pages 47, 124, and 126.)

[36] S. Gleason, "A Real-Time On-Orbit Signal Tracking Algorithm for GNSS Surface Observations," *Remote Sensing*, vol. 11, no. 16, p. 1858, aug 2019. (Cited on pages 48, 77, and 186.)

[37] A. Camps, "Spatial Resolution in GNSS-R Under Coherent Scattering," *IEEE Geoscience and Remote Sensing Letters*, vol. 17, no. 1, pp. 32–36, jan 2020. (Cited on pages 49, 51, 257, and 274.)

[38] F. Zimmermann, B. Schmitz, L. Klingbeil, and H. Kuhlmann, "GPS Multipath Analysis Using Fresnel Zones," *Sensors*, vol. 19, no. 1, p. 25, dec 2018. (Cited on page 50.)

[39] A. O'Brien, "Global Navigation Satellite System Reflectometry (GNSS-R)," in *IEEE GRSS Workshop on Microwave Remote Sensing*, 2019. (Cited on page 50.)

[40] A. Alonso, "Contributions to Land, Sea, and Sea-Ice Remote Sensing Using GNSS-Reflectometry," Ph.D. dissertation, Universitat Politècnica de Catalunya, 2016. (Cited on pages 52, 68, 69, 70, and 79.)

[41] V. U. Zavorotny and A. G. Voronovich, "Scattering of GPS signals from the ocean with wind remote sensing application," *IEEE Transactions on Geoscience and Remote Sensing*, vol. 38, no. 2, pp. 951–964, mar 2000. (Cited on pages 52, 56, 63, and 124.)

[42] Egido, "GNSS Reflectometry for Land Remote Sensing Applications," Ph.D. dissertation, Universitat Politècnica de Catalunya, 2013. (Cited on page 53.)

[43] C. Hu, C. Benson, H. Park, A. Camps, L. Qiao, and C. Rizos, "Detecting Targets above the Earth's Surface Using GNSS-R Delay Doppler Maps: Results from TDS-1," *Remote Sensing*, vol. 11, no. 19, p. 2327, oct 2019. (Cited on page 54.)

[44] H. Park, A. Camps, J. Castellvi, and J. Muro, "Generic Performance Simulator of Spaceborne GNSS-Reflectometer for Land Applications," *IEEE Journal of Selected Topics in Applied Earth Observations and Remote Sensing*, vol. 13, pp. 3179–3191, 2020. (Cited on pages 55 and 85.)

[45] D. Schiavulli, A. Ghavidel, A. Camps, and M. Migliaccio, "GNSS-R Wind-Dependent Polarimetric Signature Over the Ocean," *IEEE Geoscience and Remote Sensing Letters*, vol. 12, no. 12, pp. 2374–2378, dec 2015. (Cited on page 57.)

[46] A. G. Voronovich and V. U. Zavorotny, "Full-Polarization Modeling of Monostatic and Bistatic Radar Scattering From a Rough Sea Surface," *IEEE Transactions on Antennas and Propagation*, vol. 62, no. 3, pp. 1362–1371, mar 2014. (Cited on page 57.)

[47] N. Rodriguez-Alvarez, X. Bosch-Lluis, A. Camps, M. Vall-llossera, E. Valencia, J. Marchan-Hernandez, and I. Ramos-Perez, "Soil Moisture Retrieval Using GNSS-R Techniques: Experimental Results Over a Bare Soil Field," *IEEE Transactions on Geoscience and Remote Sensing*, vol. 47, no. 11, pp. 3616–3624, nov 2009. (Cited on page 61.)

[48] J. Querol, "Radio Frequency Interference Detection and Mitigation Techniques for Navigation and Earth Observation," Ph.D. dissertation, Universitat Politècnica de Catalunya, 2018. (Cited on pages 61, 79, 143, and 294.)

[49] W. Li, D. Yang, S. D'Addio, and M. Martín-Neira, "Partial interferometric processing of reflected GNSS signals for ocean altimetry," *IEEE Geoscience and Remote Sensing Letters*, vol. 11, no. 9, pp. 1509–1513, sep 2014. (Cited on pages 62 and 107.)

[50] J. F. Marchán-Hernández, N. Rodríguez-Álvarez, A. Camps, X. Bosch-Lluis, I. Ramos-Pérez, and E. Valencia, "Correction of the sea state impact in the L-band brightness temperature by means of delay-doppler maps of global navigation satellite signals reflected over the sea surface," *IEEE Transactions on Geoscience and Remote Sensing*, vol. 46, no. 10, pp. 2914–2923, oct 2008. (Cited on pages 64 and 70.)

[51] H. Park, E. Valencia, N. Rodriguez-Alvarez, X. Bosch-Lluis, I. Ramos-Perez, and A. Camps, "New approach to sea surface wind retrieval from GNSS-R measurements,"

in *International Geoscience and Remote Sensing Symposium (IGARSS)*. IEEE, jul 2011, pp. 1469–1472. (Cited on page 64.)

[52] A. Alonso-Arroyo, A. Camps, H. Park, D. Pascual, R. Onrubia, and F. Martín, "Retrieval of significant wave height and mean sea surface level using the GNSS-R interference pattern technique: Results from a three-month field campaign," *IEEE Transactions on Geoscience and Remote Sensing*, vol. 53, no. 6, pp. 3198–3209, jun 2015. (Cited on pages 65 and 124.)

[53] A. G. Voronovich and V. U. Zavorotny, "The Transition From Weak to Strong Diffuse Radar Bistatic Scattering From Rough Ocean Surface," *IEEE Transactions on Antennas and Propagation*, vol. 65, no. 11, pp. 6029–6034, nov 2017. (Cited on page 65.)

[54] ——, "Bistatic Radar Equation for Signals of Opportunity Revisited," *IEEE Transactions on Geoscience and Remote Sensing*, vol. 56, no. 4, pp. 1959–1968, apr 2018. (Cited on page 65.)

[55] R. De Roo and F. Ulaby, "Bistatic specular scattering from rough dielectric surfaces," *IEEE Transactions on Antennas and Propagation*, vol. 42, no. 2, pp. 220–231, 1994. (Cited on page 65.)

[56] E. Loria, A. O'Brien, V. Zavorotny, B. Downs, and C. Zuffada, "Analysis of scattering characteristics from inland bodies of water observed by CYGNSS," *Remote Sensing of Environment*, vol. 245, p. 111825, aug 2020. (Cited on page 65.)

[57] S. Gleason, S. Hodgart, Y. Sun, C. Gommenginger, S. Mackin, M. Adjrad, and M. Unwin, "Detection and processing of bistatically reflected GPS signals from low earth orbit for the purpose of ocean remote sensing," *IEEE Transactions on Geoscience and Remote Sensing*, vol. 43, no. 6, pp. 1229–1241, jun 2005. (Cited on pages 67, 80, and 96.)

[58] G. Foti, C. Gommenginger, P. Jales, M. Unwin, A. Shaw, C. Robertson, and J. Roselló, "Spaceborne GNSS reflectometry for ocean winds: First results from the UK TechDemoSat-1 mission," *Geophysical Research Letters*, vol. 42, no. 13, pp. 5435–5441, jul 2015. (Cited on pages 67 and 106.)

[59] A. Alonso-Arroyo, V. U. Zavorotny, and A. Camps, "Sea Ice Detection Using U.K. TDS-1 GNSS-R Data," *IEEE Transactions on Geoscience and Remote Sensing*, vol. 55, no. 9, pp. 4989–5001, sep 2017. (Cited on page 67.)

[60] A. Rius, E. Cardellach, and M. Martín-Neira, "Altimetric analysis of the sea-surface GPS-reflected signals," *IEEE Transactions on Geoscience and Remote*

Sensing, vol. 48, no. 4, pp. 2119–2127, apr 2010. (Cited on pages 66, 81, 88, 98, and 118.)

[61] J. F. Munoz-Martin, R. Onrubia, D. Pascual, H. Park, A. Camps, C. Rüdiger, J. Walker, and A. Monerris, "Untangling the Incoherent and Coherent Scattering Components in GNSS-R and Novel Applications," *Remote Sensing*, vol. 12, no. 7, p. 1208, apr 2020. (Cited on pages 67, 69, 126, and 185.)

[62] F. Martín, S. D'Addio, A. Camps, and M. Martín-Neira, "Modeling and analysis of GNSS-R waveforms sample-to-sample correlation," *IEEE Journal of Selected Topics in Applied Earth Observations and Remote Sensing*, vol. 7, no. 5, pp. 1545–1559, may 2014. (Cited on pages 67, 106, and 162.)

[63] A. Camps, H. Park, I. Sekulic, and J. Rius, "GNSS-R Altimetry Performance Analysis for the GEROS Experiment on Board the International Space Station," *Sensors*, vol. 17, no. 7, p. 1583, jul 2017. (Cited on page 67.)

[64] F. Martín, "Interferometric GNSS-R Processing: Modeling and Analysis of Advanced Processing Concepts for Altimetry," Ph.D. dissertation, Universitat Politècnica de Catalunya, 2015. (Cited on page 68.)

[65] E. Valencia, A. Camps, N. Rodriguez-Alvarez, I. Ramos-Perez, X. Bosch-Lluis, and H. Park, "Improving the accuracy of sea surface salinity retrieval using GNSS-R data to correct the sea state effect," *Radio Science*, vol. 46, no. 6, dec 2011. (Cited on page 69.)

[66] H. Carreno-Luengo, "Contributions to GNSS-R Earth Remote Sensing for Nano-Satellites," Ph.D. dissertation, Universitat Politècnica de Catalunya, 2016. (Cited on pages 69 and 79.)

[67] F. Martin, A. Camps, F. Fabra, A. Rius, M. Martin-Neira, S. D'Addio, and A. Alonso, "Mitigation of direct signal cross-talk and study of the coherent component in GNSS-R," *IEEE Geoscience and Remote Sensing Letters*, vol. 12, no. 2, pp. 279–283, feb 2015. (Cited on pages 69, 106, 118, and 185.)

[68] W. Li, E. Cardellach, F. Fabra, A. Rius, S. Ribó, and M. Martín-Neira, "First spaceborne phase altimetry over sea ice using TechDemoSat-1 GNSS-R signals," *Geophysical Research Letters*, vol. 44, no. 16, pp. 8369–8376, aug 2017. (Cited on page 69.)

[69] Huaizu You, J. Garrison, G. Heckler, and V. Zavorotny, "Stochastic voltage model and experimental measurement of ocean-scattered GPS signal statistics," *IEEE*

Transactions on Geoscience and Remote Sensing, vol. 42, no. 10, pp. 2160–2169, oct 2004. (Cited on pages 69, 124, 161, 242, 254, 256, and 257.)

[70] E. Valencia, A. Camps, J. F. Marchan-Hernandez, N. Rodriguez-Alvarez, I. Ramos-Perez, and X. Bosch-Lluis, "Experimental determination of the sea correlation time using GNSS-R coherent data," *IEEE Geoscience and Remote Sensing Letters*, vol. 7, no. 4, pp. 675–679, oct 2010. (Cited on pages 69, 70, 81, 161, 242, 247, 254, 255, 256, and 257.)

[71] N. Rodríguez-Álvarez, "Contributions to earth observation using gnss-r opportunity signals," Ph.D. dissertation, Universitat Politècnica de Catalunya, 2012. (Cited on page 70.)

[72] N. Rodriguez-Alvarez, D. M. Akos, V. U. Zavorotny, J. A. Smith, A. Camps, and C. W. Fairall, "Airborne GNSS-R Wind Retrievals Using Delay–Doppler Maps," *IEEE Transactions on Geoscience and Remote Sensing*, vol. 51, no. 1, pp. 626–641, jan 2013. (Cited on page 70.)

[73] E. Valencia, V. U. Zavorotny, D. M. Akos, and A. Camps, "Using DDM asymmetry metrics for wind direction retrieval from GPS ocean-scattered signals in airborne experiments," *IEEE Transactions on Geoscience and Remote Sensing*, vol. 52, no. 7, pp. 3924–3936, 2014. (Cited on pages 70 and 108.)

[74] D. Guan, H. Park, A. Camps, Y. Wang, R. Onrubia, J. Querol, and D. Pascual, "Wind direction signatures in GNSS-R observables from space," *Remote Sensing*, vol. 10, no. 2, p. 198, jan 2018. (Cited on page 70.)

[75] M. P. Clarizia, C. S. Ruf, P. Jales, and C. Gommenginger, "Spaceborne GNSS-R Minimum Variance Wind Speed Estimator," *IEEE Transactions on Geoscience and Remote Sensing*, vol. 52, no. 11, pp. 6829–6843, nov 2014. (Cited on page 70.)

[76] N. Rodriguez-Alvarez and J. L. Garrison, "Generalized Linear Observables for Ocean Wind Retrieval From Calibrated GNSS-R Delay–Doppler Maps," *IEEE Transactions on Geoscience and Remote Sensing*, vol. 54, no. 2, pp. 1142–1155, feb 2016. (Cited on page 70.)

[77] Q. Yan, W. Huang, and C. Moloney, "Neural Networks Based Sea Ice Detection and Concentration Retrieval From GNSS-R Delay-Doppler Maps," *IEEE Journal of Selected Topics in Applied Earth Observations and Remote Sensing*, vol. 10, no. 8, pp. 3789–3798, aug 2017. (Cited on page 70.)

[78] F. Wang, D. Yang, B. Zhang, and W. Li, "Waveform-based spaceborne GNSS-R wind speed observation: Demonstration and analysis using UK TechDemoSat-1

data," *Advances in Space Research*, vol. 61, no. 6, pp. 1573–1587, mar 2018. (Cited on page 70.)

[79] Y. Liu, I. Collett, and Y. J. Morton, "Application of Neural Network to GNSS-R Wind Speed Retrieval," *IEEE Transactions on Geoscience and Remote Sensing*, vol. 57, no. 12, pp. 9756–9766, dec 2019. (Cited on page 70.)

[80] J. Reynolds, M. P. Clarizia, and E. Santi, "Wind Speed Estimation From CYGNSS Using Artificial Neural Networks," *IEEE Journal of Selected Topics in Applied Earth Observations and Remote Sensing*, vol. 13, pp. 708–716, 2020. (Cited on page 70.)

[81] E. Valencia, A. Camps, J. F. Marchan-Hernandez, H. Park, X. Bosch-Lluis, N. Rodriguez-Alvarez, and I. Ramos-Perez, "Ocean surface's scattering coefficient retrieval by delay-Doppler map inversion," *IEEE Geoscience and Remote Sensing Letters*, vol. 8, no. 4, pp. 750–754, jul 2011. (Cited on page 71.)

[82] C. Gommenginger, P. Thibaut, L. Fenoglio-Marc, G. Quartly, X. Deng, J. Gómez-Enri, P. Challenor, and Y. Gao, "Retracking Altimeter Waveforms Near the Coasts," in *Coastal Altimetry*. Berlin, Heidelberg: Springer Berlin Heidelberg, 2011, pp. 61–101. (Cited on pages 72 and 76.)

[83] R. Stosius, G. Beyerle, A. Helm, A. Hoechner, and J. Wickert, "Simulation of space-borne tsunami detection using GNSS-Reflectometry applied to tsunamis in the Indian Ocean," *Natural Hazards and Earth System Science*, vol. 10, no. 6, pp. 1359–1372, jun 2010. (Cited on page 73.)

[84] A. Egido and W. H. F. Smith, "Fully Focused SAR Altimetry: Theory and Applications," *IEEE Transactions on Geoscience and Remote Sensing*, vol. 55, no. 1, pp. 392–406, jan 2017. (Cited on page 75.)

[85] G. S. Brown, "The Average Impulse Response of a Rough Surface and Its Applications," *IEEE Journal of Oceanic Engineering*, vol. 2, no. 1, pp. 67–74, jan 1977. (Cited on pages 76 and 96.)

[86] H. Park, E. Valencia, A. Camps, A. Rius, S. Ribó, and M. Martín-Neira, "Delay tracking in spaceborne GNSS-R ocean altimetry," *IEEE Geoscience and Remote Sensing Letters*, vol. 10, no. 1, pp. 57–61, jan 2013. (Cited on pages 77, 106, and 186.)

[87] H. Park, D. Pascual, A. Camps, F. Martin, A. Alonso-Arroyo, and H. Carreno-Luengo, "Analysis of spaceborne GNSS-R delay-doppler tracking," *IEEE Journal of Selected Topics in Applied Earth Observations and Remote Sensing*, vol. 7, no. 5, pp. 1481–1492, may 2014. (Cited on pages 77 and 186.)

[88] J. Mashburn, A. O'Brien, P. Axelrad, C. Zuffada, S. Lowe, R. Shah, A. Voronovich, and V. Zavorotny, "A Comparison of Waveform Model Re-Tracking Methods Using Data from CYGNSS," in *International Geoscience and Remote Sensing Symposium (IGARSS)*. IEEE, jul 2018, pp. 4289–4292. (Cited on pages 77 and 186.)

[89] J. Park, J. T. Johnson, and S. T. Lowe, "A study of the electromagnetic bias for GNSS-R ocean altimetry using the choppy wave model," *Waves in Random and Complex Media*, vol. 26, no. 4, pp. 599–612, oct 2016. (Cited on pages 77 and 78.)

[90] A. Ghavidel, D. Schiavulli, and A. Camps, "Numerical Computation of the Electromagnetic Bias in GNSS-R Altimetry," *IEEE Transactions on Geoscience and Remote Sensing*, vol. 54, no. 1, pp. 489–498, jan 2016. (Cited on pages 78 and 266.)

[91] A. Ghavidel and A. Camps, "Impact of Rain, Swell, and Surface Currents on the Electromagnetic Bias in GNSS-Reflectometry," *IEEE Journal of Selected Topics in Applied Earth Observations and Remote Sensing*, vol. 9, no. 10, pp. 4643–4649, oct 2016. (Cited on pages 78 and 266.)

[92] O. Nogués, A. Sumpsi, A. Camps, and A. Rius, "A 3 GPS-Channels Doppler-Delay Receiver for Remote Sensing Applications," in *International Geoscience and Remote Sensing Symposium (IGARSS)*, vol. 7. IEEE, 2003, pp. 4483–4485. (Cited on pages 78 and 80.)

[93] O. Nogués-Correig, E. C. Galí, J. S. Campderrós, and A. Rius, "A GPS-reflections receiver that computes doppler/delay maps in real time," *IEEE Transactions on Geoscience and Remote Sensing*, vol. 45, no. 1, pp. 156–174, jan 2007. (Cited on pages 78 and 81.)

[94] A. Alonso, A. Camps, D. Pascual, H. Park, A. Alcayde, S. Chavero, P. Martinez, L. Crespo, M. Angulo, and A. Rius, "PAU instrument aboard INTA MicroSat-1: Flight model tests," in *International Geoscience and Remote Sensing Symposium (IGARSS)*. IEEE, jul 2012, pp. 1038–1041. (Cited on pages 78 and 81.)

[95] E. Valencia, A. Camps, J. F. Marchan-Hernandez, X. Bosch-Lluis, N. Rodriguez-Alvarez, and I. Ramos-Perez, "Advanced architectures for real-time Delay-Doppler Map GNSS-reflectometers: The GPS reflectometer instrument for PAU (griPAU)," *Advances in Space Research*, vol. 46, no. 2, pp. 196–207, 2010. (Cited on pages 78, 81, 167, and 192.)

[96] M. Unwin, P. Jales, J. Tye, C. Gommenginger, G. Foti, and J. Rosello, "Spaceborne GNSS-Reflectometry on TechDemoSat-1: Early Mission Operations and

Exploitation," *IEEE Journal of Selected Topics in Applied Earth Observations and Remote Sensing*, vol. 9, no. 10, pp. 4525–4539, oct 2016. (Cited on pages 78 and 79.)

[97] A. Camps, J. F. Marchan-Hernandez, X. Bosch-Lluis, N. Rodriguez-Alvarez, I. Ramos-Perez, E. Valencia, J. M. Tarongi, H. Park, H. Carreno-Luengo, A. Alonso-Arroyo, D. Pascual, R. Onrubia, G. Forte, and J. Querol, "Review of GNSS-R instruments and tools developed at the Universitat Politecnica de Catalunya-Barcelona tech," in *International Geoscience and Remote Sensing Symposium (IGARSS)*. IEEE, 2014, pp. 3826–3829. (Cited on page 79.)

[98] M. Unwin, S. Gleason, and M. Brennan, "The Space GPS Reflectometry Experiment on the UK Disaster Monitoring Constellation Satellite," in *Proceedings of ION GPS/GNSS*, no. September, 2003, p. 2656. (Cited on pages 79 and 80.)

[99] M. Unwin, P. Jales, P. Blunt, S. Duncan, M. Brummitt, and C. Ruf, "The SGR-ReSI and its application for GNSS reflectometry on the NASA EV-2 CYGNSS mission," in *Aerospace Conference*. IEEE, mar 2013, pp. 1–6. (Cited on pages 79 and 82.)

[100] C. S. Ruf, S. Gleason, Z. Jelenak, S. Katzberg, A. Ridley, R. Rose, J. Scherrer, and V. Zavorotny, "The CYGNSS nanosatellite constellation hurricane mission," in *International Geoscience and Remote Sensing Symposium (IGARSS)*. IEEE, jul 2012, pp. 214–216. (Cited on pages 79 and 82.)

[101] J. L. Garrison, S. J. Katzberg, and C. T. Howell, "Detection of ocean reflected GPS signals: theory and experiment," in *SoutheastCon*. IEEE, 1997, pp. 290–294. (Cited on page 80.)

[102] S. T. Lowe, C. Zuffada, J. L. LaBrecque, M. Lough, J. Lerma, and L. E. Young, "Ocean-altimetry measurement using reflected GPS signals observed from a low-altitude aircraft," in *International Geoscience and Remote Sensing Symposium (IGARSS)*. IEEE, 2000, pp. 2185–2187. (Cited on page 80.)

[103] S. Lowe, P. Kroger, G. Franklin, J. LaBrecque, J. Lerma, M. Lough, M. Marcin, R. Muellerschoen, D. Spitzmesser, and L. Young, "A delay/Doppler-mapping receiver system for GPS-reflection remote sensing," *IEEE Transactions on Geoscience and Remote Sensing*, vol. 40, no. 5, pp. 1150–1163, may 2002. (Cited on page 80.)

[104] S. T. Lowe, C. Zuffada, Y. Chao, P. Kroger, L. E. Young, and J. L. LaBrecque, "5-cm-Precision aircraft ocean altimetry using GPS reflections," *Geophysical Research Letters*, vol. 29, no. 10, pp. 1–4, may 2002. (Cited on page 80.)

[105] S. T. Lowe, T. Meehan, and L. Young, "Direct Signal Enhanced Semicodeless Processing of GNSS Surface-Reflected Signals," *IEEE Journal of Selected Topics in Applied Earth Observations and Remote Sensing*, vol. 7, no. 5, pp. 1469–1472, may 2014. (Cited on page 80.)

[106] R. N. Treuhaft, S. T. Lowe, C. Zuffada, and Y. Chao, "2-cm GPS altimetry over Crater lake," *Geophysical Research Letters*, vol. 28, no. 23, pp. 4343–4346, 2001. (Cited on page 80.)

[107] J. Mashburn, P. Axelrad, S. T. Lowe, and K. M. Larson, "An Assessment of the Precision and Accuracy of Altimetry Retrievals for a Monterey Bay GNSS-R Experiment," *IEEE Journal of Selected Topics in Applied Earth Observations and Remote Sensing*, vol. 9, no. 10, pp. 4660–4668, oct 2016. (Cited on page 80.)

[108] M. Martin-Neira, M. Caparrini, J. Font-Rossello, S. Lannelongue, C. C. S. Vallmitjana, M. Martm-Neira, M. Caparrini, J. Font-Rossello, S. Lannelongue, and C. C. S. Vallmitjana, "The PARIS concept: an experimental demonstration of sea surface altimetry using GPS reflected signals," *IEEE Transactions on Geoscience and Remote Sensing*, vol. 39, no. 1, pp. 142–150, 2001. (Cited on page 80.)

[109] M. Martin-Neira, P. Colmenarejo, G. Ruffini, and C. Serra, "Altimetry precision of 1 cm over a pond using the wide-lane carrier phase of GPS reflected signals," *Canadian Journal of Remote Sensing*, vol. 28, no. 3, pp. 394–403, jun 2002. (Cited on page 80.)

[110] F. Soulat, "Sea surface remote-sensing with GNSS and sunlight reflections," Ph.D. dissertation, Universitat Politècnica de Catalunya/Starlab, 2003. (Cited on page 80.)

[111] G. Ruffini, F. Soulat, M. Caparrini, O. Germain, and M. Martín-Neira, "The Eddy experiment: Accurate GNSS-R ocean altimetry from low altitude aircraft," *Geophysical Research Letters*, vol. 31, no. 12, p. L12306, 2004. (Cited on page 80.)

[112] S. Dunne, F. Soulat, M. Caparrini, O. Germain, E. Farres, X. Barroso, and G. Ruffini, "Oceanpal, a GPS-reflection coastal instrument to monitor tide and sea-state," in *Europe Oceans*. IEEE, 2005, pp. 1351–1356 Vol. 2. (Cited on page 80.)

[113] M. Caparrini, A. Egido, F. Soulat, O. Germain, E. Farrès, S. Dunne, and G. Ruffini, "Oceanpal: Monitoring sea state with a GNSS-R coastal instrument," in *International Geoscience and Remote Sensing Symposium (IGARSS)*. IEEE, 2007, pp. 5080–5083. (Cited on page 80.)

[114] A. Helm, G. Beyerle, and M. Nitschke, "Detection of coherent reflections with GPS bipath interferometry," *Canadian Journal of Remote Sensing*, jul 2004. (Cited on page 81.)

[115] O. Nogués-Correig, S. Ribó, J. C. Arco, E. Cardellach, A. Rius, E. Valencia, J. M. Tarongí, A. Camps, H. Van Der Marel, and M. Martín-Neira, "The proof of concept for 3-CM altimetry using the PARIS Interferometric Technique," in *International Geoscience and Remote Sensing Symposium (IGARSS)*. IEEE, jul 2010, pp. 3620–3623. (Cited on pages 81 and 82.)

[116] A. Rius, F. Fabra, S. Ribo, J. C. Arco, S. Oliveras, E. Cardellach, A. Camps, O. Nogues-Correig, J. Kainulainen, E. Rohue, and M. Martin-Neira, "PARIS Interferometric Technique proof of concept: Sea surface altimetry measurements," in *International Geoscience and Remote Sensing Symposium (IGARSS)*. IEEE, jul 2012, pp. 7067–7070. (Cited on pages 81 and 82.)

[117] F. Martín, A. Camps, H. Park, F. Fabra, A. Rius, M. Martin-Neira, S. D'Addio, W. Li, and D. Yang, "Typhoon observations using the interferometric GNSS-R technique," in *International Geoscience and Remote Sensing Symposium (IGARSS)*. IEEE, jul 2014, pp. 3790–3793. (Cited on page 81.)

[118] F. Martin, A. Camps, M. Martin-Neira, S. D'Addio, F. Fabra, A. Rius, and H. Park, "Significant wave height retrieval based on the effective number of incoherent averages," in *International Geoscience and Remote Sensing Symposium (IGARSS)*. IEEE, jul 2015, pp. 3634–3637. (Cited on pages 81 and 138.)

[119] E. Cardellach, F. Fabra, O. Nogués-Correig, S. Oliveras, S. Ribó, and A. Rius, "GNSS-R ground-based and airborne campaigns for ocean, land, ice, and snow techniques: Application to the GOLD-RTR data sets," *Radio Science*, vol. 46, no. 6, dec 2011. (Cited on page 81.)

[120] E. Cardellach, A. Rius, M. Martin-Neira, F. Fabra, O. Nogues-Correig, S. Ribo, J. Kainulainen, A. Camps, and S. D'Addio, "Consolidating the Precision of Interferometric GNSS-R Ocean Altimetry Using Airborne Experimental Data," *IEEE Transactions on Geoscience and Remote Sensing*, vol. 52, no. 8, pp. 4992–5004, aug 2014. (Cited on page 81.)

[121] F. Fabra, E. Cardellach, A. Rius, S. Ribó, S. Oliveras, O. Nogués-Correig, M. Belmonte Rivas, M. Semmling, and S. D'Addio, "Phase altimetry with dual polarization GNSS-R over sea ice," *IEEE Transactions on Geoscience and Remote Sensing*, vol. 50, no. 6, pp. 2112–2121, jun 2012. (Cited on page 81.)

[122] S. Ribó, J. C. Arco, E. Cardellach, O. Nogués-Correig, A. Rius, M. T. Álvarez, and J. Taberot, "ASAP, towards a PARIS instrument for space," in *International Geoscience and Remote Sensing Symposium (IGARSS)*. IEEE, 2007, pp. 2916–2919. (Cited on page 81.)

[123] A. Helm, O. Montenbruck, J. Ashjaee, S. Yudanov, G. Beyerle, R. Stosius, and M. Rothacher, "GORS - A GNSS occultation, reflectometry and scatterometry space receiver," in *Proceedings of ION GNSS*, vol. 2, sep 2007, pp. 2011–2021. (Cited on page 81.)

[124] A. M. Semmling, J. Wickert, S. Schön, R. Stosius, M. Markgraf, T. Gerber, M. Ge, and G. Beyerle, "A zeppelin experiment to study airborne altimetry using specular Global Navigation Satellite System reflections," *Radio Science*, vol. 48, no. 4, pp. 427–440, jul 2013. (Cited on page 81.)

[125] M. Semmling, G. Beyerle, J. Beckheinrich, M. Ge, and J. Wickert, "Airborne GNSS reflectometry using crossover reference points for carrier phase altimetry," in *International Geoscience and Remote Sensing Symposium (IGARSS)*. IEEE, jul 2014, pp. 3786–3789. (Cited on page 81.)

[126] A. M. Semmling, G. Beyerle, R. Stosius, G. Dick, J. Wickert, F. Fabra, E. Cardellach, S. Ribó, A. Rius, A. Helm, S. B. Yudanov, and S. D'Addio, "Detection of Arctic Ocean tides using interferometric GNSS-R signals," *Geophysical Research Letters*, vol. 38, no. 4, feb 2011. (Cited on page 81.)

[127] A. M. Semmling, T. Schmidt, J. Wickert, S. Schn, F. Fabra, E. Cardellach, and A. Rius, "On the retrieval of the specular reflection in GNSS carrier observations for ocean altimetry," *Radio Science*, vol. 47, no. 6, dec 2012. (Cited on page 81.)

[128] A. Camps, N. Rodriguez-Alvarez, X. Bosch-Lluis, J. F. Marchan, I. Ramos-Perez, M. Segarra, L. Sagues, D. Tarrago, O. Cunado, R. Vilaseca, A. Tomas, J. Mas, and J. Guillamon, "PAU in SeoSAT: A proposed hybrid L-band microwave radiometer/GPS reflectometer to improve Sea Surface Salinity estimates from space," in *Microwave Radiometry and Remote Sensing of the Environment (MicroRad)*. IEEE, 2008, pp. 1–4. (Cited on page 81.)

[129] J. F. Marchan-Hernandez, I. Ramos-Perez, X. Bosch-Lluis, A. Camps, N. Rodríguez-Álvarez, and D. Albiol, "PAU-GNSS/R, a real-time GPS-refleetometer for earth observation applications: Architecture insights and preliminary results," in *International Geoscience and Remote Sensing Symposium (IGARSS)*, 2007, pp. 5113–5116. (Cited on page 81.)

[130] A. Camps, J. F. Marchán, E. Valencia, I. Ramos, X. Bosch-Lluis, N. Rodriguez, H. Park, A. Alcayde, A. Mollfulleda, J. Galindo, P. Martínez, S. Chavero, M. Angulo, and A. Rius, "PAU instrument aboard INTA MicroSat-1: A GNSS-R demonstration mission for sea state correction in L-band radiometry," in *International Geoscience and Remote Sensing Symposium (IGARSS)*, 2011, pp. 4126–4129. (Cited on page 81.)

[131] A. Alonso-Arroyo, A. Camps, D. Pascual, H. Park, A. Alcayde, S. Chavero, P. Martinez, L. Crespo, M. Angulo, and A. Rius, "PAU Instrument aboard INTA MicroSAT-1: Initial results of the FM model from an airborne experiment," in *Workshop on Reflectometry Using GNSS and Other Signals of Opportunity (GNSS+R)*, oct 2012. (Cited on page 81.)

[132] E. Valencia, J. F. Marchan-Hernandez, A. Camps, N. Rodriguez-Alvarez, J. Miguel Tarongi, M. Piles, I. Ramos-Perez, X. Bosch-Lluis, M. Vall-llossera, and P. Ferré, "Experimental relationship between the sea brightness temperature changes and the GNSS-R delay-Doppler maps: Preliminary results of the albatross field experiments," in *International Geoscience and Remote Sensing Symposium (IGARSS)*. IEEE, jul 2009, pp. 741–744. (Cited on page 81.)

[133] E. Valencia, A. Camps, M. Vall-llossera, A. Monerris, X. Bosch-Lluis, N. Rodriguez-Alvarez, I. Ramos-Perez, J. F. Marchan-Hernandez, J. Martínez-Fernández, N. Sánchez-Martín, and C. Pérez-Gutiérrz, "GNSS-R Delay-Doppler Maps over land: Preliminary results of the GRAJO field experiment," in *International Geoscience and Remote Sensing Symposium (IGARSS)*. IEEE, jul 2010, pp. 3805–3808. (Cited on page 81.)

[134] A. Rius, O. Nogués-Correig, S. Ribó, E. Cardellach, S. Oliveras, E. Valencia, H. Park, J. M. Tarongí, A. Camps, H. van der Marel, R. van Bree, B. Altena, and M. Martín-Neira, "Altimetry with GNSS-R interferometry: First proof of concept experiment," *GPS Solutions*, vol. 16, no. 2, pp. 231–241, apr 2012. (Cited on pages 82 and 88.)

[135] K. Yu, C. Rizos, and A. G. Dempster, "Sea Surface Roughness Estimation Using Signals from Multiple GNSS Satellites," in *Proceedings of International Global Navigation Satellite Systems Society Symposium (IGNSS)*, nov 2011. (Cited on page 82.)

[136] ——, "GNSS-Based Model-Free Sea Surface Height Estimation in Unknown Sea State Scenarios," *IEEE Journal of Selected Topics in Applied Earth Observations and Remote Sensing*, vol. 7, no. 5, pp. 1424–1435, may 2014. (Cited on page 82.)

[137] K. Yu, C. Rizos, and A. Dempster, "Sea surface wind speed estimation based on GNSS signal measurements," in *International Geoscience and Remote Sensing Symposium (IGARSS)*. IEEE, jul 2012, pp. 2587–2590. (Cited on page 82.)

[138] H. Carreno-Luengo, A. Camps, I. Perez-Ramos, and A. Rius, "PYCARO's instrument proof of concept," in *Workshop on Reflectometry Using GNSS and Other Signals of Opportunity (GNSS+R)*, oct 2012. (Cited on page 82.)

[139] H. Carreno-Luengo, A. Camps, I. Ramos-Perez, and A. Rius, "Experimental Evaluation of GNSS-Reflectometry Altimetric Precision Using the P(Y) and C/A Signals," *IEEE Journal of Selected Topics in Applied Earth Observations and Remote Sensing*, vol. 7, no. 5, pp. 1493–1500, may 2014. (Cited on page 82.)

[140] H. Carreno-Luengo and A. Camps, "A GNSS-R experiment over wave channel surface," in *International Geoscience and Remote Sensing Symposium (IGARSS)*. IEEE, jul 2013, pp. 366–369. (Cited on page 82.)

[141] H. Carreno-Luengo, A. Camps, J. Querol, G. Forte, R. Onrubia, and R. Diez, "A stratospheric balloon GNSS-R experiment: The 3Cat-2 project in DLR/SNSB BEXUS," in *International Geoscience and Remote Sensing Symposium (IGARSS)*. IEEE, jul 2014, pp. 3626–3629. (Cited on page 82.)

[142] H. Carreno-Luengo, A. Amezaga, A. Bolet, D. Vidal, J. Jane, J. F. Munoz, R. Olive, and A. Camps, "Multi-constellation, dual-polarization, and dual-frequency GNSS-R stratospheric balloon experiment over boreal forests," in *International Geoscience and Remote Sensing Symposium (IGARSS)*. IEEE, jul 2015, pp. 5107–5110. (Cited on page 82.)

[143] H. Carreno-Luengo and A. Camps, "First Dual-Band Multiconstellation GNSS-R Scatterometry Experiment Over Boreal Forests From a Stratospheric Balloon," *IEEE Journal of Selected Topics in Applied Earth Observations and Remote Sensing*, vol. 9, no. 10, pp. 4743–4751, oct 2016. (Cited on page 82.)

[144] H. Carreno-Luengo, A. Camps, J. Querol, and G. Forte, "First Results of a GNSS-R Experiment From a Stratospheric Balloon Over Boreal Forests," *IEEE Transactions on Geoscience and Remote Sensing*, vol. 54, no. 5, pp. 2652–2663, may 2016. (Cited on page 82.)

[145] H. Carreno-Luengo, A. Camps, I. Perez-Ramos, G. Forte, R. Onrubia, and R. Diez, "3Cat-2: A P(Y) and C/A GNSS-R experimental nano-satellite mission," in *International Geoscience and Remote Sensing Symposium (IGARSS)*. IEEE, jul 2013, pp. 843–846. (Cited on page 82.)

[146] H. Carreno-Luengo, A. Amezaga, A. Bolet, D. Vidal, J. Jane, J. F. Munoz, R. Olive, A. Camps, J. Carola, N. Catarino, M. Hagenfeldt, P. Palomo, and S. Cornara, "3CAT-2: A 6U CubeSat-based multi-constellation, dual-polarization, and dual-frequency GNSS-R and GNSS-RO experimental mission," in *International Geoscience and Remote Sensing Symposium (IGARSS)*. IEEE, jul 2015, pp. 5115–5118. (Cited on page 82.)

[147] R. Olive, A. Amezaga, H. Carreno-Luengo, H. Park, and A. Camps, "Implementation of a GNSS-R Payload Based on Software-Defined Radio for the 3CAT-2 Mission," *IEEE Journal of Selected Topics in Applied Earth Observations and Remote Sensing*, vol. 9, no. 10, pp. 4824–4833, oct 2016. (Cited on page 82.)

[148] H. Carreno-Luengo, A. Camps, P. Via, J. F. Munoz, A. Cortiella, D. Vidal, J. Jane, N. Catarino, M. Hagenfeldt, P. Palomo, and S. Cornara, "3Cat-2 An Experimental Nanosatellite for GNSS-R Earth Observation: Mission Concept and Analysis," *IEEE Journal of Selected Topics in Applied Earth Observations and Remote Sensing*, vol. 9, no. 10, pp. 4540–4551, oct 2016. (Cited on page 82.)

[149] Y. Zhang, L. Tian, W. Meng, Q. Gu, Y. Han, and Z. Hong, "Feasibility of Code-Level Altimetry Using Coastal BeiDou Reflection (BeiDou-R) Setups," *IEEE Journal of Selected Topics in Applied Earth Observations and Remote Sensing*, vol. 8, no. 8, pp. 4130–4140, aug 2015. (Cited on page 82.)

[150] Z. Yun, L. Binbin, T. Luman, G. Qiming, H. Yanling, and H. Zhonghua, "Phase Altimetry Using Reflected Signals From BeiDou GEO Satellites," *IEEE Geoscience and Remote Sensing Letters*, vol. 13, no. 10, pp. 1410–1414, oct 2016. (Cited on page 82.)

[151] P. F. Silva, T. Peres, R. Castro, J. Carola, T. Mendes, R. Capote, J. Bandeiras, J. Silva, and N. Catarino, "GNSS-Reflectometry Observables with Galileo E5 Signals," 2015. (Cited on page 82.)

[152] D. Pascual, H. Park, A. Camps, A. Alonso, and R. Onrubia, "Comparison of GPS L1 and Galileo E1 signals for GNSS-R ocean altimetry," in *International Geoscience and Remote Sensing Symposium (IGARSS)*. IEEE, jul 2013, pp. 358–361. (Cited on pages 85 and 95.)

[153] D. Pascual, H. Park, A. Camps, A. A. Arroyo, and R. Onrubia, "Simulation and analysis of GNSS-R composite waveforms using GPS and galileo signals," *IEEE Journal of Selected Topics in Applied Earth Observations and Remote Sensing*, vol. 7, no. 5, pp. 1461–1468, may 2014. (Cited on page 85.)

[154] H. Park, A. Camps, D. Pascual, A. Alonso, F. Martin, and H. Carreno-Luengo, "Improvement of the PAU/PARIS End-to-end Performance Simulator (P2EPS) in preparation for upcoming GNSS-R missions," in *International Geoscience and Remote Sensing Symposium (IGARSS)*. IEEE, jul 2013, pp. 362–365. (Cited on pages 85, 88, 98, 106, and 108.)

[155] H. Park, A. Camps, D. Pascual, R. Onrubia, A. Alonso-Arroyo, and F. Martin, "Evolution of PAU/PARIS End-to-end Performance Simulator (P2EPS) towards GNSS reflectometry, radio occulation and Scatterometry simulator (GEROS-SIM)," in *International Geoscience and Remote Sensing Symposium (IGARSS)*. IEEE, jul 2015, pp. 4757–4760. (Cited on page 85.)

[156] H. Park, A. Camps, D. Pascual, A. Alonso-Arroyo, J. Querol, and R. Onrubia, "Improvement of PAU/PARIS end-to-end performance simulator (P2EPS): Land scattering including topography," in *International Geoscience and Remote Sensing Symposium (IGARSS)*. IEEE, jul 2016, pp. 5607–5610. (Cited on page 85.)

[157] D. Pascual, "GNSS-Matlab," *Remote Sening Code Library (RSCL)*, 2017. (Cited on pages 85 and 245.)

[158] J. Ó. Winkel, "Modeling and Simulating GNSS Signal Structures and Receivers," Ph.D. dissertation, University FAF Munich, Neubiberg, Germany, 2000. (Cited on pages 86 and 302.)

[159] E. S. Lohan, A. Lakhzouri, and M. Renfors, "Complex double-binary-offset-carrier modulation for a unitary characterisation of Galileo and GPS signals," *IEE Proceedings: Radar, Sonar and Navigation*, vol. 153, no. 5, pp. 403–408, 2006. (Cited on page 86.)

[160] A. B. Carlson, *Communication systems*, 2nd ed. New York, NY: McGraw-Hill, 2005. (Cited on pages 88, 89, 96, and 303.)

[161] S. Ribo, J. C. Arco, S. Oliveras, E. Cardellach, A. Rius, and C. Buck, "Experimental results of an x-band PARIS receiver using digital satellite TV opportunity signals scattered on the sea surface," *IEEE Transactions on Geoscience and Remote Sensing*, vol. 52, no. 9, pp. 5704–5711, sep 2014. (Cited on page 88.)

[162] D. Pascual, A. Camps, F. Martin, H. Park, A. A. Arroyo, and R. Onrubia, "Precision bounds in GNSS-R ocean altimetry," *IEEE Journal of Selected Topics in Applied Earth Observations and Remote Sensing*, vol. 7, no. 5, pp. 1416–1423, may 2014. (Cited on page 95.)

[163] J. P. Dumont, "Estimation optimale des paramètres altimétriques des signaux radar POSEIDON," Ph.D. dissertation, Institut National Polytechnique de Toulouse, Toulouse, France, 1985. (Cited on page 96.)

[164] E. Rodríguez, "Altimetry for non-Gaussian oceans: Height biases and estimation of parameters," *Journal of Geophysical Research*, vol. 93, no. 11, nov 1988. (Cited on page 96.)

[165] D. T. Sandwell and W. H. Smith, "Retracking ERS-1 altimeter waveforms for optimal gravity field recovery," *Geophysical Journal International*, vol. 163, no. 1, pp. 79–89, oct 2005. (Cited on page 96.)

[166] C. Mailhes, J. Y. Tourneret, J. Severini, and P. Thibaut, "Cramér-Rao bounds for radar altimeter waveforms," in *European Signal Processing Conference*, Laussane, Switzerland, 2008, pp. 214–216. (Cited on page 96.)

[167] J. Severini, C. Mailhes, P. Thibaut, and J. Y. Tourneret, "Bayesian estimation of altimeter echo parameters," in *International Geoscience and Remote Sensing Symposium (IGARSS)*, vol. 3, no. 1. IEEE, 2008, pp. 238–241. (Cited on page 96.)

[168] A. Ollivier, "Nouvelle approche pour l'extraction de paramètres géophysiques des mesures en altimétrie radar," Ph.D. dissertation, Institut National Polytechnique de Grenoble, Grenoble, France, 2006. (Cited on page 96.)

[169] J. Severini, "Estimation et Classification des Signaux Altimétriques," Ph.D. dissertation, Institut National Polytechnique de Toulouse, Toulouse, France, 2010. [Online]. Available: https://tel.archives-ouvertes.fr/tel-00526100 (Cited on page 96.)

[170] S. T. Lowe, J. L. LaBrecque, C. Zuffada, L. J. Romans, L. E. Young, and G. A. Hajj, "First spaceborne observation of an Earth-reflected GPS signal," *Radio Science*, vol. 37, no. 1, pp. 1–28, jan 2002. (Cited on page 96.)

[171] H. L. V. Trees, *Detection, Estimation and Modulation Theory. Part III: Radar-Sonar Signal Processing and Gaussian Signals in Noise.* New York, NY: Wiley, 1968. (Cited on pages 96, 97, 99, 100, 143, and 151.)

[172] O. Germain and G. Ruffini, "A revisit to the GNSS-R code range precision," in *Workshop on Reflectometry Using GNSS and Other Signals of Opportunity (GNSS+R)*, 2006. (Cited on page 96.)

[173] S. D'Addio, F. Martin, H. Park, A. Camps, and M. Martin-Neira, "Height precision prediction of the PARIS in orbit demonstrator based on Cramer-Rao bound analysis," in *International Geoscience and Remote Sensing Symposium (IGARSS)*. IEEE, jul 2012, pp. 7063–7066. (Cited on page 96.)

[174] M. I. Skolnik, *Radar Handbook*. NY: McGraw-Hill, 1970. (Cited on pages 96 and 143.)

[175] H. Park, A. Camps, and E. Valencia, "Impact of Doppler frequency compensation errors on spaceborne GNSS-R altimetry," in *International Geoscience and Remote Sensing Symposium (IGARSS)*. IEEE, jul 2012, pp. 2661–2664. (Cited on page 98.)

[176] X. Bosch-Lluis, I. Ramos-Perez, A. Camps, N. Rodriguez-Alvarez, E. Valencia, and H. Park, "A general analysis of the impact of digitization in microwave correlation radiometers," *Sensors*, vol. 11, no. 6, pp. 6066–6087, jun 2011. (Cited on pages 100 and 127.)

[177] B. Sadler and R. Kozick, "A Survey of Time Delay Estimation Performance Bounds," in *Workshop on Sensor Array and Multichannel Processing*. IEEE, 2006, pp. 282–288. (Cited on pages 101 and 150.)

[178] D. Pascual, H. Park, A. Camps, A. Alonso-Arroyo, R. Onrubia, and J. Querol, "Cross-talk Statistics of Interferometric GNSS-R," in *Workshop on Reflectometry Using GNSS and Other Signals of Opportunity (GNSS+R)*, 2015. (Cited on page 105.)

[179] D. Pascual, H. Park, R. Onrubia, A. A. Arroyo, J. Querol, and A. Camps, "Crosstalk Statistics and Impact in Interferometric GNSS-R," *IEEE Journal of Selected Topics in Applied Earth Observations and Remote Sensing*, vol. 9, no. 10, pp. 4621–4630, oct 2016. (Cited on pages 105 and 106.)

[180] "Systems Tool Kit 10." [Online]. Available: http://www.agi.com/products/stk/ (Cited on pages 106 and 186.)

[181] A. Ishimaru, *Wave propagation and scattering in random media*. Academic Press. (Cited on page 124.)

[182] F. G. Bass and I. M. Fuks, *Wave Scattering from Statistically Rough Surfaces*. Pergamon, 1979. (Cited on page 124.)

[183] T. Elfouhaily, D. Thompson, and L. Linstrom, "Delay-Doppler analysis of bistatically reflected signals from the ocean surface: theory and application," *IEEE Transactions on Geoscience and Remote Sensing*, vol. 40, no. 3, pp. 560–573, mar 2002. (Cited on page 124.)

[184] C. Zuffada and V. Zavorotny, "Coherence time and statistical properties of the GPS signal scattered off the ocean surface and their impact on the accuracy of remote sensing of sea surface topography and winds," in *International Geoscience and Remote Sensing Symposium (IGARSS)*. IEEE, 2001, pp. 3332–3334. (Cited on page 124.)

[185] A. Alonso-Arroyo, J. Querol, C. Lopez-Martinez, V. Zavorotny, H. Park, D. Pascual, R. Onrubia, and A. Camps, "SNR and Standard Deviation of cGNSS-R and iGNSS-R Scatterometric Measurements," *Sensors*, vol. 17, no. 12, p. 183, jan 2017. (Cited on pages 124, 126, and 143.)

[186] A. Papoulis, *Probability, Random Variables, and Stochastic Processes*. McGraw-Hill, 1965. (Cited on page 126.)

[187] S. Ribó, O. Nogués-Correig, and A. Rius, "One-bit digital cross-correlation in the PARIS-IOD," in *International Geoscience and Remote Sensing Symposium (IGARSS)*. IEEE, jul 2011, pp. 2069–2072. (Cited on page 127.)

[188] S. Lloyd, "Least squares quantization in PCM," *IEEE Transactions on Information Theory*, vol. 28, no. 2, pp. 129–137, mar 1982. (Cited on page 129.)

[189] J. P. Imhof, "Computing the Distribution of Quadratic Forms in Normal Variables," *Biometrika*, vol. 48, no. 3, p. 419, dec 1961. (Cited on pages 136 and 137.)

[190] Jeremiah Hu and N. Beaulieu, "Accurate closed-form approximations to Ricean sum distributions and densities," *IEEE Communications Letters*, vol. 9, no. 2, pp. 133–135, feb 2005. (Cited on pages 137 and 308.)

[191] J. Lopez-Salcedo, "Simple Closed-Form Approximation to Ricean Sum Distributions," *IEEE Signal Processing Letters*, vol. 16, no. 3, pp. 153–155, mar 2009. (Cited on pages 137 and 308.)

[192] J. Hu and N. C. Beaulieu, "Accurate simple closed-form approximations to Rayleigh sum distributions and densities," *IEEE Communications Letters*, vol. 9, no. 2, pp. 109–111, feb 2005. (Cited on pages 137 and 309.)

[193] J. C. S. Santos Filho and M. D. Yacoub, "Highly accurate η - μ approximation to the sum of M independent nonidentical Hoyt variates," *IEEE Antennas and Wireless Propagation Letters*, vol. 4, no. 1, pp. 436–438, 2005. (Cited on pages 137, 140, and 308.)

[194] S. Lowe, "Voltage Signal-to-Noise Ratio (SNR) Nonlinearity Resulting From Incoherent Summations," Tech. Rep., 1999. (Cited on pages 137 and 150.)

[195] A. Camps, H. Park, E. Valencia i Domènech, D. Pascual, F. Martin, A. Rius, S. Ribo, J. Benito, A. Andrés-Beivide, P. Saameno, G. Staton, M. Martin-Neira, S. Daddio, and P. Willemsen, "Optimization and performance analysis of interferometric GNSS-R altimeters: Application to the PARIS IoD mission," *IEEE Journal of Selected Topics in Applied Earth Observations and Remote Sensing*, vol. 7, no. 5, pp. 1436–1451, may 2014. (Cited on pages 138 and 152.)

[196] H. J. Hilhorst, "Central limit theorems for correlated variables: some critical remarks," *Brazilian Journal of Physics*, vol. 39, no. 2a, aug 2009. (Cited on page 138.)

[197] C. Strassle, D. Megnet, H. Mathis, and C. Burgi, "The Squaring-Loss Paradox," in *Proceedings of the 20th International Technical Meeting of the Satellite Division of The Institute of Navigation (ION GNSS 2007)*, 2007, pp. 2715–2722. (Cited on pages 150 and 151.)

[198] D. Pascual, R. Onrubia, A. Alonso-Arroyo, H. Park, and A. Camps, "The microwave interferometric reflectometer. Part II: Back-end and processor descriptions," in *International Geoscience and Remote Sensing Symposium (IGARSS)*. IEEE, jul 2014, pp. 3782–3785. (Cited on pages 153 and 199.)

[199] O. Cervelló, D. Pascual, R. Onrubia, and A. Camps, "Advanced GNSS-R signals processing with GPUs," in *Workshop on Reflectometry Using GNSS and Other Signals of Opportunity (GNSS+R)*. IEEE, 2019. (Cited on page 153.)

[200] ——, "Advanced GNSS-R Signals Processing With GPUs," *IEEE Journal of Selected Topics in Applied Earth Observations and Remote Sensing*, vol. 13, pp. 1158–1163, 2020. (Cited on page 153.)

[201] O. Cervelló, "Advanced GNSS-R signals procesing with GPUs," B.Sc. Thesis, Universitat Pompeu Fabra, 2019. (Cited on pages 153, 181, 182, 183, and 184.)

[202] D. M. Akos and M. Pini, "Effect of Sampling Frequency on GNSS Receiver Performance," *Navigation*, vol. 53, no. 2, pp. 85–95, jun 2006. (Cited on page 159.)

[203] "Labsat webpage." [Online]. Available: https://www.labsat.co.uk/ (Cited on page 159.)

[204] J. Leclere, C. Botteron, and P.-A. Farine, "Comparison Framework of FPGA-Based GNSS Signals Acquisition Architectures," *IEEE Transactions on Aerospace and Electronic Systems*, vol. 49, no. 3, pp. 1497–1518, jul 2013. (Cited on page 165.)

[205] N. C. and A. G., "Baseband Hardware Designs in Modernised GNSS Receivers," in *Global Navigation Satellite Systems: Signal, Theory and Applications*, S. Jin, Ed. InTech, feb 2012. (Cited on page 165.)

[206] K. Sun, "Signal Acquisition and Tracking Loop Design for GNSS Receivers," in *Geodetic Sciences - Observations, Modeling and Applications*. InTech, may 2013. (Cited on pages 165 and 185.)

[207] D. Proakis, J.G.; Manolakis, *Digital Signal Processing*. Prentice-Hall, 1983. (Cited on page 171.)

[208] A. V. Oppenheim and R. W. Schafer, *Discrete-Time Signal Processing.* Prentice-Hall, 1989. (Cited on pages 171 and 193.)

[209] "FFTW Webpage." [Online]. Available: http://www.fftw.org/ (Cited on page 177.)

[210] "cuFFT CUDA Toolkit Documentation." [Online]. Available: https://docs.nvidia.com/cuda/archive/10.0/cufft/index.html (Cited on page 177.)

[211] C. Casas, "Design and Implementation of a Calibration Network for Antenna Arrays of a GNSS Signal Reflectometer," M.Sc. Thesis, Universitat Politècnica de Catalunya, 2015. (Cited on page 199.)

[212] L. Garrucho, "Attitude Determination System for a Phased Array Beamformer," Ph.D. dissertation, Escola Tècnica d'Enginyeria de Telecomunicació de Barcelona, Universitat Politècnica de Catalunya, 2015. [Online]. Available: https://upcommons.upc.edu/handle/2099.1/25264 (Cited on page 199.)

[213] R. Onrubia, D. Pascual, A. Camps, A. Alonso-Arroy, and H. Park, "MIR: The microwave interferometric reflectometer, a new airborne sensor for GNSS-R advanced research," in *International Geoscience and Remote Sensing Symposium (IGARSS).* IEEE, jul 2013, pp. 109–112. (Cited on pages 199 and 205.)

[214] R. Onrubia, D. Pascual, A. Camps, A. Alonso-Arroyo, and H. Park, "MIR: the Microwave Interferometric Reflectometer, a New Airborne Sensor to Experiment Different GNSS-R Techniques," in *URSI Com. F Microwave Signatures*, 2013. (Cited on page 199.)

[215] ——, "The Microwave Interferometric Reflectometer. Part I: Front-end and beamforming description," in *International Geoscience and Remote Sensing Symposium (IGARSS).* IEEE, jul 2014, pp. 4046–4049. (Cited on pages 199 and 205.)

[216] R. Onrubia, L. Garrucho, D. Pascual, H. Park, J. Querol, A. Alonso-Arroyo, and A. Camps, "Advances in the MIR instrument: Integration, control subsystem and analysis of the flight dynamics for beamsteering purposes," in *International Geoscience and Remote Sensing Symposium (IGARSS).* IEEE, jul 2015, pp. 4765–4768. (Cited on pages 199 and 205.)

[217] D. Pascual, R. Onrubia, J. Querol, A. Alonso-Arroyo, H. Park, and A. Camps, "First Delay Doppler Maps obtained with the Microwave Inteferometric Reflectometer (MIR)," in *International Geoscience and Remote Sensing Symposium (IGARSS).* IEEE, jul 2016, pp. 1993–1996. (Cited on page 199.)

[218] D. Pascual, R. Onrubia, J. Querol, H. Park, and A. Camps, "Calibration of GNSS-R receivers with PRN signal injection: Methodology and validation with the microwave interferometric reflectometer (MIR)," in *International Geoscience and Remote Sensing Symposium (IGARSS)*, 2017, pp. 5022–5025. (Cited on page 199.)

[219] R. Onrubia, D. Pascual, J. Querol, H. Park, and A. Camps, "Beamformer characterization of the MIR instrument: The microwave interferometric reflectometer," in *International Geoscience and Remote Sensing Symposium (IGARSS)*, 2017, pp. 5026–5029. (Cited on page 199.)

[220] ——, "The Global Navigation Satellite Systems Reflectometry (GNSS-R) Microwave Interferometric Reflectometer: Hardware, Calibration, and Validation Experiments," *Sensors*, vol. 19, no. 5, p. 1019, feb 2019. (Cited on pages 199, 205, and 206.)

[221] J. Castellvi-Esturi, A. Camps, J. Corbera, R. Onrubia, R. Alamús, D. Pascual, J. Querol, and H. Park, "3 CAT-3/MOTS, an experimental nanosatellite for multispectral and GNSS-R earth observation: Airborne optical and GNSS-R campaign," in *International Geoscience and Remote Sensing Symposium (IGARSS)*. IEEE, jul 2018, pp. 1414–1417. (Cited on pages 202 and 243.)

[222] R. Onrubia, D. Pascual, J. Querol, J. Castellvi-Esturi, J. Corbera, H. Park, and A. Camps, "Preliminary altimetry results of the MALYGNSS instrument in the HUMIT project," in *International Geoscience and Remote Sensing Symposium (IGARSS)*. IEEE, jul 2018, pp. 3331–3334. (Cited on pages 203, 244, and 245.)

[223] R. Onrubia and A. Camps, "Antena Multibanda Tipo Parche con Sistema de Alimentación Cruzada." (Cited on page 206.)

[224] "Anechoic chamber of the Antenna Lab. of UPC." [Online]. Available: https://www.tsc.upc.edu/en/facilities/anechoic-chamber (Cited on page 206.)

[225] I. Pérez, X. Bosch-Lluis, A. Camps, N. Alvarez, J. F. Hernandez, E. Domènech, C. Vernich, S. De la Rosa, and S. Pantoja, "Calibration of Correlation Radiometers Using Pseudo-Random Noise Signals," *Sensors*, vol. 9, no. 8, pp. 6131–6149, 2009. (Cited on pages 221 and 231.)

[226] Rohde & Schwarz, "R&S SMU200A Vector Signal Generator." [Online]. Available: https://www.rohde-schwarz.com/vn/product/smu200a (Cited on page 238.)

[227] D. Pascual, R. Onrubia, J. Querol, J. Castellvi-Esturi, H. Park, and A. Camps, "Determination of sea correlation time at L-band with airborne reflected new GNSS

signals," in *International Geoscience and Remote Sensing Symposium (IGARSS)*. IEEE, jul 2018, pp. 3185–3188. (Cited on pages 241, 249, and 258.)

[228] J. Querol, R. Onrubia, D. Pascual, J. Castellvi-Esturi, H. Park, and A. Camps, "RFI analysis and mitigation in airborne GNSS-R campaign," in *International Geoscience and Remote Sensing Symposium (IGARSS)*. IEEE, jul 2018, pp. 1237–1240. (Cited on page 244.)

[229] R. Onrubia, D. Pascual, J. Querol, H. Park, A. Camps, C. Rüdiger, and J. P. Walker, "Preliminary end-to-end results of the MIR instrument: The microwave interferometric reflectometer," in *International Geoscience and Remote Sensing Symposium (IGARSS)*. IEEE, jul 2018, pp. 2027–2030. (Cited on page 259.)

[230] R. Onrubia, D. Pascual, H. Park, A. Camps, C. Rüdiger, J. Walker, and A. Monerris, "Satellite Cross-Talk Impact Analysis in Airborne Interferometric Global Navigation Satellite System-Reflectometry with the Microwave Interferometric Reflectometer," *Remote Sensing*, vol. 11, no. 9, p. 1120, may 2019. (Cited on pages 259, 284, and 285.)

[231] "Oznet Webpage." [Online]. Available: http://www.oznet.org.au/ (Cited on pages 260 and 275.)

[232] "Jon Johanson article in Wikipedia." [Online]. Available: https://en.wikipedia.org/wiki/Jon_Johanson (Cited on page 261.)

[233] "Google Maps Downloader." [Online]. Available: http://www.allmapsoft.com/gmd/index.html (Cited on page 272.)

[234] T. Grelier, J. Dantepal, A. Delatour, A. Ghion, and L. Ries, "Initial observations and analysis of compass MEO satellite signals," *Inside GNSS*, vol. 2, no. 4, pp. 39–43, 2007. (Cited on page 299.)

[235] "Navipedia Webpage." [Online]. Available: https://gssc.esa.int/navipedia/index.php/Main_Page (Cited on page 299.)

[236] V. A. Aalo, G. P. Efthymoglou, and C. Chirasil, "On the envelope and phase distributions for correlated Gaussian quadratures," *IEEE Communications Letters*, vol. 11, no. 12, pp. 985–987, dec 2007. (Cited on pages 306, 307, and 309.)

[237] P. Beckmann, "Statistical distribution of the amplitude and phase of a multiply scattered field," *Journal of Research of the National Bureau of Standards*, vol. 66D, no. 3, p. 231, may 1962. (Cited on page 307.)

[238] B. Zhu, Z. Zeng, J. Cheng, and N. C. Beaulieu, "On the Distribution Function of the Generalized Beckmann Random Variable and Its Applications in Communications," *IEEE Transactions on Communications*, vol. 66, no. 5, pp. 2235–2250, may 2018. (Cited on page 307.)

[239] M. Yacoub, G. Fraidenraich, and J. Santos Filho, "Nakagami-m phase-envelope joint distribution," *Electronics Letters*, vol. 41, no. 5, p. 259, 2005. (Cited on page 309.)

[240] F. McNolty, "A Contour-Integral Derivation of the Non-Central Chi-Square Distribution," *The Annals of Mathematical Statistics*, vol. 33, no. 2, pp. 796–800, jun 1962. (Cited on page 311.)

List of Publications

Journal Articles

[JA1] **D. Pascual**, R. Onrubia, J. Querol, H. Park, and A. Camps, "Design Considerations for Real-time GNSS-R Back-end Receivers," *Remote Sensing*, (in progress).

[JA2] **D. Pascual**, J. Querol, H. Onrubia, Raul Park, and A. Camps, "Stochastic Properties and Metrics of Quantized GNSS-R Signals," *IEEE Transactions on Geoscience and Remote Sensing*, (in progress).

[JA3] O. Cervelló, **D. Pascual**, R. Onrubia, and A. Camps, "Advanced GNSS-R Signals Processing With GPUs," *IEEE Journal of Selected Topics in Applied Earth Observations and Remote Sensing*, vol. 13, pp. 1158–1163, 2020.

[JA4] J. F. Munoz-Martin, R. Onrubia, **D. Pascual**, H. Park, A. Camps, C. Rüdiger, J. Walker, and A. Monerris, "Untangling the Incoherent and Coherent Scattering Components in GNSS-R and Novel Applications," *Remote Sensing*, vol. 12, no. 7, p. 1208, apr 2020.

[JA5] A. Camps, A. Alonso-Arroyo, H. Park, R. Onrubia, **D. Pascual**, and J. Querol, "L-Band Vegetation Optical Depth Estimation Using Transmitted GNSS Signals: Application to GNSS-Reflectometry and Positioning," *Remote Sensing*, vol. 12, no. 15, p. 2352, jul 2020.

[JA6] R. Onrubia, **D. Pascual**, J. Querol, H. Park, and A. Camps, "The Global Navigation Satellite Systems Reflectometry (GNSS-R) Microwave Interferometric Reflectometer: Hardware, Calibration, and Validation Experiments," *Sensors*, vol. 19, no. 5, p. 1019, feb 2019.

[JA7] R. Onrubia, **D. Pascual**, H. Park, A. Camps, C. Rüdiger, J. Walker, and A. Monerris, "Satellite Cross-Talk Impact Analysis in Airborne

Interferometric Global Navigation Satellite System-Reflectometry with the Microwave Interferometric Reflectometer," *Remote Sensing*, vol. 11, no. 9, p. 1120, may 2019.

[JA8] D. Guan, H. Park, A. Camps, Y. Wang, R. Onrubia, J. Querol, and **D. Pascual**, "Wind direction signatures in GNSS-R observables from space," *Remote Sensing*, vol. 10, no. 2, p. 198, jan 2018.

[JA9] H. Park, A. Camps, **D. Pascual**, Y. Kang, R. Onrubia, J. Querol, and A. Alonso-Arroyo, "A Generic Level 1 Simulator for Spaceborne GNSS-R Missions and Application to GEROS-ISS Ocean Reflectometry," *IEEE Journal of Selected Topics in Applied Earth Observations and Remote Sensing*, vol. 10, no. 10, pp. 4645–4659, 2017.

[JA10] J. Querol, R. Onrubia, A. Alonso-Arroyo, **D. Pascual**, H. Park, and A. Camps, "Performance Assessment of Time-Frequency RFI Mitigation Techniques in Microwave Radiometry," *IEEE Journal of Selected Topics in Applied Earth Observations and Remote Sensing*, vol. 10, no. 7, pp. 3096–3106, 2017.

[JA11] A. Alonso-Arroyo, J. Querol, C. Lopez-Martinez, V. Zavorotny, H. Park, **D. Pascual**, R. Onrubia, and A. Camps, "SNR and Standard Deviation of cGNSS-R and iGNSS-R Scatterometric Measurements," *Sensors*, vol. 17, no. 12, p. 183, jan 2017.

[JA12] **D. Pascual**, H. Park, R. Onrubia, A. A. Arroyo, J. Querol, and A. Camps, "Crosstalk Statistics and Impact in Interferometric GNSS-R," *IEEE Journal of Selected Topics in Applied Earth Observations and Remote Sensing*, vol. 9, no. 10, pp. 4621–4630, oct 2016.

[JA13] R. Onrubia, J. Querol, **D. Pascual**, A. Alonso-Arroyo, H. Park, and A. Camps, "DME/TACAN impact analysis on GNSS reflectometry," *IEEE Journal of Selected Topics in Applied Earth Observations and Remote Sensing*, vol. 9, no. 10, pp. 4611–4620, oct 2016.

[JA14] J. Querol, A. Alonso-Arroyo, R. Onrubia, **D. Pascual**, H. Park, and A. Camps, "SNR Degradation in GNSS-R Measurements under the Effects of Radio-Frequency Interference," *IEEE Journal of Selected Topics in Applied Earth Observations and Remote Sensing*, vol. 9, no. 10, pp. 4865–4878, oct 2016.

[JA15] A. Alonso-Arroyo, A. Camps, A. Monerris, C. Rüdiger, J. P. Walker, R. Onrubia, J. Querol, H. Park, and **D. Pascual**, "On the Correlation

between GNSS-R Reflectivity and L-Band Microwave Radiometry," *IEEE Journal of Selected Topics in Applied Earth Observations and Remote Sensing*, vol. 9, no. 12, pp. 5862–5879, dec 2016.

[JA16] A. Alonso-Arroyo, A. Camps, H. Park, **D. Pascual**, R. Onrubia, and F. Martín, "Retrieval of significant wave height and mean sea surface level using the GNSS-R interference pattern technique: Results from a three-month field campaign," *IEEE Transactions on Geoscience and Remote Sensing*, vol. 53, no. 6, pp. 3198–3209, jun 2015.

[JA17] **D. Pascual**, A. Camps, F. Martin, H. Park, A. A. Arroyo, and R. Onrubia, "Precision bounds in GNSS-R ocean altimetry," *IEEE Journal of Selected Topics in Applied Earth Observations and Remote Sensing*, vol. 7, no. 5, pp. 1416–1423, may 2014.

[JA18] **D. Pascual**, H. Park, A. Camps, A. A. Arroyo, and R. Onrubia, "Simulation and analysis of GNSS-R composite waveforms using GPS and galileo signals," *IEEE Journal of Selected Topics in Applied Earth Observations and Remote Sensing*, vol. 7, no. 5, pp. 1461–1468, may 2014.

[JA19] H. Park, **D. Pascual**, A. Camps, F. Martin, A. Alonso-Arroyo, and H. Carreno-Luengo, "Analysis of spaceborne GNSS-R delay-doppler tracking," *IEEE Journal of Selected Topics in Applied Earth Observations and Remote Sensing*, vol. 7, no. 5, pp. 1481–1492, may 2014.

[JA20] A. Camps, H. Park, E. Valencia i Domènech, **D. Pascual**, F. Martin, A. Rius, S. Ribo, J. Benito, A. Andrés-Beivide, P. Saameno, G. Staton, M. Martin-Neira, S. Daddio, and P. Willemsen, "Optimization and performance analysis of interferometric GNSS-R altimeters: Application to the PARIS IoD mission," *IEEE Journal of Selected Topics in Applied Earth Observations and Remote Sensing*, vol. 7, no. 5, pp. 1436–1451, may 2014.

[JA21] F. Martín, A. Camps, H. Park, S. D'Addio, M. Martín-Neira, and **D. Pascual**, "Cross-correlation waveform analysis for conventional and interferometric GNSS-R approaches," *IEEE Journal of Selected Topics in Applied Earth Observations and Remote Sensing*, vol. 7, no. 5, pp. 1560–1572, may 2014.

[JA22] A. Alonso-Arroyo, A. Camps, A. Aguasca, G. Forte, A. Monerris, C. Rüdiger, J. P. Walker, H. Park, **D. Pascual**, and R. Onrubia, "Improving the accuracy of soil moisture retrievals using the phase difference of the dual-polarization GNSS-R interference patterns," *IEEE Geoscience and Remote Sensing Letters*, vol. 11, no. 12, pp. 2090–2094, dec 2014.

[JA23] A. A. Arroyo, A. Camps, A. Aguasca, G. F. Forte, A. Monerris, C. Rüdiger, J. P. Walker, H. Park, **D. Pascual**, and R. Onrubia, "Dual-polarization GNSS-R interference pattern technique for soil moisture mapping," *IEEE Journal of Selected Topics in Applied Earth Observations and Remote Sensing*, vol. 7, no. 5, pp. 1533–1544, may 2014.

Conference Proceedings

[CP1] J. F. Munoz, R. Onrubia, **D. Pascual**, H. Park, A. Camps, C. Rüdiger, and J. Walker, "First experimental evidence of wind and swell signatures in L5 GPS and E5A Galileo GNSS-R waveforms," in *International Geoscience and Remote Sensing Symposium (IGARSS)*, 2020.

[CP2] J. F. Munoz, R. Onrubia, **D. Pascual**, H. Park, A. Camps, C. Rüdiger, J. Walker, and A. Monerris, "Untangling the GNSS-R coherent and incoherent components: experimental evidences over the ocean," *International Geoscience and Remote Sensing Symposium (IGARSS)*, 2020.

[CP3] **D. Pascual**, R. Onrubia, J. Querol, J. Castellvi-Esturi, H. Park, and A. Camps, "Determination of sea correlation time at L-band with airborne reflected new GNSS signals," in *International Geoscience and Remote Sensing Symposium (IGARSS)*. IEEE, jul 2018, pp. 3185–3188.

[CP4] R. Onrubia, **D. Pascual**, J. Querol, H. Park, A. Camps, C. Rüdiger, and J. P. Walker, "Preliminary end-to-end results of the MIR instrument: The microwave interferometric reflectometer," in *International Geoscience and Remote Sensing Symposium (IGARSS)*. IEEE, jul 2018, pp. 2027–2030.

[CP5] R. Onrubia, **D. Pascual**, J. Querol, J. Castellvi-Esturi, J. Corbera, H. Park, and A. Camps, "Preliminary altimetry results of the MALYGNSS instrument in the HUMIT project," in *International Geoscience and Remote Sensing Symposium (IGARSS)*. IEEE, jul 2018, pp. 3331–3334.

[CP6] H. Park, A. Camps, **D. Pascual**, J. Querol, and R. Onrubia, "Spaceborne GNSS-R end-to-end simulator: Topography and vegetation effects," in *International Geoscience and Remote Sensing Symposium (IGARSS)*. IEEE, jul 2018, pp. 3157–3160.

[CP7] J. Querol, R. Onrubia, **D. Pascual**, J. Castellvi-Esturi, H. Park, and A. Camps, "RFI analysis and mitigation in airborne GNSS-R campaign," in *International Geoscience and Remote Sensing Symposium (IGARSS)*. IEEE, jul 2018, pp. 1237–1240.

[CP8] J. Castellvi-Esturi, A. Camps, J. Corbera, R. Onrubia, R. Alamús, **D. Pascual**, J. Querol, and H. Park, "3 CAT-3/MOTS, an experimental nanosatellite for multispectral and GNSS-R earth observation: Airborne optical and GNSS-R campaign," in *International Geoscience and Remote Sensing Symposium (IGARSS)*. IEEE, jul 2018, pp. 1414–1417.

[CP9] **D. Pascual**, R. Onrubia, J. Querol, H. Park, and A. Camps, "Calibration of GNSS-R receivers with PRN signal injection: Methodology and validation with the microwave interferometric reflectometer (MIR)," in *International Geoscience and Remote Sensing Symposium (IGARSS)*, 2017, pp. 5022–5025.

[CP10] R. Onrubia, **D. Pascual**, J. Querol, H. Park, and A. Camps, "Beamformer characterization of the MIR instrument: The microwave interferometric reflectometer," in *International Geoscience and Remote Sensing Symposium (IGARSS)*, 2017, pp. 5026–5029.

[CP11] J. Querol, R. Onrubia, **D. Pascual**, H. Park, and A. Camps, "A radio-frequency interference detector for GNSS navigation and GNSS-reflectometry applications," in *International Geoscience and Remote Sensing Symposium (IGARSS)*, 2017, pp. 1266–1269.

[CP12] **D. Pascual**, R. Onrubia, J. Querol, A. Alonso-Arroyo, H. Park, and A. Camps, "First Delay Doppler Maps obtained with the Microwave Inteferometric Reflectometer (MIR)," in *International Geoscience and Remote Sensing Symposium (IGARSS)*. IEEE, jul 2016, pp. 1993–1996.

[CP13] H. Park, A. Camps, **D. Pascual**, A. Alonso-Arroyo, J. Querol, and R. Onrubia, "Improvement of PAU/PARIS end-to-end performance simulator (P2EPS): Land scattering including topography," in *International Geoscience and Remote Sensing Symposium (IGARSS)*. IEEE, jul 2016, pp. 5607–5610.

[CP14] J. Querol, R. Onrubia, **D. Pascual**, A. Alonso-Arroyo, H. Park, and A. Camps, "Comparison of real-time time-frequency RFI mitigation techniques in microwave radiometry," in *Microwave Radiometry and Remote Sensing of the Environment (MicroRad)*. IEEE, apr 2016, pp. 68–70.

[CP15] R. Onrubia, J. Querol, **D. Pascual**, H. Park, A. Alonso-Arroyo, and A. Camps, "Assessment of DME/TACAN RFI mitigation techniques in GNSS-R," in *International Geoscience and Remote Sensing Symposium (IGARSS)*. IEEE, jul 2016, pp. 4811–4814.

[CP16] A. Camps, H. Park, R. Onrubia, **D. Pascual**, J. Querol, A. Alonso-Arroyo, J. Benito, A. Andres-Beivide, S. Moreno, X. Ballesteros, M. Segarra, R. Vilaseca, A. Rius, and M. Martin-Neira, "Altimetric performance of the GEROS experiment at the ISS," in *International Geoscience and Remote Sensing Symposium (IGARSS)*. IEEE, jul 2016, pp. 5621–5624.

[CP17] H. Park, A. Camps, I. Sekulic, J. M. Rius, **D. Pascual**, A. Alonso-Arroyo, J. Querol, and R. Onrubia, "Impact of multi-path by ISS structure on GEROS-ISS measured waveforms," in *International Geoscience and Remote Sensing Symposium (IGARSS)*. IEEE, jul 2016, pp. 5603–5606.

[CP18] J. Querol, E. M. Julian, R. Onrubia, A. Alonso-Arroyo, **D. Pascual**, and A. Camps, "Preliminary results of FENIX: Front-End GNSS Interference eXcisor," in *2016 IEEE International Geoscience and Remote Sensing Symposium (IGARSS)*. IEEE, jul 2016, pp. 5627–5630.

[CP19] A. Alonso-Arroyo, J. Querol, A. Camps, R. Onrubia, H. Park, and **D. Pascual**, "Can we measure vegetation water content and vegetation opacity at L-band with a single GPS receiver?" in *International Geoscience and Remote Sensing Symposium (IGARSS)*. IEEE, jul 2016, pp. 1985–1988.

[CP20] A. Alonso-Arroyo, A. Camps, A. Monerris, C. Rüdiger, J. P. Walker, Y. Gao, J. Querol, H. Park, **D. Pascual**, and R. Onrubia, "On The Comparison Between Airborne L-Band Brightness Temperature And Gnss-Reflectivity: A Case Study In Australia," in *Microwave Radiometry and Remote Sensing of the Environment (MicroRad)*, 2016.

[CP21] H. Park, A. Camps, **D. Pascual**, R. Onrubia, A. Alonso-Arroyo, and F. Martin, "Evolution of PAU/PARIS End-to-end Performance Simulator (P2EPS) towards GNSS reflectometry, radio occulation and Scatterometry simulator (GEROS-SIM)," in *International Geoscience and Remote Sensing Symposium (IGARSS)*. IEEE, jul 2015, pp. 4757–4760.

[CP22] R. Onrubia, L. Garrucho, **D. Pascual**, H. Park, J. Querol, A. Alonso-Arroyo, and A. Camps, "Advances in the MIR instrument: Integration, control subsystem and analysis of the flight dynamics for beamsteering purposes," in *International Geoscience and Remote Sensing Symposium (IGARSS)*. IEEE, jul 2015, pp. 4765–4768.

[CP23] J. Querol, A. Alonso-Arroyo, R. Onrubia, **D. Pascual**, and A. Camps, "Assessment of back-end RFI mitigation techniques in passive remote sensing,"

in *International Geoscience and Remote Sensing Symposium (IGARSS)*. IEEE, jul 2015, pp. 4746–4749.

[CP24] A. Alonso-Arroyo, S. Torrecilla, J. Querol, A. Camps, **D. Pascual**, H. Park, and R. Onrubia, "Two dedicated soil moisture experiments using the scatterometric properties of GNSS-reflectometry," in *International Geoscience and Remote Sensing Symposium (IGARSS)*. IEEE, jul 2015, pp. 3921–3924.

[CP25] A. Alonso-Arroyo, A. Camps, N. Sanchez, M. Pablos, A. Gonzalez-Zamora, J. Martinez-Fernandez, M. Vall-Llosera, and **D. Pascual**, "An airborne GNSS-R field experiment over a vineyard for soil moisture estimation and monitoring," in *International Geoscience and Remote Sensing Symposium (IGARSS)*. IEEE, jul 2015, pp. 4761–4764.

[CP26] **D. Pascual**, R. Onrubia, A. Alonso-Arroyo, H. Park, and A. Camps, "The microwave interferometric reflectometer. Part II: Back-end and processor descriptions," in *International Geoscience and Remote Sensing Symposium (IGARSS)*. IEEE, jul 2014, pp. 3782–3785.

[CP27] R. Onrubia, **D. Pascual**, A. Camps, A. Alonso-Arroyo, and H. Park, "The Microwave Interferometric Reflectometer. Part I: Front-end and beamforming description," in *International Geoscience and Remote Sensing Symposium (IGARSS)*. IEEE, jul 2014, pp. 4046–4049.

[CP28] H. Park, A. Camps, **D. Pascual**, A. Alonso-Arroyo, F. Martin, H. Carreno-Luengo, and R. Onrubia, "Simulation study on tropicial cyclone tracking from the ISS using GNSS-R measurements," in *International Geoscience and Remote Sensing Symposium (IGARSS)*. IEEE, jul 2014, pp. 4062–4065.

[CP29] A. Alonso-Arroyo, A. Camps, A. Monerris, C. Rüdiger, J. P. Walker, G. Forte, **D. Pascual**, H. Park, and R. Onrubia, "The light airborne reflectometer for GNSS-R observations (LARGO) instrument: Initial results from airborne and Rover field campaigns," in *International Geoscience and Remote Sensing Symposium (IGARSS)*. IEEE, jul 2014, pp. 4054–4057.

[CP30] ——, "The dual polarization GNSS-R interference pattern technique," in *International Geoscience and Remote Sensing Symposium (IGARSS)*. IEEE, jul 2014, pp. 4058–4061.

[CP31] A. Camps, J. F. Marchan-Hernandez, X. Bosch-Lluis, N. Rodriguez-Alvarez, I. Ramos-Perez, E. Valencia, J. M. Tarongi, H. Park, H. Carreno-Luengo,

A. Alonso-Arroyo, **D. Pascual**, R. Onrubia, G. Forte, and J. Querol, "Review of GNSS-R instruments and tools developed at the Universitat Politecnica de Catalunya-Barcelona tech," in *International Geoscience and Remote Sensing Symposium (IGARSS)*. IEEE, 2014, pp. 3826–3829.

[CP32] **D. Pascual**, H. Park, A. Camps, A. Alonso, and R. Onrubia, "Comparison of GPS L1 and Galileo E1 signals for GNSS-R ocean altimetry," in *International Geoscience and Remote Sensing Symposium (IGARSS)*. IEEE, jul 2013, pp. 358–361.

[CP33] A. Camps, **D. Pascual**, H. Park, F. Martin, A. Rius, S. Ribo, J. Benito, A. Andres, P. Saameno, G. Staton, M. Martin-Neira, S. D'Addio, and P. Willemsen, "Altimetry performance and error budget of the PARIS in-orbit demonstration mission," in *International Geoscience and Remote Sensing Symposium (IGARSS)*. IEEE, jul 2013, pp. 370–373.

[CP34] R. Onrubia, **D. Pascual**, A. Camps, A. Alonso-Arroy, and H. Park, "MIR: The microwave interferometric reflectometer, a new airborne sensor for GNSS-R advanced research," in *International Geoscience and Remote Sensing Symposium (IGARSS)*. IEEE, jul 2013, pp. 109–112.

[CP35] H. Park, A. Camps, **D. Pascual**, A. Alonso, F. Martin, and H. Carreno-Luengo, "Improvement of the PAU/PARIS End-to-end Performance Simulator (P2EPS) in preparation for upcoming GNSS-R missions," in *International Geoscience and Remote Sensing Symposium (IGARSS)*. IEEE, jul 2013, pp. 362–365.

[CP36] A. Alonso-Arroyo, G. Forte, A. Camps, H. Park, **D. Pascual**, R. Onrubia, and R. Jove-Casulleras, "Soil moisture mapping using forward scattered GPS L1 signals," in *International Geoscience and Remote Sensing Symposium (IGARSS)*. IEEE, jul 2013, pp. 354–357.

[CP37] F. Martin Alemany, S. D'Addio, A. Camps, M. Martin-Neira, H. Park, and **D. Pascual**, "Comparison of GNSS-R processing techniques for spaceborne ocean altimetry," in *International Geoscience and Remote Sensing Symposium (IGARSS)*. IEEE, jul 2013, pp. 2939–2942.

[CP38] A. Alonso, A. Camps, **D. Pascual**, H. Park, A. Alcayde, S. Chavero, P. Martinez, L. Crespo, M. Angulo, and A. Rius, "PAU instrument aboard INTA MicroSat-1: Flight model tests," in *International Geoscience and Remote Sensing Symposium (IGARSS)*. IEEE, jul 2012, pp. 1038–1041.

Co-directed Bachelor Final Degree Projects

[DP1] C. Casas, "Design and Implementation of a Calibration Network for Antenna Arrays of a GNSS Signal Reflectometer," M.Sc. Thesis, Universitat Politècnica de Catalunya, 2015.

[DP2] O. Cervelló, "Advanced GNSS-R signals processsing with GPU," B.Sc. Thesis, Universitat Pompeu Fabra, 2019.

Workshops

[WS1] O. Cervelló, **D. Pascual**, R. Onrubia, and A. Camps, "Advanced GNSS-R signals processing with GPUs," in *Workshop on Reflectometry Using GNSS and Other Signals of Opportunity (GNSS+R)*, 2019.

[WS2] R. Onrubia, **D. Pascual**, J. Querol, H. Park, and A. Camps, "Antena Bi-banda con conformación de dos haces simultáneos para sistemas GNSS-R," in *Simposium Nacional de la Unión Científica Internacional de Radio (URSI)*, 2018.

[WS3] ——, "The Microave Interferometric Reflectometer: Development Status And Beam-Forming Validation Tests," in *Workshop on Reflectometry Using GNSS and Other Signals of Opportunity (GNSS+R)*, 2017.

[WS4] H. Park, A. Camps, **D. Pascual**, J. Querol, R. Onrubia, and E. Lancheros, "E2ESimulation Of Spaceborne GNSS-R For Land Applications," in *Workshop on Reflectometry Using GNSS and Other Signals of Opportunity (GNSS+R)*, 2017.

[WS5] J. Querol, R. Onrubia, **D. Pascual**, H. Park, and A. Camps, "RFI mitigation for GNSS-Rinstruments: FENIX, the Front-End GNSS Interference eXcisor," in *Workshop on Reflectometry Using GNSS and Other Signals of Opportunity (GNSS+R)*, 2017.

[WS6] A. Camps, H. Park, E. Lancheros, R. Onrubia, **D. Pascual**, and J. Querol, "Ionospheric scintillation impact on GNSS-R altimetry," in *Workshop on Reflectometry Using GNSS and Other Signals of Opportunity (GNSS+R)*, 2017.

[WS7] **D. Pascual**, H. Park, A. Camps, A. Alonso-Arroyo, R. Onrubia, and J. Querol, "Cross-talk Statistics of Interferometric GNSS-R," in *Workshop on Reflectometry Using GNSS and Other Signals of Opportunity (GNSS+R)*, 2015.

[WS8] ——, "Study of the Cross-Talk Effect in GNSS Reflectometry," in *IEEE Young Professionals Conference in Geoscience and Remote Sensing*, 2015.

[WS9] H. Park, **D. Pascual**, A. Camps, A. Alonso-Arroyo, R. Onrubia, F. Martin, and J. Querol, "Antenna Beam Impact on GEROS-ISS Instrument Observables," in *Workshop on Reflectometry Using GNSS and Other Signals of Opportunity (GNSS+R)*, 2015.

[WS10] ——, "GEROS Instrument Simulator Built by Using P2EPS," in *Workshop on Reflectometry Using GNSS and Other Signals of Opportunity (GNSS+R)*, 2015.

[WS11] R. Onrubia, J. Querol, **D. Pascual**, A. Alonso-Arroyo, H. Park, and A. Camps, "DME/TACAN Interference Impact in Interferometric GNSS-R," in *Workshop on Reflectometry Using GNSS and Other Signals of Opportunity (GNSS+R)*, 2015.

[WS12] ——, "DME/TACAN Impact Analysison Spaceborne iGNSS-R," in *IEEE Young Professionals Conference in Geoscience and Remote Sensing*, 2015.

[WS13] J. Querol, R. Onrubia, **D. Pascual**, A. Alonso-Arroyo, H. Park, and A. Camps, "Impact of Radio-Frequency Interference on Conventional GNSS-Reflectometry," in *IEEE Young Professionals Conference in Geoscience and Remote Sensing*, 2015.

[WS14] J. Querol, A. Alonso-Arroyo, R. Onrubia, **D. Pascual**, and A. Camps, "SNR degradation in conventional GNSS-R measurements under the effects of radio frequency interference," in *Workshop on Reflectometry Using GNSS and Other Signals of Opportunity (GNSS+R)*, 2015.

[WS15] A. Alonso-Arroyo, J. Querol, C. Lopez, A. Camps, H. Park, **D. Pascual**, and D. Onrubia, "GNSS-R Correlation Peak Statistics, SNR Estimation and its Relation to Geophysical Parameters," in *Workshop on Reflectometry Using GNSS and Other Signals of Opportunity (GNSS+R)*, 2015.

[WS16] R. Onrubia, **D. Pascual**, A. Camps, A. Alonso-Arroyo, and H. Park, "MIR: the Microwave Interferometric Reflectometer, a New Airborne Sensor to Experiment Different GNSS-R Techniques," in *URSI Com. F Microwave Signatures*, 2013.

[WS17] H. Park, A. Camps, **D. Pascual**, H. Carreno-Luengo, A. Alonso-Arroyo, F. Martin, and R. Onrubia, "System Performance Simulation of Spaceborne GNSS-R Altimeters," in *URSI Com. F Microwave Signatures*, 2013.

[WS18] A. Alonso-Arroyo, G. Forte, A. Camps, H. Park, **D. Pascual**, and R. Onrubia, "The Light Airborne Reflectometer for GNSS-R Observations (LARGO) Instrument: Towards Soil Moisture Retrievals," in *URSI Com. F Microwave Signatures*, 2013.

[WS19] A. Alonso-Arroyo, A. Camps, **D. Pascual**, H. Park, and others., "PAU Instrument aboard INTA MicroSAT-1: Initial results of the FM model from an airborne experiment," in *Workshop on Reflectometry Using GNSS and Other Signals of Opportunity (GNSS+R)*, oct 2012.

[WS20] H. Park, A. Camps, E. Valencia, H. Carreno-Luengo, F. Martin, A. Alonso, and **D. Pascual**, "Analysis of GNSS-R delay and Doppler tracking errors," in *Workshop on Reflectometry Using GNSS and Other Signals of Opportunity (GNSS+R)*, oct 2012.

Open-source software

[CODE1] **D. Pascual**, "GNSS-Matlab," *Remote Sening Code Library (RSCL)*, 2017.